SMSI 2023

Sensor and Measurement Science International

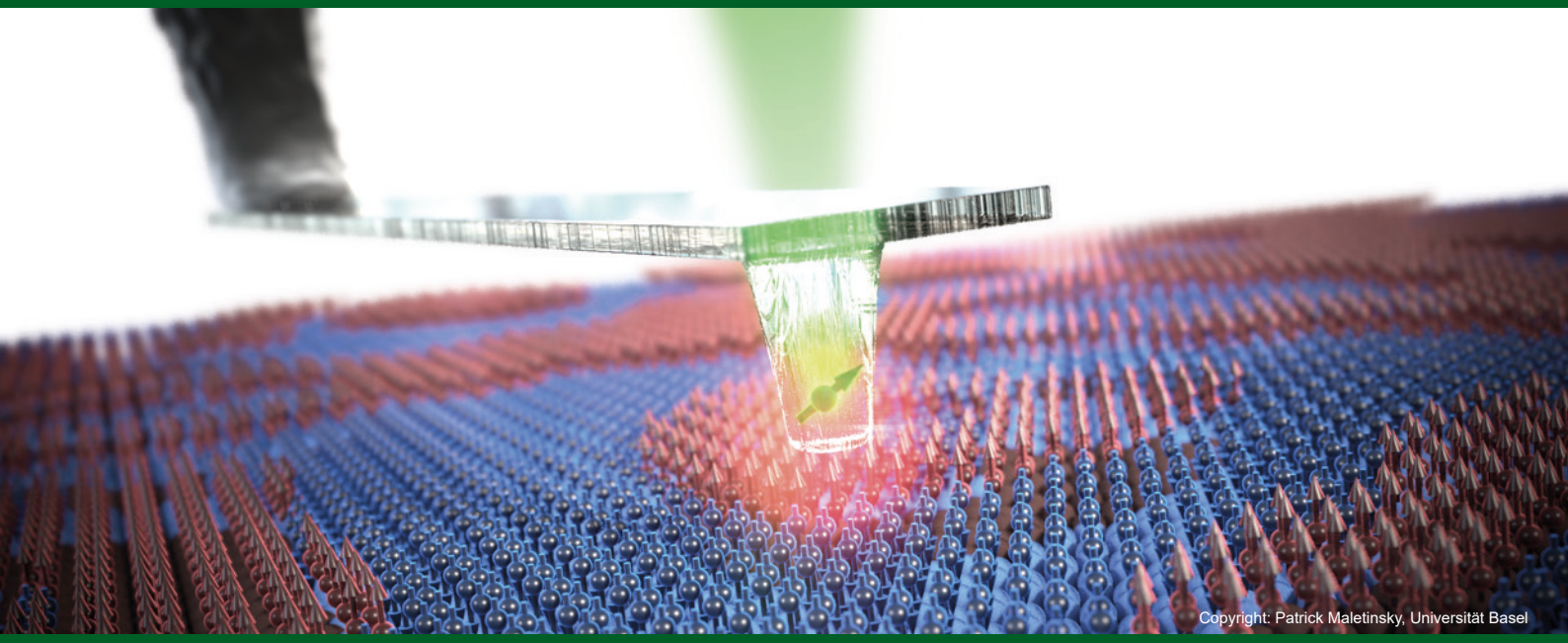

Proceedings

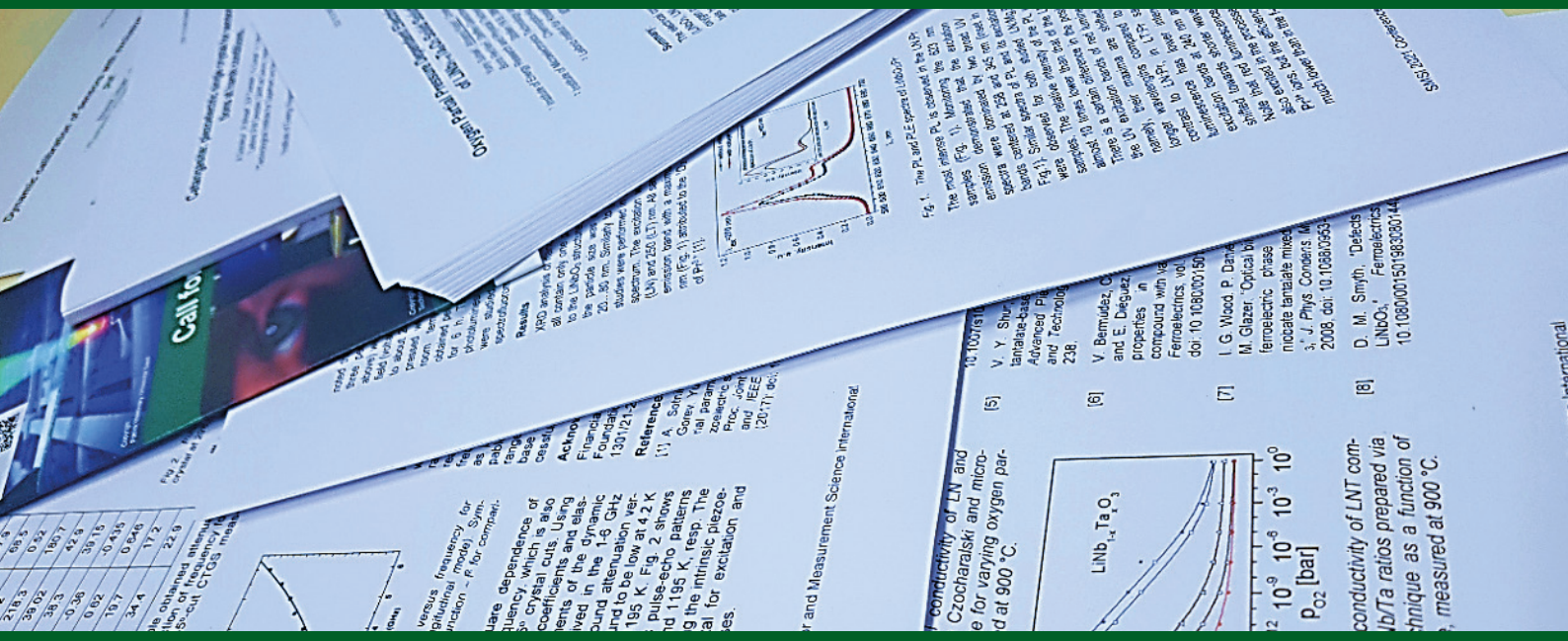

www.smsi-conference.com

AMA Verband für Sensorik + Messtechnik

AMA Association for Sensors and Measurement

Proceedings

SMSI 2023 Conference
Sensor and Measurement Science International

These proceedings cover the short papers of the lectures of the SMSI 2023 Sensor and Measurement Science International Conference.

The authors are responsible for form and content of the papers.

AMA Service GmbH accepts no responsibility for the correctness and completeness of the details and the consideration of private rights of third parties.

Herausgeber / Publisher:

AMA Service GmbH
Von-Münchhausen-Str. 49
31515 Wunstorf / Germany
Tel. +49 5033 9639-0
info@ama-service.com
www.ama-service.com / www.sensor-test.com
www.ama-science.org / www.smsi-conference.com

ISBN 978-3-9819376-8-8

SMSI 2023

Preface by the Conference Chairmen

Urlich Schmid

Michael Heizmann

Klaus-Dieter Sommer

We are pleased to meet you in person for this year's SMSI Conference. We cordially invite you to an intensive, professional exchange in a relaxing atmosphere about the latest research results, developments, and future trends around the topics of sensor technology, measurement, and metrology.

Meet international experts from the fields of sensors and instrumentation, measurement science and metrological infrastructure. Continue the success story of AMA relaxing atmosphere about the latest research results, developments, and future trends around the topics of sensor technology, measurement, and metrology scientific conferences related to sensors and metrology in Nuremberg. Use and strengthen our network, which for more than three decades has connected institutions and organizations from science, industry, research, and development to exchange ideas and to initiate successfully joint scientific projects.

SMSI 2023 thematically focuses on three pillars: sensors and instrumentation, measurement science as well as the system of units and metrological infrastructure. The sessions pursue an interdisciplinary, scientific focus with the aim of highlighting new trends, theories, methods, findings, and applications in these trendsetting topical areas. This year's highlight topics are quantum sensing, quantum metrology, optical biosensors, smart measurement and sensor systems, metrology in the digital age, nanometrology and nanofabrication, and Kibble and Planck scales, just to name a few.

In addition to technical talks, tutorials, a science slam and poster presentations, we invite you to attend the plenary talks given by internationally renowned peers. Among them, Wolfgang Koch from Fraunhofer FKIE will highlight the prospects for AI-driven systems for fusing data from multiple sensors. Emma Wooliams from the National Physical Laboratory (UK) will present Metrology in Earth Observation. Heinrich Heiss from Infineon Technologies AG will report on MEMS audio activities. Dariusz Krakowski from Airbus will discuss sensor applications in aircraft, and Georg E. Fantner from the Ecole Polytechnique Fédérale de Lausanne will present latest results on AFM metrology at nanoscale level.

SMSI will take place in parallel and conjunction with SENSOR+TEST, the world's largest trade fair for measurement and testing industry, thus offering an additional, practice-oriented exchange between academia, industry, and non-academic research organizations. And of course: Join us for our attractive social program and a lovely gala dinner in the historic city of Nuremberg.

We look forward to your expertise and a lively exchange. With the present conference proceedings, you already hold a comprehensive insight into the SMSI 2023 in your hands. It contains the peer-reviewed, two-page short papers submitted by the authors in response to the Call for Papers. We hope you enjoy browsing through the conference proceedings and gain many new insights.

Finally, our special thanks go to the members of the SMSI Conference Committee, the Topical Chairs of the conference pillars, the session chairs, and especially to the authors.

Ulrich Schmid
General Chair

Michael Heizmann
General Co-Chair

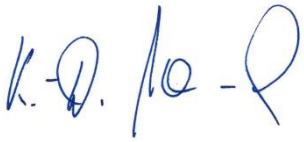

Klaus-Dieter Sommer
General Co-Chair

SMSI 2023 Conference Committee

General Chair

U. Schmid	Technische Universität Dresden (Germany)

General Co-Chair

M. Heizmann	Karlsruher Institut für Technologie (Germany)

General Co-Chair

K.-D. Sommer	Technische Universität Ilmenau (Germany)

Sensors and Instrumentation

Topical Chairs

C. Baratto	National Institute of Optics INO (Italy)
A. Bergmann	Graz University of Technology (Austria)
G. Gerlach	Technische Universität Dresden (Germany)
T. Ortlepp	CiS Forschungsinstitut für Mikrosensorik GmbH
S. Rupitsch	University of Freiburg (Germany)
S. Wood	National Physical Laboratory NPL, London (United Kingdom)

Members

J. Auge	Hochschule Magdeburg-Stendal (Germany)
J. Czarske	Technische Universität Dresden (Germany)
C. Corleto	STIL SAS, Aix-en-Provence (France)
M. da Silva	Federal University of Technology Parana, Curitiba-PR (Brasil)
M. Deilmann	KROHNE Messtechnik GmbH, Duisburg (Germany)
G. Fischerauer	University Bayreuth (Germany)
M. Fleischer	Siemens AG, München (Germany)
J. Gramich	Kistler Instrumente AG, Winterthur (Switzerland)
B. Jakoby	Johannes Kepler Universität, Linz (Austria)
U. Kaiser	Endress + Hauser, Reinach (Switzerland)
U. Kienitz	Optris GmbH, Berlin (Germany)
R. Kirchner	Technische Universität Dresden (Germany)

Members

A. König	Technical University Kaiserslautern (Germany)
M. Kraft	University of Liege (Belgium)
P. Lieberzeit	University Wien (Austria)
A. Spetz	University of Linköping (Sweden)
W. Minkina	Czestochowa University of Technology (Poland)
R. Moos	Universität Bayreuth (Germany)
D. Platz	Technical University Vienna (Austria)
M. Penza	Italian National Agency for New Technology, Energy and Sustainable Economic Development, Brindisi (Italy)
L. Reindl	Albert-Ludwigs-University Freiburg (Germany)
V. Schauer	HENSOLDT Optronics GmbH, Oberkochen (Germany)
J. Schieferdecker	Heimann Sensor GmbH, Dresden (Germany)
G. Schrag	Technische Universität München (Germany)
A. Schütze	Saarland University, Saarbrücken (Germany)
S. Semancik	National Institute of Standards and Technology, Gaithersburg (USA)
E. Starke	SICK Engineering GmbH, Ottendorf-Okrilla (Germany)
H. Trieu	Technical University Hamburg-Harburg (Germany)
G. Urban	Albert-Ludwigs-University Freiburg (Germany)
M. Vellekoop	University Bremen (Germany)
M. Walther	Fraunhofer IAF, Freiburg (Germany)
J. Wöllenstein	Fraunhofer IPM, Freiburg (Germany)
S. Zimmermann	Leibniz University Hannover (Germany)
J. Zosel	Kurt-Schwabe-Institut für Mess- und Sensortechnik e.V., Meinsberg (Germany)

Measurement Science

Topical Chairs

K.-D. Sommer	Technische Universität Ilmenau (Germany)
E. Benoit	Université Savoie Mont Blanc (France)
J. Sousa	Portuguese Quality Institute IPQ (Portugal)
B. Zagar	Johannes-Kepler-Universität Linz (Austria)

Members

Y. Aloimonos	University of Maryland, Baltimore (USA)
F. Fang	University of Dublin, Dublin (Ireland)
A. Fischer	University of Bremen (Germany)
A. Forbes	NPL National Physical Laboratory, Teddington (GB)
T. Fröhlich	Technische Universität Ilmenau (Germany)
C. Gulka	NCSL International Inc., Boulder (USA)
E. Hazarian	California State University, Carson (USA)
M. Heizmann	Karlsruhe Institute of Technology - KIT (Germany)
B. Henning	University Paderborn (Germany)
B. Jeckelmann	Muntelier (Switzerland)
W. Jian	NIM National Institute of Metrology, Beijing (P. R. China)
R. Kacker	National Institute of Standards and Technology -NIST, Gaithersburg (USA)
D. Knopf	Physikalisch-Technische Bundesanstalt (PTB), Braunschweig (Germany)
A. König	Technical University Kaiserslautern (Germany)
E. Manske	Technische Universität Ilmenau (Germany)
R. Morawski	Warsaw University of Technology (Poland)
A. Schäfer	Hottinger Brüel & Kjaer GmbH, Darmstadt (Germany)
A. Schütze	Saarland University, Saarbrücken (Germany)
R. Tutsch	University Braunschweig (Germany)
J. Valdes	Universidad Nacional de San Martín – UNSAM (Argentina)

System of Units and Metrological Infrastructure

Topical Chairs

B. Jeckelmann	Muntelier (Switzerland)
M. Bartholmai	BAM Bundesanstalt für Materialforschung (Germany)
P. Neyeshmakov	COOMET (Ukraine)
F. Lienesch	Physikalisch-Technische Bundesanstalt PTB (Germany)

Members

C. Corleto	CFM Collège Français de Métrologie, Paris (France)
A. Ganesh	CEN-CENELEC - European Committee for Standardization (CEN) and European Committee for Electrotechnical Standardization (CENELED), (Belgium)
E. Georgin	Centre Technique des Industries Aérauliques et Thermiques - CETIAT, Villeurbanne (France)
J. Hendricks	National Institute of Standards and Technology - NIST, Gaithersburg (USA)
F. Ogheard	Centre Technique des Industries Aérauliques et Thermiques - CETIAT (France)
G. Rietveld	VSL Dutch Metrology Institute, Delft (The Netherlands)
C. Tiebe	Federal Insititute for Materials Research and Testing (BAM), Berlin (Germany)
M. Melzer	Federal Institute for Materials Research and Testing (BAM), Berlin (Germany)
J. Zosel	Kurt-Schwabe-Instut für Mess- und Sensortechnik e.V., Meinsberg (Germany)

SMSI 2023: Planary Talks

Sensors and Instrumentation

A1: Digital Transformation in the Quality Infrastructure

Chair: Sascha Eichstädt, Physikalisch-Technische Bundesanstalt (PTB), Berlin (Germany)

A2: Sensor Systems for nondestructive Evaluation of Materials

Chair: Bernd Valeske, Fraunhofer-Institut - IZFP - für Zerstörungsfreie Prüfverfahren, Saarbrücken (Germany)

A3: Metrology in the Digital Age

Chair: Ulrich Kaiser, DHBW Lörrach, Lörrach (Germany)

A4: Smart Sensors

Chair: Michael Heizmann, Karlsruhe Institute of Technology KIT, Karlsruhe (Germany)

A5: Hydrogen Sensing

Chair: Jens Zosel, Kurt-Schwabe-Institut für Mess- und Sensortechnik e.V. Meinsberg, Waldheim (Germany)

A6: Quantum Magnetometry and its Applications

Chair: U. Schmid, Technical University Vienna, Vienna (Austria)

A7: Quantum Standards

Chair: Klaus-Dieter Sommer, Technische Universität Ilmenau Fakultät für Maschinenbau Institut für Prozessmess- und Sensortechnik, Ilmenau (Germany)

B1: Optical Biosensors

Chair: Camilla Baratto, University of Brescia, Brescia (Italy)

B2: Quantum Sensing

Chair: Nicolas Spethmann, Physikalisch-Technische Bundesanstalt, Braunschweig (Germany)

B3: Sensor Systems

Chair: Stefan J. Rupitsch, Albert-Ludwigs-Universität Freiburg IMTEK - Institut f. Mikrosystemtechnik, Freiburg (Germany)

B4: Gas Sensors

Chair: K. Trieu, Hamburg Univertiy of Technology, Hamburg (Germany)

B5: IV-VI - Infrared Photodetectors - Technology & Applications

Chair: S. Zimmermann, Leibniz University of Hannover, Hannover (Germany)

B6: Kibble and Planck balances I

Chair: Thomas Fröhlich, Technische Universität Ilmenau Fakultät für Maschinenbau Inst. f. Prozessmess- und Sensortechnik, Ilmenau (Germany)

B7: Kibble and Planck balances II

Chair: Thomas Fröhlich, Technische Universität Ilmenau Fakultät für Maschinenbau Inst. f. Prozessmess- und Sensortechnik, Ilmenau (Germany)

C1: NIST on a Chip for Sensing Metrology and One-Step Tracebility

Chair: Jay H. Hendricks, National Institute of Standards and Technology, Gaithersburg (USA)

C2: Prospects for Measurement Science and Metrology

Chair: Frank Lienesch, Physikalisch-Technische Bundesanstalt Laseranwendungen, Braunschweig (Germany)

C3: Photo Acustic Gas Sensors

Chair: Alexander Bergmann, Technische Universität Graz Institut für Elektrische Messtechnik, Graz (Austria)

C4: Acoustic MEMS

Chair: Leander Claes, Universität Paderborn EIM-E, Elektrische Messtechnik, Paderborn (Germany)

C5: Modern Developments in Measurement and Sensor Technology with Application Focus

Chair: Matthias Bartholmai, BAM Bundesanstalt für Materialforschung und -prüfung, Berlin (Germany)

C6: Simulation

Chair: Stefan J. Rupitsch, Albert-Ludwigs-Universität Freiburg IMTEK - Institut f. Mikrosystemtechnik, Freiburg (Germany)

C7: Digital Calibration Certificate

Chair: Shanna Schönhals, Physikalisch-Technische Bundesanstalt, Braunschweig (Germany)

D1: Magnetic Sensors for Process Control of Forming Processes

Chair: Olfa Kanoun, Technische Universität Chemnitz Fakultät für Elektrotechnik und Informationstechnik, Chemnitz (Germany)

D2: New Developments in Mathematics for Metrology

Chair: Markus Bär, Physikalisch-Technische Bundesanstalt (PTB), Berlin (Germany)

D3: Raman Spectroscopy

Chair: Sebastian Wood, National Physical Laboratory, Teddington (United Kingdom)

D4: Robotics

Chair: André Schäfer, Hottinger Brüel & Kjaer GmbH, Darmstadt (Germany)

D5: Metrology of Compound Semiconductors for Manufacturing Power Electronics

Chair: Sebastian Wood, National Physical Laboratory, Teddington, Middlesex TW11 0LW (United Kingdom)

D6: Nanomeasurements and Nanofabrication

Chair: Thomas Kissinger, Technische Universität Ilmenau, Ilmenau (Germany)

D7: Machine Learning in Measurement

Chair: Joao Alves Sousa, Instituto Portugues da Qualidade, Caparica (Portugal)

E5: Integrated Temperature Sensing

Chair: Nikolai Klimov, National Institute of Standards and Technology, Gaithersburg (USA)

E6: Sensor Interface Electronics

Chair: André Schäfer, Hottinger Brüel & Kjaer GmbH, Darmstadt (Germany)

E7: New Measurement and Sensor Approaches

Chair: Andreas Schütze, Universität des Saarlandes Lehrstuhl für Messtechnik, Saarbrücken (Germany)

Poster

Plenary Talks

Plenary Talk
DOI 10.5162/SMSI2023/PT4

Metrology for Climate Observation: European Coordination

Emma Woolliams[1], Céline Pascale[2], Paola Fisicaro[3], Nigel Fox[1]
[1] National Physical Laboratory (NPL), Teddington UK
[2] Federal Institute of Metrology (METAS), Bern-Wabern, CH
3 Laboratoire national de métrologie et d'essais (LNE), Paris, FR
Emma.woolliams@npl.co.uk

Summary:
The European Metrology Network for Climate and Ocean Observation coordinates the European metrological community to become the European contribution to the global effort to bring metrological principles into the observations of the climate and broader observations of the ocean to support the quality assurance, stability and international consistency of the measurements that make up the global climate observing system. Here we describe activities of the network, and the requirements for metrology it has identified.

Keywords: climate change, observations, European Metrology Network, metrological framework,

Introduction

Measurements from space, air, ground, and sea provide comprehensive information on the state of the environment. Service providers, commercial and nonprofit organisations, local and national governments, and international organizations use information from observations to support social and economic development and address global and local challenges: natural hazards, climate change, biodiversity, and energy, water, and food security.

The Global Climate Observing System (GCOS) is a key component of the United Nations Framework Convention on Climate Change (UNFCCC). The 2022 GCOS implementation plan [1] describes observations as central to climate action: "At a fundamental level what we do not observe we cannot understand and what we cannot understand we cannot predict, adapt to and mitigate". That plan highlights how observation systems are critical to both the scientific analysis and to providing tailored climate information to decision makers and the public. It calls for more systematic observation of the water, carbon and Earth energy cycles, as well as a coordinated, high-quality, free, and open access to climate data.

There are references to metrological principles and techniques throughout the 2022 GCOS implementation plan. SI-traceability, robust uncertainty analysis and comparison approaches are explicitly mentioned.

In response to this increasing coordination of observation systems, and recognition of the value of metrology, it is timely for the metrology community to consider how it can also coordinate its efforts to provide systematic and sustainable metrological support for the climate observing system.

The European Metrology Network for Climate and Ocean Observation

In 2019, the European Association of National Metrology Institutes (EURAMET) established the European Metrology Network (EMN) for climate and ocean observation [2] as one of the first set of EMNs to provide coordination for metrology for societal benefit areas. The EMN has 24 member institutions from 19 European countries and its mission is to be the 'European contribution to a global effort to bring metrology into climate and ocean observations".

In its first three years, the EMN has performed a review of the needs of the climate and ocean observation communities and created a strategic research agenda in response. It has held several internal and stakeholder workshops and presented the metrological approach to key relevant conferences and organisations. The EMN also was key to organising the 2022 BIPM-WMO Metrology for Climate Action Workshop which is currently preparing recommendations for global collaboration between metrologists and the observation community.

Key common requirements

There are more than 50 ECVs, many of which can be measured in different ways, and there are many applications for climate observation data. While this broadens the scope of the EMN, its stakeholder needs reviews have identified some common requirements for metrological collaboration. These include:

- Providing guidelines, tailored to the observations community, for metrological terminology and how to apply the Guide to the Expression of Uncertainty in Measurement (GUM) to observational data
- Supporting the establishment of tiered networks with high-quality SI-traceable reference measurements, linked higher density operational observations and local information from low-cost sensors
- Supporting the development of methodologies to intercompare and combine local and satellite-based measurements and models, with different spatial and temporal scales
- Developing methods for metrological traceability and uncertainty analysis for data processing through neural network algorithms

Most generally, many observation communities welcome the participation of metrologists in their committees and research projects.

Example engagement with the satellite community

Collaboration between metrologists and the satellite observation community led to the Quality Assurance Framework for Earth Observation (QA4EO), which was endorsed by CEOS in 2008. QA4EO establishes the principle that Earth observations should have an associated quality indicator (e.g., uncertainty) and provide traceability to a community-agreed reference (ideally SI). Following the agreement of this principle, and particularly through research projects funded by the European space agencies ESA and EUMETSAT and the EU research programmes, collaboration has led to defined guidelines (on [3]) for applying uncertainties and traceability to satellite observations and the “fiducial reference measurement” suborbital observations that support them. It has also led to the first metrology satellite: TRUTHS, a satellite that will fly the primary optical radiometric standard into space, is in development for a ~2030 launch [4].

Example engagement in atmospheric chemistry

The metrology community is already involved with several atmospheric measurement communities, including the WMO-Global Atmosphere Watch (WMO-GAW) [5]. The WMO-GAW works towards a single coordinated global understanding of atmospheric composition and its changes, as well as improving understanding of how the atmosphere, oceans, and biosphere interact with one another. By coordinating high-quality atmospheric composition observations across global to local scales, GAW drives impactful science and produces the next generation of research-enabled products and services. Some components of the GAW observational network are recognized as comprehensive and baseline networks within GCOS. The GAW Implementation Plan 2016-2023 [6] embeds metrology in its data quality objectives on measurement and requires traceability to agreed references (ideally SI). Several metrology institutes already contribute actively by being assigned as a central calibration laboratory within WMO-GAW, and both communities participate in regular experts' meetings.

Example engagement with the marine science community

Collaboration between metrologists and the marine science community recently started via the MINKE [7] (Metrology for Integrated Marine Management and Knowledge-Transfer Network) initiative, under H2020. In addition to integrating key European marine metrology research infrastructures, it coordinates their use and development, and proposes a framework for monitoring and managing marine ecosystems based on high-quality oceanographic data. The MINKE consortium incorporates all key research infrastructures working on marine calibration, such as metrological and oceanographic institutions, and mature participatory networks around Europe, while targeted actions in the Networking Activities foresee the active involvement of technological partners, international institutions, including intergovernmental bodies, EU and International Networks and EU Research infrastructures.

Conclusions

This presentation will discuss the different needs and approaches to bring metrological principles into climate and ocean observation.

References

[1] 2022 GCOS Implementation Plan, https://gcos.wmo.int/en/publications/gcos-implementation-plan2022

[2] www.euramet.org/climate-ocean

[3] www.qa4eo.org

[4] https://doi.org/10.3390/rs12152400

[5] https://community.wmo.int/activity-areas/gaw

[6] https://public.wmo.int/en/resources/library/wmo-global-atmosphere-watch-gaw-implementation-plan-2016-2023

[7] https://minke.eu/

Lectures

DOI 10.5162/SMSI2023/A1.1

Towards a structural foundation of a quality infrastructure in the digital world

Jens Niederhausen[1], Helga Hansen[1], Sascha Eichstädt[1]
[1] Physikalisch-Technische Bundesanstalt, Braunschweig and Berlin, Germany
Jens.Niederhausen@ptb.de

Summary:
We offer a vision of a digitally transformed quality infrastructure (QI). Specifically, we analyze the interplay and data flow between the QI institutions and present digital certificates, cloud infrastructures as well as requirements with respect to interoperability that will enable a digitally-transformed QI.

Keywords: quality infrastructure, metrology, digital transformation, digital certificates, cloud

Introduction

The quality infrastructure (QI) is an established and effective system to guarantee the quality of products, services, and processes. Currently the world is undergoing a twin-transition. New digital technologies become available that fundamentally change industrial processes and enable completely new products and services. At the same time, the green transition requires a speedy transition towards renewable energy sources and more environmentally friendly production methods. The QI must transform itself to promptly address these novel technologies and create trust and acceptance by the consumers.

Here we analyze relevant QI processes, describe the digital tools that allow fully digital workflows, and report the most current developments related to digital certificates, cloud infrastructures and an interoperable digital QI.

Results

Business partners, authorities, factory control systems, end consumers need trustworthy information about a product or a service. In the QI, this information is provided in the form of test reports or certificates.

In the digital age, the information about a product – its “QI status” – must be provided in a digital, machine-readable way. An already well-developed use case is the digital calibration certificate (DCC), which has been available in a stable format since 2021 [1]. It uses the flexible and internationally recognized Extensible Markup Language (XML) format. The DCC XML scheme is based on the minimum requirements for the machine-readable exchange of metrological data as described, for instance, in the "Digital System of Units" (D-SI) metadata model and complies with all international standards and guidelines required for such a document, including the SI units, the International vocabulary of metrology (VIM), the GUM, the CODATA table review, and ISO/IEC 17025 [1]. The DCC can be equipped with an electronic signature, as a means for its cryptographic protection against manipulation. The DCC therefore allows to avoid media discontinuity in calibration services, and it permits an error-free transmission of the corresponding data and information. The structure of the DCC is divided into four areas: administrative data, measurement results, comments, and the analogue calibration certificate as human readable. This approach can be adapted to certificates of conformity and other result reports. As part of the initiative “QI-Digital”, the PTB is developing a digital, digital Certificate of Conformance (D-CoC) for conformity assessments according to ISO/IEC 17065 in legal metrology (D-CoC M) as well as in the legally regulated area of explosion protection (D-CoC Ex) [2].

The accreditation of a laboratory or company attests the competence for a certain type of service or product. In some cases, the accreditation of a conformity assessment body or calibration laboratory is required. In that case, this information must be made available via a central database or be provided with the certificate (e. g. as a digital signature) [3].

Conformity assessments thus form the contact points between QI and product and usually invoke the interplay of several QI elements. A digital QI platform must be aimed at optimizing the conformity assessment workflow - maximizing its efficiency while also guaranteeing cyber security and data autonomy.

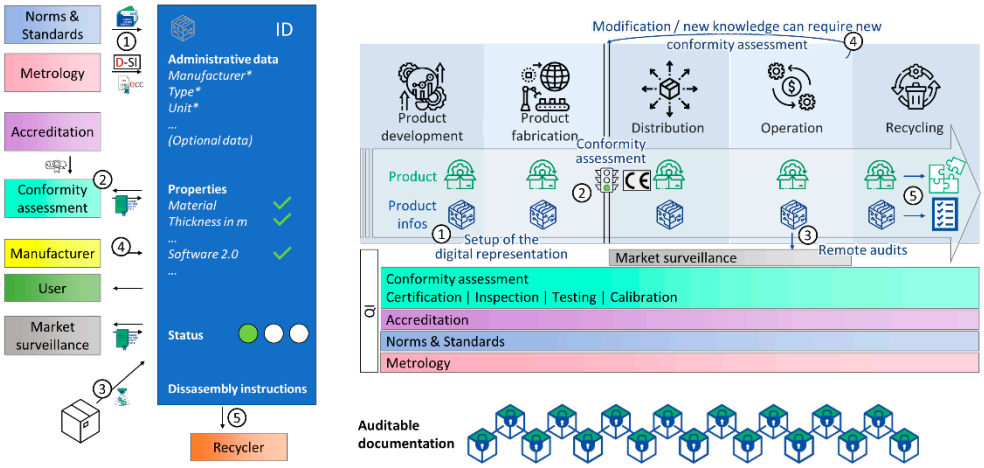

Fig. 1.: Critical points along a product's life cycle as well as corresponding QI processes and stakeholders.

From Fig. 1 we can collect important workflows for a digital QI platform: process initiation, retrieval of relevant norms and standards, providing product data relevant for the assessment (administrative data, test results, information from a calibration certificate, the accreditation status of the issuing laboratory), certificate distribution. In case the product is a digital asset (e. g., a software update), it should also be distributed over the same platform. Immutable process documentation, e. g. in form of a blockchain, makes the system auditable.

Initial developments towards the mutual access to information and data relevant for the digitalization of processes in the QI were undertaken in the initiative "European Metrology Cloud" [4]. The "Metrology Cloud" is a secured network of participants from the quality infrastructure. In this concept, data owners share their data with the network via mutual interfaces provided with the Metrology Cloud. That is, no data is circulated between parties unnecessarily, whilst still being able to support and streamline processes in the QI. A software could realize the automation of the QI processes based on the available data. Moreover, each network participant has a certain role, which specifies the information that is visible and accessible. As part of the initiative "QI-Digital" [2], the original Metrology Cloud will be further developed into an infrastructure that supports the digitalization of general processes in the quality infrastructure – the "QI Cloud".

Interoperability is the prerequisite to implement digital processes that involve more than one QI organization and to allow data flow between them via mutual interfaces. Moreover, it also allows to connect with the local infrastructures of companies and to enable them to readily integrate their own IT systems.

Importantly, the information should be distributed across the various sources, provided it can be found and accessed. Therefore, emphasis should be put on the adherence to the FAIR principles (findable, accessible, interoperable, and re-usable) in the design of the digital QI. Interoperability of data models is particularly important. For instance, information and data representation in a calibration certificate should ideally be very close, at least consistent, with the representation of similar information in a digital standard, an accreditation platform, etc. This minimizes the need for converters that add complexity and the potential for software bugs. This enables other entities (e.g., private companies) to contribute their solutions (e.g., lab software) to assist in improving and further streamlining the QI workflow. Automatically finding relevant information requires semantic information (PIDs, ontologies, etc.) and, thus, includes the transformation of human-oriented glossaries and definition lists into machine-readable knowledge representations.

In conclusion, we have described the digital tools for a fully digital QI. Note that likely also the regulatory framework will have to be adapted to fully support the digital processes.

References

[1] Hackel, S. et al.: The Digital Calibration Certifcate, PTB-Mitteilungen 127 (2017), Heft 4, p. 75, doi: 10.7795/310.20170403

[2] More info at www.qi-digital.de/en/

[3] Kuch, S. (2022): 2nd international DCC-Conference 01-03 March 2022 Proceedings, p. 207, doi: 10.7795/820.20220411

[4] Thiel, F. et al. (2018) "A Digital Quality Infrastructure for Europe: The European Metrology Cloud" PTB-Mitteilungen. Volume 127 (2017), Issue 4, p 83. ISSN 0030-834

DOI 10.5162/SMSI2023/A1.2

Digital Testing Platform for Artificial Intelligence: A modular and scalable concept

M. Liebl[1], D. Hutzschenreuter[1], A. Kofler[1], C. Kolbitsch[1], S. Eichstädt[1] and F. Härtig[1]
[1] Physikalisch-Technische Bundesanstalt (PTB), Braunschweig and Berlin, Germany
Maik.Liebl@ptb.de

Summary:
Artificial intelligence (AI) technologies in medicine require advanced testing approaches to assess and ensure the quality of applications. Here, we present a modular and scalable platform concept for quality assessment of AI technologies to accomplish this in a fast automated and digital way. We describe the design and functionality of the platform and its application to AI-based image reconstruction in accelerated magnetic resonance imaging (MRI) as a use-case example.

Keywords: Artificial Intelligence, Digital platform for AI testing, Medical AI applications

Introduction

Artificial Intelligence (AI) is a rapidly growing field of innovation which is producing powerful software solutions, e.g. in the healthcare sector. However, for their successful application in clinical routine, quality assessment is essential. For this purpose, the European Information Technology for the Future of Cancer (ITFoC) consortium demands independent tests that go beyond the common internal testing and validation during development [1]. In the future, regulation on AI-based software in the medical sector is likely as these applications are ranked as “high-risk” in the AI Act of the EU commission [2]. Thus, a key question will be how the existing quality infrastructure can be adjusted to carry out independent tests without slowing down the innovation potential.

AI testing platform (ATP)

Developing a digital AI testing platform (ATP) is an important step towards a fast and automated assessment of AI based software. The single modules of the ATP concept we propose are depicted in Figure 1. An IT platform handling client interactions, documentation and quality management forms its foundation. Five modules are connected to the IT platform that are used to perform and evaluate results of an AI software test. Data creation, e.g. using collection of existing data, provides independent, and application-specific test data serving as ground truth or ‘numerical reference artifact’. The Application Programming Interface (API) randomly picks a test data set and performs data preprocessing to emulate unknown test cases for the client. By the given ground truth, the API estimates the predefined performance metrics specified in the test criteria. Ideally, a non-AI-based reference procedure is available to determine a baseline for the performance metrics. Additionally, the test protocol is validated on AI test models.

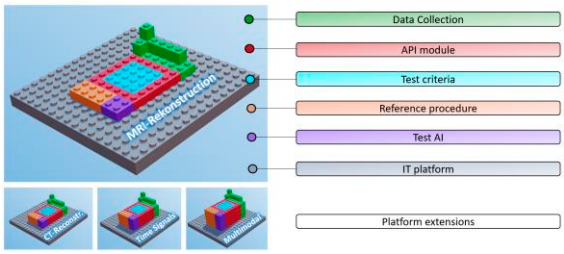

Figure 1: Modular and scalable design principle of the ATP. An IT platform carries five components: data collection, Application Programming Interface (API), test criteria, reference procedure, and test AI, required to develop and perform the AI software test.

While IT platform and API module can serve for various AI applications, the other modules are application-specific, e.g. to test AI-based image reconstruction techniques in accelerated magnetic resonance imaging (MRI). An easy and fast exchange of these modules is envisioned to tailor the AI testing platform to multiple AI-based applications as currently applied for computed tomography (CT) reconstruction, time signals as the electrocardiogram (ECG) or data sets from multiple modalities.

Service chain of the ATP

The service chain of the ATP is depicted in Figure 2. After registration on the IT platform, the client can order an AI software test. Triggered by an incoming order, the ATP provides test data for the client to download. The client uses this test data as input for the AI under test and

uploads the output to the ATP. The ATP then compares the test result with the ground truth to generate a test report. Finally, the test report is sent to the client.

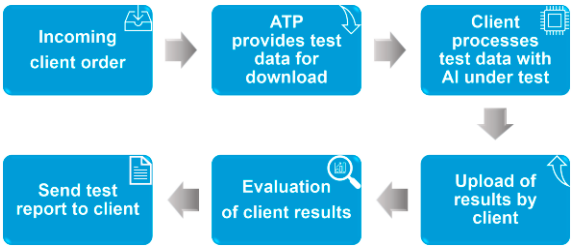

Figure 2: Service chain of the ATP. Triggered by an incoming client order, the ATP provides a test data set for the client to download. The client processes this data with his AI under test and uploads the results. The ATP then compares the test results with the ground truth and sends the test report to the client.

ATP applied to the MRI use-case

AI-based approaches enable MR image reconstruction with fewer measurements of the patient [3, 4]. This allows to speed-up the image acquisition process up to a factor of ten compared to conventional sampling schemes. Quality assessment with independent test data can help to increase the confidence of the society in AI-based methods. One possibility to accomplish this are so-called “grand-challenges” [3], that are, however, resource-binding, and competitive. With the ATP, we aim to provide an alternative way for the industry to test their AI-based software with independent data. Therefore, the concept of the ATP is applied to the example as shown in Figure 3: A data collection provides fully sampled MRI data serving as ground truth. Further, the data collection contains predefined parameters to add noise and emulate under-sampled (fast) MRI data by k-space masks.

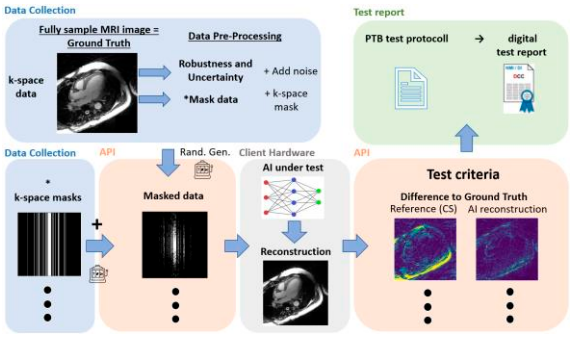

Figure 3: Workflow of the ATP applied to fast MRI reconstruction techniques. The client is provided with masked MRI data, where only the ATP knows the ground truth. By comparing the output of the AI-based client software with the ground truth, the ATP generates a digital test report listing the achieved results of the performance metrics. MRI images are adapted from Kofler et al. [4] with permission under the Creative Commons Attribution 3.0 license.

The API automatically generates the masked data using a random generator and sends this data to the client. The client reconstructs the under-sampled MRI data with their AI under test and sends the reconstructed images to the ATP. The API then calculates the difference between reconstruction and ground truth to determine the quality measures. In image reconstruction, possible performance metrics are normalized mean square error, peak signal-to-noise ratio, structural similarity, and L2 Error [3]. In this and many other AI use-cases, a non AI-based reference procedure is available to determine a baseline that the results of the AI under test should not undergo.
Finally, a test report is generated that contains the estimated results of the performance metrics for the AI under test and the reference procedure. This test report is sent to the client. After the ATP service is online, also benchmarking information might be sent confidentially to the client, e.g. the average scores obtained over all AI software tests performed so far.

Discussion and Conclusion

We presented the concept of a digital ATP that builds a framework for advanced AI software testing and quality assessment. In the design process, we considered extensions and advancements of the ATP by a modular structure. With this, we aim to provide the digital infrastructure and basis for AI software testing with independent data as currently recommended by the ITFoC.
While the ATP can provide the infrastructure, its success and possible extensions will depend on two key components: First, the expertise in the application scenarios to develop performance metrics. Second, creation of data with well characterized quality and uncertainty for each application. For future development, we plan to explore further possibilities to use existing IT platforms such as TraCIM [5] for implementing the ATP service chain.

References

[1] R. Tsopra, X. Fernandez, A. Burgin et al., A framework for validating AI in precision medicine: considerations from the European ITFoC consortium, *BMC Medical Informatics and Decision Making* 21, 247 (2021); doi: 10.1186/s12911-021-01634-3

[2] European Commission, Proposal for a Regulation of the European parliament and of the council laying down harmonized rules on artificial intelligence (Artificial Intelligence Act) and amending certain union legislative acts, (2021); https://artificialintelligenceact.eu/the-act/

[3] J. Zbontar, F. Knoll, Y. W. Lui et al., fastMRI: An Open Dataset and Benchmarks for Accelerated MRI (2019), arXiv:1811.08839v2 [cs.CV]

[4] A. Kofler, T. Schaeffter, C. Kolbitsch et al., Neural networks-based regularization for large-scale medical image reconstruction, *Physics in Medicine and Biology* 65, 135003 (2020); doi: 10.1088/1361-6560/ab990e

[5] TraCIM PTB, https://tracim.ptb.de/

DOI 10.5162/SMSI2023/A1.3

Digital Transformation of Processing Metrological Services

Anke Keidel, Catharina Kulka-Peschke, Alexander Oppermann, Samuel Eickelberg, Manuel Meiborg
Physikalisch-Technische Bundesanstalt (PTB), Abbestr. 2-12, 10587 Berlin, DE
Corresponding Author's e-mail address: anke.keidel@ptb.de

Summary:
The realization of an end-to-end digital workflow for the metrological services of the PTB, such as calibrations, conformity assessments, and more, requires the future-oriented integration of three essential aspects: processes, data, and interfaces. We present our strategy to approach these individual three key factors while considering the holistic digital workflow for the PTB and acquiring our contribution for a future IT landscape beyond the PTB.

Keywords: Interoperable processes, digital transformation, digital calibration certificate, metadata, metrology, digital workflow

Introduction

The digital transformation of metrological services at the German National Metrology Institute "Physikalisch-Technische Bundesanstalt" (PTB) demonstrates how an overall digital process can be created by sensibly combining individual processing steps whilst considering the necessary data formats.

A product-oriented approach was chosen to theorize the digital workflow from the product back to the points of data input to determine and priorities necessary process factors and to optimize their interactions. In our case, the product is the generation of the digital calibration certificate (DCC) for which the required data are regulated by international standards and therefore clearly defined [1]. Once the points of data input are determined, the workflow can be harmonized into a seamless digital process. During the development of this process framework, data integrity always remains our top prioritized.

Data

One key factor for a seamless digital workflow is that data is collected once only, meaning that - once collected - their distribution is automatized and occurs from one database in order to minimizes the risk of falsification by transmission errors. For this purpose, the PTB has developed a web-based customer portal, which will allow the customer to directly provide and maintain their administrative data. This portal, namely the E-Service, will then enable the costumer to place a digital service request and deposit all necessary documents online. Furthermore it allows to track the process status along the way. The administrative data that had been provided by the costumer can be automatically integrated into the internal data management system of the PTB, the so-called E-Files [2]. For the generation of the DCC, the metrological data, generated in the laboratory, will be combined with the administrative data, which is available from the E-Files system (see Fig. 1).

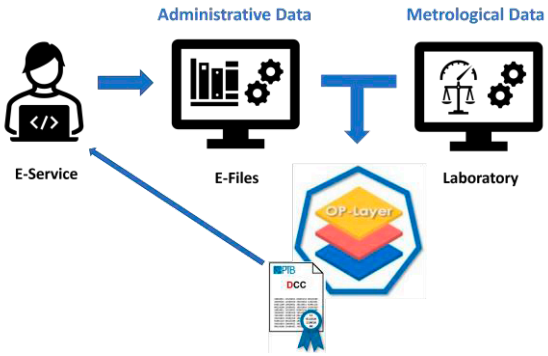

Fig. 1. Schematic illustration of the digital workflow of metrological services, including E-Files, the central data management system, OP-Layer that merges the administrative data provided by the E-Files and the metrological data, provided by the laboratories, to create a digital calibration certificate. The E-Service online portal enables the costumer to supply and maintain his administrative data. Furthermore, it allows to submit a digital calibration application and to ultimately receive a DCC.

Interfaces

A seamless digital workflow requires data integration without media discontinuity and thus suitable interfaces. Since the metrological data can be provided in different formats - depending on the individual necessities of the distinct

laboratories - an interoperable system of holistic data integration is required. Currently, the PTB is developing an open-type infrastructure with standardized interfaces, the so-called Operation Layer (OP-Layer) [3]. As a connector between all PTB systems, such as the E-Files system and the individual software solutions in the laboratories, the OP-layer can access administrative and metrological data of different formats and implement them jointly in a target document. The development of the OP-Layer is currently impelled by the automated generation of a digital calibration certificate (DCC) as first sample application (see Fig. 1).

Processes

Successful digital transformation requires streamlined, preferably linear processes and with this provides the opportunity to rethink and optimize existing non-digital workflows. In order to meet these requirements, the PTB is deploying a comprehensive process management system. On the basis of initial process analysis and assessment of their efficiency, future processes are modeled. For the construction of such interoperable digital processes it is crucial to establish a standardization of process modules to pave the way for a complete automation of the overall process.

Automation

We aim for a fully automated digital workflow to manage the metrological services within the PTB. This comprises the following process steps; order acceptance and order processing, calibration or conformity assessment, as well as the generation of the DCC and the digital provision of all necessary documents to the customer. This highest degree of automation requires uniform data structures concerning the involved documents as well as the utilized IT systems.

Once the digital workflow will have been established for the PTB, our gained knowledge, strategies, and IT infrastructure can be transferred beyond our institution and facilitate the creation of an international, interoperable IT system that enables the exchange of information and data automatically. To successfully acquire a comprehensive IT system in the future, the appropriate data structures and formats for the DCC, such as the digital SI (D-SI [4]), are currently coordinated internationally [5].

Conclusion

The digital transformation of PTB‘s metrological services aims for a holistically automated end-to-end process and, thus, requires standards. With regard to the key components described above (i.e., processes, data, and interfaces) the following requirements can be derived, while the integrity of the data remains top priority. One crucial precondition to recognize processual requirements is the critical examination of the existing work procedures as well as their considered harmonization into a streamlined digital process. Furthermore, secure and suitable data formats need to be selected that can be archived immutably and long-term. Additionally, standardized interfaces must be created for the automated merging of data into digital certificates. Moreover, for a universal and interoperable IT landscape standardized interfaces are paramount to facilitate future developments beyond the scope of PTB‘s metrological services [6].

References

[1] Siegfried Hackel, Frank Härtig, Julia Hornig, Thomas Wiedenhöfer, “The Digital Calibration Certificate”, PTB-Mitteilungen 127 (2017), Heft 4, 75-81; doi: 10.7795/310.20170403

[2] A. Keidel and S. Eichstädt, "Interoperable processes and infrastructure for the digital transformation of the quality infrastructure," 2021 IEEE International Workshop on Metrology for Industry 4.0 & IoT (MetroInd4.0&IoT), 347-351 (2021), doi: 10.1109/MetroInd4.0IoT51437.2021.9488563.

[3] A.Oppermann, S. Eickelberg, P. Kruse, Digital Transformation: Towards a Cloud Native Architecture for highly automated and event driven processes, IMEKO TC6 International Conference on Metrology and Digital Transformation, 19-21.09.2022, Berlin, Germany

[4] D. Hutzschenreuter et al.,"SmartCom Digital System of Units (D-SI) Guide for the use of the meta data format used in metrology for the easy-to-use, safe, harmonised and unambiguous digital transfer of metrological data”, doi: 10.5281/zenodo

[5] BIPM: CIPM MRA: Mutual recognition of measurement standards and of calibration and measurement certificates issued by national metrology institutes (1999).

[6] Sascha Eichstädt, Anke Keidel, Julia Tesch, “Metrology for the digital age”, *Measurement: Sensors* 18 (2021): 100232; doi: 10.1016/j.measen.2021.100232.

DOI 10.5162/SMSI2023/A1.4

A Cloud Native Architecture for automated Metrological Services

Manuel Meiborg, Alexander Oppermann, Samuel Eickelberg, Anke Keidel, Catharina Kulka-Peschke
Physikalisch-Technische Bundesanstalt (PTB), Abbestr. 2-12, 10587 Berlin, DE

Corresponding Author's e-mail address: alexander.oppermann@ptb.de

Summary:

The Operation-Layer is an applied architectural concept to interconnect and digitally transform PTB's internal processes. It consists of of three main pillars to modernize PTB's digital infrastructure: a modern self contained container environment; a state-of-the-art identity access management solution; harmonized software development guidelines to ensure streamlined, secure and pointedly special tailored applications in a cloud native environment. Breaking up data silos, streamlining process flows and simplifying IT management while centralizing administrative IT environments will have a tremendous positive effect on the every-day-workflow for any employee at PTB.

Keywords: *Digital Transformation, Universal Service Hub, Metrological Processes, Digital Calibration Certificate, Robotic Process Automation*

Introduction

In contrast to other public bodies, the Physikalisch-Technische Bundesanstalt (PTB) consists of very specialized and independent departments, working groups as well as laboratories. Each group has unique technical requirements due to their specific metrological task. The working groups have little to no overlap in their daily work. Furthermore, these groups often represent the national or international standard of calibration or the current state of research. Depending on the grade of digitalization and exisiting programming skills, some of these groups write and operate very advanced software systems. Despite of the high complexity and maintenance effort, these information systems, are usually maintained by very few non IT experts. These special tailored systems often compromise security, reusability, generic coding patterns and coding quality due to limited time, knowledge and interest. In defiance of the introduced security issues, this operating principle does not advertise innovative solutions and prevents other parts of the organization to participate and to profit from the invested time and effort for automatizing work flows. Best case scenario is unnecessary repetition. However, most working groups lack the required IT-skill and therefore are stuck with their labor-intensive manual work flow.

Cloud Native Architecture

This problem area will be addressed by the Operation Layer (OP-Layer) introducing a harmonized, centralized and containerized software development platform for special tailored applications (see Fig. 1). By offering a secure framework with harmonized interfaces and identity access management, the research groups can focus on their actual problem solving method and outsource the maintenance as well as security to the centralized IT department.

The OP-Layer offers an internal service hub to host special tailored application ideally with a generic entitlement to serve several working groups. By reducing the administrative

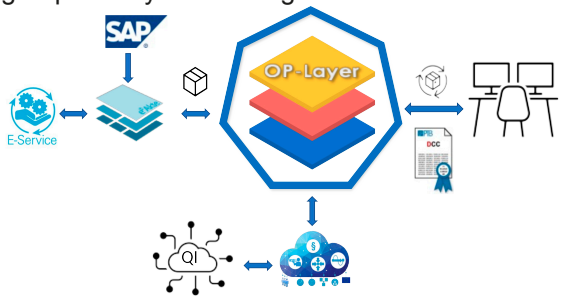

Fig. 1. Workflow overview with a scalable cloud native infrastructure at heart. The OP-Layer harmonizes interfaces, exchange formats and processes throughout the organization.

overhead for the research staff more time can be claimed for original research and in addition increasing security and quality for special tailored applications. The OP-Layer development is defined by three main pillars:

1. **Container Environment**: A self hosted sophisticated container environment with prepared CI/CD pipelines, secured networking and resource-management – Kubernetes is the current state-of-the-art solution.

2. **Identity and Access Management**: A central solution for handling authentication (with organization-wide PTB-ID) and access control for services in the OP-Layer – the de-facto-standard solution Keycloak is employed.

3. **Service Guidelines**: Providing and enforcing principles of modern software design for distributed services. Furthermore, it is encouraged to publish the code as Open Source. A service should be as lightweight as possible, provide REST-interfaces and come with some basic documentation.

Digital Calibration Certificate Process

Facilitating the adoption of the OP-Layer within PTB, reference implementations are provided of commonly used services with high impact factors. Thus, the Digital Calibration Certificate (DCC [3]) process has been entirely digitally transformed and implemented [4] within the OP-Layer.

The digital calibration process starts with the E-Service Portal. A customer portal, which offers a calibration certificate application. After applying for a calibration certificate for a measuring instrument, the process continues with a automatically created file in the E-File System. All data is automatically transferred and archived in a file. The responsible department checks the validity of the application. At this point in the process, the OP-Layer offers a convenient way to automatically transfer all necessary data to the calibration laboratory via unified REST interfaces. Moreover, a DCC service is built that automatically imports administrative data from the E-File System, in order to create a proper DCC. The resulting DCC can be automatically uploaded via the OP-Layer into an existing file within the E-File System. From there, the file handler submits the DCC to the E-Service Portal.

The OP-Layer offers also a modularized web application frontend (Fig. 2) to demonstrate the abilities of the OP-Layer.

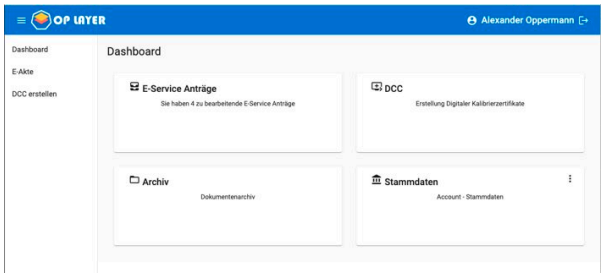

Fig. 2. Dashboard of the OP-Layer with special tailored applications such as DCC Service, E-File Service, Archive and Core Data Service. The tiles can display dynamic data from each advertised service.

Conclusions and Future Work

The first implemented Digital Calibration Certificate Process has shown a huge potential for automation and optimization. Especially for future use cases it has proven the efficiency gains and the simplicity of a digital transformed process. However, transforming the process also highlighted the challenges in defining mandatory standards and minimal shared requirements within a federal organized body such as PTB.

The next phase is to onboard working groups to the OP-Layer service infrastructure. These early adopters will have enough IT skills to export their special tailored application to the OP-Layer. This will enhance the service guidelines and is a great opportunity to connect the development community within PTB. Moreover, harmonizing development and deployment procedures increases tremendously IT security of the whole organization.

References

[1] A.Oppermann, S. Eickelberg, P. Kruse, Digital Transformation: Towards a Cloud Native Architecture for highly automated and event driven processes, IMEKO TC6 International Conference on Metrology and Digital Transformation, 19-21.09.2022, Berlin, Germany

[2] R. Heeks, Centralised vs. decentralised management of public information systems: a core-periphery solution." Information Systems for Public Sector Management Working Paper 7 (1999).

[3] Siegfried Hackel, Frank Härtig, Julia Hornig, Thomas Wiedenhöfer, “The Digital Calibration Certificate”, PTB-Mitteilungen 127 (2017), Heft 4, 75-81; doi: 10.7795/310.20170403

[4] A. Keidel and S. Eichstädt, "Interoperable processes and infrastructure for the digital transformation of the quality infrastructure," 2021 IEEE International Workshop on Metrology for Industry 4.0 & IoT (MetroInd4.0&IoT), 347-351 (2021), doi: 10.1109/MetroInd4.0IoT51437.2021.9488563.

NDE Sensors for Traceability by Material Fingerprints

Kevin Jacob[1]
[1] *Fraunhofer Institute for Nondestructive Testing IZFP*
Campus E3 1 66123 Saarbrücken Germany
kevin.jacob@izfp.fraunhofer.de

Summary:
The clear identification and traceability of components during and after processing is an essential prerequisite for the development of self-organizing, adaptive value chains. Conventional object markings such as labels, barcodes, etc. usually cannot remain permanently and undamaged on the object. Therefore, a markerfree technique is developed and first results are shown.

Keywords: Identification, markerfree, fingerprint, coldforming, traceability

Background, Motivation an Objective

In public, the topic of traceability is mainly considered from the point of view of legal regulations, standards and guidelines. In the increasingly globally networked world of production, however, this "traceability" also serves to safeguard production and reliably detect product counterfeits. Only the complete traceability of products, semi-finished products and raw materials enables the comprehensive monitoring and control of globalized flows of goods. Artificially applied object markings are only suitable for this task to a limited extent, since they cannot remain permanently and undamaged on the object. Even optically detected "natural" features of the surface can only be used to the extent that the surface of the component is heavily modified by a processing step (e.g. forming or painting). To overcome these limitations, a traceability system for metallic materials, with a focus on coldforming applications, is developed, which uses information from the interior of the component, i.e. intrinsic structural features of the material, similar to a fingerprint of the component, to identify the latter as a unique individual.

Description of the New Method or System

First experiments were carried out on tensile-samples made from HC280LAD steel. This sample geometry was used, because it provides a flat measuring surface and it allows to apply a defined uniaxial tension in order to generate different levels of plastic deformation. This allows to investigate, if the sample still can be identified after plastic deformation, as it will occur in sheet forming process. In a next step, the fingerprint method was tested on press parts from real industrial production. Here, a heavily formed press part was used. The first test were performed with a conventional single coil eddy-current system. The eddy-current sensor was moved over the measuring area of the tensile-samples in 2D meandering scan. Subsequently, a low-cost alternative in the form of Texas Instruments inductance to digital converter (LDC) was used. In order to extract information from the measurement data acquired in this way that allows the components to be identified, preprocessing is required. This means that disturbance variables such as temperature-related signal changes and lift-off effects must be compensated. The effect of lift-off on the fingerprint in terms of SNR is shown in Figure 1.

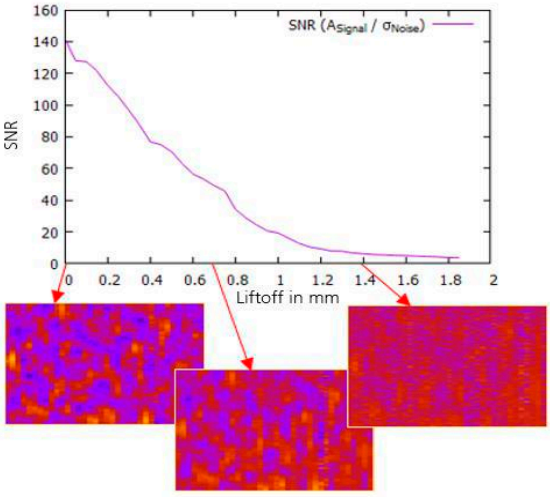

Fig. 1. Effect of the Liftoff on the SNR of the calculated fingerprint.

Since temperature changes are expressed approximately linearly in the measured impedance of the eddy current measurements, they are compensated by using simple linear regression.

Subsequently, lift-off effects are compensated. For this purpose, lift-off curves are first determined on a large number of measurement positions on the material to be investigated, from which a (material-sensor specific) mean lift-off curve is then calculated. The information used for identification (hereinafter referred to as the fingerprint) results from the deviation of the individual measured impedance values from the mean lift-off curve. Various machine learning tools can be used to compare two fingerprints to determine if they come from the same measurement position of the same component. While for small datasets good results could be obtained from a combination of optical flow and correlation, for large datasets better results are obtained using Siamese convolutional neural networks.

Results

In the case of simple tensile specimens, the fingerprint is merely stretched to the same extent as the tensile specimen. In this case, an accuracy of 100% was achieved for the identification. The measurement and identification of real components is somewhat more difficult. Figure 2 shows the fingerprint of a measurement position on a sheet metal, which was subsequently formed into a part for the rear lamp. Figure 3 shows the fingerprint after deformation, where in the upper right corner one can see artifacts or noise, because the material is bent away there. The measurement position of the deformed component is shown in Figure 4.

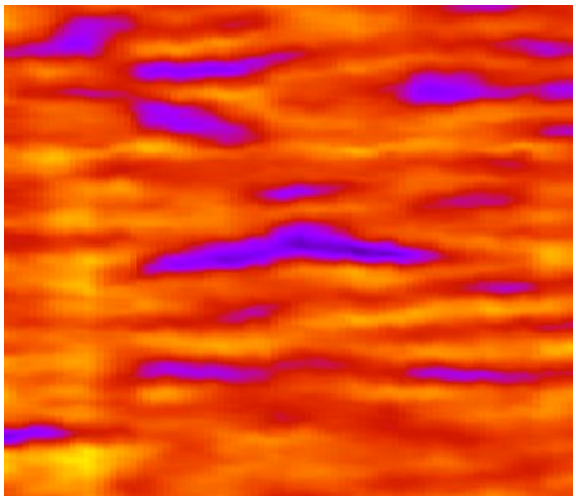

Fig. 2. Fingerprint image on the plane unformed sheet

It can be clearly seen that for identification purposes, frugal features are repeatedly measurable even after deformation. Due to the small number of samples and the resulting small data set in combination with the rather large change of the fingerprint, it was not yet possible to successfully train a classifier. With greater volume of training data, this can be addressed.

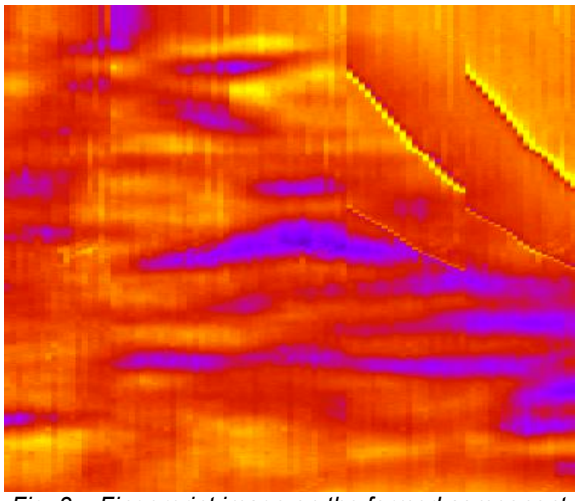

Fig. 3. Fingerprint image on the formed component

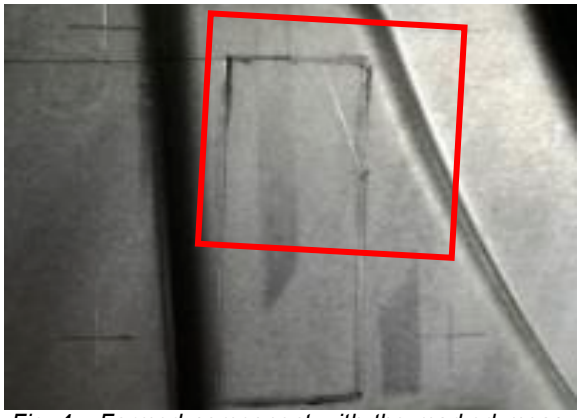

Fig. 4. Formed component with the marked measuring position

Conclusions

The basic feasibility of the developed method was thus demonstrated. However, further work is needed to develop this into an industry-ready solution. The following work includes investigations of the relationship between the microstructure and the measured fingerprints, optimization of the compensation of disturbances, minimization of the measurement time and the necessary development of an array solution.

It is obvious, that especially the combination of both electromagnetic NDE applications – material characterization and part identification - carries enormous potential for process improvements in the value added chain of sheet metal processing, e.g. in automotive industry. The possibility to trace a metal sheet with all its material properties "from the cradle to the grave" would offer complete new possibilities for self-organizing, cross-company production networks.

DOI 10.5162/SMSI2023/A2.2

Non-destructive inline sensors for digital material twin in the carbon fiber tape laying process

Jan Oswald[1], Jannik Summa[1], Christian Jungmann[1], Dirk Koster[1], Ute Rabe[1]
[1] Fraunhofer Institute for Nondestructive Testing IZFP, 66123 Saarbrücken, Germany
Jan.oswald@izfp.fraunhofer.de

Summary:
The use of inline sensors during production enables the detection of quality-relevant material fluctuations. Thus, machine parameters can be quickly adjusted in case of occurring flaws to minimize waste. In addition, semantic integration of sensors and their data into a data ecosystem enables the analysis of complex correlations. As an example, the implementation of a multimodal thermography and laser thickness inspection system with DICONDE standard in the manufacturing of unidirectional reinforced carbon fiber tapes is presented.

Keywords: carbon fibre reinforced tapes, inline inspection, thermography, laser thickness inspection, DICONDE

Introduction

Continuous fibre-reinforced thermoplastic composites exhibit high stiffness at low weight. Using unidirectional fiber reinforced (UD) tapes in the process chain of cutting, laying, consolidation and hot-forming can lead to complex shaped components. The result is a good compromise in terms of mechanical properties and economical production. The consolidation of the fabrics into 3D components in closed molds and the functionalization, e.g. stiffeners or mounting brackets, in the injection molding process enable the efficient production of lightweight structures in large series [1].

However, safety requirements demand high stiffness and breaking strength, high reproducibility while asking for low weight and efficiency. At the same time, we are experiencing a time with growing demands for resource-conserving production. To meet these requests, the application of sensors, mainly in the context of digitization, is still growing [2,3]. When it comes to quality assurance, defects must be avoided and variations of the material properties must be documented. For this purpose, optical sensors and thermographic methods are already in use in the so-called Automated Fibre-Placement (AFP) process for thermoplastic composite production [4]. A project at Fraunhofer [5, 6] goes beyond defect detection. The digital twin is created from simulated data and by recording and localizing individual material properties of the real component and merging them into a data ecosystem representing the complete process chain. The focus of the presented paper relates to one process step of the digital twin, the manufacturing of UD carbon tapes.

Inline Sensor System

A pilot test system with thermographic and a laser thickness inspection systems was integrated into the production of the UD tapes (fig. 1). The test data is automatically related to the spatial coordinates on the tape and stored in DICONDE-standard [7] on a data server. Since the latter is integrated into a data ecosystem (MySQL) the ndt-data can be correlated with simulated, machine or production data as well.

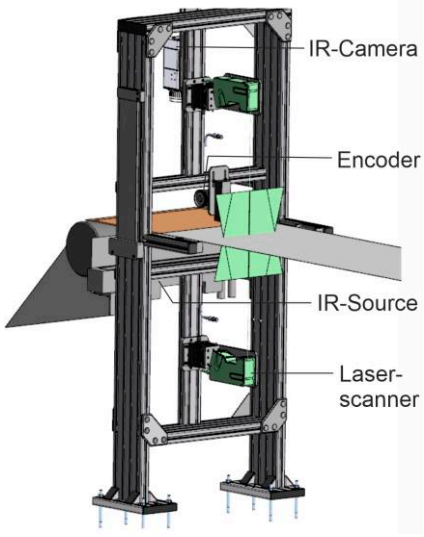

Fig. 1. 3D CAD model of the system assembly with tape moving from left to right side

The inline inspection system is placed just before the rewind station. Due to an encoder with

a friction wheel, the acquired data are related to the spatial coordinates on the tape.

The thermography system consists of a line IR-source (IRD S750SM by Optron) and a bolometer camera (VarioCam® HD Head 800 by InfraTec). The thickness inspection system incorporates two laser profilometers with CMOS sensors facing each other. The most relevant defects to detect are the tape thickness, homogeneity, impregnation as well as the C-fibre volume content.

Results

Exemplary results from the inline inspection are given for thermography and thickness inspection in figs. 2. a and b, respectively.

The displayed section of the tape has a length of 4 m. The thermographic image displays the full width of 500 mm of the tape, the thickness inspection system covers a width of 320 mm.

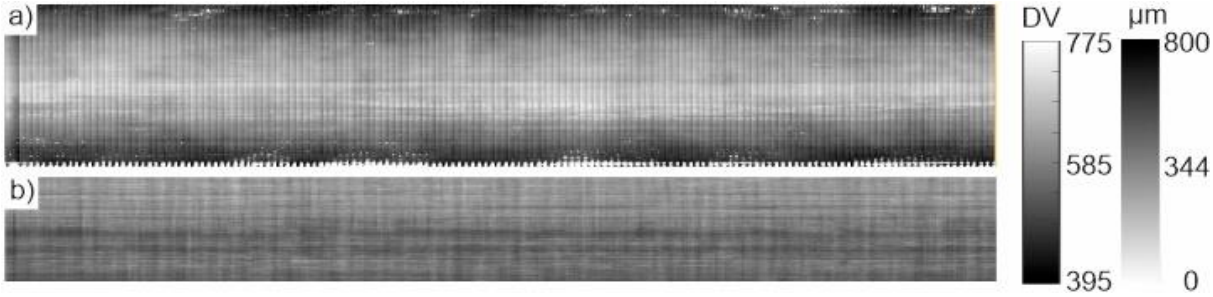

fig. 2. a) digital value of thermography intensity (DV) of the inspected tape, b) corresponding thickness values in µm

The images show the slightly asymmetrical thickness profile of the tape. Typically, greater thickness occurs in the center as the tool deforms due to high pressure. The IR intensity indicates the grade of transparency of the tape to the IR radiation emitted by the line source. The intensity contrasts and their spatial distribution is useful to infer defects. In particular, bright lines indicate gaps and small cracks.

The combination of the two modalities offers additional value, for example to investigate questions, such as whether the occurrence of defects is correlated with the tape thickness or where defects tend to occur. In order to allow the examination of cross-correlations by machine learning and other algorithms, the images are saved in DICONDE format at the end of each imaging cycle and automatically uploaded to the DICONDE server. The information provided by the DICONDE server is connected to a data ecosystem ruled by an ontology specifically adapted to the process which was developed with partners during the project. Hence, the inspection data can be analyzed and compared for example with the machine data to investigate the effect of influencing factors like tool temperature, on the defect frequency, and the data are available for further, more comprehensive process analyses.

References

[1] M. Kropka, M. Muehlbacher, T. Neumeyer, V. Altstaedt, From UD-tape to final part – a comprehensive approach towards thermoplastic composites, Procedia CIRP 66 (2017) 96-100.

[2] Sensor Market Size, Share and Industry Analysis | Forecast – 2028 (alliedmarketresearch.com)

[3] Level Sensor Market Size, Sales Analysis & Opportunity | FMI (Futuremarketinsights.com)

[4] S. Sun, Z. Han, H. Fu, H. Jin, J. S. Dhupia, Y. Wang, Defect Characteristics and Online Detection Techniques During Manufacturing of FRPs Using Automated Fiber Placements: A Review, Polymers 2020, 12, 1337.

[5] Fraunhofer funded project “Digital TPC, der digitale Zwilling für den Thermoplast-Leichtbau“, Fraunhofer IMWS, ICT, SCAI, IZFP.

[6] D. Koster, J. Summa, C. Jungmann, U. Rabe, H.-G. Herrmann, T. Link, M. John, F. Nagel, R. Schlimper, A. Delforouzi, J. Roggenbruck, K. Wolf, Inlinetauglichkeit von zerstörungsfreien Prüfmethoden für den digitalen Zwilling von thermoplastischen Carbonfaser-Tabes, DGZfP Jahrestagung 2021, http://www.ndt.net/?id=26258

[7] American Society for Testing Materials. (2015). Standard Practice for Digital Imaging and Communication in Nondestructive Evaluation (DICONDE). Designation: E2339 -15.

DOI 10.5162/SMSI2023/A2.3

Information recycling of NDE data sets

Frank Leinenbach[1], *Bernd Sprau*[1], *Christopher Stumm*[1]
[1] *Fraunhofer IZFP, Institute for Nondestructive Testing, Campus E3.1, 66123 Saarbruecken, Germany*
frank.leinenbach@izfp.fraunhofer.de

Summary:
NDE data provides essential information for the evaluation and characterization of materials and components. These could be used along the entire value chain, for example, for process optimization or as training data for AI applications. However, this requires not only the unique identification of the component or material, but also the continuous readability of the NDE data sets. In this presentation, technical challenges, and solutions for the development of a data cycle are presented.

Keywords: NDE 4.0, Data Cycle, DICONDE, SPARQL, NDE Data Space

Motivation

Today, only a few aspects of current Industry 4.0 goals are reflected in the performance of non-destructive evaluation (NDE). Files are often saved on hard disks and inspection reports are usually stored as PDFs and then deleted again after a specified safekeeping period.

But besides this, NDE methods can be valuable data suppliers for the optimization of e.g., manufacturing processes [1]. However, this is currently affected by the fact that NDE data sets usually do not guarantee a uniform structure, data format or the completeness of all relevant information. These changes are part of the ongoing digital transformation of the NDE towards NDE 4.0 [2] and include, among other things, the structured digital archiving of NDE data sets with the long-term goal of establishing an NDE data space using current networking technologies.

In addition to the direct use of the information, e.g., as part of KPI analyses, the recycling of the collected data sets offers significant advantages over the current state of the art in the long term, from which AI applications in particular benefit. For the training of an ANN, for example, a multitude of suitable and diverse data sets are needed and, in case of a shortage of real data sets, often synthetic data sets are generated and included, whereas real data sets are always preferred [3]. Also, NDE data sets of the whole history of a component could be used for optimization of recycling processes.

In the following, an approach is presented that allows the recycling of NDE data sets based on a data cycle.

The Data Cycle

The sub-aspects for realizing a data cycle can be divided into five essential steps. These are technically independent in their implementation but build on each other technologically. In the following, the sub-steps and their requirements are discussed in general terms, followed by the specific processes used to achieve the results. The sub-aspects are data generation, data archiving, database, data extraction, and the reuse of the data sets.

The data cycle always begins with the generation of data sets. At best, these are carried out during the product life cycle of the product as part of in-service inspection or in case of malfunctions. This already represents a first critical point, because whether data sets are suitable for reuse depends on several factors. The most obvious characteristic is thereby the correctness and valency of the measurement [4]. Since this is influenced by essentially the correct execution of the inspection, this point is unfortunately difficult to verify afterwards. However, it is equally important for reuse that all relevant meta data is recorded as completely as possible. In addition to the information for interpretation of the measurement data, this should also contain as much information as possible about the circumstances under which the results were generated. This includes, among other things, the measurement points, information about the inspected component and, if applicable, other environmental conditions. At the same time, it is difficult to estimate at the time of creation whether an information is relevant for later use, which makes it difficult to freely structure the measurement data and meta data.

The knowledge of the essential factors of suitable data generation has a significant impact on the second step of the data cycle, the archiving of the data sets and thus also the data format. There is a conflict between the proprietary data formats usually specified by the manufacturers of inspection systems and the manufacturer-independent generic data formats. Whereas manufacturer-dependent data formats already combine an extensive structure of raw and meta data in their data sets, the further processing of the data sets is usually only possible with company-specific software. Generic data formats such as XML or CSV, on the other hand, ensure readability by third parties, but the structures are user-specific and thus offer scope for misinterpretation. An alternative is provided by structured open data formats such as DICONDE (Digital Imaging and Communication for Nondestructive Evaluation) [5] and AQDEF (Advanced Quality Data Exchange Format) [6], which offer a specific data structure and open access. These can also be extended by further information fields, if necessary, whereby this again brings potential for misinterpretation of information with itself. The DICONDE data format is particularly suitable for NDE applications since it specifically addresses inspection tasks and is already standardized for common NDE methods.

The specific structuring of the data sets is important for the implementation of a database. This allows data sets to be separated based on their meta data and found by means of a suitable query. For this purpose, SQL (Structured Query Language) or SPARQL (SPARQL Protocol And RDF Query Language) are suitable database languages. These technologies thereby allow complex search queries, whereby relevant data sets can be identified based on the meta values. In a simple file system, on the other hand, it is usually only possible to search and select by file name, format, and creation date. The contents of the files can usually only be viewed in the case of text files, for example.

By structuring the data sets combined with the database, concrete queries can now be processed by the database, which then outputs a series of matching data sets for data extraction. Depending on the technology, the storage location or a UID (Unique Identifier) is used to extract the data from an archive or folder. What remains is the individual use of the data set for a new application. At this point the data cycle closes as soon as the new data sets, which are obtained in this new application, are archived again according to the described pattern, and transferred to the database.

Implementation and outlook

During implementation, ultrasound data was addressed as the first application. These were stored in DICONDE format and archived on a DIMATE DICONDE server. Since the search function of the DICONDE server only allows simple queries, e.g., several criteria cannot be specified as conditions at the same time, an Apache Jena Fuseki SPARQL server was set up in parallel to the DICONDE server, which allows structured queries of the archived data sets based on the DICONDE ontology. The result provides their UID, which allow extraction from the DICONDE server and can be used afterwards for further applications such as extending training data with real data sets for AI algorithms.

The described procedure will be transferred to other NDE methods in the next development iterations. In addition to established NDE methods such as thermography and eddy current, more complex methods such as 3MA will also be addressed. This work represents an essential basis for the implementation of an NDE data space, in which the mentioned setup allows a cross-company data access. However, this also requires a focus on the usage and access rights.

References

[1] D. Böttger, B. Stampfer, D. Gauder et al., Concept for soft sensor structure for turning processes of AISI4140, *tm - Technisches Messen* 87(12), 745-756 (2020); doi: 10.1515/teme-2020-0054

[2] J. Vrana, R. Singh, NDE 4.0—A Design Thinking Perspective, *Journal of Nondestructive Evaluation* 40 (8), (2021); doi: 10.1007/s10921-020-00735-9

[3] U. Faltings, T. Bettinger, S. Barth, M. Schäfer, Impact on Inference Model Performance for ML Tasks Using Real-Life Training Data and Synthetic Training Data from GANs, *Information 2022* 13 (9), (2022); Doi: 10.3390/info13010009

[4] D. Petri, P. Carbone, L. Mari, Quality of Measurement Information in Decision-Making, *IEEE Transactions on Instrumentation and Measurement* 70, 1-16 (2021); doi: 10.1109/TIM.2020.3047954

[5] B. Valeske, R. Tschuncky, F. Leinenbach, et al., Cognitive sensor systems for NDE 4.0: Technology, AI embedding, validation and qualification, *tm - Technisches Messen* 89 (4), 253-277 (2022); doi: 10.1515/teme-2021-0131

[6] D, Edgar. Geeignete Messprozesse – Valide Informationen, *tm - Technisches Messen* 86 (9), 528-539 (2019); doi: 10.1515/teme-2019-0104

DOI 10.5162/SMSI2023/A2.4

Deep Learning-Assisted Optimal Sensor Placement in Ultrasound NDT

Han Wang[1], Eduardo Pérez[1,2], Florian Römer[1]
[1] Fraunhofer Institute for Nondestructive Testing IZFP, Saarbrücken, Germany,
[2] Technische Universität Ilmenau, Ilmenau, Germany
han.wang@izfp.fraunhofer.de

Summary:
In this work we employ model-based deep learning to optimally select the sensing locations of single-channel synthetic aperture measurements in ultrasound nondestructive testing. We use the Fisher information as an optimization target to obtain task-agnostic selection matrices. We then link this result to prior findings on the behavior of the Fisher information matrix.

Keywords: channel selection, deep learning, signal recovery, ultrasound NDT

Background and Motivation

The mutually-related problems of optimal sensor placement and sparse array design are challenging, as they are often non-convex and combinatorial [1]. Recent advances in model-based deep learning have enabled data-driven solutions to these problems. In [1] and [2], soft-max neural networks are employed to achieve the desired structure of a selection matrix while retaining differentiability. Soft-max networks have been successfully applied to MIMO beam pattern design [1], joint optimization of communications and sensing [3], and the subsampling of various multi-channel ultrasound modalities [2].

In our previous work [4], we have analyzed the Cramér-Rao bound (CRB) for target localization in Synthetic Aperture (SA) Ultrasound Nondestructive Testing (UNDT). We highlighted the suitability of the CRB as an optimization target by showing that, in the far-field regime, can be written in terms of properties of the insonification signal and the geometry of the scenario. In this work, we revisit this problem by optimizing the Fisher Information Matrix (FIM). We consider a grid of discrete sensor locations to leverage soft-max neural networks with the goal of choosing the optimal coordinates for the collection of single-channel SA measurements.

Data Model

We consider a 2-D SA scenario with a single scatterer. The transducer is allowed to move along the x-axis. Using a modulated Gaussian pulse as insonification signal, the noiseless amplitude scan (A-scan) measured by placing the transducer at the l^{th} position is modeled in the frequency domain as

$$h(f,\tau_l) = a e^{-\frac{\pi^2}{\beta}(f-f_\mathrm{c})^2 + j(\phi - 2\pi f \tau_l)}, \qquad (1)$$

where a is the scattering amplitude, β regulates the bandwidth, f_c and ϕ are the frequency and phase of the carrier, and τ_l is the time delay between the scatterer and the transducer which depends on the coordinates (x, z) of the scatterer.

Sampling (1) over the frequency f, a vector $\boldsymbol{h}_l \in \mathbb{C}^{N_\mathrm{f}}$ is obtained. All L of the noiseless A-scans are then stacked into the vector $\boldsymbol{h} \in \mathbb{C}^{N_\mathrm{f}\cdot L}$. In practice, $\boldsymbol{h}$ can only be observed in the presence of noise. We model the measurement data as $\boldsymbol{y} = \boldsymbol{h} + \boldsymbol{n}$ with $\boldsymbol{n} \sim \mathcal{CN}(\boldsymbol{0}, \sigma^2 \boldsymbol{I}_{N_\mathrm{f}\cdot L})$, where $\boldsymbol{I}_N$ is an identity matrix of size $N \times N$. When subsampling $\boldsymbol{y}$, only $K \ll L$ A-scans are gathered, which can be represented as

$$\boldsymbol{\Phi y} = \boldsymbol{\Phi h} + \hat{\boldsymbol{n}} \in \mathbb{C}^{N_\mathrm{f}\cdot K}. \qquad (2)$$

In (2), the subsampling matrix $\boldsymbol{\Phi}$ has the structure $\boldsymbol{\Phi} = \boldsymbol{S} \otimes \boldsymbol{I}_{N_\mathrm{f}}$, where $\boldsymbol{S} \in \mathbb{R}^{K\times L}$ is a selection matrix. Furthermore, $\otimes$ denotes the Kronecker product and the subsampled noise obeys $\hat{\boldsymbol{n}} \sim \mathcal{CN}(\boldsymbol{0}, \sigma^2 \boldsymbol{I}_{N_\mathrm{f}\cdot K})$.

Proposed Optimization Target

We propose to maximize the elements along the main diagonal of the FIM. This maximizes the sensitivity of the data model to changes in the parameters. However, the FIM is often poorly conditioned, and its trace can be dominated by a small number of parameters that may not be of interest. Let $\boldsymbol{\xi} = [a, x, z]^{\mathrm{T}}$ be a vector containing all the unknown model parameters. The proposed optimization problem is

$$\min_{\boldsymbol{\Phi}} \sum_{i\in\mathcal{I}} -\left\| \boldsymbol{\Phi} \frac{\partial \boldsymbol{h}}{\partial \xi_i} \right\|_2^2 + \lambda \|\boldsymbol{\Phi}\boldsymbol{\Phi}^{\mathrm{T}} - \boldsymbol{I}_K\|_2^2, \qquad (3)$$

where $\mathcal{I}$ is a set containing the indices of the parameters of interest and λ is a hyperparameter. When $\mathcal{I}$ contains all the parameter indices, the first term in (3) is equivalent to the trace.

Simulations

Prior knowledge of the specimen's geometry is available in most NDT applications, which can be used to infer the Region of Interest (ROI). The sensor placement design is optimized such that the image quality in the ROI is prioritized and one can localize critical flaws.

In the pulse echo model (1), the center frequency is $f_\mathrm{c} = 4\ \mathrm{MHz}$ and the bandwidth factor is $\beta = f_\mathrm{c}^2$. The phase is set as a constant $\phi = -2.6143$. As to the measurements, we utilize $L = 48$ sensor locations with horizontal distance $\Delta\mathrm{x} = 0.5\ \mathrm{mm}$ to collect A-scans. Each A-scan consists of $N_\mathrm{f} = 46$ Fourier coefficients.

In the simulated scenario, we consider a single point scatterer existing in the specimen. Then, we randomly vary the values of model parameters $\boldsymbol{\xi}$ to generate a training dataset containing 1 million data. The point scatterer locates in the predefined ROI with a higher probability and their scattering amplitudes follow the Gaussian distribution $a \sim \mathcal{N}(15, 3)$.

By importing (3) as the loss function, a soft-max neural network is built to select $K = 24$ optimal sensor locations. The code is implemented in PyTorch and the training process runs on an NVIDIA A100 GPU node.

Results

The Optimal Sensor Placement (OSP) is successfully derived and illustrated in the Fig. 1. In addition, we bring in the Full Sensor Placement (FSP) and Uniform Sensor Placement (USP) for comparison. Because the FSP can serve as a reliable reference and the USP is the easiest sensor placement method to implement in simulation and practice.

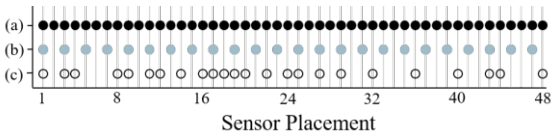

Fig. 1. Sensor placement illustration: (a) Full Sensor Placement (b) Uniform Sensor Placement (c) Optimal Sensor Placement

Furthermore, we apply FISTA to recover the measurement signals that are sampled by the three methods. The three procedures are termed as FISTA + FSP, FISTA + USP and FISTA + OSP, respectively. The reconstructed image quality plays a significant role in the performance evaluation. For further quantitative assessment, we consider the commonly-used Contrast-to-Noise Ratio (CNR) as the metric, which depends on the correctness of the scatterer's location.

Following the same data generation strategy, we create an evaluation dataset with $N_\mathrm{Evaluation} = 1000$. We compute the Cumulative Density Function (CDF) of CNR for the three sensor placement designs and illustrate them in Fig. 2.

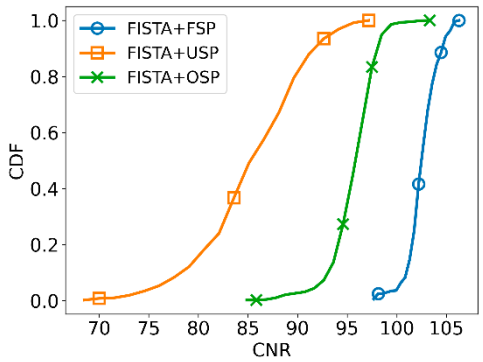

Fig. 2. CDF of CNR for FISTA+FSP, FISTA+USP and FISTA+OSP (right curve indicates a better performance)

By observing the CDF against CNR curves, the right curves indicate a better performance due to a higher CNR of the reconstructed image. Therefore, the image quality of FISTA + OSP is obviously better than FISTA + USP and approaches FISTA + FSP.

Conclusions

This paper demonstrates the application of a soft-max neural network in optimal sensor placement in ultrasound NDT. We take the CRB-related Fisher Information Matrix into account when designing the optimization target. The evaluation results show the feasibility of the optimal spatial subsampling. Furthermore, the algorithm can be applied in sparse array design and be promising in adaptive sensing methods.

References

[1] K. Diamantaras, Z. Xu, A. Petropulu, Sparse Antenna Array Design for MIMO Radar using Soft-max Selection, (2021)

[2] I. A. M. Huijben, B. S. Veeling, K. Janse, M. Mischi, R. J. G. van Sloun, Learning Sub-Sampling and Signal Recovery with Applications in Ultrasound Imaging, *IEEE Transactions on Medical Imaging* 39(12), 3955-3966 (2020); doi: 10.1109/TMI.2020.3008501

[3] Z. Xu, F. Liu, A. Petropulu, Cramér-Rao Bound and Antenna Selection Optimization for Dual Radar-Communications Design, *IEEE ICASSP,* 5168-5172 (2022); doi: 10.1109/ICASSP43922.2022.9747651

[4] E. Pérez, J. Kirchhof, S. Semper, F. Krieg, F. Römer, Cramér-Rao Bounds for Flaw Localization in Subsampled Multistatic Multichannel Ultrasound NDT Data, *IEEE ICASSP*, 2020; doi: 10.1109/ICASSP40776.2020.9053523

DOI 10.5162/SMSI2023/A3.1

Making AI Measureable - Approaches within the “Metrology for Artificial Intelligence in Medicine Programme” of PTB

Hans Rabus[1]
[1] *Physikalisch-Technische Bundesanstalt (PTB), Abbestrasse 2-12, 10587 Berlin, Germany*
hans.rabus@ptb.de

Summary:
PTB's program "Metrology for Artificial Intelligence in Medicine" was launched in 2021 as part of the QI Digital initiative, which aims at the digital transformation of the quality infrastructure system. The program comprises thirteen projects addressing the key quality aspects of artificial intelligence, - explainability, robustness, uncertainty - in medical applications, with a focus on generic methods that can be transferred to other areas of metrology.

Keywords: Explainability, robustness, uncertainty, data quality

Background and Motivation

Artificial intelligence (AI) methods are increasingly being used in medicine with the main application Being in imaging [1,2]. Currently, AI methods are also increasingly used in other areas such as intensive care [3–5], radiotherapy [6,7], and laboratory medicine [8].

There is currently no legal framework for the certification of AI-enabled medical devices. Standards are being developed to underpin the forthcoming EU law on AI. However, the development of standards addressing concrete test specifications and criteria for conformity assessment according to ISO/IEC 17067 had to be put on hold. The reason for this is the lack of a sound and generally accepted scientific basis for the criteria and procedures to be used.

QI Digital and M4AIM

The German QI Digital initiative was launched in 2019 to pioneer the digital transformation of quality infrastructure in Europe. Funded by the German government for a period of four years starting 2021, QI Digital is now being implemented as a joint project between the key players in the German quality infrastructure to demonstrate the approach through several use cases.

Use case 3 of QI Digital concerns artificial intelligence in medical engineering and is addressed by PTB’s research programme "Metrology for AI in Medicine (M4AIM)" [9]. The program aims to build competence in AI for metrology and to provide a metrological basis for the evaluation of quantifiable performance criteria of AI methods as a prerequisite for their certification.

The program focuses on quantitative measures and criteria for the explainability and robustness of AI algorithms and the uncertainty of their predictions. As an essential prerequisite, the program also includes the development of evaluated reference datasets.

The Projects

Thirteen PhD students and post-doctoral fellows are working on research projects that address the key performance aspects of AI algorithms mentioned above. Some projects were delayed in starting due to difficulties in recruiting staff, and two projects are currently suspended due to parental leave of the investigators.

All projects address specific topics of medical relevance with the aim of developing generic methods that can also be used in other applications of AI in metrology.

One of the more fundamental projects is investigating the potential of active learning to overcome the need for large datasets in supervised machine learning by creating optimal datasets for training neural networks.

Another project addresses methods of explainable or interpretable artificial intelligence (XAI), for which theoretical verification and empirical validation have been lacking. Using a toolkit of transparently manipulated ground truth data, the reliability of existing XAI methods is assessed and quantitative metrics for explanatory performance are explored.

Two projects are looking at AI applications in critical care. One evaluates causal machine learning approaches for analysing heterogeneous datasets consisting of asynchronous time series.

The other project is exploring ways to generate realistic synthetic reference datasets for training and testing AI algorithms to circumvent the problem of patient data privacy.

Three of the projects are related to medical imaging using CT or MRI techniques. One project is investigating the suitability of deep neural networks for image optimization in CT imaging, with a focus on developing test criteria for robustness evaluation. The other two projects are investigating the benefits of physical learning for the robustness of reconstructing images from noisy (low field) or insufficiently sampled MRI measurements and the associated uncertainties.

Another three projects investigate the use of AI-based approaches for dose calculation in radiation therapy of cancer. One of the projects investigates AI-based methods in adaptive radiotherapy, including faster analysis of measurements for quality assurance and direct dose calculation. The two other projects investigate generic methods to accelerate the generation of synthetic reference by simulations based on physical models and the uncertainties associated with detailed simulation results and the derived synthetic data.

Of the remaining three projects, one is investigating the potential of invertible neural networks for dealing with measurement error, model error, hyperparameters, and multimodal posterior distributions, and for applying the network to hemodynamic problems. Another is investigating a normative modeling approach to the problem of data heterogeneity, such as in clinical databases for mental illness. The third project is investigating uncertainties in simultaneous quantitative measurement of metabolites and machine learning analysis of potential biomarkers for early diagnosis of Parkinson's disease.

Conclusions

A review day was held in October 2022, one year after the program's launch, to report on the progress of ongoing projects to a panel of external reviewers. Feedback was generally positive and helped to establish further cross-connections between several projects. For one of the projects that had stalled due to insurmountable technical difficulties, a decision was made to realign the scope of the project.

In addition to the research activities of junior scientists, some of the major investors are involved in standardization committees such as the joint AI for Health (AI4H) focus group of ITU and WHO and ISO/IEC JC1/SC42. The development of metrology services for AI quality assurance is also being explored..

Acknowledgment

The programme “Metrology for Artificial Intelligence in Medicine” (M4AIM) is funded by the German Federal Ministry for Economic Affairs and Climate Action (BMWK) in the frame of the “QI-Digital” initiative.

References

[1] Z. Fang et al., Deep Learning for Fast and Spatially Constrained Tissue Quantification from Highly Accelerated Data in Magnetic Resonance Fingerprinting, *IEEE Transactions on Medical Imaging* 38 23642374 (2019); doi: 10.1109/TMI.2019.2899328

[2] L. Vandewinckele et al. Overview of artificial intelligence-based applications in radiotherapy: Recommendations for implementation and quality assurance. *Radiotherapy and Oncology* 153, 55–66 (2020); doi: 10.1016/j.radonc.2020.09.008

[3] A. Meyer et al., Machine learning for real-time prediction of complications in critical care: a retrospective study, *The Lancet Respiratory Medicine* 6, 905–914 (2018); doi: 10.1016/S2213-2600(18)30300-X

[4] N. Tomašev et al., A clinically applicable approach to continuous prediction of future acute kidney injury, *Nature* 572, 116–119 (2019); doi: 10.1038/s41586-019-1390-1

[5] G. Lichtner et al., Predicting lethal courses in critically ill COVID-19 patients using a machine learning model trained on patients with non-COVID-19 viral pneumonia *Scientific Reports* 11, 13205 (2021); doi: 10.1038/s41598-021-92475-7

[6] H. Arabi, H. Zaidi, Applications of artificial intelligence and deep learning in molecular imaging and radiotherapy, *European Journal of Hybrid Imaging* 4, 17 (2020); doi: 10.1186/s41824-020-00086-8

[7] D. Sarrut et al., Artificial Intelligence for Monte Carlo Simulation in Medical Physics, *Frontiers in Physics* 9, 738112 (2021); doi: 10.3389/fphy.2021.738112

[8] J.-P. Trezzi et al., Metabolic profiling of body fluids and multivariate data analysis, *MethodsX* 4, 95–103 (2017); doi: 10.1016/j.mex.2017.02.004

[9] https://www.m4aim.ptb.de/

DOI 10.5162/SMSI2023/A3.2

Co-Calibration in Distributed Homogeneous Sensor Networks

Maximilian Gruber[1], *Anupam P. Vedurmudi*[1], *Sascha Eichstädt*[1]
[1] *Physikalisch-Technische Bundesanstalt, Abbestraße 12, 10587 Berlin, Germany*
maximilian.gruber@ptb.de

Summary:
A co-calibration method suited only for (strictly) homogeneous sensor networks is applied to distributed homogeneous sensor networks. This is achieved by relying on spatial and temporal interpolation models to provide virtual reference measurement points at the location of the device under test. The interpolation method is evaluated in a simulation of an existing real-world use case dealing with room-temperature monitoring using distributed sensors.

Keywords: co-calibration, distributed sensor networks, spatio-temporal interpolation

Background and Motivation

Current work by the authors is focused on uncertainty-aware co-calibration of local homogeneous sensors, as well as spatial interpolation using machine-learning approaches [1].

Requiring sensors to be quasi non-distributed is a strong assumption that greatly limits the potential applicability of co-calibration in practical scenarios. To overcome this limitation, it is shown that distributed sensors can provide virtual reference values by augmenting interpolation models with GUM uncertainty evaluation [2]. Moreover, multiple interpolation models can be evaluated in parallel at a given spatio-temporal point, which can then be robustly combined via sensor fusion into a single virtual reference measurement. The approach is implemented inside a proof-of-concept simulation environment representing temperature sensors distributed inside a room.

Idea Outline

A co-calibration is similar to a calibration according to the VIM [3], but is carried out under non-ideal conditions, e.g., inside an industrial process. The result of a co-calibration method are traceable estimates of parameters characterizing a sensor's transfer behavior (e.g., linear-affine). It is of interest to provide a method for co-calibration of homogeneous sensors that is capable to also operate on spatially distributed and temporally non-synchronous input measurement.

Such a co-calibration involves spatial and temporal interpolation with a use case specific model. The interpolation model has the available measurements by reference devices as inputs and provides virtual reference measurements at the spatio-temporal positions required for the co-calibration of the device under test. The interpolation model can thus be interpreted as a means of performing virtual measurements.

Setting

Consider the case of N distributed calibrated reference sensors monitoring a quantity $\phi(\vec{x}, t)$. The n-th ($n = 1, \dots, N$) reference sensor is spatially located at $\vec{x}_n$ and provides estimates $\widehat{\phi}_n\left(\vec{x}_n, t_{n,j}\right)$ of ϕ at discrete points in time $t_{n,j}$. Sensor readings are not expected to be synchronized but are assumed to refer to the same time base. Locations and timestamps could also have associated uncertainty. The co-calibration expects M time-series of length K as reference measurement $\hat{\phi}_m^*(\vec{x}_{dut}, t_k)$ with uncertainty $u\left(\hat{\phi}_m^*(\circ)\right)$ at the position $\vec{x}_{dut}$ of the device under test as well as its indicated values $y(t_k)$ at the same consecutive time-points t_k with $k = 1, \dots, K$. From the input, the co-calibration iteratively estimates the parameters $\left(a, b, \sigma_y\right)$ of a linear-affine transfer behavior with gain a, offset b and noise $\varepsilon \sim \mathcal{N}\left(0, \sigma_y^2\right)$ using Bayesian updates. The sensor's transfer model is assumed to be given by

$$y(t_k) = a \cdot \phi(\vec{x}_{dut}, t_k) + b + \varepsilon_i \,.$$

As it can in general not be expected that $\vec{x}_n = \vec{x}_{dut}$ or $t_{n,j} = t_k$ for any n, j or k, the available measurement data from the reference sensors does not match the input requirements of the co-calibration routine. The task to be solved is to obtain an estimate $\hat{\phi}_m^*(\vec{x}_{dut}, t_k)$ (and corresponding uncertainty) of ϕ at location $\vec{x}_{dut}$ and timestamps t_k by means of interpolation.

Methods

A method to carry out uncertainty-aware interpolation in space using Kriging methods was recently investigated [1]. This method can also be extended to cover the asynchronous case. The time-signal of each reference sensor is first interpolated onto the same synchronized timestamps t_k, e.g., using [4]. A spatial Kriging interpolation is then applied to each of these timestamps t_k, resulting in functions over time that can be evaluated at the position of the device under test $\vec{x}_{dut}$.

Here, another approach is presented that does not interpolate independently in time and space, but simultaneously using an adjusted 4D nearest neighbor regression. In a rather low-informative approach, the quantity field $\phi(\vec{x}, t)$ over some finite time interval is approximated in a local multidimensional first order approach.

$$\tilde{\phi}(\vec{x}_0, t_0) = \vec{\nabla}_s \cdot \left(\begin{bmatrix} \vec{x}_0 \\ t_0 \end{bmatrix} - \begin{bmatrix} \vec{x}_s \\ t_s \end{bmatrix} \right) + \phi_s$$

Where the gradient $\vec{\nabla}_s$, offset ϕ_s and point of support $\vec{x}_s, t_s$ are obtained from available reference data of the nearest L measurement points using heuristics and a least-squares fit. Neighborhood is defined by the "p=2"-norm of a combined spatio-temporal vector $\begin{bmatrix} \vec{x} \\ t \end{bmatrix}$. The neighborhood of $(\vec{x}_0, t_0)$ is denoted as $\mathcal{N}_L(\vec{x}_0, t_0)$ and the interpolation model given by:

$$\phi_s = \text{median}\left(\hat{\phi}_n(\vec{x}_n, t_{n,j}) \,:\, (n,j) \in \mathcal{N}_L(\vec{x}_0, t_0) \right),$$

$$\vec{x}_s = \text{mean}(\{\vec{x}_n :\ (n,j) \in \mathcal{N}_L(\vec{x}_0, t_0)\}),$$

$$t_s = \text{mean}(\{t_{n,j} :\ (n,j) \in \mathcal{N}_L(\vec{x}_0, t_0)\}),$$

$$\vec{\nabla}_s = \underset{\vec{\nabla}}{\text{argmin}} \sum_{(n,j) \in \mathcal{N}_L(\vec{x},t))} \left\| \hat{\phi}_n(\vec{x}_n, t_{n,j}) - \tilde{\phi}(\vec{x}_n, t_{n,j}) \right\| .$$

The parameters $\vec{\nabla}_s, \phi_s$ have associated uncertainties. The uncertainty $u(\phi_s)$ is given by those of the median element(s). The covariance matrix $U(\vec{\nabla}_s)$ is obtained from a (repeated) Monte-Carlo-evaluation of the minimization routine. Applying the "law of propagation of uncertainty" [2] then yields for the uncertainty of $\tilde{\phi}(\vec{x}, t)$:

$$u\left(\tilde{\phi}(\vec{x}_0, t_0)\right) = \sqrt{\left(\begin{bmatrix} \vec{x}_0 \\ t_0 \end{bmatrix} - \begin{bmatrix} \vec{x}_s \\ t_s \end{bmatrix} \right) U(\vec{\nabla}_s) \left(\begin{bmatrix} \vec{x}_0 \\ t_0 \end{bmatrix} - \begin{bmatrix} \vec{x}_s \\ t_s \end{bmatrix} \right)^T + u(\phi_s)^2}.$$

Interpolation schemes based on different (potentially overlapping) neighborhoods could be used in parallel. A consequence of the chosen model for ϕ is an increased uncertainty for the interpolated value at points further away from the point of support.

Application

The outcome of applying the proposed interpolation method to a simulated temperature room use case is shown in Figures 1 and 2. The true field is given by the following equation (with spatially dependent amplitude, offset and phase):

$$\phi(\vec{x}, t) = 2|\vec{x}| + |\vec{x}| * \sin(t + |\vec{x}|)$$

Depending on the distribution of the sensors (black circles in Figure 2), closer reference measurements result in better estimates of the field ϕ. The GUM-propagated uncertainty of the second interpolation model supports this observation by providing higher uncertainty values in regions (4D) that are further away from existing reference measurements.

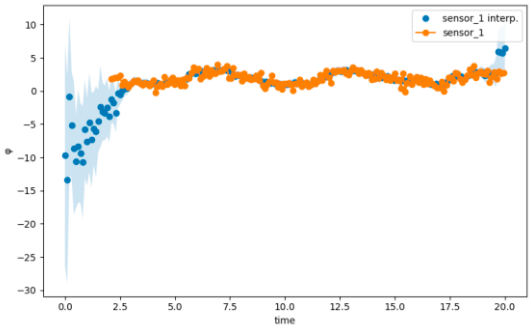

Figure 1: Interp. at position of an existing sensor.

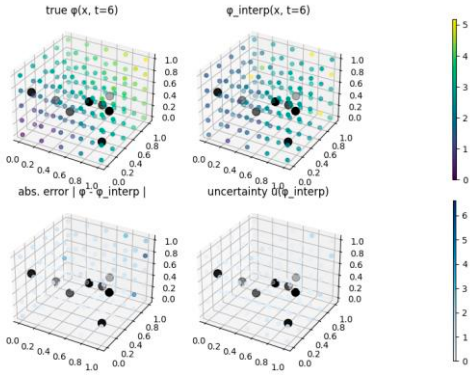

Figure 2: Interpolation at t=6 over the obs. volume. Sensor positions are drawn as black circles.

Conclusion and Outlook

Two uncertainty-aware spatio-temporal interpolation methods are proposed. One is presented in detail to use non-synchronized spatially distributed sensor network data as input for a homogeneous co-calibration method. Both approaches propagate the uncertainty into the interpolated value, but do not weight measurement data based on uncertainty.

It is of interest to further adapt, compare and explore existing and new interpolation schemes.

References

[1] Vedurmudi et al., Uncertainty-aware Temperature Interpolation for Measurement Rooms using Ordinary Kriging, 2022 (submitted)
[2] JCGM 100, Evaluation of measurement data, 2008
[3] JCGM 200, International vocabulary of metrology, 2012
[4] White, Propagation of Uncertainty and Comparison of Interpolation Schemes, 2017

DOI 10.5162/SMSI2021/A3.3

Active Display Registration in Phase Measuring Deflectometry

Yann Sperling[1], Ralf B. Bergmann[1,2]
[1] BIAS – Bremer Institut für angewandte Strahltechnik, Klagenfurter Str. 5, 28359 Bremen, Germany,
[2] University of Bremen, Faculty Physics and Electrical Engineering, Otto Hahn Allee 1, 28359 Bremen, Germany
sperling@bias.de

Summary:
We present the first experimental realization of phase measuring deflectometry (PMD) with active display registration. A stereo camera system determines the position and shape of the display that is used in PMD for active pattern generation. As an example, we measure the shape of two mirrors.

Keywords: Optical metrology, phase measuring deflectometry, generic camera model, specular surfaces, shape reconstruction

Introduction

Phase measuring deflectometry (PMD) [1] is a robust and low cost full-field shape measurement method for specular surfaces. It is based on the reflection of light rays. A display is showing sinusoidal fringe patterns which are reflected by a surface under test (SUT) and recorded with a camera. Using phase shifting technique, this establishes a correspondence between camera pixels and phase angles of the sine patterns, encoding positions on the display. This phase information is used to determine the shape of the SUT by means of inverse ray tracing.

The phase information does not uniquely determine the shape of the SUT [1]. Regularization is the process of incorporating additional information to make the shape reconstruction feasible. Setups with multiple cameras, with a translation stage moving the display or with a distance sensor provide additional information for regularization.

Active Display Registration in PMD

Bartsch and Bergmann [2] proposed the idea of Active Display Registration (ADR). A schematic setup is depicted in Fig. 1. A stereo camera system observes the PMD display directly to register its position and shape. By moving the display to several distances from the SUT, regularization can be obtained. Because ADR captures the display shape, it has the potential to reduce systematic errors caused by display nonplanarity. Additionally, ADR allows for more freedom in setup geometry as the display is not fixed. This in term may simplify the measurement of SUTs with high curvature or large size.

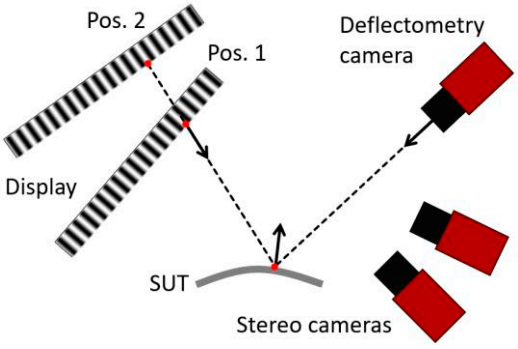

Fig. 1 Schematic of PMD with ADR. The stereo camera pair observes the display. The deflectometry camera observes the display via reflection on the SUT. The display is moved to several positions.

Zhang et al. [3] introduced a similar method based on speckle digital image correlation instead of PMD. However, their method relies on sufficient focus to capture the speckle image, and their setup is limited to the measurement of nearly flat SUTs.

In this paper, we present the first experimental realization of PMD with ADR.

Experimental Setup

Figure 2 shows our setup. All three cameras capture fringe images shown on the display to obtain phase information. Utilizing the principle of fringe projection [4], the stereo camera system determines a mapping from phase to 3D coordinates. This mapping is used to translate the phase measured by each pixel of the deflectometry camera into a 3D reference point. By moving the display to several positions,

each deflectometry camera pixel corresponds to multiple reference points, through which a line can be fitted. The line is intersected with the corresponding camera ray of vision to obtain a surface point of the SUT. This procedure is done for all camera pixels, which yields the SUT shape. Each two intersecting lines also yield a surface normal vector, as can be seen from Fig. 1. Because PMD is a high-sensitivity slope measuring technique, we can therefore use integration [1] to improve the result.

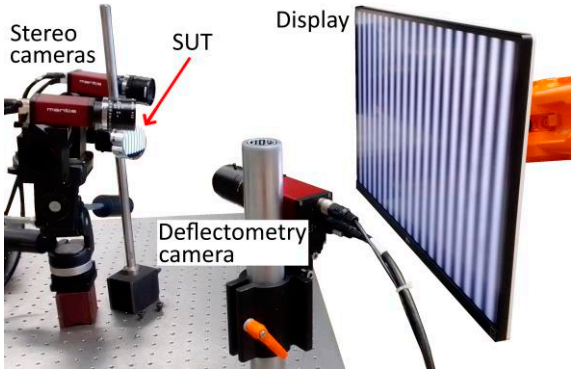

Fig. 2 Experimental setup of PMD with ADR. The display can be moved by a robot manipulator.

Calibration

We describe all cameras with the generic camera model and calibrate them with vision ray calibration [4]. The stereo system cameras are calibrated simultaneously and do not need an extrinsic calibration step for their relative position. The external calibration of the stereo system to the deflectometry camera is achieved with the procedure outlined in [5] using a planar mirror.

Results

We measure the shape of a λ/20 planar mirror and a λ/2 convex spherical mirror. The spherical mirror has a radius of curvature of (201.97±0.02) mm, which was determined with a coordinate measuring machine.

Figure 3 shows the resulting shape deviations. For the planar mirror we obtain a deviation of PV (2±0.03) µm and RMS (0.5±0.03) µm. For the spherical mirror we obtain PV (5.4±0.4) µm and RMS (1.2±0.4) µm. These errors are factor of 2 to 3 higher than that of comparable measurements using an advanced PMD method [6].

The deviations are dominated by low frequency components which indicates systematic errors in the shape measurement. We assume that our current measurement accuracy is essentially limited by the comparatively low resolution of 1.5 MPixel of the stereo system cameras, resulting in a rather sparse mapping of measured phase to 3D coordinates. This uncertainty translates into calibration as well as into shape measurement uncertainty.

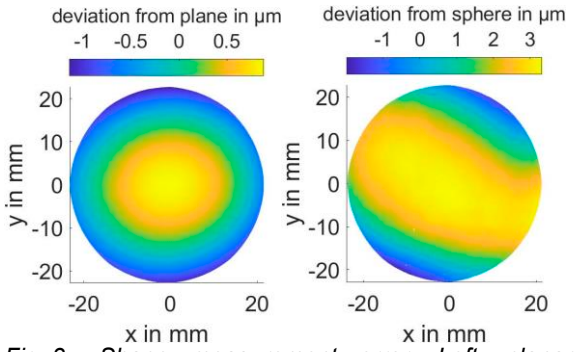

Fig. 3 Shape measurement error. Left: planar mirror (PV 2 µm, RMS 0.5 µm); right: spherical mirror (PV 5.4 µm, RMS 1.2 µm).

Summary and Outlook

We have experimentally realized a phase measuring deflectometry (PMD) setup with active display registration (ADR) and measured the shape of two mirrors. Presently, the PV deviations and the RMS values are a factor of 2 to 3 higher than those of comparable previous measurements [6]. We plan to further investigate systematic errors caused during calibration by independently measuring the tilting of the planar calibration mirror.

Acknowledgement

The authors thank the German Research Foundation (Deutsche Forschungsgemeinschaft, DFG) for financial support under grant 444018140. Y. Sperling acknowledges valuable discussions with J. Bartsch.

References

[1] L. Huang, M. Idir, C. Zuo, A. Asundi, Review of phase measuring deflectometry, Optics and Lasers in Engineering 107, 247-257 (2018); doi: 10.1016/j.optlaseng.2018.03.026

[2] J. Bartsch, R. B. Bergmann, Phasenmessende Deflektometrie mit aktiver Displayregistrierung, DGAO-Proceedings 2020 (2020)

[3] X. Zhang, D. Li, R. Wang, Active speckle deflectometry based on 3D digital image correlation, Optics Express 29, 28427-28440 (2021); doi: 10.1364/OE.437531

[4] J. Bartsch, Y. Sperling, R. B. Bergmann, Efficient vision ray calibration of multi-camera systems, Optics Express 29, 17125-17139 (2021); doi: 10.1364/OE.424337

[5] J. A. Hesch, A. I. Mourikis, S. I. Roumeliotis, Determining the Camera to Robot-body Transformation from Planar Mirror Reflections, 2008 IEEE/RSJ International Conference on Intelligent Robots and Systems, 3865-3871 (2008); doi: 0.1109/IROS.2008.4651121

[6] J. Bartsch, M. Kalms, R. B. Bergmann, Improving the calibration of phase measuring deflectometry by a polynomial representation of the display shape, J. Eur. Opt. Soc.-Rapid Publ. 15, 20 (2019); doi: 10.1186/s41476-019-0116-1

DOI 10.5162/SMSI2023/A3.4

Digital approach of certification in quality infrastucture

Keerthana Nattuveettil, Carlo Tiebe, Nanine Brunner, Michael Melzer, Marcus Thomas, Sergej Johann, Patrick P Neumann, Matthias Bartholmai
Bundesanstalt für Materialforschung -und prüfung (BAM)
keerthana.nattuveettil@bam.de

Summary:

QI-Digital is a joined project aiming at digitalising Quality Infrastructure (QI) processes involving standardization, conformity assessment, accreditation, metrology, and market surveillance [1]. Federal institute of material research and testing (BAM) is working on the creation of a digital calibration certificate (DCC) to achieve digital metrological traceability and conformity assessment. The utilisation of machine readable and executable DCCs in the XML format is demonstrated on an example of a temperature measurement at a hydrogen refueling station. The certificates will be retrieved and analysed automatically at a Process Control System or at a Digital Twin.

Keywords: Quality Infrastructure, Digital Certificates, temperature calibration, digitalisation, hydrogen technology

Motivation

To ensure the quality of “Made in Germany” in the era of digitalisation, Quality Infrastructure (QI) processes are digitalised by Federal Ministry of Economic Affairs and Climate Action (BMWK) and other stakeholders of the QI-Digital project. A holistic approach to digitalise different workflows can contribute to a paper-free documentation [1]. As an accredited calibration and testing lab, the Federal Institute of Material Research and Testing (BAM) is working on the generation and implementation of digital certificates, following the good practice guidelines established by national metrological institute. Currently, the focus is on digital calibration certificates (DCC) for temperature sensors. The concept of DCC is explored within the QI-Digital project on a hydrogen refuelling station and the use-case of temperature measurement for developing novel approaches for quality assurance.

Generation of Digital Calibration Certificate

DCCs are analogous to paper-based certificates but they are machine readable, interpretable, and executable. Therefore, they need to have a harmonised structure in a language like XML. DCC structures for different measurement quantities are defined by the respective technical committees of the German forum for calibration services (DKD), within the framework of the XML Scheme for DCCs, defined by the Physikalisch-Technische Bundesanstalt (PTB). These harmonised certificates are automatically generated by a self-developed middleware using python and LabVIEW. The final XML files are digitally signed via the Public-Key-Infrastructure (PKI) provided by the German accreditation body (DAkkS), which validates the accreditation of the issuing calibration lab. To comply with the current standards, a human-readable certificate in PDF format will also be handed over to the customers.

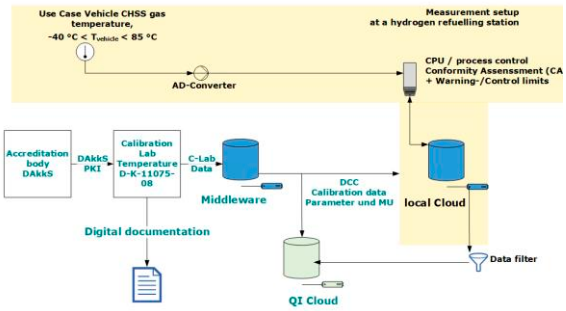

Fig. 1. Creation of calibration certificate for sensors used to measure CHSS temperature

Use of DCC in Hydrogen Refuelling Station

The DCCs generated at BAM, are transferred in a machine-interpretable XML format to a cloud which will be retrieved by Process control system (PCS) or at a Digital Twin (DT). As a practical example, the temperature measurement at

the Compressed Hydrogen Storage System (CHSS) during the fuelling of hydrogen vehicles will be used to implement and use the DCC. The real-time temperature is measured and analysed, and a conformity assessment (CA) of the process is done in real-time by PCS or DT. The calibration and measurement uncertainty values from the DCC are retrieved automatically and analysed, in order to be taken into account for the CA decisions. The process flow is shown in figure 2. The temperature limits are set via the ISO 19880-1 standard [2].

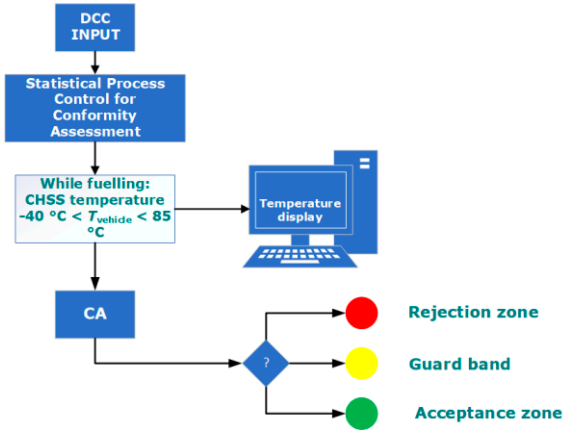

Fig. 2. Process flow diagram for conformity assessment

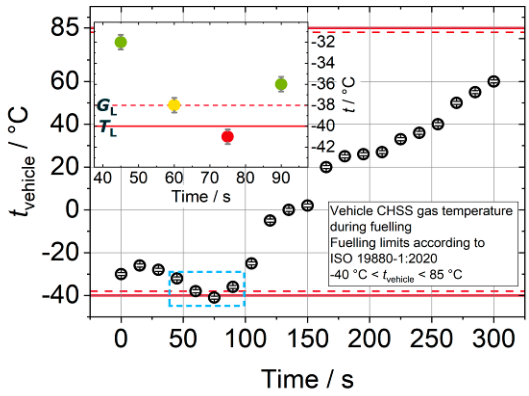

Fig. 3. Measurement data and conformity assessment results.

In figure 3, the process data acquired and the respective CA, is shown. The data is recorded at a rate of 15 seconds. The region of interest is shown in the blue box.A moving average and the standard deviation of the process are calculated. The uncertainty is derived according to DKD-R 5-1 [3].

The expanded uncertainty (k=2) of the vehicle temperature is expressed by

$$2\times\sqrt{u(CAL)^2 + u(t\_SD)^2} \qquad (1)$$

where u(CAL) is the uncertainty from the calibration process and $u(t_{SD})$ is the process standard deviation by means of the moving average.

The conformity is accepted if the hypothesis H_0 in equation (2) is true

$$H_0 = P(T_L \leq t\_vehicle \leq T_U) \geq (1-\alpha) \qquad (2)$$

Where T_L is the lower and T_U is the upper temperature limit as given in [2]. If H_0 is false, the values are rejected.

Once the probability is calculated, the values are either accepted, as indicated by green dots or they are rejected as indicated by red dots, in figure 3. The yellow values lie in the guard band, which means that the magnitude of the offset from the specification limit to the acceptance or rejection zone boundary is small.

Conclusion and Outlook

As the first step to digitalise calibration certificates, DCC for temperature sensors are generated and used in hydrogen refueling station. This will ensure digital metrological traceability and an automated conformity assessment of the processes. The use of digital signature makes it easier to validate the authenticity of the certificates. These digitalised processes will make it easier and faster to assure the quality of processes and products in general.

References

[1] S. Eichstädt, D. Hutzschenreuter, the quality infrastructure in the digital age: beyond machine-readable documents, IMEKO TC6 International Conference on Metrology and Digital Transformation (2022), https://www.m4dconf2022.ptb.de/fileadmin/documents/m4dconf2022/Material/Paper/IMEKOTC6-M4Dconf-2022-P65-EICHSTAEDT-et-al.pdf.

[2] ISO 19880-1 2020-03 Gaseous Hydrogen- Fuelling Stations -Part 1- General requirements, https://www.iso.org/standard/71940.html.

[3] DKD-R 5-1 Kalibrierung von Widerstandsthermometern 2018, https://doi.org/10.7795/550.20180828ACRU.

DOI 10.5162/SMSI2023/A4.1

Boosting Energy Efficient Machine Learning in Smart Sensor Systems

Julio Wissing, Stephan Scheele
Fraunhofer IIS, Fraunhofer Institute for Integrated Circuits IIS,
Division Smart Sensing and Electronics, Erlangen, Germany
julio.wissing@iis.fraunhofer.de, stephan.scheele@iis.fraunhofer.de

Summary:

Smart intelligent sensor systems are key for many application areas in the domain of ubiquitous computing like embedded autonomous systems, wireless sensor networks, internet of things and wearables. In this article, we provide an overview of recent approaches to improve the design, structure and deployment of machine learning methods for smart sensor systems in order to make them as lightweight and energy efficient as possible. The techniques considered cover both hardware and software perspectives.

Keywords: Smart Sensor Systems, Machine-Learning, Energy Efficiency, Hierarchical Machine-Learning, Industry 4.0

Introduction

Smart Sensor Systems combine advanced signal processing and data-fusion techniques with machine learning (ML) algorithms to ensure low-latency processing of sensor and measurement data directly at the edge device. They found numerous applications in Industry 4.0, IoT, medical diagnostics, smart cities, autonomous embedded systems etc.

In recent years, a growing interest in optimizing machine learning methods with respect to their energy efficiency can be observed as challenging and attractive research topics in both academia and industry. In particular**,** facing a recent global energy crisis, it seems more appropriate than ever to improve the energy efficiency of AI methods and their sparing use of computational resources, as used in countless smart sensing devices worldwide.

Optimization Methods

As discussed, optimizing the resource efficiency for smart sensor systems is a crucial point to ensure the viability of a TinyML approach. Key requirements of intelligent sensor systems are low-latency processing at a high data rate, high reliability, data security and a long battery lifetime[3]. During the development life cycle of such systems, there are multiple optimization points that a developer can utilize for efficient processing at the edge. In the following, we will go through the life cycle step by step to highlight possible optimization mechanisms and pitfalls to ensure the most efficient execution. In this short overview we will cover the hardware side only briefly and focus on methodical optimizations on the software side.

Pre-processing and Feature Extraction

Before any data is fed into the ML-pipeline, the sensor data needs to be prepared to be more efficiently processed. At this point, denoising and data filtering methods can be applied, so that only needed data is passed to the model. After the data preprocessing step, the remaining sensor data is fed into the feature extraction stage. Here, the dimensionality is reduced to contain only relevant information. This has the benefit of quicker training and the possibility to use more efficient models in the next stage. However, creating a viable set of features can be hard to achieve. Usually, some sort of expert knowledge is needed to identify patterns, possible transformations or meaningful statistical moments. Additionally, some features might not be as influential as others and may therefore be left out. To overcome this issue, feature pruning or search can be included in the process. This is achieved by either tracing back through the machine learning model to find the most relevant inputs [4] or by applying search algorithms like random search, genetic algorithms or reinforcement learning. Additionally, a standard feature extraction might be unnecessary in the case of NNs, which inherently identifies meaningful input data in the

training process but come with the downside of increased computational complexity.

Machine Learning Model Optimization

After feature extraction, a machine learning algorithm is applied to transform the given inputs into the desired output format. We divide possible optimizations into two groups: Ante and post-hoc optimization. The first one can be applied before the actual training and comes down to a meta-approach of choosing the most efficient classifier. In a greedy fashion, the most efficient model wrt. energy usage and precision can be selected. It must be noted that for suitable models not only different kinds of neural networks (NNs) should be considered. Even though a neural architecture search is an applicable approach to find efficient models, classical methods like decision trees might be a suitable option with a good working feature extraction.

Post-hoc optimization can be applied after training. This step is very dependent on the chosen ML-Method but can broadly be described in either reducing the bit width of calculations or leaving out unnecessary parts of the model. The first one is referred to as quantization [2], which brings down a model from floating point to integer 8-bit precision or lower. The second approach falls into the category of pruning, which might be pruning branches in a decision tree, omitting classifiers in an ensemble, or leaving out neurons in a NN [2].

Hierarchical Machine Learning

In some applications it might be possible to divide a classification into smaller sub-tasks. In a divide-and-conquer fashion, instead of using one ML-model to solve the task, smaller and more efficient models are used. Consider an industry 4.0 scenario with a smart accelerometer to find bearing damages in a machine. A standard approach would be to classify every time frame of sensor data with a big NN or a support-vector-machine. In the hierarchical case, we can implement an event-wake-up-trigger and split the task into three stages: Anomaly detection, fault localization and severity classification. Because of the smaller sub-problems, the first stage can be solved with a linear classifier, the second one with a random forest and the third one with a selection of tree-based classifiers [1].

Hardware selection

From the hardware perspective, the platform can highly impact the resulting efficiency of a system and must be selected alongside with the software. The algorithms should be tested for the lowest precision possible and for the need of floating point calculations. Most optimally, all calculations can be done in 16 or 8 bit and a floating point unit can be omitted. Additionally, further hardware modules are helpful to accelerate the execution of certain algorithms. Usually, the more specialized an acceleration unit is, the more efficient the execution becomes if the algorithm can utilize it. A DSP-unit is one of the broader kind of accelerators, which can optimize various calculations like vector/matrix operations, Fourier-transformations, or statistics. Furthermore, typical SIMD-Accelerators like vector or neural processing units can accelerate both NNs and matrix-operations. NNs can also utilize extremely specialized hardware like analog Neuromorphic circuits, which can cut down latency and energy usage drastically [5]. A final consideration when picking hardware platform(s) is software support. A lot of silicon manufacturers and IP-providers are delivering software-librarys alongside their chips that help to utilize their hardware more efficiently. Typical examples for that are ARM-CMSIS or STM32-Cube AI.

Conclusion and Outlook

We presented an overview of methods to improve the efficiency of machine learning algorithms for smart sensor systems. Depending on the application or ML-model, these can be applied before, during, or after training an ML model. Existing results show that a good trade-off between model efficiency and accuracy can be achieved, significantly increasing efficiency (e.g. reduction of 47% energy consumption [1]) without sacrificing the ML model accuracy and fidelity.

References

[1] J. Wissing, S. Scheele, A. Mohammed, D. Kolossa, und U. Schmid, HiMLEdge – Energy-Aware Optimization for Hierarchical Machine Learning, *Advanced Research in Technologies, Information, Innovation and Sustainability*, 15-29 (2022); doi: 10.1007/978-3-031-20316-9_2

[2] T. Liang, J. Glossner, L. Wang, S. Shi, X. Zhang, Pruning and quantization for deep neural network acceleration: A survey, *Neurocomputing* 461, 270-403 (2021) ; doi:10.1016/j.neucom.2021.07.045.

[3] S. Li, L. Xu, S. Zhao, 5G Internet of Things: A survey, *Journal of Industrial Information Integration 10*, 1-9 (2018); doi:10.1016/j.jii.2018.01.005.

[4] S. Yeom, P. Seegerer, S. Lapuschkin, A. Binder, S. Wiedemann, K. Müller, W. Samek, Pruning by explaining: A novel criterion for deep neural network pruning, Pattern Recognition 115 (2021), doi:10.1016/j.patcog.2021.107899.

[5] R. Müller et al., Hardware/Software Co-Design of an Automatically Generated Analog NN, *Embedded Computer Systems: Architectures, Modeling, and Simulation*, 385–400 (2022); doi: 10.1007/978-3-031-04580-6_26

DOI 10.5162/SMSI2023/A4.2

Correction of Inconsistent Sensor Timing: Missing Samples and Clock Deviations

Yogesh Kapoor[1], Walter Lang[1], Reiner Jedermann[1]
[1] Institute for Microsensors, -Actuators and –Systems (IMSAS), University Bremen, Otto-Hahn-Allee 1, Germany
rjedermann@imsas.uni-bremen.de

Summary:
Sensor data, transferred by wireless sensor networks, must often be resampled for correcting missing samples or timing deviations. The direct application of the well-known Shannon theorem is limited to uniform sampling. For the non-uniform case, the resampling accuracy can be improved by Local Regression. Several cases, such as low/high signal frequency and noise were tested in combination with different scales of non-uniformity from missing single samples to fully arbitrary sampling.

Keywords: Arbitrary resampling, missing samples, clock jitter, Whittaker-Shannon Interpolation, sensor data processing, non-uniform sampling.

Problem and Motivation

The timing of measurement data, transmitted via wireless sensor networks, is often inconsistent. Samples might be missing or delayed due to network failures or overload. The CPU clock of the sensor nodes might deviate or be out-of-sync with other sensor nodes. Subsequent processing of the sensor data mostly requires uniform sampling at identical time points for different sensor nodes. The measurements must be resampled accordingly for digital twins and IoT based data processing.

In practice, often only the simple approach of “keeping the last measured value” is applied, or, in technical terms, a Zero Order Hold function (ZOH). The Whittaker-Shannon Interpolation (WSI) according to the sampling theorem of Shannon [1] offers full reconstruction from a theoretical point of view under some restrictions by filtering the input with a sin(x)/x function. The first restriction, that the signal is bandlimited to half of the sampling rate, is mostly assumed to be fulfilled. However, other restrictions often cannot be complied with in practice. Sampling must be uniform and free of noise. The signal must be infinite in time. Especially the latter one is problematic for real-time processing of sensor data, where only the past values are known.

In this contribution, we test different alternate methods, in order to provide an improved solution adapted to the sampling conditions.

Methods and test cases

In addition to WSI and ZOH, we tested Local Polynomial Regression (LPR) [2], also known as Locally Estimated Scatterplot Smoothing (LOESS), and linear connection of neighboring measurement points (LIN).

Sine waves at different frequencies, a random signal created by Gaussian process, and temperature measurements in a building were applied as test signals. Reference signals were generated at 10fold sampling frequency. A set of samples was picked from this reference set at lower sampling frequency as example measurement data. Signals with low/high frequency and with/without noise were tested. Besides uniform sampling for f=1Hz, different inconsistent timing conditions were tested, such as missing samples, clock jitter, and arbitrary time points with a maximum distance of 1.5 s.

For comparing the accuracy of the different methods, they were applied to resample the signal to the reference frequency. The Root Mean Square Error (RMSE) was calculated between the resampled and the reference signal. The reconstruction was tested for the off-line case with a measurement set of defined length, as well as real-time case where only past measurements are known, and the reconstructed signal must be updated after each new measurement.

Results

Fig. 1 shows a test signal created by a Gaussian process with a covariance width of 1. Different algorithms were tested to reconstruct the full signal by samples takes in intervals of 1 s. All methods had problems to approximate short peaks in the signal. Best results were achieved

by WSI with an RMSE of 0.060 followed by LPR with 0.111.

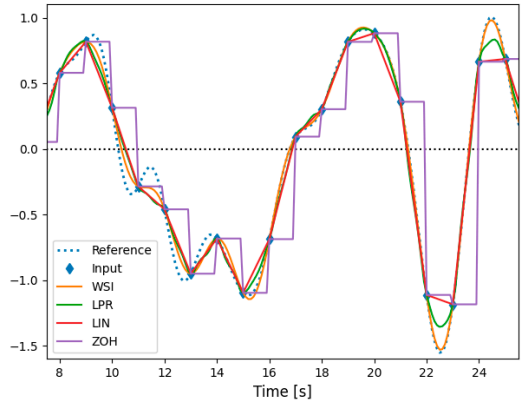

Fig 1. Gauss process test signal (covariance = 1) and resampling

For further testing of the frequency sensitivity of the different methods, sinus waves were applied as test signal. WSI is the method of choice for signals with frequencies close to the theoretical limit for the relation between highest signal and sampling frequency of r=50% (Fig. 2). If r drops below 20%, LPR provides the same or even better accuracy. For low frequencies r<3%, LIN can be used without losing accuracy.

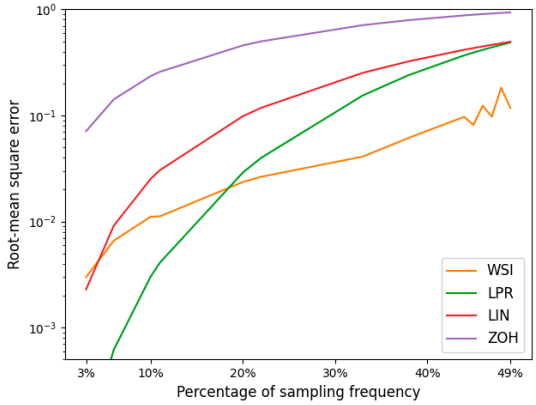

Fig. 2. Prediction error as function of frequency

The effect of inconsistent sensor timing was further tested for WSI and LPR. For the test of clock jitter, the sampling time point was varied by ±10% of the sampling interval. In a second test, an updated signal prediction was calculated after each new measurement with only the past data known.

WSI turned out to be very sensitive towards deviating clock timing, or cutting the input to past values, as the high RMSE indicates (Fig. 3, orange solid lines).

LPR (green) was hardly affected by jitter but for the update case, the RMSE increased by a factor ~3. Leaving out two samples gave about the same error as the update case. Arbitrary sampling gave similar results as the update case for LPR, but the highest RMSE for WSI.

For signal frequencies below 20% of the sampling frequency, LPR provides acceptable accuracy for non-uniform sampling, but for higher frequencies, an accurate method is still missing.

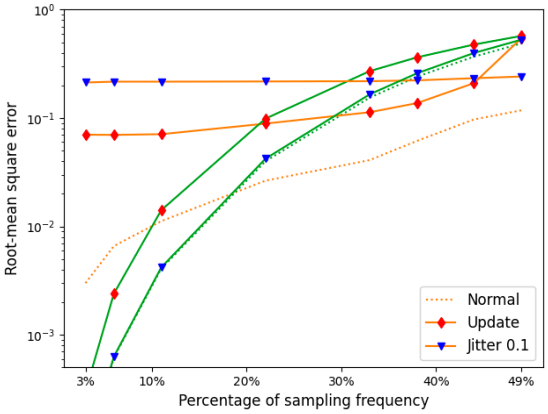

Fig 3. Effect of non-uniform sampling (WSI orange, LPR green)

Discussion

LIN was always better than ZOH for all test signal frequencies, e.g., by a factor of 4 for r=20%. The error can be further reduced by using LPR, e.g., by an additional factor of 3 at r=20%. Only for higher frequencies with r>20%, WSI achieved better results.

LPR is also suitable for the update case and non-uniform sampling with r<20%. However, there is still a lack of good methods for higher frequencies with r>20%. Last results concerning improved methods will be presented at the conference, including Kriging [2], Akima [3], and a newly developed modified local regression method. A Digital Twin platform for sensor data processing was presented at the previous conference [4]. The suggested resampling methods provide the necessary extension for inclusion of sensor data with timing deviations.

References

[1] J. M. Whittaker, Interpolatory function theory: The University Press (1935)

[2] R. Jedermann, Feasibility of Low Latency, Single-Sample Delay Resampling - A New Kriging Based Method, *Algorithms* 16, no. 4: 203; doi: 10.3390/a16040203

[3] A. Patki, G. Thiagarajan, Low complexity, low latency resampling of asynchronously sampled signals, *International Conference on Signal Processing and Communications (SPCOM),* 2016

[4] R. Jedermann, K. Singh, W. Lang, P. Mahajan, Digital twin concepts for linking live sensor data with real-time models, *J. Sens. Sens. Syst.,* 2023, Vol. 12(1), pp. 111-121; doi: 10.5194/jsss-12-111-2023

DOI 10.5162/SMSI2023/A4.3

Concept of a Self-X Sensory System and its first implementation on an XMR-based Angular Decoder Demonstrator

Elena Gerken[1] , *Andreas König*[1]
[1] *Cognitive Integrated Sensor Systems, TU Kaiserslautern Deutschland,*
gerken@eit.uni-kl.de

Summary:
The methodology and case study presented in this article reveals the impact of self-X properties on long-term system reliability. The studies were conducted on the data received from XMR-based angular decoders used as a demonstration setup and Red Pitaya platform used for real-time measurement. A new approach inspired by the biological immune system was explored to detect anomalies and novelties in the field of one-class classification (OCC) XMR sensor properties. The accuracy of the proposed methodology was 96.2 %. Due to the implementation of the self-X (self-healing, self-calibration, self-repairing, etc.) properties, it is possible to increase the efficiency of the physical demonstrator by maintaining satisfactory system performance, despite the defects that occur during the operation.

Keywords: Self-X system, Artificial immune system, Positive selection algorithm, XMR-based angular decoder, Tuning knobs

Background, Motivation, and Objective

Driven by the rapid growth of information technology in manufacturing, industry 4.0 focuses on intelligent monitoring using machine learning and optimization techniques [1].
One of the main goals of industry 4.0 is to predict the anomalous behaviour of the system. Fault diagnosis, early detection of defects, and increased system reliability are essential to lower operational costs [2]. Numerous methodologies are presented in the literature [3-6] to reduce maintenance costs and prevent unplanned downtime in the production chain due to equipment failures.
This research presents a self-X approach based on the extension of condition monitoring of instrumented processes to self-monitoring of the involved sensors, focusing on real-time anomaly detection and elimination. For this goal, inspired by the adaptability and autonomy of living beings, the concept of a holistic and robust system with self-X properties is proposed.

Proposed Methodology

This study aims to create a self-X system that will diagnose and evaluate the operation of controlled equipment while providing its monitoring with subsequent correction of errors and malfunctions. Thus, it will increase the system's reliability and ensure satisfactory performance without human interference due to the existence of the self-X properties. The flowchart of the proposed methodology is presented in Fig. 1.

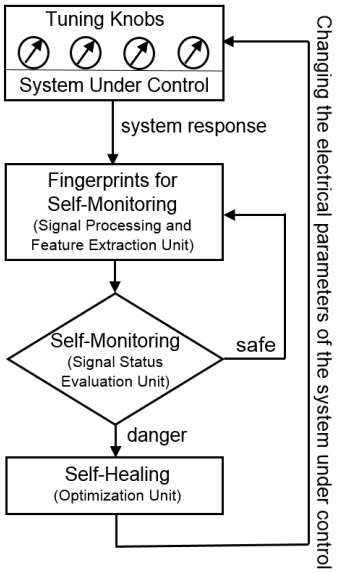

Fig. 1. Self-X mechanisms implementation.

In this approach, the data received from the system under examination is processed with new features extraction. Self-monitoring mechanism, based on the principles of the biological immune system, produces a one-class classification according to signal features, similar to the definition of self and non-self cells in the body of living beings. OCC uses a Positive Selection Algorithm (PSA) [7] based on the NOVAS filtering approach proposed by König [8], where only safe

signal features are used as a set of detectors during the training phase. Hence, the often impossible task of comprehensively describing the set of errors is eliminated [8]. The self-healing property is based on changing the parameters of the input signal using the tuning knobs, bringing the output signal into a safe zone.

Results

An XMR-based angular decoder demonstrator with error incubation capability is used as an experimental setup (Fig. 2). The Red Pitaya platform was used as a real-time measuring system. The motor speed was set to 1413.63 rpm, while the sampling rate of the Red Pitaya's ADC was 1907.35 Hz. One period was sampled with 81 samples, the number of samples in the experiment was limited to 16384 samples [9].

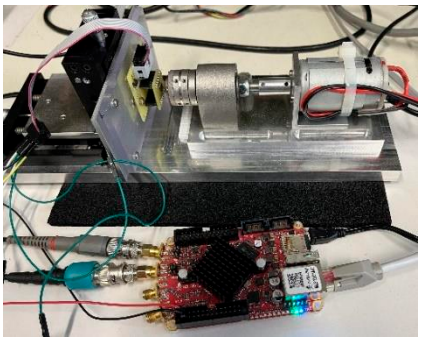

Fig. 2. Demonstrator with error incubation capability.

This experiment is the first step to move from synthesized [10] to real measured data acquired by the Red Pitaya platform. In current studies fault injection is still done simulated on real data acquisition and was labelled as distorted signal, while the measured data were labelled as good samples (Fig. 3). Extracted features from measured and synthesized data are still basic and uncorrelated and will be complemented in the next step to full complexity met, e.g., in [5].

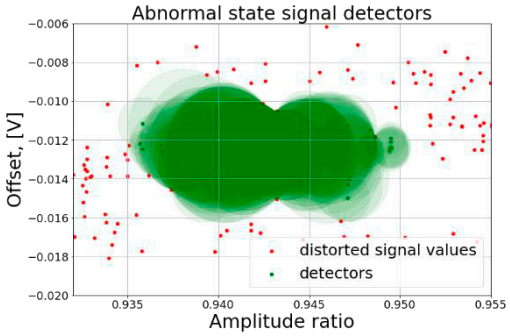

Fig. 3. Set of detectors with different radius.

At the training stage, a set of detectors with different radii [11] are determined (Fig. 3). The allowed minimum radius was 0.0004, while the max and min radii obtained by the training algorithm phase were 0.00353 and 0.00063. When an abnormal value is observed, the self-healing property will be activated. Self-healing (see Fig. 1) can follow in the same footsteps as the extrinsic or intrinsic evolution of electronics pursued in [5], but needs a different cost function. The cost function to minimize in the optimization loop of Fig. 1 in our approach relies on the condition monitoring itself. In previous work, the accuracy of synthesized data was 98.16% [10], while on the real measurement, the accuracy was 96.2%. The accuracy of the actual hardware is slightly lower than the synthesized data but still falls in an acceptable range. Further work will be based on extension for continuous online measurement and adaptation based on the Red Pitaya platform. To advance the experiment studies, it is intended to inject the real-world faults at the mechanical, sensory, and electronics level before acquisition of measurement data.

References

[1] Diez-Olivan, Alberto, Javier Del Ser, Diego Pascual Galar and Basilio Sierra. "Data fusion and machine learning for industrial prognosis: Trends and perspectives towards Industry 4.0." *Inf. Fusion* 50 (2019): 92-111.

[2] Ersoy, Yusuf. (2022). The Advantages and Barries in Implementing of Industry 4.0 and Key Features of Industry 4.0. The Journal of International Scientific Researches. 7. 207-214.

[3] Singh, Sarbjeet, Diego Pascual Galar, David Baglee and Sten-Erik Björling. "Self-maintenance techniques: a smart approach towards self-maintenance system." International Journal of System Assurance Engineering and Management 5 (2014): 75-83.

[4] Brooks Sam, Roy Rajkumar. (2021). Complexity of self-engineering systems across the life cycle – Biological and engineering systems. Procedia CIRP. 98. 121-126. 10.1016/j.procir.2021.01.016.

[5] Zaman Qummar, Andreas König "Self-x integrated sensor circuits immune to measurement noise in the presence of input perturbation by using robust optimization." (2019).

[6] L. Fasanotti, "A distributed intelligent maintenance system based on artificial immune approach and multi-agent systems," 2014 12th IEEE International Conference on Industrial Informatics (INDIN), 2014, pp. 783-786, doi: 10.1109/INDIN.2014.6945613.

[7] Stibor, Thomas, Jonathan Timmis and Claudia Eckert. "A Comparative Study of Real-Valued Negative Selection to Statistical Anomaly Detection Techniques." ICARIS (2005).

[8] A. König et al. Visual Inspection in Industrial Manufacturing. IEEE Micro, Vol. 15, No. 3, pp. 26-31, June, 1995.

[9] "2.4. Command-line tools — Red Pitaya 0.97 documentation." https://redpitaya.readthedocs.io/en/latest/appsFeatures/command_line_tools/com_line-_tool.html. Accessed: 16-11-2022.

[10] Elena Gerken, Andreas König "Application of artificial immune system for Self-X measurement and automation systems in industry 4.0: analysis and survey" Measurement, Sensor Systems and Applications Conference (MeSSAC) 24-26 Aug, 2022.

[11] Chmielewski, Andrzej & Wierzchon, Slawomir. (2006). V-Detector algorithm with tree-based structures. 11-16.

DOI 10.5162/SMSI2023/A4.4

Telemetric angle and position sensing using millimeter-wave metamaterial and a FMCW chip

Alexander Schossmann[1], Michael Töfferl[1], Christoph Schmidt[1], Christof Michenthaler[2], Dirk Hammerschmidt[2], Alexander Bergmann[1]
[1] Christian Doppler Laboratory for Structured Matter Based Sensing, Institute of Electrical Measurement and Sensor Systems, Graz University of Technology, Austria
[2]Infineon Technologies Austria AG, Villach, Austria
alexander.schossmann@tugraz.at

Summary:
A fully telemetric sensor concept is presented for real-time angle and position measurement using millimeter-wave metamaterials that exhibit Fano resonant behavior. The idea is to determine the angle of rotation from the reflection signals of a millimeter-wave transceiver chip. A metamaterial geometry exhibiting Fano resonance behavior has been designed and implemented on low-cost FR4 laminates. In addition, we show numerical and experimental analysis of the sensing effect and present the implementation with a frequency-modulated continuous wave (FMCW) chip.

Keywords: Angle measurement, position measurement, telemetric sensor, metamaterial, millimeter-wave

Introduction

Real-time position measurement, rotary as well as linear, is a fundamental quantity in powertrains and robotics. In this context, there is also a high demand for telemetric and contactless position sensors [1,2].

Sensor concept

It has been shown that planar metamaterials can exhibit Fano-type resonances that significantly determine their reflectivity [3]. The basic idea of our sensor concept is to exploit these Fano resonances which, due to their anisotropy, strongly depend on the orientation of the unit cell with respect to the polarization of the electric field. This results in an angle-dependent reflection of the metamaterial target, which can be used to determine the angle of rotation.

Numerical analysis

The metamaterial used in this work has a unit cell structure as shown in Fig. 1a. The metamaterial elements were fabricated on Panasonic R-1755M laminates with a thickness of 1.2 mm using standard PCB technology. We performed finite element simulations (FEM) in COMSOL Multiphysics®, extrapolating the material parameters of the laminate to the millimeter-wave range. The geometrical parameters were optimized to set the resonance frequency of the Fano type in the frequency range of the FMCW chip, which ranges from 58.0 GHz to 63.5 GHz.

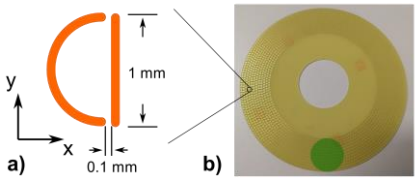

Fig. 1. Metamaterial. a: Sketch of unit cell. b: Array on FR4 disc. The dotted circle marks the illuminated area.

We simulated S11 amplitude spectra for various angles ϕ between the electric field polarization and the x-axis in Fig 1a. Results are shown in Fig 2 for ϕ in the range between $0°$ and $90°$.

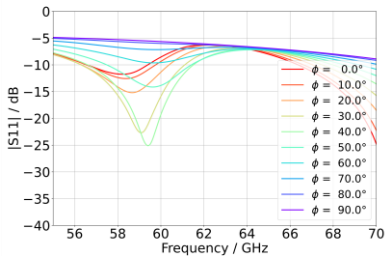

Fig. 2. Simulation of metamaterial S11 spectra.

Due to the symmetry of the unit cell, the curves in the range from $90°$ to $180°$ overlap with those from $0°$ to $90°$. The curve for $\phi = 40°$ shows a distinct minimum close to $60\,\mathrm{GHz}$ which comes

from the Fano-type resonance. Thus, the coupling to this mode is maximum for $\phi = 40°$. Most importantly, the data shows that varying ϕ significantly changes the reflectance in the frequency range close to the Fano resonance, which in turn allows to determine the rotation angle by measuring the reflectance.

VNA measurement results

The metamaterial is produced as a single layer on a 10 cm diameter disc in a circular arrangement (see Fig. 1b). All unit cells are aligned parallel to each other. The disk is mounted on an aluminum axis together with a degree disk for reading the angle of rotation. Reflectance measurements were performed using an Anritsu MS4647B vector network analyzer and a horn antenna. The measurement distance to the metamaterial was 1 cm. The area of the metamaterial array irradiated with this setup is outlined as a green circle in Fig. 1b. In a post-processing step, we performed time domain gating. Fig. 3 shows the measurement results.

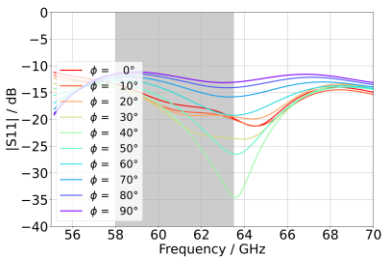

Fig. 3. VNA measurement of metamaterial S11 spectra. Grey area: Bandwidth of FMCW chip.

There is an overall horizontal shift of the curves compared to the simulation results (Fig 2). This indicates that the dielectric constant of the laminate is smaller than the value we extrapolated. In the range from $40°$ to $90°$ the change of the curves with increasing ϕ agrees well with the simulated ones. Furthermore, the coupling to the Fano-type resonance is maximum at $40°$. For ϕ between $0°$ and $30°$ the data in Fig 3 shows a shift of the minimum towards higher frequencies whereas the simulated curves show a shift towards lower frequencies. We explain this by the fact that in the FEM simulations plane wave incidence was assumed. Due to the small measurement distance, this is not strictly fulfilled in the experiment, which leads to a different coupling behavior for small values of ϕ. Nevertheless, the measured curves show the proposed sensor behavior for frequencies in the FMCW chip bandwidth (grey in Fig 3).

FMCW chip measurement results

We installed the FMCW chip at 3 cm distance to the metamaterial, considering the FMCW chirp bandwidth of 5.5 GHz. We calculated the amplitude spectra using the on-chip FFT routine and identified the peak that corresponds to the reflection from the metamaterial. Fig 4 shows the measured amplitude as a function of ϕ.

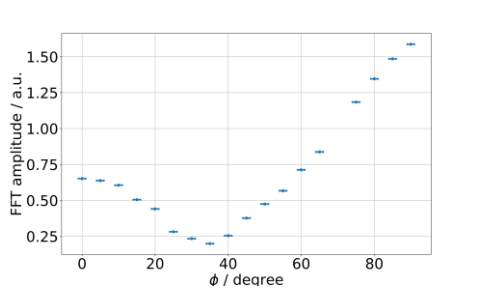

Fig. 4. Millimeter-wave transceiver: FFT amplitude as function of the rotation angle ϕ.

The horizontal error bars show the estimated reading error of the setup. The data clearly shows the angle-dependent change in the reflectance of the metamaterial. However, the curve in Fig 4 is not a bijective function over the whole range of ϕ. This is explained by the resonant behavior observed in simulations as well as measurements (Fig 2 and Fig 3) which show that the coupling to the Fano-type resonance is maximum at $\phi = 40°$. Our implementation can measure the rotation angle fully telemetric in the range from $40°$ to $90°$. However, the implementation of a sine encoder would be straightforward by varying the orientation of the unit cells in the metamaterial array such that the reflectance changes sinusoidally as a function of the sample's rotation angle or movement as sketched in Fig 5.

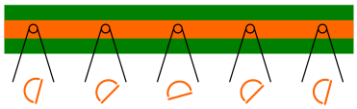

Fig. 5. Possible implementation of sine encoder

We are confident that our proposed sensor concept potentially paves the way toward a new angle and position sensor technology based on millimeter-wave metamaterials.

References

[1] S.R. Ruocco, Robot sensors and transducers, *Open University Press Robotics Series,* ISBN: 978-94-011-6870-0

[2] D. Nyce, Linear position sensors: theory and application. *John Wiley & Sons.,* ISBN: 978-0-471-23326-8

[3] V. Fedotov, M.Rose, S. Prosvirnin, et al., Sharp Trapped-Mode Resonances in Planar Metamaterials with a Broken Structural Symmetry, *Physical Review Letters, 99, 14 2007,* doi: 10.1103/PhysRevLett.99.147401

DOI 10.5162/SMSI2023/A5.1

Measurement of Dissolved Hydrogen in Biogas Fermentation Media

Jens Zosel[1], Rodrigo Renato Retamal Marín[1], Eike Janesch[2], Peter Neubauer[2], Stefan Junne[2,3], Michael Mertig[1,4]
[1] Kurt-Schwabe-Institut für Mess- und Sensortechnik Meinsberg e.V., Waldheim, Germany
[2] Bioprocess Engineering, Institute of Biotechnology, Technische Universität Berlin, Germany
[3] Section for Bioscience and Engineering, Aalborg University Esbjerg, Denmark
4 Physikalische Chemie, Technische Universität Dresden, Dresden, Germany
jens.zosel@ksi-meinsberg.de

Summary:
Hydrogen is a cofactor in many microbial transformation processes and therefore important to achieve a high product yield. The measurement of dissolved hydrogen in biogas processes is complex, because it is conducted at conditions, which may disturb stability and precision of the measured value. A new approach for the measurement of dissolved hydrogen in biogas culture broth by using semiconducting metal oxide gas sensors is presented.

Keywords: metal oxide gas sensor, dissolved hydrogen, biogas culture broth, micro fluidic system

Introduction

Hydrogen (H_2) is a cofactor in many microbial transformation processes and therefore important to achieve a high product yield. It needs to be dissolved in the liquid phase for utilization in cellular transformation. In anaerobic digestion, H_2 occurs usually at partial pressures below 10 Pa [1]. Thus, the provision of cells with sufficient amounts of H_2 is crucial, since it offers only low solubility. This requires a trade-off between expensive improvement of H_2 input rate and its limited availability for a cell.

The measurement of dissolved hydrogen ($H_{2,diss}$) in biogas fermentation media is complex, because it is usually conducted at conditions, which disturb stability and precision of the measured value [2]. These conditions concern biofilm formation on sensitive surfaces as well as hydrogen consumption on surfaces in the fermenter headspace by microbes with access to traces of oxygen. It could be shown in the past that these issues can be circumvented successfully by enabling a membrane-free extraction of dissolved hydrogen ($H_{2,diss}$) into a clean chamber before its detection [3]. This chamber is rinsed with a constantly flowing carrier gas, which is analyzed subsequently for its H_2 concentration ($c(H_2)$). Initially, an automated chromatographic system was used for this task, which is highly sensitive and selective, but it requires a high installation effort. This is associated with costs that exceed the usual scope of biogas production.

This contribution describes a new approach for the measurement of $H_{2,diss}$ in biogas culture broth by using semiconducting metal oxide gas sensors (MOX). These low-cost sensors can be installed with a significantly diminished effort compared to chromatographic systems. Unfortunately, these sensors usually degrade within days when they are in direct contact with biogas. Therefore, within this new approach they are combined with a miniaturized fluidic arrangement based on a small gas-flushable chamber for the MOX.

Methods

The new sensor system consists of a gas supply, a micro-fluidic system with the sensor chamber and a PLC for controlling gas flows and valves and for data logging as shown in Fig. 1.

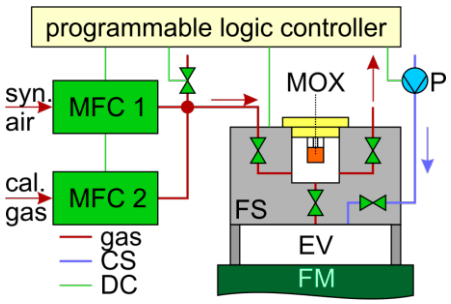

Fig. 1. Scheme of the sensor system: CS = cleaning solution, DC = data/control line, EV = extraction volume, FM = fermentation medium, FS = fluidic system, MFC = mass flow controller, MOX = metal oxide gas sensor, P = pump

The sensor chamber inlet is connected to the gas supply, while the outlet is vented into the environment. A third line connects the sensor chamber to an extraction volume via a solenoid valve. The gas supply provides humidified air or a calibration gas with known c(H_2) during the periods, when the $H_{2,diss}$ in the fermentation media equilibrates with the gas atmosphere in the extraction volume through a membrane-free gas/liquid boundary. After complete equilibration, the flushing gas flow through the sensor chamber is interrupted by closing the valves at the in- and outlet. Subsequently, the connection between sensor chamber and extraction volume is opened for 90 s to allow the extracted H_2 to diffuse into the sensor chamber. The peak of the sensor signal, occurring immediately after this opening, is a stable measure for p($H_{2,diss}$) in the culture broth. After the diffusion step, the extraction volume is filled with fresh air again, and the next equilibration/measurement cycle starts.

Results

The system was characterized in the laboratory in deionized water as model fluid with different concentrations of $H_{2,diss}$. The fluid was held at 25 °C and the partial pressure p($H_{2,diss}$) was adjusted by introducing small gas bubbles of a H_2/N_2 mixture with defined p(H_2) between 1 and 100 Pa.

The resulting calibration curve is shown in Fig. 2 for two independently operating sensor systems. It proves that stable plateau values are achieved at each adjusted value of p($H_{2,diss}$) with a noise below 5 %. The relatively long response time concerns the concentration change in the model fluid, which is significantly longer than the sensor response. The signal is moving back rapidly exactly to the initial 100 Pa level after 120 h measurement, demonstrating a sufficient long-term stability of the sensor.

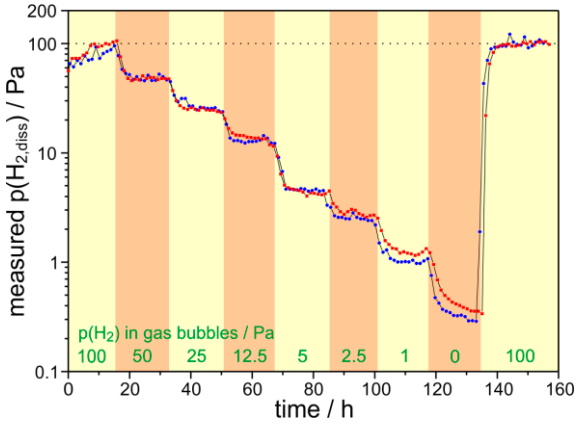

Fig. 2. Calibration curves of two independently operated sensor systems in model media with p($H_{2,diss}$) = 0 … 100 Pa.

After laboratory characterization, the system was installed in a laboratory fermenter and operated for 900 h. The curve in Fig. 3 demonstrates that stable measurements are achievable over this long period.

The peaks of p($H_{2,diss}$) occur immediately after feeding, demonstrating the short sensor response time and the role of H_2 as an intermediate substance in the biogas process and its rapid transfer to the methane producing bacteria. The small fermenter volume of less than 2 liters prevents water cleaning of sensors, due to intolerable dilution of the culture broth. Therefore, the sensor has been cleaned externally, which is also reflected in its signal.

The new sensor system is suited for broad commercialization of dissolved hydrogen monitoring in biotechnological processes.

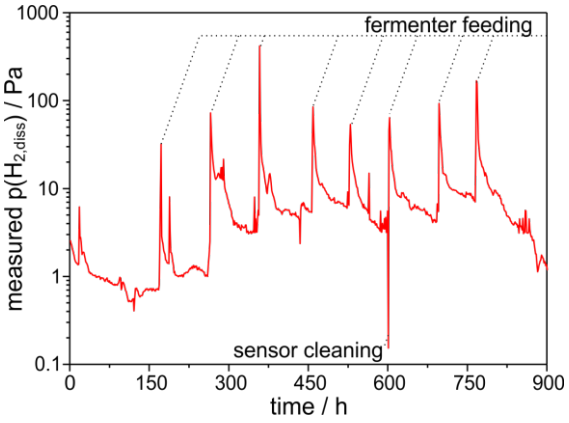

Fig. 3. Long-term measurement of p($H_{2,diss}$) in a laboratory biogas fermenter.

References

[1] X. Wu, H. Yang, L. Guo, Effect of operation parameters on anaerobic fermentation using cow dung as a source of microorganisms, *International Journal of Hydrogen Energy* 35. 46–51, (2010); doi: 10.1016/j.ijhydene.2009.10.039

[2] A. Pauss, G. Andre, M. Perrier, S. Guiot, Liquid-to-gas mass transfer in anaerobic processes: inevitable transfer limitations of methane and hydrogen in the biomethanation process, *Applied and Environmental Microbiology* 56, 1636–1644 (1990); doi: 10.1128/aem.56.6.1636-1644.1990

[3] M. Schelter, J. Zosel, W. Oelßner, M. Mertig, A novel method for measuring dissolved gases in liquids, *Sensors and Actuators B* 193, 113– 120 (2014); doi 10.1016/j.snb.2013.11.070

Acknowledgement

The authors acknowledge funding of the project consortium “ProPhaSep” by the BMWK within the framework program "Biomass energy use", FKZ No. 03EI5409. Das Kurt-Schwabe-Institut Meinsberg wird mitfinanziert durch Steuermittel auf der Grundlage des vom Sächsischen Landtag beschlossenen Haushaltes.

DOI 10.5162/SMSI2023/A5.2

Hydrogen Sensors for Energy Applications

J.R. Stetter[1,2], M.W. Findlay[1], D. Peaslee[2], T. Russ[2], V. Patel[1], B. Meulendyk[1], and E.F. Stetter[1,2]
[1] KWJ Engineering, Inc., 8430 Central Avenue Suite C, 94560 Newark, CA, USA
[2] SPEC Sensors LLC, 8430 Central Avenue Suite D, 94560 Newark, CA, USA
Corresponding Author: jrstetter@gmail.com

Summary:

Over the recent decade, H_2 has become more and more important for multiple industries. The fuel industry especially has been increasing their efforts to use H_2, a carbon-free fuel source. Since H_2 may be a significant indirect contributor to climate change and global warming, a device capable to detect and, more importantly, quantify leaks along the supply chain to both prevent H_2 product loss but also assess impacts on our atmosphere must be develop. Ideally, these devices and "apps" are adaptable to various concentration ranges, environments, and both fixed stations and mobile/wearable devices.

Keywords: Hydrogen, indirect greenhouse gas, electrochemical sensor, nano-TCD, IoT-capable

Background, Motivation and Objective

Since the colorless and odorless gas Hydrogen, H_2, has increasingly important applications in new pollutant free energy sources, like batteries and fuel cells for cars and satellites, to remove friction-heat in turbines, as cryogenic fuel in rockets as well as a lift gas in weather balloons [1], the demand for H_2 sensors has been increasing as well. As every other energy source, H_2 has certain drawbacks. Firstly, if mixed with air, H_2 is flammable, or even explosive above a certain threshold (4 – 75 V%) [1]. Secondly, and more importantly, H_2 was found to be an indirect greenhouse gas [2]. It is called an indirect greenhouse gas because H_2 on its own does not do much damage, however, the products of the reactions involving H_2 in the troposphere and stratosphere are problematic: (i) H_2 reacts with OH radicals in the troposphere resulting in higher lifetimes of methane by effectively reducing the amount OH radicals that can react with methane, (ii) the oxidation of H_2 ultimately leads to the formation of tropospheric O_3, and (iii) the reaction of H_2 in the stratosphere results in an increase in water vapor resulting in an increasing infrared radiative capacity which lead to warming effects [2].

The severe effects H_2 has on the climate require a strict control of possible H_2 sources. In order to cover all applications throughout the H_2 supply chain – including production, transport, storage, and use – a high volume of adaptable monitoring devices that are IoT capable are needed. The adaptable monitoring devices must be capable to detect very small concentrations (low ppb levels) as well as high levels of H_2 while being deployable in fixed stations, portable, mobile, wearable and distributable applications. Prior work has introduced the use of amperometric H_2 sensors [3] in safety applications and herein discussion is extended to low-level environmental monitoring applications.

To summarize, the primary H_2 sensor applications include: 1**)** safety because H_2 is flammable and explosive, 2**)** process control for purity and mixed methane-hydrogen feedstocks, and 3**)** environmental concerns about secondary greenhouse effects.

Experimental Methods

There are two primary technologies for H_2 detection reported here including a small, ultra-low power, high sensitivity electrochemical sensor and a nano-TCD sensor for higher concentrations. The small, low-cost electrochemical sensor is capable of H_2 detection at ppb-levels while requiring next to no power [3]. The nano-TCD sensor combines the superb detection range of 100 ppm to 100 % H_2 of currently available TCD devices while consuming significantly less power than current TCD because of its lower mass.

The devices were exposed to controlled levels of H_2 in air in one of our standard measurement systems. The sensors were operated at room temperature and in 50% RH air and alternatingly exposed to H_2/air mixtures (50% RH). Sensor characterization of sensitivity, selectivity, response time and stability are measured to calibrate the devices and interpret data from field measurements.

Results

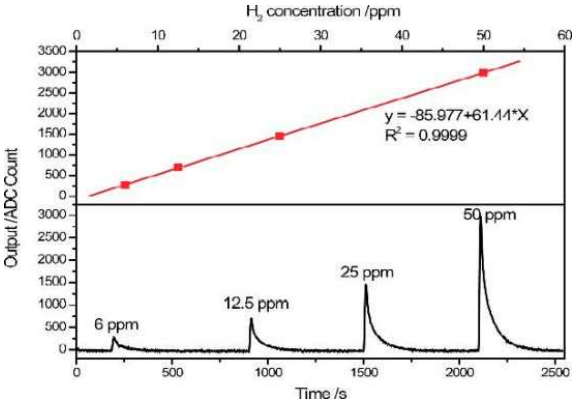

Figure 1: bottom: output of the electrochemical sensors in the presence of varying concentrations of H_2. Top: calibration curve of the sensor output shown at the bottom.

The results of the small, ultra-low power electrochemical sensor are promising (Figure 1). We observed a linear correlation between the output and the H_2 concentration at low level exposure. We were able to detect low ppm levels of H_2 in air with relatively rapid response.

The results obtained with the nano-TCD were similarly promising. Due to experimental limitations, we were not able to measure the response to H_2 concentrations greater than 2% as of now. However, the data in Figure 2 clearly shows a linear dependence of the output (resistance) on the concentration.

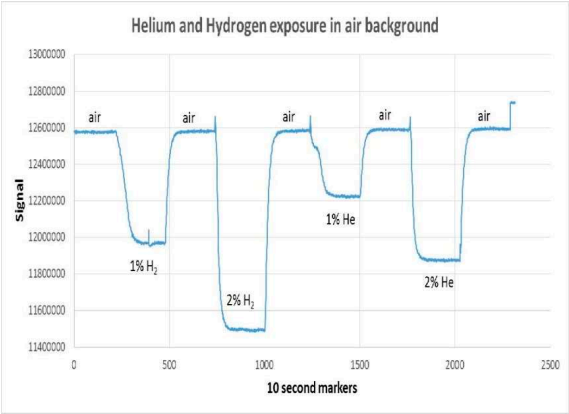

Figure 2: output of a nano-TCD sensor in the presence of various H_2 and He concentrations

Conclusion

The electrochemical sensor shows promising results for ppb-level detection of H_2 in ambient conditions. Similar observations are made for the nano-TCD exposed to high levels of H_2. These two sensors integrated into a single device could provide accurate measurements for concentrations from lower than 1 ppm to 100%. This would allow for environmental assessments as well as safety applications. Both sensors are low power and could be packaged in a simple, low-cost and intrinsically safe package heretofore not possible. The differing selectivity of the sensors can reduce false alarms. Additional studies of the sensor characteristics over time, temperature, and RH will provide data for autocorrection of concentration readings. And there are additional ways to optimize the sensors as they are prepared to be deployed in arrays of devices that can communicate with user interfaces and provide spatial and temporal details about H_2 concentrations in the vicinity of leaks. Data from arrays of local low-cost sensors can be combined with atmospheric data and in AI/ML developed models to locate the leak source as well as provide quantitative data on amount of leaked H_2. This work and the future planned measurements will show that combining these two types of sensors can provide flexible and adaptable sensing devices for a range of applications from fixed site to low-cost, low-power distributed applications.

References

[1] G. Korotcenkov, S. do Han, J.R. Stetter, Review of electrochemical hydrogen sensors, Chem Rev. 109 (2009) 1402–1433. https://doi.org/10.1021/cr800339k.

[2] I.B. Ocko, S.P. Hamburg, Climate consequences of hydrogen emissions, Atmos Chem Phys. 22 (2022) 9349–9368. https://doi.org/10.5194/acp-22-9349-2022.

[3] T. Wischmeyer, J.R. Stetter, W.J. Buttner, V. Patel, D. Peaslee, Characterization of a selective, zero power sensor for distributed sensing of hydrogen in energy applications, Int J Hydrogen Energy. 46 (2021) 31489–31500. https://doi.org/10.1016/j.ijhydene.2021.07.015.

DOI 10.5162/SMSI2023/A5.3

Differential Thermal Conductivity Hydrogen Sensor

Sophie Emperhoff[1,2], Matthias Eberl[2], Julia Perez Barraza[2], Florian Brandl[2] and Jürgen Wöllenstein[1,3]
[1] Department of Microsystems Engineering (IMTEK), Albert-Ludwigs-Universität Freiburg, 79085 Freiburg im Breisgau, Germany,
[2] Infineon Technologies AG, 81549 Neubiberg, Germany,
[3] Fraunhofer IPM, 79110 Freiburg, Germany
Sophie.emperhoff@infineon.com

Summary:
In this work, a thermal conductivity sensor for the detection of hydrogen in fuel cell applications is presented. The sensor uses a differential measuring concept with two cavities combined on one semiconductor-die where one of those cavities is hermetically sealed and filled with nitrogen as a reference gas. The sensors were characterized with hydrogen concentrations between 0 and 3.5 % at different heater temperatures. A 3σ-noise level of 0.06 % hydrogen was achieved with the prototype sensor.

Keywords: thermal conductivity, MEMS, hydrogen, gas sensor, automotive

Introduction

Greenhouse gases such as carbon dioxide are drivers of climate change. Many governments are increasing their commitment to climate protection in order to slow down the warming of the planet. For example, Germany is aiming for greenhouse gas neutrality by 2050 [1]. Within the transportation sector, activities toward electrification and zero-emission drives continue to increase. Using hydrogen as a fuel is one pillar to allow decarbonization where electrification is not possible or reasonable [2].

To avoid endangering passengers or pedestrians, the use of hydrogen as a vehicle fuel also increases the demand of hydrogen gas sensors. Since the thermal conductivity of hydrogen at room temperature is seven times higher than that of air, measuring thermal conductivity is a feasible method to detect hydrogen. Even though other sensor principles like electrochemical and catalytic sensors may show higher sensitivities and selectivity toward hydrogen, they show some major drawbacks regarding an application in the automotive sector such as a short lifetime and vulnerability to poisoning, respectively [3]. A thermal conductivity sensor implemented as a micro-electrical-mechanical system (MEMS) offers additional advantages such as miniaturization, low production costs and low power consumption.

The measurement principle itself is based on resistivity changes of an electrically heated freestanding resistive element. This hot element is a resistor which is heated by short pulses. The resistor should be thermally decoupled from the substrate so that most thermal energy is transferred via the surrounding gas. The hot element cools down when hydrogen is present, and a change of resistivity can be measured.

A MEMS-based sensor using thermal conductivity to measure hydrogen concentrations below the lower explosive limit of 4 % is presented. A differential measurement concept with four geometrically identical elements is used, two located in a hermetically sealed cavity containing a reference gas.

Method

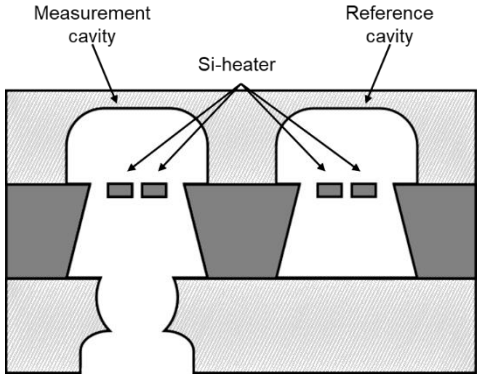

Fig. 1. Schematic cross-section of the MEMS structure. A sensor detects the thermal conductivity of the ambient gas while a reference sensor in a hermetically sealed cavity is surrounded by a defined reference gas.

The MEMS consists of a silicon wafer into which two cavities are etched. One is later used as a measurement cavity with an open port to the surrounding gas. The other cavity is hermetically sealed and filled with a reference gas which

should most closely resemble the measurement environment. For the application as a leakage sensor in fuel cell vehicles, the cavity is filled with nitrogen.

Certain areas of the wafer are made conductive by doping. These areas are exempted during the process and later form the electrical leads and sensing elements.

The structured silicon wafer is encapsulated by two glass wafers under nitrogen atmosphere, resulting in a hermetically sealed nitrogen-filled cavity (fig. 1).

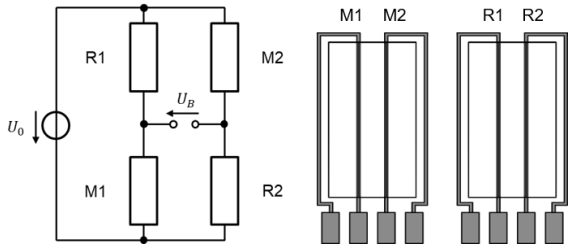

Fig. 2. Schematic top view of sensor structure with four resistors separated in a measurement (M1, M2) and a reference cavity (R1, R2) connected as a Wheatstone bridge.

Each cavity contains two resistors made of doped silicon which act as heater and sensor elements. Two heaters are exposed to the measured medium while the other two heaters are in the reference gas. The heaters are connected in a Wheatstone bridge. Only two of the four resistors are exposed to a change of thermal conductivity in the presence of hydrogen. This differential measurement concept leads to very precise and low-noise measurements. The bridge circuit reduces temperature and aging effects.

Results

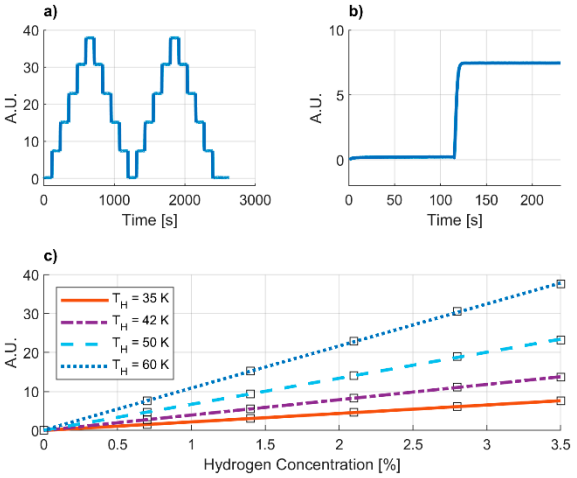

Fig. 3. (a) Raw data of hydrogen concentration measurement from 0 to 3.5 % in 0.7 % steps (T_H = 60 K), (b) the first two concentration steps on a smaller scale and (c) mean values of concentration measurements at four different temperatures T_H of the heaters.

The gas sensing attributes of the sensor were characterized during exposure to varying hydrogen concentrations ranging from 0 to 3.5 % in dry air at a constant gas flow of 500 sccm, at room temperature and ambient pressure. Each concentration step was held for two minutes. The carrier gas was dry air generated by a zero-air generator. The hydrogen concentration was gradually increased from 0 to 3.5 % in 0.7 % steps, then reduced back to 0 %. Then, this sequence was repeated.

The measurement was repeated at four different supply voltages of the bridge. Changing the supply voltage leads to different temperatures of the Si-heater. The performance of the sensor was determined at four different heater temperatures T_H. Fig. 3 a) shows the raw data of a measurement at T_H = 60 K as a visualization of the measurement sequence and the resulting sensor output. Fig. 3 b) shows the first change of concentration on a smaller scale. The response time of the sensor is a few seconds.

Tab. 1: 3σ-noise level of the sensor at different heater temperatures T_H.

T_H [K]	35	42	50	60
3σ-noise [%H_2]	0.17	0.12	0.09	0.06

With this sensor and measurement configuration a 3σ-noise level of 0.06 % hydrogen in air (at T_H = 60 K) is achieved. Table 1 shows the noise level at all measured temperatures.

The measurements show that a higher temperature of the heater results in a higher sensitivity and a better resolution of the sensor. Lower temperatures though reduce power consumption which is very valuable for many applications. The sensor still shows good results at lower heater temperatures and could be used as a leakage detection sensor for hydrogen in the future.

Acknowledgements

This project received funding from the German Federal Ministry of Economic Affairs and Climate Action (BMWK) within the research project HySABi under No. 03EN5009A.

References

[1] Bundesministerium für Umwelt, Naturschutz, Bau und Reaktorsicherheit (BMUB), Ed., Klimaschutzplan 2050 – Klimaschutzpolitische Grundsätze und Ziele der Bundesregierung (2016).

[2] C. Robinson, A. Davies, and J. Wainwright, Global hydrogen balance: Outlook to 2050 - Inflections and Green Rules, *IHS Markit* (2022).

[3] T. Hübert, et al., Hydrogen sensors – A review, *Sensors and Actuators B: Chemical* 157, 329-352 (2011); doi: 10.1016/j.snb.2011.04.070

DOI 10.5162/SMSI2023/A5.4

Rapid Characterisation of Mixtures of Hydrogen and Natural Gas by Means of Ultrasonic Time-Delay Estimation

Jorge M. Monsalve[1], Uwe Völz[1], Björn Betz[1], Christinne Ruffert[1], Jörg Amelung[1], Sandro G. Koch[1], Marcus Wiersig[2]
[1] Fraunhofer IPMS, Maria-Reiche-Straße 2, 01109 Dresden, Germany,
[2] German fuel institute DBI, Halsbrücker Str. 34, D-09599 Freiberg, Germany
jorge.mario.monsalve.guaracao@ipms.fraunhofer.de

Summary:
In this work we present a possible application of ultrasonic time-delay estimation to characterise mixtures of natural gas and hydrogen by the speed of sound. We constructed two prototypes based on two variants of micromachined ultrasonic transducers, both out-of-plane (CMUT) and in-plane (L-CMUT), operating at different frequencies (1.6 MHz and 40 kHz respectively). A calibration of these devices under controlled conditions will enable their assessment as potential hydrogen-sensitive gas counters.

Keywords: hydrogen, natural gas, CMUT, ultrasound, pitch-catch

Introduction

In the coming years, hydrogen will be widely distributed in the German pipeline network as a mixture with natural gas, seeking to enable its application in domestic and industrial environments [1]. Monitoring the hydrogen content in this mixture at different stages of the distribution network will therefore become a need, considering that different components of the gas infrastructure (e.g. pipes, compressors, turbines) offer different levels of tolerance to hydrogen, and that this gas mixture possesses a lower calorific value per unit volume in comparison to natural gas [2,3]. Although the composition of such mixtures can be accurately measured in gas chromatographs, a fast, on-site, and low-cost method—even if less accurate—would offer a significant advantage for monitoring hydrogen in households and factories.

Ultrasonic transducers have been widely implemented in pipelines for monitoring volume flow, and a minimal adjustment in their control unit enables a further report of the speed of sound of the fluid, given that both variables are directly calculated from the two measurements of the time of flight (upstream and downstream) [4]. By monitoring the speed of sound of the hydrogen-enriched mixture, a first, quick estimation of its composition can be performed. If mixture were binary (e.g. H_2 in CH_4), the speed of sound would offer a direct measurement of the hydrogen content, provided that the temperature of the mixture is known. This can be evidenced in Laplace's equation for the speed of sound in ideal gases (1), which reveals its dependence on three variables (C_p, C_v, M) that in turn depend directly (in fact, linearly) on the amount of each substance [5].

$$c = \sqrt{\frac{\gamma P}{\rho}} = \sqrt{\left(\frac{C_p}{C_v}\right)\frac{RT}{M}} \qquad (1)$$

Nonetheless, natural gas does not consist purely of methane, but is itself a mixture that includes ethane, propane, nitrogen and other gases. Depending on the geographical source and the extraction method, the content of CH_4 in natural gas can vary from 98%vol to around 80%vol [6]. If, however, the source of natural gas is kept constant, its composition varies only very slightly, and the concentration of hydrogen can be calibrated with a series of measurements of the speed of sound—or with the knowledge of the composition of the respective sort of natural gas.

Method

We have constructed two prototypes to measure the speed of sound by means of a "pitch-catch" measurement of an ultrasonic wave packet. The devices are designed to act as a new kind of gas counter that reports not only the volume flow but also the hydrogen content, including a temperature correction (for which a corresponding sensor is included). The first prototype relies on a CMUT (Capacitive Micromachined Ultrasonic Transducer) that operates at a frequency of 1.6 MHz [7]. Given the high attenuation losses at this operation frequency, the travelling range of

the waves is kept at 11 mm. The second prototype relies on a low-frequency, laterally oscillating CMUT [8] that generates a wave packet with a centre frequency of 40 kHz. This wave packet is then detected by a MEMS microphone (Knowles® SPU1410LR5H) located at a distance of 150 mm from the "L-CMUT" transmitter. A scheme of these two prototypes is found in Figure 1.

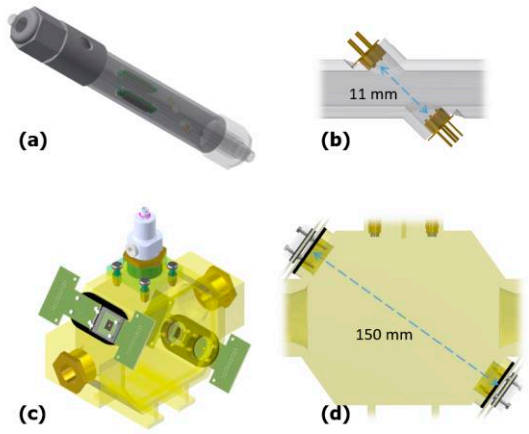

Fig. 1. Overview of the two MUT-based devices through which the speed of sound of the gas mixture is characterised. (a) CMUT device and a detail view (b) of the location of the transducers. (c) L-CMUT device and a detail view (d) of the location of the transducers.

The calibration of the speed of sound for different mixtures of hydrogen and natural gas is to be performed under controlled conditions. A mass flow controller (Brooks® 5851S) is used to regulate the mixture, whose composition is then monitored with a gas chromatograph (Thermo Scientific® TRACE 1310). A drum-type gas meter (Ritter® TG5/1) is implemented to control the flow that enters the devices. With this set-up, both the concentration of hydrogen and the volume flow can be adjusted in order to calibrate the ultrasonic devices.

Results

A preliminary test was performed to verify that the MUTs can operate under natural gas and pure hydrogen. The exposure to both gases was well withstood by both types of sensors, CMUT and L-CMUT. Figure 2 shows a representative measurement of the time of flight in a pilot L-CMUT set-up (a measurement chamber with 10 cm side length) under natural gas and hydrogen. It is evident how the speed of sound was increased when hydrogen was introduced. The results of the calibration under controlled conditions will be presented in the full version of this article.

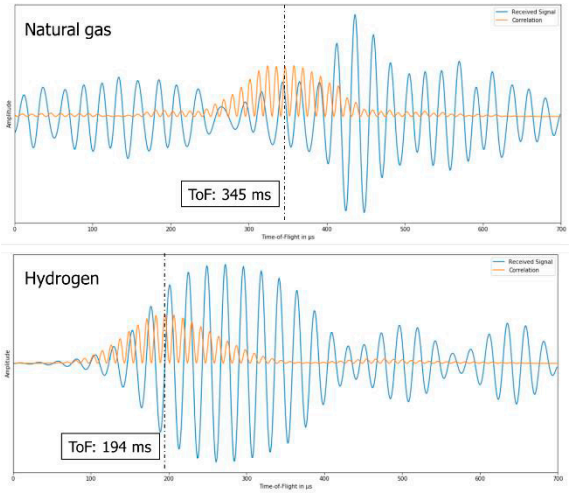

Fig. 2. Preliminary test with the L-CMUT transducers exposed to natural gas and hydrogen, observing a clear reduction of the time of flight.

References

[1] Die Nationale Wasserstoffstrategie, *Bundesministerium für Wirtschaft und Energie (BMWi)*, (2020)

[2] G. Müller-Syring, M. Henel, Wasserstofftoleranz der Erdgasinfrastruktur inklusive aller assoziierten Anlagen, *DVWG Deutscher Verein des Gas- und Wasserfaches e.V.*, G 1-02-12 (2014)

[3] P. Götze, P. Pietsch, M. Wiersig, Wasserstoffwirkung auf die Gaszählung, *Vulkan-Verlag GmbH,* 05398, (2021)

[4] Measurement of Gas by Multipath Ultrasonic Flow Meters, *American Gas Association*, AGA Report No. 9 (1998)

[5] H. Dixon, G. Greenwood, On the Velocity of Sound in Mixtures of Gases, *Proceedings of the Royal Society A,* Vol. 109, No. 752 (1925); doi: 10.1098/rspa.1925.0145

[6] G. Cerbe, B. Lendt, Grundlagen der Gastechnik (8 ed.), *Carl Hanser Verlag GmbH & Co. KG* (2016)

[7] S. Koch, U. Völz, N. Lange, *et al.*, Empowering Robots for Multimodal Tactile Gripping using Capacitive Micromachined Ultrasonic Transducers, *2021 Smart Systems Integration (SSI)* (2021); doi: 10.1109/SSI52265.2021.9467023

[8] J. M. Monsalve, A. Melnikov, M. Stolz, *et al.*, Proof of Concept of an Air-coupled Electrostatic Ultrasonic Transducer Based on Lateral Motion, *Sensors and Actuators A: Physical*, Vol. 345 (2022); doi: 10.1016/j.sna.2022.113813

DOI 10.5162/SMSI2023/A6.1

Magnetic Flow Metering with Optically Pumped Magnetometers (OPM)

Leonhard Schmieder[1], *Peter A. Koss*[1], *Frank Kühnemann*[1]
[1] *Fraunhofer IPM, Georges-Koehler-Allee 301, 79110 Freiburg i.Br., Germany*
Leonhard.Schmieder@IPM.Fraunhofer.de

Summary:
We present a novel non-invasive flow metering procedure where the flow velocity of a fluid is determined using polarized hydrogen nuclei of the fluid as magnetic markers. The metering procedure is based on a time-of-flight method in which magnetic information is applied to the liquid using a permanent magnet and a radiofrequency (RF) pulse. Downstream, the magnetic information is read-out by optically pumped magnetometers (OPM) by measuring the magnetic field produced by the hydrogen. We discuss results, application cases and challenges for industrial usability.

Keywords: Flow Metering, Magnetometry, OPM, ZULF-NMR, Time-Of-Flight Measurement

Introduction

Nuclear magnetic resonance (NMR) based flow metering has proven to be a viable tool for multiphase flow detection [1] with a range of industrial applications [1,2,3]. However, high-field NMR measuring devices are costly, show a high system integration effort and don't work with metallic pipes [4]. These aspects limit the methods applicability [5]. The recent commercialization of highly sensitive OPM [6] allowed us to develop a novel magnetic flow metering procedure in the zero-to-ultra-low-field (ZULF) regime [7]. The procedure allows flow detection through metal pipes, and, because the procedure does not require high magnetic fields, its implementation is effortless compared to the established high field NMR pendant [8]. The research presented is a continuation of the proof of principle for magnetic flow metering presented in [7]. As we continue to test the industrial potential of the procedure, we now analyze the viability of metering the flow of water flowing through industry standard steel pipes. In addition, a commercial electromagnetic flow meter is used to benchmark our flow metering results.

Materials and Methods

A schematic overview of the magnetic flow metering procedure is shown in Fig. 1. To determine the flow velocity of a fluid, polarized hydrogen atoms are magnetometrically monitored by OPM operating at nanotesla ambient field strength. The OPM have a sensitivity of <15 fT/Hz$^{0.5}$. In the presence of an external magnetic field, short resonance RF pulses change the fluids magnetic background, creating local magnetic marks. These marks are used as timestamps to perform a time-of-flight (TOF) measurement of the flow velocity.

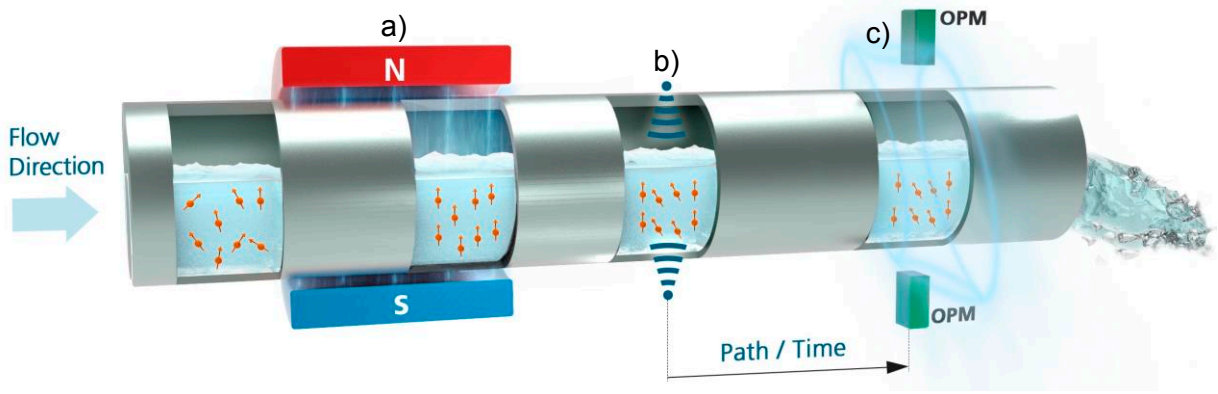

Fig. 1. Time-of-flight based measurement of a flow velocity. a) The fluid is magnetized by a strong magnet. b) A short and resonant RF pulse is applied to the fluid which creates a "notch" in a magnetized background. c) This notch is monitored by OPM downstream. The flow velocity is simply given by path over time where the timing information is given by the creation and detection of the notches.

To determine the flow velocity of the fluid we use the following relation:

$V=\Delta L/\Delta t$ (1),

Where ΔL is distance between the RF coil and the OPM. The timing information between pulse application and detecting its effect on the fluid polarization is given by Δt. The water is guided in a ½ inch stainless steel pipe. The results are compared to a commercial electromagnetic flow meter.

Results

The procedure was tested with tap water flowing at a constant velocity of 59 cm/s. The total measurement time was 10 min. Figure 2 shows an extract of the raw data used to determine Δt. The measurement results of the flow velocity detection are shown in Fig. 3. The average relative error of the magnetic flow metering apparatus is 0.5%. The commercial flowmeter showed an average relative error of 0.1%

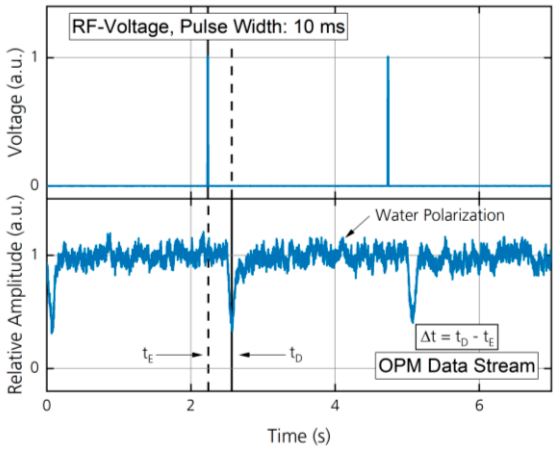

Fig. 2. Determination of Δt. The upper graph shows the voltage applied to the RF coil. Every 2.5 s a delta pulse is applied to the fluid. The lower graph displays the magnetic response of the fluid. After each pulse the water magnetic field is "marked". The relative position of pulse application and detection yields Δt.

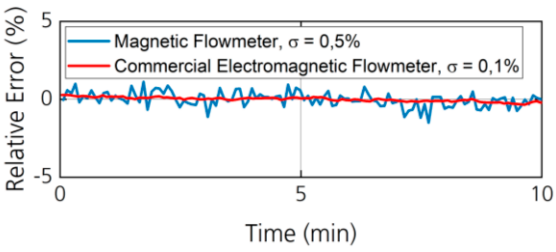

Fig. 3. Comparison of the flow velocity detected by the commercial electromagnetic flowmeter and the magnetic flow meter. The relative error of metering a constant flow velocity of 59 cm/s is plotted against the measurement time.

Conclusion and Outlook

The conducted experiment demonstrates a successful magnetic flow metering performed with industry standard steel pipes. The relative deviation of 0.5% when metering a flow rate of 59 cm/s with the current experimental setup shows the viability of magnetic flow metering in this configuration. Comparing the magnetic flowmeter's performance to the commercial flowmeter underlines this statement.

Further research on the magnetic flow metering procedure will address the signal preparation section. Potential use cases range from inline fill level detection to resolving a flow profile with limited two-phase resolution. As the procedure is also non-invasive, we aim for a clamp-on demonstrator.

Funding

This work was supported as a Fraunhofer LIGHTHOUSE PROJECT (QMag). In equal parts, this work was funded by the Ministry of Economic Affairs, Labour and Housing of the State of Baden-Württemberg, Germany.

References

[1] Thorn, R.; Johansen, G.A.; Hjertaker, B.T. Three-phase flow measurement in the petroleum industry. *Meas. Sci. Technol*. 2013, 24, 12003; doi: 10.1088/0957-0233/24/1/012003

[2] Davydov R, Davydov V, Myazin N, Dudkin V. The Multifunctional Nuclear Magnetic Flowmeter for Control to the Consumption and Condition of Coolant in Nuclear Reactors. Energies. 2022; 15(5):1748. https://doi.org/10.3390/en15051748

[3] Tessier, J.J.; Packer, K.J. The characterization of multiphase fluid transport in a porous solid by pulsed gradient stimulated echo nuclear magnetic resonance. Phys. Fluids 1998, 10, 75–85. https://doi.org/10.1063/1.869551

[4] O'Neill, K. T., Klotz, A., Stanwix, P. L., Fridjonsson, E. O., & Johns, M. L. (2017). Quantitative multiphase flow characterisation using an Earth's field NMR flow meter. Flow Measurement and Instrumentation, 58, 104-111.

[5] Falcone, G., Hewitt, G. F., Alimonti, C., & Harrison, B. (2002). Multiphase Flowmetering: Current Trends and Future Developments. JPT 54 (4): 77–84. SPE-74689-MS. DOI: 10.2118/74689-MS.

[6] Budker, Dmitry, and Michael Romalis. "Optical magnetometry." Nature physics 3.4 (2007): 227-234. https://doi.org/10.1038/nphys566

[7] Schmieder L, Koss PA, Lambrecht A, Kühnemann F. Noninvasive Magnetic-Marking-Based Flow Metering with Optically Pumped Magnetometers. Applied Sciences. 2022; 12(3):1275. https://doi.org/10.3390/app12031275

[8] Neugebauer, Reimund. Quantum Technologies. Stuttgart: Fraunhofer Verlag, 2022. Print.

DOI 10.5162/SMSI2023/A6.2

Quantum magnetometry as an enabling technology in the NewSpace domain

Stephan Busch[1], Peter A. Koss[2], Martin Rother[3], Monika Korte[3]

[1] Fraunhofer EMI, Ernst-Zermelo-Str. 4, 79104 Freiburg, Germany
[2] Fraunhofer IPM, Georges-Koehler-Allee 301, 79110 Freiburg, Germany
[3] Helmholz-Zentrum Potsdam GFZ, Albert-Einstein-Straße 42-46, 14473 Potsdam, Germany
stephan.busch@emi.fraunhofer.de

Summary: Quantum magnetometry advances rapidly, leading to compact sensors with high sensitivity and absolute accuracy without the need for cryogenic cooling which makes them a promising technology for the NewSpace domain. Small satellite technology provides economic access to space, and when launched in large constellations, they open new possibilities for global applications with high temporal and spatial resolution. This contribution shows benefits of emerging technologies for magnetic cleanliness verification and spaceborne geomagnetic observation.

Keywords: small satellites, geomagnetism, magnetic cleanliness

Introduction

Quantum magnetometry uses the connection between light and atomic systems to measure magnetic fields [1]. Specifically, optically pumped magnetometers (OPM), have seen significant advancements in terms of sensitivity and compactness, as cryogenic cooling is not required. Due to the atomic origin of their signals, OPM have an extremely high magnetic sensitivity and they can operate calibration-free. Thus, OPM are likely to become an enabling technology, in particular for small satellite applications in the NewSpace domain.

Small satellites are currently revolutionizing the space sector as they are significantly cheaper and easier to launch than traditional large satellites. Thus, they are popular for a variety of applications such as Earth observation, satellite communication, and scientific research. When launched in large constellations, they open new possibilities, with the potential to offer worldwide coverage with high temporal and spatial resolution.

The benefits of OPM technology might be exploited for two relevant applications:

1. Magnetic Cleanliness Verification
2. Spaceborne Geomagnetic Observation

Magnetic Cleanliness of Small Satellites

The use of small satellites in scientific and commercial applications presents new and unique challenges, particularly for the pointing requirements where small disturbance torques from residual magnetic dipoles interact with the magnetic field in low Earth orbits. The verification of magnetic cleanliness requirements is particularly challenging for small satellite systems, due to increased utilization of commercial-off-the-shelf (COTS) technology, as well as scaling and signal-to-noise ratio issues. Spatially distributed high accuracy magnetic field measurements can precisely characterize the spacecrafts magnetic properties which allows to compensate their effects on attitude control. For example, the qualification of the Fraunhofer small satellite ERNST [2], lead to the development of a cutting-edge test setup for precise characterization of small residual dipole moments [3].

Geomagnetic Observation on Constellations of Small Satellites

The use of OPM onboard resource-limited small satellites has several advantages as they can be extremely small and lightweight with comparably low power requirements, while the technology allows extremely sensitive measurements without the need for calibration. Considering emerging capabilities of commercial devices to measure also magnetic field vector components, economic small satellite constellations have the potential to provide high-resolution measurements of the Earth's magnetic field simultaneously at many locations and local times. This is particularly useful for studying the Earth's magnetic field in regions where it

is particularly complex, such as the polar regions or at very low orbital altitudes. This enables studies of geomagnetic field variations to infer about Earth's interior dynamics or space weather [4].

Meeting Scientific Requirements

In order to assess the potential of the current capabilities regarding small satellite technology and OPM sensors, scientific observation requirements were estimated in *Tab. 1*, which are based on observations described in [5] and [6]. All requirements for magnetic flux and attitude knowledge are given as goal specification and corresponding threshold values, describing minimal requirements to ensure valuable observations.

Tab. 1: Scientific observation requirements

Parameter	Goal	Threshold
B, Dyn. Range	±65000 nT	±65000 nT
B, Accuracy	1 nT	5 nT
B, Precision	0.1 nT	1 nT
|B|, Cadence	16 Hz	0.25 Hz
$B_{i=x,y,z}$, Cadence	128 Hz	0.25 Hz
Attitude Accuracy	1 arcsec	30 arcsec

A first analysis on current capabilities of OPM technology shows promising results. Scalar sensors with less than 100 fT/Hz$^{1/2}$ noise floor were built recently [6] and the extraction of vector information with an angular resolution better than 2 arcsec is also possible [7]. It is assumed, that miniaturized OPM which meet the scientific requirements will become commercially available within the next years. Especially mass, size, and power consumptions of commercially available devices qualify them as potential scientific instrument for miniature spacecrafts.

The power requirement of such a payload could likely be met by an efficient 1-2U cubesat platform as described in [8], optimized for the instrument operation such that any electrical currents would be minimized during measurements. Attitude knowledge better than 6 arcsec could be achieved by two orthogonal star trackers on a shared optical bench, mounted as close as possible to the OPM. This instrument assembly could easily be deployed from the satellite with a flexible boom as shown in Fig. 1.

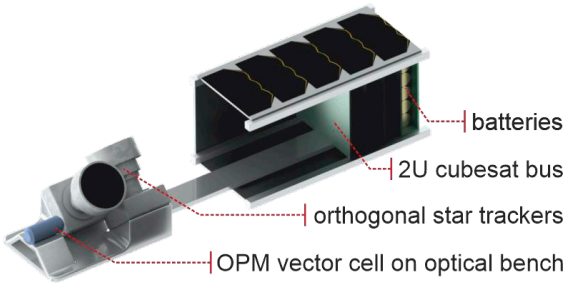

Fig. 1. A satellite concept with an OPM onboard.

Sufficient attitude stabilization to allow for acquisition of the star trackers could be realized by efficient magnetic attitude control [9], operated between the sampling periods. This way, the satellite would create minimal magnetic noise during measurements to meet the challenging magnetic cleanliness requirements.

Conclusions

Recent advances in the development of OPM provides great potential for future small satellite applications. On small satellites, they can be used for high quality platform magnetometer missions, covering many local times to support dedicated science missions [10], and they might be developed into full high-quality magnetic science missions in the future.

References

[1] C. L. Degen, F. Reinhard, und P. Cappellaro, „Quantum sensing“, *Rev. Mod. Phys.*, Bd. 89, Nr. 3, S. 035002, Juli 2017, doi: 10.1103/RevModPhys.89.035002.

[2] M. Schimmerohn *u. a.*, „ERNST: Demonstrating Advanced Infrared Detection from a 12U CubeSat“, in *SmallSat*, Logan UT, 2022, S. SSC22-WKVIII-03.

[3] S. Busch *u. a.*, „Magnetic Cleanliness Verification of Miniature Satellites for High Precision Pointing“, gehalten auf der 73rd International Astronautical Congress, Paris, France, 2022, S. IAC-22,B4,6A,x69376.

[4] Doornbos, E. *u. a.*, „Feasibility of using platform magnetometers to observe and detect Space Weather events“, ESA contract AO-i8735/16/NL/LF, 2018.

[5] L. Tøffner-Clausen, V. Lesur, N. Olsen, und C. C. Finlay, „In-flight scalar calibration and characterisation of the Swarm magnetometry package“, *Earth Planets Space*, Bd. 68, Nr. 1, Dez. 2016, doi: 10.1186/s40623-016-0501-6.

[6] V. Gerginov, M. Pomponio, und S. Knappe, „Scalar Magnetometry Below 100 fT/Hz $^{1/2}$ in a Microfabricated Cell“, *IEEE Sens. J.*, Bd. 20, Nr. 21, S. 12684–12690, Nov. 2020, doi: 10.1109/JSEN.2020.3002193.

[7] S. Afach *u. a.*, „Highly stable atomic vector magnetometer based on free spin precession“, *Opt. Express*, Bd. 23, Nr. 17, S. 22108, Aug. 2015, doi: 10.1364/OE.23.022108.

[8] S. Busch, *Robust, Flexible and Efficient Design for Miniature Satellite Systems*. Universität Würzburg, 2016. doi: 10.25972/OPUS-13652.

[9] S. Busch, P. Bangert, und K. Schilling, „Attitude control demonstration for pico-satellite formation flying by UWE-3“, in *Proceedings of the 4S-Symposium, Mallorca*, 2014.

[10] I. Michaelis, K. Styp-Rekowski, J. Rauberg, C. Stolle, und M. Korte, „Geomagnetic data from the GOCE satellite mission“, *Earth Planets Space*, Bd. 74, Nr. 1, S. 135, Sep. 2022, doi: 10.1186/s40623-022-01691-6.

DOI 10.5162/SMSI2023/A6.3

Quantum Magnetometry for Material Testing

Kerstin Thiemann[1], Andreas Blug[1], Alexander Bertz[1]
[1] Fraunhofer Institute for Physical Measurement Technologies IPM, 79110 Freiburg, Germany, kerstin.thiemann@ipm.fraunhofer.de

Summary:
Optically pumped zero-field magnetometers (OPM) are extremely sensitive to small variations in magnetic stray fields. However, their spatial resolution limits their application in non-destructive test-ing. With the help of flux guides these challenges can be overcome. This paper shows an example how the combination of OPM and flux guide can be used to measure magnetic stray fields of partial penetration weld seams in ferromagnetic steel sheets from the bottom side.

Keywords: Quantum sensing, non-destructive testing, magnetic testing, ferromagnetic materials

Introduction

Residual stresses are one of the major issues in welded parts since they could be detrimental to the integrity of components and structure [1]. Within ferromagnetic materials, these stresses alter the local magnetization and therefore the external magnetic field of the component [2, 3]. As magnetometers measure the average change of magnetization in a measurement volume, highly sensitive and commercially available quantum sensors like optically pumped magnetometers (OPM) measuring magnetic field B in a vapor cell are promising candidates for non-destructive testing with small measurement volumes or high spatial resolution [4].

In fatigue trials on mesoscale ferritic steel specimen with a loaded volume of about 0.1 mm³, the external magnetic field changed by about 5 nT when mechanical stress was altered from negative to positive yield stress [5, 6]. In principle, the sensitivity of the sensor of 15 fT/√Hz [7] would be sufficient to measure stress concentrations prior to crack initiation. However, the measurement volume inside the component and therefore the lateral spatial resolution at the surface of OPM sensors are limited by the physical distance between component surface and the vapor cell inside the sensor to several millimeters. To overcome this problem, Kim and Savukov used flux guides from Mn-based ferrites to measure the lateral component of the magnetic field with high spatial resolution [8].

In this paper, we use a different flux guide geometry measuring the normal component of the external magnetic field. This geometry should be appropriate for NDT of ferromagnetic components with high relative permeability μ_r as their magnetic stray field is refracted towards the normal at the surface. At the example of two neighboring weld seams, we demonstrate the improvement of the lateral spatial resolution compared to a OPM sensor only.

Material and Methods

A sketch of the experimental setup is shown in Fig. 1. A conically shaped flux guide (relative permeability μ_r = 2300) is attached to the OPM with the aid of a 3D printed housing and placed into a magnetic shielding via the top opening. The horizontal axis is externally motorized and carries the sample. All components are placed in such a way that the point of measurement is in the center of the magnetic shielding and the sample moves along the flux guide.

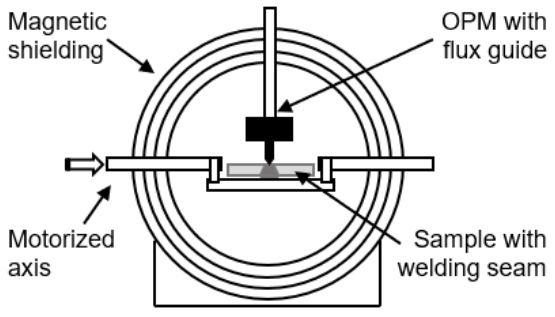

Fig. 1. Sketch of setup: inside the magnetic shielding on the vertical axis a OPM is placed where a flux guide can be attached. The horizontal axis is externally motorized and holds the sample.

The sample shown in Fig. 2 consists of two partial penetration welding seams which are 4 mm apart, attaching a second layer of ferromagnetic steel [9]. To show the effects of the flux guide, measurements are performed with just the OPM and the with the OPM flux guide combination. The sample is moved with

0.1 mm/s and the sampling frequency of the OPM is 200 Hz. The distance d between sample surface and point of measurement are kept as small as possible (d < 1 mm, excluding the distance from the housing to the center of the vapor cell within the OPM).

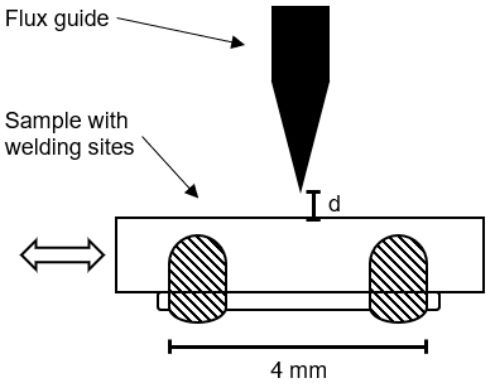

Fig. 2. Detailed sketch of the sample with two partial penetration welding seams spaced 4 mm apart. The sample is moved in a distance d along flux guide to measure magnetic stray fields from the bottom side.

Results

The comparison between the measurements with only the sensor (blue) and the combination of OPM and flux guide (red) is shown in Fig. 3. The sample has a magnetic gradient across the scanned line. However, the location of the welding sites (indicated in grey pattern) are only clearly visible in the measurements including the flux guide.

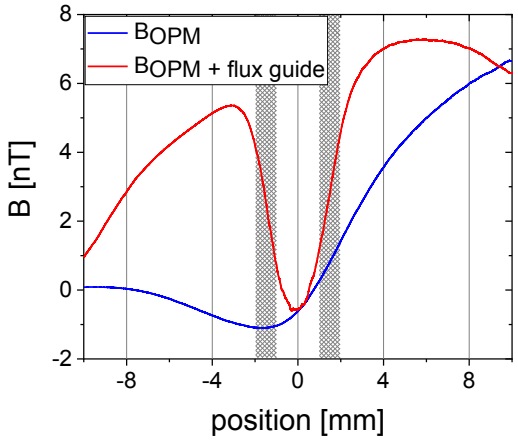

Fig. 3. Comparison of the two measurements using OPM only (blue) and using the OPM with the flux guide attached (red). The changes of the magnetic field (B) on the surface of the sample across a welding site (grey patterned).

Conclusion and outlook

This works illustrates that the use of a flux guide significantly enhances the spatial resolution of OPM. The spatial resolution is very dependent on the distance between the vapor cell inside the OPM sensor and the measurement site. Implementing a flux guide simplifies to control spatial resolution and measurement volume in the sample. In this respect, significant progress by optimizing the geometry of the flux guide is expected.

Further research on the geometry, material and hysteresis behavior of flux guides will provide more insight into their benefit. Potentially providing a high spatial resolution without sacrificing sensitivity. Allowing to perform accurate and localized analysis for material testing, including local stress concentrations and defects.

Acknowledgements

This work was supported as a Fraunhofer LIGHTHOUSE PROJECT (QMag). We acknowledge financial support from the Ministry of Economic Affairs, Labor and Housing of the State of Baden-Württemberg, Germany. Thanks also to Ralph Sperling from Fraunhofer IMM for manufacturing the flux guides.

References

[1] F. Giudice and A. Sili, “A theoretical approach to the residual stress assessment based on thermal field evaluation in laser beam welding,” Int J Adv Manuf Technol, vol. 123, 7-8, pp. 2793 (2022).

[2] D. C. Jiles, “Theory of the magnetomechanical effect,” J. Phys. D: Appl. Phys, no. 28, p. 1537 (1995).

[3] M. Roskosz and M. Bieniek, “Evaluation of residual stress in ferromagnetic steels based on residual magnetic field measurements,” NDT & E International, vol. 45, no. 1, pp. 55 (2012).

[4] M. W. Mitchell and S. Palacios Alvarez, “Colloquium: Quantum limits to the energy resolution of magnetic field sensors,” Rev. Mod. Phys., vol. 92, no. 2 (2020).

[5] P. Koss, A. R. Durmaz, A. Blug, G. Laskin, O. S. Pawar, K. Thiemann, et al., “Optically Pumped Magnetometer Measuring Fatigue-Induced Damage in Steel”, *Applied Sciences* 12 (3), pp. 1329 (2022).

[6] K. Thiemann, A. Blug, P. Koss, A. Durmaz, G. Laskin, A. Bertz, F. Kühnemann, T. Straub, “Using optically pumped magnetometers to identify initial damage in bulk material during fatigue testing,” *Proc. SPIE 12133, Quantum Technologies 2022*, 121330F (2022).

[7] Gen-2 Zero-Field Magnetometer (QZFM). QuSpin, Inc., 331 South 104th Street, Suite 130, Louisville, CO 80027, USA. QuSpin.com (20.01.2023)

[8] Y.J. Kim, I. Savukov, “Ultra-sensitive Magnetic Microscopy with an Optically Pumped Magnetometer,” *Scientific reports* 6, 24773 (2016).

[9] A. Blug, F. Abt, L. Nicolosi, A. Heider, R. Weber, D. Carl, et al. “The full penetration hole as a stochastic process: controlling penetration depth in keyhole laser-welding processes,” *Appl. Phys. B* 108 (1), pp. 97 (2012).

DOI 10.5162/SMSI2023/A6.4

Diamond-Based Magnetic Widefield-Microscopy of Domain Patterns in Electric Steel

Simon Philipp[1], Niklas Mathes[2], Marvin Feuerhelm[1], Ali Riza Durmaz[1], Shayan Deldar[3], Ivan Soldatov[3], , Rudolf Schäfer[3], Xavier Vidal[2], Thomas Straub[1]
[1] Fraunhofer Institute for Mechanics of Materials IWM, Wöhlerstraße 11, 79108 Freiburg, Germany,
[2] Fraunhofer Institute for Applied Solid State Physics IAF, Tullastraße 72, 79108 Freiburg, Germany
[3] Leibnitz institute for Solid State and Materials Research IFW, Helmholtzstraße 20, 01069 Dresden, Germany
simon.philipp@iwm.fraunhofer.de

Summary
In this work, we demonstrate magnetic stray field imaging on a grain-oriented FeSi electric steel micro sample after cyclic loading, using a home-built NV widefield microscope. The image is compared with a corresponding magnetic domain image of the same sample area acquired via Magneto Optical Kerr Effect (MOKE) microscopy.

Keywords: NV center, Widefield Microscopy, Magnetic Imaging, Non-Destructive Testing, Quantum Magnetometry

Introduction

Microscopic testing of magnetic materials has been utilized for the measurement of a variety of relevant properties for material sciences and engineering, some of which being residual stress, microstructure, or hardness. Recently, it has been shown [1] that measuring the stray field induced from the the inverse magneto-strictive, or Villari effect [2] can potentially be exploited to retrieve a magnetic signature of fatigue and early-stage crack initiation in micro-mechanical samples.
To find a magnetic signature in these measurements, it is essential to understand the evolution of the magnetic state in the sample, based on the structural and mechanical behavior of the material under different loading conditions. One route towards this, is by imaging the magnetic domain patterns, as can be done by Magneto-Optical Kerr Effect (MOKE) microscopy. Despite being an established method, it has the drawback of only providing information on the magnetization but not on the magnetic stray field [3].
Magnetic sensing techniques that utilize the nitrogen-vacancy (NV) center in diamond have been established in a wide variety of research, ranging from Bio- and solid-state magnetism over electronics to chemical analysis for magnetic, electric, thermal and strain sensing [4]. NV-center-based magnetic widefield microscopy, involves a dense layer of NV-centers rather than an individual one. In this way, a magnetic stray field distribution can be imaged over a wide area of hundreds of micrometers in only a few minutes of time, while still maintaining a diffraction optics spatial resolution. In this work, we demonstrate magnetic stray field imaging on a FeSi electric steel micro sample using a home-built NV widefield microscope and compare the results with a corresponding magnetic domain image acquired prior and in-situ during cyclic mechanical loading of the sample via MOKE microscopy.

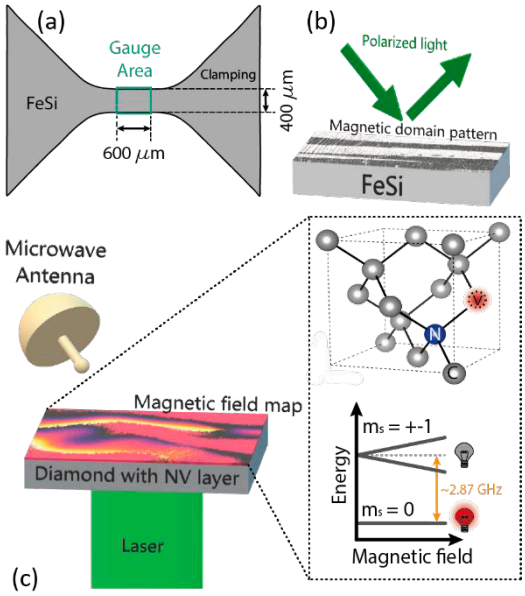

Fig. 1. (a) Schematic of a micro sample. The gauge area is highlighted (b) Schematic of a MOKE measurement. (c) Schematic of the widefield-NV setup. The inset shows the crystal structure and ground state energy levels of a single NV.

Experiment

The micro samples were cut from a single grain of grain oriented FeSi electric steel using wire erosion to minimize heat-affected zones along the edges. The specimens have a thickness of 220 µm, with a gauge section of 600x400 µm² which widens on both ends into a clamping area. A schematic of a micro sample with the geometry used here is shown in Fig. 1 (a). For the in-situ MOKE measurements, as schematically described in Fig. 1 (b), a micro-tensile apparatus, integrated into a Kerr microscope, was used. On the sample shown here, we performed a fatigue test in the elastic regime with a stress amplitude of a_S = 195 MPa and a load ratio of R = 0.1 at a frequency of f = 30 Hz. After that, the sample showed severe plastic deformation and the image in Fig. 2 (c) was taken at 0 MPa after 1651 cycles.

Wide-field NV microscopy was performed utilizing a dense layer of nitrogen-vacancy (NV) centers. The nitrogen doped diamond was homegrown by chemical vapor deposition (CVD) (Fig. 1 (c)). The sample was later electron irradiated and finally the NV-centers were formed in a thermal annealing procedure. Initialization and readout of the of the NV-center's spin state is performed optically with a green laser at λ = 532 nm. The magnetic resonance is obtained by tuning the frequency of a microwave irradiation from a nearby antenna. The red fluorescence is detected with a CMOS camera. This, together with the spin-dependent photo luminescence of the NV center allows for the measurement of the magnetic field from the field-dependent spin splitting of the m_s = ±1 states (see inset in Fig. 1 (c) and Fig. 2 (a)) via optically detected magnetic resonance (ODMR) spectroscopy.

Results

Fig. 2 (a) shows an averaged ODMR spectrum of multiple NV centers, as recorded for each pixel of the acquired image. The splitting of the dips is directly proportional to the magnetic field and is plotted for each pixel in (b). Fig. 2 (b) and (c) show the same area of a plastically deformed FeSi micro sample. The map of the ODMR splitting in (b) has a resolution of around 1 µm and took around 20 minutes recording time for an image size of 250x250 µm². The splitting is proportional to the distribution of the magnetic field generated due to the effective magnetic anisotropy of the sample, which is mainly a superposition of the crystal anisotropy of the material and the shape of the sample in the investigated area. The fatigue process and the plastic deformation of the material induce defects like dislocations,

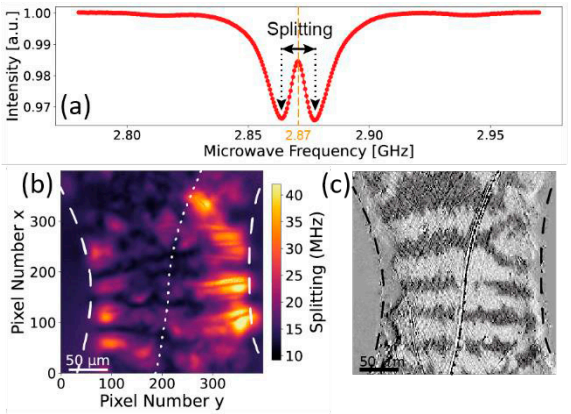

Fig. 2. (a) Averaged ODMR spectrum of the NV layer at one pixel. (b) Map of the magnetic field dependent splitting of the ODMR signal. (c) MOKE image of the same area as in (b).

slip and shear bands, inclusions, or precipitations, which can act as pinning cites for the magnetic domains [5]. This potentially causes the complex domain pattern displayed in (c), as recorded by MOKE microscopy. Comparison of the two images shows, that the magnetic field distribution in (b) and the domain pattern in (c) can be correlated reasonably well with each other. The lines in the images serve as guides to the eye and highlight characteristic features of the sample, such as the edges (dashed) and a scratch in the center (dotted), which can clearly be identified in both images. In conclusion, we have shown that NV-center based wide-field magnetometry as a quantum technology, can potentially be used in materials testing for imaging of the magnetic field distribution in micro samples. The NV map is clearly related to the underlying domain pattern imaged by MOKE microscopy but adds additional information about the magnetic stray field. This could be of advantage to find a magnetic fingerprint for early state fatigue damage in ferromagnetic materials.

[1] P. A. Koss *et al.*, Optically Pumped Magnetometer Measuring Fatigue-Induced Damage in Steel, Applied Sciences **12**, 1329 (2022). DOI: 10.3390/app12031329

[2] G. Riesgo *et al.*, Villari Effect at Low Strain in Magnetoactive Materials, Materials **13** (2020). DOI: 10.3390/ma13112472

[3] I. V. Soldatov and R. Schäfer, Selective sensitivity in Kerr microscopy, The Review of scientific instruments **88**, 73701 (2017). DOI: 10.1063/1.4991820

[4] S. C. Scholten *et al.*, Journal of Applied Physics **130**, 150902 (2021).

[5] A. Seeger, H. Kronmüller, H. Rieger, and H. Träuble, Effect of Lattice Defects on the Magnetization Curve of Ferromagnets, Journal of Applied Physics **35**, 740 (1964). DOI: 10.1063/1.1713460

DOI 10.5162/SMSI2023/A7.1

What did the current SI do to the uncertainties in measurement of defining constants?

Raghu N. Kacker[1]
[1] *National Institute of Standards and Technology, Gaithersburg, MD 20899, USA,*
raghu.kacker@nist.gov

Summary:
We present a brief axiomatic description of the current SI. A set of seven defining fundamental constants were assigned an exact value in the SI based on their best-known quantity values in terms of the previous SI units. The defining constants so established redefine the SI base and other units. The previous uncertainties in measurement of the defining constants did not evaporate. They were shifted to the physical realizations of the SI units of related quantities.

Keywords: Avogadro number, Kilogram, Planck constant, Uncertainty, Unit of measurement

Introduction

The current SI (ninth edition, dated 2019) has established new definitions for the SI base units by fixing the numerical values for a chosen set of seven fundamental or technical constants of nature referred to as the defining constants. The base units of the SI are still second (s), meter (m), kilogram (kg), ampere (A), kelvin (K), mole (mol), and candela (cd). The seven defining constants chosen to redefine the base units are the hyperfine transition frequency of the 133-cesium atom ($\Delta\nu_{Cs}$), the speed of light in vacuum (c), the Planck constant (h), the elementary charge (e), the Boltzmann constant (k), the Avogadro constant (N_A), and the luminous efficacy of monochromatic radiation of frequency 540×10^{12} Hz (K_{cd}). The best-known quantity values in terms of the previous SI units were assigned to the defining constants. Informally, the measurement uncertainties associated with the assigned quantity values were zeroed. The quantity values of the defining constants so established redefine the SI units [1].

In the SI, a metrological expression for a quantity value Q is a product of a number {Q} and a unit of measurement [Q]. That is, Q = {Q} [Q]. The quantity is compared with a physical realization of the unit [Q] to determine the number {Q}. The number {Q} is uncertain due to imperfections of measurement (including incomplete description of the quantity measured). For most applications, this uncertainty is much larger than the uncertainty in the physical realization of the SI units.

In the current SI, seven defining constants were chosen as the quantity Q*. A suitable number {Q} was determined for each defining constant. Then the ratio Q*/{Q} was set as the revised unit [Q] for that defining constant [1]. The suitable number for each defining constant was determined such that the current SI units are backward compatible with the previous SI units.

An SI unit of measurement must be (1) a constant, (2) backward compatible with the previous SI units to maintain continuity, (3) and convenient for physical realization to develop measurement standards. The backward compatibility to previous units subsumes (i) that the units are of practical size, and (ii) that the SI is an interconnected system of coherent units. Physical realizability was an important consideration in the choice of defining constants. The chosen defining constants allow for practical realizations with smallest uncertainties. In principle, defining constants are available to everyone and at all times. A link to special artifacts is not needed [1].

The defining constants are unique invariant quantities. So, a defining constant can, in principle, be used as a unit of measurement for quantities of the same kind. As potential units, the defining constants are either too small or too large for practical use. So, a practical unit of measurement [Q] would be proportional to the defining constant Q*; that is [Q] = κ Q* for some constant of proportionality κ. A fundamental requirement is that a revised definition must be backward compatible with the previous SI units. Suppose {Q} is the numerical part of the established value of a defining constant Q* in terms

of the previous SI unit. Consider the following definition of a unit of measurement

$$[Q] = \{Q\}^{-1}\, Q^* \qquad (1)$$

where $\{Q\}^{-1}$ is the constant of proportionality. The equation (1) can be written as

$$Q^* = \{Q\}\,[Q] \qquad (2)$$

The equation (2) is profound for it states that the magnitude of the SI unit [Q] is such that the established value {Q} [Q] is exactly equal to the defining constant Q* (quantity). This is the foundation of the current SI based on the established values of seven defining constants. Per equation (1), the SI units based on defining constants are unique invariant quantities (constants). Per equation (2), the SI units based on the defining constants are backward compatible with the previous SI units. Table 1 is reproduced from the current (ninth) edition of the SI Brochure [1].

Table 1. The seven defining constants of the SI and the seven corresponding units they define.

Defining constant	Symbol	Numerical value	Unit
hyperfine transition frequency of Cs	$\Delta\nu_{Cs}$	9 192 631 770	Hz
speed of light in vacuum	c	299 792 458	m s^{-1}
Planck constant	h	6.626 070 15 × 10^{-34}	J s
elementary charge	e	1.602 176 634 × 10^{-19}	C
Boltzmann constant	k	1.380 649 × 10^{-23}	J K^{-1}
Avogadro constant	N_A	6.022 140 76 × 10^{23}	mol^{-1}
luminous efficacy	K_{cd}	683	lm W^{-1}

The symbols Hz, J, C, lm, and W represent the units hertz, joule, coulomb, lumen, and watt, which are defined as 1 Hz = 1 s^{-1}, 1 J = 1 kg m^2 s^{-2}, 1 C = 1 A s, 1 lm = 1 cd m^2 m^{-2}, and 1 W = 1 kg m^2 s^{-3}, respectively. The column 1 lists the names of the defining constants (quantities). The symbols in column 2 are for both the defining constants and their established values. The products of the numerical values in column 3 and the corresponding units in column 4 are the established values of the defining constants. The revised SI units are of such magnitude that the defining constants are exactly equal to their established values. The defining constants divided by their numerical values are the current definitions of their SI units. These SI units of defining constants are algebraically solved to obtain the current definitions of the SI base units (s, m, kg, A, K, and cd), and the other SI units given in the current SI Brochure [1]. The hyperfine transition frequency of the 133-cesium atom, the speed of light in vacuum, and the luminous efficacy were established in 1967, 1975, and 1979, respectively [1]. Thus, the world was already using the definitions of the second, the meter, and the candela that were based on establishing the values of defining constants. The current SI updated earlier definitions.

Previous uncertainties in measurement of defining constants were shifted to physical realizations of the units of related quantities

The SI is an inter-connected system of units. When the uncertainty associated with one quantity value changes, the uncertainties in the related quantity values also change. The zeroing of uncertainties in measurement of defining constants to establish their values had the consequence of shifting those uncertainties to physical realizations of the units of related quantities [2]. The 2017 recommended value of the Planck constant h, for example, had a relative standard uncertainty of 1 × 10^{-8}. In the revised SI, this uncertainty was shifted to the mass of the international prototype of kilogram (IPK). As of 2019, the mass of the IPK has quantity value 1 kg with a relative standard uncertainty of 1 × 10^{-8} [1]. The 2017 recommended value of the molar Planck constant $N_A h$ had a relative standard uncertainty of 4.5 × 10^{-10}. In the current SI, this uncertainty was shifted to the molar mass of carbon 12, $M(^{12}C)$. As of 2019, $M(^{12}C)$ has quantity value 0.012 kg/mol with a relative standard uncertainty of 4.5 × 10^{-10} [1]. The relative standard uncertainty associated with the 2017 recommended value of the Boltzmann constant k was close to 3.7 × 10^{-7}. This uncertainty was shifted to the Triple point of water, T_{TPW}. As of 2019, T_{TPW} has quantity value 273.16 K with a relative standard uncertainty of 3.7 × 10^{-7} [1]. In the future these uncertainties will be determined experimentally.

Disclaimer These findings, and conclusions do not necessarily reflect the views or policies of NIST or the United States Government.

Acknowledgment Thanks to Eite Tiesinga, Richard Steiner, and David Flater for their suggestions. Thanks to Ron Boisvert, and Tim Burns for their support, and to Klaus Sommer for his encouragement.

References

[1] The International System of Units (SI), 9th edition (2019); https://www.bipm.org/utils/common/pdf/si-brochure/SI-Brochure-9-EN.pdf

[2] CODATA recommended values of the fundamental physical constants: 2018; https://doi.org/10.1103/RevModPhys.93.025010

DOI 10.5162/SMSI2023/A7.2

Title: **The hunt for mineral resources with quantum magnetometers**

Authors: Ronny Stolz[1,2], Markus Schiffler[1], Michael Becken[3], Anneke Thiede[3], Michael Schneider[4], Glenn Chubak[5], Ockert Terblanche[6]

Affiliations:

1 Dept. Quantum Systems, Leibniz Institute of Photonic Technology, Albert-Einstein-Str. 9, D-07745 Jena, Germany

2 Advanced Electromagnetics Group, Technische Universitaet Ilmenau, Helmholtzplatz 2, D- 98684 Ilmenau

3 Institute of Geophysics, University of Münster, Corrensstr. 24, D-48149 Münster, Germany

4 supracon AG, An der Lehmgrube 11, D-07751 Jena, Germany

5 DIAS Geophysical Ltd., 2131 Airport Drive, Saskatoon, SK, Canada, S7L 7E1

6 AngloGold Ashanti, 140 St Georges Terrace, Perth, Western Australia, 6010

Abstract Quantum sensing provides advanced technologies which significantly improves sensitivity and accuracy for sensing changes of motion, gravity, electric and magnetic field. Therein, quantum sensors for the detection of magnetic fields, so-called quantum magnetometers, are one of the most promising technological realizations.

In this work, we firstly will provide an overview on methods in geophysical exploration. There are various methods in exploration which would benefit from vastly improved magnetic field sensing technologies.

Then attention will be paid to state-of-the-art quantum magnetometers usable for this purpose. We will introduce recent developments on Superconducting Quantum Interference Devices, so called SQUID, based sensors and optically pumped magnetometers, so-called OPMs, as specific implementations of a quantum magnetometer.

These sensors have already today impact in mineral exploration. We will introduce some SQUID instrument implementations, related field operation demonstrations and case studies. For instance, airborne vector magnetometer devices with ultra-low noise of < 10 $fT/Hz^{1/2}$ and ultra-high dynamic range of real > 32 bit as well as a full tensor magnetic gradiometer with ultra-low gradient noise of < 100 $fT/(m \times Hz^{1/2})$ were already realized. Successful case studies will be presented and discussed.

Ground-based receivers for the transient electromagnetic method are already a mature technology being in commercial use for more than a decade. These quantum magnetometers led to a number of discoveries of conductive ore bodies. Also, a related case study will be presented.

Since there exist expectations about their use in geophysics, this work will provide a brief overview on the various developing quantum technologies and their individual state of the art for implementing quantum magnetometers.

Finally, future prospects of using quantum magnetometers in geophysical exploration and other applications will be discussed.

Keywords: Mineral exploration, Magnetics, Electromagnetic methods, Magnetic method, Quantum sensors, SQUID, OPM

DOI 10.5162/SMSI2023/A7.3

New developments for the programmable quantum current generator

Sophie Djordjevic[1], Wilfrid Poirier[1]
[1]Laboratoire national de métrologie et d'essais, 29 avenue Roger Hennequin, 78197 Trappes, France, sophie.djordjevic@lne.fr

Summary:
This paper describes the latest improvements of the programmable quantum current generator. Here we focus on the fabrication of the new cryogenic current comparator, which will allow implementing the triple connection between the quantum Hall resistance standard and the programmable Josephson voltage standard, necessary step to reduce the correction on the generated current from few parts in 10^7 to few parts in 10^{10}. Other on-going developments towards a laboratory dedicated to a new ampere traceability are also introduced.

Keywords: Current measurements, metrology, quantum standards, cryogenic current comparator.

Introduction

The first implementation of the PQCG demonstrated that the ampere could be realized from the elementary charge, e, with a 10^{-8} relative uncertainty in the mA range down to the µA range [1]. The high accuracy is obtained by applying Ohm's law in a circuit connecting directly a quantum Hall resistance standard (QHRS) and a programmable Josephson voltage standard (PJVS) with a multiple connection scheme and by amplifying the quantized current with a cryogenic current comparator (CCC). Our next goal is to develop a more compact and even more accurate version of the PQCG in a dedicated laboratory. We already demonstrated noise improvements of the set-up and reported in a comparison with the Ultrastable Low-Noise Current Amplifier (ULCA) from PTB at 50 µA [2]. An important target is the development of a new CCC, which allows implementing the triple connection of the QHRS to the PJVS in order to reduce to a negligible value the cable correction, which was amounting to a few 10^{-7} in the double connection scheme previously implemented. Hence the goal is to generate a quantum current simply given by GN_Jef_J , where G is the gain of the CCC, and N_J and f_J are the number of Josephson junctions and the Josephson frequency respectively. This important step will not only reduce the Type B uncertainty budget to a few parts in 10^9 but also results into a significant simplification of the system by avoiding the measurement of the cable resistances. After a detailed description of the new CCC, we will give some details about the other on-going developments towards a more compact version of the PQCG and we will discuss the advantage to use the PQCG to calibrate resistances.

Design of the new CCC

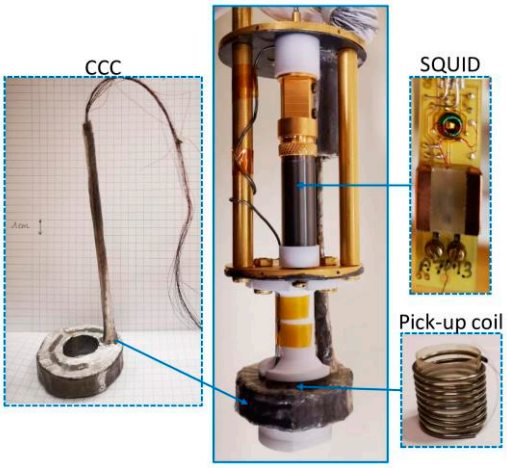

Fig.1: CCC mounted in the cryoprobe.

The new CCC is based on an architecture similar to the one presented in [3] but with 5 additional windings. The total number of turns is 8789. The CCC is made of 20 windings of 1, 1, 1, 2, 2, 16, 16, 16, 32, 64, 128, 128, 160, 160, 465, 465, 1600, 1600, 2065 and 2065 turns. The triple connection will be possible for the windings of 1, 2, 16, 128, 160, 465 and 1600 turns. The possibility to connect the circuit containing the PJVS and the QHRS to three windings of 465 turns will allow enhancing in an optimum way the signal-to-noise ratio while preventing the Johnson-Nyquist noise of the QHRS at 1.3 K from becoming the dominant contribution [2]. The windings were glued with a two-component epoxy adhesive. Each winding

is made of insulated 80-µm-diameter Cu clad NbTi superconducting wire. We used 150-µm-thick Pb foils and Pb/Sn/Bi superconducting solder with a low melting temperature to realize the toroidal shielding around the windings. To prevent flux leakage, the toroidal shield is made of three electrically insulated turns corresponding to two overlap turns. The inner and outer diameter of the toroidal shield are 19 mm and 47 mm respectively. The chimney is about 125 mm high. The CCC is fixed by a nut on a screw made of machinable glass ceramic (Macor) at the bottom of the cryogenic probe. The CCC is enclosed in a first 0.5-mm-thick Pb superconducting cylindrical screen with an inner diameter of 57 mm and a height of 83 mm. The lead foil is maintained mechanically into a gold plated brass cylinder. Based on the geometries of the CCC and of the superconducting shield, the calculated effective inductance of the CCC is 14.5 nH.

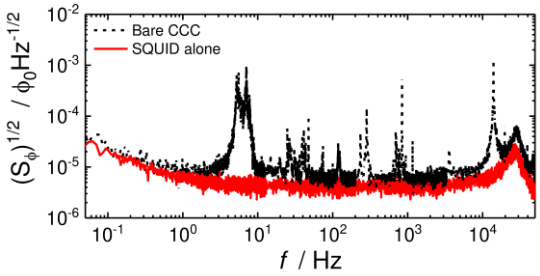

Fig.2: Noise spectrum of the bare CCC and the SQUID alone.

Fig.1 shows the mounting of the CCC into a cryoprobe, which was designed to reduce the mechanical vibrations leading to electrical noise in measurements. It is equipped with a Quantum Design Inc. DC SQUID, which has a white noise level of 3 $\mu\phi_0 Hz^{-1/2}$, where ϕ_0 is the superconducting flux quantum, and a 1/*f* corner frequency f_c = 0.3 Hz. The SQUID is placed in a separate superconducting Nb shield. It is coupled to the CCC via a superconducting flux transformer composed of a wire wound sensing coil placed as close as possible to the inner surface of the CCC. The coil is made of a 100-µm diameter NbTi wire inserted in a lead tube to increase the effective radius of the wire. The coupling is obtained with a sensing coil of N_p = 9 turns, leading to a measured sensitivity of 8 µA.turns/ϕ_0. Forty copper alloy wires with a stainless steel shield are connected to the CCC wires on a PTFE plate in the helium bath. Two concentric magnetic shields are added: a Pb superconducting shield enclosing the SQUID and the CCC stages and a Cryoperm shield surrounding the whole. The expected overall magnetic attenuation is about 202 dB. The noise spectrum of the CCC and of the SQUID alone are presented in Fig.2. The base noise level of the CCC amounts only to 7 $\mu\phi_0 Hz^{-1/2}$, slightly above the base SQUID level, which proves the shielding efficiency. At frequencies below f_c, one can observe the dominant contribution of the 1/*f* SQUID noise.

Other developments and conclusion

The developments for the new version of the PQCG are done in a new laboratory dedicated to the metrology of the ampere. Two pits 3 m apart are dedicated to the QHRS on one side and to the CCC or two PJVS systems on the other side. The latter hosts a cryogenic system based on a pulse tube refrigerator, which has been shielded with a 3 mm pure iron screen reducing the magnetic field to less than 20 µT when the QHRS is operated at 10 T. A new external voltage controlled current source has been developed delivering currents from the nA range to the mA range.

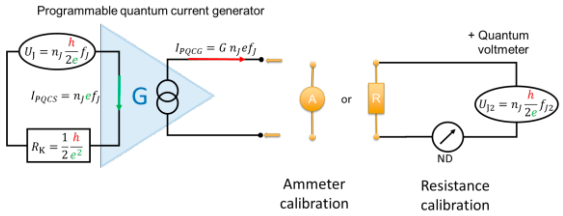

Fig.3: Calibration set-up for the calibration of currents or resistances using the PQCG.

One of our objectives is to investigate the possibility of using the PQCG for the direct calibration of resistances in conjunction with a quantum voltmeter (PJVS associated with a voltage null detector) as described by the sketch of Fig.3. We expect reaching relative uncertainties down to a few 10^{-9} in a more flexible way than with resistance comparison bridges: no need of transfer resistance, wide range of resistance values from 1 Ω to 1 GΩ, more flexibility on the value of the measurement current, reduction of the effect of the current leakage owing to the low impedance of the PJVS. Hence, the PQCG realizing the ampere would constitute the skeleton of a future quantum calibrator.

References

[1] J. Brun-Picard *et al*, Practical quantum realization of the ampere from the elementary charge", *Physical Review X*, 6, 041051 (2016). Doi:10.1103/PhysRevX.6.041051

[2] S. Djordjevic *et al,* Improvements of the programmable quantum current generator for better traceability of electrical current measurements, *Metrologia*, 58, 045005 (2021). Doi: 0.1088/1681-7575/ac0503

[3] W. Poirier *et al*, A Resistance Bridge based on a cryogenic current comparator achieving Sub-10^{-10} measurement uncertainties, *IEEE Transactions on Instrumentation and Measurement*, 70, 1000314 (2021). Doi :10.1109/TIM.2020.3010111

DOI 10.5162/SMSI2023/A7.4

Bias-Tee quantum current sensor with temperature tracking based on modulated cw-ODMR with NV centers

Jens Pogorzelski, Jonas Homrighausen, Ludwig Horsthemke, Dennis Stiegekötter, Lara Lindloge, Julian Teuber, Markus Gregor, Peter Glösekötter
FH Münster – University of Applied Sciences, Stegerwaldstraße 39, 48565 Steinfurt, Germany
pogorzelski.jens@fh-muenster.de

Summary:
A new current measurement setup is presented, which based on randomly orientated NV ensembles in diamonds with a diameter of 150µm. Diamonds are applied directly on a printed circuit board (PCB) track which is used as a Bias-Tee to combine DC current and microwave (MW) excitation. By scanning the MW frequency, characteristic dips in fluorescence intensity are used to deduce DC current and temperature in a measurement range of 2 A to 8 A and 300 K to 380 K.

Keywords: NV center, room temperature, quantum sensor, current sensor, temperature tracking

Background, Motivation and Objective

Quantum magnetometry based on optically detected magnetic resonance (ODMR) of nitrogen vacancy centers (NV-Centers) in nano- or micro-diamonds is a promising technology for precise and small magnetic field sensors and resulting from this current sensors [1]. Nevertheless, few practical approaches have been pursued so far to translate this technology into viable approaches to concrete current sensing setups [1][2].

Here, we propose a new measurement setup based on the idea of a Bias-Tee that combines a DC current and the MW needed to drive the quantum states of the NV center on one simple printed circuit board (PCB) track with only a few surface mounted device (SMD) components and randomly orientated 150 µm diamonds (Adámas Nanotechnologies). Additionally the specific shifts of the zero field splitting (ZFS) could be used to track the temperature of the PCB track. The DC current can be measured directly or used after calibration to bias an external magnetic field. The use of standard components and randomly oriented diamonds makes the setup cost effective and mechanically simple to assemble compared to other sensing setups [1][2].

Description of the New Method or System

The proposed system is based on a two layer 18 µm copper thickness, 0.5 mm FR4 PCB. For coupling MW into the DC current track coupling capacitor C1 is used (Fig. 1). Inductors L1 and L2 (also L3 and L4) together with the respective filter capacities Cf build a LC filter with a theoretical corner frequency of 1.5 MHz. In the area where DC current and MW are combined five diamonds are applied across the trace (Fig. 1). The diamonds have a diameter of about 150 µm and a NV-Center concentration of approx. 2.5-3 ppm. This results in a bright fluorescence.

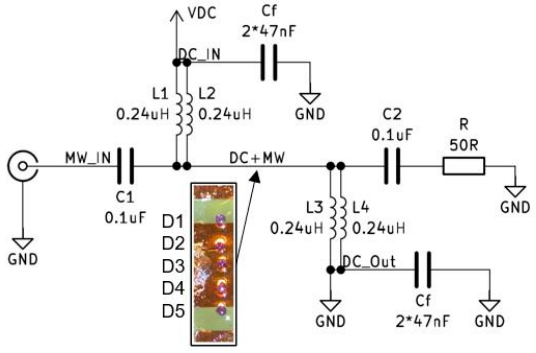

Fig. 1 Schematic of Bias Tee. The sensing area is located at the track where MW and DC Current are combined. Five diamonds are applied to the PCB track in the sensing area to investigate the properties of the setup. DC current direction is changeable.

Diamonds are excited with a 520 nm Laser diode focused onto the diamond by a microscope objective. The fluorescence beam is split by a dichroic mirror and detected with photodiode. The MW is provided by a Rohde & Schwarz SMBV100B and continuously amplitude modulated with a frequency of 5 kHz to improve signal to noise ratio [3] using a lock in amplifier (Zurich Instruments MFLI). The temperature is tracked by an FLIR E40 infrared camera.

Results

As shown in Fig. 2 it is possible to shift the resonance frequencies of the NV center with rising

currents. As mentioned, the diamonds are not aligned, which leads to significantly different spectra (Fig. 2a). With the well know physics of the NV ground state and the geometric properties of the diamond lattice [4], the total magnetic magnitude can be estimated from the eight, partially overlaid, resonance frequencies in the ODMR spectrum. The results are shown in Fig 2c.

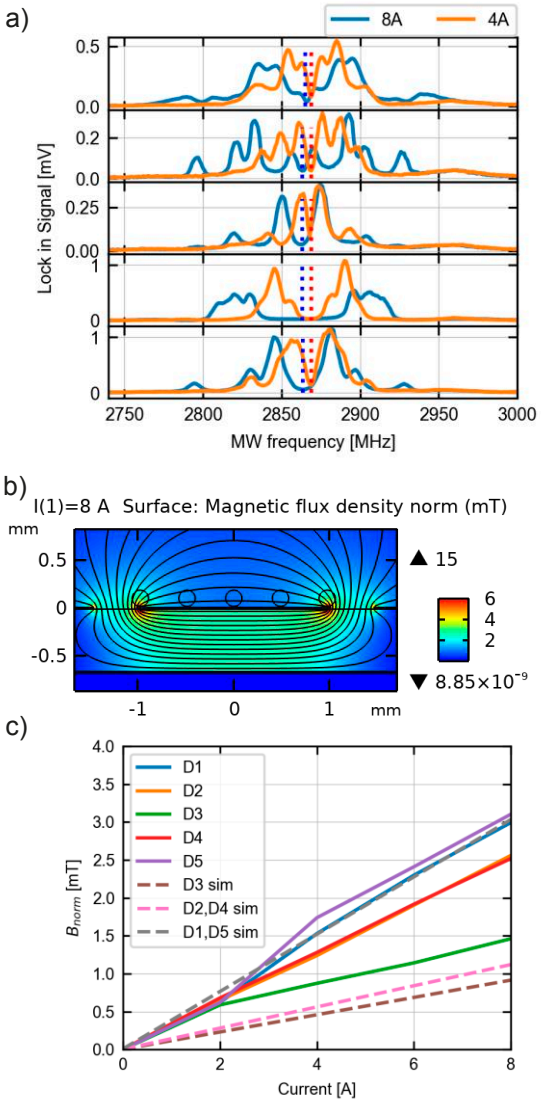

Fig. 2a) Exemplary spectra measured at 8 A and 4 A DC current on all five diamonds D1 to D5. Shifts in the ZFS between different current values (dotted line). b) 2D COMSOL simulation of 8 A DC current with combined MW excitation of 10 dBm c) measured and simulated magnetic field from all five diamonds over a current range from 0 A to 8 A.

The magnitude increases in the diamonds at the outer edges which follows the theoretical simulation (Fig. 2b). However, measurement results and simulation for D1 and D5 differ on average by 8.8 %. For D3 by 46.3 % and for D2 and D4 even by 56.2 %. Nevertheless through the linear dependence between magnitude and current on every diamond it is shown that a current sensor could be easily calibrated.
Furthermore one can see a shift in the ZFS on higher current values (Fig 2a – dotted line) and therefor higher temperatures [5]. Due to the small cross-section of the PCB trace, high temperatures are reached. These do not affect the linear behavior of the measured field in the present measurements. Current and temperature measurement can therefore be performed simultaneously and independent.

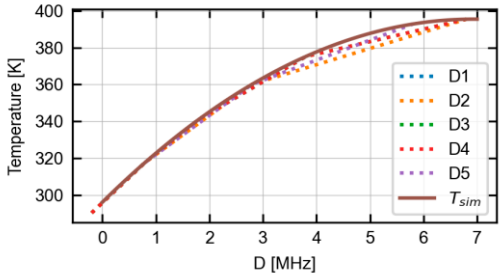

Fig. 3 Temperature Values calculated from $D = f_{ZFS0A} - f_{ZFS}$ of every diamond.

By a reference measurement a polynomial function is fit to calculate the current temperature directly from $D = f_{ZFS} - f_{ZFS0A}$ (Fig 3), where at 297.05 K the ZFS frequency at 0 A f_{ZFS0A} is measured as 2869.8 MHz.
The results show a cost effective and scalable way to use randomly orientated diamonds with NV centers in a quantum sensor application.

References

[1] Hatano, Y. et.al., High-precision robust monitoring of charge/discharge current over a wide dynamic range for electric vehicle batteries using diamond quantum sensors. Sci Rep 12, 13991 (2022). doi: 10.1038/s41598-022-18106-x

[2] Z. Long et.al., The Design of Current Sensor Based on Diamond Magnetometer, 2022 IEEE International Conference on Electrical Engineering, Big Data and Algorithms (EEBDA), (2022), pp. 685-687, doi: 10.1109/EEBDA53927.2022.9745017

[3] Haitham A. R. El-Ella et.al., Optimised frequency modulation for continuous-wave optical magnetic resonance sensing using nitrogen-vacancy ensembles, Opt. Express 25, 14809-14821 (2017) , doi: 10.1364/OE.25.014809

[4] M.W. Doherty et.al., Theory of the ground state spin of the NV- center in diamond: II. Spin solutions, time-evolution, relaxation and inhomogeneous dephasing, Phys. Rev. B 85, 205203 (2012), doi: 10.48550/arXiv.1111.5882

[5] V. M. Acosta, E. Bauch, M. P. Ledbetter, A. Waxman, L.-S. Bouchard, and D. Budker, Temperature Dependence of the Nitrogen-Vacancy Magnetic Resonance in Diamond, Phys. Rev. Lett. 104, 070801, Erratum Phys. Rev. Lett. 106, 209901 (2011), doi: 10.1103/PhysRevLett.104.070801

DOI 10.5162/SMSI2023/B1.1

Chemo/Biosensing with Optical Fibres

Francesco Baldini
[1] Istituto di Fisica Applicata "Nello Carrara", CNR,Via Madonna del Piano 10,Sesto Fiorentino (FI), Italy
f.baldini@ifac.cnr.it

Summary:
Chemo/biosensing with optical fibres has played an important role since the 1980s mainly thanks to their invasive capabilities and unique performance that have allowed measurements inside the human body otherwise impracticable. Optical fibre-based platforms for biosensing have been also proposed, by exploiting the refractive index (RI) changes induced on chemical/biochemical recognition layers deposited on fibre surface. Long period gratings (LPGs) and lossy mode resonance (LMR) are among the two most interesting approaches, being characterized by high sensitivity to external RI changes.

Keywords: Optical fibre sensor, bile, pH, long period gratings, lossy mode resonance

Introduction

One of the first invasive optical fibre chemical sensor was a sensor for blood pH developed by Peterson in 1980 [1]. Since then many examples of invasive optical fibre sensors have been described for the measurement of chemical and biochemical parameters. But optical fibres are also being proposed in the last years as essential elements for label-free biosensing by exploiting the changes of refractive index (RI) induced by chemical interaction within a recognition layer deposited on the optical fibres, obtaining comparable performances if not higher than those based on surface plasmon resonance.

Invasive optical fibre sensors

In gastroesophageal apparatus optical fibres have been used to monitor refluxes by measuring bile and pH [2].

The bile presence is measured by measuring the absorption of bilirubin, the main biliary pigment, which is characterized by a strong absorption spectrum in the blue region. The sensor utilizes two light emitting diodes, as sources (λ=465 nm and λ =570 nm for the signal and the reference, respectively) and an optical fibre bundle of 250 µm plastic fibres to transport the light from the sources to the probe and back to the photodetector; the probe is a miniaturised spectrophotometric cell of 3 mm external diameter (Fig.1).

Fig. 1. The optical fibre probe for the bile detection.

Bilitec2000 is the industrialised version of the bile sensor available on the market, produced by Cecchi srl and distributed by Medtronic up to 2007 and now by EBNeuro.

As for detection of gastroesophageal pH, the main hindrance to the development of an optical sensor has been the wide pH range of clinical interest (1.0-8.0 pH units). The first attempts involved the simultaneous use of two pH indicators, being each of them generally able to cover 2-3 pH units. Methyl red was shown to be able to cover the whole range after its covalent immobilization on controlled pore glasses [2]. On this basis an optical fibre probe was developed immobilizing the CPGs with methyl red at the distal end of 500 µm plastic fibres (Fig.2).

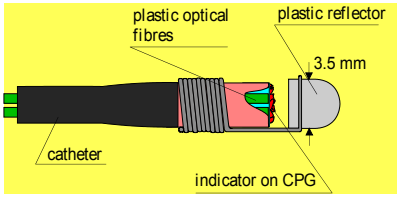

Fig. 2. The optical fibre probe for the pH detection.

The possibility of combining pH and bile measurement using a single fibre catheter is actually under study by reducing the dimension of the fibres for pH detection to 250 µm and integrating them in the same tubing containing the fibres for bile detection. A clinical study is starting with the first measurements on patients.

Besides bile and pH, pressure is the other essential parameter to perform exhaustive diagnosis in gastroesophageal reflux pathologies. An all-optical device was developed for their simultaneous measurement within the European project OPTIMO (http://www.optimo-project.eu) and

makes use of a catheter where plastic optical fibres (POFs) for bile and pH measurement and a glass fibre for pressure measurement are integrated [3]. The catheter is formed by an elastomer capable to transfer the radial esophageal pressure in longitudinal strain, extruded on a glass fibre with 10 fiber Bragg gratings. POFs are located on the external surface of the elastomer and a polymeric tubing covers the whole structure which has a diameter of 4 mm. Lateral windows allows the entrance of esophageal content for the measurement of bile and pH.

Gastric carbon dioxide (CO_2) is another important parameter in the gastro-esophageal apparatus. Its monitoring can provide essential information on tissue perfusion, since the stomach is the first organ in the body affected in cases of shock and the last to be restored. An optical fibre sensor using a single 600 µm glass fibre terminating with a probe was developed. The sensor is based on the measurement of the pH change induced by the CO_2 diffusion inside the probe, constituted by a plastic head containing the CO_2-sensitive layer (Fig.3). The sensor was tested on critically ill patients demonstrating the superiority of the optical fibre approach with respect to the traditional one based on gastric tonometry [2].

Fig.3. The pCO_2 probe (left) with the disassembled 500 µm optical fibre (right).

Label-free optical fibre biosensors

Measurements of refractive index in biological fluids are being used since many years for the quantitative measurements of analytes, by means of the use of chemical/biochemical recognition layers deposited on suitable substrates. LPGs [4] and the generation of LMRs allows measuring precisely and accurately surface RI changes [5].

LPGs are characterized by a periodic modulation of a single-mode optical fiber core and they are highly sensitive to the RI changes of the medium surrounding the fiber due to the coupling occurring between the fundamental core mode and different cladding modes. Any interaction occurring along the sensing region modifies the transmission spectrum and this can be evaluated in real-time by recording the shift of the LPG resonance wavelengths (Fig.4). Deposition of nanometric layers of high RI materials along the fibre allows to achieve limit of detection of the order of ng/mL^{-1} in the IgG/anti-IgG immunoassays [6, 7].

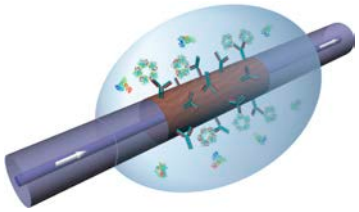

Fig.4. Schematic illustration of the surface sensing of biomolecules by an LPG. (from ref 4).

LMR is an optical phenomenon which takes place when an optical fiber is coated with nm-thick films with a complex refractive index; under specific conditions, coupling between fiber guided modes and guided modes of the thin film (the so-called lossy modes) occurs, leading to the formation of attenuation bands in the transmission spectrum. RI changes in the environment surrounding gives rise to changes in the coupling condition which caused shifts of the attenuation bands, which can be detected. As it occurs in LPGs, biosensing is achieved by means of the deposition of a molecular recognition layer on the fiber surface, with the shift of the resonance taking place following the interaction of the investigated analyte with the sensing layer. With this approach, limit of detections of 100 ng/mL for D-dimer in diluted serum [8] and of 110 pg/ml for tau protein in cerebrospinal fluid [9] were achieved.

References

[1] J.I.Peterson et al., Fiber optic pH probe for physiological use, *J Anal Chem* 52, 864-869 (1980).

[2] F.Baldini, In vivo monitoring of the gastro-oesophageal system using optical fibre sensors," *Anal Bioanal Chem* 375, 732-743 (2003).

[3] K.Schroeder et al., Fiber Optical Sensing System for Simultaneous Manometry, pH-metry and Bilimetry in Oesophagus, SMSI 2020, 222-223 (2020).

[4] F.Chiavaioli et al., Biosensing with optical fiber gratings, *Nanophotonics* 6 (4), 663- 679 (2017).

[5] I.Del Villar et al., Design rules for lossy mode resonance-based sensors, *Appl Opt* 51, 4298-4307 (2012).

[6] F.Chiavaioli et al., Sol-gel based titania-silica thin film overlay for long period fiber grating-based biosensors", Anal Chem 87, 12024-120131 (2015).

[7] F.Esposito et al., Long period grating in double cladding fiber coated with graphene oxide as high-performance optical platform for biosensing, *Biosens Bioelectr* 172, 112747 (2021).

[8] P.Zubiate et al., Fiber-based early diagnosis of venous thromboembolic disease by label-free D-dimer detection", *Biosens Bioelectr*: *X* 2, 100026 (2019).

[9] F.Chiavaioli et al., Ultrahigh Sensitive Detection of Tau Protein as Alzheimer's Biomarker via Microfluidics and Nanofunctionalized Optical Fiber Sensors, *Adv Photonics Res* 2200044 (2022).

DOI 10.5162/SMSI2023/B1.2

Colorimetric Detection of Oxygen in Food Packaging

Laura Engel[1,2], Katrin Schmitt[1,2], Jürgen Wöllenstein[1,2]
[1] IMTEK, Laboratory for Gas Sensors, Georges-Köhler-Allee 102, 79110 Freiburg, Germany
[2] Fraunhofer IPM, Georges-Köhler-Allee 301, 79110 Freiburg, Germany
laura.engel@ipm.fraunhofer.de

Summary:
We present a simple method to monitor the oxygen (O_2) concentration within food packages based on a UV resettable colorimetric indicator. The basis is a material combination of the redox color dye methylene blue (MB) with a titanium dioxide (TiO_2) nanopowder and glycerol. The work comprises different paste approaches suitable for screen printing and discusses the influencing factors to achieve the desired sensor properties based on investigations in an application-related scenario.

Keywords: Colorimetry, screen-printing, oxygen, food packing, optical gas sensor.

Background, Motivation and Objective

Approximately 12 million tons of food waste are generated in Germany every year, 52% of them in private households [1]. According to the Federal Ministry of Food and Agriculture, a targeted halving of the food waste in private households could save six million tons of CO_2 equivalents of greenhouse gas emissions annually. The generation of waste through discarded food is therefore not only associated with an immense economic loss, but also indispensable for the pursuit of rational climate and resource protection, which is a social task. Looking at the situation globally, it is assumed that a total of 1.3 billion tons of the food produced is not used every year [2]. According to estimates, the resulting total damage amounts to around 2.6 trillion US dollars, which corresponds to around 4% of global gross domestic product [2]. The food industry must deal with an increasingly complex, globalized environment of legal regulation and standards. With increasing use of additives in agriculture and animal husbandry, the risk of leaving residues in plant or animal products that are harmful to the health of consumers increases, too. Statistics show that the cause of 43% of all foodborne infections in Germany cannot be identified [3]. Increasing complexity of the value chain and increasing output per production facility complicate the traceability in the case of contaminated food. Furthermore, the distribution process also poses a risk to the quality of the food. Examples for this are a lack of compliance within the cold chain or violations of hygiene standards. However, independent from the multitude of influencing factors food quality could be monitored with the help of an integrated gas sensor. The goal of this work is the development of a printable, colorimetric gas sensor label (O_2, H_2S, amines, etc.), which gives a general description of the packaging's gas composition und thus on the condition of the product (see Fig. 1.).

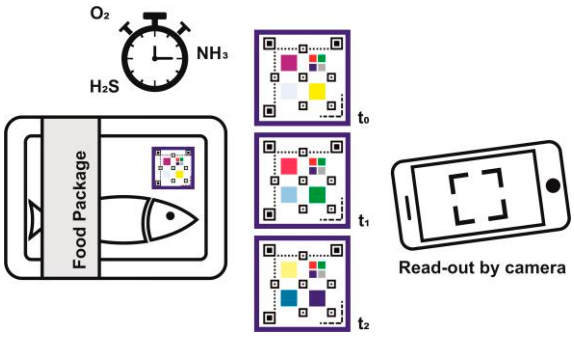

Fig. 1. Scheme of the sensor principle with three different colorimetric indicators. The integration of the colorimetric layers into a machine-readable pattern and the incorporation of a color reference enables an assessment of the color change that is independent from the illumination and the camera used.

In the present work the material development was focused on the example of an O_2 indicator. The shelf life of most packaged foods is affected by the presence of O_2. This gas leads to oxidation-related spoilage, accelerates the microbial growth of aerobics microorganisms, and is therefore excluded or reduced as far as possible in the protective gas atmosphere. To extend the shelf life, a reliable monitoring of the O_2 concentration could contribute to capture the current state of the goods.

Description of the New Method

Main challenge for the development of an O_2 indicator is the presence of O_2 in nearly every environment. Many goods are very sensitive to

O_2, and the packaging materials used show different barrier properties as well as a certain O_2 level of the already sealed packaging. The aim of this work is the development of a colorimetric indicator for the detection of O_2 that allows the time at which the measurement starts to be determined and that presupposes that "low" O_2 concentrations are negligible over the planned measurement period. As a part of this work an approach based on methylene blue (MB), titanium dioxide (TiO_2) and glycerol is used as gas sensitive material for the detection of O_2. The detection method is based on a photo-induced reduction of the redox dye MB to its leuco form, which in turn can be oxidized to its blue condition again by the presence of O_2 [4]. This method allows the sensor to be handled in an O_2 environment. Packed with the goods in a protective gas atmosphere, the measurement can be stated by resetting the gas sensitive layer with UV light. After the reset, the package is covered with a UV blocking foil to avoid a reverse reaction of the gas sensitive material through the given lighting conditions. For the manufacture of the gas sensitive layer different paste approaches were pursued. For the manufacturing of the paste, MB (indicator grade, Roth) and TiO_2 nanopowder (AEROXIDE TiO_2 P25, Evonik) were wet grinded in a planetary ball mill (PM 100, Retsch) using different solvents for the respective paste approach. Additives (defoamer, dispersant and thixotropic agent) were added to support the milling process to form a homogeneous paste structure on the one hand and to support the printing process on the other. Finally, glycerol (≥99.5%, Sigma-Aldrich) was added to the raw dispersion. To characterize the printability of the pastes, measurements were performed using a rotational rheometer (KINEXUS lab+, Netzsch) to determine the viscosity and the thixotropy of the pastes. A printing process was developed on a precision screen-printing machine (Thieme Lab 1000, Thieme GmbH & Co. KG) using a 120-30 PE mesh for the prints. Fig. 2 shows a 1-layer print by the example of a paste approach based on propylene glycol. The printed sensor layers were characterized by UV/Vis spectroscopy and in-situ readout station, which allows to analyze the color change via RGB values recorded with a camera. The in-situ readout station enables the indicators to be measured in a real-world perspective from 5 °C and is, in addition, coupled with a mass spectrometer to define the exact O_2 entry into the measurement chamber used to simulate food-packaging. Fig. 3 shows the sensor response of the exemplary selected layer towards 20% O_2 measured by UV/Vis spectroscopy. The respective camera images can be seen in Fig. 4.

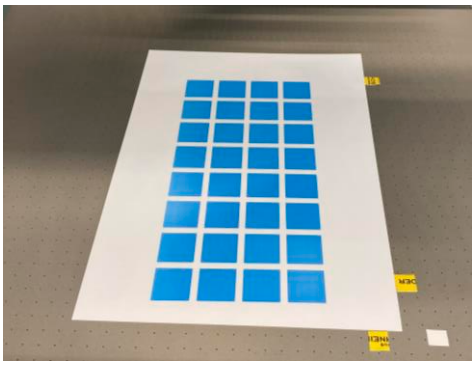

Fig. 2. Colorimetric sensor layers on A4 sheet.

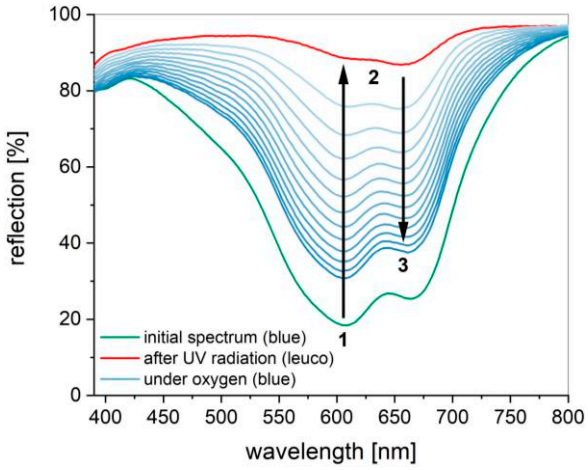

Fig. 3. Change in spectrum of the O_2 sensitive layer under the influence of 20% O_2 for 1 hour at room temperature and a relative humidity of 40%. Recording of the spectrum every 5 minutes.

Fig. 4. Screen-printed sensor layer at ambient condition (1), after rest with UV light under N_2 (2) and after exposure to 20% O_2 for one hour (3).

Results

Within this work we developed and characterized colorimetric sensor layers for the detection of O_2 in food packages over a defined period (~weeks). For the manufacture of the sensors, different screen-printing pastes were developed and characterized with respect to printability, sensitivity towards O_2, possible interfering gases and the influence of relative humidity.

References

[1] BMEL, https://www.bmel.de/DE/themen/ernaehrung/lebensmittelverschwendung.html, 15.11.2022

[2] GobalCom, https://www.cleanenergy-project.-de/umwelt/ressourcen-management, 15.11.2022

[3] IUFoST Konferenz, 2005

[4] A. Mills, D. Hazafy, A solvent-based intelligence ink for oxygen, *The Analyst*, 213-2018 (2008); doi: 10.1039/b713450a

DOI 10.5162/SMSI2023/B1.3

CMOS Based Integration Technology for Solid State pH-Measurement

Olaf R. Hild[1], Christian Kunath[1], Eberhard Kurth[1], Christopher D. Beale[1], Falah Q. Al Falahi[1]
[1] Fraunhofer IPMS, Maria Reiche Str. 2, 01109 Dresden, Germany
Corresponding Author's e-mail address: olaf.hild@ipms.fraunhofer.de

Summary:
The measurement of pH with ion-sensitive field-effect transistors (ISFETs) as a half-cell, in combination with a silver/silver chloride reference electrode as a second half-cell, is state of the art. Here we present an integration technology that allows for the fabrication of an ISFET with a solid-state reference element (REFET) on one chip, while permitting connectivity to IC-CMOS technology.

Keywords: ISFET, REFET, pH-Measurement, CMOS integration, solid-state reference electrode, counter electrode

Background, Motivation and Objective

The pH-ISFET has been in use for many years, and the device is an alternative measuring probe to the conventional glass electrode. Unlike the glass electrode, the pH-ISFET has no internal buffer solution and its output impedance is about 5 kΩ rather than more than 100 kΩ for the glass electrode, with the lower impedance being more favorable from a measurement standpoint. In order to reliably measure pH in an aqueous ionic solution with an ISFET, a reference electrode is typically required for providing the reference potential. However, typical reference electrodes have an internal electrolyte, the constituents of which can diffuse into the solution to be measured. Diffusion also means a change in the concentration-defined reference potential and contamination of the measured solution. Thus, for a solid-state pH sensor, a pure solid-state reference electrode as a field-effect transistor, or REFET, would be an improvement. However, to compensate for the low impedance of the reference electrode to the measured solution, a counter electrode is also required, where the potential difference of the ISFET with respect to the REFET is used to determine the pH. The measurement thus requires that the ISFET and the REFET be electrically isolated from each other.

Description of the New Method or System

For an efficient sensor design, everything should be integrated on one chip along with the measurement electronics. Here, the p-channel FETs, ISFET and REFET, are fabricated separately in 2 n-wells in a p-EPI-Si wafer, with the EPI layer on a highly doped p-Si substrate. Thus, the two FETs are electrically separated, where this structure corresponds to that of CMOS technology. In the first stage of development, normal pH-ISFETs are implemented in the new environment and their metrological effects are characterized. For an optimal ISFET topology having a good wetting of the measuring solution with the ISFET surface, the LOCOS technology was chosen. Fig. 1 shows the basic vertical structure and topology of an n-well ISFET and a substrate contact.

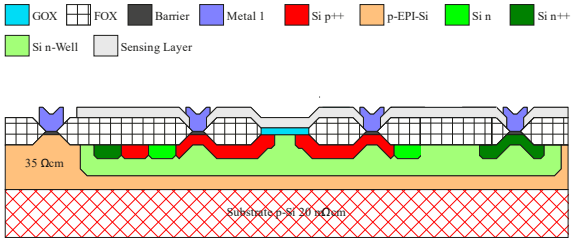

Fig. 1 ISFET cross-section. Not to scale.

Fig. 2 shows microscope images of an n-well ISFET and ISFET plus REFET on one chip. The sensing layer was deposited according to Wong et al. [1].

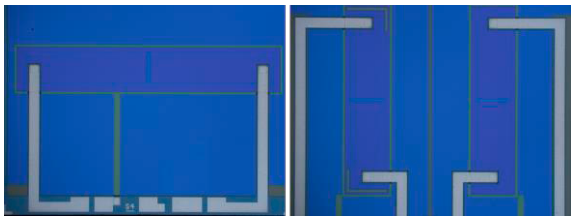

Fig. 2: Microscope images of sensor chips left: ISFET and right: Integrated ISFET + REFET (currently not functionable)

Fabrication sequence:

1. Adjustment mark/implantations n-, n++, n (well, well contact, inversion-stopper, guard)
2. LOCOS (LP nitride hard mask)
3. Implantation p++ (source, drain)
4. GOX/Sensor layer/Annealing
5. Lithography/RIE
6. Contact free etching/lithography/metal/lithography/RIE
7. Forming gas/electrical characterization

Results

The ISFETs were equally distributed over a 200 mm wafer. After sawing the wafer, the ISFETs were bonded to ceramic boards, wire bonded and encapsulated. Transfer curves were then measured in pH 7.00 ± 0.02 buffer solution (Na-K-phosphate) at 25.0 °C, where these curves are shown in Fig. 3. It can be seen that all 30 curves overlay each other very closely, and there is an excellent good homogeneity over the wafer. This means that a very low scattering of the operating point is to be expected.

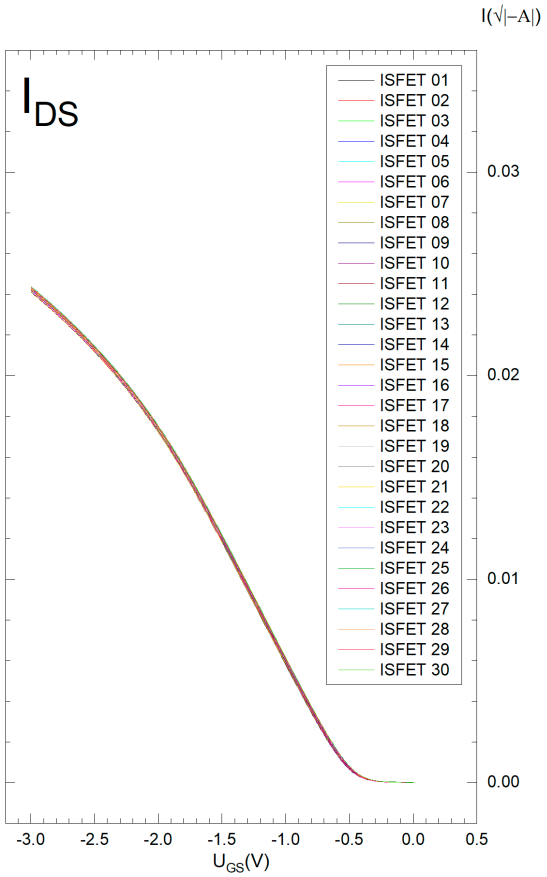

Fig. 3 Transfer curves of 30 ISFETs evenly distributed across a 200 mm wafer.

Fig. 4 shows the U_{GS} signal curve after switching on at 25 °C and pH 7. The ISFET needs about 30 min until its measuring accuracy reaches ±0.02 pH, after which drift occurs. The drift value is determined by filling a new buffer solution into the measuring cell after about 16 h. The operating point of the ISFET was roughly at its isothermal point. The ISFET parameters and the drift values are in Tab. 1.

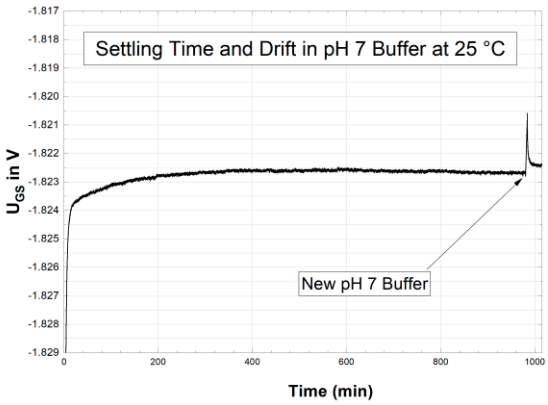

Fig. 4: Operating point drift of an ISFET over time, with the pH buffer replaced at the end of the measurement.

Tab. 1: ISFET operating point parameters, the settling time and the drift value.

ISFET Parameters	Parameter Values
U_{DS}	-0.95 V
I_{DS}	-260 µA
U_{GS}	-1.822 V
T	25 °C
pH	7
Settling time to ± 0.02 pH	30 min
Drift	75 µV/h

References

[1] H. S. Wong, M. White, A self contained CMOS integrated sensor, IEDM 1988, 658-660

DOI 10.5162/SMSI2023/B1.4

Development of Simple, Reusable and Sensitive Electrochemical Sensor based on Silver Nanoparticles Modified Gold Screen-Printed Electrode for the Detection of Nitrate in Water

*Najib Ben Messaoud, Marília B. dos Santos, Begoña Espiña, Raquel B. Queirós**
International Iberian Nanotechnology Laboratory
Avenida Mestre José Veiga, 4715-330 Braga, Portugal
**raquel.queiros@inl.int*

Summary
A simple, reusable and sensitive electrochemical sensor based on silver nanoparticles modified gold screen-printed electrode has been developed for the detection of nitrate in water for animal feed. The sensor exhibited a wide linear response to nitrate from 50 µM to 10000 µM with a detection limit of 4.38 µM (N=4) which is significantly lower than the maximum contaminant level admitted for watering dairy cattle ($3.22X10^3$ µM), and within the sensor linear range. The sensor presented good reproducibility (<10%) and repeatability (2%) as well as selectivity with respect to common interferents found in water.

Keywords: Nitrate; Silver Nanoparticles; Electrochemical sensor; Water monitoring

Introduction

Nitrate (NO_3^-) is widely found in water, resulting mainly from the usage of agricultural fertilizers and the discharge of untreated wastewater from human activities [1]. However, high levels of nitrate can cause serious harms for both aquatic ecosystems and human health [2]. According to regulation EC 183/2005 of the EU [3], the maximum admitted value of nitrate for watering dairy cattle is of $3.22X10^3$ µM. Therefore, there is great interest in developing fast, accurate and portable sensing devices for the determination of nitrate in the field, where electrochemical sensors are one of the most promising. The modification of the surfaces of such sensors with nanomaterials can enhance the sensitivity of those devices, as several have already been reported [4]. However, the pretreatments, preparation and modifications of such sensors in the reported studies are complex and time-consuming. In the present work, a simple, reusable and sensitive electrochemical sensor for nitrate detection consisting of silver nanoparticles (AgNPs) modified gold screen-printed electrode (AuSPE) has been developed. The optimal electrodeposition time of AgNPs has been determined to obtain the highest sensing performances. The electrochemical behavioor of the modified electrode was investigated by Square Wave Voltammetry (SWV). Finally, the selectivity with respect to common interferents in water was demonstrated.

Experimental

Potassium nitrate (KNO_3), silver nitrate ($AgNO_3$) and sodium chloride (NaCl) were purchased from Sigma Aldrich. Stock solution of nitrate and interferents were dissolved in NaCl solution (0.6 M). $AgNO_3$ (3.5 mM) dissolved in KNO_3 electrolyte solution (100mM). Cleaned AuSPEs have been conditioned in H_2SO_4 solution (10 mM) by cyclic voltammetry (CV) between 0 V and 1.5 V at 100 mVs^{-1}. Next, the electrode modification was achieved by the electrodeposition of silver onto AuSPE using the chronoamperometry method at −0.2 V, at controlled time. Thus, t=7s was selected as the optimum time in order to maximise the sensitivity for the determination of nitrate. SWV measurements were carried out at the pulse amplitude of 60 mV with a frequency of 100 Hz. The potential varied from 0.0 V to −1.4 V. Figure 1 shows the fabrication process of the proposed NO_3^- sensor. According to the references, the modification of gold electrodes with AgNPs can lead to the formation of a catalyst that can be used for the selective electrochemical reduction of NO_3^- to NO_2^- according to the following reaction [5]:

$$NO_3^- + 2H^+ + 2e^- \rightarrow NO_2^- + H_2O \quad (1)$$

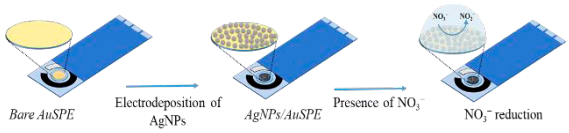

Fig. 1. Schematic illustration of the fabrication process and the detection mechanism of the proposed nitrate (NO3−) sensor.

Results and discussion

The surface of the modified electrode was characterised by Scanning Electron Microscopy (SEM) (Fig. 2). Fig. 2a shows the SEM image,

where the AgNPs deposition was confirmed. The homogeneous distribution of AgNPs (blue color) on the electrode surface is reported in the EDX mapping in Fig. 2b.

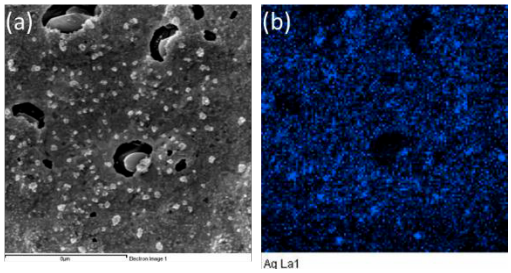

Fig. 2. SEM micrograph (a) and mapping analysis (b) of the AgNPs deposited on the AuSPE electrode surface.

Then, the sensor was characterized by SWV. A significant change of the current value was noted after the modification of the bare electrode with the AgNPs, confirming the surface modification. The influence of scan rate on the reduction of the nitrate was studied by CV (results not shown), indicating that the reduction was controlled by diffusion processes. The electroanalytical determination of NO_3^- using the AgNPs/AuSPE was performed by SWV. The electrochemical curves obtained for varying NO_3^- concentrations are shown in Fig. 3. The calibration plot constructed from the obtained SWV response, illustrated in inset of Fig. 3, shows a wide linear range from 50 to 10000 µM. The calculated detection limit was 4.38 µM (N=4). NaCl electrolyte solution (pH= 7) was used which can provide the opportunity to directly detect nitrate in real water samples without the need to change the electrolyte pH and without interfering with the sensor's performance. Few reported sensors have been developed for nitrate reduction reaction within neutral pH, indeed acidic electrolyte has been used in most cases to obtain better sensitivity. The relative standard deviation (RSD) found for the measurement of 400 µM, 1500 µM and 10000 µM of NO_3^- at four different electrodes, prepared in the same way, was 8.6 %, 5.6% and 5.2% respectively, showing good reproducibility. The repeatability (N= 10) of the sensor was successfully carried out obtaining an RSD of 2.0 %. The selectivity of the sensor towards NO_3^- was investigated in the presence of the most common interfering compounds (Ca^{2+}, K^+, NO_2^-, HCO_3^-, CH_3COO^- and Mg^{2+}) at concentrations 10-fold higher than of NO_3^-. None of the interferents exhibited a significant change in the NO_3^- response.

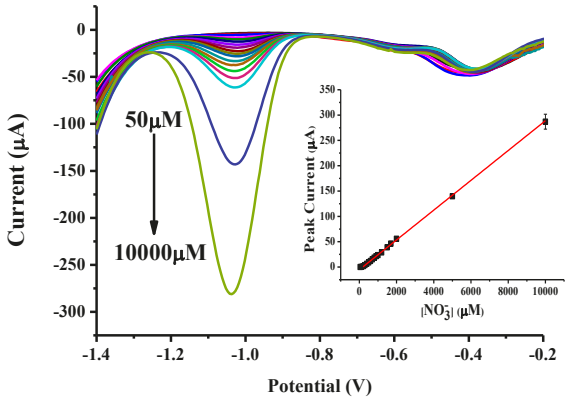

Fig. 3. SWV of different concentration of NO_3^- from 50 µM to 10000 µM at AgNPs/AuSPE in NaCl (0.6M). Inset: corresponding calibration curve.

Conclusion

A simple, reusable and sensitive electrochemical sensor for NO_3^- based on AgNPs has been developed. Important performances such as a low detection limit of 4.38 µM (N=4), wide detection range from 50 µM to 10000 µM and excellent selectivity of the developed sensor were achieved. This could be very promising for the detection of NO_3^- in real water samples.

Acknowledgements

The authors acknowledge the financial support of the project RW Clean (POCI-01-0247-FEDER-070109), co funded by COMPETE 2020 under the PT2020 partnership Agreement, through ERDF.

References

[1] O. Alagha, M.S. Manzar, M. Zubair, I. Anil, N.D. Mu'azu, A. Qureshi, Comparative adsorptive removal of phosphate and nitrate from wastewater using biochar-MgAl LDH nanocomposites: coexisting anions effect and mechanistic studies, *Nanomaterials* 10, 336 (2020); doi.org/10.3390/nano10020336

[2] M.E.E. Alahi, S.C. Mukhopadhyay, Detection methods of nitrate in water: A review, *Sensors and Actuators A: Physical* 280, 210–221 (2018); doi.org/10.1016/j.sna.2018.07.026

[3] Regulation (EC) nº 183/2005, of the European Parliament and of the Council of January 12 (2005).

[4] R. Ahmad, K.S. Bhat, M.-S. Ahn, Y.-B. Hahn, Fabrication of a robust and highly sensitive nitrate biosensor based on directly grown zinc oxide nanorods on a silver electrode, New Journal of Chemistry. 41, 10992–10997 (2017) ;doi10.1039/C7NJ02526B

[5] M. Huang, J. B. Henry, B. B. Berkes, A. Maljusch, W. Schuhmann, A. S. Bondarenko, non-stationary electrocatalytic systems, *Analyst* 137, 631–640 (2012); doi.org/10.1039/C1AN15671C.

DOI 10.5162/SMSI2023/B2.1

B2.1 Concepts and Applications of QT, including Quantum-Referenced Sensing and Relevance for QComputing & Qcommunication

N. Spethmann, Physikalisch-Technische Bundesanstalt, Braunschweig (Germany)

The short paper of this contribution is not available

DOI 10.5162/SMSI2023/B2.1

B2.1 Concepts and Applications of QT, including Quantum-Referenced Sensing and Relevance for QComputing & Qcommunication

N. Spethmann, Physikalisch-Technische Bundesanstalt, Braunschweig (Germany)

The short paper of this contribution is not available

DOI 10.5162/SMSI2023/B2.2

B2.2 Nitrogen-Vacancy Centers for Quantum Sensing

N. Aslam, Technische Universität Braunschweig, Braunschweig (Germany)

The short paper of this contribution is not available

DOI 10.5162/SMSI2023/B2.2

B2.2 Nitrogen-Vacancy Centers for Quantum Sensing

N. Aslam, Technische Universität Braunschweig, Braunschweig (Germany)

The short paper of this contribution is not available

DOI 10.5162/SMSI2023/B2.3

B2.3 Magnetometry (Quantum [OPM] and Classic) for Battery Cells for Electromobility

G. Kendall, CDO2 Ltd., Brighton (United Kingdom)

The short paper of this contribution is not available

DOI 10.5162/SMSI2023/B2.3

B2.3 Magnetometry (Quantum [OPM] and Classic) for Battery Cells for Electromobility

G. Kendall, CDO2 Ltd., Brighton (United Kingdom)

The short paper of this contribution is not available

DOI 10.5162/SMSI2023/B2.4

B2.4 Integrated Quantum Sensors based on Atomic Gases

M. Krutzik, Ferdinand-Braun-Institut gGmbH, Leibniz-Institut für Höchstfrequenztechnik, Berlin (Germany)

The short paper of this contribution is not available

DOI 10.5162/SMSI2023/B2.4

B2.4 Integrated Quantum Sensors based on Atomic Gases

M. Krutzik, Ferdinand-Braun-Institut gGmbH, Leibniz-Institut für Höchstfrequenztechnik, Berlin (Germany)

The short paper of this contribution is not available

DOI 10.5162/SMSI2023/B3.1

A universally applicable condition monitoring system for efficiency evaluation of low-voltage motors

Andreas Grundmann[1], *Thomas Reuter*[1], *Álvaro Oteros Pérez*[1], *Jens Schmidt*[1]
[1] *Institut Chemnitzer Maschinen und Anlagenbau e.V.,*
Otto-Schmerbach-Straße 19, 09117 Chemnitz, Germany
a.grundmann@icm-chemnitz.de

Summary:
A compact universal Condition-Monitoring-System for predictive maintenance and efficiency evaluation has been developed for monitoring low-voltage motors. The analysis for edge processing of glass sheets showed energy savings of up to 50 % and machine utilization of 30 %. This enabled unfavorable processes to be identified and improvement procedures to be initiated.

Keywords: Electric drives, Condition-Monitoring-System, Energy saving, Efficiency evaluation, Machine utilization

Motivation

As announced by the Federal Environment Agency in various publications, electric drives in industry and manufacturing consume almost two-fifths of all electricity in Germany. At the same time, this shows the great potential for savings in electric drives and driven units for pumps, fans, or ventilators, for example, as well as all types of conveyor technology. For driven pumps alone, the potential energy savings are estimated at five billion kilowatt hours [1]. A similar conclusion was reached by the German Association for Electrical, Electronic & Information Technologies (VDE) in its 2008 study "Efficiency and Savings Potentials of Electrical Energy in Germany," which shows the prospects and need for action up to the year 2025. The study showed that the key role in energy savings will be played by electric motors. The consumption focus here is seen in three-phase motors in the power range from 0.75 kW to 40 kW (related to electric drives of pumps, fans, and ventilators), as these have the greatest number of operating hours per year [2]. At the same time, in addition to energy saving, the maintenance of electric drives and driven units is of crucial importance, since sudden failures can have serious consequences for safety as well as high costs for repair or production downtime [3, 4]. Maintenance is based on permanent condition monitoring of electric drives [5, 6]. A universally applicable condition monitoring system was implemented for comprehensive monitoring of uncontrolled electric drives, which covers the two criteria of condition monitoring and efficiency evaluation. In this paper, the main focus will be on efficiency evaluation based on the energy data. This results from the comparison of the specified motor characteristics and the actual measured active power. The condition monitoring part was explained in [7].

Condition-Monitoring-System

The purpose of the Condition-Monitoring-System is the continuous monitoring of uncontrolled drives. For this purpose, the motor monitoring module is to be mounted on the terminal box of the drive. The recorded data is made available to the various user groups with the appropriate access rights via a gateway or a cloud (see Fig 1). The electrical contact of the motor monitoring module is made via the terminal board of the uncontrolled drive. The motor monitoring module consists of a measurement board and a communication board, which are connected to each other via plug contacts (sandwich construction). The measurement board contains the power supply for the module as well as all individual controllers and sensors for the acquisition of the electrical measured variables, the temperature (PT1000), and the acceleration (KX122). The individually acquired data is collected on a microcontroller and transmitted to the communication board. The W-LAN chip implemented on it transmits the data to a gateway or to a cloud.

Power determination

An energy measuring chip (power meter), which operates according to the Aron circuit [8], is used to record the energy data. Here, only two-phase voltages and two-phase currents are measured in a three-phase system to determine the power of the drive. The voltage is deter-

mined directly and the current indirectly via two Rogowski coils. The two Rogowski coils used are induction coils in which a conductor wire is uniformly wound around a non-ferromagnetic core. The limiting factors of this measuring principle are the measuring range of the coils, which in the case shown is 40 kW, and the wire cross-section of the motor's connecting cable. The accuracy of the power determination is 5 %.

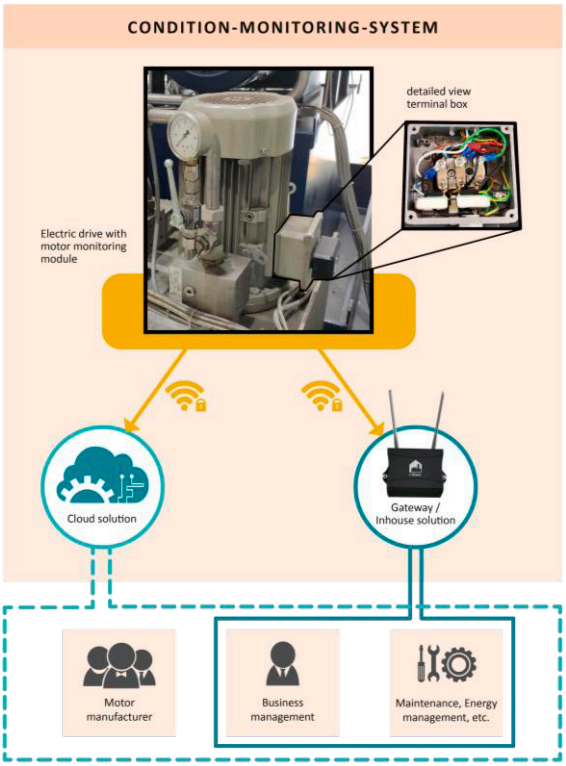

Fig. 1. Functional principle of the Condition-Monitoring-System.

Pilot study

For the pilot study, a machine for edge processing of glass sheets was equipped with the Condition-Monitoring-System. The aim was to determine the efficiency of the motor (Pmech = 3 kW), the actual processing time per work piece and the utilization of the machine.

Results

The energy analysis showed a motor idle power of 0.2 kW, an average active power in the tool engagement of 1.2 kW and a max. active power of 1.7 kW. Thus, an energy saving of 50 % can be achieved by using a smaller motor (e.g., 1.5 kW motor). With regard to the processing time, it could be determined that the glass sheets to be produced most frequently are processed between 13 s and 29 s. With this knowledge, conclusions can be drawn about the glass sheet sizes and considered in investment activities. The actual machine utilization was 30 %. Based on these findings, the peripheral processes were analyzed, unfavorable processes were identified and improvement measures were initiated.

Outlook

In the future, the Condition-Monitoring-System will also focus on controlled electric drives. Furthermore, the development of AI-based evaluation algorithms will be addressed.

References

[1] M. Pehnt, Endbericht: Energieeffizienz: Potenziale, volkswirtschaftliche Effekte und innovative Handlungs- und Förderfelder für die Nationale Klimaschutzinitiative, Hg.: ifeu - Institut für Energie- und Umweltforschung Heidelberg; Heidelberg, 10/2011

[2] E. Baake, VDE Studie: Effizienz- und Einsparpotentiale elektrischer Energie in Deutschland, Hg.: VDE Verband der Elektrotechnik Elektronik Informationstechnik e.V., Frankfurt am Main, 01/2008

[3] M. Kande, A.J. Isaksson, R. Thottappillil, N. Taylor, Rotating Electrical Machine Condition Monitoring Automation—A Review, Machines 5, 1-24 (2017); doi: 10.3390/machines5040024

[4] P. Tavner, L. Ran, J. Penman, H. Sedding, Condition Monitoring of Rotating Electrical Machines. Power and Energy Series 56, The Institution of Engineering and Technology, 2008

[5] R.B. Randall, Vibration-based Condition Monitoring. John Wiley and Sons, 2011; doi:10.1002/9780470977668

[6] M. Tshilidzi, Condition Monitoring Using Computational Intelligence Methods - Applications in Mechanical and Electrical Systems. Springer-Verlag, London, 2012; doi: 10.1007/978-1-4471-2380-4

[7] T. Reuter, J. Schmidt, A. Grundmann, Entwicklung eines Condition-Monitoring-Systems für Niederspannungsmotoren: Teil 1: Untersuchung von Belastungs- und Schadensfällen mittels Schwingungsmessung, Zeitschrift für wirtschaftlichen Fabrikbetrieb 117, 659-666 (2022); doi: 10.1515/zwf-2022-1139

[8] H. Linse, R. Fischer, Grundlagen der Elektrotechnik. In: Elektrotechnik für Maschinenbauer. 12. Aufl., Vieweg+Teubner Verlag, Wiesbaden, 2005

DOI 10.5162/SMSI2023/B3.2

Robust Sensor System for Condition Monitoring of Lubricated Rail Vehicle Components

K. Dubek[1,2], *Ch. Schneidhofer*[1], *N. Dörr*[1], *U. Schmid*[2]
[1] *AC2T research GmbH, Viktor-Kaplan-Straße 2/C, 2700 Wiener Neustadt, Austria*
[2] *TU Wien, Institute of Sensor and Actuator Systems, Gußhausstraße 27-29, 1040 Wien, Austria*
Krisztian.Dubek@ac2t.at

Summary:
Sensor systems for monitoring lubricated components must provide a high-level of robustness against various environmental impacts like temperature, humidity, and vibrational load to operate reliably over a long-term period. Therefore, a lab-to-field development environment was established to mimic the influence of these factors under controlled laboratory conditions. The sensor-based monitoring of water in grease-lubricated axle box bearings on wheelsets for railway application is presented to account for water content as critical lubricant parameter, as water can damage or even destroy bearings.

Keywords: Humidity sensor, axle box bearing, grease, water content, condition monitoring

Overview and Motivation

A fast and reliable method for evaluating the suitability of a sensor system for an application is provided by the technology readiness levels (TRL) [1]. In the context of this work, suitability means that the sensor system must be sufficiently robust regarding hardware, *i.e.*, sensor components must withstand harsh conditions and environments during operation, as well as software, *i.e.*, easy-to-interpret sensor signals [1]. For this purpose, laboratory-based evaluations [2] or laboratory bench tests [3] can be carried out to simulate the degradation mechanism(s) in sensor performance. The aim is a rapid development of the sensor system up to TRL 5 in the laboratory before field demonstration takes place.

For the sensor development, the step from the laboratory-based validation (TRL 4-5) into the field demonstration (TRL 6) is most important. Key to the solution is the transferability of laboratory results to the field application, which is implemented using the so-called lab-to-field approach (see Fig. 1). Applied to sensors, core element of such an approach is the environment for sensor development that simulates relevant field conditions in the research laboratory.

In this work, the focus was placed on sensor-based monitoring of water in grease-lubricated axle bearings for railway application. This is because water can lead to corrosion as well as cavitation and in further consequence, can stimulate irreparable metal fracture [1]. Thus, key element of the sensor system is the Humidity Sensor in Axle Bearings (HSAB) mounted in the cover of the latter component. In the case of an unwanted penetration of water into the grease the HSAB system will give feedback on an increased air humidity close to the bearing.

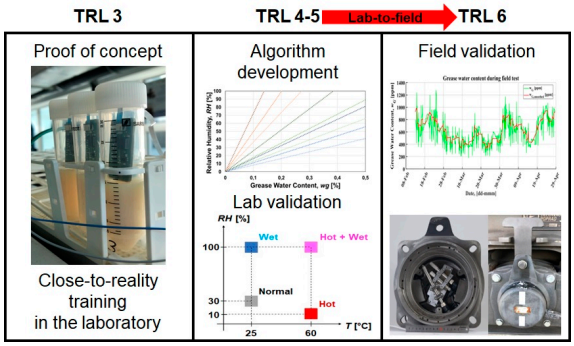

Fig. 1. Lab-to-field approach for the development of sensor systems with stepwise increase in TRL.

Methodology and Results

After the proof of concept, the HSAB system was tested for TRL 4 according to the international standard IEC 60068-2-38, among others, in which the sensor system is exposed to increased, changing climatic loads (see Fig. 2). As the sensor system remained functional after this validation test, the test result was “passed” and thus TRL 4 approved.

For the validation for TRL 5, the sensor system was assembled via a mounting unit inside the bearing cover as planned in the field. The entire system was than equipped onto a shaker and tested beyond the standard IEC 61373 “Category 3 Axle mounted” in which simulated long-

life and shock tests with increased amplitude of factor up to 1.7 were carried out.

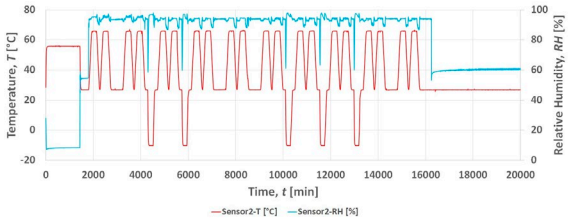

Fig. 2. Measurement results following standard IEC 60068-2-38.

Simultaneously, the entire system was subjected to four relevant climatic conditions at rail application (see Fig. 3). Both functionality and mechanical integrity stayed intact, thus the test result was “passed” and TRL 5 was approved.

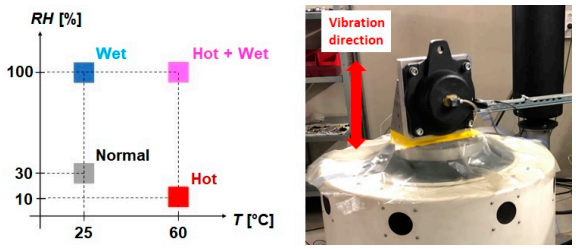

Fig. 3. Setup of mechanical and environmental testing (right) of HSAB system according to diverse climatic conditions (left).

In the last step, the HSAB system was demonstrated in field to achieve TRL 6. Therefore, the fully assembled system was fixed at the axle box of an Y25 bogie of a freight wagon. Also, a reference weather sensor was installed on the bogie to log weather data. Fig. 4 shows the trend of the recorded sensor signals during a drive from Salzburg to Graz (Austria). Deviations between the sensor signals are due to the different positioning of the sensors. As all sensor provided reliable signals with no abnormalities, TRL 6 has been approved.

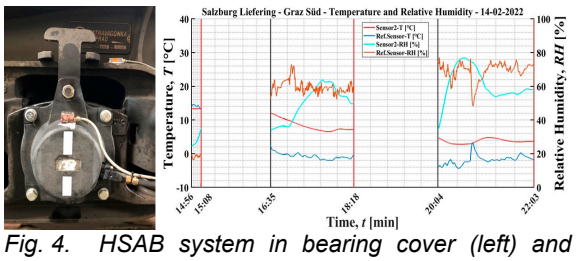

Fig. 4. HSAB system in bearing cover (left) and signals during a drive from Salzburg to Graz (right).

As part of the robustness validation of the HSAB system, also an algorithm under laboratory conditions was developed to correlate the grease water content and the relative air humidity measured by the HSAB system. This algorithm was then used to properly calculate the grease water content throughout the field test (see Fig. 5) based on sensor signals. As can be seen, the water content of the grease remained at acceptable levels (w_G < 1000 ppm).

In addition, dry and wet periods in time are clearly detected. Therefore, the HSAB system is considered appropriate and robust to work under rail vehicle operating conditions, which makes a valuable contribution to the reliable and safe operation of freight wagons.

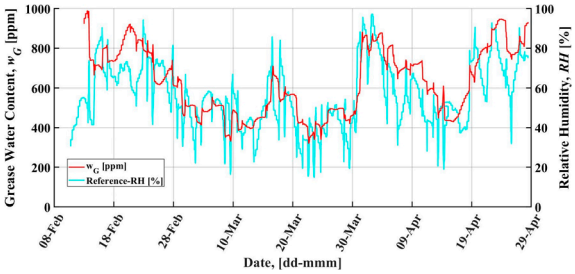

Fig. 5. Calculated grease water content and relative humidity of the reference sensor during field test.

Conclusion

The usability of the lab-to-field approach was demonstrated enabling a rapid development of the HSAB system up to TRL 5 and keeping the efforts for field validation at a lower level. The correlation between grease water content and relative humidity of the environment confirmed the applicability of the HSAB. The grease water content changes due to interaction with the environment at the shaft seal resulting in accordingly changes of the climatic conditions prevailing at the sensors in the bearing cover.

Acknowledgements

This work has received funding from the Shift2Rail Joint Undertaking (JU) under grant agreement no 826206 and no 101004051. The JU receives support from the European Union’s Horizon 2020 research and innovation program and the Shift2Rail JU members other than the Union. Simulation of lubricant degradation was supported by the project COMET InTribology1 (FFG project no. 872176). The work was carried out at AC2T research GmbH. The team thanks Steiermärkische Landesbahnen for the support of the field demonstration.

References

[1] Ch. Schneidhofer, K. Dubek, N. Dörr, Robust sensors enabling condition-based maintenance of lubricated components in locomotives and wagons, *Transportation Research Procedia (TRA) Conference* (2022); accepted

[2] Ch. Schneidhofer, A. Grafl, K. Adam, Online Zustandsüberwachung von Hydraulikölen in der Stahlindustrie, *Berg- und Hüttenmännische Monatshefte* 163, 193-198 (2018); doi: 10.1007/s00501-018-0707-y

[3] D. Coronado, C. Kupferschmidt, Assessment and validation of oil sensor systems for on-line oil condition monitoring of wind turbine gearboxes, *Procedia Technology* 15, 747-754 (2014); doi: 10.1016/j.protcy.2014.09.047

DOI 10.5162/SMSI2023/B3.3

A UHF RFID sensor tag system with externally connected sensor component

M. Lenzhofer[1], L. Neumaier[1], J. Kosel[1]
[1] Silicon Austria Labs GmbH, Europastrasse 12, 9524 Villach, AUSTRIA
Martin.Lenzhofer@silicon-austria.com

Summary:
The presented work focuses on the development of RFID sensor tags utilizing external sensor devices via long cable connections of up to 4 m, which is often needed to overcome spatial restrictions in different machines of industrial processes, due to fully metallic housings or limited space conditions. The influences of the large distances between sensor element and RFID integrated circuit on the tag of the RFID sensor system itself are analyzed and practical issues are addressed to enable a measurement over a long read-out range with a standard UHF reader device.

Keywords: RFID sensor system, UHF reader, wireless measurement, sensor tag, RFID technology

Introduction

Radio frequency identification (RFID) sensor technology is an upcoming technology that is more and more applied in many applications and already implemented in the industrial field, where process control, health state monitoring and condition recognition are of main interest. There are several companies on the market, like IDENTIV, microsensys, XERAFY and HID that develop RFID sensor tags. Mainly, the chip sets of the company ASYGN or AXZON are employed in existing solutions. While ASYGN offers an integrated circuit (IC) with a fully integrated sensor front-end circuit, to connect either external sensor devices to the chip or utilize internal sensors, the company AXZON targets solutions with a different approach. They realize the discretization of the measured quantity by directly influencing the antenna structure and analyzing the relative strength signal indicator (RSSI) value, which can be read-out by their integrated engine, called CHAMELEON. Therefore, the antenna structure itself acts as sensing device, which leads on one hand to a cost reduction, but on the other hand offers limited sensing capabilities with only a few discrete values. An intense market review revealed that the commercially available RFID sensor tag solutions, use different types of chips of the previously mentioned chip manufacturers, exploiting only their internally integrated sensor devices.

In the literature several solutions for sensor attached RFID systems [1], including optimized antenna structures for long read-out ranges [2] are reported, which are even applied in industrial applications [3], but always without long sensor wires.

Development of the RFID Sensor Tag

In the presented sensor tag the ASYGN chip AS3212, which includes a fully integrated sensor front-end circuit to attach a Wheatstone bridge configuration is used. To measure the temperature at hard-to-reach places, where it is not possible to install a tag antenna structure or transmitter antenna due to a metallic environment, long connection wires between the sensor tag and the sensing element are required. In this case several issues arise. First, the overall input resistance of the connected bridge circuit should be matched to about 1 kΩ. Secondly, the low bridge supply voltage of 1 V must be considered. Finally, it must be ensured that the measured value can be correlated to the real physical quantity, for example temperature.

Beside these boundary conditions, a long cable within the configuration introduces a non-negligible inductivity with an effective area that might induce high voltage peaks, if being exposed to an electromagnetically disturbed environment. Additionally, a copper wire itself is sensitive to any pressure. To overcome this, a common technique is to twist the supply and return conductor to the sensor component, avoiding a wire loop and hence the induction of any unwanted signal.

Long connection wires also add a not neglectable resistance value, that falsify the measured temperature with the PT1000. This is particularly relevant, if the wires are very thin, like 100 µm in diameter and 4 m long. Thereby,

due to the twisting of the wires, an additional length extension of up to 5% can be expected. This value leads to an absolute error that must be compensated. Figure 1 shows a commonly used arrangement that does not offer this possibility.

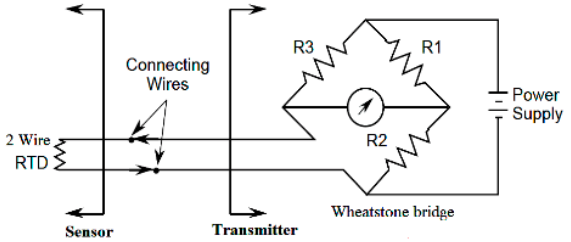

Fig. 1. Common setup of a Wheatstone bridge for temperature measurements.

To compensate the effect of the long connecting wires, an additional wire with a short circuit is connected between R3 and its power supply feeding pin depicted in Figure 2.

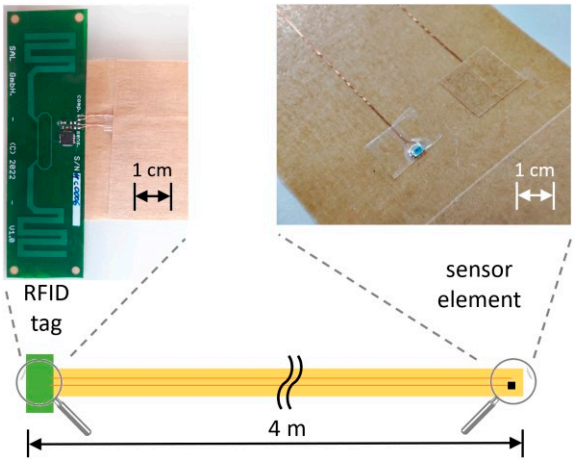

Fig. 2. Developed sensor system with RFID chip, antenna and connected sensor with parallel compensation wire to equalize the resistance value.

Measurement Results

As the AS3212 is a UHF-based RFID chip, the IC with the attached sensor implemented in the Wheatston bridge is connected to an antenna structure. To minimize the component count, also the matching circuit is realized as a lumped element structure.

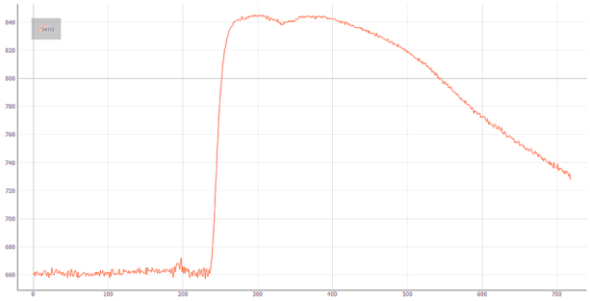

Fig. 3. Temperature measurement with 4 m long sensor wires. Binary values just represent the voltage difference within the bridge configuration.

As the sensor circuitry represents an additional load to the chip, also the matching circuitry is affected. A detuning increases the power consumption by additionally reducing the read-out range. Therefore, this load scenario must be considered. Figure 3 depicts a typical temperature measurement result, achieved by heating up the sensor with a hot air gun up to +100°C.
The read-out over a range of up to 2 m is performed with a Impinj Speedway R420 reader unit, connected to a 11 dBi antenna of Kathrein.

Conclusion and Outlook

The presented work describes the setup of a UHF RFID sensor tag, that is capable to be connected to external sensor elements with long wires and therefore enables the possibility to read out temperature values wirelessly, even if the measurement point of interest is hardly accessible. Although the wiring introduces a high resistive load to the RFID chip, by optimizing the matching circuitry wireless read-out ranges of up to 2 m could be achieved.
These promising results, show the great potential of such a UHF RFID sensor system to be used in many types of industrial applications, where no appropriate solution exist. Nevertheless, further improvements and optimizations regarding the matching must be performed to enhance the read-out range and additionally investigations in the system performance for different sensor wire lengths might be useful, to be able to offer solutions for any kind of problems in the industrial environment in the future.

Acknowledgement

This work has been jointly supported by the Industry partner Hasslacher Norica Timber and by Silicon Austria Labs (SAL), owned by the Republic of Austria, the Styrian Business Promotion Agency (SFG), the federal state of Carinthia, the Upper Austrian Research (UAR), and the Austrian Association for the Electric and Electronics Industry (FEEI).

References

[1] F. Costa, S. Genovesi, M. Borgese, A. Michel, F. A. Dicandia, and G. Manara, “A Review of RFID Sensors, the New Frontier of Internet of Things,” Sensors, vol. 21, no. 9, p. 3138, Apr. 2021, doi: 10.3390/s21093138.

[2] Abdulghafor, R., Turaev, S., Almohamedh, H., Alabdan, R., Almutairi, B., Almutairi, A., & Almotairi, S. Recent advances in passive UHF-RFID tag antenna design for improved read range in product packaging applications: A comprehensive review. IEEE Access, 9, 63611-63635.

[3] Zhang, K., Li, Z., Meng, Z., Zhou, W., Gao, N., & Zhang, Z. (2022). UHF-HF integrated RFID sensor: A novel information interface for industrial integration. IEEE Sensors Journal, 22(15), 15477-15487.

DOI 10.5162/SMSI2023/B3.4

Energy-Autonomous Wireless Sensor Node for Monitoring of Wind Turbine Blades

Thomas Schaechtle[1,2], Christian Heim[1], Gudrun Bruckner[3], Alfred Binder[3], Leonhard M. Reindl[1], and Stefan J. Rupitsch[1]
[1] University of Freiburg, Laboratory for Electrical Instrumentation and Embedded Systems, Freiburg, Germany
[2] Fraunhofer Institute for Highspeed Dynamics, Ernst Mach-Institute, Freiburg, Germany
[3] Silicon Austrian Labs, Villach, Austria
thomas.schaechtle@imtek.uni-freiburg.de

Summary:
In this contribution, we propose an energy-autonomous wireless sensor node for monitoring wind turbine blades. To allow a placement of the sensor node on the leading edge of the wind turbine blade with minimal influence to its performance, the electronics have to be ultra-thin and mechanically flexible. The concept of the sensor system is presented with a main focus on the eigenfrequency analysis of the rotor blade based on MEMS accelerometers. The sensor system is demonstrated on a small-scale wind turbine blade with a length of 1.07 m.

Keywords: wireless sensor node, energy-autonomous, eigenfrequency analysis, predictive maintenance, wind turbine monitoring, MEMS accelerometer

Motivation

Wind turbines are exposed to harsh environmental conditions, which have a particularly strong impact on their rotor blades. In order to be able to determine the present state and predict aging effects, it is of great interest to acquire local measurement data on the rotor blade itself. This can contribute to a safe operation of wind turbines after its intended life span and reduce safety downtimes. For this, the monitoring of ice layer thickness and the detection of mechanical peak loads due to impacts for example of birds, bats, ice shedding or wind gusts will be investigated. For this purpose, an energy-autonomous, ultra-thin and flexible wireless sensor system is required to be retrofittable.

In the following, we present the concept of a wireless sensor node. Furthermore, an eigenfrequency analysis is implemented and evaluated on a test setup to subsequently estimate the power consumption for energy-autonomous operation.

Concept of the Wireless Sensor Node

Eigenfrequencies are affected by alterations in geometry and material parameters and can, therefore, be exploited to detect faults in rotor blades. The eigenfrequencies can be obtained by a spectral analysis of the rotor blades vibration measured with MEMS accelerometers [1].

Modern MEMS accelerometers provide ultra-low-power operation modes with high sampling rates for spectral measurements or for continuously detecting mechanical impacts. Here, we implemented a continuous impact detection (ID) with a wake-up at a threshold of 30 g to detect randomly occurring mechanical peak loads with the accelerometer Analog Devices *ADXL273* featuring a measurement range of up to 200 g. A vibration signal is obtained by the accelerometer Bosch Sensortec *BMA400* with optimized resolution in the measurement range of 16 g either at scheduled intervals or after an impact is detected. The vibration signal is read out from the accelerometers memory into a microcontroller (µC) and is further processed according to Fig. 1. The eigenfrequencies are extracted and transmitted (Tx peaks) with an integrated 2.4 GHz radio transceiver.

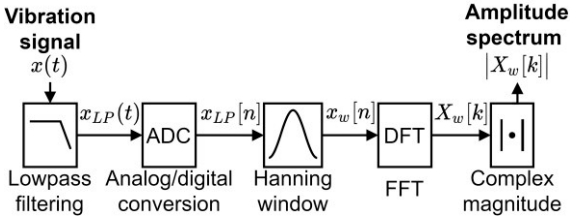

Fig. 1. Block diagram of the spectral analysis.

The first five obtained eigenfrequencies are transmitted to a base station. Thereby, long-term changes for a predictive maintenance database can be acquired. The used microcon-

troller Nordic *nRF52840* is mostly operated in a sleep mode with a real time clock (RTC) for scheduled tasks. A prototype of the sensor node was fabricated on a 0.6 mm thick FR4 substrate shown in Fig. 2. A subsequent sensor node will be integrated on a flexible printed circuit board with a 200 µm polyimide substrate together with a low-profile battery and energy harvester resulting in a total thickness of less than 1.3 mm.

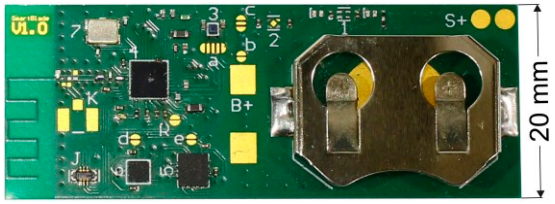

Fig. 2. Picture of the wireless sensor node.

Demonstration on a Small-Scale Rotor Blade

The eigenfrequencies of a small-scale rotor blade were determined by the wireless sensor node and evaluated with a scanning laser Doppler vibrometer. The 1.07 m long rotor blade is composed of a glass fiber reinforced polymer procured from *IstaBreeze*®.

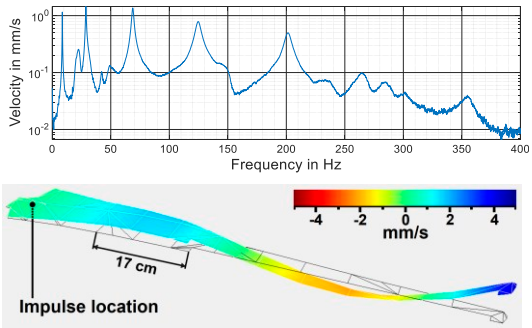

Fig. 3. Measurement results of the scanning laser Doppler vibrometer: (a) Average amplitude spectrum of the entire rotor blade. (b) Graphical representation of the third flap-wise mode at 68.83 Hz.

The statically fixed rotor blade was excited at the bottom side with a mechanical impulse generated by an electrodynamic shaker with an attached force sensor at the hammer tip. With this setup, almost solely flap-wise modes have been excited. The sensor node was positioned at the tip of the rotor blade, with the further analyzed acceleration axis, facing out of the flat side of the rotor blade.

Tab. 1: Accuracy of the eigenfrequency analysis of the first three flap-wise modes.

Flap-wise mode	Vibrometer: Frequency in Hz	Sensor Node: Frequency in Hz
1st	8.44 ± 0.08	8.6 ± 0.2
2nd	28.83 ± 0.08	29.0 ± 0.2
3rd	70.00 ± 0.16	69.9 ± 0.2

Results

Based on the coherently scanned surface of the rotor blade with the laser Doppler vibrometer, the eigenmodes can be visually determined with an exemplary of the third flap-wise mode given in Fig. 3 (b). The corresponding eigenfrequencies can be matched to the averaged spectrum of all points in the scanned area in Fig. 3 (a) and the spectrum obtained by the wireless sensor node in Fig. 4 (b).

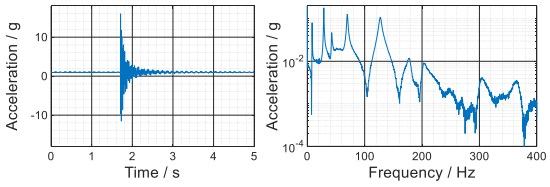

Fig. 4. Measurement result of the wireless sensor node: (a) Vibration signal in the time domain before applying a Hanning window. (b) Vibration signal in the frequency domain.

In Fig. 4 (a), measurements of an excitation impulse can be seen with an exponentially decaying amplitude in the time domain measured with 800 Hz. A fast Fourier transform (FFT) is exploited with 4096 samples to obtain the eigenfrequency analysis (EFA) in Fig. 4 (b). The eigenfrequencies of the first three flap-wise modes are averaged over 30 measurements and listed in Tab. 1.

Tab. 2: Current consumption of the sensor node at an operating voltage of 1.8 V.

Tasks	Current in µA	Duration in ms
ID & RTC	5.3 ± 0.7	-
µC & EFA	6520 ± 783	5119.00 ± 0.02
Tx peaks	7520 ± 903	0.62 ± 0.02

With the averaged current consumptions of the described tasks listed in Tab. 2, the applicability of the MEMS sensor for continuous impact detection for an energy-autonomous sensor node is shown and an estimation of measurement and transmission intervals for future work can be derived.

Acknowledgement

We gratefully acknowledge the funding of this work by the Austrian Research Promotion Agency (FFG) within the ASSIC project.

References

[1] M. McGugan, L. Mishnaevsky Jr, Damage mechanism based approach to the structural health monitoring of wind turbine blades. MDPI Coatings, 10(12), 1223 (2020); doi: 10.3390/coatings10121223

DOI 10.5162/SMSI2023/B4.1

Chemiresistive Methane Gas Sensing Properties of Triphenylene-based Metal-organic Frameworks

Sachin T. Navale[1,2,], Ignasi Fort-Grandas[1,2], Yuzelfy Mendoza[1,2], Paolo Pellegrino[1,2], Mauricio Moreno[1,2], Daniel Sainz[2,3], Anton Vidal-Ferran[2,3,4], Albert Romano-Rodriguez[1,2]*
[1] Dept. of Electronic and Biomedical Engineering, Universitat de Barcelona, 08028 Barcelona, Spain
[2] Institute of Nanoscience and Nanotechnology, Universitat de Barcelona, 08028 Barcelona, Spain
[3] Dept. of Inorganic and Organic Chemistry, Universitat de Barcelona, 08028 Barcelona, Spain
[4] Catalan Institution of Research and Advanced Studies (ICREA), 08010 Barcelona, Spain
**E-mail address: stnavale2@ub.edu*

Summary:
The emission of methane (CH_4), a potent greenhouse gas (GHG), into the atmosphere is one of the causes of global warming and climate change. To address these challenges, we must continue to reduce CH_4 emissions, which ultimately require miniaturised low-power sensor systems with better precision for monitoring, reporting, and validation of CH_4 levels. In this respect, the use of triphenylene-based metal-organic frameworks (TP-MOFs), as sensing materials, to detect CH_4 is described here. Thanks to their high surface area and porosity, TP-MOFs detect low CH_4 levels at room temperature.

Keywords: nanomaterials, MOFs, gas sensors, electrical response, GHGs

Background, Motivation and Objective

Over the last several years, climate change and global warming have been a major concern and are considered to be one of the greatest global threats. Increasing human actions has led to a rapid increase in GHGs emissions, particularly CH_4 and carbon dioxide (CO_2), into the Earth's atmosphere, which has resulted in a gradual warming of the atmosphere [1]. Notably, CH_4 is a potentially explosive gas and it has more than 84 times the warming power of CO_2 [2]. As a result, it is highly responsible for global warming. Therefore, measuring and reliably quantifying CH_4 emissions into the environment is a top priority for tackling the climate change. In this respect, detecting and monitoring CH_4 is the first step in seeking a solution for managing and reducing its concentration in the Earth's atmosphere. In order to meet this demand, substantial research into new materials-based highly sensitive and low-cost gas sensor systems for detecting CH_4 is underway [1-2]. For this, chemiresistive gas sensors are very attractive because they are cost-effective, easy to manufacture, simple to operate, and show response towards various gases. These chemiresistive sensor devices are mostly made from metal oxides, whose properties have been achieved through intensive research on micro- and -nanofabrication of the materials [3]. However, despite considerable efforts, these sensors are still suffering from the drawbacks of poor selectivity, stability, and higher working temperatures. These problems of chemiresistive sensors can be circumvented by replacing metal oxides with advanced MOFs as gas sensing materials. Basically, MOFs are crystalline materials consisting of metal nodes and organic linkers that form a rigid cage-like structure with an extremely high surface area and porosity that makes MOFs an ideal candidate for gas detection, since chemiresistive sensors highly rely on surface reactions [3]. Thus, the main objective of present study is to detect low CH_4 levels using advanced TP-MOFs as detection materials.

Here we used a prominent group of TP-MOFs, which can be chemically altered either with hydroxyl or amino or thiol ligating groups. We targeted the series containing hexahydroxytriphenylene (HHTP) as an organic ligand and Cu^{2+} or Ni^{2+} as metal-ions. We demonstrate that Cu- or Ni-HHTP-based MOFs can be used as sensing materials for detecting low levels of CH_4 at room temperature.

Experimental details

During Cu-HHTP MOF synthesis, suitable amounts of HHTP-ligand and Cu-acetate were mixed in 2 ml of distilled water and sonicated for 10 min. Subsequently, 0.15 ml of dimethylformamide was added into the above mixture and sonicated for another 10 min., after which it was kept in an oven at 80 °C for 6 hrs. After the reaction, the powder product was collected by centrifugation and washed several times with distilled water and ethanol and dried. Similar conditions were applied to the synthesis of Ni-HHTP MOF

with Ni-acetate as metal salt [4]. The chemical structure of Cu/Ni-HHTP MOF is shown in Fig. 1.

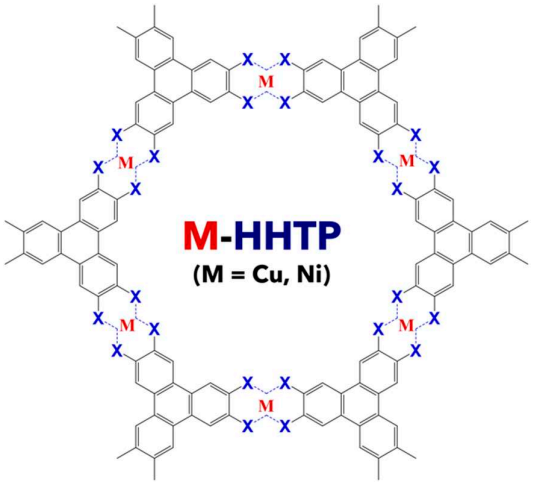

Fig. 1. Chemical structure of Cu/Ni-HHTP MOF.

Gas sensing results

Gas sensing studies on Cu/Ni-HHTP MOFs were conducted, using dynamic gas measurement setup, towards different concentrations of CH_4 at room temperature. The electrical resistance change of Cu/Ni-HHTP MOFs upon CH_4 interaction was recorded and plotted over time. For electrical resistance measurement, chips with interdigited electrodes (90 pairs of Au-electrodes) were used. For sensor fabrication, a small amount of Cu/Ni-HHTP powders were dispersed into the distilled water and sonicated for 20 minutes. Afterwards, 10 µl (≈1 drop) of the suspension was drop-casted onto the interdigited chips and dried, before being used as sensing element. During gas sensing measurements, prior to CH_4 injection, Cu/Ni-HHTP sensors were stabilized for 2 hrs in dry synthetic air. A sensor response was calculated as: Response=[$|R_a$-$R_g|/R_a$]*100, where, R_a and R_g are the resistances of Cu/Ni-HHTP sensors in air and CH_4 gas, respectively. Fig. 2 shows the response of Cu- and Ni-HHTP sensors to various CH_4 concentrations at room temperature, wherein resistance values of both the sensors found to be increased upon CH_4 interaction, with complete recovery kinetics. A higher response was observed for the Cu-HHTP sensor relative to the Ni-HHTP sensor. The calculated response, at 12.5 ppm CH_4 is 10% for the Cu-HHTP sensor, which is almost 9 times that of the Ni-HHTP sensor (1.15%), suggesting excellent response to CH_4 with Cu-HHTP MOFs. More importantly, the Cu-HHTP sensor detects very low CH_4 concentration, 1.2 ppm, which is below the atmospheric CH_4 concentration (1.9 ppm) reported by Global Monitoring Laboratory for the year 2022 [5]. Thus, the sensing results clearly illustrate the potential of TP-HHTP MOFs as active sensing materials in the development of low-power chemiresistive sensors to detect GHGs, especially CH_4.

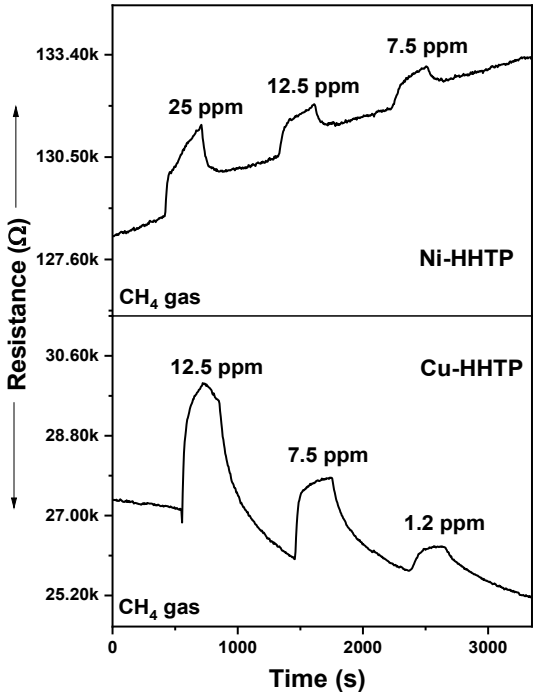

Fig. 2. Dynamic resistance plot of Cu/Ni-HHTP MOF sensor at various levels of CH_4 at room temperature.

Acknowledgements

This research has received funding from the European Union's Horizon 2020 research and innovation programme under Marie Sklodowska-Curie grant agreement No. 101030015 and from the Spanish Ministerio de Economía e Innovación, through project PID2019-107697RB C41/AEI/10.13039/501100011033.

References

[1] K. Santhanam, N. Ahamed, Greenhouse gas sensors fabricated with new materials for climatic usage: A review, *Chemengineering* 2, 38 (2018); doi: 10.3390/chemengineering2030038

[2] M. Bezdek, S. Luo, K. Ku, T. Swager, A chemiresistive methane sensor, *PNAS* 118, 1-6 (2021); doi:10.1073/pnas.2022515118

[3] W. Koo, J. Jang, I. Kim, Metal-organic frameworks for chemiresistive sensors, *Chem* 5, 1938-1963 (2019); doi: 10.1016/j.chempr.2019.04.013

[4] R. Dey et al., Single crystals of electrically conductive two-dimensional metal-organic frameworks: Structural and electric transport properties, *ACS Cent. Sci.* 5, 1959-1964 (2019); doi: 10.1021/acscentsci.9b01006

[5] X. Lan, K. Thoning, E. Dlugokencky, Trends in globally-averaged CH_4, N_2O, and SF_6 determined from NOAA Global Monitoring Laboratory measurements, (2022); doi:10.15138/P8XG-AA10

DOI 10.5162/SMSI2023/B4.2

Multi-Parameter Gas Monitoring System for Natural Gas with Hydrogen

Christof Huber[1], Fabio Schraner[1], Sandro Schwab[1]
[1]TrueDyne Sensors AG, Christoph-Merian-Ring 20, 4153 Reinach, Switzerland,
christof.huber@endress.com

Summary:

We demonstrate the use of a newly developed multi-parameter gas property MEMS chip, that is designed to measure density, dynamic viscosity and thermal conductivity of gases, for the characterisation of hydrogen-containing combustion gas mixtures. The sensor is able to measure combustion gas with hydrogen directly in the process line independent of the process conditions (pressure, temperature and flow) and without complex gas conditioning. The chip design is aimed at ensuring that cost-sensitive mass applications can also be served with this sensor in the future.

Keywords: micro cantilever, gas thermophysical properties, natural gas, hydrogen, calorific value

Background and Motivation

Monitoring gas compositions in realtime at low costs directly in the process becomes more and more important in different fields of applications. Using MEMS sensors is an adequate way to solve this demand. By means of correlative methods, various desired quality properties of gas mixtures can be derived from thermophysical properties like density, viscosity and thermal conductivity of gases in an application-specific manner. For example, the composition of multi-component process gas mixtures such as welding shield gases or gases in food packaging (MAP) can be characterised and monitored online. Another important application for such a measuring system are combustion gases such as natural gas or biogas, which can also contain large quantities of hydrogen. The properties that are relevant here are calorific value, Wobbe index, methane number, hydrogen concentration, inert gas content, molar mass and reference density [1,2].

Description of the System

Our silicon chip contains two micro cantilevers, piezoelectrically activated (see Fig. 1). As shown in previous publications, this chip can be used to measure thermophysical properties of gases. On the one hand, the 1st cantilever is vibronically excited to its resonance frequency. The density and viscosity can be derived from the determined oscillation properties frequency, f, and quality factor, Q [2,3,4]. What is new about this chip version is that by heating the second cantilever with a constant heating power and simultaneously measuring the temperature difference that arises between the two cantilevers, the thermal conductivity of the gas can also be determined. This measurement can be carried out simultaneously or alternately with the density and viscosity measurement. With the help of the different temperature sensors on the chip, the gas temperatures associated with the measured variables density, dynamic viscosity and thermal conductivity can also be precisely tracked at any time. In conjunction with a pressure measurement the measured gas can be completely characterised independently of the process conditions.

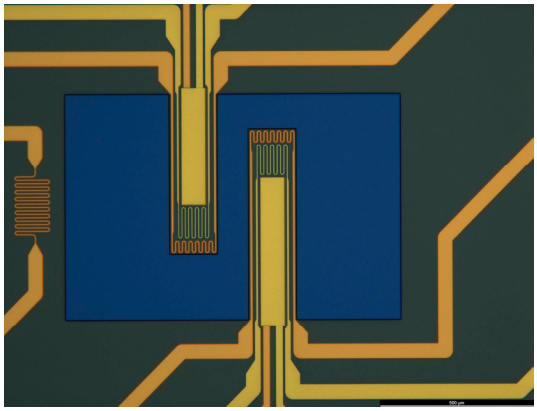

Fig. 1. Picture of the MEMS chip containing two micro cantilevers of slightly different lengths (500 and 600 µm), which can be piezo electrically driven and read out. The two cantilevers are each equipped with a temperature sensor and a heating element. In addition, there is another temperature sensor on the frame of the chip (left side).

With our chip it is possible to measure in a temperature range from approx. -40 to 80°C and in a pressure range from approx. 0.5 to 10 bar. No

complex gas conditioning and branching is necessary, which makes the installation simple and inexpensive.

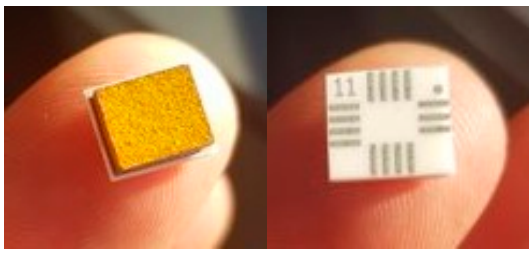

Fig. 2. Pictures of the packed chip from top and bottom. The MEMS chip is flip chip bonded to a ceramic PCB (right) and covered with a porous filter cap (left).

To protect the sensing cantilevers and to be able to measure reliably in the process under changing conditions and with possibly contaminated gases, the MEMS chip was covered with a filter cap (see Fig. 2). The cap consists of a porous structure made of sintered bronze with pore sizes in the range of a few micrometers. The filter cap also prevents gas convection at the chip, which would interfere with the measurement of thermal conductivity. Nevertheless, due to the small chip dimension, the filter cap allows a very fast diffusive gas exchange in the range of < 2 sec and thus measurements almost in realtime.

Results

The following shows the achievable measurement performance of such a measurement system for methane and natural gas mixtures with hydrogen contents up to 20% mol in a wide temperature and pressure range. For the experiments, the sensor was mounted together with a pressure sensor in a pressure tight measuring cylinder. The complete system was placed in a climate chamber and various gas mixtures (see Tab. 1) were measured at pressures between 2 and 6 bar and temperatures between 0 and 50°C. The results can be seen in Figs. 3 and 4. The calorific value and the Wobbe Index of the gases could be determined with an accuracy of 1 to 1.5% over the entire measuring range.

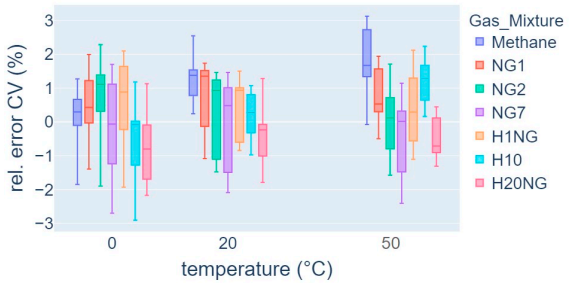

Fig. 3. Relative error of the calorific value determination of 7 different gas mixtures at different temperatures. Each box plot includes measurements performed at three pressures (2, 4 and 6 bar).

The hydrogen content was determined to <0.5% mol and the total inert gas content to approx. 1% mol.

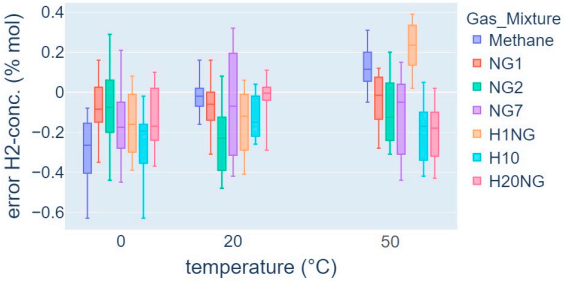

Fig. 4. Error of the hydrogen concentration determination of 7 different gas mixtures, containing up to 20% mol hydrogen, at different temperatures. Each box plot includes measurements performed at three pressures (2, 4 and 6 bar).

Tab. 1. Composition of the measured gases.

gas	NG1	NG2	NG7	H1 NG	H20 NG	H10
CH_4	93	85	84	91.8	74.1	90
C_2H_6	4.2	9	5	4.1	3.4	0
C_3H_8	0.8	1.5	2	0.8	0.7	0
C_4H_{10}	0.3	0.5	0.5	0.3	0.3	0
N_2	1.3	2.5	4	1.3	1	0
CO_2	0.7	1.4	4	0.6	0.5	0
H_2	0	0	0	1	20	10

References

[1] C. Huber, A. Badarlis, A method for determining properties of a hydrocarbon containing gas mixture and device for the same, *EP3362790B1*, (2015)

[2] C. Huber, P. Reith and A. Badarlis. Gas Density and Viscosity Measurement with a Micro-cantilever for Online Combustion Gas Monitoring. *Proceedings of the 19th GMA/ITG-Fachtagung Sensoren und Messsysteme*, 26–27 (2018); ISBN 978-3-8007-4683-5

[3] A. Badarlis, A. Pfau, A. Kalfas, Measurement and Evaluation of the Gas Density and Viscosity of Pure Gases and Mixtures Using a Micro-Cantilever Beam, *Sensors* 15, 24318-24342 (2015); doi: 10.3390/s150924318

[4] C. Huber, M.P. Pina, J.J. Morales, A. Mehdaoui, A Multiparameter Gas-Monitoring System Combining Functionalized and Non-Functionalized Microcantilevers, *micromachines* 11, 283 (2020); doi: 10.3390/mi11030283

DOI 10.5162/SMSI2023/B4.3

Highly Sensitive Hydrogen Sensor Based on ZnO/MWCNTs Nanocomposite Material

M.S. Aleksanyan, A.G. Sayunts, G.H. Shahkhatuni, Z.G. Simonyan, G.E. Shahnazaryan
Center of Semiconductor Devices and Nanotechnologies, Yerevan State University, 1 Alex Manoogian, 0025, Yerevan, Armenia
Corresponding Author's e-mail address: sayuntsartak@ysu.am

Summary:
The development of a flexible hydrogen sensor based on ZnO/MWCNTs (Multi-Walled Carbon Nanotubes) is presented in this work. The sensor was prepared by an electron-beam deposition method, when gas sensitive ZnO/MWCNTs thin film was deposited onto a flexible polyimide substrate. The produced sensor demonstrated excellent gas sensing characteristics to hydrogen at 150°C operating temperature, where the resistance of the sensor decreased more than 100 times in the presence of 25 ppm of hydrogen demonstrating the linear dependence of the sensor response on hydrogen concentration. The obtained results proved that ZnO/MWCNTs based flexible structure may become an excellent material for hydrogen monitoring devices.

Keywords: Gas sensor, hydrogen, flexible sensor, carbon nanotube, zinc oxide.

Introduction

Hydrogen is widely used in various fields of human activity and the need for its application continues to increase year by year becoming one of the promising alternatives to traditional energy sources. Consequently, the highly flammable nature of hydrogen and its explosive characteristics under certain conditions increase the interest in hydrogen sensors in all areas where hydrogen technologies are used [1].

Resistive gas sensors based on metal oxide semiconductors are attractive in their simple structure, high response, low cost, availability of the electric signal, low power consumption, and high reliability [2]. However, metal oxide semiconductor gas sensors have poor electron conductivity and a small surface area which worsens their sensing properties. The presence of MWCNTs in main metal oxide materials improves the gas sensing properties of the sensors, decreases the operating temperature (even to room temperature), and gives stability to the sensors [3].

Compared with non-flexible sensors, flexible ones are more conducive to applications in wearable electronics, they are lightweight and have low cost and low power consumption. Due to their high flexibility and small sizes, these sensors can be easily integrated into the surfaces of any flexible objects [1, 4].

In this work, a new nanocomposite ZnO/MWCNTs material is proposed, which is distinguished by a relatively high response to hydrogen and low operating temperature.

Experimental

The ZnO/MWCNTs (Nanoshel-UK Ltd., UK, with 99% purity) based sensing layer was deposited on a polyimide flexible substrate with 130 μm thickness (Zhongcheng Insulating Material Ltd., China) on which were pre-deposited gold interdigitated electrodes (Fig. 1).

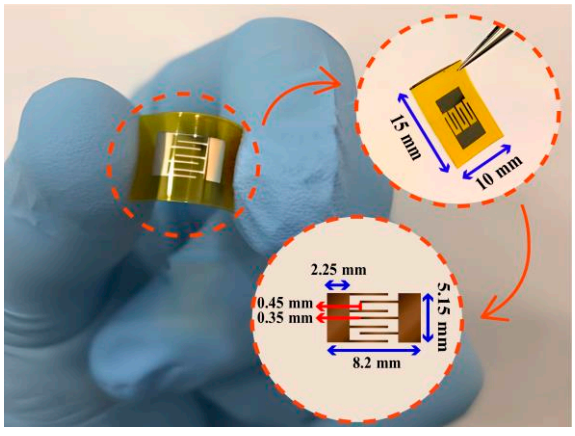

Fig. 1. Actual photo of the flexible hydrogen sensor.

The electron-beam deposition process of ZnO/MWCNTs material was conducted under the following conditions: 40 mA anode current, 0.4 kV anode voltage, 100 °C substrate temperature, 75 mm distance between the target and substrate, 3×10^{-3} Pa base pressure,

5×10^{-1} Pa deposition pressure and 15 minutes duration of sputtering using pre-prepared ZnO/MWCNTs target. Then, palladium catalytic particles were sputtered on the active surface of the ZnO/MWCNTs material by an ion-beam sputtering method.

Results

Gas sensing properties of the ZnO/MWCNTs material were studied in the air and in the presence of hydrogen by laboratory-designed (automated) gas sensor testing setup. The response of the sensor is defined as the resistance ratio of the sensor in the air and in the atmosphere of the target gas, respectively (R_a/R_g, where R_a and R_g are the resistance of the sensor in the air and in the presence of target gas, respectively). The sensing characteristics of the sensor were investigated in the temperature range of 25–250°C (Fig.2).

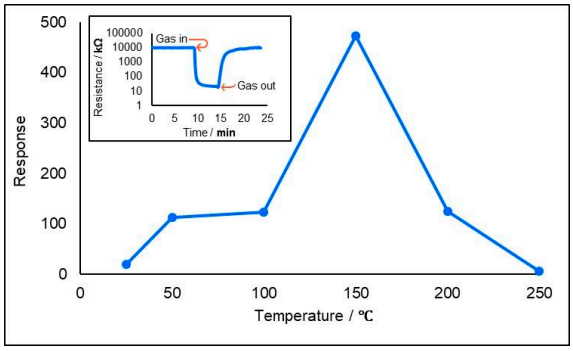

Fig. 2. Dependence of the ZnO/MWCNTs sensor response on temperature in the presence of 100 ppm hydrogen and the dynamic change in the sensor resistance at 150°C (inside of the picture).

As Fig. 2 shows, the sensor demonstrated the best response to 100 ppm at 150°C temperature where its resistance changed more than 472 times and response and recovery times were 15 s and 4.5 s minutes, respectively. The ZnO/MWCNTs structure showed a response to 100 ppm hydrogen even at room temperature, where its resistance changed about 20 times during 18 minutes and recovered after 5 hours.

The dynamic response curves under the influence of different concentrations of hydrogen at 150°C temperature as well as the dependence of sensor response on hydrogen concentration are shown in Fig. 3. The ZnO/MWCNTs flexible gas sensor reacted to 25 ppm hydrogen at the operating temperature with a response value of 100. It is important to mention that sensor response changed linearly toward hydrogen concentration which allows for estimating different concentrations of hydrogen in real environments.

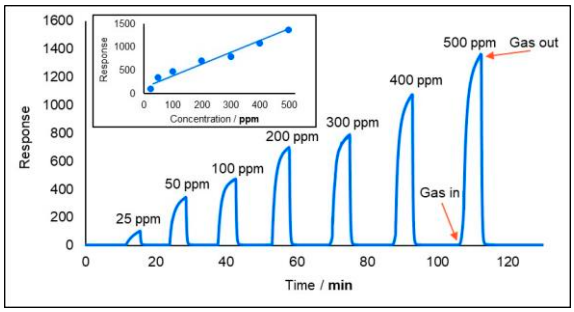

Fig. 3. Dynamic response curves of the ZnO/MWCNTs sensor for different concentrations of hydrogen and the dependence of the response on hydrogen concentration at the operating temperature (inside of the picture).

Conclusion

In summary, the fabricated ZnO/MWCNTs based flexible sensor showed a high response (~100) to 25 ppm hydrogen at 150°C operating temperature. Besides, the sensor demonstrated the linear response dependence on hydrogen concentration toward 25-500 ppm at that temperature. The ZnO/MWCNTs structure also exhibited good sensitivity toward 100 ppm hydrogen even at room temperature.

Acknowledgment

The work was supported by the Science Committee of MESCS RA, in the frames of the research project № 21APP-2J001.

References

[1] M.S. Aleksanyan, A.G. Sayunts, G.H. Shahkhatuni, Z.G. Simonyan, V.M. Aroutiounian, G.E. Shahnazaryan, Flexible sensor based on multi-walled carbon nanotube-SnO_2 nanocomposite material for hydrogen detection, *Advances in Natural Sciences: Nanoscience and Nanotechnology* 13, 035003 (2022); doi: 10.1088/2043-6262/ac8671

[2] S.R. Jamnani, H.M. Moghaddam, S.G. Leonardi, G. Neri, PANI/Sm_2O_3 nanocomposite sensor for fast hydrogen detection at room temperature, *Synthetic Metals* 268, 116493 (2020); doi: 10.1016/j.synthmet.2020.116493

[3] S. Vijayakumar, S. Vadivel, A. Biruntha, T. Brindhasri, P.A. Desika, Design and fabrication of clad modified fiber optic gas sensor based CeO_2/MWCNTs hybrid sensors by facile hydrothermal technique, *Diamond and Related Materials* 109, 108006 (2020); doi: 10.1016/j.diamond.2020.108006

[4] F. Zhang, Q. Lin, F. Han, Z. Wang, B. Tian, L. Zhao, T. Dong, Z. Jiang, A flexible and wearable NO_2 gas detection and early warning device based on a spraying process and an interdigital electrode at room temperature, *Microsystems & Nanoengineering* 8, 40 (2022); doi: 10.1038/s41378-022-00369-z

DOI 10.5162/SMSI2023/B4.4

Dielectric Properties of Materials used for a Radio-Frequency based NO_x Dosimeter

Stefanie Walter[1], *Jaroslaw Kita*[1], *Daniela Schönauer-Kamin*[1], *Gunter Hagen*[1], *Ralf Moos*[1]
[1] *Department of Functional Materials, University of Bayreuth, 95447 Bayreuth, Germany*
functional.materials@uni-bayreuth.de

Summary:
To detect low concentrations of nitrogen oxides (NO_x), a new radio-frequency dosimeter is being developed. The storage of NO_x in a functional material results in a change of its dielectric properties, that can be detected via a resonance structure. To optimize the sensor design, the dielectric properties of different sensor substrates as well as of the sensitive barium-based NO_x storage materials itself were analyzed.

Keywords: radio frequency (RF), dosimeter, dielectric properties, LTCC, NO_x storage materials

Introduction

Nitrogen oxides (NO_x) cause substantial damage to both human health and environment. To ensure air quality, monitoring of NO_x is necessary. For this purpose, a dosimeter capable of measuring average NO_x concentrations over long time periods is being developed.

Sensor Design

Many materials cannot be used for conventional resistive sensors due to their high electrical resistivity. An alternative is offered by radio frequency (RF) sensors, which can detect changes in the dielectric properties of a functional material.

The sensor setup, as shown in Fig. 1, is modified compared to a previous design in [1]. The stripline to excite the resonant structure is now shielded on both sides by a ground plane. LTCC (Low Temperature Cofired Ceramics) is used as the sensor substrate. For higher stability, the functional material can be placed in a recess in the top LTCC layer. This is necessary, since a layer thickness of several hundred micrometers is advisable for a high sensor signal.

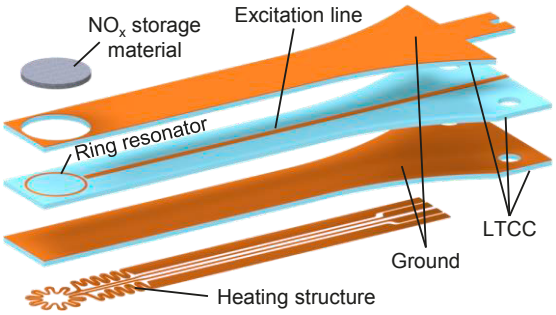

Fig. 1. Schematic setup of the planar RF-based NO_x dosimeter.

Dosimeters measure a time-integrated gas concentration. Thus, for dosimetric detection of NO_x, the functional material has to store NO_x continuously proportional to the NO_x concentration [2]. This can then be measured via the parameters of the excited resonant mode. Since the adsorption behavior of such materials is often temperature-dependent, a heating structure is implemented to vary the sensor temperature. This can also be used for sensor regeneration, as NO_x is often desorbed at higher temperatures [2].

Microwave Cavity Perturbation

To obtain an optimal sensor signal, the geometry of the resonant structure has to be designed in dependence of the dielectric properties of the LTCC substrate and the barium-based NO_x storage material. These can determined by the Microwave Cavity Perturbation (MCP), whose basic working principle has already been described in detail in [3].

By placing a sample in a cylindrical cavity, in which electromagnetic resonances can be excited, a shift of the resonant frequency Δf and of the invers quality factor $\Delta(1/Q)$ occurs. Following Eqs. 1 and 2, they can be used to infer the permittivity ε_r' and the dielectric losses ε_r'' of the material sample:

$$\Delta f \sim (\varepsilon_r' - 1) \tag{1}$$

$$\Delta\left(\frac{1}{Q}\right) \sim \varepsilon_r'' \tag{2}$$

However, depending on the sample properties, multiple corrections regarding the correlations in Eqs. 1 and 2 must be made as indicated in [3] in order to be able to infer the correct material properties.

Properties of LTCC

Two different types of LTCC material were analyzed: the DuPont GreenTape 951 and the DuPont GreenTape 9K7, a low-loss material optimized for radio frequency applications. According to the manufacturer's data sheet, the latter has a loss factor $\tan\delta$, which describes the ratio of ε_r'' to ε_r', of only 0.001 at 10 GHz compared with 0.014 for the LTCC 951. However, these values refer to room temperature. Since the sensor will be operated in a wide temperature range, knowledge of the temperature-dependent behaviour of the material properties is essential. The values for ε_r' and $\tan\delta$ measured by the MCP in a temperature range from 20 to 600 °C are shown in Fig. 2.

For both LTCC materials, their permittivity ε_r' is almost independent of temperature. Therefore, a shift in resonant frequency can be attributed mainly to dielectric changes occurring in the NO_x storage material. The loss factor affects the attenuation of the electromagnetic wave during its propagation along the excitation line and in the resonance structure and therefore determines the quality of the sensor signal. For both LTCC materials, $\tan\delta$ increases exponentially with temperature, however at different rate. Therefore, 951 exhibits lower dielectric losses than 9K7 at temperatures above 500 °C. Since the RF-dosimeter is intended to be operated mainly in a temperature range between 200 and 400 °C, 9K7 is still preferred as substrate for this application.

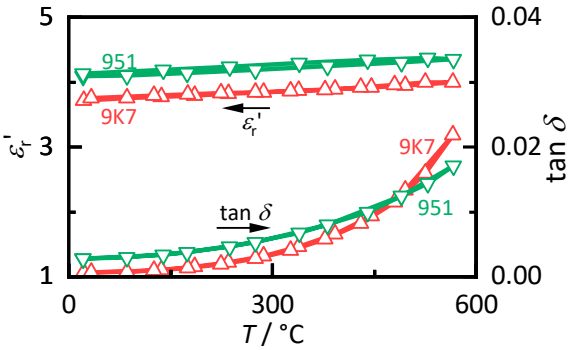

Fig. 2. Permittivity ε_r' and loss factor $\tan\delta$ of different LTCC materials; red: DuPont 9K7; green: DuPont 951.

Properties of NO_x Storage Materials

To detect the NO_x loading of the functional material, it has to change its dielectric properties thereby. In barium-based materials, this is the case due to the conversion of carbonate to nitrate during NO_x storage. Such materials are commonly used in automotive storage catalysts, exhibiting significant changes in their dielectric properties during NO_x storage [4].

With the MCP the dielectric properties of barium carbonate ($BaCO_3$) and barium nitrate ($Ba(NO_2)_3$) were measured. The permittivity of the two powders differs only slightly. Therefore, only their losses - shown in Fig. 4 - are relevant for NO_x detection. The dielectric losses ε_r'' of $BaCO_3$ increase only slightly with temperature and remain below 0.05. In contrast, those of $Ba(NO_2)_3$ increase rapidly. While below 100 °C ε_r'' of both powders are in the same range, at 400 °C the losses of nitrate are already 20 times higher. Thus, operation at high temperatures would be preferable for the RF-dosimeter. However, due to the NO_x adsorption behavior, a dosimeter-like sensor behavior is only expected at temperatures up to 400 °C. In addition, the signal quality decreases with higher temperature due to higher losses of the LTCC.

Furthermore, using pure barium carbonate as the functional material seems problematic due to its slow NO_x adsorption reaction rate, as it has only a small surface area of 1.6 m²/g. Therefore in future measurements, the barium will be coated on a highly porous aluminum oxide powder to increase the reaction surface.

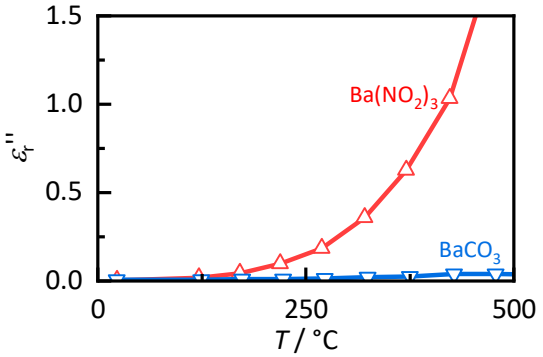

Fig. 3. Dielectric losses ε_r'' of barium-based NO_x storage materials; $BaCO_3$ in blue, $Ba(NO_2)_3$ in red.

References

[1] S. Walter, et al., Novel radio-frequency-based gas sensor with integrated heater, *J. Sens. Sens. Syst.* 8, 49–56 (2019); doi: 10.5194/jsss-8-49-2019.

[2] A. Geupel, et al., Integrating nitrogen oxide sensor: A novel concept for measuring low concentrations in the exhaust gas, *Sens. Actuators B* 145, 756–761 (2010); doi: 10.1016/j.snb.2010.01.036.

[3] C. Steiner, et al., Determination of the Dielectric Properties of Storage Materials for Exhaust Gas Aftertreatment Using the Microwave Cavity Perturbation Method, *Sensors* 20, 6024 (2020); doi: 10.3390/s20216024.

[4] S. Walter, et al., Radio Frequency-Based Determination of the Oxygen and the NO_x Storage Level of NO_x Storage Catalysts, *Top. Catal.* 62, 157–163 (2019); doi: 10.1007/s11244-018-1079-y.

Funding

This research was funded by the Deutsche Forschungsgemeinschaft DFG, (MO 1060/42-1).

DOI 10.5162/SMSI2023/B5.1

PbSe Photoconductors: Understanding Behavior and Concept for Upgrade Towards DC Stability

Davorin Babic[1], Shankar Baliga[1], Johannes Kunsch[2], Rudolf Mühlenbein[3], Weylin Pigg[1], Juan San Roman[1]
[1] Laser Components Detector Group, 2277 North Nevada Str, 85225 Chandler AZ, USA,
[2] Laser Components Germany GmbH, Werner-von-Siemens-Str. 15, 82140 Olching, Germany
[3] Mühlenbein, Lilienweg 24, 53501 Grafschaft, Germany
j.kunsch@lasercomponents.com

Summary:
Laser Components is a manufacturer of infrared detectors and with the mission to “Maintain and Upgrade IR Classics”. PbSe polycrystalline mid-wave infrared detectors are integral part of our product portfolio. They are linear p-type photoconductors over wide bias and temperature ranges. Current flows mostly uniform across grains and connecting tissue. Photoconductivity follows the “numbers modulation” model. Practical improvement of the devices is forecasted by using sort of balanced detection scheme.

Keywords: Infrared Semiconductor Detector, PbSe, Mid-Infrared, Photoconductor, Polycrystalline, Uncooled.

Introduction

PbS and PbSe infrared photoconductors belong to the family of thin film photodetectors (TFPD) and have been around for decades and successfully used in commercial and defence applications since. However, industrial usage of those materials has been based on RoHS exemptions and therefore strong efforts towards replacement were initiated. PbS and PbSe have been challenged for RoHS several times, but there is good news: Another exemption until July 2028 has been recommended and a longer-term co-existence of lead salt detectors and new DWRS (Detectors Without RoHS Substances) is forecasted. [1]

This paper is dedicated to PbSe and there is a mystery that needs to be explained: Typical D* for an uncooled PbSe device is 1.8 x 10^{10} Jones which is well above competing uncooled mid-wave infrared (MWIR) photodiodes. So, why do polycrystalline devices outperform single crystal based devices? Recently, broader investigations have been started in the community [2] triggered partially by A. Rogalski who called for more detailed information on PbSe [3]. This paper will contribute to a better understanding of the material and uses data from [4].

In practical use, dynamic behaviour becomes important and this paper will pave the road towards PbSe detectors with more “usability” as well.

Material Related Investigations

Basically, PbSe photoconductors belong to the group of TFPD (thin-film photodetectors). Complex material characterization has been performed at several stages of CBD (chemical bath deposition): Deposited, oxidized and iodized. The deposited film by itself has no photosensitivity. Iodization of this film does not result in photoconductivity. A weak sensitization is achieved by oxygen. Full sensitization requires subsequent iodization. Effects on carrier density, mobility and resistivity can be seen in Tab.1

Tab. 1: Hall effect data of PbSe (23°C, p-type carriers)

Production step	Relative Concentration	Relative Mobility	Relative Resistivity
Deposited	1.000	1.0	1
Oxidized	0.024	11.3	3
Iodized	0.018	0.5	110

Obviously, the resistance plays a major role in photosensitivity. In a typical application, the detector resistance is changed by 0.1% under illumination. We found out as well, that iodization is mandantory for a linear device. Our ma-

terial is always p-type with a typical film thickness of 1 µm. No signatures of barriers could be found in I-V characteristics. Surface XPS did indicate a mixture of PbO with SeO2, below it is mostly PbSe. A weak iodine signal is present as well. Photocurrent curves vs. 1/T are parallel for different light intensities. This is the signature of the number model. So, photoconductivity is achieved by increased hole concentration and increased hole lifetime since electrons are trapped.

Fig. 1 does give a visualition of what is going on inside the material structure: Deposition does result in crystallites that are stacked very closely. Oxidization starts to loosen this structure and after iodization it has turned into “grains that are surrounded by lots of connecting tissue”.

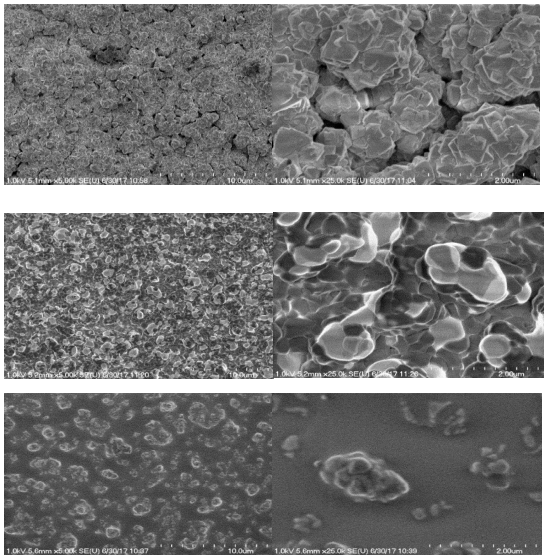

Fig.1. SEM images of PbSe at various production steps. Top: Deposited. Middle: Oxidized. Bottom: Iodized

Kelvin probe microscopy images do indicate that grains have higher electron energy which leads to the assumption that they act as traps. However, it turned out as well, that current does flow mostly uniform across grains and tissues.

Improved Usability

PbSe detectors have to follow recent user expectations as best as possible and recent users do expect a stable baseline after switch on. We followed an old approach to dampen the effects of temperature variations without using Peltier cooling.

PbSe elements are usually driven in a voltage divider configuration, i.e. the PbSe and a load resistor are connected in series. The idea is to use a blinded PbSe element as load resistor. In case of identical twins, the resistance among load and photoresistor will always be matched over temperature and bias will be constant. In some aspects, this can be seen as “balanced detection”. At pretests, the DC signal was found to be stable within 0.5 % immediately after switch on. This result was surprising to experienced users, since they have been used to initial settling times of approximately 10 minutes. [5]

Results

Transport in PbSe has been investigated. In some aspects, our data show consistency with [6]. As a little special, we found a grain-tissue morphology, a mostly uniform current and the importance of iodization for a linear device. [4] Evidence for the numbers model has been found in contrast to the standard literature [3], that favors the Petritz model.

We report a “balanced” approach that results in PbSe detectors with a stable baseline immediately after switch on. At the moment, we are working on scaling up.

Our PbSe devices work well. However, we have been unable to find barriers as predicted by recent models. [6] So, further investigation by the community is needed.

Acknowledgement

The authors gratefully acknowledge Prof. H.-Y. Zhang and his group work at Arizona State University for performing the Hall effect and other measurements.

References

[1] Study to assess requests for renewal of 16 exemptions to Annex 2011/65/EU, ISBN 978-92-76-56150-7, doi:10.2779/281264, August 2022, p. 159ff

[2] M.C. Gupta, J.T. Harrison, M.T. Islam, Photoconductive PbSe thin films for infrared imaging, Mater. Adv. 2021, 2, 3133

[3] A. Rogalski, *Infrared and Terahertz Detectors*, 3rd Edition, CRC Press (2019), p. 542 ff

[4] D. Babic, Understanding Behaviour of Lead Salt Photoconductors, *2nd Infrared Sessions*, January 19, 2021

[5] R. Mühlenbein, *private communication*

[6] M.H. Jang, S.S Yoo, M.T. Kramer, N.K. Dhar, M.C. Gupta, Electrical transport properties of sensitized PbSe thin films for IR imaging sensors, *Semicond. Sci. Technol.* 34 (2019) 065009

DOI 10.5162/SMSI2023/B5.2

PbS Detectors for Portable Near-Infrared Spectroscopy

Robert Lovrincic[1] , Michael Hanke[1], Daniel Kaelblein[1], and Wilfried Hermes[1]

[1]trinamiX GmbH, Industriestraße 35, 67063 Ludwigshafen am Rhein, Germany

Near-infrared spectroscopy (NIRS) has been a working horse in high-end analytics for decades. It covers the wavelength range from 0.9 to 2.5 µm (or 11000 to 4000 cm^{-1}). This spectral range allows to measure overtone (0.9 to 2 µm) and combination bands (2 to 2.5 µm) of molecular vibrations in organic materials. The overtone bands are 1st, 2nd, and 3rd order overtones:

	Range	Rel. intensities
1st overtones:	1700 - 2000 nm	1
2nd overtones:	1100 - 1700 nm	0.1
3rd overtones:	850 - 1100 nm	0.01

The combination bands carry very detailed information on the samples under test, e.g., the fatty acid composition in oilseeds or the amino acid profile in protein. Hence, laboratory spectrometers capable of measuring up to 2500 nm are widely used in agriculture for quality control and pricing.

Figure 1: trinamiX's mobile NIR spectrometer. The device is battery-powered, connects to smartphone or computer via *Bluetooth*®, and has an integrated lamp module for measurements in diffuse reflectance. The sensor unit consists of a 256-pixel PbS line array detector, fabricated in Ludwigshafen.

Fairly recently, NIR spectrometers have managed to break out of their well-controlled laboratory environment by becoming smaller, lighter, and scalable. In general, there are two approaches for handheld NIR spectrometers: (i) devices based on muti-pixel line array detectors, where the dispersive element splits the wavelength range in space and each pixel detects a certain wavelength; (ii) devices based on single-pixel detectors using an

interferometer with mechanically moving parts as dispersive element, such as MEMS Fourier-Transform (FT) or Fabry-Perot interferometers (FPI). Whereas the PbS detector technology is compatible with both approaches, InGaAs detectors are only used with option (ii) as extended InGaAs line array detectors are too scarce for widespread utilization in handheld devices. PbS is fabricated by chemical bath deposition, a process that is fast, scalable, and does not depend on lattice matched substrates.

trinamiX GmbH, a subsidiary of BASF SE based in Ludwigshafen, has introduced a portable NIR spectroscopy system to the market (see Fig. 1). This system consists of software, cloud-based NIR calibrations, and in-house developed spectrometer. The heart of the trinamiX spectrometer technology is its 256-pixel PbS line array detector, fabricated at cleanrooms in Ludwigshafen, Germany.

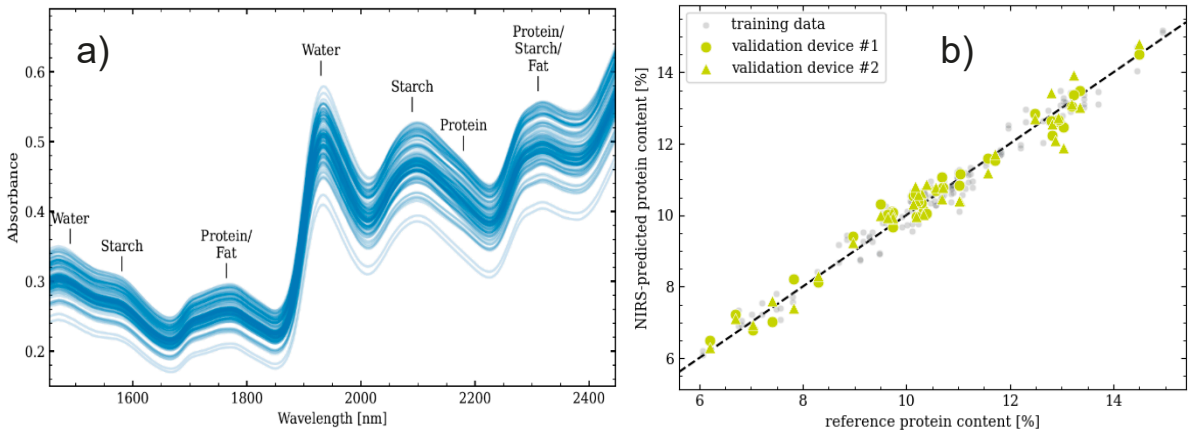

Figure 2: Portable NIRS of wheat. a) Spectra obtained from 108 wheat samples with the trinamiX handheld device. The chosen representation is absorbance (-log R) vs. wavelength in nm. To guide the eye, vertical black lines indicate the approximate positions and attributable species that are mainly responsible for the spectral appearance at those points. b) Reference crude protein content according to wet chemistry on the abscissa versus model predictions on the ordinate axis.

As an indication for the performance of the trinamiX NIRS system, Fig. 2 depicts the results of measurements on 108 wheat samples with known protein content and the subsequent data analysis. Fig. 2a) displays the raw NIR spectra of all samples measured with two trinamiX devices. Fig. 2b) shows how well the protein content of these samples can be predicted from their NIR spectra. The resulting standard error of prediction is 0.3 %, close to the accuracy that can be obtained by orders of magnitude larger and more expensive benchtop spectrometers.

Besides the classical NIRS application fields in the farm-to-fork environment, making the technology portable and affordable allows it to develop into markets far beyond the laboratory. Non-invasive biomarker monitoring is a huge trend in consumer electronics but still limited by the availability and affordability of detectors above 1000 nm detection range. PbS with its scalable and cost-effective production method (CBD) and broad wavelength detection range

enables consumers to track additional biomarker and therefore monitor their physical condition in real time. Seamless integration into consumer electronic devices, such as smartphones and watches, are in the focus.

Figure 3: Reference phone with an integrated NIR spectrometer module and a hydration application embedded in a health app.

DOI 10.5162/SMSI2023/B5.3

Augmented Vision Enabled by Imagers Based on PbS Quantum Dots

Paweł E. Malinowski*, Vladimir Pejovic*,**, Itai Lieberman*, Joo Hyoung Kim*, Naresh Chandrasekaran*, Nikolas Papadopoulos*, Myung Jin Lim*, Luis Moreno Hagelsieb*, Tom Verschooten*, Jonas Bentell*, Steven Thijs*, Paul Heremans*,**, and David Cheyns*

***imec, Kapeldreef 75, 3001 Leuven, Belgium**
****ESAT, KU Leuven, Kasteelpark Arenberg 10, 3001 Leuven, Belgium**

Cameras are omnipresent in our daily lives, with several billions image sensor units deployed annually. The imaging revolution was possible with the introduction of CMOS (complementary metal-oxide-semiconductor) technology and streamlining the manufacturing process based on the semiconductor ecosystem. CMOS image sensors (CIS) are relying on light detection by a silicon photodiode, which is perfectly suited for replicating human vision (visible wavelength range) and beyond (e.g. NIR – near infrared or UV - ultraviolet). At the same time, longer wavelengths such as short-wave infrared (SWIR) are inaccessible by Si due to the energy bandgap, setting the cut-off wavelength at around 1100 nm.

SWIR range is typically defined above 1400 nm (which is the onset of "eye-safe" region as the human eye is several orders of magnitude less sensitive to radiation above that wavelength) until approximately 2500 nm (which is the onset of mid-wave infrared, MWIR) [1]. This range is interesting both for active and passive illumination systems. In the former case, one can take advantage of less background radiation coming from the Sun (with irradiance at 1400 nm significantly lower than at e.g. 940 nm typically used in systems such as FaceID). The latter can provide vision in low-light conditions (e.g. using "night glow"). Applications include recognition of visually similar materials (sorting), high contrast for water (moisture detection), vision through fog/smoke/clouds (driver assistance in automotive) or low-light imaging (security cameras).

The incumbent approach of accessing SWIR wavelengths was to use hybrid imagers with a CMOS readout chip flip-chip bonded to a detector chip. This detector chip would be made of low bandgap III-V or II-VI materials such as InGaAs or HgCdTe. The low throughput epitaxial growth process together with die-to-die bonding process result in very high sensor cost. This in turn results in SWIR range being limited to high-end applications in machine vision, scientific and space imaging, with global annual volumes estimated at around 11'000 image sensors. Recent advances focus on the bonding process to realize sensors with pixel pitch down to 5 µm [2].

An alternative approach is to realize "monolithic hybrid" integration of the detector material other than Si directly on the readout chip. From the family of thin-film photodetectors (TFPD), colloidal quantum dots (CQD) seem as a very attractive candidate material family [3]. Thanks to the tunability of the cut-off wavelength with the nanocrystal size, one can select the appropriate spectrum by tuning the material synthesis process. Deposition by coating directly on the CMOS readout wafer enables significant throughput increase with wafer-level manufacturing. This can lead to high volumes of image sensors driving the cost down to levels suitable even for consumer and automotive applications.

QD image sensors are composed of the readout front-end (circuitry) including the pixel engine and the photodiode stack. The stack contains the QD absorber, electron and hole transport layers and semi-transparent top contact, plus an encapsulation layer. Depending on the readout architecture, the QD photodiode may have different polarity: "e2ROIC" (readout accepting electrons) or "h2ROIC" (readout accepting holes). The QD absorber in most reported implementations is based on lead sulfide (PbS), as this material can be tuned from the quantum confinement peak at 940 nm all the way to above 2200 nm (Fig. 2). Other materials include InAs [4], which promises to deliver much faster response (even below ns) and HgTe, enabling cut-off wavelengths in the MWIR range [5].

We have fabricated QD image sensor prototypes with VGA+ resolution (768x512 pixels) and 5 µm pixel pitch. External quantum efficiency (EQE) in the current generation imager is around 40% at the wavelength of 1450 nm at the reverse bias voltage below -3 V and at room temperature. Some imaging examples in machine vision applications are shown in Fig. 3-6, highlighting possibilities in sorting and inspection. Fig. 7 shows our modular camera with interchangeable boards allowing to adjust the functionality to the specific use case. This system helps to define specifications required by different applications and customize the image sensor accordingly. One example of customization is reducing the pixel pitch to enable high image quality and compact for factors. We demostrated SWIR imagers with pixel pitch down to 1.82 µm [6], with the most recent publications reducing that further to 1.62 µm [7].

Quantum dot image sensors are a new approach to access the SWIR wavelength range. With the monolithic integration of PbS QD photodiode on CMOS readout, high pixel density and high-resolution focal plane arrays can be realized. Efforts to enable manufacturing upscaled to wafer-level show the path towards cost reduction allowing applications that could not implement SWIR imaging. Further improvements of maturity of this technology will bring miniaturized SWIR cameras to new markets and augment information acquired by vision systems.

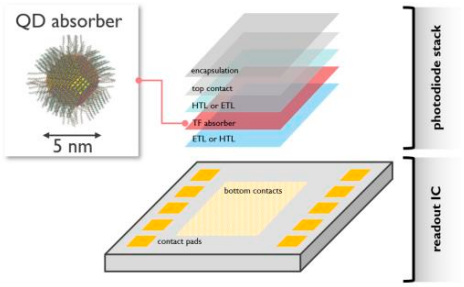

Fig. 1. Schematic structure of a “monolithic hybrid” quantum dot image sensor.

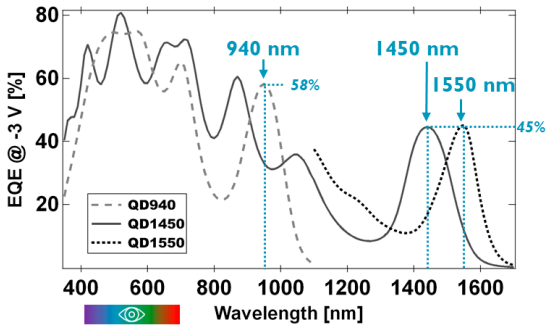

Fig. 2. External quantum efficiency (EQE) for photodiodes using different sizes of PbS QD.

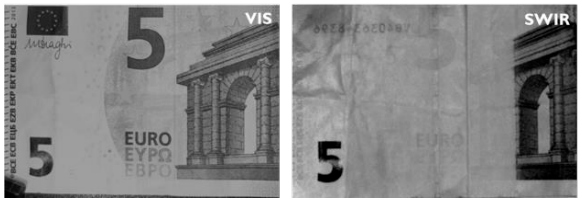

Fig. 3. SWIR imaging example: banknotes in the visible (VIS, left) and SWIR range (right).

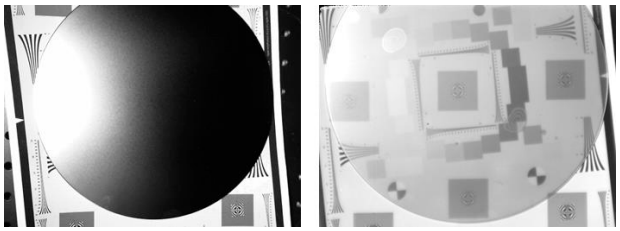

Fig. 4. SWIR imaging example: silicon wafer inspection (VIS, left) and SWIR (right).

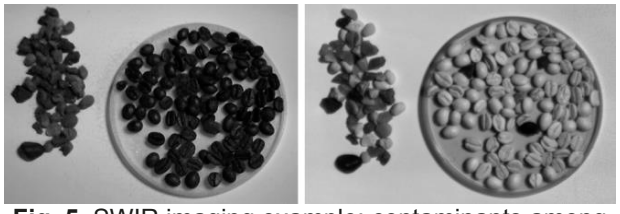

Fig. 5. SWIR imaging example: contaminants among coffee beans (VIS, left) and SWIR (right).

Fig. 6. SWIR imaging example: food inspection through plastic packaging (VIS, left) and SWIR (right).

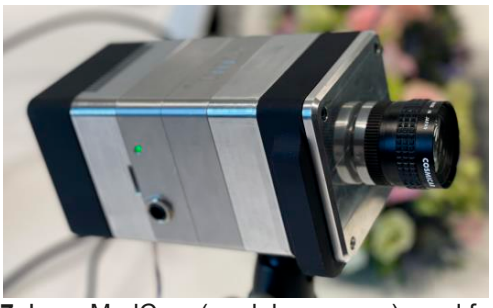

Fig. 7. Imec ModCam (modular camera) used for use case studies with QD image sensors.

References

[1] A. Rogalski, “History of infrared detectors,” Opto-Electronics Rev.,vol. 20, no. 3, pp. 279–308, Jan. 2012, doi: 10.2478/s11772-012-0037-7.

[2] S. Manda et al., “High-definition visible-SWIR InGaAs image sensor using Cu–Cu bonding of III–V to silicon wafer,” in IEDM Tech. Dig., Dec. 2019, pp. 7–16, doi: 10.1109/IEDM19573.2019.8993432.

[3] V. Pejovic et al., “ Infrared Colloidal Quantum Dot Image Sensors,” IEEE Transactions on Electron Devices, vol. 69, no. 6 (2022), DOI: 10.1109/TED.2021.3133191

[4] J. Leemans et al., “Colloidal III–V Quantum Dot Photodiodes for Short-Wave Infrared Photodetection,“ Advanced Science, vol. 9, no. 17 (2022), DOI: 10.1002/advs.202200844.

[5] A. Chu et al., “HgTe nanocrystals for SWIR detection and their integration up to the focal plane array,” ACS Appl. Mater. Interfaces, vol. 11, no. 36, pp. 33116–33123, (2019), DOI: 10.1021/acsami.9b09954.

[6] J. Lee et al., “Imaging in Short-Wave Infrared with 1 . 82 µm Pixel Pitch Quantum Dot Image Sensor,” IEDM, paper 16-5 (2020)

[7] J. Steckel et al., “1.62µm Global Shutter Quantum Dot Image Sensor Optimized for Near and Shortwave Infrared.,” IEDM, paper 23-4 (2021)

DOI 10.5162/SMSI2023/B5.4

PbS-based Detector for Industrial Fire Prevention – a Hidden Champion

Michael Mehlhorn[1], *Nils Vespermann*[1], *Mario Haas*[1]
[1] *Fagus-GreCon Greten GmbH & Co. KG, Hannoversche Straße 58, 31061 Alfeld, Germany*
michael.mehlhorn@fagus-grecon.com, *nils.vespermann@fagus-grecon.com*, *mario.haas@fagus-grecon.com*

Summary:
Lead sulfide-based spark detectors have been successfully used for more than four decades to safely detect highly mobile ignition sources in pneumatic transport, protecting countless industrial plants and human lives from fire and explosion incidents. The physics of infrared radiation, targeted field measurements and simulations are used to classify ignition sources in pneumatic transport into four types and to describe their detection reliability with established sensor materials even under high loads.

Keywords: PbS, Lead Sulfide, Fire Prevention, IR Detection, Industrial Application, Spark Detector. Explosion Protection, Ignition Sources, Black Body Radiation, Pneumatic Transport

Challenges in Industrial Fire Prevention

In many industries such as wood processing, food and animal feed production, plastics or metal processing, combustible dusts or bulk materials are generated. During the processing, for example, frictional heat can create potentially dangerous ignition sources. In pneumatic transport, these ignition sources are transported to other production areas and can cause fires or even explosions. Preventive fire protection begins with process design and regular maintenance, which can reduce many of the origins of these ignition sources (Fig. 1).

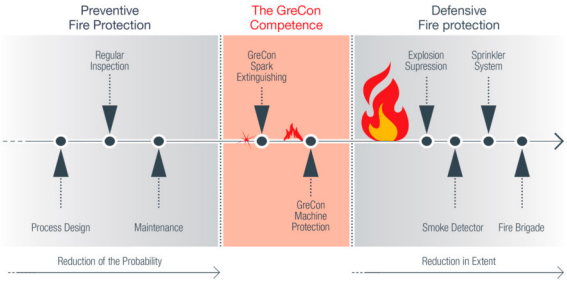

Fig. 1. Sensor-based protection of industrial plants at the edge of preventive to defensive fire protection.

To prevent fires and explosions from still occurring ignition sources and to prevent defensive fire protection from taking effect, these ignition sources must be reliably detected and eliminated. This is where spark extinguishing systems come into play.

Spark Extinguishing Systems

Spark extinguishing systems work in a minimally invasive way, protecting tens of thousands of industrial plants worldwide and the people who work there, almost invisibly and unnoticed. They consist of IR-detectors for the detection of ignition sources. Via an automatic control panel these are connected to an automatic extinguishing system, which eliminates the ignition sources with the aid of water mist a few hundred milliseconds and thus a few meters after detection (Fig. 2).

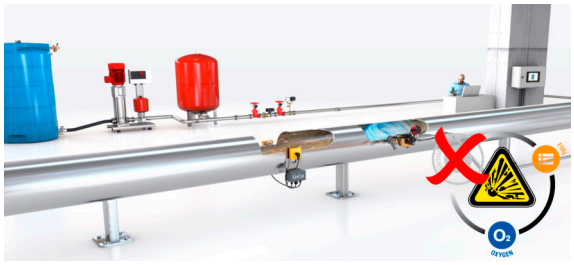

Fig. 2. Safe detection and elimination of highly mobile ignition sources in pneumatic transport by spark extinguishment systems.

Classification of Ignition Sources

Thanks to the studies of the University of Wuppertal, we have gained some important insights into ignition energy and ignition-effective particles in pneumatic transport. There was a long-term research project in the years 2015 to 2018 with the aim of investigating the controlling of ignition sources in pneumatic transport. With a multitude of results [1], [2].

The most important finding is that these so-called highly mobile ignition sources can be classified into four different types with different risk potential. Properties such as size, lifetime (LT), temperature (T) (which can lead to igni-

tion), active burning, from which their risk potential (RP) can be deduced:

(1) Mechanically generated sparks: E: small, T>1200°C, inert, LT<1 sec, RP:3

(2) Burning Particles: E small to medium, T<900°C, active, LT<1 min, RP: 5

(3) Hot Particles: E: high, T >400°C, inert, LT>1 min, RP: 7

(4) Smoldering Nests: E: high, T <350°C, active, LT>5 min, RP: 10

The first type are mechanically generated sparks. These are produced during metal processing or are generated by fans. If, for example, the bearing is damaged.

The second type are the burning particles, which occur during drying processes, for example with direct heating or during mechanical processing.

The third type are hot particles. In other words, impurities that are created in shredding processes. They can also be welding balls, i.e., very hot particles that do not burn itself, but are so hot that they can cause dust deposits to ignite.

The last type are smoldering nests. They are created wherever there is drying or where self-ignition can occur due to environmental influences.

From Ignition Sources to the Best Fitting Sensor Material

Since the invention of the spark extinguishing system in the mid-1970s, two sensor materials have become established. On the one hand, they have the necessary robustness and detectivity and, on the other hand, they operate continuously and reliably under rough industrial conditions between -40°C and 70°C (ambient) or 300°C (process): silicon (Si) and lead sulfide (PbS). The detectors developed from these materials are very often located in potentially explosive atmospheres, which places special demands on the power supply. The smaller the power requirement, the more feasible and affordable, and thus more suitable for practical use, the detector is.

To a first approximation, each particle with a specific temperature emits a continuous spectrum of electromagnetic radiation comparable to blackbody radiation. If enough emitted radiation falls within the spectral sensitivity window of the sensor material, these particles can be reliably detected. Figure 3 shows the typical blackbody spectra of the sun, the visible glowing and the ambient light. The positions of the 4 types of ignition sources, where sufficient detectable radiation is still present, are marked. Additionally, the spectral sensitivity of the two sensor materials is shown.

The less hot the ignition source is, the more important is the reliable detection by PbS-based detectors. Especially smoldering nests, which are "cold" on the outside and very hot inside and whose lifetime is often several minutes, present a very high risk potential.

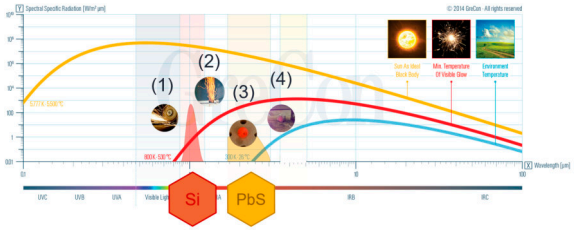

Fig. 3. Spectral specific radiation and spectral sensitivity of spark detecting sensors vs. radiation wavelength for the four different types of ignition sources

Modelling-based predictability of detection reliability

Knowledge of the types of ignition sources in pneumatic transport allows the calculation of models that consider specific application parameters and material properties. Supported by experiments validated in the lab and test field, the detection reliability and its limits can be determined for each ignition source and both sensor materials. This enables the optimal selection and parameterization of the spark detector used. Fig. 4 shows an example of such signal characteristics on Si- and PbS-based detectors. The signal heights are used to select the sensitivity and which detector should preferably be used. The less hot the ignition source, the more the signal height shifts towards PbS-based detectors.

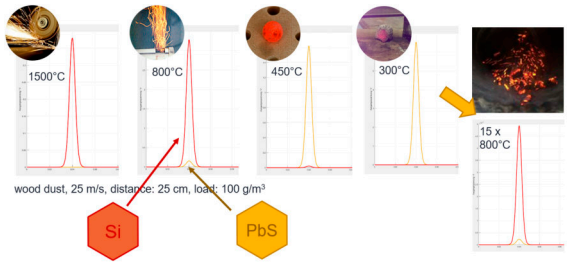

Fig. 4. Example of modeled signal characteristics on Si- und PbS-based detectors for the different types of ignition sources.

References

[1] B. Liske, U. Barth, Zündquelle Glimmnest, VDI Wissensforum GmbH (Hg.): Sichere Handhabung Brennbarer Stäube 2017. Bd. 2314

[2] J. Bechem, B. Liske, N. Vespermann, U. Barth, Ignition Source: Hot Particle, *5th Magdeburg Fire and Explosion Days*, 23/24.03.2017

DOI 10.5162/SMSI2023/B6.1

A Kibble balance as part of a quantum measurement institute in one room at NIST

Lorenz Keck[1, 2], Frank Seifert[1, 3], Stephan Schlamminger[1], David Newell[1], René Theska[2], Darine Haddad[1]
[1] National Institute of Standards and Technology, Gaithersburg, MD, USA,
[2] Technische Universitaet Ilmenau, Ilmenau, Thuringia, GE,
[3] University of Maryland, College Park, MD, USA
Lorenz.Keck@nist.gov

Summary:
The new Kibble balance at the National Institute of Standards and Technology (NIST) is part of the Quantum Electro-Mechanical Metrology Suite (QEMMS). Two quantum standards are incorporated directly in the electrical circuit of the Kibble balance for the realization of the unit of mass. This eliminates the need for external calibration in the Kibble balance experiment. The targeted uncertainty is 2 µg on a 100 g mass and a range from 10 g to 200 g will be covered. We introduce the measurement concept of the QEMMS, show the current state of development and publish first measurements proving the performance of the newly designed balance mechanics.

Keywords: quantum measurements, quantum SI, mass metrology, Kibble balance, mechanism

Introduction

Highly accurate Kibble balances today can provide primary realizations of the kilogram with relative combined uncertainties of 2 parts in 10^8 [1]. Until 2019 a worldwide effort has been made towards redefining the kilogram within the International System of Units (SI) to create a definition of this fundamental base-unit traceable to unchanging constants of nature, and not a physical object. The Kibble balance was developed to fix a value of the last puzzle piece of quantum constants missing for the success of the redefinition: Planck's constant. It was measured based on the current value of the International Prototype Kilogram (IPK). Thus, balances were designed for a 1 kg mass measurement and due to sufficient agreement of various other experiments on the part per billion level, a value for Planck's constant could be agreed upon. Now this value can be used to define the kilogram through the Kibble balance.

The QEMMS

Not only the Planck's constant is important for traceability in the Kibble balance experiment, also the speed of light, charge of an electron, and the definition of the second are vital for operation. Voltage, resistance, time and length measurements are traced back to these constants and thus they build the foundation of calibration of the Kibble balance itself. All quantities except for electrical resistance are typically directly measured by their respective primary standards.

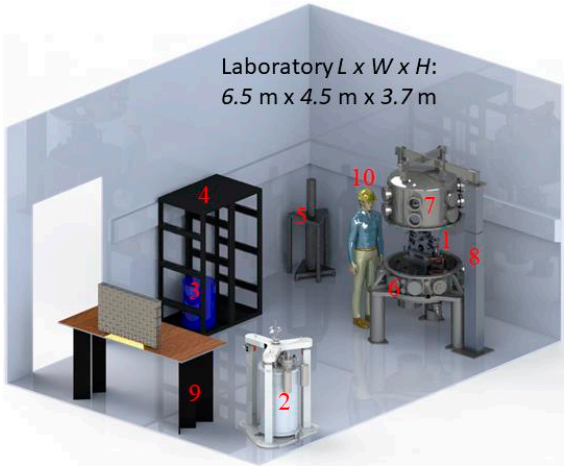

Fig. 1. The QEMMS in the lab at NIST. 1 – Kibble balance; 2 – Cryostat with graphene quantum Hall array standard; 3 – PJVS; 4 – hardware rack; 5 – absolute gravimeter; 6, 7, 8 – vacuum chamber and lift; 9 – desk with PC; 10 – operator

During the weighing mode electric current through the coil needs to be measured to quantify the magnitude of generated electromagnetic force from the magnet-coil system. Here, mostly calibrated resistors are being used and a precisely measurable voltage drop over these can be analyzed to quantify current according to Ohm's law. Recently, scientists at NIST were able to build a graphene quantum Hall array standard capable to maintain quantization dur-

ing constant exposure with currents up to 0.3 mA [2], which, for the first time, opens the doors for implementing this instrument directly in the Kibble balance's electrical circuit as a primary reference for resistance. This led to the idea of building a new version of the Kibble balance at NIST, the Quantum Electro-Mechanical Metrology Suite (QEMMS), with the objective to eliminate the calibration uncertainty for resistance by providing full metrological traceability by a metrology institute in one room including all primary references for the measurement. It features an absolute gravimeter, a graphene quantum Hall array standard, a Programmable Josephson Voltage Standard (PJVS), and the Kibble balance, see Fig. 1. Furthermore, since it is easier and more practical to scale mass measurements up than down, a lower mass range is targeted (10 g to 200 g), but with the same relative combined uncertainty as 1 kg-balances. This tightens the requirements for design especially for subsystems with absolute uncertainty contributions as, e.g., the mechanical system/mechanism.

The new balance mechanics

Another new approach in the QEMMS is the mechanical system, which, for the first time, is based on one single flexure-based mechanism (see Fig. 2) for both modes of operation, the velocity and the weighing mode. A detailed description of the mechanism can be found in [3].

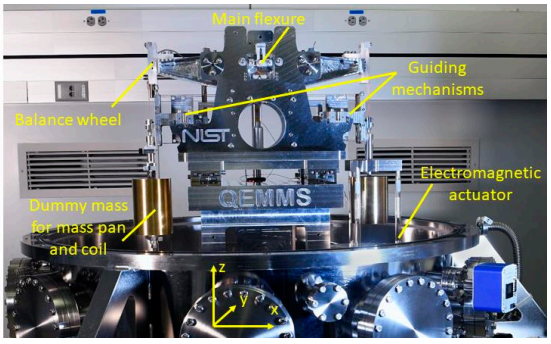

Fig. 2. Picture of the state of construction of the Kibble balance in the QEMMS. The newly designed mechanism is under experimental investigation in the vacuum chamber.

The challenge was to develop a mechanism that minimizes mechanical hysteresis, which is why we use a flexure mechanism over a knife edge one, but also provide sufficient travel during the velocity mode. The latter requires to integrate two functions in the flexure mechanism that are usually separated in flexures: (1) suspending relevant components (15 kg suspended weight), and (2) providing large travel, here ±30 mm. Furthermore, a dedicated sub-mechanism for mechanism is used to define the trajectory of the coil.

First measurement

A recent success was a measurement of the balance trajectory which indicates that we can use this mechanism to guide the coil in the velocity mode with deviations from the vertical of less than ±3 µm on the whole travel range, see Fig. 3. This is sufficient for the experiment.

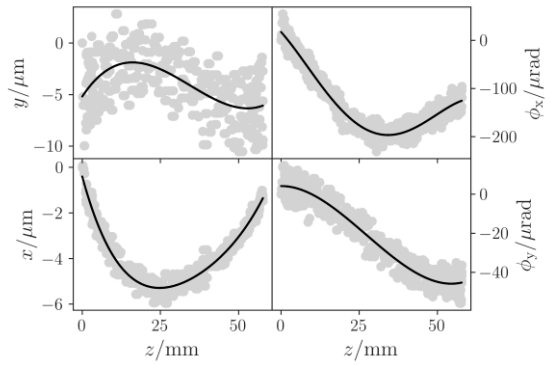

Fig. 3. Preliminary measurement of verticality and angular deviation of balance motion measured with a fully loaded balance mechanism. The mechanism oscillated freely with its eigenfrequency in z.

The result required thorough alignment of the components in the mechanics with respect to both each other and gravity. Currently the quality of alignment is limited by its sensitivity and the types of alignments we can perform with the mechanism in situ. Furthermore, ambiguity remains as to whether one flexure mechanism for both modes of operation is useable from a standpoint of repeatability in mass measurement, especially with views on hysteretic losses in the mechanics.

Conclusion

At NIST a new Kibble balance is under development. Two novelties are featured: (1) all quantum measurements take place directly in the instrument so that there is no need for external calibration anymore, and (2) one single flexure mechanism is used to guide the coil in velocity mode and to perform the weighing phase. The proof of travel quality was given – now a hysteresis/repeatability test of mass measurements is underway for ultimate proof of performance of the concept.

References

[1] S. Davidson, M. Stock, "Beginning of a new phase of the dissemination of the kilogram", Metrologia, vol. 58, 2021.

[2] A. R. Panna, et al., "Graphene quantum Hall effect parallel resistance arrays", Phys. Rev. B 103, 075408, 2021.

[3] L. Keck, et. al, "Design of an enhanced mechanism for a new Kibble balance directly traceable to the quantum SI", EPJ Techniques and Instrumentation, vol. 9, no. 7, July 2022.

DOI 10.5162/SMSI2023/B6.2

Fiber-Interferometric Sensor for Velocity Measurement in the Planck-Balance

Vitalii Shmagun[1], *Thomas Kissinger, Thomas Fröhlich*
Institute of Process Measurement and Sensor Technology, Technical University of Ilmenau, Ehrenbergstraße 29, 98693 Ilmenau, Germany
[1] *vitalii.shmagun@tu-ilmenau.de*

Summary:
This work describes the use of a compact fiber-interferometric sensor for velocity measurements for the Kibble balance method. Our fiber-interferometric sensor was compared within a Planck-balance setup with a commercial reference interferometer. Results show that the fiber-interferometric sensor is capable of high accuracy velocity measurement comparable with the reference interferometer. High performance and compactness of the sensor head allow it to be integrated into small-size systems, where the use of the conventional interferometer systems is limited or not possible.

Keywords: Interferometer, Kibble Balance, Planck calibration, Velocity Measurement

Introduction

Interferometric displacement measurement plays an important role in force measurement instruments, as it allows non-contact measurement with high accuracy and traceability to the meter definition. Laser interferometers are the primary tool for traceable velocity measurement during the Planck calibration in Kibble balance systems [1], which is the focus of the paper. Interferometers are also used in other precise force measurement instruments, such as calibration stages for characterization of force transducers for dynamic measurements or for calibration of force-displacement curves (spring constant) of AFM cantilevers [2].

Conventional interferometer systems used in the instruments mentioned above are based on helium-neon lasers, which provide very high frequency stability and coherence, but have large size and short lifetime, which is considered being the main drawback of the He-Ne laser in industrial applications. In addition, the complicated optical design of a conventional interferometer leads to precise alignment requirements and limited integration ability due to the large size of the interferometer [3].

With the rapid development of telecommunication technology, more and more semiconductor lasers appear on the market with performance characteristics suitable for interferometry applications. The major advantages of a laser diode are its long lifetime and the possibility to directly modulate the laser frequency by modulating the laser injection current.

Laser frequency modulation allows the use of various modulation techniques [4, 5] in low-finesse Fabry-Perot configurations, avoiding a complex optical interferometer setup, since the second optical quadrature signal for the phase demodulation does not need to be measured directly. Thus, the optical setup may consist of only a compact fiber-coupled collimator as a sensor head, pointing at the measurement surface.

The compact measurement head allows to integrate the interferometer into small-size systems, where the use of a conventional interferometer would be limited.

Fiber-Interferometric Sensor

The basic setup of the fiber-interferometric sensor is shown in Fig. 1. The light from the laser diode passes through the circulator to the fiber-coupled collimator. Part of the light is reflected from the fiber end back to the fiber, forming the reference beam. The transmitted light passes through the collimator lens, is reflected off the mirror and is coupled directly to the fiber. The reflections from the fiber end and the target surface form an interference signal that is fed back through the circulator to a photodetector.

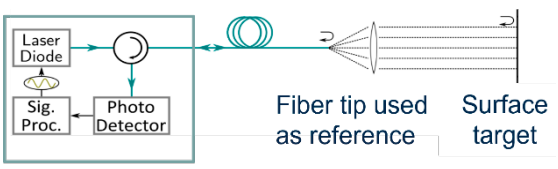

Fig. 1. Basic setup of the fiber-interferometric sensor

To demodulate the phase of the interference signal, a range-resolved interferometry [5] method is used, which allows to distinguish between single-pass and double-pass modes [6] of the fiber interferometric sensor and exhibits high linearity of demodulation.

To ensure traceability to the meter unit, part of the laser output is split with a coupler and directed to a hydrogen cyanide gas cell with a separate photodetector behind it. The offset current of the laser diode is manually adjusted to the center of the gas absorption line using the amplitude of a photodetector signal as feedback.

Velocity Measurement in the Planck-Balance

Our recently developed Planck-Balance (PB2) system [1] is based on the Kibble-Balance principle. In the velocity mode of the balance, the electromagnetic force factor Bl of the coil-magnet system is determined and can then be used in the force mode to calculate the force applied to the coil.

During velocity mode, the coil oscillates in the magnetic field and the coil position x is measured with an interferometer through several complete cycles, simultaneously to the measurement of the induced voltage U with a digital voltmeter. The Bl is then defined as

$$Bl = \frac{U_0}{\omega \cdot x_0}, \qquad (1)$$

where U_0 is the amplitude of the induced voltage in the coil, $\omega = 2\pi f$ and x_0 are the frequency and the amplitude of the coil displacement, respectively. These parameters are usually determined with a sine-fitting algorithm and for PB2 are in the following range $f = 1...10$ Hz, $x_0 = 10...40$ µm.

Experimental Setup

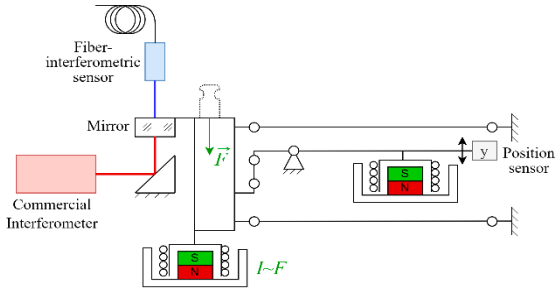

Fig. 2. Planck-balance setup.

The fiber-interferometric sensor was installed in the Planck-Balance setup (Fig. 2) so that the sensor and the commercial interferometer are pointed at the same mirror from opposite sides. It allows to directly compare displacement and velocity measurements taken with a sensor and a commercial interferometer. A multichannel data acquisition unit is used for synchronous data acquisition from both interferometers.

Results

Several measurements were made in which the coil was moved sinusoidally at a frequency of 1 Hz and an amplitude of 20 µm, and the coil position was measured for 10 seconds simultaneously using a commercial interferometer and the fiber interferometer sensor. The velocity amplitude $v = \omega \cdot x_0$ was then estimated with a sine-fitting algorithm for both displacement signals and compared. The comparison shows that the velocity amplitude v_{fiber} obtained with the fiber interferometric sensor has a systematic deviation $\Delta_{sys} = -18$ nm/s from the amplitude v_{int} obtained with the commercial interferometer. The systematic error is believed to be caused mainly by the mechanical misalignment of the sensor and will be the subject of further investigation. Fig. 3 compares the extracted velocity amplitudes for each interferometer type over 6 repeats of the measurement, with the discussed systematic error subtracted from v_{fiber}. The velocity measurements with the fiber interferometric sensor are found to be in very good agreement with the readings of the reference interferometer, with a remaining standard deviation between the two interferometer types of only 0.1 nm/s.

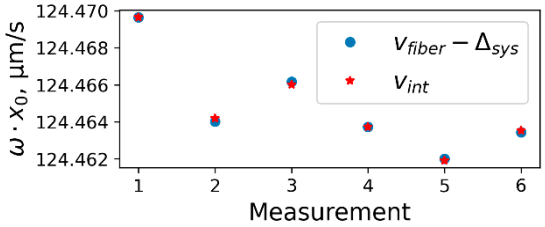

Fig. 3. Calculated velocity amplitude for each measurement.

References

[1] S. Vasilyan, et al., *tm - Technisches Messen*, Vol. 88 (Issue 12), 731-756 (2021); doi: 10.1515/teme-2021-0101

[2] C. Diethold, et al., *Measurement,* Vol 51, 343-348 (2014); doi: 10.1016/j.measurement.2014.02.034

[3] A. J. Fleming, *Sensors and Actuators A: Physical*, 190, 106-126 (2013); doi: 10.1016/j.sna.2012.10.016

[4] A. Bruyant, et al., (2017), *Optical Interferometry*, IntechOpen, London; doi: 10.5772/66657.

[5] T. Kissinger, T. O.H. Charrett, and R. P. Tatam, *Opt. Express* 23, 9415-9431 (2015); doi: 10.1364/OE.23.009415

[6] K. Thurner, et al., *Applied optics* 54.10, 3051-3063 (2015); doi: 10.1364/AO.54.003051

DOI 10.5162/SMSI2023/B6.3

Actuator design considerations for the Planck-Balance

Norbert Rogge[1], *Thomas Fröhlich*[1]
[1] *TU Ilmenau, PF 100565, 98684 Ilmenau, Germany,*
Norbert.rogge@tu-ilmenau.de

Summary:
The paper presents crucial design considerations for the actuators in a table-top Kibble balance, especially its influence on the uncertainty contribution by the voltage measurements. The resulting contribution is exemplary shown for the PB2 version of the Planck-Balance and constraints are discussed that limit the possibilities to optimize the geometric factor of the measurement actuator.

Keywords: Kibble balance, uncertainty evaluation, mass metrology, electromagnetic force compensation, dynamic force measurement

Motivation

The Planck-Balance is a tabletop Kibble balance that was developed in a joint project of PTB and TU Ilmenau. Both versions of the Planck-Balance – the PB1 for calibration of class E1 weights and the PB2 for class E2 – utilize a commercial load cell for carrying the load, but have an additional voice coil actuator to carry out the Kibble experiment (measurement actuator). However, the internal voice coil actuator (drive actuator) of the electromagnetic force compensated (EMFC) load cell is used to move the load carrier of the balance in order to excite the coil of the measurement actuator relative to its magnetic field. From the ratio the induced voltage U_{ind} in the measurement coil and its velocity v, which is measured by an interferometer, the geometric factor Bl can be determined (velocity mode) as

$$Bl = \frac{U_{\mathrm{ind}}}{v}. \qquad (1)$$

This factor also equates the ratio of force, which is used to counterbalance the gravitational force F_{G} of the weight, and the current I_m through the measurement coil (force mode), which is measured as voltage drop U_R over a shunt resistor with the known value R.

$$Bl = \frac{F_{\mathrm{G}}}{I_m} = \frac{m \cdot g \cdot R}{U_R} \qquad (2)$$

Combining the measurements of velocity mode and force mode, the mass m of the weight can be determined with

$$m = \frac{U_R \cdot U_{\mathrm{ind}}}{v \cdot g \cdot R}, \quad (3)$$

and a known local gravitational acceleration g.

This allows a mass calibration that is independent from a calibration weight and traceable to natural constants like Planck's constant h via the electrical quantities.

Influence on uncertainty

The value of the geometric factor Bl can be influenced by the cross-section area A_{W} of the coil wire and therefore the Number of turns N that are immersed into the air gap of the magnet system, which provides a flux density B. The flux density and the air gap volume V_{W} are less convenient for a tuning process of the actuator, supposed that the geometrical constraints are already used to full capacity and an extensive redesign of the system should be omitted. However, he ratio between power dissipation and the compensation force is independent from the wire diameter and must not be taken into account during its optimization [1].

Even though, the geometric factor Bl is canceled out due to combination of the results of both measurement modes, the value of Bl is crucial to the uncertainty contribution of the voltage measurements. Assuming a lower absolute limit ΔU of the uncertainty of the voltage measurement, the best relative uncertainty is achieved with higher voltages. In the velocity mode the induced voltage is increased with a high value of Bl, while a high value of voltage drop is generated for small values of Bl in the force mode.

Therefore, the sensitivity coefficient $c_{U;\mathrm{rel}}$, which equates the contribution of the voltage measurement uncertainty to the relative uncertainty of mass determination, has a minimal value for a geometrical factor Bl_{opt} of

$$Bl_{\mathrm{opt}} = \sqrt{\frac{m \cdot g \cdot R}{v}}, \qquad (4)$$

If the same voltage uncertainty is assumed in both modes [2].

This minimum is valid for given values of the other parameters, but one has to keep in mind that this also applies to the sensitivity coefficient

$$c_{U;\mathrm{rel}}(Bl_{\mathrm{opt}}) = \sqrt{\frac{2}{v \cdot m \cdot g \cdot R}}. \qquad (5)$$

In contrast to the value of *Bl* that minimizes the coefficient, the coefficient for this optimized geometric factor itself decreases with increasing gravitational force or resistance of the shunt.

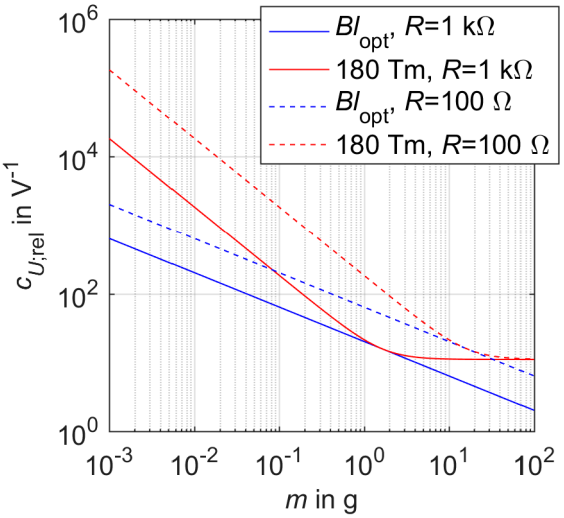

Fig. 1. Sensitivity coefficient of the contribution of voltage measurement uncertainty.

For illustration, the calculated sensitivity coefficient is shown in Fig. 1 in the measurement range of the PB2 system and its current design and uncertainty parameters that are taken from [3]. Since it is not reasonable to exchange the coil of the measurement actuator for every mass value within the measurement range in order to have the optimal *Bl*, the sensitivity coefficient is also shown for the fixed value that was chosen in the PB2 system. With an appropriate choice for the value of shunt resistor, the sensitivity coefficient can even be smaller than with an optimized *Bl*, but a lower resistance.

Constraints of optimization

The shown example illustrates the possibility to optimize the achievable measurement uncertainty with the choice of the coil parameters and the shunt resistor. However, these possibilities are limited by several additional aspects.

Voltage measurements with very low relative measurement uncertainties can only be done within a measurement range of up to 10 V with devices like the Keysight 3458A that represent the current state of the art. In a similar way, this provides also a lower limit for the *Bl*, but also an upper limit for the geometric factor *Bl*, since the induced voltage should not exceed this measurement range. Furthermore, it also provides an upper limit for an optimization with the shunt resistance in order to avoid a too high voltage drop in the force mode.

The choice of the shunt resistance is further limited by the factor that also an appropriate current source that provides the coil current in force mode has also a limited supply voltage U_{max}. This voltage needs to be bigger than the sum of voltage drops over the shunt and the actuator coil, which is not independent from *Bl*, if it is mainly optimized due to the choice of the cross-section area A_{W} of the wire. This constraint provides an upper limit for the shunt resistance that equates to

$$R_{\mathrm{max}} = \frac{U_{\mathrm{max}} \cdot B \cdot A_{\mathrm{W}} - \rho_{\mathrm{W}} \cdot m \cdot g}{v \cdot m \cdot g \cdot B^2 \cdot {A_{\mathrm{W}}}^2}. \qquad (6)$$

Drive actuator

In addition to the obvious necessity to optimize the measurement actuator, also the characteristics of the drive actuator need to be considered.

In the PB2 system, this actuator is used to excite the system in the velocity mode and therefore its ac characteristics are relevant for choosing an appropriate current source. These characteristics are composed of the coil's resistance and inductance as well as its geometrical factor *Bl*, which should not be too high in order to avoid back EMF. But since the drive actuator is also used to generate offset forces in the force mode [3], its *Bl* should also not be too small.

References

[1] J. Schleichert, S. Vasilyan, L. Günther. Magnet system for the Planck-balance. *Engineering for a Changing World: Proceedings. 59th IWK, Ilmenau Scientic Colloquium*,Technische Universität Ilmenau, (2017)

[2] S. Li, S. Schlamminger. The irony of the magnet system for Kibble balances – a review, Metrologia 59, 022001, (2022); doi: 10.1088/1681-7575/ac464a

[3] S. Vasilyan, N. Rogge, C. Rothleitner, S. Lin, I. Poroskun, D. Knopf, F. Härtig, T. Fröhlich. The progress in development of the Planck-Balance 2 (PB2): A tabletop Kibble balance for the mass calibration of E2 class weights. *tm - Technisches Messen*, 88(12), 731–756, (2021). doi: 10.1515/teme-2021-0101.

DOI 10.5162/SMSI2023/B6.4

A vertically positionable permanent magnet system for the Planck-Balance

Johannes Konrad[1], *Christian Rothleitner*[1], *Jonas Kloß*[1], *Thomas Fröhlich*[2]
[1] *Physikalisch-Technische Bundesanstalt, Bundesallee 100, 38116 Braunschweig, Germany*
[1] *Technische Universität Ilmenau, Gustav-Kirchhoff-Straße 1, 98693 Ilmenau, Germany*
Correspondence: Johannes.Konrad@ptb.de

Summary:

The Planck-Balance is a compact version of a Kibble balance, allowing a direct measurement of mass by means of electromagnetic force compensation (EMFC). Consequently, effects due to deformation have to be considered. The vertical position adjustment of the magnet relative to the coil, which is discussed in this article, can reduce many errors, such as errors due to deformations during weighing, which lead to a non-proportional correlation between the current in the compensation coil and the compensated mass. In the current setup of the Planck-Balance, these relative errors may be up to about $8 \cdot 10^{-6}$ the case of a 100 g mass. In addition, there are other problems such as a deviation due to drift of the zero crossing position as well as a relative bias of the voltage amplitude of the fundamental frequency in the velocity mode, which may also be reduced.

Keywords: planck-balance, force factor, watt balance, kibble balance, mass, kilogram

1. Background and motivation

It would be desirable to be able to determine masses directly without having to calibrate the weighing instrument beforehand with other already calibrated masses. This is possible since the redefinition of the kilogram. One of the advantages is that the maximum achievable accuracy is no longer limited by the uncertainty of the calibrated masses [1].

2. Introduction to the Planck-Balance

There are already realized Kibble balances in the world, but in most cases they are very large and heavy [2]. In our working group, we are improving the Planck-Balance, developed in a collaboration between the PTB and TU Ilmenau [3]. The working principle can be seen in figure 1.

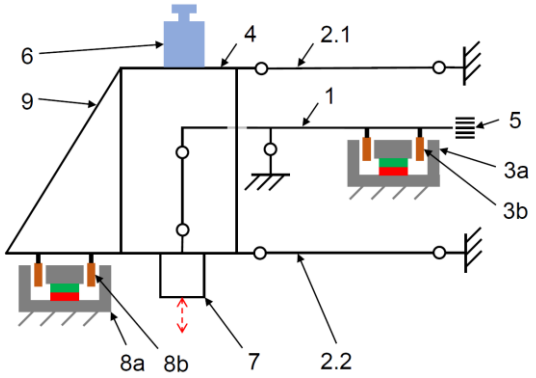

Figure 1: Principle of the modified weighing cell (Planck-Balance).

The load carrier (4) is suspended from a lever (1) and is constrained by a parallel guiding mechanism (2.1, 2.2). In the conventional method, the gravitational force of the mass (6) is compensated by the electromagnetic force of the coil and permanent magnet system (3b and 3a). The force equilibrium is verified by using the optical position indicator (5). In the Planck-Balance, the load cell was extended by an adapter (9) to which a second coil (8b) (with a corresponding stationary permanent magnet system (8a)) is attached. These serve as the new measuring actor of the Planck-Balance whose functionality will be described later. Furthermore, a reflector (7) is mounted to the load carrier, with which its vertical position can be measured interferometrically in order to determine the force factor *BI* of the voice coil actuator (8b and 8a). *BI* describes the product of *B*, which is the magnetic flux density and *I*, the coil length. It is also a quantification of the link between the current flowing through the coil and the Lorentz force acting on it.

3. Influence of elastic deformation

The force factor *BI* depends on the position of the coil and permanent magnet relative to each other. The vertical dependence of the force factor of the magnet and coil combination (8a and 8b) to be expected is shown in Figure 2, and was extrapolated. Its dependence in the measuring range was determined by weighing the same mass at different vertical positions (Figure 3). If a mass is placed on top of the load carrier and its weight being compensated by means of a

current flowing through the coil (8b), all components involved in the flow of forces are elastically deformed. In the following, only the coil and its attachment will be considered. The same applies to the permanent magnet, but the effect there is much smaller due to the higher stiffness. Figure 4 shows the displacement of the adapter when compensating a 100 g mass, calculated by means of the finite element method (FEM).

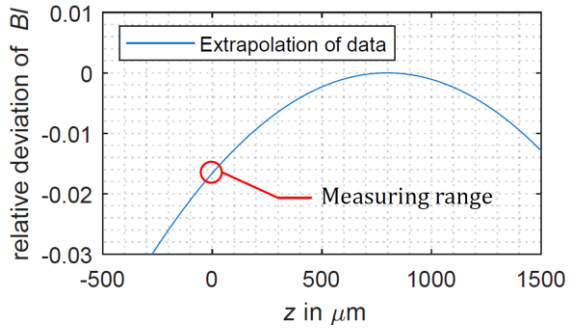

Figure 2: Extrapolated relative deviation of the force factor from its set/weighing position (z = 0) as a function of the vertical position z.

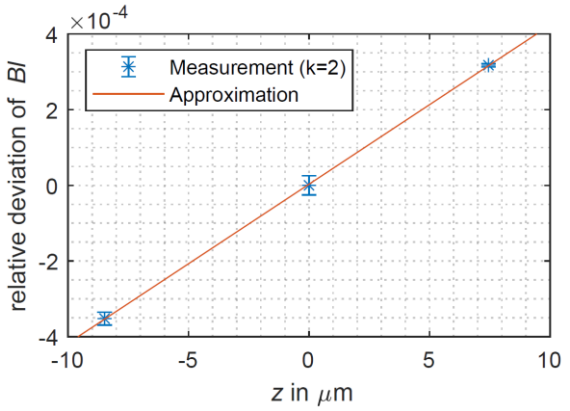

Figure 3: Measuring range of Figure 2, linearly approximated.

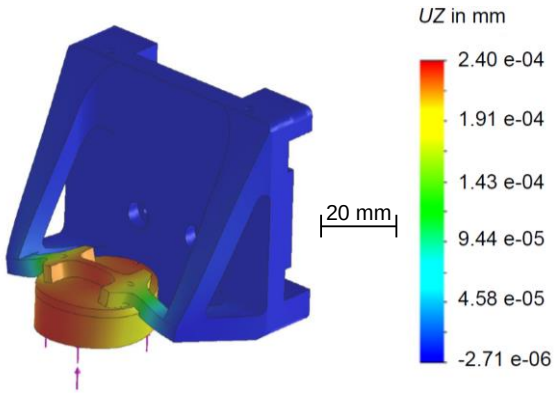

Figure 4: Vertical displacement of the components at a force corresponding to 100 g (FEM-model).

The average displacement of the coil along its axis due to the deformation of the adapter is about 200 nm for a force equivalent to a 100 g mass. This displacement in turn leads to a different vertical position of the coil and thus to a different effective force factor. In the case of a mass of 100 g, this results in a Bl-value of about $8.4 \cdot 10^{-6}$ higher than at the zero position. Assuming the deformation induced displacement to be proportional to the force, combined with the position-dependent force factor described in Figure 3, this results in a measurement error that increases linearly with the mass to be weighed.

4. Approaches to reduce the error

Several design changes are to be implemented into the system, e. g. a magnet holder intended to enable vertical positioning (Figure 5). The magnetic circuit (1) is attached to a cylindrical mount (3), which is located in the guiding cylinder (4) so that it is secured against rotation and can be moved vertically. By turning the adjusting ring (5), which is coupled to the guiding cylinder by the connecting piece (6), the magnet can be moved vertically relative to the coil and its – also to be manufactured – more rigid holder (2, 7). In this way the electrical center of the coil is intended to be vertically positioned at the vertex of the *Bl*-profile – which can be expected to have a global maximum like in Figure 2 – reducing the error. A scale on the adjusting ring allows the magnet to be positioned with a resolution of 10 µm, which is sufficient for our application.

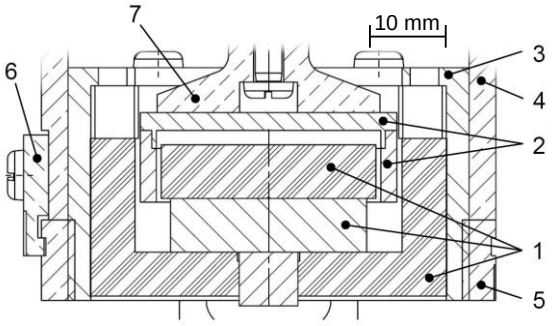

Figure 2: Sectional view of the new magnet holder including adjacent parts.

Since the position-dependent *Bl* may cause other errors, such as a deviation due to drift of the zero crossing position in the velocity mode, an increase in accuracy can be expected. Results are anticipated to be available at the time of the conference.

[1] I. Robinson, S. Schlamminger, The watt or Kibble balance: a technique for implementing the new SI definition of the unit of mass, *Metrologia* 53 A46 (2016); doi:10.1088/0026-1394/53/5/A46

[2] D. Kim et al., Design of the KRISS watt balance, *Metrologia* 51 (2014), S.96 - S.100; doi:10.1088/0026-1394/51/2/S96

[3] S. Vasilyan et al., The progress in development of the Planck-Balance 2 (PB2): A tabletop Kibble balance for the mass calibration of E2 class weights. *tm-Technisches Messen,* 88(12):731-756, 2021; doi:10.1515/teme-2021-0101

DOI 10.5162/SMSI2023/B7.1

SI Traceable Small Force Generation and Measurements via Photon Momentum

Suren Vasilyan[1], Norbert Rogge[1], Thomas Fröhlich[1]
[1] Institute of Process Measurement and Sensor Technology, Technische Universität Ilmenau, 98693 Ilmenau, Germany,
suren.vasilyan@tu-ilmenau.de

Summary:
In this contribution we present the concept of photon momentum enabled SI-traceably made small force generation and measurements below the conventionally accepted limits. The developed instrumentations, the measurement infrastructure and the obtained results demonstrate the advantages of this concept and further are extended to present the means of systematization of the force measurements covering the range below 10 µN to several tens of nN. The prospects to reduce the relative measurement uncertainties of small force and small weight measurements are discussed.

Keywords: Photon momentum, small force, small weight, laser power, Planck-balance.

Background

Since the year 2019 the unit of the mass, the kilogram, in the International System of Units (SI) [1] is defined by a natural constant, namely through the fixed numerical value of the Planck constant. According to the present definition, the value of the Planck constant is h= 6.62607015×10^{-34} Js, expressed in base units kg m^{2}s^{-1} [1]. There exist two well established methods for practical realization of the kg. One is based on counting the atoms of a silicon sphere by X-ray crystal density method (based on concept of the inertial mass) and later disseminating the value using gravitational mass measurements. The other is the Kibble balance (KB) method [2] that exploits the gravitational force (gravitational mass) and compares the effective compensation force measured as a mechanical power with the electrical powers of the sensor obtained from a two-step experiment both steps based on electromagnetic interaction and with direct traceability to macroscopic quantum effects: the Josephson effect and the quantum Hall effect. Until now the primary realization and subsequent key-comparisons are made only for 1 kg. All other smaller values are still obtained using conventional accepted standard methods and instrumentations. Improvements/drawbacks have not been seen while undergoing this big change in mass metrology. Since the SI traceable calibrated force measurements are directly connected and are referenced with the mass values including for very small values, therefore in force metrology no substantial changes are noticeable as well. The KB allows to realize methods and determining a mass of any value in terms of the Planck constant without the use of any other mass standard including for lowest levels (>1 mg) and for any arbitrary value (e. g. 3.247 g) directly without the need of interpolation between standard mass values (e. g. 1 g, 2 g, 5 g, 10 g) and for all other derived units such as force, torque, etc. Therefore, a new class of the specially designed apparatuses would potentially simplify the calibration procedures and minimize the necessary time and, as a consequence, the respective economic burden. There exists already a table-top version of KB, e.g. Planck-Balance 2 (PB2) [3], an apparatus that allows SI traceable instrumentation based standard mass calibrations from 100 g down to 1 mg with measurement uncertainties corresponding to the weights of E2 class in air following OIML R 111-1 [4]. At 1 mg the typical uncertainties are about 0.3% and it grows to high % as the scale reaches to µg level due to very well described material and instrumentation limitations.

Photon momentum method

A complementary method using the photon momentum generated small forces offers powerful means to test and to reduce the uncertainty of the measurements and characterize instrumentations in a SI-traceable manner. This method relies on the option to reference the measured small forces in relation with the magnitude of the measured optical power of lasers in accordance to the

$$F = \frac{Power}{c}(1 + R_L)\cos\theta \qquad (1)$$

where Power is given by calibrated optical detector, c is the speed of the light, R_L is the reflectivity coefficient of the mirror on which the force is generated while laser is impinging and reflecting from it. The force exerted by a CW laser source with 1.5 W average optical power

is equal to 10 nN, which is equivalent to the gravitational (*g*) force acting on the approx. 1-µg-mass piece, to be determined as

$$F = mg \tag{2}$$

If highly reflective and well-characterized mirror is used, a multiple reflection can be created with negligible optical power loses by which amplification of forces can be achieved as

$$\sum_{i=1}^{N} F_i = \frac{(1+R_L)}{c} \sum_{i=1}^{N} Power_i, \qquad \sum_{i=1}^{N} \mathrm{Power}_i = \mathrm{Power}_1 \sum_{i=1}^{N} {R_L}^{i-1} \tag{3}$$

For example, a reference force of appox. 10 µN (1 mg) can be generated with 100 W power and 15-reflections. As a result, a short SI traceability chain can be constructed with minimal uncertainty contributing parameters, i.e. combined uncertainty of the optical power detector and the reflectivity value of the mirror [5]. Combining eqs. 1 and 2 yields

$$m = Power \frac{1+R_L}{c \cdot g} \tag{4}$$

$$\frac{u(m)}{m} = \sqrt{\left(\frac{u(\mathrm{Power})}{\mathrm{Power}}\right)^2 + \left(\frac{u(R_L)}{R_L}\right)^2 + \left(\frac{u(g)}{g}\right)^2} \tag{5}$$

The value of *u(g)/g* can be determined by means of a (free-fall) absolute gravimeter to approximately 0.2 ppm and below better than 0.01 ppm. The values of $u(R_L)/R_L$ for the ultra-high reflective mirrors in accordance with most datasheets provided by different manufacturers varies in the range of 10 ppm to 70 ppm. The *u(*Power*)/*Power typically varies dependent from absolute magnitude of the applied laser. For example, in accordance with PTB provided calibration services for the detector calibration in reference with primary standard it is approximately 0.1%-0.5% for 100 W and by the use of state-of-the-art cryogenic primary standards as low as nW orders of powers can be detected, with the upper limit typically given for below 1 mW power level with an expanded measurement uncertainty of about 0.002 %.

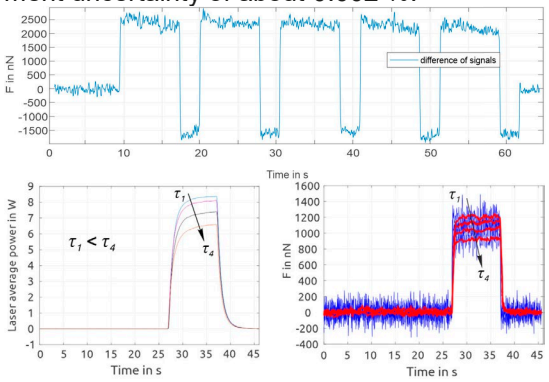

Figure 1. Measured forces via photon momentum and referenced by input laser power. [6]

The *u(m)/m* known from conventional mass metrology, from the 'uncertainties of the weights of the classes E1, E2, F1, and F2 according to OIML R111' is not specified below 1 mg that has already 0.3 % error limits (permissible tolerances). Thus, if the photon momentum is used for generation of forces referenced by high-precision SI-traceable conventional measurement methods and converted to mass values, then better uncertainty can be obtained both practically and by computations (eq. 5).
In practice, at Institute of Process Measurement and Sensor Technology in TU Ilmenau, such measurements are already realized for the force generation below this 1 mg (10µN) limits (Fig.1). In upper panel up-to-now measured maximum forces generated by the input high-power pulsed lasers of 17 W level at 33-reflection configuration with 75% duty cycle (10s) operation of periodic on-and-off signal is presented. In lower panel, the input laser power during each 10s is modulated by tuning the pulse width at 250ns, 1.5µs, 5µs, 10µs, and the corresponding force measurements in case of 21-reflections are shown. The current progress in referencing the photon momentum generated forces via optical power measurements of the input laser is limited to below 0.5% due to yet existing minor technical implementation problematics, e.g. proper choice of the laser and high-reflectivity mirror that should be optimized for the lasers' wavelength.

Outlook

Future steps in these developments are directed to implement a comprehensive uncertainty analyzes of the force measurements and scale calibration using a special apparatus known as Photon momentum setup that utilizes at the same time the principle of the KB similar to PB2 setup [6]. With the setup, preliminary, an uncertainty of approximately 0.1% for 10 µN, 1 µN, 100 nN force measurements referenced by photon momentum generated forces are expected.

[1] BIPM Cons. Com. Units. Mise en pratique for the definition of the kilogram in the SI, 2019.

[2] I. A. Robinson and S. Schlamminger, Metrologia 53, A46, (2016).

[3] S. Vasilyan, N. Rogge, C. Rothleitner, S. Lin, I. Poroskun, D. Knopf, F. Härtig, and T. Fröhlich, tm, 88(12):731–756, (2021).

[4] OIML. OIML R111-1 e04, 2004(E).

[5] S. Vasilyan, M. López, N. Rogge, M. Pastuschek, H. Lecher, E. Manske, S. Kück, T. Fröhlich, Metrologia, 58(1):015006, (2021).

[6] S. Vasilyan, N. Rogge, T. Fröhlich, tm, 89(11):757-777, (2022).

DOI 10.5162/SMSI2023/B7.2

Monolithic Guiding Mechanism and Adjustment Devices for an Electrostatic Force Balance at LNE

K. Dougdag[*], *F. Beaudoux*[*] *and M. Thomas*[*]

[1] LNE (Laboratoire National de Métrologie et d'Essais) 29 Rue Roger Hennequin, 78190 Trappes, France
(matthieu.thomas@lne.fr)

Summary:

A measurement apparatus that uses an electrostatic force generator is being developed at LNE, toward the realization of small masses and forces in the International System of Units (SI). Two of the main parts are designed, i.e. a parallelogram balance mechanism, and two capacitance actuators. The balance mechanism is fully monolithic as well as the two adjustment systems of the electrostatic actuators. Special attention has been paid to the overall symmetry of the system and to cost efficiency.

Keywords: Balance, electrostatic force, measurement, mass.

Introduction

The principle of the electrostatic balance method for measuring small forces (range 1 mN to 1 nN) and thus small masses (range 100 mg to 100 µg) proposed by [1], [2], can be used to realize mass at the 1 mg level with a standard uncertainty below 10 ppm [3].

When a voltage V is applied on a capacitor, an electrostatic force F is generated:

$$F = -\frac{1}{2}\frac{\mathrm{d}C}{\mathrm{d}z}V^2 \qquad (1)$$

where $\mathrm{d}C/\mathrm{d}z$ is the spatial gradient of the capacitance. This force can be used to balance the gravity force acting on a mass artefact m by using a balance mechanism. It allows to compare forces along its compliant axis: to achieve that, one of the electrode of the capacitor is affixed on the balance mechanism, whereas the second one is set immobile in laboratory referential. In a first approximation, the mass value can be determined as:

$$m = \frac{1}{2\,g}\frac{\mathrm{d}C}{\mathrm{d}z}\left(V_{\mathrm{off}}^2 - V_{\mathrm{on}}^2\right) \qquad (2)$$

where g is the local acceleration of gravity and V_{off} (resp. V_{on}) the voltage needed to equilibrate at the z_0 altitude the balance mechanism without the mass sample (resp. with the mass sample).

Determining $\mathrm{d}C/\mathrm{d}z$ requires translating one of the electrode of the capacitance (by using the balance mechanism as a guiding stage, and usually by using a second capacitance as an actuator) and measuring C at different z: the value $\mathrm{d}C/\mathrm{d}z$ at z_0 is then usually obtained by a polynomial fit [4].

Mechanical Design of Balance Mechanism

Different systems can be used to build a highly compliant mechanism, with linear or quasi-linear movement and parallel motion linkage, Peaucellier–Lipkin linkage… have been investigated. At last, a simple parallelogram has a bunch of desirable feature, as noted by [5] and is probably the easier to machine, has only 4 axis of rotation (see figure 1) and deviates only of 5 µm from a linear trajectory (with the dimensions describes lower) on a 1 mm vertical travel.

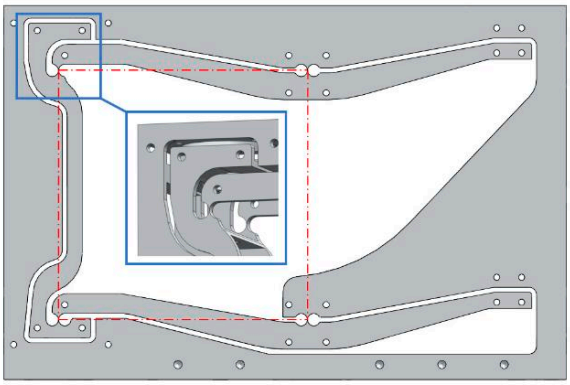

Fig. 1. CAD lateral view of the balance parallelogram mechanism. On the left, the vertical segment (pan) is the one on which gravity and electrostatic force will be compared. The horizontal arms (swings) are the actual guiding stage and the right extent of the swing are used to have a naturally equilibrated system, when no electrode is fixed on it. The red dashed line indicates the parallelogram position at weighing point (length 100 mm). The inset in the blue square shows a closer view of one hinge.

Flexures hinges have several key advantages over other solutions, and monolithic design, with for example a wire electrical discharge machining (WEDM), yields major benefits [5], and notably ensure the alignment of this delicate mechanism [6].

The chosen hinges are circular ($r = 2.5$ mm) with a thickness t of 40 µm. In order to improve transverse stiffness without compromise on the torsional stiffness, each hinge is indeed a comprised of two single hinges of width w 3 mm separated by 34 mm. Being electro-machined in aluminium EN AW-7075 T651, each half hinge will have a flexure stiffness of [7]:

$$\kappa_{\text{half hinge}} = \frac{2\,E\,w}{9\,\pi}\sqrt{\frac{t^5}{r}} = 3.1 \cdot 10^{-3}\ \text{N m rad}^{-1} \quad (3)$$

with $E = 72\ \text{GPa}$ the Young's modulus. Of course, its stiffness is slightly modified once the hinge is loaded.

Regarding the dimensions of the whole system, following [5], we have chosen a length $b = 100\ \text{mm}$ for each of the arms of the apparatus. Thus the vertical stiffness of the balance mechanism, comprised of its eight half hinges will be [8]:

$$K = \frac{\kappa}{b^2} = 2.5\ \text{N m}^{-1} \quad (4)$$

The balance mechanism is ready to welcome a spring system in the near future to lower this stiffness [8].

Capacitance and Adjustment Mechanism

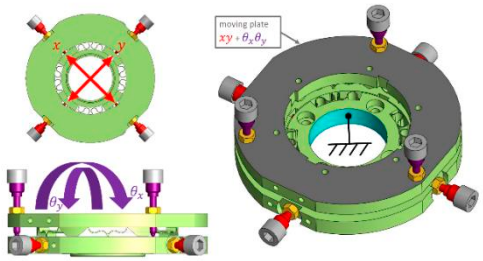

Fig. 2. CAD lateral view of the 5 dof (z not shown on figure) monolithic adjustment system which will be used to tune the relative position of the outer electrode with respect to the inner one.

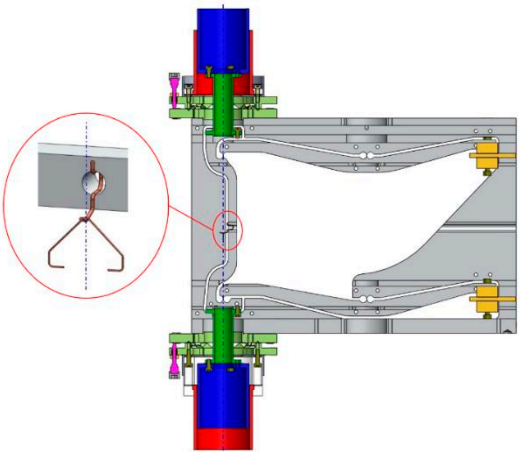

Fig. 3. CAD sectional general view of the balance parallelogram mechanism, capacitance and adjustment system, mass pan (red circle) and equilibrium mass (orange at left). The close up shows a possible configuration for the mass pan.

In order to weight 100 mg with a voltage of around 1000 V, the $\mathrm{d}C/\mathrm{d}z$ should be equal to $2\ \text{nF/m}$ at the weighing point. The electrodes are then chosen circular, the capacitance gradient is then constant and depending only (at first approximation) of the ratio of the radii of the electrodes R_1 and R_2:

$$\mathrm{d}C/\mathrm{d}z = \frac{2\,\pi\,\varepsilon_0}{\ln\left(R_2/R_1\right)} \quad (5)$$

To obtain a compact electrode set, we've chosen electrodes of 18.00 mm and 18.50 mm of radii. With 30 mm superposition at the weighing point, the total capacitance will be 60 pF. The electrodes must be coaxial in order to get a constant capacitance gradient.

To achieve that, 2 monolithic adjustment systems with seven flexure hinges of 0.3 mm thickness can displace each outer electrode on 5 degrees of freedom (dof) (see figure 2).

Each adjustment system resolution of 1 µm and 10 µrad when using microthreaded screws; relative movements can be followed by capacitives sensors.

Assembly

Each capacitor is directly fixed on the balance mechanism (see figure 3), which is itself fastened on an aluminum board by a Kelvin connection and 3 springs, in order to minimize the mechanical stress on balance.

Conclusion

LNE has begun the conception and machining of an electrostatic force balance, aiming at realizing the mass unit at the milligram level. The balance mechanism is a monolithic simple parallelogram whereas the actuator is a cylindrical capacitor with monolithic adjustment system.

Some parts of the system are already machined and delivered, and first results should be presented at the conference.

References

[1] V. Bego, J. Butorac, G. Gasljevic, and K. Poljancic, "Volt Balance Realization of the Volt At Etf in Zagreb.," *IEEE Trans. Instrum. Meas.*, vol. IM–36, no. 2, pp. 185–189, 1986.

[2] V. Bego, J. Butorac, and K. Poljančić, "Voltage Balance for Replacing the Kilogram," *IEEE Trans. Instrum. Meas.*, vol. 44, no. 2, pp. 579–582, 1995.

[3] G. A. Shaw *et al.*, "Milligram mass metrology using an electrostatic force balance," *Metrologia*, vol. 53, no. 5, pp. A86–A94, 2016.

[4] J. Stirling and G. A. Shaw, "Realising traceable electrostatic forces despite non-linear balance motion," *Meas. Sci. Technol.*, vol. 28, no. 5, p. 055003, May 2017.

[5] L. Keck, G. Shaw, R. Theska, and S. Schlamminger, "Design of an Electrostatic Balance Mechanism to Measure Optical Power of 100 kW," *IEEE Trans. Instrum. Meas.*, vol. 70, 2021.

[6] I. M. Choi, M. S. Kim, S. Y. Woo, and S. H. Kim, "Parallelism error analysis and compensation for micro-force measurement," *Meas. Sci. Technol.*, vol. 15, no. 1, pp. 237–243, 2004.

[7] P. Pinot *et al.*, "Static phase improvements in the LNE watt balance," *Rev. Sci. Instrum.*, vol. 87, no. 10, Oct. 2016.

[8] J. R. Pratt, D. B. Newell, and J. A. Kramar, "A flexure balance with adjustable restoring torque for nanonewton force measurement," *VDI Berichte*, no. 1685, pp. 77–82, 2002.

DOI 10.5162/SMSI2023/B7.3

Beam Horizontality Determination in the LNE Kibble Balance Experiment

D. Ziane[1], P. Espel[1], and M. Thomas[1]

[1] LNE (Laboratoire National de Métrologie et d'Essais) 29 Rue Roger Hennequin, 78190 Trappes, France
(matthieu.thomas@lne.fr)

Summary:

Determination of a mass in the LNE Kibble balance experiment requires, among other things, a precise control and knowledge of position and spatial orientation of its major comparator force element : the beam. This paper presents, with simple geometric assumptions, our automated method to determine, in vacuum, and without any additional device, the ideal beam setpoint position to use during weighing phase

Keywords: beam, Kibble balance, precision measurements, uncertainty.

Introduction

The Kibble balance principle consists of the comparison between virtual electromagnetic and mechanical powers measured during interlaced static and dynamic phases [1], [2].

One requirement for reducing unwanted force during weighing (or static) phase is to balance the beam as close to its horizontal position in order to not be sensitive to horizontal parasitic forces. Indeed, the aim of the static phase is to measure a vertical force F_z without bias. However, if a parasitic force F_x (horizontal and parallel to the longitudinal axis of the beam) is exerted at the end of the beam, with a beam separated from the horizontal by an angle α, a relative biais ε_{F_z} on F_z appears [3]:

$$\varepsilon_{F_z} = \alpha \frac{F_x}{F_z} \qquad (1)$$

The LNE Kibble balance beam is a single-piece symmetrical 100 mm length arms with three double flexure pivots [4], [5] . Under charge, these three centers of rotation are aligned by design and therefore define the segment which is supposed to be aligned with the horizontal during a static phase. The challenge remains to be able to match this segment with the horizontal line in order to maintain ε_{F_z} on the order of 10 ppb.

Experimental conditions

During weighing phase, the weight of a standard mass m subject to a gravitational acceleration g is balanced by the Laplace force F_z exerted on a coil, immersed in a magnetic induction field B, in which flows a current I. The servo control error signal is provided by the vertical position of the beam end, relatively to a fixe point, measured by a compact commercial interferometer.

At any time the vertical position of the coil is measured by three interferometers relatively to three points materialized by the apex of three corner cube reflectors equally distributed on the perimeter of its circular support.

In a same way three position sensors based on vertical propagating Gaussian beams intercepted by screens located at the periphery of the coil support are used to measure the coil displacement in the horizontal plane (x and y).

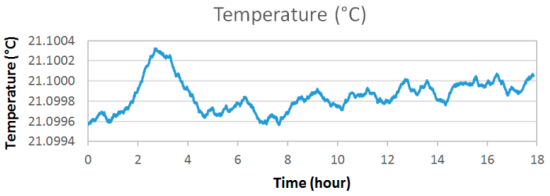

Fig. 1. Temperature of the magnetic circuit during the experiments

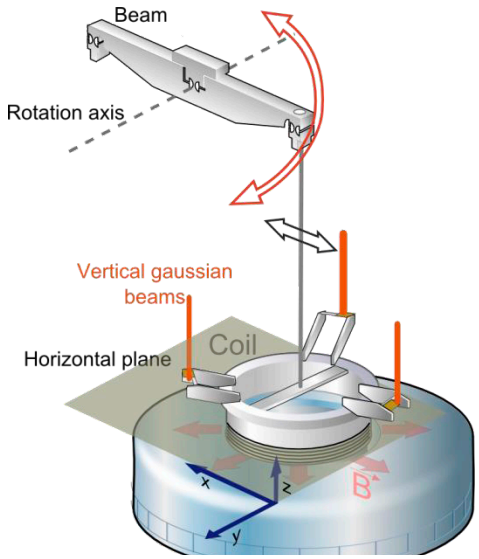

Fig. 2. Schematic view of the experimental set up. From top to bottom: balance beam, coil suspension, coil immersed in the magnetic circuit.

The most stable environmental conditions are required: the whole balance must have reached, in vacuum, a thermal equilibrium, in particular the magnetic circuit.

Fours heating resistors driven by a regulation system maintain the temperature of magnetic circuit at a fraction of millikelvins (Fig. 1).

Hypothesis and principle

The method consists in monitoring and relating the coil displacement with the beam position during a weighing phase when a low frequency (~5.10^{-5} Hz) sinusoidal setpoint is applied to the beam position (Fig. 1). If the coil is hanging vertically and its sensor Gaussian beams are vertical, then the coil position in the horizontal plane ($x0y$), reach an extremum when the beam crosses its horizontal position. During the process the beam end path travel is an arc of circle whose vertical projection is the coil trajectory. Even if the rotation beam axis is itself tilted with respect to the horizontal, the trajectory of the coil continues to present a turnaround point when the horizontality of the beam is crossed.

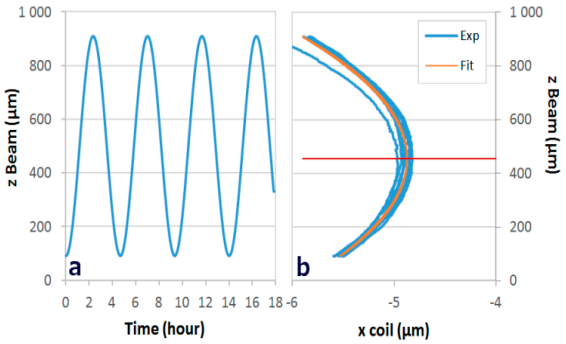

Fig. 3. a) Low frequency sinusoidal movement of the beam, b) Vertical beam displacement according to horizontal coil displacement during a horizontality beam determination. The red horizontal line shows the horizontal position of the beam end.

Improvements

In usual weighing mode, beam displacement imply also a vertical displacement of the coil immersed in the magnetic circuit, therefore, a non-uniform vertical magnetic field in the explored range, could add a bias in our measurements. To avoid this issue, the LNE kibble balance design allows to maintain constant the vertical position of the coil, despite the beam oscillation, since the balance beam plus its suspension can be moved as a single element [2], by activating the translation stage used in dynamic phase.

Measurements

The beam can be balanced between two mechanical stops spaced 1 mm apart, the lower one being our position reference (0 µm). A current is injected and adjusted in the coil in order to slowly oscillate the beam with an 0.8 mm amplitude at the end.

The vertical motor of the translation stage is commanded to move in an opposite way to always nullify the vertical coil motion.

Simultaneously, the three Gaussian beam signals are acquired with an integration time of 10 s and converted to *x* and *y* positions.

Results

Fig.3 shows in its left part, the evolution of the vertical imposed displacement of the beam end versus time; in the right part the blue line represents the corresponding measured horizontal excursion of the coil. As expected, the coil reaches repeatedly (8 times) an extremum. The coil trajectory can be locally and fit to a parabola (orange line) and finally the horizontal beam position can be extracted (red line), in this case at 455 µm. Repeated measurements show dispersion less than 10 µm. Estimation of the uncertainty associated is still under investigations.

Conclusion

The beam is used in the weighing phase as a force comparator. It must be aligned with the horizontal to reduce the contributions of some parasitic forces to negligible levels. The technique used to carry out this alignment is a non-perturbative method which allows an automated determination of the beam horizontally position, in a mass determination conditions i.e. in vacuum, and with no additional devices.

References

[1] B. P. Kibble, “Measurement of the gyromagnetic ratio of the proton by the strong field method,” 1976.

[2] M. Thomas *et al.*, “A determination of the Planck constant using the LNE Kibble balance in air,” *Metrologia*, vol. 54, no. 4, pp. 468–480, 2017.

[3] C. A. Sanchez and B. M. Wood, “Alignment of the NRC watt balance: Considerations, uncertainties and techniques,” *Metrologia*, vol. 51, no. 2, 2014.

[4] P. Pinot, Y. Liu, P. Espel, M. Thomas, D. Ziane, and F. Piquemal, “French watt balance experiment: Design of a single-piece balance beam and study of its mechanical behavior | Expérience française de balance du watt : conception d’un fleaú de balance monobloc et étude de son comportement mécanique,” *17th Int. Congr. Metrol. CIM 2015*, p. 2015, 2015.

[5] P. Pinot *et al.*, “Static phase improvements in the LNE watt balance,” *Rev. Sci. Instrum.*, vol. 87, no. 10, Oct. 2016.

DOI 10.5162/SMSI2023/B7.4

Novel Method for Determining the Mechanical Stiffness of Weighing Cells

Martin Wittke, Maximilian Darnieder, Mario André Torres Melgarejo, René Theska
Technische Universität Ilmenau, Department of Mechanical Engineering, Ilmenau, Germany
Institute for Design and Precision Engineering, Precision Engineering Group
martin.wittke@tu-ilmenau.de

Summary:
Weighing cells with electromagnetic force compensation are frequently used in precision balances and mass comparators. The kinematic structure is given by a compliant mechanism with concentrated compliances. Thin flexure hinges enable highly reproducible motion but limit the sensitivity to mass changes due to their rotational stiffness. To achieve the desired sensitivity, the stiffness of the mechanism must be further reduced by mechanical adjustments. To optimize the adjustment parameters, the initial stiffness of the mechanism needs to be characterized accurately.
For this purpose, a novel self-testing method was developed. It allows accurate determination of the elastic stiffness of the weighing cell and the geometric stiffness caused by the masses of the linkages. The method uses static stiffness measurements in three orientations. The gravity vector must be orthogonal to the plane of motion to characterize the elastic stiffness. Determining the geometric stiffness requires the system to be in the working orientation. The upside-down orientation is used to confirm the results. This paper considers the novel method analytically and simulates using a rigid body model and the finite element method. The measurement of the stiffness of a weighing cell prototype is taken to validate the method.

Keywords: weighing cell, electromagnetic force compensation, compliant mechanism, flexure hinge, stiffness measurement

Introduction

Weighing cells with electromagnetic force compensation are frequently used in precision balances and mass comparators due to their high measurement resolution and robust behavior [1]. The kinematic structure of the weighing cell is a compliant mechanism with concentrated compliance. It enables highly reproducible behavior and high sensitivity to mass changes on the weighing pan. Due to technological manufacturing limits [2] of the thin flexure hinges, stiffness adjustment is required to achieve the desired specifications. To optimize the adjustment, the initial stiffness of the mechanism must be known accurately. For this purpose, a novel measurement method was developed. It allows a self-testing characterization of the elastic and geometric stiffness by measurements in three orientations.

State of the Art

There are several methods for determining the stiffness of mechanical structures or compliant systems. They can be divided into three main categories: dimensional methods, dynamic experimental methods, and static experimental methods. The dimensional methods use the dimensions and the material properties of the mechanism to calculate its stiffness. However, they have high overall uncertainty. Dynamic experimental methods measure the natural frequency or thermal noise, from which the stiffness can be determined. As a prerequisite, the moving masses need to be known. Uncertainty in the range of 10% to 25% can be estimated [3]. Static experimental methods achieve the lowest measurement uncertainties of less than 5% [3]. The stiffness can be determined by measuring the force-displacement curve for example with a reference balance [4], a reference spring, or a calibrated actuator [5].

Determination Principle

Trim masses are typically used to reduce the stiffness of a weighing cell [6]. When selecting the adjustment parameters, the intrinsic mass of the linkages is often neglected. This leads to complicated readjustment to achieve minimal stiffness.
The developed method precisely characterizes the elastic and geometric stiffness of the mechanism and enables optimal adjustment. Static

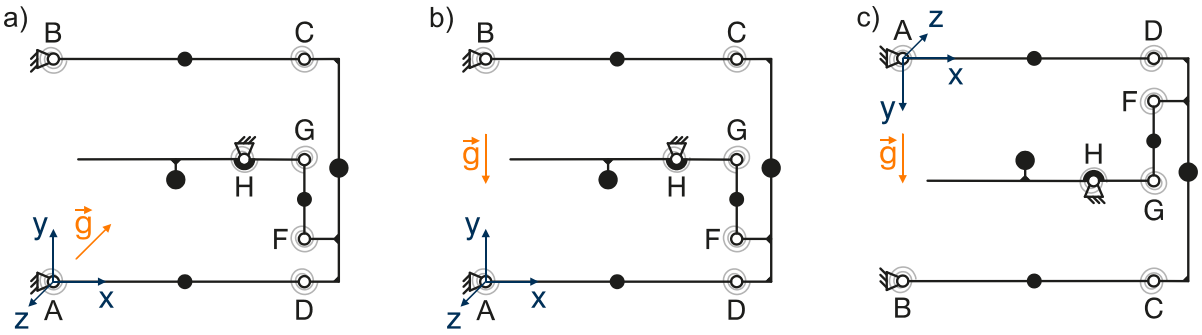

Fig. 1. Orientations required for the stiffness determination method. a) Horizontal. b) Working. c) Upside-down.

stiffness measurements in three orientations of the system are carried out. The horizontal orientation (see Fig. 1. a)) is used to determine the pure elastic stiffness $C_{M,e}$ of the mechanism. The gravity vector $\vec{g}$ is orthogonal to the plane of motion. Thus, there is no impact by linkage masses, i.e. no geometric stiffness. Characterizing the stiffness $C_{M,w}$ in the working direction (see Fig. 1. b)) includes the elastic and the geometric stiffness. The geometric part $C_{M,g}$ of the stiffness can be calculated from Equation (1).

$$C_{M,g} = C_{M,w} - C_{M,e} \quad (1)$$

The upside-down orientation (see Fig. 1. c)) is used to verify the results. The measured stiffness $C_{M,u}$ includes a reversed impact by linkage masses. Thus, equation (2) can be applied to confirm the determined values.

$$C_{M,e} = \frac{C_{M,w} + C_{M,u}}{2} \quad (2)$$

These equations are valid only for minimal deflections. This corresponds to the applications. Larger deflections would lead to a significant difference in the geometric stiffness $C_{M,g,w,}$ in the working orientation and the geometric stiffness $C_{M,g,u}$ in the upside-down orientation due to the nonlinearity of the torque-angle characteristic of the geometric stiffness.

Simulation and Measurement Results

Rigid body and finite element simulations of a demonstrator were carried out to determine the elastic stiffness in the horizontal orientation and geometric stiffnesses in the working and the upside-down orientation. The simulation results (see Tab. 1) verify the analytical considerations.

Tab. 1: Comparison of elastic and geometric stiffness.

	$C_{M,e}$ /(Nm^{-1})	$C_{M,g,w}$ /(Nm^{-1})	$C_{M,g,u}$ /(Nm^{-1})
Rigid body model	50.57	-0.84	+0.85
Finite element method	50.58	-1.29	+1.31
Measurement results*	36.58 ±0.27	-1.84 ±0.26	+1.75 ±0.33

*Standard deviations k = 1.

Deviations in geometric stiffness result from considered deformations of the frame and numerical errors in the finite element model. Experimental results confirm the method as well (see Tab. 1). Differences in the absolute values result from dimensional deviations of the manufactured joints.

Summary and Outlook

This paper presents a novel self-testing method for determining the stiffness of weighing cells. It uses static force-displacement measurements in three orientations to characterize the elastic and geometric parts of the stiffness. The method was considered theoretically and validated by simulations and measurements.

As a next step, a metrological model will be elaborated using the guide to the expression of uncertainty in measurement (GUM). The measuring setup used will be optimized to further reduce uncertainty. Additionally, the investigations will be repeated with comparable force measurement applications.

References

[1] R.R. Marangoni, Traceable multicomponent force and torque measurement, *Dissertation* (2019)

[2] J.P. Bacher, C. Joseph, R. Clavel, Flexures for high precision robotics, *Ind. Robot* 29, 349–353 (2002); doi: 10.1108/01439910210432911

[3] C. Clifford, M. Seah, The determination of atomic force microscope cantilever spring constants via dimensional methods for nanomechanical analysis, *Nanotechnology* 17, 1666-1680 (2005); doi: 10.1088/0957-4484/16/9/044

[4] M.-S. Kim, J.-H. Choi, J.-H. Kim, Y.-K. Park, SI-traceable determination of spring constants of various atomic force microscope cantilevers with a small uncertainty of 1%, *Meas. Sci. Technol.* 18, 3351–3358 (2007); doi: 10.1088/0957-0233/18/11/014

[5] N. Yan, High Resolution Force Measurement System for Lorentz Force Velocimetry, *Dissertation* (2019)

[6] M. Darnieder, M. Pabst, R. Wenig, L. Zentner, R. Theska, T. Fröhlich, Static behavior of weighing cells, *Journal of Sensors and Sensor Systems* 7.2, 587–600 (2018); doi: 10.5194/jsss-7-587-2018.

DOI 10.5162/SMSI2023/C1.1

One-Step Traceability with NIST on a Chip: A Case for the Emergence of Quantum-Based Methods for Metrology and Sensing of Pressure, Vacuum, Temperature, Electric Fields, Mass, Force, and Torque, all enabled by the New SI.

J. Hendricks[1], B. Goldstein[1], A. Artusio-Glimpse[1], C. Holloway[1], M. Simons[1], N. Prajapati[1], A. Rotunno[1], S. Berweger[1], K. Campbell[2], and M. Jayaseelan[2] N. Klimov[1], Z. Ahmed[1], D. Barker[1], S. Eckel[1], J. Fedchak[1], J. Ricker[1], K. Douglass[1], T. Herman[1], M. Chojnacky[1], J. Scherschligt[1], S. Schlamminger[1], L. Chao[1], Z. Comden[1], J. Draganov[1] T. Bui[1]

[1]National Institute of Standards and Technology, Gaithersburg, MD 20899, USA,
[2]University of Colorado, Boulder, CO 80305, USA

Summary:
The world is changing. Measurements are everywhere. As sensors are embedded into everyday products and electronics, the importance of sensors that give “the right answer” or “none at all” is of growing importance. The traditional role of the national metrology institute (NMI) is also changing with the 2019 revision of the international system of units. This revision removed long-standing artifact-based standards in favor of fundamental constants of nature. Sensors that are built on fundamental physics, constants of nature, and in many cases quantum-based systems will open a new paradigm for metrology. NIST has developed the “NIST on a Chip” program with a far-reaching vision that the future of metrology will be based on a new suite of sensor technologies that effectively removes the need for calibration instruments or artifacts to be returned to the NMI for periodic recalibration. This will be due to the inherent stability of these sensors that ideally will be small, compact, take advantage of nanomanufacturing, nanophotonics, future development of on-chip lasers, frequency combs, photon sources and detectors, etc. This paper will briefly discuss the promise for sensors and standards of pressure, vacuum, temperature, electric field, mass, force, and torque.

Keywords:

NIST on a Chip, NOAC, pressure, vacuum, cold atoms, fixed length optical cavity, Fabry Perot, quantum, nanophotonics, national metrology institute, temperature metrology, thermometry, photonics, Rydberg atoms, electrometry, revised SI, radio frequency, sensing, communications, Kibble balance, revised SI, force measurements, torque measurements

Introduction

The role of NIST as a National Metrology institute (NMI) is changing due to a world-wide redefinition of units that occurred on May 20th, 2019. The re-definition of units is now aligned with physical constants of nature and fundamental physics which has now opened new realization routes with quantum-based sensors and standards. The NIST on a Chip program (NOAC) is strategically positioned to take advantage of this change. The re-definition of the SI units enables new ways to realize the units for the pascal (pressure and vacuum), the kelvin (temperature), and the kilogram (mass). These quantum-based systems, however exciting, do raise new challenges and several important questions. Can these new realizations enable the size and scale of the realization to be miniaturized to the point where it can be imbedded into everyday products? What will be the role of metrology institutes in this new ecosystem of metrology and measurement? What will be the NMI role for quality systems and measurement assurance for these new quantum-based systems? [1] This paper will briefly review several emerging technologies for measurements of pressure, vacuum, temperature, electric fields, mass, force and torque. These methods are viewed through the redefinition of units that occurred in 2019 and the overall viewpoint of potential impact to the NIST on a Chip (NOAC) program.

Pressure

The next generation of pressure standards will provide a new route of SI traceability for the pascal. By taking advantage of light interacting with a gas the pressure-dependent refractive index of helium can be precisely predicted from fundamental, first-principles quantum-chemistry calculations. This enables a new route for realizing the pascal which has now been demonstrated.

From a metrology standpoint, the new quantum-based SI pascal will move us from the classical force/area definition to an energy density (joules per unit volume) definition. Should the technique be further miniaturized, it will lead to a revolution in pressure metrology, enabling a photonics-based device that serves both a gas pressure sensor and a portable gas pressure standard all in one. In the future, the mercury barometer will be replaced with a new standard based on quantum chemistry calculations.

Figure 1: Fixed Length Optical Cavity developed under a CRADA (Collaborative Research and Development Agreement) with MKS Instruments. The FLOC will enable the replacement of artifact-based mercury manometers world-wide. Photo courtesy of MKS Instruments.

The new method relies on a pair of optical cavities, each consisting of a set of mirrors on a spacer with the gas/vacuum filling the space between the mirrors. To improve upon this design, the reference cavity is always kept at vacuum to help eliminate noise and other systematic errors. This device, referred to as a Fixed Length Optical Cavity (FLOC), is shown in Figure 1. The FLOC is made of a glass with Ultra-Low thermal Expansion (ULE) to prevent changes in interferometer length with temperature. The upper cavity consists of a slot to allow gas to easily flow in and out, whereas the reference cavity is a hole drilled through the glass block and sealed at either end via mirrors.[2-5] The FLOC shown in Figure 1 was developed under a CRADA (Collaborative Research and Development Agreement) between NIST and MKS Instruments.

Vacuum

For vacuum measurements, NIST efforts to develop a new vacuum standard for measuring and understanding the pascal at the lowest pressures is underway. To achieve this, the Cold-Atom Vacuum Standard (CAVS) has been developed which uses a cold atom trap to sense pressure. [6] Since the earliest days of neutral atom trapping, it has been known that the background gas in the vacuum limits the trap lifetime (the characteristic time that atoms remain trapped). NIST is taking advantage of this well-known effect to create a quantum-based standard and sensor for vacuum measurement.

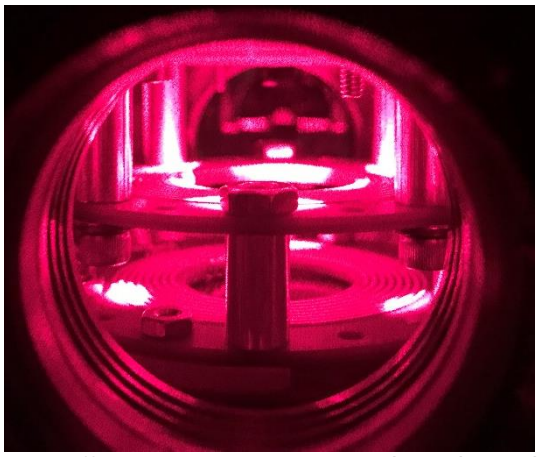

Figure 2: NIST CAVS table-top prototype version with a cloud of trapped Li atoms.

Because the measured loss-rate of ultra- cold atoms from the trap depends on a fundamental atomic property (the loss-rate coefficient, related to the thermalized cross section) such atoms can be used as an absolute sensor and primary vacuum standard. Researchers have often observed that the relationship between the trap lifetime and background gas can be an indication of the vacuum level, and several research groups have pursued using cold atom traps as vacuum sensors. [8,9] However, an absolute vacuum standard, sufficient for use as an international standard, has not yet been realized. To do this requires rigorous attention to all potential error sources, from both the atomic perspective and the vacuum perspective. Moreover, a primary CAVS requires the collision cross section between trapped ultra-cold atoms and the background gas to be traceable to an ab initio theoretical determination. NIST has built a laboratory-scale CAVS apparatus, developed the measurement scheme, and done preliminary theoretical calculations, all of which show promising early results. In addition, NIST is developing a small, portable version that uses a grating-based trap (shown in Figure 2) that will eventually enable users to realize and measure vacuum pressures in their lab without relying on calibrated sensor artifacts.

Temperature

For temperature measurements, NIST efforts to develop a method of measuring temperature using a photonic-based method are underway. Temperature measurements and sensors play a crucial role in various aspects of modern technology ranging from medicine and manufacturing process control to environmental borehole monitoring. Among various temperature

measurement solutions, resistance-based thermometry is a time-tested method of disseminating temperature standards. [10]

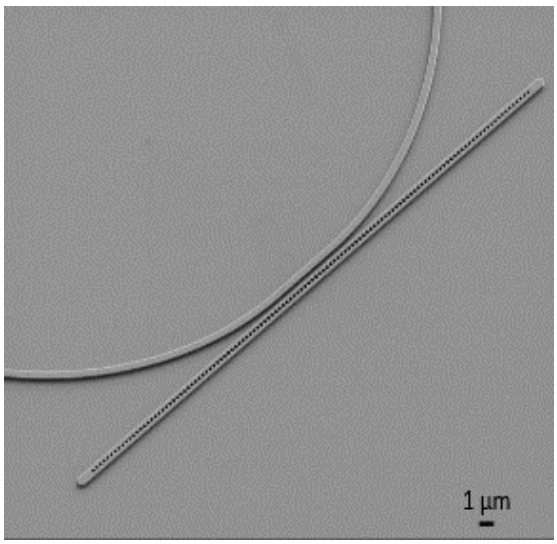

Figure 3. Silicon photonic crystal cavitythermometer fabricated at NIST

Although industrial resistance thermometers can routinely measure temperatures with uncertainties of 10 mK, their performance is sensitive to multiple environmental variables such as mechanical shock, thermal stress and humidity. These fundamental limitations of resistance thermometry, as well as the desire to reduce sensor ownership cost, have ignited a substantial interest in the development of alternative temperature measurement solutions such as photonics-based temperature sensors [11,12]. These sensors are Fabry-Perrot cavity type silicon photonic devices that are based on a Photonic Crystal nanobeam Cavity (PhCC), whose high-Q resonant frequency mode is highly sensitive to even ultra-small temperature variations. Measurement results show the NIST photonic nanothermometers can detect changes of temperature as small as sub-10 µK and can achieve measurement capabilities that are on-par or even better than the state-of-the-art platinum resistance thermometry.

Electric Field Measurements

Absolute measurements of electric fields are vital in various applications, such as precision metrology, communications, and sensing. However, measuring the electric field's strength accurately is a challenging task due to the lack of reliable calibration standards. The traditional calibration methods rely on accurate measurements of the geometry of the sensing probe and a chain of calibrations to determine absolute field strength with an order of 5 % uncertainty. NIST is developing an alternative approach that utilizes Rydberg atoms for measuring electric fields with improved accuracy and simplicity.

Rydberg atoms made with alkali atoms such as rubidium have a single valance electron which enables the accurate calculation of the quantum mechanical response of these atoms to radio frequency electric fields. The researchers employ a spectroscopy technique known as electromagnetic induced transparency (EIT) and a resonant effect known as Autler-Townes (AT) splitting to measure the Radio Frequency (RF) field strengths exposed to the atoms [13].

The Rydberg atom-based technique provides a direct traceability path for RF electric field strength to be determined directly from fundamental units of the SI, namely the Planck constant accomplished through the calculable response of the atoms given by the dipole moment and dictated by quantum mechanics.

Using this technique, Rydberg atom sensors have been shown to achieve sensitivities down to 5 $\mu Vm^{-1}Hz^{-1/2}$ [14] and as receivers of amplitude, frequency, and/or phase modulated signals [15,16].

Mass, Force and Torque

The reciprocity in Maxwell's equations that Bryan Kibble saw in 1975 [17] proved to be a powerful principle for high-precision metrology and allows the precise comparison of electrical power to mechanical power with relative uncertainties close to 1 part in 10^8. With the 2019 redefinition, the kilogram (kg) is now defined in terms of the Planck constant. This eliminated the artifact-based standard for mass. NIST has built systems based on the Kibble principle [18,19] that are high accuracy, full laboratory scale instruments. With the 2019 redefinition, NIST is now showing that the Kibble principle has fantastic potential be useful in mass-produced devices for mass, torque, and force. NIST has developed table-top prototype instruments that calibrate mass, force, and torque using Kibble's principle. For the torque project, NIST researchers have shown the performance on a device that can measure torques ranging from order 1 mN·m to 18 mN·m.

Conclusion

Sensors that are built on fundamental physics, constants of nature, and in many cases quantum-based systems are being developed worldwide at National Metrology Institutes. NIST has developed the NIST on a Chip program with a long-term vision that the future of metrology will be based on a new suite of sensor technologies. While the example technologies discussed in this paper are emergent, NIST has

demonstrated several tabletop versions. Should these be further developed by industry, reduced in size, weight and power and integrated into commercial products, a new paradigm will emerge that will reduce or eliminate the need for instrument recalibration. This will be due to the inherent stability of these sensors that ideally will be small, compact, take advantage of other quickly developing fields and technologies, including nanomanufacturing, nanophotonics, future development of on-chip lasers, frequency combs, photon sources and detectors, to name a few.

References

[1] Tzalenchuk, A., Spethmann, N., Prior, T. *et al.* The expanding role of National Metrology Institutes in the quantum era. *Nat. Phys.* **18**, 724–727 (2022).

[2] P. Egan, J. Stone, J. Hendricks, J. Ricker, G. Scace, G. Strouse, “Performance of a dual Fabry–Perot cavity refractometer,” Opt. Letters, Vol. 40, No. 17, August 2015

[3] M. Puchalski, K. Piszczatowski, J. Komasa, B. Jeziorski, K. Szalewicz, 2016, “Theoretical determination of the polarizability dispersion and the refractive index of helium,” Amer. Phys. Soc., Phys. Rev. A

[4] P. Egan, J. Stone, J. Ricker, J. Hendricks, 2016, “Metrology for comparison of displacements at the picometer level,” Amer. Inst. of Phys., Rev. of Sci. Inst. 87, 053113

[5] J. Stone, P. Egan. J. Hendricks, G. Strouse, D. Olson, J. Ricker, G. Scace, D. Gerty, 2015 “Metrology for comparison of displacements at the picometer level,” Key Eng. Mat. Vol. 625 p 79-84

[6] J. Scherschligt, J. A. Fedchak, D.S. Barker, S. Eckel, N. Klimov, C. Makrides, and E. Tiesinga, Metrologia 54, S125 (2017).

[7] D.E. Fagnan, J. Wang, C. Zhu, P. Djuricanin, B.G. Klappauf, J.L. Booth, and K.W. Madison, Phys. Rev. A - At. Mol. Opt. Phys. 80, 1 (2009).

[8] T. Arpornthip, C.A. Sackett, and K.J. Hughes, Phys. Rev. A - At. Mol. Opt. Phys. 85, 1 (2012).

[9] S. Eckel, D. Barker, J. Fedchak, N. Klimov, E. Norrgard and J. Scherschligt, Metrologia 2018 55 S182–93

[10] Strouse, NIST Spec. Publ. 250, 81 (2008).

[11] Kim et al., Opt. Express 18, 22215 (2010).

Proceedings Volume 10923, Silicon Photonics XIV; 109230L (2019) https://doi.org/10.1117/12.2505898 Event: SPIE OPTO, 2019, San Francisco, California, United States

[12] M. Tanasittikosol, et al., “Microwave dressing of Rydberg dark states,” J. Phys. B 44, 184020, 2011.

[13] M. Jing, et al., “Atomic superheterodyne receiver based on microwave-dressed Rydberg spectroscopy,” Nature Physics 16(9), 911-915, 2020.

[14] D. Anderson, et al., “An atomic receiver for AM and FM radio communication,” IEEE Trans. on Antenn. and Prop. 69, 2455, 2021.

[15] C. Holloway, et al., “Detecting and receiving phase-modulated signals with Rydberg atom-based receiver,” IEEE Antenn. And Wireless Prop. Lett. 18, 1853, 2019.

[16] B.P. Kibble, A measurement of the gyromagnetic ratio of the proton by the strong field method, in Atomic Masses and Fundamental Constants 5th ed, edited by J.H. Sanders and A.H. Wapstra.

[17] D. Haddad et al. Invited Article: A precise instrument to determine the Planck constant, and the future kilogram, Rev. Sci Instrum, 87:061301, 2022, https://doi.org/10.1063/1.4953825.

[18] F. Seifert et al. A macroscopic mass from quantum mechanics in an integrated approach. Communications Physics, 5:321, 2022, http://dx.doi.org/10.1038/s42005-022-01088-7.

DOI 10.5162/SMSI2023/C1.2

Rydberg Atoms for One-Step Traceability for Sensing Electric Fields

A. Artusio-Glimpse[1], C. L. Holloway[1], M. T. Simons[1], N. Prajapati[1], A. Rotunno[1], S. Berweger[1], K. Campbell[2], and M. Jayaseelan[2]
[1] National Institute of Standards and Technology, Boulder, CO 80305, USA,
[2] University of Colorado, Boulder, CO 80305, USA,
alexandra.artusio-glimpse@nist.gov

Summary:
Absolute electric field measurements present a “chicken-and-egg” situation where calibration of field probes relies on accurate knowledge of the field while precise determination of the field involves measurements with a calibrated probe. Metrology institutes overcome this dilemma by employing careful geometric measurements, Maxwell’s equations, and a long chain of calibrations to determine absolute field strength with order of 5% uncertainty. We describe an alternative approach using Rydberg atoms that ties radio frequency electric field strength to Planck’s constant through calculable quantum properties of the atoms for improved accuracy and simplicity. In addition to improved calibrations, Rydberg atom probes can be used as sensors and receivers for a wide swath of applications that we describe.

Keywords: Rydberg atoms, electrometry, revised SI, radio frequency, sensing, communications

Introduction

Rydberg atoms are highly excited atoms with high sensitivity to electric fields making them attractive for measurements and sensing. By selecting alkali atoms, like rubidium (Rb) or cesium (Cs), which have a single valance electron, we can accurately calculate the quantum mechanical response of these atoms to incident radio frequency (RF) electric fields. We employ a spectroscopy technique known as electromagnetic induced transparency (EIT) and a resonant effect known as Autler-Townes (AT) splitting to precisely determine RF field strengths radiated onto the atoms [1]. These techniques and some use cases are described in this paper.

One-Step Traceability with EIT/AT

We begin with a vapor cell filled with room temperature alkali atom vapor. A probe laser, resonant with the transition between the ground state $|1\rangle$ and first excited state $|2\rangle$ of the atoms is strongly absorbed as it propagates through the vapor cell before being measured by a photodetector as depicted in Fig. 1. Due to the motion of the room temperature atoms state, the resonant absorption line is broad, on the order of 100s of MHz as depicted in Fig 2. However, a narrow <10 MHz transmission window can be induced by applying a second (coupling) laser that is resonant with state $|2\rangle$ and a Rydberg state $|3\rangle$ and produces EIT.

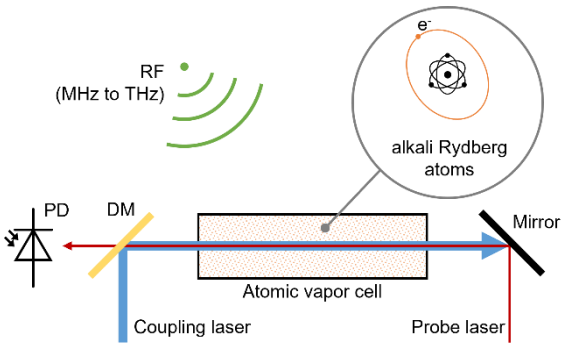

Fig. 1. Diagram of the electric field measurement setup. PD-photodetector, DM-dichroic mirror.

By using the coupling laser to excite the atoms to a Rydberg state, an RF field can be applied that is resonant with state $|3\rangle$ and a second Rydberg state $|4\rangle$ causing the EIT spectral line in Fig. 2 to split, an effect known as AT splitting. The frequency separation Δf between the split AT lines is directly proportional to the amplitude of the incident RF electric field $|E|$ with $\wp$, the atomic dipole moment of the RF transition, and h, Planck’s constant, as proportionality constants: $|E| = (h/\wp)\,\Delta f$.

This splitting is valid for a wide range of RF frequencies, from MHz to THz, and the resulting field measurement can be completed with 1% uncertainty [2]. Very strong RF fields (>10 V/m) cause an additional Stark shifting effect that goes as $|E|^2$ and require a more complicated Floquet analysis [5]. Very weak fields

(<10 mV/m), on the other hand, induce splitting that is not resolvable, but a linear response can still be achieved by applying a second RF field as a local oscillator (LO) detuned from the test field by an intermediate frequency (IF) on the order of kHz. When the frequency of probe and coupling lasers is locked, the photodetector signal turns into a sine wave at the IF with an amplitude and phase that is proportional to the test RF field [6]. Using this technique, Rydberg atom sensors have been shown to achieve sensitivities down to 5 $\mu Vm^{-1}Hz^{-1/2}$ [7] and as receivers of amplitude, frequency, and/or phase modulated signals [9,10].

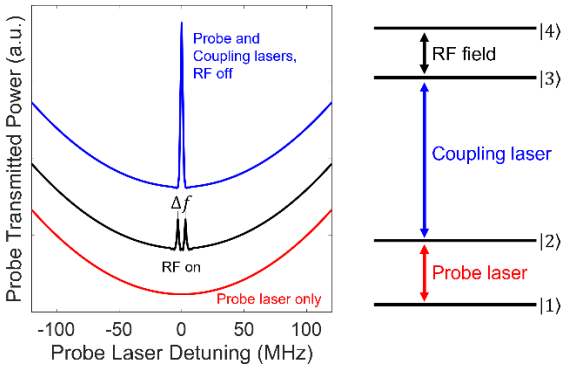

Fig. 2. EIT signal with Doppler background as probe laser frequency is detuned. Frequency separation between the two peaks generated when the RF field is on provides a traceable measurement of the RF electric field strength.

Rydberg atoms for sensing and receiving

In the AT splitting regime, the Rydberg atom-based technique provides a direct traceability path for RF electric field strength to the fundamental units of the SI, namely Planck's constant, through the calculable response of the atoms, the dipole moment $\wp$, dictated by quantum mechanics. Not only is this an excellent tool for field strength metrology, but the Rydberg atoms also turn out to be useful in sensing, communications, and RF power metrology.

At NIST, we have demonstrated the use of Rydberg atoms for in situ, traceable measurements of power in waveguide [11], voltage reference measurements [12], and determination of the angle of arrival of an over the air test signal [13]. We have studied a scheme that extends the sensitivity of the Rydberg atoms to lower, few MHz, RF frequencies by applying an additional GHz field to engineer the desired Rydberg atom response [14]. Dressing the atoms with other RF fields also allows us to stretch the resonant AT behavior over a continuous range of RF frequencies [15]. Most recently, we have demonstrated an interferometric technique that enables detection of RF phase without the need for an RF LO [16]. Rydberg atom-based receivers operate over an extremely wide band of RF frequencies (MHz to THz). They also can be electrically small, and the dielectric sensor head minimizes scattering of the incident field. These features of Rydberg atoms are unlike classical antennas.

Conclusion

We define the benefits of using Rydberg atoms for one-step traceability for sensing RF electric fields. In addition, we review many other applications that are under investigation at NIST using these atoms, highlighting the unique features of this measurement system as compared to classical antennas.

References

[1] M. Tanasittikosol, et al., "Microwave dressing of Rydberg dark states," J. Phys. B 44, 184020, 2011.

[2] C. Holloway, et al., "Electric field metrology for SI traceability: Systematic measurement uncertainties in electromagnetically induced transparency in atomic vapor," J. of App. Phys. 121(23), 233106, 2017.

[5] D. Anderson, et al., "Two-photon microwave transitions and strong-field effects in a room-temperature Rydberg-atom gas," Phys. Rev. A 90, 043419, 2014.

[6] M. Simons, et al., "A Rydberg atom-based mixer: measuring the phase of a radio frequency wave," Appl. Phys. Lett. 114, 114101, 2019.

[7] M. Jing, et al., "Atomic superheterodyne receiver based on microwave-dressed Rydberg spectroscopy," Nature Physics 16(9), 911-915, 2020.

[9] D. Anderson, et al., "An atomic receiver for AM and FM radio communication," IEEE Trans. on Antenn. and Prop. 69, 2455, 2021.

[10] C. Holloway, et al., "Detecting and receiving phase-modulated signals with Rydberg atom-based receiver," IEEE Antenn. And Wireless Prop. Lett. 18, 1853, 2019.

[11] C. Holloway, et al., "A quantum-based power standard: Using Rydberg atoms for a SI-traceable radio-frequency power measurement technique in rectangular waveguides," Appl. Phys. Let. 113, 094101, 2018.

[12] C. Holloway, et al., "Electromagnetically induced transparency based Rydberg-atom sensor for traceable voltage measurements," AVS Quantum Sci. 4, 034401, 2022.

[13] A. Robinson, et al., "Determining the angle-of-arrival of a radio-frequency source with a Rydberg atom-based sensor," Appl. Phys. Lett. 118, 114001, 2021.

[14] A. Rotunno, et al., "Pseudo-resonant detection of low frequency VHF electric fields via Ravi matching with Autler-Townes splitting in Rydberg atoms," arXiv:2212.03304, 2022.

[15] S. Berweger, et al., "Rydberg state engineering: A comparison of tuning schemes for continuous frequency sensing," arXiv:2209.14407, 2022.

[16] S. Berweger, et al. "Phase-resolved Rydberg atom field sensing using quantum interferometry," arXiv:2212.00185, 2022.

DOI 10.5162/SMSI2023/C1.3

Integrated Nanophotonics for One-Step Traceability for Temperature Measurements

Nikolai N. Klimov[1], *Kevin O. Douglass*[1], *Tobias Herman*[1], *Zeeshan Ahmed*[1], *Michal J. Chojnacky*[1]
[1] *National Institute of Standards and Technology, Gaithersburg, MD 20899, USA,*
nklimov@nist.gov

Summary:
We report on the development of the next-generation photonics-based thermometry at National Institute of Standards and Technology (NIST). We provide details on design, fabrication, and performance of ultra-high resolution photonic thermometers. Our device shows a noise floor of sub-10 µK when measured at water triple point and gallium fixed-point cells, demonstrating the potential for photonic thermometry that is on-par or even better than the state-of-the-art resistance thermometry.

Keywords: temperature metrology, thermometry, photonics

Introduction

Temperature measurements play a crucial role in various aspects of modern technology. Among various temperature measurement solutions, resistance-based thermometry is a time-tested method of disseminating temperature standards [1]. Although industrial resistance thermometers can routinely measure temperatures with uncertainties of 10 mK, their resistances drift over time due to sensors' sensitivity to multiple environmental variables. These fundamental limitations of resistance thermometry, as well as the desire to reduce sensor ownership cost, have ignited a substantial interest in the development of alternative temperature measurement solutions such as photonics-based temperature sensors [2]–[4]. Here we present the results of our efforts at NIST in developing novel on-chip integrated silicon photonic temperature sensors with a nanoscale footprint and ultra-high resolution as an alternative solution to legacy resistance thermometers. These nanophotonic sensors operate in telecom frequency range and have a high-quality (high-*Q*) resonant frequency mode that is highly sensitive to even ultra-small temperature variations. We present a direct comparison of our photonic thermometers to Standard Platinum Resistance Thermometers (SPRT), the best-in-class resistance temperature sensors used to disseminate the International Temperature Scale of 1990. Our preliminary results indicate that our photonic thermometers are capable of detecting changes of temperature as small as sub-10 µK and can achieve measurement capabilities that are on-par or better than state-of-the-art resistance thermometry.

Device design, fabrication, and packaging

The integrated photonic thermometers described in this work are silicon photonic crystal cavity (Si PhCC) nanoresonators that have a very sharp resonance optical mode in their transmission spectra [3]. The mode frequency shifts with temperature due to high thermo-optic coefficient of silicon [5] and can be used to trace temperature variations with high precision. Our photonic thermometer features Fabry-Perot cavity that is shaped out of two symmetrical photonic crystals (Fig. 1). To design photonic crystal cavity we follow a deterministic approach of Ref. [6] with additional optimization.

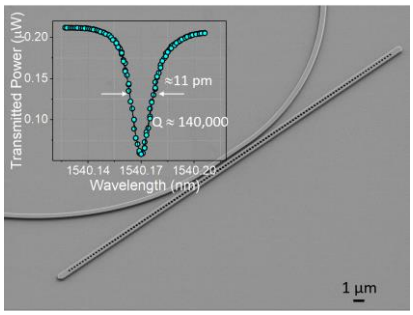

Fig 1: SEM image of silicon photonic thermometer. The insert shows the resonant absorption peak of the sensor.

The photonic chip with integrated silicon photonic thermometers was fabricated at the NIST NanoFab facility [7]. The integrated sensors were patterned on silicon-on-insulator substrate. The substrate consists of 220 nm-thick silicon, 3 µm-thick buried silicon dioxide, and 670 µm of silicon handle. The devices were patterned via electron-beam lithography followed by inductively coupled plasma reactive ion etch (ICP RIE) of the patterned topmost

silicon layer. After the ICP RIE etch, devices were top-cladded with a silicon dioxide layer with a thickenss of 1500 nm . After device fabrication, we fiber-coupled the photonic chip on a custom-built photonic chip packaging station by bonding a v-groove fiber array to the input/output ports on the chip using ultraviolet light curable adhesive. The fiber-coupled device was then placed in a sheath tube and sealed under inert gas.

Results

The fabricated photonics thermometer has a resonance peak at ≈1540 nm wavelength at 300 K and a temperature sensitivity of ≈67 pm/K. The photonic thermometer is interrogated using a telecom tuneable laser and a laser dither locking technique. To realize a dither lock a laser frequency is modulated via a low-frequency laser current modulation. When the laser frequency is close to the photonic crystal cavity resonance, the frequency modulation produces an amplitude modulation of the photodiode signal. A transmission signal from the cavity is sent to a phase-sensitive detector, which transforms this modulation signal into a derivative signal. The produced “error” signal is used in a feedback loop to adjust the laser frequency to constantly track the PhCC resonance shift. Once a laser lock is realized, the laser frequency is locked to the top of the fringe of photonic crystal cavity resonance. Whenever the PhCC resonance frequency shifts due to external temperature variations, the laser frequency is automatically adjusted via a feedback loop.

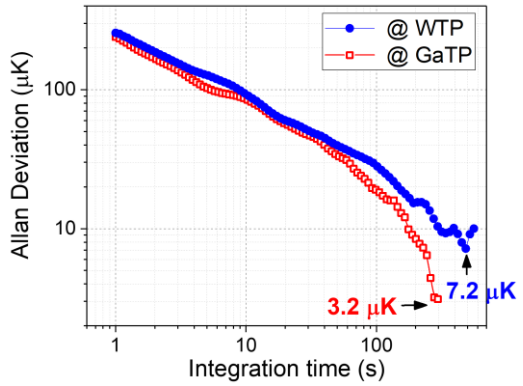

Fig. 2: Allan deviation plot of photonic thermometer TP-W and TP-Ga.

To access sensor’s performance, we calibrated our photonic thermometer against two fixed-point cells with phase-transition temperatures defined within the International Temperature Scale of 1990 (ITS-90): the triple-point of water (TP-W, 273.16 K) and the triple-point of gallium (TP-Ga, 302.9166 K). These two temperatures bracket the most frequently used range of ITS-90 [9]. The resonance frequency of the photonic thermometer changes monotonically with temperature. Calibration of the resonance frequencies at the two fixed-point temperatures allows the thermometer to make absolute temperature measurements referenced to the ITS-90 temperature scale. The measured noise floor for TP-W and TP-Ga are at the 10 µK level (Fig. 2).

Conclusion

In conclusion, we fabricated an ultra-sensitive photonic temperature sensor and demonstrated its performance at TP-W and TP-Ga in water and gallium fixed-point cells. The photonic thermometer shows a noise floor below 10 µK and is comparable to the performance of SPRT. Moreover, the photonic thermometer is more robust against mechanical shock and temperature stress than SPRTs. The results from this study show the potential for photonic thermometers to serve as future standards for the dissemination of ITS-90 to commercial calibration laboratories and as transfer standards for international measurement comparisons between National Metrology Institutes.

References

[1] G. F. Strouse, “Standard Platinum Resistance Thermometer Calibrations fromthe Ar TP to the Ag FP,” *NIST Spec. Publ.*, vol. 250, no. 250, p. 81, 2008.
[2] AD. Kersey and T. A. Berkoff, “Fiber-optic Bragg-grating differential-temperature sensor,” *IEEE Photonics Technol. Lett.*, vol. 4, no. 10, pp. 1183–1185, Oct. 1992.
[3] N. N. Klimov *et. al*, “On-chip silicon photonic thermometers: from waveguide Bragg grating to ring resonators sensors,” May 2015, p. 948609.
[4] N. N. Klimov *et. al*, “On-chip silicon waveguide Bragg grating photonic temperature sensor,” *Opt. Lett.*, vol. 40, no. 17, p. 3934, Sep. 2015.
[5] G. Cocorullo *et. al*, “Temperature dependence of the thermo-optic coefficient in crystalline silicon between room temperature and 550 K at the wavelength of 1523 nm,” *Appl. Phys. Lett.*, vol. 74, no. 22, pp. 3338–3340, May 1999.
[6] Q. Quan and M. Loncar, “Deterministic design of wavelength scale, ultra-high Q photonic crystal nanobeam cavities,” *Opt. Express*, vol. 19, no. 19, pp. 18529–18542, Sep. 2011.
[7] “Disclaimer: Certain commercial fabrication facility, equipment, and materials are identified in this paper in order to specify device fabrication, and the experimental procedure adequately. Such identification is not intended to imply endorsement by the National Institute of Standards and Technology, nor is it intended to imply that the facility, equipment, or materials identified are necessarily the best available.”
[8] F. Van Laere *et al.*, “Compact and Highly Efficient Grating Couplers Between Optical Fiber and Nanophotonic Waveguides,” *J. Light. Technol.*, vol. 25, no. 1, pp. 151–156, Jan. 2007.
[9] H. Preston-Thomas, “The International Temperature Scale of 1990 (ITS-90),” *Metrologia*, vol. 27, no. 1, pp. 3–10, Jan. 1990.

DOI 10.5162/SMSI2023/C1.4

Using the Kibble Principle for One-Step Traceability for Mass, Force, and Torque

S. Schlamminger[1], L. Chao[1], Z. Comden[1], J. Draganov[1], T. Mametja[1]
[1] National Institute of Standards and Technology, Gaithersburg, MD 20899, USA,
stephan.schlamminger@nist.gov

Summary:
Many technologies contributed to the 2019 revision of the international system of units. Notable is a mechanical apparatus, the Kibble balance. It allows the precise comparison of electrical power to mechanical power with relative uncertainties close to 1 part in 10^8. Here, we show the basic principle of this device and discuss several exciting future applications.

Keywords: Kibble balance, revised SI, force measurements, torque measurements

Introduction

In 1975, Bryan Kibble, a metrologist at the National Physical Laboratory in the UK, had an insight [1] that would eventually lead to the revision of the international system of units (SI) in 2019. As is the case with many eureka moments, in hindsight, they are obvious, but they solve a long-standing problem. In this particular case, Kibble's ideas allowed us to obtain precisely the force of a current-carrying wire in a magnetic field, an almost century-old struggle at the time. And precise it is. The world's best measurements utilizing Kibble's idea have relative uncertainties of 1 part in 10^8. Clearly, such a powerful insight must be treasured and understood. An explanation is attempted below.

Kibble's idea in a nutshell

The energy of a coil in a magnetic flux density, B, is given by the number of turns, N, times the current, I, encircling the area of the coil, A, or

$$E = NIBA. \qquad (1)$$

Note, the product BA is the flux through the coil opening, abbreviated as $\phi = BA$. From eq. (1), the forces and torques on the coil can be obtained by the partial derivatives in the corresponding direction. So, for example, the force in the z direction is given by

$$F_z = -\frac{\partial E}{\partial z} = -NI\,\frac{\partial \phi}{\partial z}. \qquad (2)$$

Even in 1975, this was nothing new. People have tried to measure forces using eq. (2), but the problem is that the product BA is difficult to know precisely. Absolute measurements of B are cumbersome and what exactly is the open area of a coil, A? Even if the coil is made from a single layer how much of the wire diameter must be considered to calculate A?

Kibble noticed that the flux through the coil appears in another equation, Faraday's law of induction,

$$U = -N\,\frac{d\phi}{dt}. \qquad (3)$$

Here U is the electromotive force (EMF) that appears at the open-ended leads of a coil as the flux through the coil varies with time. Now assume, the coil is moved, by some undescribed mechanism, through a magnetic field that is constant in time but not in space in a purely vertical trajectory, the time derivative can be replaced in the following way,

$$U = -N\,\frac{\partial \phi}{\partial z}\,\frac{d\,z}{d\,t} = -N\,\frac{\partial \phi}{\partial z}\,v_z. \qquad (3)$$

By measuring the induced EMF and the vertical velocity, v_z, the derivative of the flux can be obtained. What makes the idea powerful is that both quantities can be measured easily and precisely.

Eliminating the flux integral in eq. (2), yields

$$F_z = \frac{I\,U}{v_z}. \qquad (4)$$

In the section above, we worked an example in the vertical direction, as is the case in the Kibble balance. The theory works, of course, in all directions and even for rotational motion. The torque, N_x, about an axis *x* can be measured using

$$N_x = \frac{I\,U}{\omega_x}. \qquad (4)$$

In eq. (4), ω_x is the angular velocity about the same axis while *U* is measured.

Work at the National Institute of Standards and Technology (NIST)

In the 2010s, a Kibble balance for a nominal mass of 1 kg was built with the purpose to aid the international effort to revise the SI and to become the primary mass standard of the United States after said revision [2]. This Kibble balance produces measurements with competitive uncertainties for masses ranging from 50 g to 2 kg [3].

After the 2019 revision of the SI, the big Kibble balance remains operative, and research has expanded to table-top-sized Kibble balances. Figure 1 shows one such balance, KIBB-g2. This balance has a load capacity ranging from 500 mg to 20 g. The goal is to measure these masses with relative uncertainties of 1×10^{-5}.

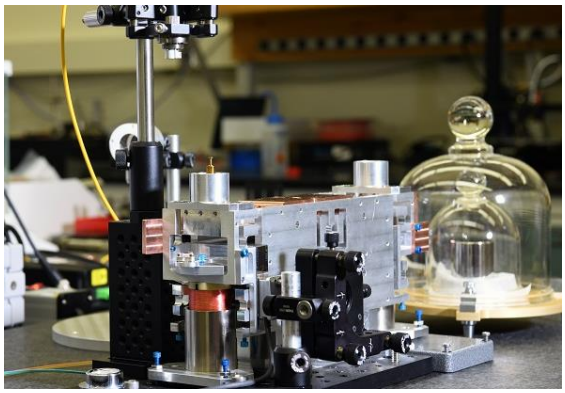

Fig. 1. Photograph of KIBB-g2. A Kibble balance that fits on a table and can be used to measure gram-level masses. Photo credit: Curt Suplee/NIST.

Furthermore, we have started a new project aiming to build a device that can calibrate torque. Our first model can calibrate torques of order 18 mN·m with relative uncertainties of order 10^{-3}.

A xylophone of devices

The big Kibble balance at NIST has shown to be able to measure masses within a factor of 40. If one is willing to incur larger uncertainties, that range can be stretched to about 100 or two decades. Hence, to cover the range from 1 mg to 1 kg, about three Kibble balances are necessary. For the smaller masses, below 30 mg, the magnetic force on a current-carrying coil is too strong and it is better to use the force between two charged capacitor plates. To cover the desired range mentioned above one would need one electrostatic balance and three Kibble balances.

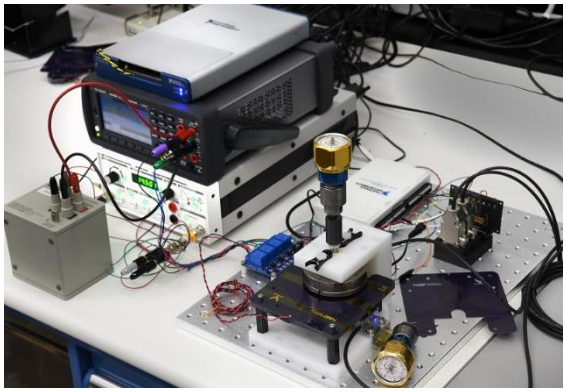

Fig. 1. The electronic NIST torque realizer. A device that calibrates torque watches at torque levels of 1 Nm with relative uncertainties of 10^{-3}. Photo credit: Curt Suplee/NIST.

For the torque project, we have shown the performance on a device that can measure torques ranging from order 1 mN·m to 18 mN·m. The next step is to build devices for larger torque ranges.

Conclusion

The reciprocity in Maxwell's equations that Kibble saw proved to be a powerful principle for high-precision metrology. However, these principles could be useful in mass-produced devices. We have shown table-top instruments that can calibrate mass, force, and torque using Kibble's principle.

References

[1] B.P. Kibble, A measurement of the gyromagnetic ratio of the proton by the strong field method, in Atomic Masses and Fundamental Constants 5th ed, edited by J.H. Sanders and A.H. Wapstra.

[2] D. Haddad et al. Invited Article: A precise instrument to determine the Planck constant, and the future kilogram, Rev. Sci Instrum, 87:061301, 2022, https://doi.org/10.1063/1.4953825.

[3] F. Seifert et al. A macroscopic mass from quantum mechanics in an integrated approach. Communications Physics, 5:321, 2022, http://dx.doi.org/10.1038/s42005-022-01088-7.

DOI 10.5162/SMSI2023C2.1

Measurement Science in Psychology: Prospects for New SI Units

William P. Fisher, Jr.

Could the instruments of psychology and the social sciences be tuned to common scales? How might humanity's relationships with the earth be harmonized for diverse ensembles? Can different tuning systems inform different cultural perspectives? In what ways might people, communities, and nations make beautiful music together, creatively improvise bent and blue notes played out in jazzy, swinging, and rocking social, economic, and political organizations?

L. L. Thurstone was a former electrical engineer turned psychologist who made foundational contributions to measurement theory and practice. In an article published in 1928, Thurstone wrote:

> "One crucial experimental test must be applied to our method of measuring attitudes before it can be accepted as valid. A measuring instrument must not be seriously affected in its measuring function by the object of measurement. To the extent that its measuring function is so affected, the validity of the instrument is impaired or limited. If a yardstick measured differently because of the fact that it was a rug, a picture, or a piece of paper that was being measured, then to that extent the trustworthiness of that yardstick as a measuring device would be impaired. Within the range of objects for which the measuring instrument is intended, its function must be independent of the object of measurement."

And so, Thurstone held that, in psychological measurement:

> "If the scale is to be regarded as valid, the scale values of the statements should not be affected by the opinions of the people who help to construct it. This may turn out to be a severe test in practice, but the scaling method must stand such a test before it can be accepted as being more than a description of the people who construct the scale."

This article has been cited in peer-reviewed research over 3,200 times. Thurstone's description of a principle of substantive unit amounts that add up in a way usefully represented by numbers set the stage for many later developments in psychological and social measurement. Rasch (1960, 1961), in particular, formalized Thurstone's ideas in individual-level models based on a parameter separation theorem, where the observed score is both necessary and sufficient to estimation (Andersen, 1977; Andrich, 1978, 2010; Fischer, 1981).

Rasch's work has formed the basis of recent collaborations of metrologists and psychometricians spelling out the terms of how measurement models, methods, concepts, and unit standards could be unified across the sciences (Cano, et al., 2019; Fisher & Cano, 2023; Mari & Wilson, 2014; Mari, Wilson, & Maul, 2021; Pendrill, 2014, 2019; Pendrill & Fisher, 2015).

Rasch's models for measurement are notable for:

- extending the implicit mathematics of everyday language into explicitly mathematical language in much the same way this was accomplished in the natural sciences;
- having the same mathematical form as many laws of nature, including intriguing implementations of multivalued quantum logic and nonequilibrium evolutionary processes;
- reproducing physical measurements of mass, length, and density from ordinal observations;
- estimating the same quantities as metrological methods when applied to the same data;
- being recognized by metrologists as paradigmatic of measurement;
- integrating explanatory models' theoretical predictions with experimental tests of units defined as retaining their properties across samples and instrument configurations;
- being applied in tens of thousands of published research articles;

- ensuring the defensibility of hundreds of millions of admissions, graduation, licensure, and certification decisions over the last 50 years and more;
- humanizing and personalizing quantitative psychology and social science by relating measurement to the fulfillment of educational, career, and health goals; and
- supporting, perhaps unexpectedly to most, a human, socially progressive, aesthetic, ethical, economical, and environmentally sustainable epistemology of science.

Tuning the instruments of psychology and the social sciences to common scales offers hopeful possibilities for harmonizing relationships in creative ways that do not reduce beauty and meaning to homogenized uniformity but instead open onto new playful improvisations and soulful innovations.

These points will be briefly elaborated in a presentation, and will be supported with referenced sources for those wishing to pursue their own interests in the relevant models and methods.

References

Andersen, E. B. (1977). Sufficient statistics and latent trait models. Psychometrika, 42(1), 69-81.

Andrich, D. (1978, December). A rating formulation for ordered response categories. Psychometrika, 43(4), 561-573.

Andrich, D. (1978). Relationships between the Thurstone and Rasch approaches to item scaling. Applied Psychological Measurement, 2, 449-460.

Andrich, D. (2010). Sufficiency and conditional estimation of person parameters in the polytomous Rasch model. Psychometrika, 75(2), 292-308.

Cano, S., Pendrill, L., Melin, J., & Fisher, W. P., Jr. (2019). Towards consensus measurement standards for patient-centered outcomes. Measurement, 141, 62-69.

Fischer, G. H. (1981, March). On the existence and uniqueness of maximum-likelihood estimates in the Rasch model. Psychometrika, 46(1), 59-77.

Fisher, W. P., Jr., & Cano, S. (Eds.). (2023). Person-centred outcome metrology: Principles and applications for high stakes decision making (G. R. R. Morawski, & others, Ed.). Springer Series in Measurement Science & Technology. Springer. https://link.springer.com/book/9783031074646

Mari, L., & Wilson, M. (2014, May). An introduction to the Rasch measurement approach for metrologists. Measurement, 51, 315-327.

Mari, L., Wilson, M., & Maul, A. (2021). Measurement across the sciences: Developing a shared concept system for measurement (R. Morawski, G. Rossi, & others, Eds.). Springer Series in Measurement Science and Technology. Springer.

Pendrill, L. R. (2014, December). Man as a measurement instrument [Special Feature]. NCSLi Measure: The Journal of Measurement Science, 9(4), 22-33.

Pendrill, L. R. (2019). Quality assured measurement: Unification across social and physical sciences. Springer.

Pendrill, L., & Fisher, W. P., Jr. (2015). Counting and quantification: Comparing psychometric and metrological perspectives on visual perceptions of number. Measurement, 71, 46-55.

Rasch, G. (1960). Probabilistic models for some intelligence and attainment tests ((Reprint, with Foreword and Afterword by B. D. Wright, Chicago: University of Chicago Press, 1980). Danmarks Paedogogiske Institut.

Rasch, G. (1961). On general laws and the meaning of measurement in psychology. In J. Neyman (Ed.), Proceedings of the fourth Berkeley symposium on mathematical statistics and probability: Volume IV: Contributions to biology and problems of medicine (pp. 321-333 [http://www.rasch.org/memo1960.pdf]). University of California Press.

Thurstone, L. L. (1928). Attitudes can be measured. American Journal of Sociology, XXXIII, 529-544. (Rpt. in L. L. Thurstone, (1959). The measurement of values (pp. 215-233). Chicago, Illinois: University of Chicago Press, Midway Reprint Series.)

DOI 10.5162/SMSI2023/C2.2

Development of a conductive MEMS-SPM for nanoelectrical characterisation of nanostructured materials

Zhi Li[1], Christian Kuhlmann[1], Khaled Kaja[2], François Piquemal[2], Karla Hiller[3], S. Hahn[3], Uwe Brand[1]
[1] Physikalisch-Technische Bundesanstalt, Bundesallee 100, 38116 Braunschweig, Germany,
[2] Laboratoire national de métrologie et d'essais, 29 Avenue Roger Hennequin, 78197, Trappes Cedex, France
[3]Fakultät für Elektrotechnik und Informationstechnik, Zentrum für Mikrotechnologien, Technische Universität Chemnitz, 09126, Chemnitz, Germany
Zhi.Li@ptb.de

Summary:
A conductive MEMS based scanning probe microscope (MEMS-SPM) has been developed to measure the mechanical and electrical properties of nanostructured materials including nanopillars and nanowires for energy harvesting devices. The MEMS-SPM features an integrated AFM cantilever gripper, with which various conductive AFM probes can be used as tactile stylus for nano-dimensional, nanomechanical and -electrical measurements. First measurement results will be presented.

Keywords: Microelectromechanical systems, scanning probe microscopy, conductive SPM, nanoelectrical measurement, nanowires energy harvesting devices

Motivation

Energy harvesting from renewable sources like solar, waste heat, and mechanical movement has become a prominent solution to create small amounts of electrical energy in areas of difficult access, and correspondingly energy harvesting devices can help to address the world energy problems. Nanowire (NW) based energy harvesting systems, including photovoltaic solar cells, thermoelectrical, and electromechanical energy nanogenerators have achieved encouraging progress. Meanwhile, the nanometer (nm) dimensions of the wires incorporated in large size of the devices (m^2) raise considerable challenges for testing and characterization. It is worth noting that averaged properties of energy harvesting devices can now be measured, but a quantitative link and correlation between the performance of single NWs and that of the overall device is lacking.
Within the frame of the EMPIR project 19ENG05 NanoWires, a microelectromechanical system (MEMS) based scanning probe microscope (MEMS-SPM) head [1] has been developed, with the aim to characterize the electrical properties of single nanowires with diameters <100 nm.

Principle of the conductive MEMS-SPM

As illustrated in Fig. 1, this innovative conductive MEMS-SPM utilizes integrated electrostatic comb-drives for force and displacement sensing with a force resolution down to nN (10^{-9} Newton) and a depth resolution < 1 nm. A passive AFM cantilever gripper has been integrated, allowing the conductive MEMS-SPM to utilize various commercially available conductive AFM probes for surface topography measurement and local electrical measurements of nanostructured materials.

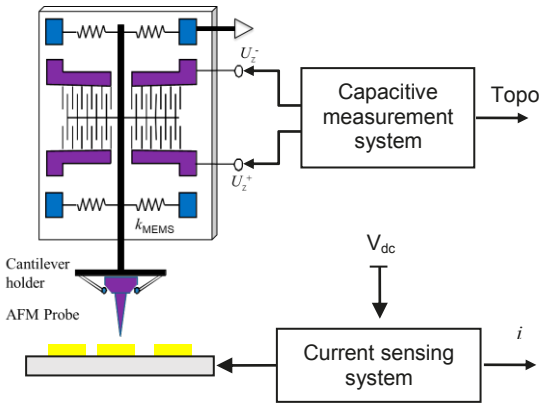

Fig. 1. Schematic of the conductive MEMS-SPM together with the data acquisition systems for nanoelectromechanical measurements.

A home-developed current sensing system with a resolution < 100 pA has been realized to measure the through-tip current with a bandwidth up to 300 Hz.

Results

The conductive MEMS-SPM has been prototyped by means of deep reactive ion etching combined with a silicon-silicon bonding step (B-DRIE) [2]. Silicon micro-structures with an aspect ratio of 25 have been fabricated. Fig. 2 shows the passive cantilever gripper in the MEMS-SPM together with a clamped AFM probe for topography and electrical measurements.

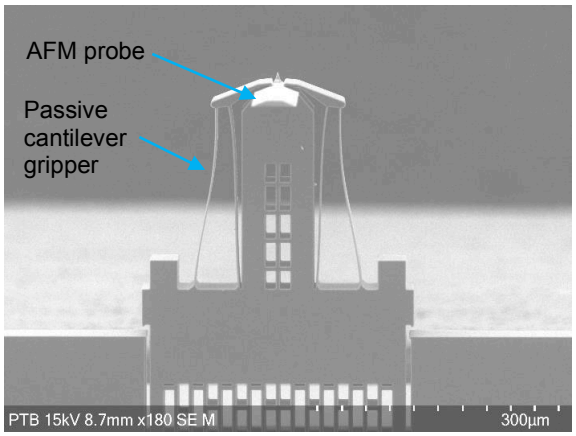

Fig. 2. Detailed view of the cantilever gripper integrated in the MEMS-SPM, in which a CDT-NCHR AFM probe is held as stylus for nanoelectromechanical measurements.

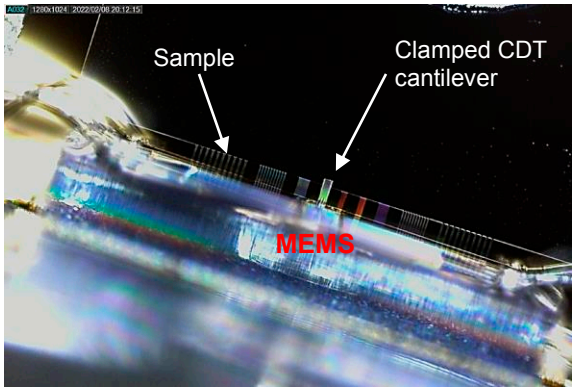

(a) Test sample under measurement

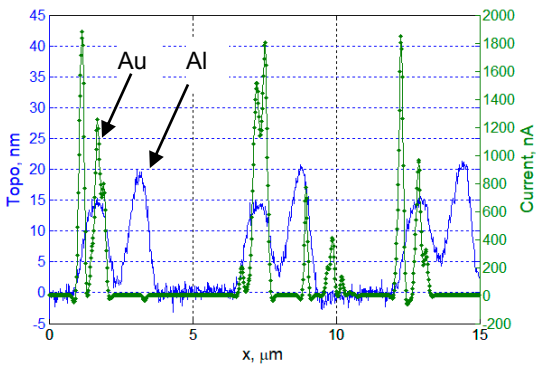

(b) Typical line profile of the test structures

Fig. 3. Topography and electrical measurements of Al and Au line arrays using the conductive MEMS-SPM prototype.

To demonstrate the capability of the MEMS-SPM prototype, a test sample with Al and Au line arrays for KPFM and EFM [3] has been measured, and the current through the Au lines has been acquired. Fig. 3 illustrates one of the typical line profiles of the test structures. It can be seen from Fig. 3 that the topography of the Au and Al lines can be well revealed, and the through-tip current on the Au line can be clearly detected.

Summary and outlook

A conductive MEMS-SPM for nanoelectromechanical characterization of nanostructured materials has been developed. First measurements of test samples indicate that the prototype of this MEMS-SPM is able to simultaneously measure the topography and electrical properties of nanostructures with a lateral resolution better than 50 nm.

The modelling and characterization of the conductive AFM probes for nano-electrical measurements belongs to one of the foci of our future work. The resolution and bandwidth of the through-tip current measurement system will be further improved to enable high-throughput surface measurements. The conductive MEMS-SPM head is also planned to be integrated into a commercial AFM for high-speed areal characterization of nanostructured materials including vertical aligned nanowires used in energy harvesting devices.

This research project is supported by the European Union and is funded within the scope of the European Metrology Programme for Innovation and Research (EMPIR) project 19ENG05 NanoWires entitled ‘High throughput metrology for nanowire energy harvesting devices’ (https://www.ptb.de/empir2020/%20nanowires/home/).

References

[1] Z Li, S. Gao, U. Brand, K. Hiller and H. Wolff, A MEMS nanoindenter with an integrated AFM cantilever gripper for nanomechanical characterization of compliant materials, *Nanotechnology* 31 305502 (2020); doi:10.1088/1361-6528/ab88ed

[2] K. Hiller, M. Kuechler, D. Billep, B. Schroeter, M. Dienel, D. Scheibner, T. Gessner, Bonding and deep RIE—a powerful combination of high aspect ratio sensors and actuators, *Proc. SPIE*, 5715 (2005) 80–91

[3] KPFM & EFM Sample, https://www.budgetsensors.com/KPFM-and-EFM-sample?gclid=Cj0KCQiAgP6PBhDmARIsAPWMq6lqyWZxvZY-MfG13U18VHgoLZAObk7wJtNkQ-VWjMLE2CLtlTFQEVMaAkPwEALw_wcB

DOI 10.5162/SMSI2023/C2.3

Optical Metrology for the Characterization of Fluids Relevant for Hydrogen Storage and Transport

Manuel Kerscher[1], Julius H. Jander[1], Maximilian Piszko[1], Patrick S. Schmidt[1], Thomas M. Koller[1], Michael H. Rausch[1], Peter Wasserscheid[2,3], Andreas P. Fröba[1,]*
[1] Institute of Advanced Optical Technologies – Thermophysical Properties (AOT-TP), Friedrich-Alexander-Universität Erlangen-Nürnberg (FAU), Paul-Gordan-Straße 8, 91052 Erlangen, Germany
[2] Forschungszentrum Jülich GmbH, Helmholtz Institute Erlangen-Nürnberg for Renewable Energy (IEK-11), Cauerstraße 1, 91058 Erlangen, Germany
[3] Institute of Chemical Reaction Engineering (CRT), Friedrich-Alexander-Universität Erlangen-Nürnberg (FAU), Egerlandstraße 3, 91058 Erlangen, Germany
**andreas.p.froeba@fau.de*

Summary:

This contribution demonstrates the application of light scattering and related optical techniques for the characterization of fluids relevant for hydrogen (H_2) storage and transport, with emphasis on the accurate determination of thermophysical properties. Conventional dynamic light scattering (DLS), surface light scattering (SLS), and the shadowgraph method were employed for broad ranges of fluid classes, temperatures, and H_2 pressures. By Raman spectroscopy, approaches for measuring H_2 concentrations in the liquid phase and the hydrogen loading of liquid organic hydrogen carriers (LOHCs) were validated.

Keywords: dynamic light scattering, hydrogen carriers, Raman spectroscopy, shadowgraph method, surface light scattering

Background and Motivation

For establishing a H_2-based energy economy, efficient and safe ways for its storage and transport are required. In the context of chemical H_2 storage, LOHCs are of increasing interest. Here, bi- or tricyclic compounds such as diphenylmethane (DPM, H0-DPM), benzyltoluene, and dibenzyltoluene are discussed. Also methanol is considered as a hydrogen carrier. For corresponding process design and optimization, thermophysical properties at process-relevant conditions including the presence of physically dissolved H_2 are necessary, but only sparsely available. Since the thermophysical properties and, thus, the reaction kinetics depend on the actual composition, knowledge on the liquid composition during the process is of special interest, too. For the large-scale storage of H_2 produced from off-shore wind energy, subsea caverns are currently discussed. Here, e.g., the mutual diffusion coefficient of H_2 in brine at storage conditions is relevant.

Light Scattering Techniques

The experimental determination of thermophysical and especially transport properties over a broad range of thermodynamic states represents a considerable challenge. For this task, optical metrology features the advantage of investigating fluids in a contactless way in or out of equilibrium. The analysis of quasi-elastically scattered light via photon-correlation spectroscopy allows for the simultaneous and accurate determination of several thermophysical properties without the need of calibration. DLS from the bulk of a binary fluid mixture gives simultaneous access to the Fick diffusion coefficient D_{11} and the thermal diffusivity a. Similarly, SLS analyzes the temporal behavior of capillary waves at fluid interfaces. For the studied fluids, the simultaneous determination of the dynamic viscosity η and surface or interfacial tension σ is possible by SLS. Contrary to many conventional methods, both DLS and SLS are applied in macroscopic thermodynamic equilibrium and can be used to study mixtures containing dissolved gases at saturation conditions. The shadowgraph method studies long-range fluctuations in the bulk of the fluid in the presence of a macroscopic temperature gradient and can enable the measurement of various thermophysical properties in one experiment. By Raman spectroscopy, intensity ratios of characteristic lines associated with vibrational modes of the functional groups in the individual scattering molecules can be studied. This allows the contactless optical determination of

the composition of fluid mixtures as well as the detection of changes in the fluid structure.

Results

By DLS, a and D_{11} in binary LOHC mixtures of H_2-lean and H_2-rich species have been studied. In a mixture of H0-DPM with dicyclohexylmethane (H12-DPM), a and D_{11} could be determined simultaneously at temperatures T up to 473 K. Investigations on the same mixture using the shadowgraph method allowed to access a, where good agreement with the values from DLS was found. For quasi-binary dibenzyltoluene/perhydrodibenzyltoluene mixtures, DLS allowed to obtain effective D_{11} values covering four orders of magnitude for T from (264 to 571) K [1].

Furthermore, DLS was successfully applied for the accurate determination of a and D_{11} of various fluids relevant for H_2 storage and transport containing dissolved H_2 at saturation conditions. Here, diffusivities in binary mixtures of H_2 in the LOHC compounds H12-DPM [2] and ortho-perhydrobenzyltoluene, in methanol as well as in water or brine were determined over a broad range of T up to 572 K and H_2 pressures p_{H2} up to 20 MPa. Fig. 1 shows a and D_{11} obtained by DLS for the example of binary mixtures of H12-DPM or methanol containing dissolved H_2 close to infinite dilution of H_2 as a function of T.

With SLS, the influences of LOHC composition and of pressurized H_2 at p_{H2} up to 7 MPa and T up to 573 K on η and σ of several LOHCs was studied [3]. For instance, measurements with DPM-based solvents as well as ortho-perhydrobenzyltoluene in the presence of dissolved H_2 revealed nearly constant η values and a slight decrease of σ by up to –6% with increasing p_{H2} for all solvents, independent of the studied T. Investigations on binary mixtures of methanol with dissolved H_2 at up to 8 MPa and 393 K by SLS showed very similar behaviors of η and σ.

To connect the information on η and σ of methanol in the presence of pressurized H_2 with the actual amount of dissolved H_2, Raman spectra from the liquid phase recorded during SLS experiments were evaluated. For calibration, spectra recorded for methanol with dissolved H_2 in a solubility apparatus with known liquid phase compositions determined from conventional solubility measurements by the isochoric saturation method were used. Here, the transfer of the calibration to the SLS setup for the determination of H_2 concentrations thereon via Raman spectroscopy was successfully demonstrated.

In a similar manner, an approach for the contactless measurement of the hydrogen loading of LOHCs, i.e. the degree of hydrogenation (*DoH*), which represents the share of reversibly bound hydrogen compared to the total uptake capacity of the LOHC, was tested and validated for the DPM-based LOHC system up to 573 K [4]. Using Raman spectra from binary mixtures of H0- and H12-DPM, a T-independent calibration was obtained and successfully applied to determine the *DoH* of partially hydrogenated reaction mixtures containing also cyclohexylphenylmethane (H6-DPM) as well as of pure H6-DPM. For the studied systems and T, the known *DoH* values could be reproduced by Raman spectroscopy with an average absolute deviation of 0.018.

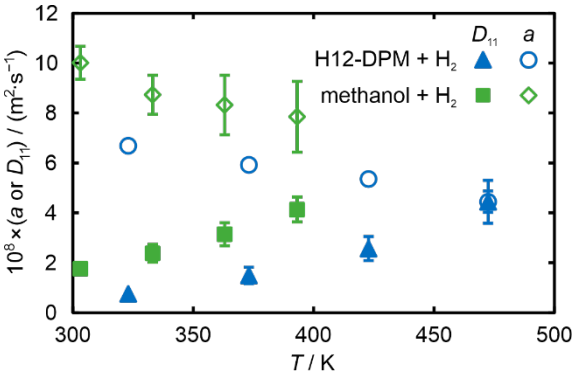

Fig. 1. Thermal diffusivities a and Fick diffusion coefficients D_{11} as a function of temperature T measured by DLS in the saturated liquid phase of binary mixtures of H12-DPM [2] or methanol with dissolved H_2 in the regime of infinite dilution at pressures p of about (3 or 8) MPa, respectively.

References

[1] A. Heller, M. H. Rausch, P. S. Schulz, P. Wasserscheid, A. P. Fröba, Binary Diffusion Coefficients of the Liquid Organic Hydrogen Carrier System Dibenzyltoluene/Perhydrodibenzyltoluene, *J. Chem. Eng. Data* 61, 504-511 (2016); doi: 10.1021/acs.jced.5b00671

[2] F. E. Berger Bioucas, M. Piszko, M. Kerscher, P. Preuster, M. H. Rausch, T. M. Koller, P. Wasserscheid, A. P. Fröba, Thermal Conductivity of Hydrocarbon Liquid Organic Hydrogen Carrier Systems: Measurement and Prediction, *J. Chem. Eng. Data* 65, 5003-5017 (2020); doi: 10.1021/acs.jced.0c00613

[3] M. Kerscher, T. Klein, P. Preuster, P. Wasserscheid, T. M. Koller, M. H. Rausch, A. P. Fröba, Influence of Dissolved Hydrogen on the Viscosity and Interfacial Tension of the Liquid Organic Hydrogen Carrier System Based on Diphenylmethane by Surface Light Scattering and Molecular Dynamics Simulations, *Int. J. Hydrogen Energy* 47, 39163-39178 (2022); doi: 10.1016/j.ijhydene.2022.09.078

[4] J. H. Jander, M. Kerscher, S. Li, M. H. Rausch, P. Wasserscheid, A. P. Fröba, Determination of Hydrogen Loading in the Carrier System Diphenylmethane/Dicyclohexylmethane by Depolarized Raman Spectroscopy, *Int. J. Hydrogen Energy* 47, 9331-9345 (2022); doi: 10.1016/j.ijhydene.2022.01.005

DOI 10.5162/SMSI2023/C2.4

Trust MEtrology – A label to ackowledge good pratices in metrology

Jérôme Lopez, Director of CFM

Sébastien Denaës, Head of Metrology, Equipment and Datascience Service at Colas

Keywords : metrology, label, industry, quality, certification

The CFM (Collège Français de Metrologie) is a french organization gathering more than 700 members from about 450 organizations in industry and in accreditated laboratories, mostly in France and french speaking countries. The CFM was founded in 2002 by three members : LNE, CETIAT (NMI-DI) and the industrial group PSA, now STELLANTIS. The primary mission of CFM is to communicate about good pratices in metrology. In order to address its mission, CFM organizes the CIM (Congrès International de Métrologie), the International Congress of Metrology, technical days, does some co-editing of technical guides with AFNOR the french normalization body, is the animator of a working group (Creative Metrology) to anticipate the needs of industry in metrology and in particular with topics like digitalization.

In 2020, the CFM decided to launch a new initiative dedicated only to industry (and not accreditated laboratories) : a label of good practices in metrology, called « Trust Metrology ». The goal was to answer the following question:

- How a company can bridge the gap between the ISO 9001 and the ISO 17025 ?

The first question is related to the observation that ISO9001 is rather limited about what it says about metrology. The paragraph 7.1.5 (Monitoring and measuring ressources) claims mainly that metrological traceability should be insured. Little is said about the organization of metrology within the company, the processing of measurement datas, nothing about the management of uncertainties. On the other hand, in ISO17025 the accreditation norm, dedicated to calibration and test laboratories, these topics are very detailed and other topics are described extensively like for instance impartiality. Some of them are not very adapted or with a level of exigence that is beyond what an industrial company can address with its field of constraints. This is actually why, many companies, in particular SMEs do not go to accreditation and decide to sub-contract partially or totally their metrology, losing sometimes the knowledge and the internal skills.

Measurements are key in monitoring and mastering the process of manufacturing and production, and metrology is the insurance to manage correctly the measuring process. That is why, a referential for good practices in metrology is needed, with a pragmatic approach, taking into account the economical, ressources and time constraints of an industrial company and in particular SMEs.

ISO1012, the norm for Measurement systems management is under revision since 2021 and should be published not before the end of 2023. We do not see it as a competitive but complementary. In particular, a label may be less constraintful when addressing critical topics like measurement uncertainty management. In addition, the label should not be applied in case of accreditated laboratories and concerns only industrial companies that use metrology to control their products and their processes.

The methodology that was chosen to build this label was first to gather metrology experts within the CFM network, with various backgounds, from industry, from calibration laboratories, and consultants.

This experts committee has then created an analysis grid, with 42 questions in 8 categories : measurement requirements, management/organization, instruments management, methods, metrological traceability, Influencing factors, uncertainties management and measurement datas management.

The process of labellisation is the following : an expert from the expert committee spends one day at the company premices with the metrology manager of the person in charge and evaluates the metrology of the company with the help of the evaluation grid. A system of grades is defined for each question and average grades are calculated for each category. Some minimal grades are mandatory depending on the catagory.

The evaluator reports his evaluation to the experts committee, which makes the final decision. The decision can be one out of three possibilities :

1- The label is given without any conditions
2- Few critical points have been identified and the company shoud address these points and proves that they have done so ; if so, the experts committee validates the labellisation
3- Two many critical points have been identified and the label is not given ; the company should address the critical points and come back later for a new evaluation.

In the three cases, the evaluation identifies improvement axis and the company can implement them in order to improve its measurement process.

Since its launch, a dozen of companies have been evaluted and have of them received the label Trust MEtrology.

We believe that trust is the most important and difficult thing to create with customers and partners and that it can be easily deconstructed. This trust should rely on solid and real things : mainly the trust in products, which relies directly on trust on measurements a company makes on its products.

CFM as a trust partner is here to promote the label Trust MEtrology, in its network. The presentation of the label to an international community, like the one present at SMSI is of great interest.

DOI 10.5162/SMSI2023/C3.1

Evaluation of photoacoustic detectors for methyl bromide sensing

H. Yassine[1], C. Weber[1,2], J. Wöllenstein[1,2], K. Schmitt[1,2]
[1] Department of Microsystems Engineering-IMTEK, Laboratory for Gas Sensors, University of Freiburg, Georges-Köhler-Allee 102, 79110 Freiburg, Germany
[2] Fraunhofer Institute for Physical Measurement Techniques IPM, Georges-Köhler-Allee 301, 79110 Freiburg, Germany
hassan.yassine@imtek.uni-freiburg.de

Summary:
We present a new approach towards measuring methyl bromide (CH_3Br) using a two-chamber photoacoustic sensor with the focus on suitable detector gas fillings. A MIR LED was selected as IR source. The absorbed spectral power in a photoacoustic detector filled with 100 vol.-% methane (CH_4) and the response of this detector to CH_3Br were simulated and compared with the response of a detector filled with 100 vol.-% CH_3Br.

Keywords: two-chamber photoacoustic gas sensor, simulation, methyl bromide, methane

Motivation

Methyl bromide (CH_3Br) is a gas used mainly in Asian countries for fumigation of containers, especially those intended for shipping [1]. This gas is highly toxic and causes harmful diseases to the human nervous system. It is therefore necessary to monitor this gas in containers to avoid fatal accidents that may occur when the container door is opened. Two-chamber photoacoustic sensors have the advantage of high sensitivity and selectivity. This is due to the fact that the detector chamber is filled with 100 vol.-% target gas and the absorption lines of this gas thus act as an IR filter. In other words, the photoacoustic detector is only sensitive to gases that absorb at the absorption lines of detector gas. In this situation, an optical filter is not necessary. A new approach to measure CH_3Br using a two-chamber photoacoustic sensor is presented. Due to the toxicity of CH_3Br we have searched for non-toxic substituent gases that have similar absorption properties in the infrared region as CH_3Br. In this way, a photoacoustic detector filled with substituent gas could be used to indirectly measure CH_3Br.

Infrared absorption of CH_3Br and CH_4

Two-chamber photoacoustic sensors generally consist of an IR source, an absorption cell and a photoacoustic detector chamber hermetically filled with the target gas or, in this case, a substituent gas. A MEMS microphone placed inside this detector cell detects the generated sound wave. In order to find a suitable substituent gas as detector filling gas, it is essential to know the absorption properties of CH_3Br.

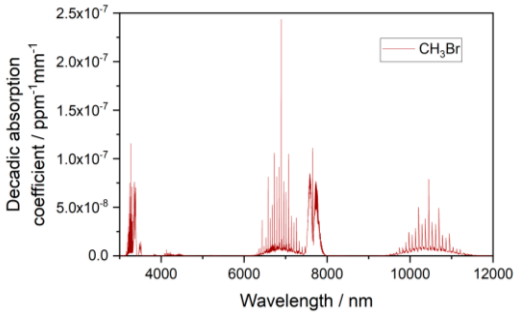

Fig. 1. Decadic absorption coefficient spectrum of CH_3Br from 3000-12000 nm from [2].

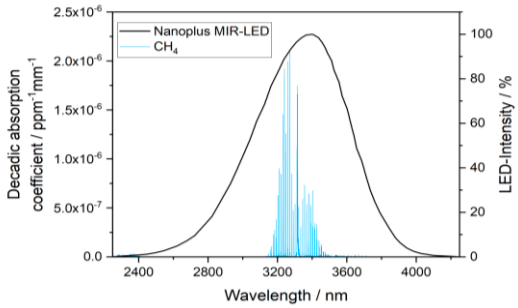

Fig. 2. Decadic absorption coefficient spectrum of CH_4 from 2250-4250 nm from [3] as well as the emission spectra of the MIR-LED from Nanoplus [4].

Fig. 1 shows the decadic absorption coefficient spectrum of CH_3Br between 3000-12000 nm from [2]. CH_3Br absorbs between 3150-3550 nm, 6300-8000 nm and between 9500-11700 nm. For various reasons, it makes most

sense to search for a substituent gas that absorbs between 3150-3550 nm. One reason is that high-power MIR LEDs are available for this wavelength region. In addition, water vapor (H_2O) does not absorb here. Methane (CH_4) could be a possible substituent gas. As can be seen in Fig. 2, CH_4 absorbs strongly at 3300 nm. The 3.4 µm MIR LED from *Nanoplus* was selected as radiation source. The emission spectrum of this LED is shown in Fig. 2.

Absorbed spectral power in the detector and the detector response to CH_3Br

Simulations have been performed to estimate whether or not CH_4 is a suitable substituent gas for CH_3Br. These simulations determine the sensitivity of a detector filled with 100 vol.-% CH_4 gas to different CH_3Br concentrations in the absorption cell at a known optical path length. The simulations were done similarly as in [5]. Fig.3 shows the absorbed spectral power in a detector chamber filled with 100 vol.-% CH_4 at two different gas concentrations in the absorption cell. The optical path length was set to 1.6 m. The results show that the absorbed spectral power in the detector has decreased much more in the wavelength range 3350-3400 nm than in the wavelength range 3200-3300 nm when the CH_3Br concentration was increased from 0 vol.-% to 1 vol.-% CH_3Br in the absorption cell. This is partly because CH_3Br has more overlapping absorption lines with CH_4 in this wavelength range than in the wavelength range 3200-3300 nm and partly because the absorption lines in this wavelength range are stronger here.

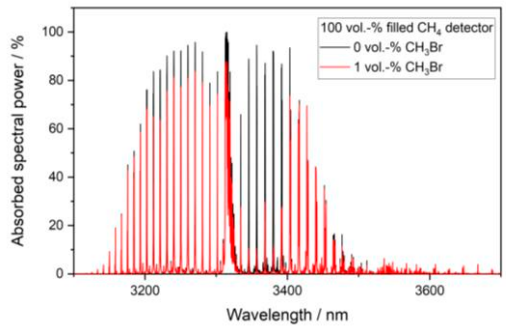

Fig. 3. Absorbed spectral power in a detector filled with 100 vol.-% CH_4 at two different CH_3Br concentrations in the absorption cell (0 vol.-% CH_3Br in black and 1 vol.-% CH_3Br in red). The optical path length was 1.6 m.

Furthermore, simulations concerning the sensitivity of a detector filled with 100 vol.-% CH_4 detector as well as a detector filled with 100 vol.-% CH_3Br to 0-1000 ppm CH_3Br (in 20 ppm steps) at an optical path length of 1.6 m were done. The variation of the signal of both detectors is linear with respect to the variation of the CH_3Br concentration in the absorption cell. The signal of the detector filled with pure CH_3Br drops to ~87.5 %, while the signal of the detector filled with pure CH_4 only to ~94.8 % when there are 1000 ppm CH_3Br in the absorption cell. This result seems reasonable because the highest sensitivity can be achieved with the target gas as detector gas. The results show that there is a possibility to use substituent gases as CH_4 as detector filling gas in order to indirectly measure CH_3Br.

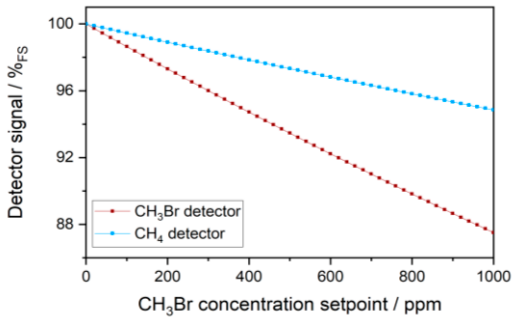

Fig. 1. Simulated variation of the signal of a detector filled with 100 vol.-% CH_3Br and one filled with 100 vol.-% CH_4 with respect to CH_3Br concentration setpoint between 0-1000 ppm.

Conclusion

The sensitivity of a CH_4 and a CH_3Br photoacoustic detector to CH_3Br was simulated. The results have shown that it is possible to replace CH_3Br with CH_4 as the detector filling to measure CH_3Br using the two-chamber photoacoustic principle. However, the signal change of the detector filled with CH_4 is ~ 41% lower than that of the detector filled with CH_3Br (assuming 1000 ppm CH_3Br in the absorption cell). These results look promising and CH_3Br can be measured using a two-chamber photoacoustic sensor without using a detector filled with CH_3Br.

References

[1] R. D. Kaushik, “Chapter 19 - Methyl bromide: Risk assessment, environmental, and health hazard,” in Hazardous Gases, J. Singh et al., Eds. Academic Press, 2021, pp. 239–250.

[2] P. M. Chu et al., “The NIST quantitative infrared database,” J. Res. Natl. Inst. Stand. Technol., vol. 104, no. 1, pp. 59–81, 1999, doi: 10.6028/jres.104.004.

[3] I. E. Gordon et al., “The HITRAN2016 molecular spectroscopic database,” J. Quant. Spectrosc. Radiat. Transf., vol. 203, pp. 3–69, 2017, doi: 10.1016/j.jqsrt.2017.06.038.

[4] Nanoplus, “Mid-Infrared LEDs” MIR LED: 2800 nm-4000 nm. 3.4 µm Datasheet, 2021

[5] C. Weber et al., “ Miniaturisiere photoakustische Detektoren für den Nachweis fluorhaltiger Kältemittel,” pp. 322–327, 2020, doi: 10.5162/sensoren2019/4.2.2.

DOI 10.5162/SMSI2023/C3.2

Using Photoacoustic Wave Interference to Improve the Signal-to-Noise Ratio in Gas Sensors

Gabriel Rodriguez Gutierrez[1], Stefan Palzer[1], Alvaro Ortiz Perez[1]
[1]Professorship for Sensors, Department of Electrical Engineering and Information Technology, TU Dortmund, Dortmund, 44227, Germany
stefan.palzer@tu-dortmund.de

Summary:
Photoacoustic-based gas sensors are particularly suited to detect molecules with strong absorption features in the mid infrared spectral range. Especially indirect photoacoustic setups allow for building miniaturized, low-cost detectors. When using mid-IR LEDs as a light source, their low optical output power results in poor Signal to Noise Ratio (SNR), which is currently a limiting factor in terms of performance. In this contribution we make use of the properties of state-of-the-art MEMS microphones and the potential for modulating arbitrary waveforms in LEDs to demonstrate how the SNR may be improved.

Keywords: noise, interference effects, sensors using photometry, processing of wave sensor data

Introduction

Even though photoacoustic-based gas sensors have been used in a variety of applications for more than 80 years, the potential of the technique in terms of miniaturization and selectivity has not been explored to its full extent. In recent years, academic and commercial efforts in direct and indirect photoacoustic spectroscopy have led to ever smaller and better performing devices.

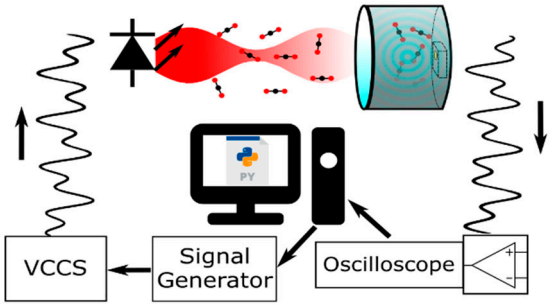

Fig. 1. Schematic diagram of the system used. Arbitrarily generated waveforms are sent as current waveforms to an LED using a Voltage-Controlled Current Source (VCCS). The photoacoustic signal resulting is amplified, then detected by an oscilloscope.

In photoacoustic non-dispersive infrared absorption spectroscopy (NDIR) setups the selectivity is mainly governed by the gas filling, which in turn opens up the possibility to use simpler light sources, e.g. thermal emitters or Light Emitting Diodes (LEDs). However, cross-sensitivities may arise when using thermal emitters as a consequence of overlapping spectral features between gases [1]. Therefore, the use of LEDs as a light source is beneficial, since their spectral range is much more limited. Additionally, current thermal emitters do not allow for modulation frequencies exceeding some tens of Hertz [2].

Currently, the optical output power of LEDs in the mid infrared spectral range is still limited to below 1 mW. Additionally, too high a modulation frequency is not desirable, because the photoacoustic signal strength decays as $1/\omega_{mod}$. Due to these factors, only reducing the noise on the sound transducer signal remains to improve the signal-to-noise ratio (SNR) for a given optical path.

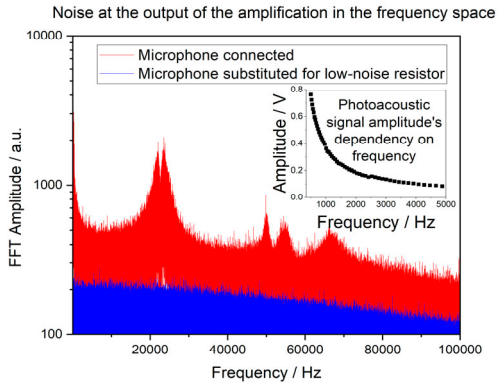

Fig. 2. Noise characterization of the detector and amplification. The dominating noise source is intrinsic to the MEMS microphone, especially at the low (<1kHz) frequencies that are used for photoacoustics because of the 1/f decaying signal amplitude. The resonant peaks of this microphone while surrounded by a CO_2 atmosphere can be observed.

In the past, quartz tuning forks have been used in indirect photoacoustic setups but their resonance frequencies are usually in the kHz range,

which offsets the advantage of their resonance due to the decaying photoacoustic amplitude. Alternatively, commercially available MEMS microphones feature a near constant sensitivity in the audible acoustic spectrum. In the past, this microphone type has been utilized to gauge the photoacoustic wave but so far, no use has been made of the capabilities of those sensors in terms of detecting various acoustic frequencies simultaneously.

System Design

The basic setup used is depicted in Figure 1 and consists of a simple, indirect photoacoustic setup with the aim to study methods to reduce the noise of the photoacoustic signal.

This system uses a mid-infrared LED from Hamamatsu Photonics with a central emission wavelength of 4.2 µm and a spectral width of ~1 µm. The photoacoustic detector is a hermetically sealed cell filled with 100% CO_2, a sapphire window for optical access, and an ICS-40720 MEMS microphone from InvenSense as sound transducer. The photoacoustic signal's amplitude is small enough to require the use of a low-noise, multi-stage, wideband amplification.

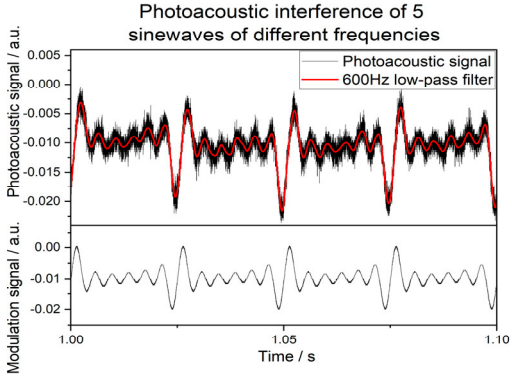

Fig. 3. Interference of 5 different sinewaves in the photoacoustic cell (above), and original modulation signal (below). Even for high numbers of interfering signals the rough shape of the current signal is preserved, with a growing degree of distortion at higher numbers of different frequencies.

Results

The amplifier circuit has been characterized to prove that most of the noise comes from the microphone, which is the limiting factor in the electronic circuit in terms of SNR. The results of this noise characterization can be observed on Figure 2, as well as the dependency of the photoacoustic signal with the modulation frequency.

Afterwards, it has been established that interference of different frequencies can take place inside the photoacoustic cell, by adding several sinewaves together at the generation of the waveform in the arbitrary signal generator. The results can be found on Figure 3.

Finally, whether or not interfering signals can increase the SNR has been studied using square-wave waveforms, which upon interference don't generate high peaks of current that could damage the light source. First a modulation frequency of 80Hz has been chosen, as it roughly maximizes the SNR for this particular microphone and configuration. A sine wave and a square wave of 100mA peak to peak and 80Hz frequency have been compared. Fourier analysis has been carried out for both waveforms as shown in Figure 4, and it has been established that a minimum 14% increase in SNR without increasing power consumption is possible for the used system.

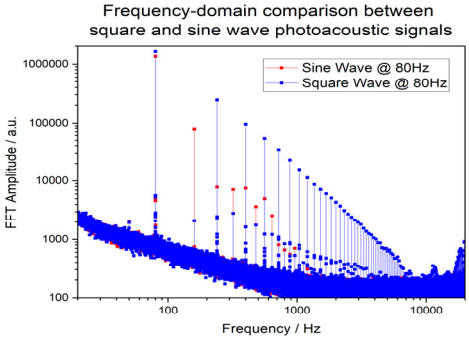

Fig. 4. Photoacoustic frequency spectrum for a sine and a square wave. The harmonics of the sinewave are due to distortion in the photoacoustic cell at low frequencies. The difference in amplitude between the harmonics of both waveforms is noticeable.

Conclusions

The combined use of LED as light source and MEMS microphones as sound transducer offers unique possibilities to improve the performance of low-cost, miniaturized NDIR-type photoacoustic gas sensors. Taking into account higher harmonics resulting from square wave form modulation, the SNR may be improved. The use of interference effects in photoacoustic detector has been explored here and has the potential for further improvements.

References

[1] Knobelspies, Stefan; Bierer, Benedikt; Ortiz Perez, Alvaro; Wöllenstein, Jürgen; Kneer, Janosch; Palzer, Stefan (2016): Low-cost gas sensing system for the reliable and precise measurement of methane, carbon dioxide and hydrogen sulfide in natural gas and biomethane. In: Sensors and Actuators B: Chemical 236, S. 885–892. DOI: 10.1016/j.snb.2016.03.022.

[2] Walden, Paul; Kneer, Janosch; Knobelspies, Stefan; Kronast, Wolfgang; Mescheder, Ulrich; Palzer, Stefan (2015): Micromachined Hotplate Platform for the Investigation of Ink-Jet Printed, Functionalized Metal Oxide Nanoparticles. In: *J. Microelectromech. Syst.* 24 (5), S. 1384–1390. DOI: 10.1109/JMEMS.2015.2399696.

DOI 10.5162/SMSI2023/C3.3

Photoacoustic Sensor for isotopologic analysis of highly concentrated methane

Marc-Simon Bahr[1,2] and Marcus Wolff[1]
[1] Hamburg University of Applied Sciences, Heinrich Blasius Institute of Physical Technologies, Berliner Tor 21, 20099 Hamburg, Germany
[2] University of the West of Scotland, High Street, PA1 2BE Paisley, United Kingdom
marc-simon.bahr@haw-hamburg.de

Summary:
Photoacoustic spectroscopy (PAS) is typically used for the detection of trace gases. However, there are a number of applications where highly concentrated mixtures need to be analyzed. In some cases especially the isotopologic composition of certain hydrocarbons needs to be determined. We present PAS-based isotopologic analyses of two digit percentage-level methane concentrations in nitrogen and its AI-based evaluation. The investigation allows conclusions to be drawn about the extent to which PAS is suitable for an isotopologic analysis of undiluted natural gas-like mixtures.

Keywords: photoacoustic spectroscopy, $^{12}CH_4$, $^{13}CH_4$, interband cascade laser, natural gas

Introduction

The impact of methane emissions on the climate change is up to 34 times higher in comparison to CO_2, due to its global warming potential [1]. Based on that fact, it is of outmost importance to detect methane, its concentrations and emission sources. Methane exhibits a source dependent individual isotopologic “signature” which depends on the $^{13}CH_4$ and $^{12}CH_4$ shares as quantified by the following equation:

$$\delta^{13}C = \left(\frac{R_{sample}}{R_{std}} - 1\right) \cdot 1000‰, \quad (1)$$

where R_{sample} is the $^{13}CH_4/^{12}CH_4$ ratio of the sample and $R_{std} = 0.0112372$. The $\delta^{13}C$ value of anthropogenic methane sources tend to be slightly higher in comparison to biogenic sources which helps to identify them and, thus, reduce their contribution to climate change [2]. Furthermore, the short-chained hydrocarbon composition of natural gas is decisive for its numerous industrial applications. The energy content of the natural gas is strongly dependent on the hydrocarbon shares and must be compensated in production processes by parameter adjusting [3]. In addition, the $\delta^{13}C$ value can be used to evaluate and optimize the natural gas conveyor technique [4].

A well-known and precise method for the analysis of gas mixtures is gas chromatography in combination with isotope-ratio mass spectrometry (IRMS) [5]. PAS is a very established method for detection of methane isotopologues in the single-digit per mill range, down to the parts per million (ppm) range [6].

In the following, we present to the best of our knowledge the first time PAS-based measurement of $^{13}CH_4$ and $^{12}CH_4$ isotopologue mixtures in the percentage range. Finally, the measurement results are then evaluated using cross-validation in conjunction with Partial Least Squares Regression (PLSR).

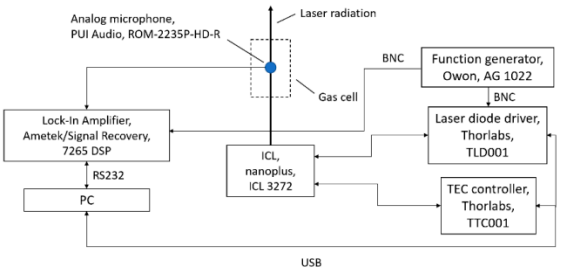

Fig. 1. Experimental setup.

Methods and Material

The measurement setup is schematically shown in Figure 1. The interband cascade laser ICL 3272 used in this investigation was manufactured by nanoplus GmbH (Gerbrunn, Germany) and exhibits a center wavelength of 3323 nm with a spectral linewidth below 20 MHz. The used measurement cell is designed according to the established H geometry featuring a longitudinal resonance around 3 kHz. The resulting measurement signal is detected by the analog microphone ROM-2235P-HD-R from PUI Audio (Fairborn, OH/United States). The Ametek / Signal Recovery lock-in amplifier DSP LIA (Berwyn, IL/United States) performs the 1*f* amplitude detection of the microphone signal. The measurement setup including the PLSR algorithm is

controlled using a MATLAB script on a PC. The gas mixtures in the gas cell are generated using the 6 Channel Gas mixer from QCAL (Munich, Germany), which is controlled by a PC.

The measurement were done for three different $^{12}CH_4$ concentration: 25%, 50% and 70% combined with three different $^{13}CH_4$ shares, as displayed in the Tab. 1. The residual gas to 100% was always N_2.

Tab. 1: $^{12}CH_4$ and $^{13}CH_4$ concentrations of the nine investigated mixtures (rest: N_2).

$^{12}CH_4$	$^{13}CH_4$
25%	0.28%, 0.75% and 1.25%
50%	0.56%, 1.75% and 2.25%
75%	0.78%, 2.25% and 3.00%

Results

Figure 2 shows exemplarily the recorded photoacoustic spectra, i.e. the PA signal as function of the average laser current for 50% $^{12}CH_4$ share. All measurements were taken at a sample temperature of 26°C and a pressure of 1016 hPa.

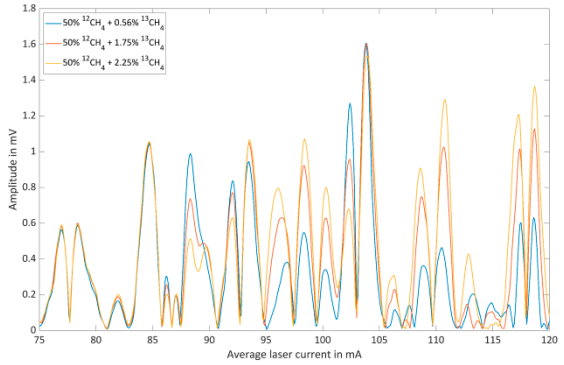

Fig. 2. Photoacoustic signal as function of the average laser current for 50% $^{12}CH_4$ with three different $^{13}CH_4$ shares in nitrogen.

Due to the complexity of the collected spectra a quantitative multivariate approach is implemented to validate the methane isotopologue mixtures and to test the suitability of the method. Figure 3 shows the true and the predicted methane isotopologue concentrations, after leave-one-out cross-validation based on PLSR was applied to all nine investigated mixtures. The mixture numbers in Fig. 3 corresponds to the order given in Tab. 1.

The absolute root-mean-square-errors for the predicted $^{12}CH_4$ and $^{13}CH_4$ concentrations were calculated to 3.08% and 0.29%, respectively.

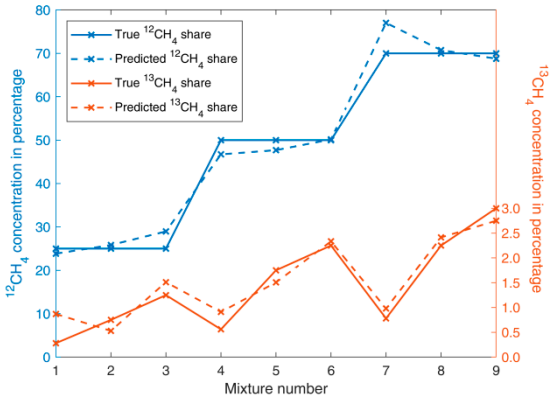

Fig. 3. Evaluation of the investigated methane isotopologue mixtures by leave-one-out cross-validation based on PLSR.

Conclusion

In conclusion, the evaluation in Fig. 3 in conjunction with the calculated errors prove to a satisfactory extent that PAS is a suitable method for the isotopologic analysis of highly concentrated methane. Adding more measurements to the training data set of the PLSR algorithm would improve the accuracy of the predictions. The presented results make it appear possible to analyze undiluted natural gas samples.

References

[1] M. Z. Jacobson, *100% clean, renewable energy and storage for everything*. Cambridge: Cambridge University Press, 2021.

[2] M. Schroll, F. Keppler, M. Greule, C. Eckhardt, H. Zorn, and K. Lenhart, “The stable carbon isotope signature of methane produced by saprotrophic fungi,” *Biogeosciences*, vol. 17, no. 14, pp. 3891–3901, 2020, doi: 10.5194/bg-17-3891-2020.

[3] J. Leicher, A. Giese, K. Görner, M. Werschy, H. Krause, and H. Dörr, “Natural gas quality fluctuations – surveys and statistics on the situation in Germany,” *Energy Procedia*, vol. 120, pp. 165–172, 2017, doi: 10.1016/j.egypro.2017.07.161.

[4] T. Zhang and B. M. Krooss, “Experimental investigation on the carbon isotope fractionation of methane during gas migration by diffusion through sedimentary rocks at elevated temperature and pressure,” *Geochimica et Cosmochimica Acta*, vol. 65, no. 16, pp. 2723–2742, 2001, doi: 10.1016/S0016-7037(01)00601-9.

[5] A. L. Sessions, “Isotope-ratio detection for gas chromatography,” *Journal of separation science*, vol. 29, no. 12, pp. 1946–1961, 2006, doi: 10.1002/jssc.200600002.

[6] A. Loh and M. Wolff, “Photoacoustic Detection of Short-Chained Hydrocarbon Isotopologues,” in *7th International Symposium on Sensor Science*, p. 23.

DOI 10.5162/SMSI2023/C3.4

Everything at once—Linearizing System Response and Enhancing Sensitivity in Photoacoustic Gas Sensors by Demodulation and Filter Tuning

Simon Essing[1], Gabriele Schrag[1], David Tumpold[2], Guillaume Dumas[2], Andrey Kravchenko[3], Mohammadamir Ghaderi[2]
[1]Chair of Physics of Electrotechnology, Technical University of Munich, Germany,
[2]Infineon Technologies AG, Neubiberg, Germany,
[3]Infineon Technologies Dresden GmbH, Dresden, Germany
simon.essing@tum.de

Summary:
We present a sophisticated method to improve the sensitivity of CO_2-detecting non-resonant MEMS-based photoacoustic gas spectroscopy systems by more than 50 % compared to state-of-the-art approaches. The method based on signal demodulation can also be used to linearize the measured system's response in order to reduce the calibration effort for future sensors. Tuning the filter transmission spectra accordingly is utilized to further increase the linearity of the system response and enhancing the sensitivity by more than 200 %.

Keywords: algorithms, demodulation, linearization, photoacoustic spectroscopy, sensitivity

Background and State of the Art

Non-resonant miniaturized photoacoustic gas sensors (PAS) comprise a light source that often consists of a MEMS infrared emitter and an optical filter, a pressure chamber and a MEMS microphone[1]. Infrared Radiation is emitted and filtered in a way that the photons entering the pressure chamber match the wavelength needed to excite the gas molecules of interest. The excited molecules transfer the absorbed energy into an acoustical signal, which is detected by the microphone. State of the art systems currently used for CO_2 detection are prone to being cross sensitive to humidity [2, 3]. One major goal in sensor development is hence to provide maximum sensitivity to CO_2 while, at the same time, preserving robustness against changing environmental conditions such as humidity. A common signal analysis approach in this respect is to bandpass the microphone signal at the excitation frequency and calculate the root mean square (RMS) for every acoustical pulse, which is a measure for the gas concentration inside the pressure chamber and hence, the sensor's sensitivity [1, 4]. Our approach addresses the increase of this sensitivity w.r.t to the state of the art.

Description of the New Method or System

In an environment enriched with the target gas, the measured signal of the PAS is assumed to be a superposition of a CO_2- and a background-signal. The Microphone detects the transient pressure signal inside the chamber which is dominated by the excitation frequency of the emitter, see Fig. 1. Band-passing the signal at the excitation frequency suppresses interfering signal components leaving only the relevant signal content, see Fig. 2.

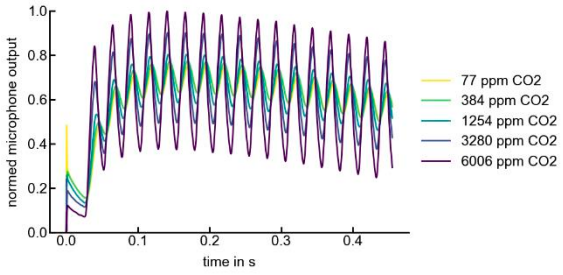

Fig. 1 Exemplary normed raw microphone output for various CO_2 concentration values.

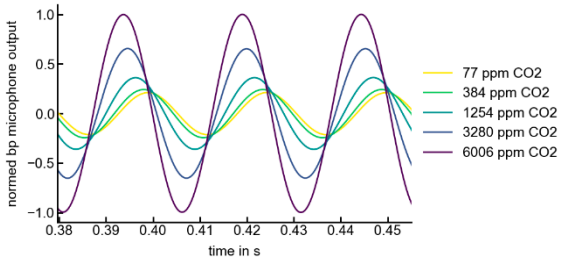

Fig. 2 Exemplary normed and band-passed microphone output showing the influence of increasing CO_2 concentrations on the overall phase and amplitude of the signal.

The basic idea behind the method is to demodulate the band-passed microphone signal into in-

phase and quadrature components w.r.t to a specifically chosen phase angle, tailored to maximize the signal amplitude of the respective gas to be measured. Choosing a phase angle, which maximizes the signal of the CO_2 phase distinctly increases the sensor sensitivity compared to the pure RMS approach. The same can be done for any other target gas by adapting the phase to maximize this response. Additionally, by demodulating the signal w.r.t. the appropriate phase, the contribution of the CO_2 to the total signal becomes more pronounced and is also linearized for lower concentrations, as can be seen in Fig. ***3***.

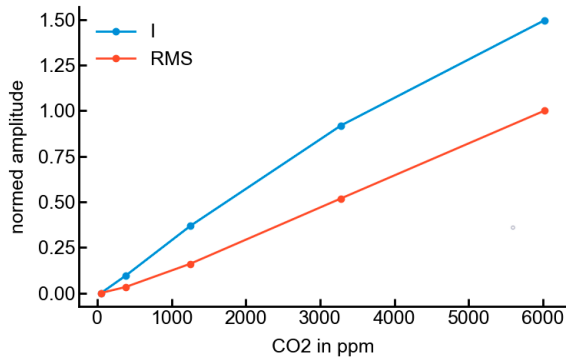

Fig. 3: Sensitivity gain of the "co2" filter to CO_2 by demodulating the microphone signal with a phase maximizing the CO_2 signal (signal "I") compared to using the root mean square analysis of the microphone output (signal "RMS"). The amplitude, and thus, the sensitivity is increased by more than 50 %.

Experimental Results and Conclusion

Applying the described demodulation approach to measurements of our PAS system, a sensitivity increase of the amplitude of around 55% for CO_2 detection is achieved, while, at the same time, we attain linearization of the system response, especially for low concentrations. Additionally, the filter is designed in such a way that the system response to CO_2 is further increased compared to a typical CO_2 filter, see Fig. 4.

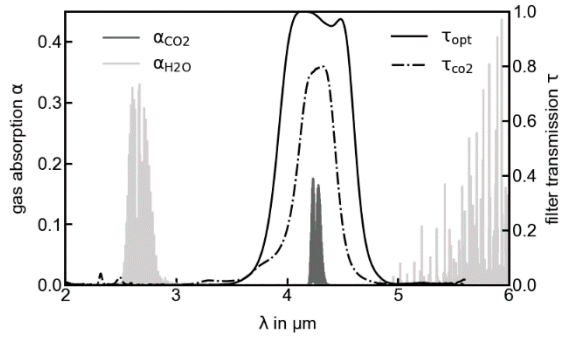

Fig. 4: Measured transmission spectra of optimized Bragg filters and the gas absorption spectra of water vapor and carbon dioxide. By expanding the transmission band for CO_2 an additional linear sensitivity of the demodulated sensor signal can be obtained, by still maintaining sufficient suppression of water bands to address cross sensitivity to relative humidity.

Fig. 4 shows the transmission spectra of a typical CO_2 Filter ("co2") and the optimized filter ("opt"), increasing the absorption band relevant for CO_2 significantly. The depicted gas absorption spectra for H_2O and CO_2 are simulated by means of Lambert-Beer's law for typical sensor dimensions under representative conditions (p = 1013 hPa, T = 295 K, RH = 60%, c_{CO2} = 420ppm).

Hence, optimizing the optical filter increases the system response of the demodulated signals further by another 200% for the detection of CO_2, see Fig. 5).

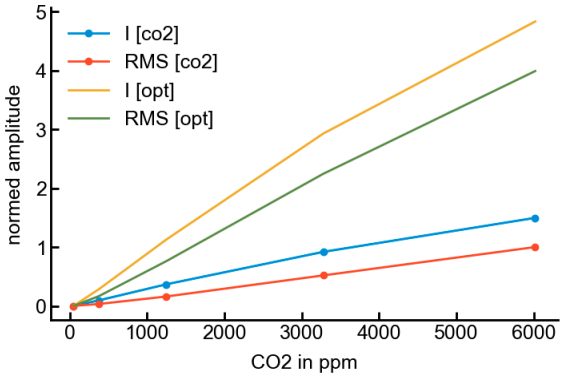

Fig. 5: Sensitivity gain of the optimized filter [opt] to CO_2 compared to the [co2] design by demodulating the microphone signal with a gain maximizing phase (signal I) compared to using a root mean square of the microphone signal (signal RMS). Optimization of the filter leads to a further increase in sensitivity by more than 200 %.

References

[1] S. Essing, G. Schrag, D. Tumpold, C. Glacer, M. Mihotek, and A. Kravchenko, "Towards predictive system-level modelling of miniaturized photoacoustic gas sensors," in *2022 23rd International Conference on Thermal, Mechanical and Multi-Physics Simulation and Experiments in Microelectronics and Microsystems (EuroSimE)*, St Julian, Malta, 4252022, pp. 1–5.

[2] S. Palzer, "Photoacoustic-Based Gas Sensing: A Review," *Sensors (Basel, Switzerland)*, vol. 20, no. 9, 2020, doi: 10.3390/s20092745.

[3] S. Knobelspies, B. Bierer, A. Ortiz Perez, J. Wöllenstein, J. Kneer, and S. Palzer, "Low-cost gas sensing system for the reliable and precise measurement of methane, carbon dioxide and hydrogen sulfide in natural gas and biomethane," *Sensors and Actuators B: Chemical*, vol. 236, pp. 885–892, 2016, doi: 10.1016/j.snb.2016.03.022.

[4] S. Gassner *et al.*, "Anodically Bonded Photoacoustic Transducer: An Approach towards Wafer-Level Optical Gas Sensors," *Sensors (Basel, Switzerland)*, vol. 22, no. 2, 2022, doi: 10.3390/s22020685.

DOI 10.5162/SMSI2023/C4.1

Electroacoustic Ice Detection Using Surface Acoustic Wave Devices

Philipp Schulmeyer[1], *Hagen Schmidt*[1]
[1] *Leibniz-Institut für Festkörper- und Werkstoffforschung, Helmholtzstr. 20, 01069 Dresden,*
p.schulmeyer@ifw-dresden.de

Summary:
Icing of infrastructure or vehicles can lead to structural failure due to increased loads. In particular aerodynamic structures like wind turbine rotor blades demand for a small, thin, retrofittable and wirelessly working ice detection sensor. This paper shows that surface acoustic wave (SAW) devices, made from piezoelectric single crystals 64° YX- and 128° YX-lithium niobate, allow to directly detect ice loaded surfaces by analysing the acoustic- and capacitive-dominated admittance behaviour of an ice-loaded interdigital transducer.

Keywords: surface acoustic wave sensor, ice detection, lithium niobate, admittance, interdigital transducer

Introduction

Surface acoustic waves (SAW) allow the development of small, lightweight and retrofittable SAW sensors which, as passive components, can be operated and interrogated by radio signal via antennas. A remotely installed interrogation unit transmits an electromagnetic signal, which is received by the sensor's antenna and converted into an acoustic wave in the interdigital transducer (IDT) via interdigitated comb electrodes. This conversion is based on the converse piezoelectric effect. The acoustic wave is reflected or sent back to the interrogation unit as an electromagnetic wave. The analysis of the output and input signal thus allows a statement about ambient conditions like surface loads. While [1] and [2] show the ability to determine liquid wetting and phase transitions from water to ice of a loaded delay line (DL), by changing propagation characteristics of the acoustic wave, this paper focuses on changes in admittance due to a water loaded IDT. A related approach considering water toxicity sensing is shown in [3].

Materials

The SAW devices considered are two-port delay lines (DL) made of piezoelectric substrates 128° YX- and 64° YX-lithium niobate ($LiNbO_3$) respectively with a thickness of 500 µm. In the following, these will be abbreviated as 128LN and 64LN. The IDT's aluminium metallisation and the passivation layer of silicon dioxide (SiO_2) have a thickness of 300 nm and 500 nm. Input and output transducers each consist of 31 finger pairs with a finger width of 30 µm. The aperture is 2 mm and the delay line has a length of 10 mm (see Fig. 1). All measurements are carried out in a temperature test chamber (Voetsch VT4002).

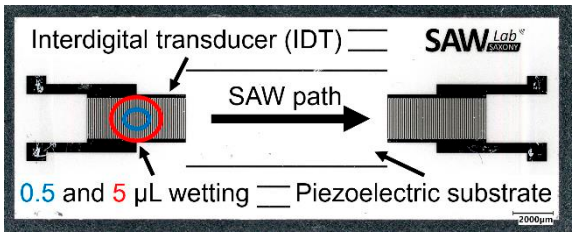

Fig. 1: SAW two-port delay line

The SAW device to be measured is located on a carrier and is connected to a vector network analyser (Agilent E5070B, short: VNA) with two spring contacts per IDT via a printed circuit board matched to 50 Ohm characteristic impedance and SMA connection. The IDT's admittance Y_{11} over frequency is calculated from S-parameters retrieved by VNA.

Measurements

First, the devices are measured at room temperature (20 °C) in dry condition. Then drops of water are placed in the centre of one IDT in 0.5 µL steps using a pipette. Slight deviations of volume due to evaporation are neglected because of a short measuring time. The maximum drop volume for this measurement is 5 µL. Subsequently, these measurements are repeated at -20 °C in the temperature test chamber.

Results

Surface loading on the IDT shows a significant influence on the admittance behaviour for 128LN and 64LN devices. Figures 2 and 3 describe the

normalised conductance and susceptance over frequency. Each curve can be zoned in an acoustically ($0.95 < f/f_s < 1.05$) and capacitively ($0.95 > f/f_s > 1.05$) dominated frequency range (f_s: synchronous frequency, where acoustic wavelength and transducer period match for maximal SAW excitation).

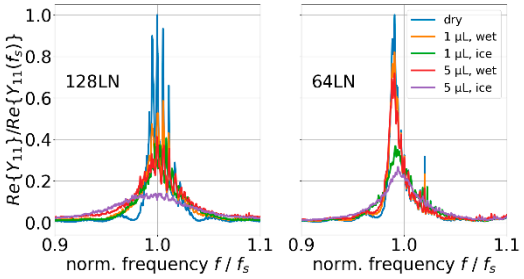

Fig. 2: Normalized conductance over frequency for 128LN (left) and 64LN (right)

IDT loading by liquid and frozen water on 128LN leads to a high decrease in conductance with a further decrease by increasing drop volume (see Fig. 2, left). 64LN device shows a significantly lower decrease in wet state but a higher decrease in conductance for frozen water. An increasing drop volume slightly decreases conductance (see Fig. 2, right). This behaviour can be explained by the different polarisation of the SAWs propagating in 128LN and 64LN. 128 LN's Rayleigh waves with a dominant surface-normal amplitude radiate bulk acoustic waves into the drop and get damped. 64LN's shear-horizontal polarised SAW does not couple at the substrate-fluid-interface due to water's low viscosity but gets damped by increasing viscosity due to freezing.

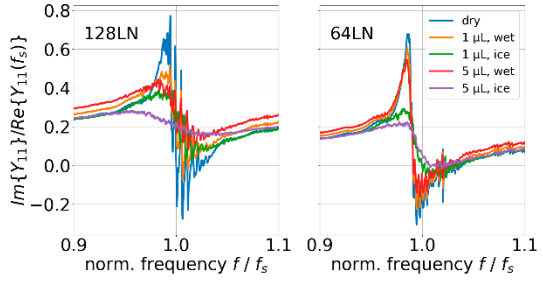

Fig. 3: Normalized susceptance over frequency for 128LN (left) and 64LN (right)

The 128LN device shows a higher susceptance compared to the 64LN device and a more significant capacitive influence in the wet state. In both cases the susceptance increases with frequency (see Fig. 3). The difference in susceptance despite of identical IDTs is caused by 128LN's higher effective dielectric constant ε_{eff}. The more significant capacitive influence in wet state and the linear increase of susceptance with frequency can be explained by the dependence to frequency and the IDT's static transducer capacitance. The susceptance increases with an increase in total effective dielectric constant of the load and frequency.

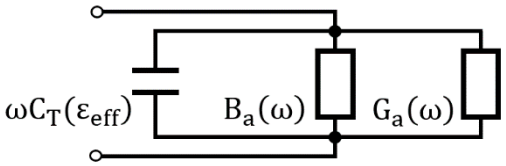

Fig. 4: Equivalent circuit regarding crossed-field model

These relations are described by the crossed-field model [4] which applies due to a parallel order of wave vector and substrate's crystallographic rotation axis [5]. The equations for conductance (1) and susceptance (2) can be derived by using an equivalent circuit (see Fig. 4):

$$G = Re\{Y\} = G_a(\omega) \quad (1)$$

$$B = Im\{Y\} = B_a(\omega) + \omega C_T(\varepsilon_{eff}) \quad (2)$$

with $\omega = 2\pi f$ and the static transducer capacity $C_T(\varepsilon_{eff})$ as well as acoustic-related G_a and B_a.

Conclusion

Both, 128LN and 64LN, devices show capabilities to gain information about a water drop's phase by analysing the loaded IDT's admittance. In the acoustically dominant region 64LN's admittance behaviour allows a differentiation between liquid and frozen water drops in the measuring range. In the frequency range where the capacitive behaviour dominates 128LN's admittance allows for the same differentiation.

References

[1] N.J. Vellekoop, et al., A Love-wave ice detector, *IEEE Ultrasonics Symposium Proc.* 1, 453-456 (1999); doi: 10.1109/ULTSYM.1999.849438

[2] W. Wang, et al., Development of a Love Wave Based Device for Sensing Icing Process with Fast Response, *J. Electr. Eng. & Techn.* 15, 1245-1254 (2020), doi: 10.1007/s42835-020-00411-y

[3] J. Furniss, et al., Love mode surface acoustic wave and impedance sensors for water toxicity sensing, *Environm. Progress & Sustainable Energy* 37, 172-179 (2017); doi: 10.1002/ep.12715

[4] W. R. Smith, et al., Analysis of Interdigital Surface Wave Transducers by Use of an Equivalent Circuit Model, *IEEE Transactions on Microwave Theory and Techniques* 17, no. 11, 856-864 (1969); doi: 10.1109/TMTT.1969.1127075.

[5] G. Martin, et al., Properties of interdigital transducers in relation to the substrate crystal symmetry, *IEEE Transactions on Ultrasonics, Ferroelectrics, and Frequency Control* 43, no. 4, 646-653 (1996); doi: 10.1109/58.503726.

DOI 10.5162/SMSI2023/C4.2

Application of Ultrasonic Shear Wave Measurements for the Assessment of Surface Hydrophobicity and Drying Dynamics of Aqueous Droplets

Ioanna Bampouri[1], *Vitaly Buckin*[1]
[1] *School of Chemistry, University College Dublin, Belfield, Dublin 04, Ireland,*
Corresponding Author's e-mail address: ioanna.bampouri@ucdconnect.ie

Summary:
The paper describes the application of ultrasonic shear wave measurements for the assessment of hydrophobicity of various surfaces and real-time non-destructive monitoring of the process of aqueous droplet evaporation. This research focuses on the quantification of surface hydrophobicity expressed through aqueous droplet contact angle and the study of the kinetics of droplet evaporation including evaporation modes (pinned and unpinned) and the characterization of watermarks left after drying.

Keywords: Surface Hydrophobicity, Contact Angle, Shear Wave Ultrasonic Spectroscopy, Admittance Analysis, Drop Shape Analysis

Background, Motivation and Objective

Wettability and droplet evaporation plays an important role in nature, daily life, and many technological applications, manufacturing engineering, chemical and medical products. Understanding the interaction and wetting dynamic of droplets with various surfaces, and the complex mechanisms of drying processes is essential [1, 2]. Moreover, the formation of drying defects and watermarks (WM), after the wet cleaning procedures in the semiconductor industry, has been identified as a serious problem [3]. Quantification of these phenomena and correlation of surface properties (i.e., roughness) and drying defects (i.e., watermarks) will provide in-depth information on the quality of the materials and cleaning liquids. This requires efficient real-time, non-destructive techniques for precision monitoring of the droplet drying process.

The current paper describes the application of shear wave ultrasonic spectroscopy for studies of aqueous droplet shape and dynamics of drying on surfaces with different hydrophobicity. This spectroscopy includes the principles usually described as Quartz Crystal Microbalance (QCM) technique [4, 5]; however, with add-on multifrequency and energy loss analysis.

Description of the Method

The shear wave spectroscopy probes the 'bottom' part of the droplet, which is in contact with the surface studied. A generated shear wave propagates through the material into the liquid and attenuates in a very thin layer of liquid that resides on top of the surface, thus providing information on the surface area and the properties of the system (surface and thin layer of liquid attached). The effective thickness of the probed liquid layer can be changed from the micron to nanometer range by changing the frequency of the wave. This allows for quantitative assessment of surface hydrophobicity and real-time characterization of different amounts of liquid positioned on the surface during the drying process, distinguishing the pinned and unpinned modes of evaporation (see Fig. 1).

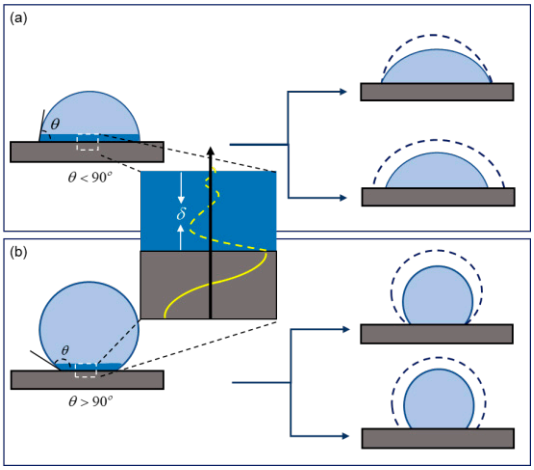

Fig. 1. Schematic illustration of the measuring principles of sessile droplets on surfaces showing the decay length (δ) and the two modes of evaporation (pinned and unpinned contact line) on; (a) hydrophilic, and (b) hydrophobic surfaces. The grey rectangle represents the piezoelectric sensor covered by the surface studied. Measurements of complex admittance produce the crystal resonance frequencies and energy losses characterized by the crystal Q factor.

Analysis of size and shape characterization of impurity depositions (i.e., 'water marks') formed, possible slip phenomena for hydrophobic surfaces, can be included as well. Figure 1 illustrates the measuring principles of characterization of droplet hydrophobicity and monitoring of the dynamics of drying for different, pinned, and unpinned, modes of evaporation.

Results

Figure 2 illustrates an example of monitoring of the evaporation process, compiled of pinned and unpinned mode, on a hydrophobic surface, represented by the difference of the resonance frequencies, δf , of the sensor with an aqueous droplet on its surface and without the droplet. The weight of the droplet decreases nearly linearly over the whole time period (high-precision gravimetric measurements). The initial value of the frequency shift can be recalculated into the amount of surface area covered by the droplet, or into the droplet contact angle.

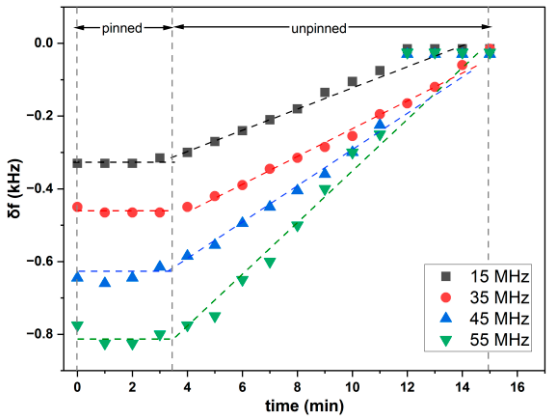

Fig 2. Experimental results of the frequency shift, δf, of a 2 µL water droplet on the hydrophobic surface (PTFE spray-coated sensor) measured in various frequencies as a function of time at room temperature.

The pinned mode of evaporation, corresponding to constant frequency shift, is observed at the time period of 0 to approximately 3.5 min (see Fig. 2). Unpinning mode occurs after this phase until the end of the drying process. Further drop shape analysis offered important information on the geometry of the droplet (height, volume, diameter), and energy loss analysis (at various frequencies) provided knowledge on viscous damping effects from the droplets, during different times of evaporation. Finally, the drying kinetics of aqueous droplets allowed for the quantification of impurity depositions on the surfaces and the characterization of watermarks formed.

References

[1] B. Murray, S. Narayanan, The Role of Wettability on the Response of a Quartz Crystal Microbalance Loaded with a Sessile Droplet, Scientific Reports, 9 (2019) 17289.
[2] H.Y. Erbil, Evaporation of pure liquid sessile and spherical suspended drops: A review, Advances in Colloid and Interface Science, 170 (2012) 67-86.
[3] A.H. Tamaddon, P.W. Mertens, J. Vermant, G. Vereecke, F. Holsteyns, M. Heyns, S. De Gendt, Role of Ambient Composition on the Formation and Shape of Watermarks on a Bare Silicon Substrate, ECS Journal of Solid State Science and Technology, 3 (2014) N3081-N3086.
[4] A. Alassi, M. Benammar, D. Brett, Quartz Crystal Microbalance Electronic Interfacing Systems: A Review, Sensors, 17 (2017) 2799.
[5] D. Johannsmann, The Quartz Crystal Microbalance in Soft Matter Research: Fundamentals and Modeling, Springer International Publishing (2014).

DOI 10.5162/SMSI2023/C4.3

In-Situ Control of Microphone Responses in an Array

Artem Ivanov[1]
[1] *Landshut University of Applied Sciences, Am Lurzenhof 1, 84036 Landshut, Germany*
Artem.Ivanov@haw-landshut.de

Summary:
A method to perform measurements of microphone responses directly in an array is proposed. It targets especially arrays built with MEMS Microphones and does not require high instrumentation effort. The method was successfully tested for calibration of two types of planar arrays in reverberant environments. Presented experimental results illustrate the application.

Keywords: MEMS microphone array, in-situ calibration

Introduction

Microphone arrays are widely used in acoustic measurements. An example can be found in acoustic cameras, where a suitable combination of single sensor signals allows to localize sound sources with the help of beam forming or to reconstruct the sound field by use of acoustic near field holography. The processing algorithms rely on exact matching between the microphones or at least on the knowledge of their amplitude and phase responses to compensate the differences, therefore extensive research was devoted to methods of calibrating microphone arrays in respect of positions of single sensors and their responses [1], [2].

The calibration task becomes especially challenging when the single microphones cannot be removed from the array after the assembly, e.g. when the array is built of miniature MEMS devices soldered onto printed circuit boards [3]. The approach proposed here allows to calibrate amplitude responses of the sensors and to control the actual condition of the microphone array. The method was developed especially for use with arrays based on low-cost MEMS Microphones and was successfully tested with planar arrays in reverberant cites.

Description of the Proposed Method

The approach targets the case when the microphones cannot be removed from the array for calibration, so the acquisition of sensor responses is performed directly by the measurement system itself in a dedicated firmware branch. In this way the influence of the whole acquisition chain microphone-preamplifier-ADC is taken into account.

To cope with the practical situation of reverberant environment excitation characterized by a distinguished first wavefront is used. The subsequent processing concentrates on this first wavefront to effectively suppress the influence of scattered waves which would arrive later. Knowing the geometry of the array and the anticipated sound pressure distribution on its elements, measurement and calibration of the microphone responses can be carried out. A suitable excitation can be produced e.g. by hands clapping or balloon popping. In our tests the most practical source turned out to be a loudspeaker driven with a rectangular voltage pulse.

Systems operated at typical audio sampling frequencies (about 40 kSps) cannot acquire all necessary details of the short wavefront. Hence the following processing is performed on interpolated signals. It is important, however, that they do not contain aliased frequencies.

After the high-pass filtering the peak amplitude of the first wavefront and its arrival time is defined from the interpolated signal. If at least one of the array microphones was previously calibrated, it can be used as the reference. Otherwise the average amplitude response over the array is used to obtain the relative amplitudes of all microphones. After performing several measurements the averaged amplitude responses are taken as the calibration factors.

Interpolation of original signals can be carried out by the zero padding in frequency domain. Good results were obtained also using interpolation by convolution with the Lanczos kernel of length 7 or higher, which can be performed on systems with very limited hardware resources.

Experimental Results

Experimental verification of the proposed calibration method was carried out with two differ-

ent measurement systems based on MEMS microphone arrays. The presented results were gathered with a system containing 128 MEMS microphones arranged in a rectangular 16 by 8 matrix and digitized at f_s = 48 kSps [4]. An example of a recorded microphone signal is given in Fig. 1. It was obtained using a loudspeaker (60 W, 4 Ohm 5¼´´ Woofer of JBL GTC5210) positioned 3 m away from the array and driven by a rectangular voltage pulse of 15.5 V amplitude and 0.25 s duration.

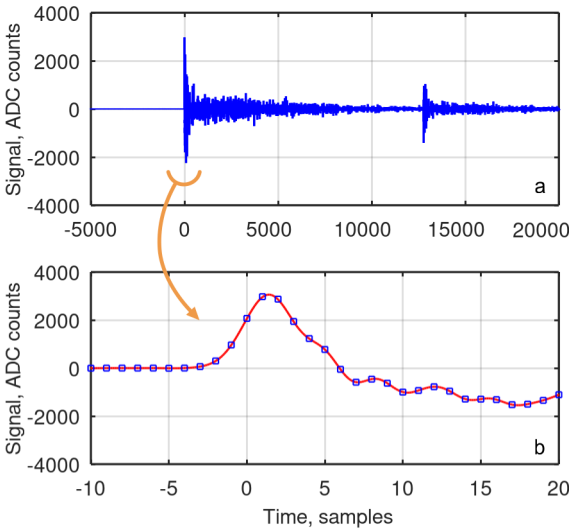

Fig. 1. Microphone signal recorded at 48 kSps (blue line and points). Red line – interpolation of the first wavefront.

Fig. 2 shows the amplitude calibration factors for all 128 sensors in the array calculated as relative responses. The variation of the microphone sensitivity is specified with ±1 dB, which is equivalent to approximately ±12% on the amplitude scale. It can be seen that all sensors lie well within the anticipated range.

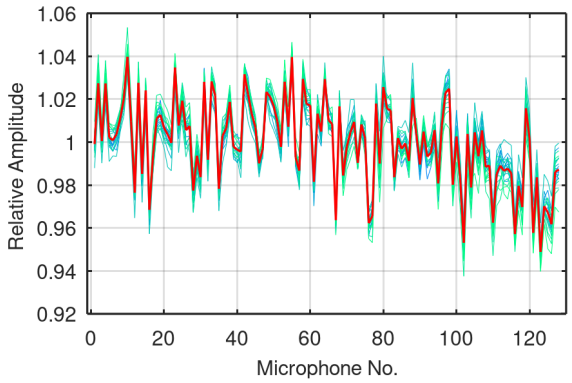

Fig. 2. Amplitude responses of 128 microphones in the array. Results of 20 measurements as blue-green lines, averaged values are shown in red.

The distances between the loudspeaker and the microphones differed over the array area by 0.5% at maximum. This variation should have a barely detectable effect on the amplitudes in Fig. 2. The apparent decrease of amplitudes at higher microphone numbers is attributed to the fact that the boards carrying microphones 97 to 128 originate from a different production batch.

The arrival time of the first wavefront is plotted in Fig. 3 for an exemplary measurement (only two of the array lines are shown for the clarity of representation). The green curve shows the theoretically anticipated arrival time based on the point source model for the given geometry (taken speed of sound is c = 344 m/s). Note the sub-sample time resolution which is possible due to the use of interpolated signals. Experiment agrees well with the theoretical model.

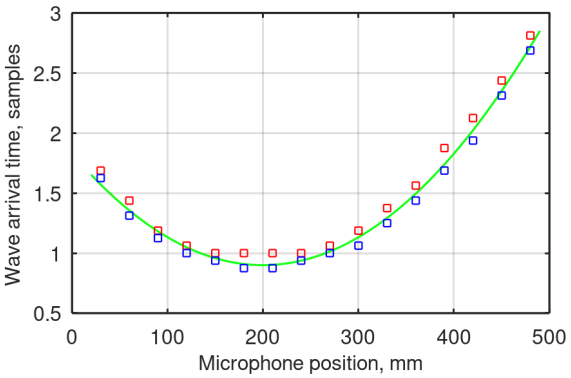

Fig. 3. First wavefront arrival time (squares) compared with the theoretical curve for 32 microphones.

Irregularities in the time response plot can be used for control of the system condition: experiments showed for example that an obstruction of a microphone port with a dirt particle can be clearly detected as a shift in the plot.

Conclusions

The presented approach allows to perform measurements of microphone responses directly in the array for their control or calibration in reverberant environments. Additionally performed comparisons with microphone calibration in a standing-wave tube confirm the validity of the results.

References

[1] N. Tashev, Gain self-calibration procedure for microphone arrays, *IEEE ICME* (2004), doi: 10.1109/ICME.2004.1394367

[2] M. Szőke, C. Bahr, L. Cattafesta, K.-S. Rossignol, Zh. Yang, Toward Efficient In Situ Microphone Calibration Procedures Using Laser-Induced Plasma, *28th AIAA/CEAS Aeroacoustics Conference* (2022), doi: 10.13140/RG.2.2.14486.42566

[3] F. Perrodin, J. Nikolic, J. Busset, R. Siegwart, Design and Calibration of Large Microphone Arrays for Robotic Applications, *IEEE/RSJ International Conference on Intelligent Robots and Systems* (2012), doi: 10.1109/IROS.2012.6385985

[4] A. Ivanov, A. Kulinna, Microphone Based System for Visualization of Vibration Patterns, *submitted for SMSI 2023*

DOI 10.5162/SMSI2023/C4.4

Characterization of a Piezo-Resistive MEMS Microphone for Aero-Acoustic Measurements

Kolja Erbacher[1], Onteru Lokesh[2], Claire Bourquard[2], Lixiang Wu[2], Piotr Mackowiak[4]
Ha Duong Ngo[3], Martin Schneider-Ramelow[4]
[1] Technische Universität Berlin, Germany, [2] Silicon Austria Labs, Austria, [3] University of Applied Sciences Berlin, Germany. [4]Fraunhofer Institute for Reliability and Microintegration IZM, Germany,
erbacher@tu-berlin.de

Summary:
This paper presents the packaging and characterization of a piezo-resistive (PR) micro-electro-mechanical system (MEMS) microphone for aero-acoustic measurements with three different membrane sizes. The thickness of the square membranes is 5 µm with an edge length of 1900 µm, 2260 µm and 2660 µm, respectively. The results of the sensors characterization show a sensitivity of up to 55 dB re 1 V/Pa when exposed to an acoustic chirp signal ranging from 5-50 kHz at 70-100 dB SPL. This paper presents a test approach necessary for chips with very thin membrane and the results of a dynamic pressure frequency response test.

Keywords: aero-acoustic, thin membrane, microphone, piezo-resistive, MEMS

Introduction

The development of new airplane generations with less noise emission and aerodynamic drag can only be enabled by novel finite element simulations, which lack of sufficient accurate calibration data in the past. This desired data can only be obtained by new aero-acoustic microphone sensor systems with high spatial resolution and dynamic range [1]. Available microphones either are packaged in large cases, which inhibits a small pitch between sensors and so a high spatial resolution, or have a low total harmonic distortion, which disables the use in flight tests, where pressures up to 175 dB SPL need to be measured. The thin and flexible array with custom designed PR MEMS microphones, presented by the author in a previous paper [2], addresses the above stated limitations. The focus of this paper is a test approach for chips with a very thin membrane and presents the results of a dynamic pressure frequency response test.

Piezo resistive microphone

The microphone consists of a 5 µm thin square membrane with the three edge lengths (1900/2260/2660 µm). The implanted piezo resistors which are configured to form a Wheatstone bridge, change their resistivity when the membrane is deflected. he membrane has an optional 10 µm ventilation hole, to release static pressures in the back chamber. A schematic drawing of the sensor is shown in Fig. 1, the detailed fabrication steps were descripted in [2].

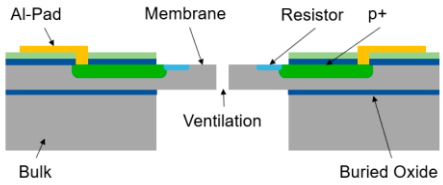

Fig. 1. Structure of the sensor chip shown in a cross-section view (not at scale)

Preparation of the Samples

To measure the response of the fabricated sensor chips dynamic pressure in test benches, it needs to be mounted on a printed circuit board (PCB) sealing the back cavity from the applied pressure. Thermomechanical stress due to different coefficients of thermal expansion of die and PCB can easily preload the thin membrane and so alter the measurement results. When using a very soft or thick applied adhesive, the structure gets to instable for wire bonding. The applied ultrasound is absorbed by the adhesive and does not form the joint of wire and pad. To prevent these effects a silicon adapter chip with a feed-through is firstly glued on the package, using epoxy resin. Then the sensor is attached with a silicone adhesive that is cured at 150 °C. This setup (Fig. 2). does work for aluminium-wire-bonding and the membrane does not get deflected, which can be detected with an optical microscope.

Measurement Setups

The dynamic pressure test was carried out in an anechoic chamber containing the electro-

static pressure source type PID 604142, one sample and an optical reference microphone type Eta250 Ultra. The distance between source and microphone was set to approx. 3 cm. The sensor output voltage was amplified by a factor of 10.

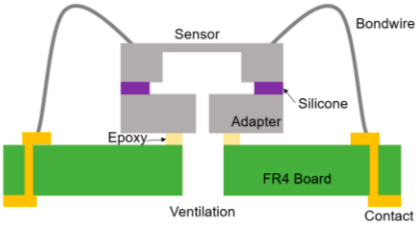

Fig. 2. Package with FR4-PCB with back chamber ventilation and silicon adapter chip

Measurement Results

The speaker was excited with a chirp signal with frequencies between 5-50 kHz. Due to a lack of DAQ-channels, firstly the reference microphone signal was recorded and secondly the device under test (DUT). To calculate the frequency response of the DUT, the values of the reference mic where divided by the known sensitivity of the ref mic and then converted into the frequency domain by Fast Fourier Transformation (FFT), giving the frequency dependent pressures at the DUT. Then the DUT voltage values where converted by FFT and then normalised by the before calculated pressure values. The resulting graphs are shown in Fig. 3-5. Four samples for each membrane size were tested with a vent hole (wv – with vent) and without a vent hole (nv – no vent).

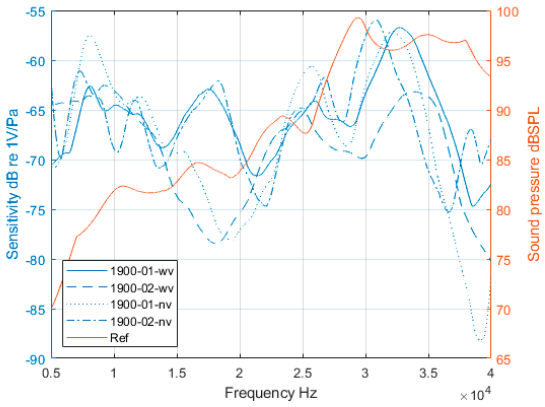

Fig. 3. Frequency response for DUTs 1900 µm

Outlook

Even though the presented measurement results show the functionality of the fabricated microphones, the tests need to be repeated with higher numbers of samples, to quantify the deviation of the frequency response for every type of sensor. The resulting trends can then be compared with the simulation results in [2] and new design adaptions can be formulated to fit the specifications.

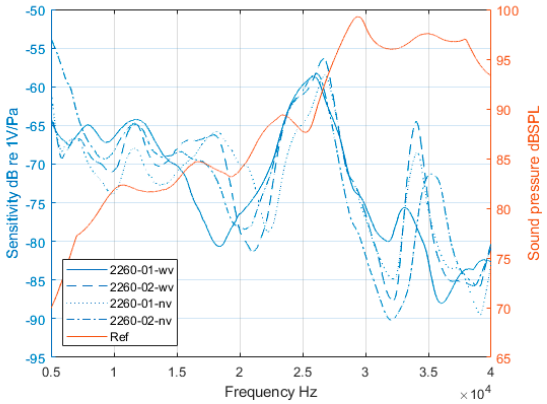

Fig. 4. Frequency response for DUTs 2260 µm

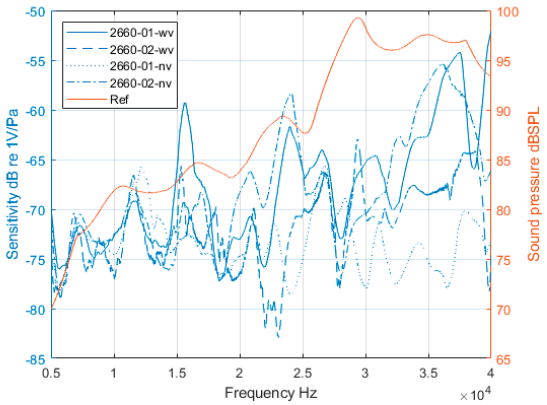

Fig. 5. Frequency response for DUTs 2660 µm

Outlook

In preparation for flight tests the samples will be investigated in the Bacchus test [3] at Airbus, where they can be exposed to the combination of flow and acoustic phenomenon. For the flight tests, the sensors will be embedded into flexible large area arrays [2].

Acknowledgement

We would like to thank our colleagues from the Aeromic consortium for contributing to this publication. This project has received funding from the Clean Sky 2 Joint Undertaking (JU) under grant agreement No 101007958.

References

[1] T. Ahlefeldt et al., Road to acquisition: Preparing a MEMS microphone array for measurement of fuselage surface pressure fluctuations, *micromachines 2021*, doi:10.3390/mi12080961

[2] K. Erbacher et al., Design and modeling of a novel piezoresistive microphone for aero acoustic measurements in laminar boundary layers using FEM and LEM, *AIAA 2022*, doi:10.2514/6.2022-1023

[3] J Derre, O Sainges, BACCHUS: an Aero-Acoustic Test Bench oriented towards Microphone Assembly and De-Noising Method Development, e-Forum Acusticum 2020, doi:10.48465/fa.2020.0665

DOI 10.5162/SMSI2023/C5.1

Revisiting Environmental Sensing Nodes: Lessons Learned and Way Forward

Nicolas P. Winkler[1], *Sergej Johann*[1], *Harald Kohlhoff*[1], *Patrick P. Neumann*[1]
[1] *Bundesanstalt für Materialforschung und -prüfung (BAM),*
Unter den Eichen 87, 12205 Berlin, Germany,
mro@bam.de

Summary:
Setting up sensors for the purpose of environmental monitoring should be a matter of days, but often drags over weeks or even months, preventing scientists from doing real research. Additionally, the newly developed hardware and software solutions are often reinventing existing wheels. In this short paper, we revisit the design of our environmental sensing node that has been monitoring industrial areas over a span of two years. We share our findings and lessons learned. Based on this, we outline how a new generation of sensing node(s) can look like.

Keywords: sensing node, sensor network, environmental monitoring, low-cost, LoRaWAN

Motivation

Scientists need data to gain new knowledge. Thanks to open-source code and maker communities, and modern embedded hardware technology, a near infinity of solutions to environmental monitoring exist. However, no inexpensive ready-to-go system has been established, which leaves individual scientists with developing a custom system nearly from scratch, taking away valuable research time to tedious development time.

To facilitate this process for future scientists, we share our experience with the development and instrumentation of our low-cost sensing nodes. We propose our current ideas that might be helpful for scientists designing environmental sensing platforms.

Lessons Learned

Literature shows that there are a lot of developments for low-cost sensing nodes [1]. It is beyond the scope of this paper, to give a detailed overview on these. Instead, we highlight lessons that we learned from own previous projects [2, 3].

In [2], we proposed a stationary sensing node with active ventilation fan for air quality monitoring. These nodes have been working in outdoor and indoor scenarios for multiple years since then.

When outdoor scenarios are addressed and power supply is limited, we emphasize that the whole system must be designed for low-power consumption holistically. Care should be taken during the selection of electronics and the design of the software architecture, as low power is only achievable to a certain degree by tuning subsystems individually from each other. Similarly, external power supply, such as batteries, need to be dimensioned adequately.

We also advise checking the orientation of sensors thoroughly. Some sensors may have mounting orientations that are better than other, e.g., dust may clutter horizontally oriented optical lenses. Similarly, a mitigation procedure for sensor drift should be thought of. Especially for low-cost (dust) sensors, it may be more sensible to replace whole sensors, instead of cleaning them in the field. As low-cost sensors are prone for unreliable readings or outages, we advise to keep a sensor replacement strategy in mind. When multiple sensing nodes are deployed in a sensor network, the network might be used to absorb outages of individual sensors [4].

Lastly, we want to highlight the accessibility of data. This is of course dependent on the scenario, but occasions may arise in which also non-experts may need easy access to the sensor data. Concretely, travel restrictions due to the global COVID-19 pandemics forced us to rely on external non-experts for data retrieval.

Design Ideas for a Revised System

To reflect the learning from our previous system, we outline, how a new environmental sensing node can look like. To ensure a high reusability and flexibility of the sensor platform, we propose a modular sensing node, that can

be quickly equipped with different sensor modules. The key idea is that each sensing node consists of a single main module, which receives data in a standardized format from the different sensor modules. By this, sensor modules must be developed and programmed only once and can then be reused in different scenarios and constellations.

To ensure seamless wireless connectivity, we will use both WLAN and LoRaWAN. LoRaWAN stands for Long Range Wide Area Network and is a network protocol that enables long-range wireless communication between devices. With LoRaWAN, distances up to 15 km over ground can be covered, while consuming low power [5]. Thus, a single LoRa gateway can ensure the coverage of various nodes in outdoor scenarios. Adding WLAN functionality helps to easily address indoor or office scenarios, where WLAN most probably already exists, and no designated gateway needs to be installed. Fig. 1 shows exemplary coverage areas for both communication protocols. We envision a unified cloud to which all gateways are connected, as shown in Fig. 2. By this, the end user may retrieve the data easily through a single access point, ideally being able to flexibly query the desired information.

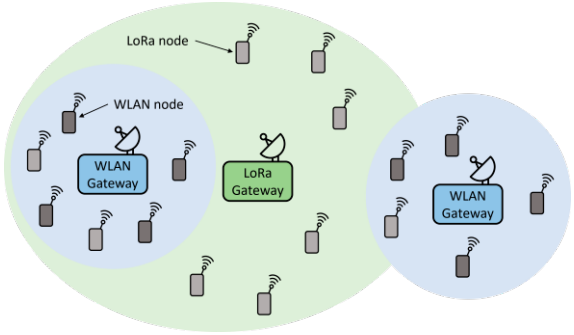

Fig. 1: Sensing nodes are transmitting their data to local gateways. These can be WLAN or LoRa gateways.

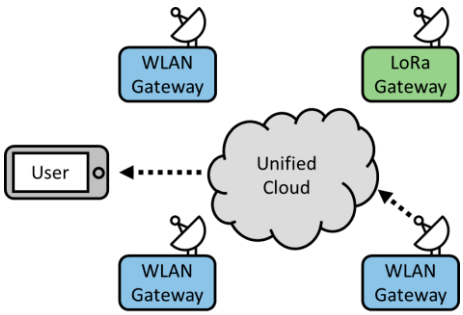

Fig. 2: All gateways transmit their data to a unified server with database. End users gather their data from this database.

Lastly, we propose to mostly use commercials off-the-shelf components for the casing of the electronics and sensors to keep hardware costs as low as possible. Two different design concepts of different price points are displayed in Fig. 3. The left concept is based on a custom-manufactured tower unit, into which different sensor modules can be embedded. While this design is more flexible regarding sensor size, manufacturing custom components is costly. In contrast, the right concept utilizes a commercially available ABS thermoplastic box for the main module, under which different sensor modules are attached, making the system more cost efficient.

Fig. 3: Different concepts for a modular sensing node. The left pictures a system, where two different modules are attached to the core 'tower unit'. On the right, four sensor modules are attached underneath a main module.

References

[1] F. Karray, M. W. Jmal, A. Garcia-Ortiz M. Abid, A. M. Obeid, A comprehensive survey on wireless sensor node hardware platforms, *Computer Networks*, 89-110 (2018); doi: 10.1016/j.comnet.2018.05.010

[2] N. P. Winkler, P. P. Neumann, H. Kohlhoff, J. Erdmann, E. Schaffernicht, A.J. Lilienthal, Development of a Low-Cost Sensing Node with Active Ventilation Fan for Air Pollution Monitoring. *SMSI 2021 Proceedings*, 260-261 (2021); doi: 10.5162/SMSI2021/D3.5

[3] J. Sergej, N. P. Winkler, M. Bartholmai, Multi-sensor system for long-term monitoring with WiFi and LoRaWAN technology, *38th Danubia-Adria Symposium on Advances in Experimental Mechanics,* (2022);

[4] N. P. Winkler, P. P. Neumann, E. Schaffernicht, A. J. Lilienthal. Using redundancy in a sensor network to compensate sensor failures, *2021 IEEE Sensors*, (2021); doi: 10.1109/SENSORS47087.2021.9639479

[5] J. Petajajarvi, K. Mikhaylov, A. Roivainen, T. Hanninen, M. Pettissalo, On the coverage of LPWANs: range evaluation and channel attenuation model for LoRa technology, *2015 14th International Conference on ITS Telecommunications (ITST),* 55-59 (2015); doi: 10.1109/ITST.2015.7377400

DOI 10.5162/SMSI2023/C5.2

Flexible Magnetic Sensors Enabling Novel Measuring Capabilities

Michael Melzer[1]
[1] *Bundesanstalt für Materialforschung und -prüfung (BAM), Unter den Eichen 87, 12205 Berlin, Germany, michael.melzer@bam.de*

Summary:
Since several years, magnetic sensor elements are available in fully flexible architectures that often reveal identical sensing properties, compared to their rigid counterparts, while being bent severely and repeatedly. Nowadays, a variety of magnetic senor principles, including well known Hall, AMR and GMR but also more exotic PHE and AHE sensors were demonstrated on such flexible platforms. The novel properties of being thin, lightweight, shapeable, and wearable enable magnetic sensory systems to be utilized in vicinities and conditions that are inaccessible for rigid and microchip-based sensors.

Keywords: flexible electronics, flexible sensors, magnetic sensors, novel applications, in-situ sensing

Introduction

The ongoing technological development of flexible electronics is motivated by the eagerness of multifunctional electronic systems towards being thin, lightweight, compliant, wearable or even implantable and transient. This requires all components of circuitry, including passive, active and responsive (sensor) elements being reshapeable on demand after fabrication and assembly. Ideally, they fully maintain their electronic properties and mechanical integrity while being severely and repeatedly distorted. Such flexible electronic designs pave the way to novel application fields like, foldable and wearable electronics, smart textiles, soft robotics, electronic skins, as well as domestic healthcare devices and functional medical implants.

Especially for sensor devices, thin and flexible architectures allow utilizing sensing elements in narrow, non-planar or soft and volatile environments that are otherwise not accessible.

Flexible magnetic sensors

Also magnetic sensors underwent the transition from rigid and microchip-based to fully flexible and other shapeable designs.[1] This is particularly mediated by the fact, that many physical effects that are exploited in magnetic sensing are occurring in layered thin film structures, that can be arranged on flat polymeric supports in order to obtain flexible devices. The main technological obstacles in this process, which are surface roughness, temperature restrictions and limited miniaturization, are tackled by means of adapted preparation procedures.[1]

Besides Hall [2], magnetoresistance (MR) [3], giant magnetoresistance (GMR) [4,5] and tunnel magnetoresistance (TMR) [6], also more exotic magnetic sensing principles, *i.e.* planar Hall effect (PHE) [7] and anomalous Hall effect (AHE) [8], have been realized on flexible platforms, recently. Hence, a variety of flexible magnetic sensor elements, covering different target field ranges, sensitivities, sensible field components and environmental working conditions, is available nowadays.

For magnetic sensing, the added value aspect of being integratable into narrow constrictions or operating in close proximity to an arbitrarily shaped surface is particularly beneficial, since the detectable magnetic field strength is rapidly decreasing with the distance from the source to be detected.

Novel measuring capabilities

A selection of application scenarios, where the compliant mechanical properties induce specific advantages for magnetic sensing are given in Fig. 1.

Magnetic particles are widely used for diagnostic or therapeutic purposes in biology and medicine by means of fluidic systems. For the detection of these particles, which are often used to label specific biological objects having target properties, flowing through a fluidic channel, flexible magnetic sensors offer an elegant approach to enhance their sensing capabilities. As depicted in Fig. 1a, a flexible sensing element can surround the entire channel cross-section.[9] In comparison to a planar sensor,

that is limited to one single face of the channel, this circumferential arrangement makes the detection of the magnetic entities less susceptible to the specific transit position inside the channel. Furthermore, magnetic sensors are often sensitive to only a single magnetic field component with respect to their orientation, which requires the magnetic objects to be aligned to the sensor upon detection. A circumferential sensor, however, gives rise to a unique isotropic sensitivity [9], omitting the need for particle alignment.

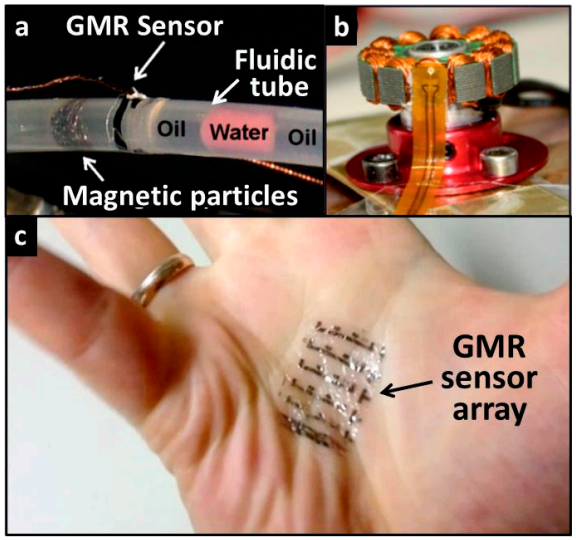

Fig. 1. Selection of novel measurement capabilities utilizing flexible magnetic sensors. (a) circumferential magnetic sensing in fluidics [9]; (b) direct flux density measurement in the air gap of electrical machines and drives [10]; (c) on-skin magnetoception [4].

Due to their thin architecture, flexible magnetic sensors can also be integrated into the narrow and curved air gaps of electrical machines and drives, *i.e.* between rotor and stator, where conventional sensors simply do not fit (see Fig. 1b). This allows measuring the strong magnetic fields directly at the position where they act to drive the machine. In particular for active magnetic bearings, this allows for direct flux-based control [10], offering more stiffness, precision and resilience in operation.

Flexible magnetic sensors can also be operated directly on the human skin.[2] Especially ultra-thin designs of only few µm total thickness are able to intimately conform to the epidermis (see Fig. 1c) and simultaneously follow their natural deformations and distortions without performance degradation. The highly compliant magnetic sensor foil is haptically not perceived by the recipient if worn on skin. This artificial magnetoception [4] gives rise to novel capabilities for touchless human-machine interaction.

References

[1] D. Makarov, M. Melzer, D. Karnaushenko, O. G. Schmidt, Shapeable magnetoelectronics, *Applied Physics Reviews* 3, 011101 (2016); doi: 10.1063/1.4938497.

[2] M. Melzer, J. I. Mönch, D. Makarov, Y. Zabila, G. S. C. Bermúdez, D. Karnaushenko, S. Baunack, F. Bahr, C. Yan, M. Kaltenbrunner, O. G. Schmidt, Wearable Magnetic Field Sensors for Flexible Electronics, *Advanced Materials* 27, 1274-1280 (2014); doi: 10.1002/adma.201405027.

[3] G. S. C. Bermúdez, H. Fuchs, L. Bischoff, J. Fassbender D. Makarov, Electronic-skin compasses for geomagnetic field-driven artificial magnetoreception and interactive electronics, *Nature Electronics* 1, 589-595 (2018); doi: 10.1038/s41928-018-0161-6.

[4] M. Melzer, M. Kaltenbrunner, D. Makarov, D. D. Karnaushenko, D. Karnaushenko, T. Sekitani, T. Someya, O. G. Schmidt, Imperceptible magnetoelectronics, *Nature Communications* 6, 6080 (2015); doi: 10.1038/ncomms7080

[5] G. S. C. Bermúdez, D. D. Karnaushenko, D. Karnaushenko, A. Lebanov, L.Bischoff, M. Kaltenbrunner, J. Fassbender, O. G. Schmidt, D. Makarov, Magnetosensitive e-skins with directional perception for augmented reality, *Science Advances* 4, eaao2623 (2018); doi: 10.1126/sciadv.aao26.

[6] S. Amara, G. A. T. Sevilla, M. Hawsawi, Y Mashraei, H. Mohammed, M. E. Cruz, Y. P. Ivanov, S. Jaiswal, G. Jakob, M. Kläui, M. Hussain, J Kosel, High-Performance Flexible Magnetic Tunnel Junctions for Smart Miniaturized Instruments, *Advanced Engineering Materials* 20, 1800471 (2018); doi: 10.1002/adem.201800471.

[7] P. N. Granell, G. Wang, G. S. C. Bermudez, T. Kosub, F. Golmar, L. Steren, J. Fassbender, D. Makarov, Highly compliant planar Hall effect sensor with sub 200 nT sensitivity, *npj Flexible Electronics* 3, 3 (2019); doi: 10.1038/s41528-018-0046-9.

[8] M. Ha, G. S. C. Bermúdez, J. A.-C. Liu, E. S. O. Mata, B. A. Evans, J. B. Tracy, D. Makarov, Reconfigurable Magnetic Origami Actuators with On-Board Sensing for Guided Assembly, *Advanced Materials* 33, 2008751 (2021); doi: 10.1002/adma.202008751.

[9] M. Melzer, D. Karnaushenko, D. Makarov, L. Baraban, A. Calvimontes, J. I. Mönch, R. Kaltofen, Y. Mei O. G. Schmid, Elastic magnetic sensor with isotropic sensitivity for in-flow detection of magnetic objects, *RSC Advances* 2, 2284-2288, (2012); doi: 10.1039/C2RA01062C.

[10] I. J. Mönch, F. Bahr, M. Melzer, D. Karnaushenko, D. Makarov, W. Hofmann, O. G. Schmidt, Flexible Hall Sensorics for Flux-Based Control of Magnetic Levitation, *IEEE Transactions on Magnetics* 51, 4004004 (2015); doi: 10.1109/TMAG.2015.2438232.

DOI 10.5162/SMSI2023/C5.3

Passive Smart Dust: A Versatile Low-Cost Sensor Platform

Tino Nerger[1,2], Patrick P. Neumann[1], Michael G. Weller[1,2]
[1] Bundesanstalt für Materialforschung und -prüfung (BAM), Unter den Eichen 87, Berlin, Germany
[2] Humboldt Universität zu Berlin, Unter den Linden 6, 10117 Berlin, Germany
Tino.Nerger@BAM.de

Summary:
We present a new approach to detect chemical hazardous substances from a safe distance. In a first step we were able to detect concentrations of dangerous acids and base by using simple paper-based snippets with a chemically modified surface. A significant color change indicates the presence of a chemical hazard and was detected with the help pf a drone and custom software.

Keywords: passive smart dust, drone, chemical sensors, optical detection

Introduction

The remote and autonomous detection of hazardous substances is an important task that can be achieved using remotely operated platforms equipped with dedicated sensors. In recent years a huge variety of methods and vehicles have been used in hazardous conditions for surveillance [1]. The term "smart dust" was initially coined in a work of science fiction and subsequently developed into a research proposal at UC Berkeley, which received funding from the Defense Advanced Research Projects Agency (DARPA). Although the idea attracted attention, it was eventually judged to be excessively intricate for the technology available at the time [2]. With the launch of the passive smart dust project, we reinterpreted the original idea with simple "chemically intelligent" passive sensor particle brought out in the target area in combination with an active sensor on an Unmanned Aerial Vehicle (UAV).

Fig. 1. Schematic presentation of the PSD concept [3].

So, we can circumvent problems of power supplies and communication modules for the smart dust particles that limited older approaches. The surface of the reactive particle can be pre-programmed in the lab to facilitate specific reactions to hazardous substances. The projected applications permit different materials to be used, such as those that can withstand the environment long-term monitoring or that are biodegradable. A frequent scenario of an industrial accident with spoiled acid, as an acute and quickly remediable problem, became the first test setting for our passive smart dust concept [3].

Materials and methodology

Drone platform

The DJI M300 RTK is a commercially available quadrocopter that is suitable to operate in harsh weather conditions. A Real Time Kinematic (RTK) ground station was used for precise determination of localization data. The drone offers maximum flight time of 55 min with a given range of up to 15 km [4]. A payload of up to 2.7 kg can be attached on the platform. In our case the DJI Zenmuse H20T was used for optical measurements. The H20T is gimbal stabilized and contains a zoom capable 20 Megapixel (MP) 1/1.7" Complementary metal-oxide-semiconductor (CMOS) sensor and a 12 MP wide range 1/2.3" CMOS sensor for visible light detection. Moreover, a VOx mircoblometer can measure wavelengths in the near infrared range and a 905 nm class 1M laser provides relevant distance information. An overflight altitude of 20 m was chosen, resulting in a reasonable image resolution and safe distance in which the smart dust is not affected by any rotor downwind.

Sensor particles

For environmental reason, paper-based particles represent the focus of the upcoming work. To be recognized by an optical camera system the used the smart dust particles need to be big enough for being detectable with commercial off-the-shelf camera systems and shall provide a big shift in the emitted light wavelength. At first commercial pH paper [CHEMSOLUTE® universal] was tested within several sizes and heights. In a next step, particles were self-manufactured and optimized.

Macherey-Nagel [MN 617] highly absorbent filtration paper was covered with a mixture of polyethyleneimine (PEI) [Mw~25000, Mn~10000, Sigma-Aldrich, Germany] and 1-Naphtholphthalein [reinst, Carl Roth, Germany] as well as PEI and Thymol blue [ACS 95%, Supelco™, Canada] respectively (Fig. 2).

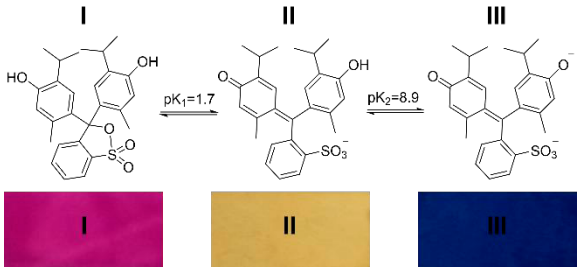

Fig. 2. Different forms of thymol blue combined with pictures of the manufactured test particles at pH value of 1(I), 7(II) and 13(III) respectively.

The used cationic PEI polymer effectively hinders a bleeding of the indicator when exposed to liquids from a time larger than 5 min which is a current problem with commercial test stripes. Both used indicators offer not only one but two color-stages and concurrent detection of strong acids or bases and negative control in the neutral pH range [6].

Evaluation

For an automated localization of contaminated areas, a detection algorithm was developed in Python. The obtained pictures in JPEG format were converted into the Hue Saturation Value (HSV) color space. Subsequently, a filter based on the particle's HUE value was used for particle identification/detection [7]. By using the Exchangeable Image File Format (EXIF) data in combination with distance and angle information from the gimbal, the particles can be localized with an error of under 2 cm. In the presence of a hazard, a warning message is automatically generated, and the identified areas are visualized in Google Earth using its Keyhole Markup Language (KML) file format.

Fig. 3. ROI of red particles indicating the presence of acid (a) After processing hazardous areas are shown on google earth via imported datapoints (b).

Results

Remote sensing of pH paper pieces formed an effective basis for the detection of acids and bases, which could be accurately detected by a camera system from a safe distance. By applying a HSV-filter, which identified the colors of particles that reacted to the presence of acid, all the Regions of Interest (ROI's) were revealed. Additionally, the EXIF data provided the exact location of the hazard. Thanks to the combination with the RTK system of the DJI M300, highly precise location data in centimeter range was obtained. To ensure easy application in the field, the positive test areas were projected onto a widely accessible digital map (Fig. 3).

References

[1] Kucharczyk M.et al., Remote sensing of natural hazard-related disasters with small drones: Global trends, biases, and research opportunties, *Remote Sensing of Environment*. **2021** (264), 112577

[2] Pister et al., Smart Dust: Wireless Networks of Millimeter-Scale Sensor Nodes, *Research Summary, UC, Berkely*, USA, **1999**

[3] Modified from: Azush Y. Khademsadegh M. https://www.behance.net/gallery/26185489/Dubai-Land Accessed March 09, **2022**

[4] https://www.theguardian.com/us-news/2023/feb/15/tucson-arizona-truck-crash-hazardous-spill Accessed February 20, **2023**

[5] https://drone-safety.de/produkt/dji-matrice- 300/ Accessed January 26, **2023**

[6] Steinegger A. et al., Optical Sensing and Imaging of pH Values: Spectroscopies, Materials, and Applications, *Chemical Reviews* **2020** 120, (22), 12357-12489

[7] Pearson B. et al., A Hue-Base Method for pH Determination, *University of Portland Chemistry Undergraduate Publications* **2015**

DOI 10.5162/SMSI2023/C5.4

From Thermographic In-situ Monitoring to Porosity Detection – A Deep Learning Framework for Quality Control in Laser Powder Bed Fusion

Simon Oster[1], Nils Scheuschner[1], Keerthana Chand[1], Philipp P. Breese[1], Tina Becker[1], Frank Heinrichsdorff[2], Simon J. Altenburg[1]
[1] Bundesanstalt für Materialforschung und -prüfung, Unter den Eichen 87, 12205 Berlin, Germany
[2] Siemens AG, Siemensdamm 50, 13629 Berlin, Germany
Simon.Oster@bam.de

Summary:
In this study, we present an enhanced deep learning framework for the prediction of porosity based on thermographic in-situ monitoring data of laser powder bed fusion processes. The manufacturing of two cuboid specimens from Haynes 282 (Ni-based alloy) powder was monitored by a short-wave infrared camera. We use thermogram feature data and x-ray computed tomography data to train a convolutional neural network classifier. The classifier is used to perform a multi-class prediction of the spatially resolved porosity level in small sub-volumes of the specimen bulk.

Keywords: Laser powder bed fusion, In-situ monitoring, Thermography, Machine Learning, Porosity

Introduction

Porosity in laser powder bed fusion (PBF-LB/M) is a major detrimental factor for the mechanical strength of safety-critical components. Thermography as an in-situ monitoring method can be used to monitor the thermal history of the component (Fig. 1). Deviations in the thermal history were shown to be an indicator for increased probability of porosity formation [1]. Thermographic in-situ monitoring of PBF-LB/M processes results in complex thermogram data of comprehensive size. The reduction to physically interpretable thermogram features can reduce the amount of data significantly. However, the layer-by-layer manufacturing increases the complexity of porosity prediction tasks due to phenomena such as remelting of subsequent layers. Machine Learning (ML) algorithms can be applied to overcome these issues. In this study, we use a convolutional neural network (CNN) to perform a spatially resolved multi-class classification of the porosity level based on thermogram feature data.

Experiments & Methods

We manufactured two cuboid specimens with identical process parametrization from Haynes 282 (Ni-based alloy) in separate build jobs using a commercial 3D printer. Laser power and scan velocity were varied in different component sections to force the formation of lack-of-fusion and keyhole porosity (Fig. 1). We monitored the manufacturing process using a short-wave infrared (SWIR) camera with a framerate of 2193 Hz and a spatial resolution of approx. 38 µm/pixel. From the resulting thermograms, we extracted features regarding the melt pool geometry and temperature, process spatter, and cooling of the solidified material. After manufacturing, both specimens were scanned using X-ray Computed Tomography (XCT) with a voxel resolution of (3x3x3) µm³. The XCT data was segmented into material and voids. We registered both datasets based on our registration methodology presented in [2]. Thermogram feature data and XCT data were used to produce a dataset for the training of the CNN model.

Enhanced prediction model

We aim to extend our prediction framework by the following aspects: Firstly, at the current state of work, we already expanded the portfolio of thermogram features by spatter features (*e.g.*, *number of ejected spatter particles*) and further cooling features (*e.g.*, *cooling rate*). These new features are considered to provide additional valuable information about the local process condition which could further improve the performance of the classifier. Secondly, we aim to use natural neighbor interpolation to produce geometrically smooth feature layer data and calculate the respective interpolation uncertainty [3]. A main motivation behind this is the spatial aliasing inherent to the thermogram feature data. Aliasing occurs since the maximum acquisition frequency of the SWIR camera

limits the sampling rate in which the melt pool can be monitored. The interpolation uncertainty will be incorporated into the CNN to weight the training samples. Thirdly, we intend to expand the model from binary classification to a multi-class classifier to predict different levels of porosity and the primal void class.

Preliminary results

The sensitivity of thermogram features to changes of the Volumetric Energy Density (VED) provides first indications about their potential for void prediction. In Fig. 2, the sensitivity of a selection of features to VED changes is shown. For better comparison between features, all data points were normalized using the results for nominal VED (57.95 J/mm³). All melt pool geometry features showed significantly decreased values for decreased VED and vice versa. In terms of spatter features, an increased *Number of ejected Particles* was present for decreased VED. For high VEDs, the feature showed very low values (< 0.25). The remaining spatter features showed overall low sensitivity to VED changes. *Time over threshold* (*TOT*) and *Sum of temperatures over threshold* (*SOTemOT*) showed comparable behavior and high sensitivity to increased VED. In contrast, the *Cooling rate* (CR) is increased for decreased VED and vice versa. The presented results indicate that especially *Number of Particles* and *Cooling rate* might include valuable information for defect prediction.

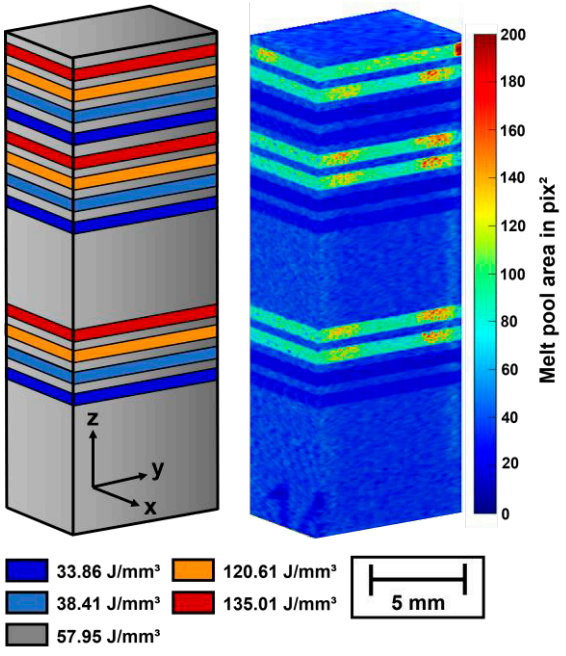

Fig. 1. Left side: Sliced representation of specimen design. Sections of changed VED are indicated by color and consist of 15 layers each. Right side: Sliced representation of thermal history indicated by melt pool area feature. Natural neighbor interpolation was used to produce the shown 3D volume.

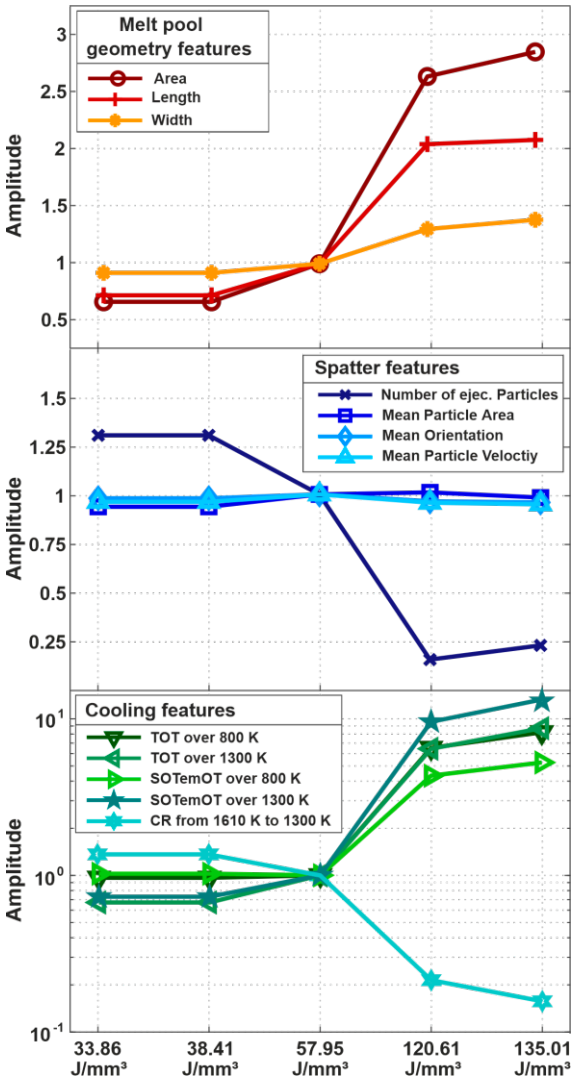

Fig. 2. Normalized mean feature response to VED changes. The abscissa shows the used VED settings, and the ordinate shows the normalized feature responses. The shown data points depict the normalized mean feature responses measured when using the given VED.

References

[1] C. S. Lough, T. Liu, X. Wang, B. Brown, R. G. Landers, D. A. Bristow, J. A. Drallmeier, E. C. Kinzel, Local prediction of Laser Powder Bed Fusion porosity by short-wave infrared imaging thermal feature porosity probability maps. *Journal of Material Processing Tech.*, 302 (2022); doi: 10.1016/j.jmatprotec.2021.117473

[2] S. Oster, T. Fritsch, A. Ulbricht, G. Mohr, G. Bruno, C. Maierhofer, S. J. Altenburg, On the Registration of Thermographic In Situ Monitoring Data and Computed Tomography Reference Data in the Scope of Defect Prediction in Laser Powder Bed Fusion, *Metals*, 12, 947 (2022); doi: 10.3390/met12060947

[3] T. R. Etherington, Discrete natural neighbour interpolation with uncertainty using cross-validation error-distance fields, *PeerJ Comput. Sci.*, 6:e282, (2020); doi: 10.7717/peerj-cs.282

DOI 10.5162/SMSI2023/C6.1

Fluid-Structure Interaction of MEMS Resonators

Daniel Platz[1], *Andre Gesing*[1], *Ulrich Schmid*[1]
[1] *TU Wien, Institute of Sensor and Actuator Systems, Gußhaustraße 27-29, 1040 Vienna, Austria*
daniel.platz@tuwien.ac.at

Summary:
The modelling of the fluid-structure interaction of MEMS resonators with a surrounding fluid is a formidable challenge. Only for resonators with slender beam geometries reliable methods are available. Here, we present a novel modelling approach that overcomes the geometry restrictions of beam-based methods while still being computationally efficient. We use this method to study the spectral response of a MEMS resonator immersed in a liquid. The results give insights into the fluid-structure interaction of MEMS resonators that could not have been achieved with established methods.

Keywords: MEMS resonators, fluid sensors, fluid-structure interaction, plate models, finite element methods

Introduction

Resonators based on microelectromechanical systems (MEMS) play a key role in numerous sensing applications. This prominent role is not only due to the small size and low cost of MEMS resonators. MEMS resonators also establish a gateway between the physical world and the digital domain. An important aspect of this gateway is that MEMS resonators comprise mechanically moveable parts that interact with their environment. Different types of interactions can be utilized to measure various physical quantities. One particular important interaction is the fluid-structure interaction (FSI) of a MEMS resonator with a surrounding fluid [1]. This fluid can either be a gas or a liquid and for practically every MEMS resonator outside vacuum or near-vacuum FSI is the dominant interaction with the environment. Despite this prominent role of FSI and the long history of MEMS development, the FSI of MEMS resonators is well understood only for a few limiting cases. Especially for resonators with beam geometries, various methods are available for determining the FSI. However, these models are only valid for resonators with slender beam geometries which severely limits their applicability. Moreover, only vibrational modes that can be found in beam geometries can be investigated with beam-based methods. These methods fall short of explaining the FSI of MEMS resonators vibrating in non-beam modes as the mode shown in fig. 1 [2]. Here, we present a novel method to investigate the FSI of MEMS resonators with non-beam geometries and demonstrate how these methods can be used for predicting the spectral response of MEMS resonators in fluids.

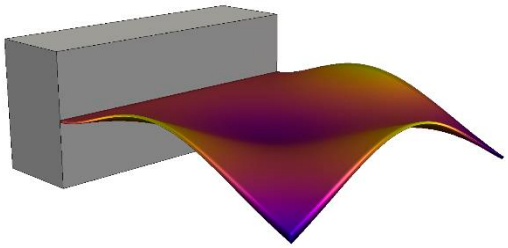

Fig. 1. Non-beam vibrational mode of a cantilevered MEMS resonator. Such modes are present in every MEMS resonator. However, they appear at frequencies of lower-order beam modes only if the width of the resonator is comparable to the resonator's length.

Description of the Method

A difficult challenge in the modelling of MEMS resonators is posed by the mismatch of scales between large resonator geometries and small fluid displacements. This scale mismatch prevents the use of conventional computational fluid dynamics (CFD) methods. We address this challenge by modelling the fluid flow with a boundary integral representation. The pressure p exerted by a fluid flow field $\boldsymbol{u}$ on the resonator surface is then determined by inverting an integral equation over the resonator surface A,

$$u(\boldsymbol{x}) = \int_A p(\boldsymbol{x}')\psi(\boldsymbol{x},\boldsymbol{x}')d\boldsymbol{x}', \qquad (1)$$

where ψ is a geometry-dependent Green's function. In doing so, we avoid a computationally costly discretization of the full fluid domain.

We assume that the resonator exhibits a thin geometry, i.e. its thickness is much smaller than the resonator's width and length, which allows for using the Kirchhoff plate equation,

$$D\,\nabla^4 w + \rho\frac{\partial^2 w}{\partial t^2} = p, \qquad (2)$$

for modelling the solid mechanics of the resonator. Here, w is the transversal displacement of the resonator, D is its flexural rigidity, ρ its density and t is the time. This approach allows for going beyond beam models while circumventing the complexity of three-dimensional continuum mechanics models. We combine equation (1) and (2) and solve the resulting equation using a non-conformal finite element method [3]. This method does not suffer from the limitations of beam-based models but avoids high computational costs.

Results

Using the method presented above, we can investigate how the FSI of a MEMS resonator changes as the geometry deviates from an ideal beam geometry [4]. As an example, we compute the spectral response of a cantilevered MEMS resonator as a function of its anchor width shown in fig. 2.

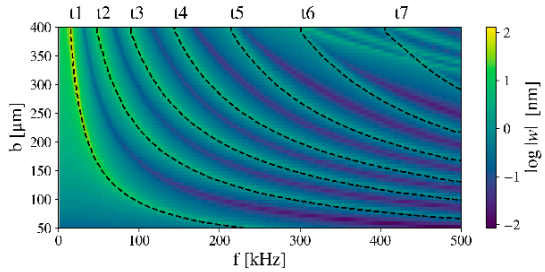

Fig. 2. Deflection spectrum as a function of resonator width for a cantilevered rectangular silicon MEMS resonator with a length of 800 µm and a thickness of 5 µm. The resonator is immersed in water and symmetrically driven at both of its free corners. The resonances of the first nine beam vibrational modes are marked by dashed lines.

At a width of 50 µm, the resonator is well approximated as a beam and only beam vibrational modes can be found in the frequency interval up to 500 kHz. These beam modes shift towards lower frequencies as the resonator width increases indicating an increased fluid-added mass. Above a width of 200 µm, additional resonances are visible in the spectral response which correspond to non-beam modes like the mode shown in fig 1. These modes experience a larger increase of the fluid-added mass than classical beam modes which results in a lager decrease of their resonance frequency as the resonator width increases.

The resonance frequency is not the only quantity that depends on the resonator width. The quality factor of all vibrational modes also changes for different resonator widths. The resonance frequencies and quality factors for different beam modes and resonator widths are shown in fig. 3. Generally, it can be observed that the quality factor increases as the width of the resonator increases.

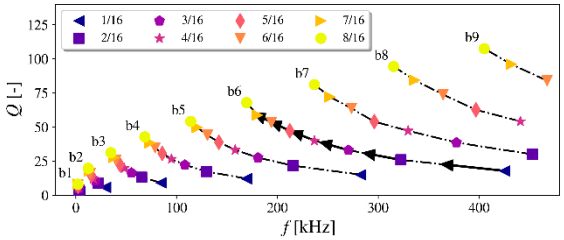

Fig. 3. Quality factors of the beam vibrational modes of the spectrum in fig. 2. The aspect ratio of the resonator is indicated by different marker symbols shown in the legend.

A similar analysis can be performed for non-beam modes. A comparison of the results reveals that the quality factor of any vibrational mode is well predicted by

$$Q = 0.23\,\beta^{0.45}, \qquad (3)$$

where β is a generalized Reynolds number.

Conclusion

We have presented a modelling approach for the FSI of MEMS resonators with non-beam geometries. The method mitigates scale mismatches that are inherent in the modelling of MEMS-FSI by combining a boundary integral fluid flow representation with plate solid mechanics. We use this approach to study the spectral response of non-slender resonators in water. The results show that the quality factor of different modes can be predicted by a generalized Reynolds number. We anticipate that the presented methods and results will play a vital role in the development of novel MEMS resonators with non-conventional geometries.

References

[1] Ho, C.-M. & Tai, Y.-C. Micro-Electro-Mechanical-Systems (MEMS) And Fluid Flows. Annual Review of Fluid Mechanics 30, 579–612 (1998)

[2] Kucera, M. et al. Characterisation of multi roof tile-shaped out-of-plane vibrational modes in aluminium-nitride-actuated self-sensing micro-resonators in liquid media. Applied Physics Letters 107, 53506 (2015).

[3] Gesing, A., Platz, D. & Schmid, U. A numerical method to determine the displacement spectrum of micro-plates in viscous fluids. Computers & Structures 260, 106716 (2022).

[4] Gesing, A., Platz, D. & Schmid, U. Viscous fluid–structure interaction of micro-resonators in the beam–plate transition. Journal of Applied Physics 131, 134502 (2022).

DOI 10.5162/SMSI2023/C6.2

Optimised FEM Simulation of Automated Acoustic Non-Destructive Testing of Spot Welds

Philipp Sachs[1], Reinhard Klambauer[1], Stefan Wunderl[2], Tobias Hötzer[2], Wolfgang Rohringer[2], Alexander Bergmann[1]
[1] Technische Universität Graz, Inffeldgasse 33/I, A - 8010 Graz,
[2] XARION Laser Acoustics GmbH, Ghegastrasse 3, A - 1030 Wien
sachs@tugraz.at

Summary:
Resistance spot welding is the prevailing technology used to join metal sheets. To guarantee weld strength and prevent structural failure, reliable quality control tests are indispensable. In an effort to automise the predominantly manually performed inspection, novel methods for automated weld spot inspection need fast simulation models with reasonable accuracy for optimisation. This work describes the process by means of a multiphysical FEM simulation of a spot weld measurement procedure. Various simulation approaches were used to obtain the best matching results with experimental data.

Keywords: Non-destructive Testing, Acoustic, Spot Weld, Simulation, Optical Microphone

Introduction

While spot welding processes are usually fully automated, the pre-dominantly used ultrasonic quality inspection is generally performed manually with handheld devices. This is associated with high labour costs and inspection results, which are prone to human errors. Consequently, car manufacturers have sought to automate this inspection process since years. The reason robot-automated testing solutions are not standard yet is related to the fact, that conventional ultrasonic testing technologies are contact-based and require a liquid coupling agent or physical contact with the weld surface itself. [1] Besides being sensitive to surface conditions like tool-imprints or roughness, such probes also require sub-mm lateral positioning, exact angular alignment and accurate contact-pressure in order to provide reliable results. [2]

A promising novel approach for automated weld-spot inspections is the combination of laser-excited ultrasound and an optical microphone, termed Laser Excited Acoustics (LEA). Typically, with LEA a contact-free scanning procedure is applied to do inspection. [3] Along the scan path, the excitation laser is pulsed on the surface, generating an impulse-like ultrasonic shockwave through thermoelastic expansion, see Fig. 1. For thin metal sheets typically used in car manufacturing, the laser excitation generates lamb waves. These waves propagate through the metal sheets and are influenced by the weld-spot geometry. Subsequently, for each laser pulse, the leaky lamb waves can be captured in air with the optical microphone at a certain distance from the excitation position. The results of LEA can be used to extract weld-spot parameters such as the nugget diameter. This work describes the setup and optimisation of a multiphysical FEM simulation model of the LEA measurement procedure. With the derived simulation model, valuable insight in the dependency of the measured signal to the experimental setup and material parameters can be gained without the need of time-consuming sample preparation and measurements.

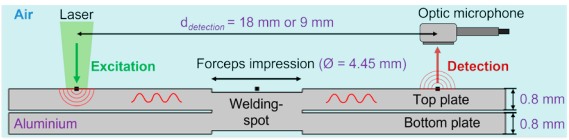

Fig. 1. 2D view of the spot weld setup with laser as optical excitation and optical microphone as detector

Simulation

For the FEM simulation the software "COMSOL Multiphysics" is used to simulate the propagating mechanical waves in the plates joint by spot welds. In this process, the interfaces "Solid Mechanics" and "Pressure Acoustics" are used to simulate the interaction between the mechanical waves in the plates and the pressure acoustics in air, for parameters see Fig. 1. With a parameter sweep and a time dependent solver the resulting signals are determined. To be

more memory and speed efficient, an iterative solver is used, instead of a direct solver. With these settings the optimised simulation should achieve a similar result as the experiment. To achieve a time optimised simulation, simplifications are used to reduce the simulation time. All applied simplifications have to retain a certain level of accuracy. Therefore, the following methods were tested: Different excitation/detection method, Pressure/displacement similarity, Geometry changes.

Results

Similar to the experiment, the 2D simulation captures the pressure in air at the detection spot. Due to the large processing and memory usage, the 3D simulation instead is reduced to capture only the displacement of the top-plate. To prove, that there is only a small difference in the results between the captured signals in air and on the surface of the top-plate, an additional simulation was used for confirmation.

In Fig. 2 profile curves, which represent the detected and processed signals, with a variety of the mentioned simplifications are shown. For all 3D simulations a smaller bottom-plate has been used to reduce the geometry. In addition to that, the sensor's field of view for signal detection for all simulations has been simplified as a point detection. The 2D mechanical (mech.) coupled, 3D mech. $d_{detection}$ = 18 mm and 3D mech. $d_{detection}$ = 9 mm simulations use a mechanical point excitation on the top plate surface, as a simplified representation of the laser beam. To see the influence of the distance between the excitation and detection a simulation with a smaller spacing ($d_{detection}$ = 9 mm) was performed. With the comparison of these two profile curves, it can be seen, that the difference is marginal and consequently a small change of distance is negligible. The fastest simulation was achieved for plane wave excitation and multiple detection points, which has the advantage to capture all detected signals in one simulation without changing the detection/excitation position.

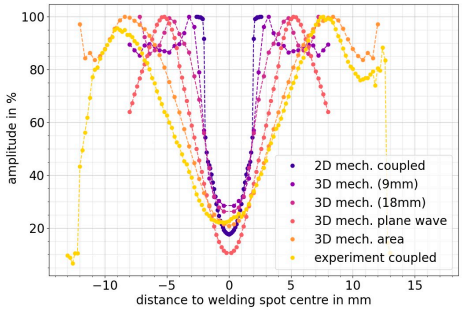

Fig. 2. Comparison of the simulated profile curves and the experiment profile curve at a welding spot diameter of 4.45 mm

For the 3D mech. area excitation simulation, which has the most similarities to the laser excitation, an area was used for the excitation. Due to the extended excitation area, the model symmetry could not be fully exploited and the model size had to be slightly increased.

In comparison to the experimental data the simulated profile curves are narrower. In course of this the 2D simulation reaches and stays at its maxima at the welding spot diameter. The 3D simulations all show a similar profile curve shape, which has a minimum in the middle, two maxima and an attenuation after the maxima. Notable is, that the distance between the two maxima of the profile curves change drastically with the change of the excitation method. Furthermore, it can be observed, that the profile curve of the experiment data is not symmetrical. The slight deviations of each side could be caused by the not perfectly symmetric welding spot and the surface conditions of the experiment.

Tab. 1: Comparison simulation runtime

Simulation type	Approx. runtime
2D mechanical and coupled	12 h to 14 h
3D mechanical, plane wave excitation	1 h to 2 h
3D mechanical $d_{detection}$ = 18mm	12 h to 16 h
3D mechanical $d_{detection}$ = 9mm	7 h to 10 h
3D mechanical, area excitation	16 h to 20 h

Conclusion

The best fitting profile curve to the experiment can be obtained by the simulation with the area excitation method, which has a longer runtime, as seen in Tab. 1 and uses more memory. Nevertheless, due to the simultaneous usage of the optimisations: excitation/detection method (area excitation / point detection), displacement similarity and geometry changes (minimised bottom plate), the experiment profile curve can be simulated in a reasonable time with limited processing resources. This allows for further studies on the dependencies on geometry and material parameters.

References

[1] Ji C., Na J.K., Lee Y., Park Y., Kimchi M., Robot-assisted non-destructive testing of automotive resistance spot welds, *Weld World 65*, 119–126 (2021); doi: 10.1007/s40194-020-01002-1

[2] Buckley J., Servent R., Improvements in Ultrasonic Inspection of Resistance Spot welds, *The British Institute of Non-Destructive Testing, 73-77* (2009); doi: 10.1784/insi.2009.51.2.73

[3] Brauns M., Lücking F., Rohringer W., Fischer. B., Single-sided contact-free ultrasound inspection of aerospace composites, *Forum Acusticum*, 49-50 (2020); doi: 10.48465/fa.2020.0993

DOI 10.5162/SMSI2023/C6.3

Theoretical Model and Simulation of a 3D Printed Multi-Material Vibration Harvester

Philipp Gawron[1], Thomas M. Wendt[1], Stefan J. Rupitsch[2]
[1] Work-Life Robotics Institute, Offenburg University of Applied Sciences, Offenburg, Germany
[2] Laboratory for Electrical Instrumentation and Embedded Systems, Department of Microsystems Engineering, University of Freiburg, 79110 Freiburg, Germany
philipp.gawron@hs-offenburg.de

Summary:
In this contribution, we present a novel 3D printed multi-material, electromagnetic vibration harvester. The harvester is based on a cantilever design and utilizes an embedded constantan wire within a matrix of polyethylene terephthalate glycol (PETG). A prototype has been manufactured with a combination of a fused filament fabrication (FFF) printer and a robot with a custom-made tool.

Keywords: energy harvesting; vibration; 3D printing; multi-material; cantilever

Introduction

Energy harvesting provides a sustainable way to power wireless sensor nodes (WSN) [1]. 3D printed energy harvesters offer the possibility to manufacture application specific harvester geometries and sizes [2]. Printing multiple materials has been utilized in the field of triboelectric harvesters [3]. 3D printing multiple materials has not been researched regarding electromagnetic vibration harvesters yet [2]. In this contribution, we propose a 3D printed cantilever made of PETG and an embedded constantan wire for electromagnetic energy harvesting.

Methods and Materials

A cantilever-geometry (clamped-free) was applied for the harvester. The dimensions are shown in Fig. 1. The red area was clamped while the green area was the free tip. The cantilever was analytically modelled as a layered Euler-Bernoulli-beam with tip mass (green area = tip) and external excitation.

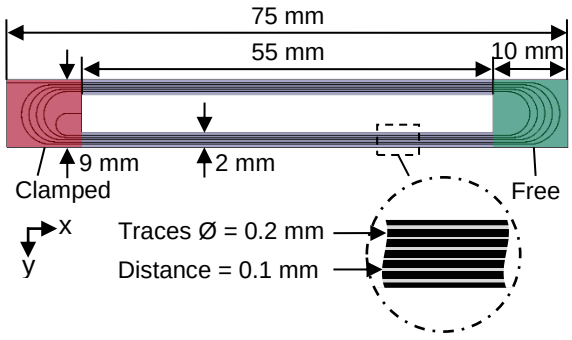

Fig. 1. Geometry and dimensions of the cantilever with embedded wire.

The equation of motion can be expressed as [4], [5]:

$$\sum_{j=1}^{s} E_j I_j \, w^{IV} + \sum_{j=1}^{s} \rho_j A_j \, \ddot{w} = W_0 \sin(\Omega t) \qquad (1)$$

With layer j, number of total layers s, Young's modulus E, deflection w, density ρ, area A, ambient amplitude W_0, excitation angular frequency Ω and time t, respectively. The moment of inertia I can be calculated with the parallel axis theorem [4]:

$$I_j = I_{y_j} + z_{s_j}^2 A_j \qquad (2)$$

The cantilever features a height of 1 mm and was printed via FFF with PETG. A constantan-wire (Ø 0.2 mm, 0.1 mm distance between traces, 5 turns) was embedded during the print with a custom-made tool and a KUKA Agilus KR 6 R900-2. A height of 1 mm was chosen in order to achieve a low resonance frequency, while still allowing the wire-embedment. Low frequencies offer more energy [6]. The composite layer was simplified for calculation and assumed as a homogenous layer as shown in Fig. 2.

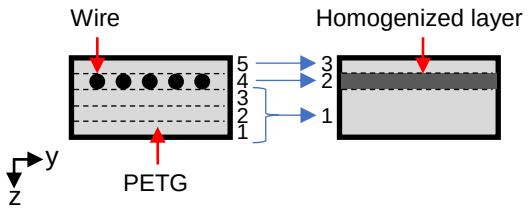

Fig. 2. Cross section of cantilever, (left) printed layers, (right) analytical layer-numbers with homogenized layer.

We combined the Young's modulus and density of the wire and PETG-matrix by the corresponding volume fraction in the layer. The displacement *w*(*x*,*t*) in z-direction is given [5]:

$$w(x,t) = [A \cdot \cos(\kappa x) + B \cdot \sin(\kappa x) + C \cdot \cosh(\kappa x) + D \cdot \sinh(\kappa x)] \cdot W_0 \sin(\Omega t) \quad (3)$$

With the boundary conditions and (3), the linear system of equations can be solved. For non-trivial solutions the determinant of the system has to be zero [5]:

$$1 + \cos(\kappa_i l)\cosh(\kappa_i l) + \varepsilon\kappa_i l[\cos(\kappa_i l)\sinh(\kappa_i l) - \sin(\kappa_i l)\cosh(\kappa_i l)] = 0 \quad (4)$$

with the length *l*, the mass-ratio ε between tip mass and cantilever and the variable κ [4], [5]:

$$\kappa^4 = \omega^2 \frac{\sum_{j=1}^{s} \rho_j A_j}{\sum_{j=1}^{s} E_j I_j} \quad (5)$$

From (4), the eigenvalues can be derived by searching for zero points as shown in Fig. 3. The resulting angular frequency can be calculated with [4], [5]:

$$\omega_i = \frac{\kappa_i^2}{l^2} \sqrt{\frac{\sum_{j=1}^{s} E_j I_j}{\sum_{j=1}^{s} \rho_j A_j}} \quad (6)$$

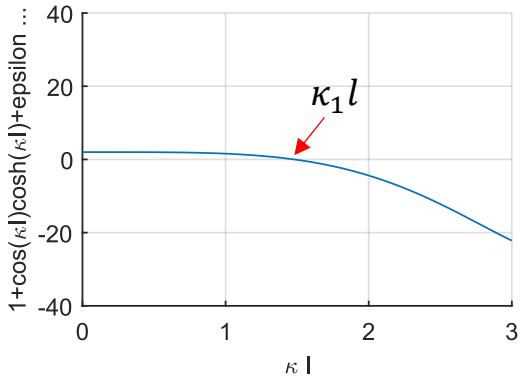

Fig. 3. Frist eigenvalue of the cantilever with tip-mass

Results and Discussion

Utilizing equation (6) an angular frequency of 261.5 s^{-1} and a resonance frequency of 41.6 Hz was calculated for the first resonance frequency. The simulation of the embedded wire-structure in COMSOL showed a resonance frequency of 37.7 Hz. A simplified simulation with a homogenized plate-material for the multi-material-layer showed 41.7 Hz which is in good agreement with the result of equation (6). Fig. 4 depicts the specimen after embedding the wire during the printing-process. Magnets will be added around the moving area of the cantilever as shown in Fig. 5 in order to electromagnetically harvest energy from mechanical vibrations.

Fig. 4. Cantilever during printing-process after embedding the wire in layer 4.

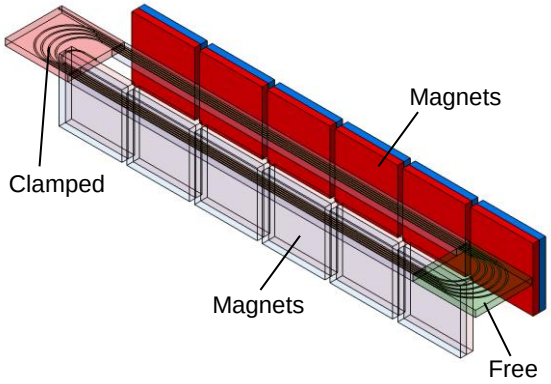

Fig. 5. Cantilever with embedded wire and magnets.

Conclusion

A theoretical model, simulation results and the fabrication of a multi-material 3D printed cantilever have been shown. Future work will focus on the characterization of the harvester and the electrical energy output.

References

[1] H. Landaluce, L. Arjona, A. Perallos, F. Falcone, I. Angulo, and F. Muralter, A Review of IoT Sensing Applications and Challenges Using RFID and Wireless Sensor Networks, *Sensors (Basel, Switzerland)*, vol. 20, no. 9, (2020); doi: 10.3390/s20092495.

[2] P. Gawron, T. M. Wendt, L. Stiglmeier, N. Hangst, and U. B. Himmelsbach, A Review on Kinetic Energy Harvesting with Focus on 3D Printed Electromagnetic Vibration Harvesters, *Energies*, vol. 14, no. 21, (2021); doi: 10.3390/en14216961.

[3] R. I. Haque, P.-A. Farine, and D. Briand, 3D Printed Materials Based Triboelectric Device for Energy Harvesting and Sensing, *Proceedings*, vol. 1, no. 4, (2017), doi: 10.3390/proceedings1040580.

[4] D. Gross, W. Hauger, J. Schröder, W. A. Wall, and J. Bonet, *Engineering Mechanics 2*. Berlin, Heidelberg: Springer Berlin Heidelberg, (2018), doi: 10.1007/978-3-642-12886-8.

[5] D. Gross, W. Hauger, and P. Wriggers, *Technische Mechanik 4: Hydromechanik, Elemente der Höheren Mechanik, Numerische Methoden,* 10th ed.: Springer Vieweg, (2018), doi: 10.1007/978-3-662-55694-8.

[6] K. Solai, M. Chandrasekaran, and J. D. Rathnasami, Miniaturized but efficient cantilever beam vibration energy harvesters for wireless bridge health monitoring applications, *Arch Appl Mech*, vol. 91, no. 12, pp. 4609–4619, (2021), doi: 10.1007/s00419-021-02058-1.

DOI 10.5162/SMSI2023/C6.4

Simulation of Damping Effects in Irregularly Perforated MEMS Devices by Physical Compact Modeling

Friederike Michael, Gabriele Schrag,
Technical University of Munich, Chair of Physics of Electrotechnology
Theresienstraße 90, 80333 Munich, Germany
friederike.michael@tum.de

Summary:
Accurate modeling of damping effects in high-end MEMS devices is a major challenge due to low feature sizes and complex device geometries. By applying a finite network approach with specially derived compact models, we are able to simulate structures with varying perforation patterns and account for the impact of the transition regions between differently perforated areas. Simulations of exemplary test structures with different perforation sizes and patterns prove the feasibility of our approach, which perspectively improves the accuracy of damping estimation beyond state of the art.

Keywords: squeeze film damping, transition flow, MEMS, Kirchhoffian networks, damping ratio

Introduction

Squeeze film damping (SQFD) significantly determines the dynamic performance of various microelectromechanical systems (MEMS), such as micro switches or accelerometers. Their moving parts are usually highly perforated due to etching steps during the manufacturing process and, more importantly, to precisely adjust damping to achieve the desired performance. State-of-the art MEMS devices exhibit therefore a complex, laterally large-scale device geometry with varying feature sizes and perforation patterns [1].

However, a reliable and fast way to accurately predict damping in such large-scale microstructures is still an issue, since most modeling approaches consider uniformly perforated plates only (e.g. [2] [3]), which does not apply to complex MEMS designs with multiple perforation patterns. In this respect, it is also vital to pay special attention to regions where different perforation patterns are adjoining, which has a non-negligible impact on the overall damping .Additionally, small feature sizes as well as packaging under low-pressure conditions require the implementation of geometry-dependent corrections, which account for deviations from continuum-flow-based models.

We present an approach enabling fast, but yet physics-based simulation of distributed damping effects in arbitrarily perforated MEMS devices by a compact modeling approach based on generalized Kirchhoffian networks (GKNs) [4] and apply it to representative test structures.

Modeling Approach and Simulation Concept

Fluidic damping strongly depends on the overall device geometry as well as on the size, shape and density of the perforations. To analyze spatially distributed damping effects the structure is discretized into several elements by a mesh, comparable to FEM, but using a flux-conserving finite network consisting of respective elements, which are classified into groups labeled as part of the boundary, of a perforation or of the non-perforated section of the plate, depending on their location.

In order to model the fluidic damping underneath the plate, we use the modified Reynolds equation with correction factors for rarefied gases at higher Knudsen numbers. It is represented by an equivalent network containing a fluidic resistance, a fluidic capacitance and the varying gap height as the source for the gas flow, see Fig. 1. To model fluid flow into, through and out of a single perforation we use three separate models. The fluidic “channel” resistance has the Hagen-Poiseuille equation as underlying model, with adaptions for square perforations. For flow into and out of the perforations the models introduced by [5] are applied. The outflow at the structure’s borders is modeled with an additional fluidic “boundary” resistance based on the equations derived in [5].

The resulting model of the entire structure is represented by a network with the above-described models attached to its nodes, which enables to read out and visualize the pressure at each node as well as the volume flow rate from one node to another. The models are written in Verilog A,

which allows implementing the GKN model into a standard circuit simulator.

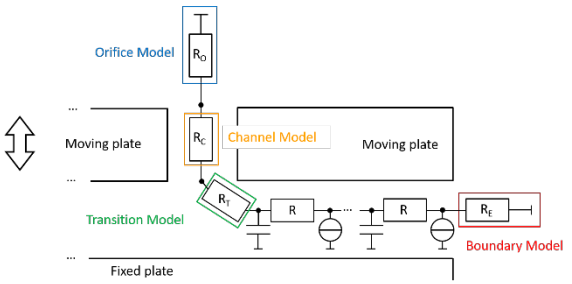

Fig. 1. Cross-sectional schematic of a vertically moving plate with resistances, sources and capacitors modeling fluid flow at the respective nodes.

This offers several advantages regarding the simulation of complex MEMS structures. Aside from the possibility to add custom models, it enables the coupling of damping models to GKN models of other energy domains and electric circuitry. Most importantly, these tools are designed to solve a large number of ordinary differential equations (i.e. our distributed finite network) within a minimum of time, which increases simulation speed significantly.

Simulation Results

The feasibility of the presented simulation concept is demonstrated for test structures with varying perforation patterns, as depicted in Fig. 2b. They consist of a thick perforated plate with two differently sized square perforations arranged in a chessboard-like manner for design convenience and to ease fabrication. However, the approach is also applicable to a design with perforations of varying size and shape, which are randomly scattered over the structure's surface.

The damping ratio is calculated for a pressure range of 1 Pa to 300 kPa. The results are presented in Fig. 2a along with the results of two structures perforated evenly with large and small square-sized perforations, respectively. The pressure-dependent damping ratio for the "chessboard" reveals to be slightly higher than those for the large square holes and lower than those for the small square holes. For pressures lower than 1000 Pa, the difference between the damping ratios remains almost constant. At higher pressure values the damping for the structure with the small holes increases notably when compared to the other two test structures. This shows that impact of the small holes in the "chessboard" is mostly compensated by the large holes, which meets the physically expected result. Newly fabricated test structures are on their way to be characterized via laser Doppler vibrometry in order to validate the simulation. Results will be presented at the conference.

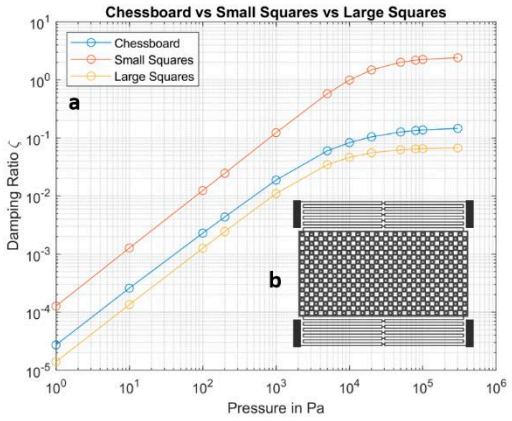

*Fig. 2 **a)** Damping ratio ζ of three differently perforated, exemplary test structures for pressures from 1 Pa to 300 kPa, with large square perforations (yellow), small squares (red) and "chessboard" perforation as depicted in Fig. 2b (blue). **b)** Test structure connected to folded cantilever springs with two differently sized square perforations, assembled in a checkered manner.*

It is noteworthy, that the simulation results for the test structures with around 650 perforations each are obtained within seconds, which shows the efficiency of our approach and the potential to apply it to more complex and large-scale devices as described e.g. in [1].

Outlook

The massive save of simulation time as well as the customization of models to specific requirements opens up new perspectives for accurate damping prediction in microsystems design beyond the current state of the art.

References

[1] J. Classen *et al.,* "Evolution of Bosch Inertial Measurement Units for Consumer Electronics," in *2020 IEEE SENSORS*, 2020, pp. 1–4, doi: 10.1109/SENSORS47125.2020.9278815.

[2] T. Veijola and P. Raback, "Methods for Solving Gas Damping Problems in Perforated Microstructures Using a 2D Finite-Element Solver," *Sensors*, vol. 7, no. 7, pp. 1069–1090, 2007, doi: 10.3390/s7071069.

[3] M. Bao, H. Yang, Y. Sun, and Y. Wang, "Squeeze-film air damping of thick hole-plate," *Sensors and Actuators A: Physical*, vol. 108, 1-3, pp. 212–217, 2003, doi: 10.1016/S0924-4247(03)00263-2.

[4] G. Schrag and G. Wachutka, "System-Level Modeling of MEMS Using Generalized Kirchhoffian Networks - Basic Principles," in *Advanced micro et nanosystems*, vol. 10, *System-level modeling of MEMS*, T. Bechtold, G. Schrag, and L. Feng, Eds., Weinheim: Wiley-VCH, 2013, pp. 19–51.

[5] R. Sattler, "Physikalisch basierte Mixed-Level Modellierung von gedämpften elektromechanischen Mikrosystemen," Technische Universität München. [Online]. Available: https://mediatum.ub.tum.de/623347

DOI 10.5162/SMSI2023/C71

C7.1 Introduction to Digital Calibration Certificates

S. Hackel, Physikalisch-Technische Bundesanstalt (PTB), Braunschweig (Germany)

The short paper of this contribution is not available

DOI 10.5162/SMSI2023/C71

C7.1 Introduction to Digital Calibration Certificates

S. Hackel, Physikalisch-Technische Bundesanstalt (PTB), Braunschweig (Germany)

The short paper of this contribution is not available

Digital Calibration Certificate as Part of a Calibration Eco-system

DOI 10.5162/SMSI2023/C7.2

Sami Koskinen, Director, Digital Transformation[1]
[1] Beamex OY AB, Ristisuonraitti 10, 68600 Pietarsaari, Finland
sami.koskinen@beamex.com

Summary:
Together with a consortium of partners, Beamex is driving the development of a digital calibration certificate (DCC) solution that will provide a standardized method to record and share calibration data. This data can then be exchanged via a DCC exchange hub, which provides stakeholders with full control over their calibration data. A DCC-based calibration ecosystem will accelerate innovation, improve efficiency, increase safety, and ultimately lead to a safer and less uncertain world for all.

Keywords: Calibration, digitalization, standardization, traceability, metrology, digital calibration certificate

Background, Motivation and Objective

As we enter the fourth industrial revolution, digital transformation is affecting most industries, and the process industry is no exception. While many process-industry players have begun their digitalization journey, for example by using a digital calibration solution with a central management system that integrates with existing ERP systems, external stakeholders like contractors still largely rely on paper-based certificates, resulting in a half-baked digital transformation.

Together with partners Boehringer Ingelheim, Orion, Bayer, PTB, Aalto University, VTT MIKES, Siemens, Vaisala, Perschmann Calibration, Testo, and Lahti Precision, Beamex has demonstrated a proof of concept (PoC) for a fully digitalized environment for calibration data generation – the digital calibration certificate, or DCC. This PoC solution is considered an effective and user-friendly method for executing calibration data exchange between stakeholders [1].

What is a DCC and why is it needed?

Paper calibration certificates are familiar, feel safe, and are a format everyone can understand. However, with the reliance on paper comes the possibility for human error, particularly in a multi-stage process like calibration. Paper certificates also negatively affect traceability, and analyzing the data from a single device to make data-driven decisions is extremely time-consuming. For process industries that use thousands or tens of thousands of devices, this quickly becomes impractical.

Calibration certificates have traditionally been used in the one-to-one relationship between the instrument owner and the calibration service provider, with each of these parties having multiple such relationships. Today's calibration systems, however, involve multiple players, with process industry customers liaising with multiple instrument manufacturers, calibration service providers, and accredited laboratories. This creates a vast and unwieldy network where data sharing, traceability, and even maintaining compliance can be exceptionally challenging, particularly for globally operating customers with tens or even hundreds of sites across different countries.

A DCC changes the game by introducing machine-readable digital calibration certificates that can be easily accessed in a repeatable and non-error prone way and information can be transferred automatically in digital format between different these stakeholders.

The MP3 of the process industry world

One way to understand what a DCC represents is to think of the MP3 music file format, which is simply a way of encoding music that makes it easily shareable and allows it to be played on a range of devices. A DCC is the MP3 of the process industry world: a standardized digital file format that is easily shared between organizations and can be read by machines.

Beamex and its consortium partners believe that the cloud is the best method for sharing DCC data as it replaces point-to-point connections between an organization and external parties, which are time consuming and costly to set up, maintain, and change. A cloud-based system also makes scaling up far easier without the need for investment in IT infrastructure.

A fit-for-purpose ecosystem for process industries

In industrial environments, process instruments are calibrated in the field, sometimes in extremely hostile conditions, while reference standards are calibrated against manufacturers'

specifications. This is markedly different from accredited environments like laboratories, which are clean, safe, calm environments where calibration is much easier to perform and control.

The DCC ecosystem of the future, which will provide a standardized way to gather and exchange information, needs to be developed to serve the unique calibration needs of the process industry if it is to be successfully adopted and to allow it to offer the level of traceability required; it also needs to support both process instrument and reference standard applications.

Building a calibration ecosystem for Industry 4.0

Digitalization and the increasing level of automation in process industries mean that the sheer volume of calibration data is becoming unmanageable with current solutions, ramping up the pressure to transition to a new kind of calibration ecosystem.

To put things into perspective, the global market for calibration services is expected to grow to close to USD 9 billion by 2027, by which time service providers are expected to be delivering 45 million calibration certificates per year. Assuming that service providers are responsible for 50% of all calibrations delivered, then by 2027 there will be 90 million calibration certificates moving between the various stakeholders.

A DCC-based calibration ecosystem simplifies the situation massively, providing a standardized method to record and exchange calibration data and breaking down the silos that exist today.

With a standardized methodology in place, process industry customers, regulators, system providers, instrument manufacturers, calibration service providers, accredited laboratories, and national metrology institutes can ‘sit around the same table’, in this case a common DCC exchange hub.

This hub would act as the central information exchange that the various stakeholders can connect to and use to send and receive relevant data. The DCC exchange hub concept provides stakeholders with full control over their calibration data, allowing them to decide how it is used and who can access it.

In addition to critical calibration data, stakeholders can also use the hub to access and share knowledge for the common good, such as established quality standards or calibration recommendations.

An innovation enabler

In addition to standardization and easier information exchange, a fit-for-purpose calibration ecosystem based on DCCs brings with it a host of other benefits:

- It makes data analysis easier and supports the creation of digital twins that can be used to identify efficiency and safety improvements.
- It supports digital traceability and smarter, data-based decision-making.
- It makes management of calibration references and instruments easier and more efficient because everything is in digital format.
- It allows process industry customers to follow their preferred calibration processes rather than mandating a specific way of working.

Join the movement

As the saying goes, a problem shared is a problem halved. Together with its partner network, Beamex has been driving the development of a PoC for the DCC concept for four years. Future work will include executing a new PoC that will examine a complete metrological traceability chain from the SI to the end user process, exploring new possibilities to exploit DCC data, and validating business opportunities.

Only by pooling knowledge and expertise can we overcome the challenges that are limiting DCC implementation. We welcome the opportunity to discuss how different organizations can contribute to the successful adoption of this much-needed solution, which will accelerate innovation, improve efficiency, increase safety, and ultimately lead to a safer and less uncertain world for all.

References

[1] J. Nummiluikki, S. Saxholm, A Kärkkäinen, S. Koskinen, Digital Calibration Certificate in an Industrial Application, *Acta IMEKO* Vol. 12, No. 1 (2023). doi: https://doi.org/10.21014/actaimeko.v12i1.1402

[2] K Riska, Digital Calibration Certificate as Part of an Ecosystem, Degree Thesis, Industrial Management and Engineering, M.Eng. Novia University of Applied Sciences, Vaasa, Finland. Retrieved from: https://www.theseus.fi/handle/10024/749631

DOI 10.5162/SMSI2023/C7.3

C7.3 Creating Machine Interpretable DCC

B. Gloger, Physikalisch-Technische Bundesanstalt (PTB), (Germany)

The short paper of this contribution is not available

DOI 10.5162/SMSI2023/C7.3

C7.3 Creating Machine Interpretable DCC

B. Gloger, Physikalisch-Technische Bundesanstalt (PTB), (Germany)

The short paper of this contribution is not available

DOI 10.5162/SMSI2023/C7.4

C7.4 Simulation of Damping Effects in Irregularly Perforated MEMS Devices by Physical Compact Modeling

F. Michael, G. Schrag, Technical University of Munich, München (Germany)

The short paper of this contribution is not available

DOI 10.5162/SMSI2023/C7.4

C7.4 Simulation of Damping Effects in Irregularly Perforated MEMS Devices by Physical Compact Modeling

F. Michael, G. Schrag, Technical University of Munich, München (Germany)

The short paper of this contribution is not available

DOI 10.5162/SMSI2023/D1.1

Qualification of Barkhausen Noise and Eddy Current Based Sensors for Online Monitoring of Strain-Induced α'-Martensite Phase Transformation During Flow Forming

Julian Rozo Vasquez[1,], Bahman Arian[2], Lukas Kersting[3], Werner Homberg[2], Ansgar Trächtler[3], Frank Walther[1]*
[1] Chair of Materials Test Engineering (WPT), TU Dortmund University, Baroper Str. 303, D-44227 Dortmund, Germany
[2] Forming and Machining Technology (LUF), Paderborn University, Pohlweg 53, D-33098 Paderborn, Germany
[3] Fraunhofer Institute for Mechatronic Systems Design (IEM), Zukunftsmeile 1, D-33102 Paderborn, Germany
** Correspondence: julian.rozo@tu-dortmund.de; Tel.: +49 231 755 8535*

Summary:
This study illustrates the sensitivity of Barkhausen noise and eddy current based sensors to monitor the evolution of micromagnetic properties during phase transformation due to plastic deformation of metastable austenitic steel AISI 304L. The phase transformation was carried out on flow formed tubes, under specific thermomechanical conditions to produce local graded areas. The results show a very good potential of both types of sensors to monitor the evolution of magnetic properties during the production process in order to use those signals in closed-loop property-control systems.

Keywords: micromagnetic testing, magnetic Barkhausen noise, eddy currents, flow forming, phase transformation.

Background Motivation and Objective

The production of components by flow forming has gained recently importance mainly in transportation industries [1]. The use of austenitic steel in combination with advanced manufacturing techniques enables the production of high-quality components. During forming of metastable austenitic steel, plastic deformation changes the geometry and microstructure of the workpieces. In particular, phase transformation from metastable austenite to α'-martensite occurs, which modifies the magnetic and mechanical properties [2]. The production of graded components with specific mechanical properties requires the development of closed-loop controlled processes. This entails the use of suitable sensors to monitor the evolution of properties during plastic deformation.

Non-destructive techniques, like micromagnetic testing have been widely used for the detection of the amount of ferromagnetic α'-martensite phase. In different studies, the magnetic Barkhausen noise (MBN) and eddy current analyses have shown a remarkable sensitivity to the changes of the ferromagnetic properties and permeability, respectively. This gives them great potential to be used within closed-loop control systems [3].

The objective of this work is to show the suitability of MBN and eddy currents to perform local measurements of α'-martensite.

Description of Methods and Systems

The specimens for the qualification of the sensors were produced in a PLB 400 spinning machine from Leifeld Metal Spinning GmbH (Ahlen, Germany) by means of flow forming (Fig. 1a). The specimens were manufactured using stainless steel AISI 304L (X2CrNi18-9, 1.4307) seamless tubes, 80 mm outer diameter. The specimens were manufactured cooling to a temperature of about -195°C during the deformation process, on the area marked in red (Fig. 1b). This favors the transformation of metastable austenite into α'-martensite during plastic deformation, according to literature [2].

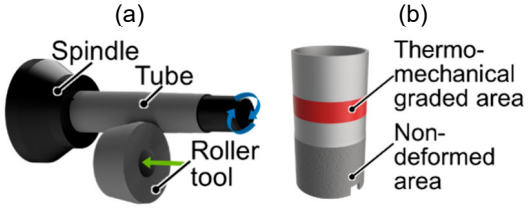

Fig. 1. Specimen manufacture: (a) flow forming process; (b) specimen specifications. The area marked in red contains a higher amount of strain-induced α'-martensite.

On the locally cooled areas, where plastic deformation occurs, a higher α'-martensite fraction is expected. On the area where plastic deformation occurs without cooling (light grey area in Fig. 1b), a less amount of α'-martensite is expected and on the non-deformed areas only austenite is present.

The characterization was carried out by means of a Feritscope FMP30 (Helmut Fischer GmbH, Sindelfingen, Germany), whose measurements are not possible to be transferred and used within a closed-loop control system. However, the measurements are an important tool to establish reference values. MBN and eddy current analysis deliver measurements over the time, that are usable as control signals and can be well correlated and calibrated with the phase transformation phenomena. In this study, the 3MA-II system (Fraunhofer IZFP, Saarbruecken, Germany) and Elotest PL600 (Rohmann GmbH, Frankenthal, Germany) were used to qualify the MBN and eddy currents methodologies, respectively, to monitor the phase transformation.

Results

The measurements were carried on three different lines along the axial position at different angular positions (Fig.2).

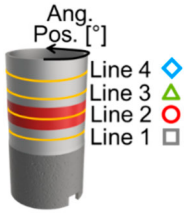

Fig. 2. Detail of measurement points on specimens.

Fig. 3 shows measurements of α'-martensite fraction determined by Feritscope FMP30. These measurements are not online transferable to a controller and are used only as comparison data.

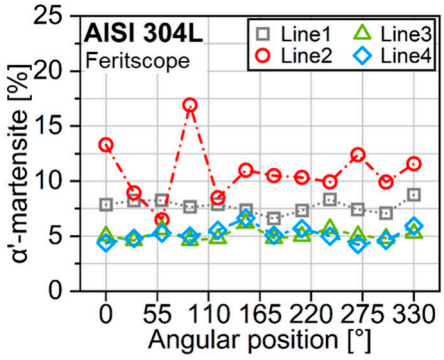

Fig. 3. Graph of strain-induced α'-martensite percentage at different measurement points.

The results show higher amounts of α'-martensite along the line 2. This area was cooled during the forming process, which favors the phase transformation during flow forming. A maximal peak is reached at an angular position of 0° and 80°. The line 1 has the second higher amount of α'-martensite due to the heat transfer direction caused by the movement of the forming tool between line 4 and 3. The deformation process without cooling warms these areas, which hinders the formation of α'-martensite.

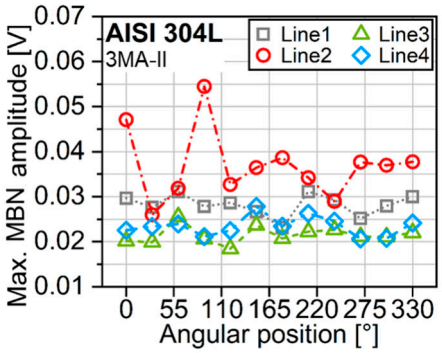

Fig. 4. Graph of maximum amplitude of MBN, measured by 3MA-II system at different points.

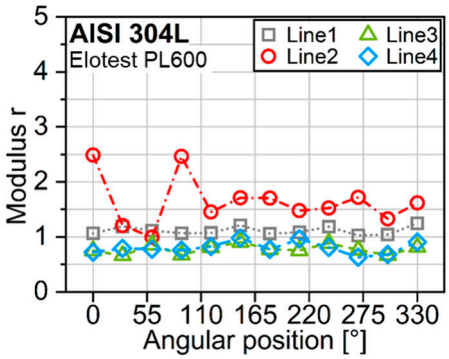

Fig. 5. Graph of the modulus r of the eddy currents method, measured by Elotest PL600 at different points.

The measurements carried out using MBN and eddy current based sensors show a promising sensitivity for applications where the phase transformation must be monitored in time. The sensors detected the phase amount peaks at 0° and around 80°. Both devices allow the transfer of the measured signals to be used in closed-loop control systems.

Acknowledgements: Funded by the German Research Foundation (Deutsche Forschungsgemeinschaft, DFG) – project number 424335026 – within the priority program SPP 2183.

References

[1] D. Marini et al., Flow forming: A review of research methodologies, prediction modes and their applications, *International Journal of Mechanical Engineering and Technology* 7 (5), 285-315 (2016).

[2] G.B. Olson, M. Cohen, Kinetics of strain-induced martensitic nucleation, *Metallurgical Transactions A* 6A, 791-795 (1975).

[3] M. Riepold et al., Model approaches for closed-loop property control flow forming, *Advances in Industrial and Manufacturing Engineering 3 (2021). https://doi.org/10.1016/j.aime.2021.100057*

DOI 10.5162/SMSI2023/D1.2

Sensitivity Analysis of Barkhausen Noise Measurements for Residual Stress Correlation

Sophie Charlotte Stebner[1], Daniel Maier[2], Ahmed Ismail[3], Michael Dölz[1], Boris Lohmann[3], Wolfram Volk[2], Sebastian Münstermann[1]
[1] Integrity of Materials and Structures (IMS), Department of Ferrous Metallurgy (IEHK), RWTH Aachen University, Intzestr. 1, 52072 Aachen, Germany,
[2] Chair of Metal Forming and Casting, TUM School of Engineering and Design, Technical University of Munich, Walther-Meißner-Str. 4, 85748 Munich, Germany
[3] Chair of Automatic Control, TUM School of Engineering and Design, Technical University of Munich, Boltzmann Str. 15, 85748 Munich, Germany
sophie.stebner@iehk.rwth-aachen.de

Summary:
As recent tendencies in the efficient design of forming processes show a clear trend towards property-control, suitable measurement techniques for inline monitoring must be identified and investigated regarding their measurement suitability. Since Barkhausen noise analysis offers a to the microstructural evolution susceptible measurement technique that may allow a correlation to residual stresses using symmetry effects seen in the measurement signal, this work introduces a sensitivity analysis of the available measurement parameter settings and their respective suitability for signal processing.

Keywords: Barkhausen noise analysis, sensitivity analysis, correlation, soft sensor, metal forming

Background, Motivation and Objective

Recent developments in the manufacturing engineering industry show a clear trend towards the development of monitoring techniques for forming processes [1,2]. Especially, the implementation of property-controlled monitoring techniques and thereupon based closed-loop control of the processes, are promised to make the process design more efficient regarding resources, time as well as economic aspects [3,4]. During forming processes, the microstructure undergoes permanent changes which then dictates the components application post forming [5]. Meaning, that for the successful implementation of property-based controls, suitable measurement techniques that detect the microstructural evolution need to be identified and investigated how they may be correlated to the properties of interest. Among many sensor systems, Barkhausen noise (BHN) analysis offers a non-destructive testing technique that is susceptible to a microstructural evolution [6]. However, dependent upon the investigated material, for BHN analysis, suitable measurement parameters need to be investigated. Hence, this work will introduce a sensitivity analysis of measurement settings of the QASS µmagnetic measurement equipment for a P235 TR1 tube steel to find the ideal measurement settings for the derivation of a property-based control.

Description of the New Method

Although, BHN analysis is very susceptible to a microstructural evolution, primary studies of the authors showed that both macrostructural evolution trends in hardness and residual stress state have a notable impact upon the signal intensity of the BHN sensor. As during the forming process the material not only hardens but also shows a significant redistribution of residual stresses, a sole investigation of the signal intensity cannot be recommended. Literature [7] however suggests, that a change in the residual stress state has an influence on the geometric characteristics of the hysteresis curve, which is also seen in the geometry of the QASS µmagnetic measurement signal. Hence, to ultimately be able to quantitatively correlate residual stresses and BHN based upon the geometry and intensity of the signal, an investigation regarding the best measurement settings is introduced. The varied parameters include the amplitude of BHN [mV] quantized in steps of 64 mV as is predefined by the equipment, frequency [Hz] in steps of 100 Hz up to 1.5 kHz, Amplification from 500:1 up to 5000:1 in steps of 100, sample rate from 30 kHz up to 4 MHZ also as predefined by the equipment and oversampling from “no oversampling” up to 64:1 during measurement. All testing was done on unbent P235 TR1 tube and results were investigated regarding their suitability for evaluation of signal intensity as well as

symmetry characteristics. Symmetry characteristics were determined in defining symmetry factors (SF) for the hill shaped signal, giving information on whether the signal is left- or right-skewed according to eq. (1).

$$S = \frac{t_{max} - t_{center}}{l} \quad (1)$$

Where l is the bottom length of the BHN hill, t_{max} is the x-coordinate of the maximum point and t_{center} the x-coordinate of the middle point. For $S = 0$, the hill is symmetrical, $S < 0$, the hill left-skewed and respectively $S > 0$, right-skewed. Thus, this work lies an important foundation for the quantitative correlation of signal intensity and signal symmetry to the residual stress state.

Results

During the systematic variation of the different measurement settings, it was observed that a variation of the oversampling as well as sample rate in most combinations led to very poor measurement results on the P235 TR1 where data processing was made impossible. Furthermore, setting the BHN amplitude to higher energies than 466 mV led to magnetic saturation, meaning the intensity of the signal plateaued. Hence, amplitudes above 466 mV are also ruled out for further processing. The parameter frequency showed, that with an increase, the signal intensity led to good results, however the detected Barkhausen hill symmetry became very irregular, leaving the authors to exclude high frequencies as that would require the signal to be smoothed strongly, thus distorting the measurement result significantly. The higher the chosen amplification, the higher the signal intensities, however at high amplifications the SF evaluation showed that both SF left and right did not differ much from zero, making it a poor choice for correlation to residual stresses. The most robust and steady results using the prototype sensor from QASS µmagnetic were ultimately identified to:

Tab. 1: Measurement settings for future testing

Amplitude [mV]	Frequency [Hz]	Sample rate [MHz]	Over sampling	Amplification
255	100	4	8	2000

Fig. 1 shows a characterization along the (a) the in- and (b) outside of a formed tube. It can be seen that the results are robust and differ from each other along the measurement points, making a correlation to residual stresses possible.

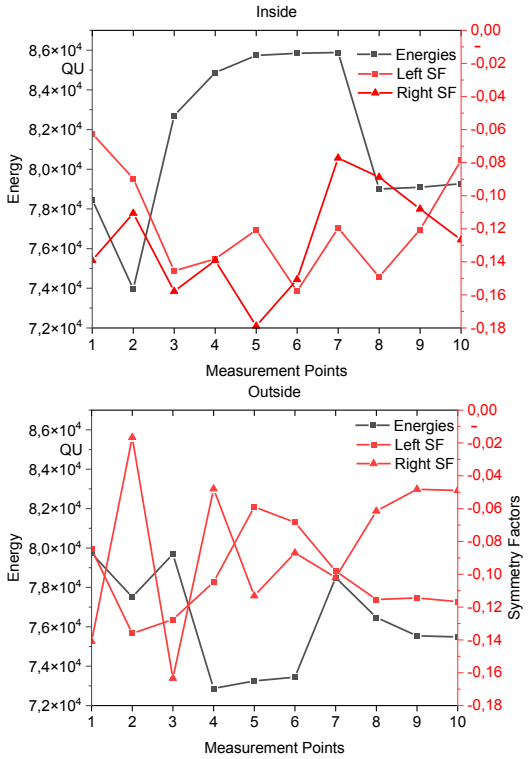

Fig. 1. Development of energies in QASS Units [QU] and symmetry factors of left and right BHN hills along (a) inside and (b) outside of a bent tube.

References

[1] A. Awasthi, K. K. Saxena, V. Arun, Sustainable and smart metal forming manufacturing process, *Materials Today: Proceedings* 44, 2069–2079 (2021); doi: 10.1016/j.matpr.2020.12.177.

[2] A. Kumar, A. Das, A nonlinear process monitoring strategy for a Metal Forming process, *Materials Today: Proceedings* 59, 368–372 (2022); doi: 10.1016/j.matpr.2021.11.327.

[3] J. M. Allwood, S. R. Duncan, J. Cao, P. Groche, G. Hirt, B. Kinsey, T. Kuboki, M. Liewald, A. Sterzing, A. E. Tekkaya, Closed-loop control of product properties in metal forming, *CIRP Annals* 65, 573–596 (2016); doi: 10.1016/j.cirp.2016.06.002.

[4] J. A. Polyblank, J. M. Allwood, S. R. Duncan, Closed-loop control of product properties in metal forming: A review and prospectus, *Journal of Materials Processing Technology* 214, 2333–2348 (2014); doi: 10.1016/j.jmatprotec.2014.04.014.

[5] E. Hornbogen, H. Warlimont, *Metallkunde: Aufbau und Eigenschaften von Metallen und Legierungen*. Springer, Berlin, Heidelberg; 2001.

[6] T. Le Manh, J. A. P. Benitez, J. H. E. Hernández, J. M. Hallen López, eds., *Barkhausen noise for non-destructive testing and materials characterization in low carbon steels*. Woodhead Publishing an imprint of Elsevier, Duxford, Cambridge, MA, Kidlington; 2020.

[7] M. Suliga, K. Chwastek, P. Pawlik, Hysteresis loop as the indicator of residual stress in drawn wires, *Nondestructive Testing and Evaluation* 29, 123–132 (2014); doi: 10.1080/10589759.2013.858717.

DOI 10.5162/SMSI2023/D1.3

Real-Time Microstructure Characterization using Eddy Current-based Soft Sensors

Sebastian Hütter[1], Gerhard Mook[1], Thorsten Halle[1]
[1] Institute of Materials and Joining Technology, Otto-von-Guericke Universität, Universitätsplatz 2, 39106 Magdeburg, Germany
sebastian.huetter@ovgu.de

Summary:
Non-destructive testing methods enable not only quality assurance but also material characterization. This is often done in offline application or as an intermediate step, in-line applications in close integration with manufacturing processes are more complex. By using a model integrated into a soft sensor on top of eddy current impedance measurement, we show that it is possible to obtain useful material data using comparatively simple sensor hardware in real time.

Keywords: eddy current, material characterization, in-process measurement, soft sensors, process technology

Introduction

In advanced manufacturing processes, often not only the shape but some microstructural properties of the workpiece are critical quality targets. The use of eddy-current measurement even for minor microstructural changes has previously been demonstrated [1]. To allow for in-process control of such properties, they must be measured in real time and with sufficiently low latency in often adverse conditions, such as in close proximity to tools, hot workpieces, cooling media, etc. It is rarely possible to suppress or control for all of these interferences. Hence, a form of sensor data processing is desired that transforms measured signals to useful outputs that are less sensitive to disturbances. The use of model-based soft sensors is one way to achieve this. This article presents a design of a soft sensor based on an eddy current system and shows its implementation in real-time application. Additionally, we briefly discuss practical use of this system in a tangential profile ring rolling process [2,3].

Measurement Hardware

Eddy current measurements were carried out using the analog frontend of an *EddyCation* testing system coupled with custom signal processing software. A two-coil probe with separate transmitter and receiver coils was used in conventional transformatoric setup. Both coils were housed in a 10 mm ferrite core as a field guide, which was then mounted in the mechanical support structure (see figure 1). An otherwise identical second probe without the mounting parts was used for testing and evaluation.

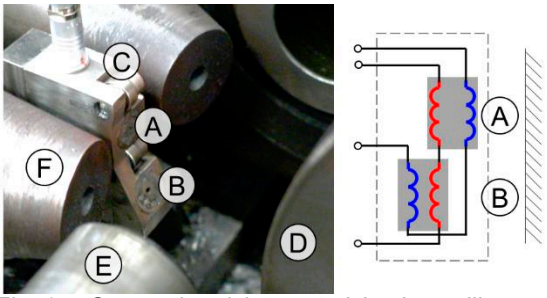

Fig. 1. Sensor head integrated in ring rolling machine (left) and schematic (right). A: Main probe, B: drift subtraction probe, C: support rollers, D: Main roll, E: mandrel, F: stabilization rolls. Shaded area indicates coils sharing one ferrite core.

Signal Processing

The transmission coil was excited using wideband pseudorandom white noise. The received signal was evaluated in the range from 1 kHz to 20 kHz, corresponding to the pass-band of the frontend filters. By transformation to frequency space and complex division, the forward transfer function H is obtained directly.

This transfer function was then modeled using a simplified lumped-element model [4]. The elements of this model are shown in figure 2. An analytical expression for the transfer function of this model can be found and while it contains many terms, the mathematical complexity is manageable. It was found that only three probe (constructive) parameters (inductivities, resistances) and three material-related parameters (ideal transformer coupling, loss resistance) are sufficient to describe the resulting transfer function.

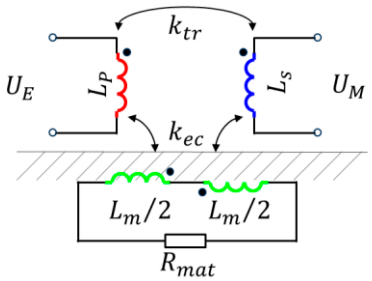

Fig. 2. Proposed equivalent lumped element model for the electro-magnetic interactions. U_E: transmitted voltage, U_M: response voltage, L_P, L_s,: probe inductivities, k_{tr}, k_{ec}: ideal transformer coupling factors, L_m: fictional ring current inductivity, R_{mat}: material loss resistance

Then, a fit is performed to find material parameters that describe the currently measured transfer function by minimizing the weighted sum of the absolute differences between measured and predicted transfer function in frequency domain. To ensure real-time applicability, the optimization must take at most as much time as the next data acquisition, ideally with constant (predictable) time lag. This is implemented by using a continuously running random gradient descent method which can be interrupted at any time. Since the current best prediction is continuously refined, this method converges quickly, but at the same time is capable of following changes in the measured signal with low response time.

Results

The presented sensor system was evaluated both in off-line and in-line application. It could be shown that using this model approach, it is possible to characterize both ferromagnetic and non-ferromagnetic materials as well as materials that exhibit a phase transformation without adjustments to signal conditioning.

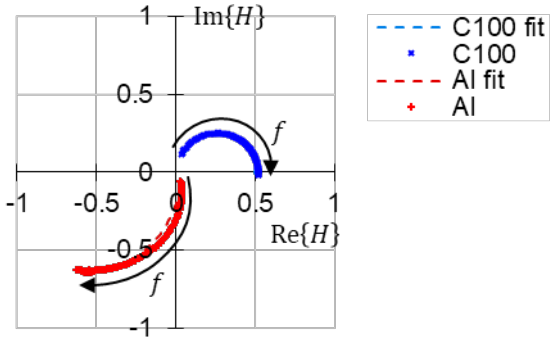

Fig. 3. Comparison of as-measured transfer function and fitted values for aluminum and ferritic C100 steel samples. Both acquired with identical device settings.

In the fully integrated application, ring rolling experiments were carried out. Figure 4 shows one result. It was found the loss resistance parameter correlates well with the total accumulated strain, including the recovery and recrystallization once forming is finished but the workpiece is still hot. Similarly, the transformatoric parameter k_{tr} relates to the permeability and magnetic domain size. This is especially interesting in this application as it also identifies the formation of bainite (which has smaller magnetic domains compared to ferrite) at around 400°C in the rest phase.

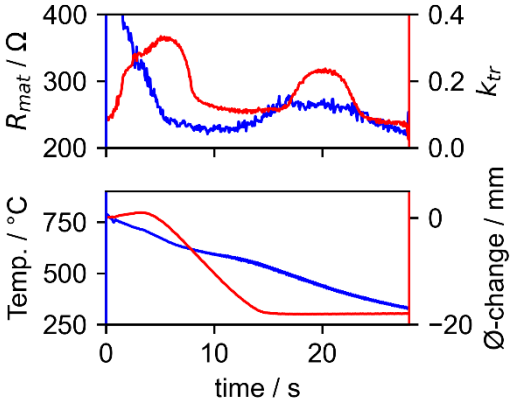

Fig. 4. Model parameters fitted in real-time during forming process (top) and process conditions (bottom).

Additional data processing can be used to identify and correlate the equivalent model's parameters to physical quantities such as concrete values of permeability, grain size, equivalent strain, etc.

Acknowledgements

The authors thank the German Research Foundation DFG for the support of the depicted research within the priority program SPP2183 through project grant no. HA 5209/11-2.

References

[1] S. Hütter, R. Lafarge, J. Simonin, G. Mook, A. Brosius, T. Halle, Determination of Microstructure Changes by Eddy-Current Methods for Cold and Warm Forming Applications, *Advances in Industrial and Manufacturing Engineering* 2C, 100042 (2021); doi:10.1016/j.aime.2021.100042

[2] A. Brosius, M. Tulke, C. Guilleaume, Non-linear model-predictive-control for thermomechanical ring rolling, in: Proceedings of the XV International Conference on Computational Plasticity - Fundamentals and Applications, CIMNE, 2009

[3] R. Lafarge, S. Hütter, O. Michael, T. Halle, A. Brosius, Property controlled thermomechanical ring rolling: process implementation and window, in: 33. Aachener Stahlkolloquium, 2022

[4] S. Hütter, G. Mook, T. Halle, Quantifizierung elektromagnetischer Eigenschaften durch Wirbelstrom-basierte Softsensoren, in: 40. Vortrags- Und Diskussionstagung Werkstoffprüfung, Deutsche Gesellschaft für Materialkunde, Dresden, 2022

DOI 10.5162/SMSI2023/D1.4

Multifrequency Multichannel Eddy Current Sensor System for the Analysis of Mechanical States in Ferromagnetic Materials

Frank Wendler[1], Robert Laue[2], Sebastian Härtel[3], Olfa Kanoun[1], Birgit Awiszus[2]
[1] Professorship Measurement and Sensor Technology, Chemnitz University of Technology, Reichenhainer Str. 70, 09126 Chemnitz, Germany
[2] Professorship Virtual Production Engineering, Chemnitz University of Technology, Reichenhainer Str. 70, 09126 Chemnitz, Germany
[3] Chair of Hybrid Manufacturing, Brandenburg University of Technology, Konrad-Wachsmann-Allee 17, 03046 Cottbus, Germany
frank.wendler@etit.tu-chemnitz.de

Summary:
In this work, we introduce the concept of a multifrequency multichannel eddy current sensor for the contactless simultaneous measurement of distance, relative magnetic permeability, the magnitude of magnetic anisotropy, angle of magnetic anisotropy, the magnitude of tilting, and direction of tilting. The System is demonstrated at a sample in a tensile test experiment.

Keywords: inductance spectroscopy, anisotropy measurement, permeability measurement, in-process measurement, material characterization

Introduction

Eddy current sensors have been already successfully applied in the field of material testing and the quantitative analysis of distance and electric and magnetic properties. Most sensor application focus on a few dominant use cases like the measurement of the distance and conductivity, when other influences are neglected or compensated. Concepts for the simultaneous measurement of multiple measurands are still subject to recent research and are challenged by the problem of effect separation. Especially the analysis of magnetic material properties could open access to several hard-to-measure quantities if the individual contribution could be isolated and quantified. The magnetic properties of ferromagnetic material depend on factors such as mechanical stress, defect density, grain size, and other changes in microstructure.

In the field of metal forming variable factors are defect density and mechanical stress, while the others can be considered constant. The increase in defects in the crystal structure reduces the ability of the material to magnetize and adjust to external magnetic fields. Mechanical stress does change the magnetic properties over the so-called Villari Effect depending on the direction of the stress. This results in stress-induced magnetic anisotropy in the material. Since both influences are expected to mutually affect each other, the novel introduced sensor approach aims at the simultaneous characterization of both effects and mutual correction. For this purpose, a multifrequency approach for the simultaneous measurement of distance and relative magnetic permeability is combined with the tilting compensated measurement of the magnetic anisotropy.

Structure of Sensor

The sensor consists of a central excitation coil and 8 angular aligned receiving coils displayed in fig. 1. The central coil can be excited at various frequencies in the range of 5 kHz to 1 MHz.

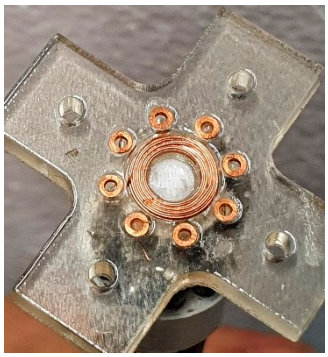

Fig. 1. Sensor head of the multisensor system with central excitation coil and 8 angular receiving coils

For each frequency current and the voltage are measured in amplitude and phase. This information can be used to calculate the spectra of

the inductance of the central coil and is the foundation for the calculation of the distance and the magnetic permeability. The eight receiving coils along the circumference of the excitation coil analyze the magnitude of the excitation field for angular variations resulting from material anisotropy.

Analysis of Distance and Magnetic Permeability

The distance and the electric and magnetic properties have a characteristic influence on the shape of the spectra of the sensor inductance. In general, the inductance is enhanced at low frequencies by the magnetic properties of ferromagnetic material and reduced at high frequencies by the eddy current effect in the material. The magnitude of this change does mainly depend on the distance. In between the high and the low-frequency case is the region where the sensor inductance does drop for increasing frequencies. The position of this region does mainly depend on the ratio between the electric conductivity and magnetic permeability. This characteristic behavior is used in combination with an eddy current model [1] and an implemented particle filter to obtain the values of the relative magnetic permeability and the distance from one spectrum of the inductance [2].

Analysis of Magnetic Anisotropy and Correction of Tilting

The obtained amplitudes of the voltages of the eight receiving coils are analyzed over a Fast Fourier Transform along the angular coordinate. Tilting does create a sine signal with one maximum and one minimum over 360° because one side of the sensor coil will get closer to the target and one side will get further away. The magnetic anisotropy will create a sine signal with two maxima and two minima over 360°. A frequency selective analysis can separate and quantify the contribution of tilting and magnetic anisotropy and analyze the respective direction.

Experimental Evaluation

The sensor system was attached to the sample of DC01 steel in a tensile test experiment. The sample was elongated 30 mm at a constant speed and then relieved in four steps of the remaining force. The loading starts at about 50 s and results in a strong increase of anisotropy (blue curve) and a strong decrease in magnetic permeability (orange curve) in figure 2. The elongation continues until 350 s. In this phase, anisotropy increases to the maximum and then decreases, which correlates with the stress in the sample. The permeability decreases to a nearly constant level. The sample remains on stationary condition till 430 s at an elongation of 30 mm while permeability and anisotropy maintain stable. Then the remaining force is relieved in four steps till the 700 seconds mark. The steps are clearly visible in the blue curve of the anisotropy, but the step height is not uniform and increases with decreasing load. For the permeability and increase is observable for the unloading cycle.

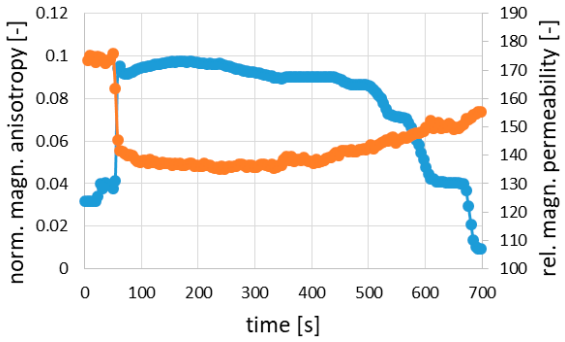

Fig. 2. Observed curves of magnetic anisotropy (blue) and relative permeability (orange) during a tensile test experiment of the DC01 steel sample

Conclusions

The multisensor system does allow the non-contact measurement of magnetic permeability and magnetic anisotropy with the compensation of the geometric influences of tilting and distance variations. The combination of two sensor concepts and measurement effects does not only allow the measurement at one spot. It creates the opportunity to mutually compensate geometric effects and isolate the origin of changes in the magnetic properties. For the investigated sample the responses of magnetic permeability and magnetic anisotropy were highly correlated but reveal characteristic differences in the detailed view. This is a necessary foundation for the separation of the underlying causes.

Acknowledgement

The authors would like to thank the German Research Foundation for funding the project (project number 424334154) within the framework of SPP2183: Property Controlled Forming Processes.

References

[1] Dodd, C. V., and W. E. Deeds. "Analytical solutions to eddy-current probe-coil problems." *Journal of applied physics* 39.6, 2829-2838 (1968); doi: 10.1063/1.1656680

[2] Lu, Mingyang, et al. "Reducing the lift-off effect on permeability measurement for magnetic plates from multifrequency induction data." IEEE Transactions on Instrumentation and Measurement 67.1,167-174 (2017); doi: 10.1109/TIM.2017.2728338

DOI 10.5162/SMSI2023/D2.1

D2.1 New developments in mathematics for metrology: Virtual experiments, machine learning and synthetic reference data

M. Baer, Physikalisch-Technische Bundesanstalt, Braunschweig (Germany)

The short paper of this contribution is not available

DOI 10.5162/SMSI2023/D2.1

D2.1 New developments in mathematics for metrology: Virtual experiments, machine learning and synthetic reference data

M. Baer, Physikalisch-Technische Bundesanstalt, Braunschweig (Germany)

Summary:

Please describe briefly the highlights of your work. The summary of max. 6 lines should be typed across both columns. Please do not leave any spaces between the short paper and the title of your first section and please do not use symbols in the summary. (style “SMSI_Conference_Bodytext”)

DOI 10.5162/SMSI2023/D2.2

Advanced Error Modelling of a Fourier Scatterometer

Marcel van Dijk[1], *Gertjan Kok*[1]
[1] *VSL, Thijsseweg 11, 2629 JA Delft, Netherlands*
mvandijk@vsl.nl

Summary:
Several error sources of a Coherent Fourier Scatterometer have been modelled to improve the accuracy and uncertainty evaluation of the measurement of geometrical dimensions of gratings, such as the critical dimension, height and pitch. Using the error model, the sensitivities of the geometrical dimensions of a grating to the error sources have been evaluated. In combination with the uncertainties of these error sources, these sensitivities can provide insight into how to improve measurements of gratings with nano dimensions, which can be of great benefit to the semiconductor industry.

Keywords: error model, virtual model, uncertainty evaluation, scatterometry, nano measurements

Coherent Fourier Scatterometry

Coherent Fourier Scatterometry (CFS) is a technique that has shown promising results in measuring nano dimensions in gratings, as shown in [1] for example. In CFS, an object is illuminated by a focused coherent light source. The scattered light is measured by means of a camera, and the geometrical parameters of the grating (such as critical dimension (CD), pitch, and height) are reconstructed from that image. A schematic sketch of the measurement set-up and the relevant geometrical parameters of the periodic sample are visualized in figure 1.

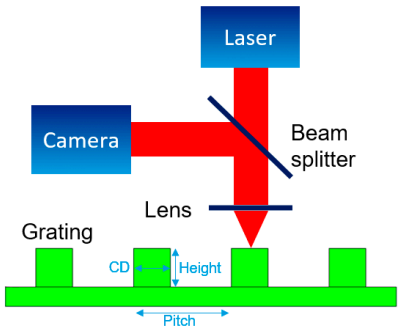

Fig. 1. Measurement set-up of CFS and relevant geometrical parameters.

The reconstruction of the parameters characterizing the sample geometry is done by inversion of the so-called forward model, in which the measurement is replicated by a virtual experiment. The aim of the model inversion is to find the set of geometrical parameters that minimizes the difference between the measured image and the simulated image.

By using a specific measurement scheme, CFS is reported to yield an enhanced sensitivity, as discussed in [2]. This is desirable in for example the semiconductor industry, given the shrinking dimensions in microchips.

The virtual experiment is a crucial ingredient in CFS. It is not only part of the measurement procedure, it also provides a means to evaluate the uncertainty associated with the estimates of the geometrical parameters. It is therefore essential for the virtual experiment to be as realistic as possible. This means that the error sources that can contribute to (a distortion in) the measurement result, should also be addressed in the virtual experiment. Although research has been performed in modelling error sources in scatterometry [3, 4], so far, relatively little research has focused on CFS.

In our research, we have focused on modelling several error sources that can occur during the CFS measurement. This enables more accurate estimates of the geometrical parameters of the grating, as well as more realistic estimates of the uncertainties associated with these estimates. We distinguish two different main sources of error: errors coming from the measurement set-up and errors coming from undesired artefacts in the grating.

Errors in measurement set-up

Errors in the measurement can come from, for example, errors in the properties of the measurement equipment or from the positioning of the grating that has to be measured.

There are several error sources that can come from the properties of the measurement equipment. For example, the numerical aperture of the lens determines the angles of the incident light. Different incident angles lead to different scattering patterns. In addition, the wavelength

of the laser is a component in determining how the light scatters from the grating. It is therefore important to consider all uncertainties in the numerical aperture of the lens as well as in the wavelength of the laser. The properties of the measurement equipment should therefore be accurately measured. This is out-of-scope for this paper.

Errors can also be introduced by the positioning of the grating. For example, it is possible that the light is not properly focused on the sample or that the sample is rotated or slightly tilted (either parallel to the grating, perpendicular to the grating, or a combination of the two). A defocused sample will, for example, alter the point at which the incident planewaves refract on the grating. This leads to a phase shift that can be incorporated into the virtual experiment.

Errors in grating

It is possible that there are artefacts in the grating that influence the scattered light. If not accounted for, these artefacts can cause a mismatch between the measurement and the virtual counterpart. This can lead to errors in the estimates of the geometrical parameters. We have modelled the following sample artefacts: rounded corners, oxide layer, bulged walls, and roughness, as shown in figure 2.

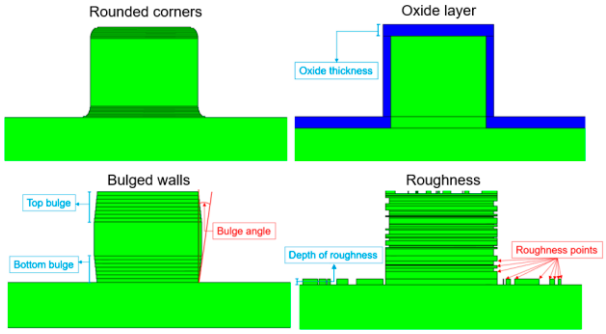

Fig. 2. Sample artefacts that have been modelled in the virtual experiment.

Sensitivities

Having included these errors in the virtual experiment, we are able to determine the sensitivity of the measurement with respect to the different error sources. Once the magnitudes of the individual errors sources have been measured of the real scatterometer, this will provide insight into which error sources have the most impact on the estimates of the geometrical parameters. Knowing the most dominant error sources, one can more effectively perform the measurement which reduces the overall uncertainty of the geometrical parameters. The sensitivities of the error sources for a particular grating and measurement set-up can be found in table 1. To ease the presentation, a nominal error with value 1 has been used, and its effect on the measured critical dimension, pitch and height has been evaluated.

Tab. 1: Sensitivities of the critical dimension (CD), pitch, and height with respect to the error sources.

Error source	Nom. Error	CD [nm]	Pitch [nm]	Height [nm]
Numerical Aperture	0.01	0.61	0.55	0.69
Laser wavelength	1 nm	0.65	1.37	0.32
Parallel tilt	1°	0.00	0.00	0.00
Perpendicular tilt	1°	0.00	0.00	0.00
Rotation	1°	0.00	0.00	0.00
Defocus	1 nm	0.09	0.25	0.53
Rounded corners	1 nm	0.00	0.00	0.00
Oxide layer	1 nm	0.98	0.36	0.44
Roughness	1 nm	1.22	0.11	0.19
Bulged walls	1°	0.94	0.44	0.92

The sensitivity coefficients can be used for determining the measurement uncertainty, e.g. an uncertainty of 0.1 nm in laser wavelength would result in an uncertainty of 0.065 nm in the CD. Note that this is not an exhaustive list of all errors and more error sources will be included at a later stage.

When the uncertainties of all the error sources have been established experimentally, the combined measurement uncertainty can be calculated. At the same time it will become clear what the dominant sources of uncertainty are. These insights can help in subsequently reducing the overall uncertainty of measurements based on CFS.

Acknowledgment

This project (20IND04 ATMOC) has received funding from the EMPIR programme co-financed by the Participating States and from the European Union's Horizon 2020 research and innovation programme.
We would also like to thank our colleague Lauryna Siaudinyté for discussions on the topic of this paper.

References

[1] N. Kumar, et. al., Reconstruction of sub-wavelength features and nano-positioning of gratings using coherent Fourier scatterometry, *Opt. Express 22*, 24678-24688 (2014); doi: 10.1364/OE.22.024678

[2] S. Roy, et. al, Interferometric coherent Fourier scatterometry: a method for obtaining high sensitivity in the optical inverse-grating problem, *Journal of Optics 15*, 07507 (2013); doi: 10.1088/2040-8978/15/7/075707

[3] T. Germer, et. al., Developing an Uncertainty Analysis for Optical Scatterometry, *Metrology, Inspection, and Process Control for Microlithography XXIII,* 72720T (2009); doi: 10.1117/12.814835

[4] M. Henn, et. al., Improved reconstruction of critical dimensions in extreme ultraviolet scatterometry by modeling systematic errors, *Measurement Science and Technology 25*, 044003 (2014); doi: 0.1088/0957-0233/25/4/044003

DOI 10.5162/SMSI2023/D2.3

Modelling in Measurement
- From classical analytical approaches to cognitive data-driven solutions –

Michael Heizmann[1], Wolfgang Koch[2], Nadine Schiering[3], Klaus-Dieter Sommer[4]
[1] Karlsruhe Institute of Technology KIT, Germany
[2] Fraunhofer Institute for Communication, Information Processing and Ergonomics FKIE, Wachtberg, Germany
[3] ZMK & ANALYTIK GmbH, Bitterfeld-Wolfen, Germany
[4] Technical University Ilmenau, Ilmenau, Germany

Summary:

Models are an inseparable part of Metrology. They make it possible to derive measurement results, including measurement uncertainties, from measurement data or output signals and knowledge about the measurement process. Models establish a functional relationship between the measurand and all relevant quantities on which the measurand depends. Models do not necessarily have to be derived from analytical-functional relationships; they are increasingly data-driven with cognitive capabilities. In general, they are used to design measurement systems, analyze measurement data, make inferences and predictions, and form the basis for evaluating measurement uncertainties.

In industrial measurement and sensor technology as well as in metrology, we have recently seen quite significant, almost revolutionary developments, primarily promoted by the digital transformation process. Probably the most important influence on measurement and sensor technology has been the rapid development of information and communication technology towards systems with cognitive capabilities for context understanding and explainability, interaction, adaptation and learning.

Significant new technological and metrological approaches in measurement and sensor technology are:

Classical modelling approaches. They are based on physical principles and are typically referred to as analytical parametric. However, with the increasing use of digital technologies, large sensor networks, and powerful computers, classical approaches are increasingly being replaced or complemented by data-driven modelling approaches. This is especially true where large, complex and flexible networked sensor systems are used and little expert knowledge of real-world and often changing contexts is available.

Due to the digital transformation, processes in industry are changing with increasing speed. Complex sensor networks are used in fully digitized production processes. Due to the increasing availability of low-cost *Industrial Internet of Things* (*IIoT*)-enabled measurement devices, sensor networks are much larger, more complex and flexible networked than in traditional measurement applications. As a result, and due to incomplete expert knowledge about the systems and their potential changes, data analysis is typically data-driven. Probably the most important influence on measurement and sensor technology has been the rapid development of information and communication technology towards systems with cognitive capabilities for context understanding, interaction, adaptation and learning. In addition, the use of digital twins, where a model of a physical object is updated based on an evolving data set, intentionally increases the flexibility of networking. With this paradigm shift in the treatment and analysis of measurement data, traditional approaches to modelling in metrology need to evolve and be complemented.

Keywords: analytical parametric modelling, data-driven modelling, digital twins, cognitive sensors

The following topics will be discussed in the paper:

- Cause-effect principle in measurement
- Forward and inverse modelling in measurement
- Classical analytical modelling
- Virtual representations in measurement
- Data-driven modelling of cognitive sensors and flexible measurement systems
- Quality and explainability of cognitive systems and abilities in measurement

References

[Aeschbacher 2014] Aeschbacher, M. Simulation unter Hochdruck. METinfo, Vol. 21, No. 2/2014.

[Bauer et al 2020] Bauer, K. Automation 2030, VDI, Juli 2020

[Heizmann 2016] Heizmann, M. und Puente León F.: Modellbildung in der Mess- und Automatisierungstechnik, DE GRUYTER OLDENBOURG tm – Technisches Messen 2016; 83(2): 63–65, DOI 10.1515/teme-2015-0126.

[Sommer 2005] Sommer, K.-D., Weckenmann, A. and Siebert, B.R.L. A systematic approach to the modelling of measurements for uncertainty evaluation. J. Phys.: Conf. Ser., 13, 052, pp. 224-227, 2005.

[Sommer 2006] Sommer, K.-D., Siebert, B.R.L. Systematic approach to the modelling of measurements for uncertainty evaluation. Metrologia, 43, pp. 200-210, 2006.

[Sommer 2021] Sommer K. D. et al. Modelling of Networked Measuring Systems ─ an Essential Component of the Factory of the Future, JSSS, 2021 – in print

[Sommer 2022] Sommer, K.-D., Heizmann, M. and Schütze, A. "Measurement systems and sensors with cognitive features" *tm - Technisches Messen*, vol. 89, no. 4, 2022, pp. 211-213.

[Stark 2020] Stark, R. et al. WiGeP-Positionspapier: „Digitaler Zwilling“. http://www.wigep.de/fileadmin/Positions_und_Impulspapiere/Positionspapier_Gesamt_20200401_V11_final.pdf (Abruf: 2020.10.07)

[Wright 2020] Wright, W. and Davidson, S. How to tell the difference between a model and a digital twin. Adv. Model. and Simul. In Eng. Sci., 7: 13, 2020. https://doi.org/10.1186/s40323-020-00147-4

DOI 10.5162/SMSI2023/D2.4

On Uncertainty Evaluation using Virtual Experiments

Gerd Wübbeler[1], Manuel Marschall[1], Clemens Elster[1]
[1] Physikalisch-Technische Bundesanstalt, Braunschweig and Berlin, Germany
Gerd.wuebbeler@ptb.de

Summary:
Virtual experiments have become increasingly important in metrology and industry. Combined with Monte Carlo methods, they are also employed for uncertainty evaluation. However, the modeling principles underlying the *Guide to the Expression of Uncertainty in Measurement* (GUM) generally differ from the concepts of a typical virtual experiment. We discuss these conceptual differences and exemplify how they can affect resulting uncertainties. We also show that for certain linear models virtual experiments can nevertheless be used to determine measurement uncertainties in line with the GUM.

Keywords: measurement uncertainty, virtual experiments, GUM, Monte-Carlo Method, linear models

Virtual experiments and the GUM

A virtual experiment is typically a numerical model of a measurement process which produces virtual data whose properties reflect those of the data observed in the real experiment. Virtual experiments have become increasingly important in modern metrology and industrial applications, e.g., to explore the accuracy of a measurement device, to specify machine tolerances needed to reach a required accuracy, or to identify significant sources of uncertainty. Combined with Monte-Carlo methods, virtual experiments have been proposed for the evaluation of measurement uncertainties [1].

However, the metrological standard for uncertainty evaluation specified in the GUM [2] does not rely on a simulation of the measurement process but rather uses a model for which one of its input quantities is represented by the outcome of the measurement process. This different role of input and output quantities for a GUM model and a typical virtual experiment is illustrated in Fig. 1.

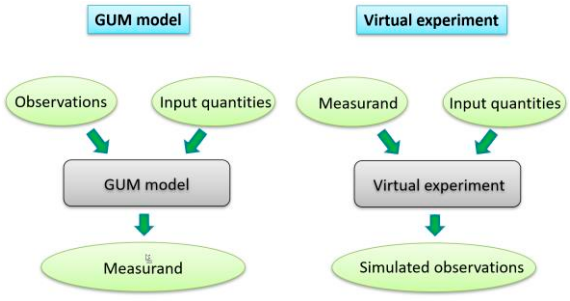

Fig. 1. Comparison of GUM model and virtual experiment.

Comparison in terms of a linear model

The difference of the two approaches is shown for a model as used in the GUM, which represents an almost direct measurement of a measurand y

$$y = x + z^3. \qquad (1)$$

Here x is a quantity for which repeated observations are given (GUM Type A information) and z a quantity with Type B information. The variance σ^2 of the distribution from which repeated observations are taken is assumed to be known. The corresponding model for the virtual experiment is

$$x_{\mathrm{VE}} = y_0 - z^3 + \varepsilon\,, \qquad (2)$$

where ε models the random error with variance σ^2 observed in repeated measurements, and y_0 is a fixed value selected for the simulated measurand. The subscript VE denotes the outcome of the virtual experiment. Each time the virtual experiment is run, different values for ε and z are taken, where a value for z is drawn from the probability density function (PDF) that encodes the knowledge about z (Type A information).

The blue line in Fig. 2 shows the PDF for the measurand y which has been obtained by applying the GUM-S1 Monte-Carlo method [3] to measurement model (1). The corresponding PDF of randomly drawn virtual data x_{VE} (red line) via the virtual experiment (2) was determined by application of a Monte-Carlo method. As can be seen, the two distributions obtained

by GUM-S1 and by the virtual experiment clearly differ with respect to the location of their mean values and, moreover, also with respect to their shape. That is, simply shifting the PDF obtained by the virtual experiment does not yield the PDF for the measurand produced by the application of GUM-S1.

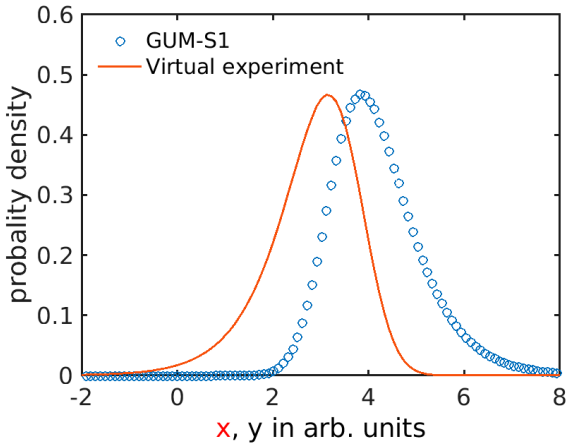

Fig. 2. Comparison of the PDFs obtained by GUM-S1 and by generation of random drawn virtual data using the virtual experiment.

GUM uncertainty evaluation using virtual experiments

While the GUM (and GUM S1) uncertainty evaluation follows rather strict rules this is not the case when applying Monte-Carlo to a virtual experiment. In fact, a Monte-Carlo virtual experiment can be carried out following rather different strategies which may even lead to markedly different resulting uncertainties as demonstrated in [4].

However, for linear models, a simple transformation of the virtual experiment (2) can be applied, such that the PDF produced by repeatedly running the procedure equals an application of GUM-S1, cf. [5]. More specifically, this can be achieved by a transformation according to

$$y = x + y_0 - x_{\mathrm{VE}}\,, \qquad (3)$$

where x denotes the real observation, y_0 the chosen virtual measurand, and x_{VE} the random outcome of the virtual experiment (2). By repeatedly running the virtual experiment and applying the transformation (3), the resulting samples equal those obtained by applying the Monte Carlo approach of GUM-S1. Fig. 3 illustrates this equivalence for the considered models and chosen PDF for z.

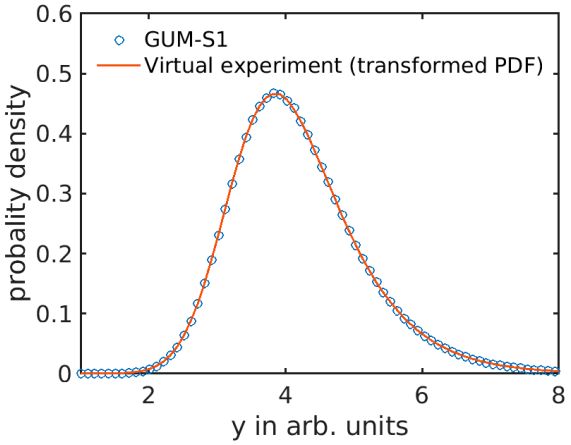

Fig. 3. Comparison of the PDFs obtained by GUM-S1 and by transformation (3) applied to the randomly drawn virtual data.

Conclusions

Virtual experiments can be helpful to develop and assess uncertainty evaluations within the framework of the GUM. For specific linear models, a simple transformation of randomly drawn virtual data yields a GUM-compliant uncertainty analysis. For nonlinear models, however, the distribution of randomly drawn virtual data can no longer be easily transformed into a GUM-compliant uncertainty evaluation. The development of corresponding approaches will be the topic of future research.

References

[1] Balsamo, A.; Di Ciommo, M.; Mugno, R.; Rebaglia, B.; Ricci, E.; Grella, R. Evaluation of CMM uncertainty through Monte Carlo simulations. CIRP Ann. 1999, 48, 425–428.

[2] Joint Committee for Guides in Metrology. Evaluation of Measurement Data—Guide to the Expression of Uncertainty in Measurement; International Bureau of Weights and Measures (BIPM): Sèvres, France, 2008; BIPM, IEC, IFCC, ILAC, ISO, IUPAC, IUPAP, and OIML, JCGM 100:2008, GUM 1995 with minor corrections.

[3] Joint Committee for Guides in Metrology. Evaluation of Measurement Data—Supplement 1 to the "Guide to the Expression of Uncertainty in Measurement"—Propagation of Distributions Using a Monte Carlo Method; International Bureau of Weights and Measures (BIPM): Sèvres, France, 2008; BIPM, IEC, IFCC, ILAC, ISO, IUPAC, IUPAP, and OIML, JCGM 101: 2008.

[4] Kok, G., Wübbeler, G., & Elster, C. (2022). Impact of Imperfect Artefacts and the Modus Operandi on Uncertainty Quantification Using Virtual Instruments. Metrology, 2(2), 311-319.

[5] Wübbeler, G.; Marschall, M.; Kniel, K.; Heißelmann, D.; Härtig, F.; Elster, C. GUM-Compliant Uncertainty Evaluation Using Virtual Experiments. Metrology 2022, 2, 114–127

DOI 10.5162/SMSI2023/D3.1

Methane-Hydrogen Raman Spectra Analysis in Binary Gaseous Mixtures

Fabio Melison[1], Lorenzo Cocola[1], Elena Meneghin[2], Daniele Rossi[2], Luca Poletto[1]
[1] CNR – Institute for Photonics and Nanotechnologies, Via Trasea 7, 35131 Padova, Italy
[2] Pietro Fiorentini S.p.A., Via E.Fermi 8/10, 36057 Arcugnano, Italy
fabio.melison@pd.ifn.cnr.it

Summary:
The combined Raman spectra of methane and hydrogen have been analyzed in a way to estimate the concentration of the two species in binary gaseous blends. The acquisitions were made with an industrial tailored Raman instrument appositely developed to measure the natural gas mixtures composition. Once acquired, the Raman spectra have been fitted using a MATLAB® routine. The results show a high correlation between the estimated and the certified gases concentrations.

Keywords: Raman spectroscopy, methane, hydrogen, gas analysis, measurement

Motivation

Hydrogen is light, storable, reactive, has high energy content per unit of mass, and it can readily produce at industrial scale. Supplying hydrogen to industrial users is now a major business globally. Demand for hydrogen in its pure form is around 70 million tons per year (MtH_2/yr) [1]. In the next few years, hydrogen will be injected in the natural gas networks in several European countries and around the world. For example, in Germany the hydrogen concentration can reach 2% by volume, growing up to 10% concentration under certain circumstances [2].

Given its intrinsic capability to determine multiple species simultaneously with a non-invasive approach, Raman spectroscopy is a suitable candidate to analyze complex gas mixtures. Starting from the results obtained from a feasibility study [3], a novel system which implements Raman spectroscopy to determine the main natural gas components has been used to analyze the combined Raman spectra of methane and hydrogen. The aim of this study is to first determine the performance and the reliability in CH_4-H_2 binary mixtures concentration detection. The focus has been set on detection and concentration estimation in four CH_4-H_2 binary mixtures.

Methods

The system employed in this study is designed to operate with a low power absorption and in a wide operative temperature range. Its final use is intended to be the on-the-field analysis of natural gas directly on the transport and distributions networks. In this experiment the instrument was kept at a fixed laboratory temperature, minimizing the sources of variability.

The Raman system employed in the experiment is shown in Fig. 1. The laser source is a solid state multi-mode diode source centered at 455 nm with an optical power set to 2W.

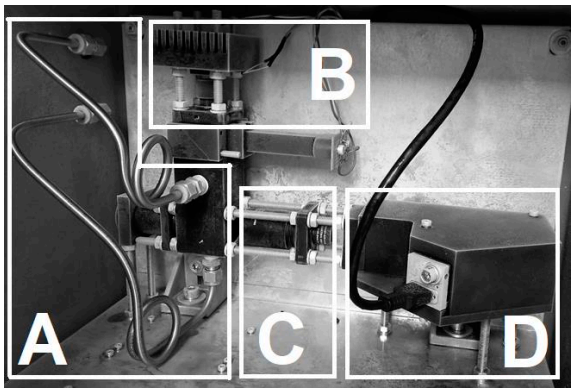

Fig. 1. Raman system employed in the experiment. Section A: gas cell, gas-in and gas-out pipes. Section B: laser source. Section C: Raman signal collecting optics. Section D: diffraction grating spectrometer.

Raman calibration spectra of methane and hydrogen were generated by averaging 30 acquisitions with 2-seconds camera exposure. The bottles used in this phase had concentrations equal to 100% for both methane and hydrogen. The calibration spectra of methane and hydrogen are plotted in Fig. 2.

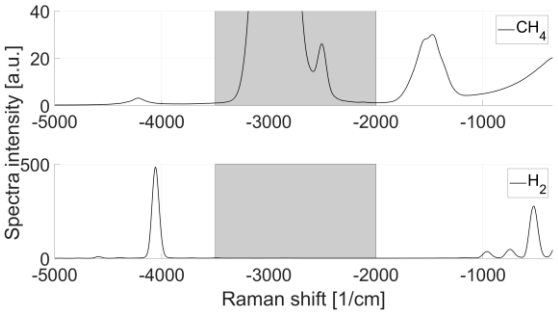

Fig. 2. Calibration Raman spectra, 100% concentration of methane (top) and hydrogen (bottom).

In Table 1 the concentrations of the four analyzed mixtures are reported.

Tab. 1: Certified mixtures concentration [%]

Label	CH_4	H_2
MIX1	98.000	2.000
MIX2	94.977	5.023
MIX3	89.940	10.060
MIX4	79.758	20.242

The analysis is performed on two spectral regions: from -350 cm^{-1} to -2000 cm^{-1} and from -3500 cm^{-1} to -5000 cm^{-1}. For each mixture, 20 experimental spectra were fitted using a fit routine appositely developed in MATLAB®, using a nonlinear least-square solver which finds the linear combination of the two calibrations that fits at best the acquired spectra. The average of the 20 fit solutions is intended to be the final estimated concentration.

Results

As an example, the elaboration for MIX3 is represented in Fig. 3. The acquired spectra and the best fit solution are plotted on the top. The residues between the acquired spectra and the synthetic spectra are plotted on the bottom.

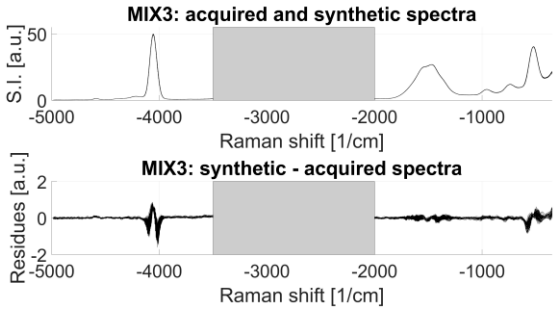

Fig. 3. Fit elaboration: acquired and synthetic spectra (top) and elaboration residuals (bottom).

The measured concentrations and the related errors are reported in Table 2. The precision of the measuring method in the measurement of concentrations is anyway better than 0.1%mol/mol for concentration of hydrogen in methane as high as 20%.

Tab. 2: Experimental mixture concentrations [%] and errors [% mol/mol]

Fit results		Result CH_4	Result H_2
MIX1	Result	98.003	1.997
	Error	0.003	-0.003
MIX2	Result	94.928	5.072
	Error	-0.049	0.049
MIX3	Result	89.849	10.151
	Error	-0.091	0.091
MIX4	Result	79.667	20.333
	Error	-0.091	0.091

Conclusions

The ability to estimate the compositions of binary methane-hydrogen mixtures has been proven, to assess the feasibility to analyze mixtures with a hydrogen content up to 20%. Mixtures containing hydrogen in natural gas will be the object of next studies.

Acknowledgments

The authors acknowledge the support from the Project PiPe4.0, part of ATTRACT that has received funding from the European Union's Horizon 2020 Research and Innovation Programme.

References

[1] IEA (2019), The Future of Hydrogen, IEA, Paris https://www.iea.org/reports/the-future-of-hydrogen, License: CC BY 4.0

[2] IEA, Limits on hydrogen blending in natural gas networks, 2018, IEA, Paris https://www.iea.org/data-and-statistics/charts/limits-on-hydrogen-blending-in-natural-gas-networks-2018, IEA. License: CC BY 4.0

[3] L. Cocola, F. Melison, N. Scarabottolo, G.Tondello, L. Poletto, Diode-based Raman sensor for fuel gas analysis, Proc. SPIE 11354, Optical Sensing and Detection VI, 113541A (2020).

DOI 10.5162/SMSI2023/D3.2

Raman Spectroscopy applied to detection of grapevine disease: the case of Esca detection

Camilla Baratto[1], *Gina Ambrosio*[1], *Guido Faglia*[2,1], *Massimo Turina*[3],
[1] *CNR-INO, PRISM Lab, Via Branze 45, 25123 Brescia, Italy,*
[2] *Department of Information Engineering, University of Brescia, 25133 Brescia, Italy*
[3] *IPSP-CNR, Strada delle Cacce,Turin, 25133, Italy*
camilla.baratto@ino.cnr.it

Summary:
We report on the use of Raman Spectroscopy (RS) and chemometric analysis as a non-invasive sensor to implement precision agriculture for early detection of the ESCA disease. Initial encouraging findings allow to identify symptomless leaves in ESCA-affected vines as belonging to a diseased vine through a change in spectroscopic properties measured by RS likely due to a change in carotenoids. To date, there is no report of RS for Esca disease detection.

Keywords: Raman Spectroscopy; Esca disease; precision agriculture; chemometric.

Introduction

Advanced detection of plant pathogens is fundamental to allow human intervention that can limit crop damages, with a proper pesticide use in sustainable crop management systems. When available, diagnostic techniques different than operator-dependent visual assessment must support the identification of pathogens. Esca disease has a tremendous economic impact [1] in all wine-producing countries: different fungi (*Phaeoacremonium aleophilum, Phaeomoniella chlamydospora, and Fomitiporia Mediterranea*) often associated to the disease, can be present also in healthy plants[2], and their inoculation often does not reproduce the disease [3]. Thus, it is difficult to support the diagnosis even with destructive techniques like Enzyme-Linked Immuno Sorbent Assay (ELISA) or Polymerase Chain Reaction (PCR), which remain inconclusive. Once symptoms of ESCA diseases are detected visually, it is already too late for a possible precision therapeutic intervention. It is thus of utmost importance to find a technique that allows for early monitoring of the disease.

Recently the applicability of Raman spectroscopy (RS) to precision agriculture has been demonstrated [4][5]. RS is a non-invasive technique that does not require sample preparation and could be readily available for in field monitoring. The advantages of Raman technique with respect to other more established optical techniques, such as reflectance spectroscopy [6], hyperspectral broad band remote sensing [7], chlorophyll fluorescence spectroscopy [8], relies on the capability of monitoring molecules associated with the plant health. The main concept of this work is to combine the sensing capabilities of the RS technique and chemometric analysis in order to develop a non-destructive analyzer for early detection of the esca disease that allows the correlation and prediction of the different symptomatic expressions of the disease (Brown Wood Streaking, Grapevine Leaf Stripe Disease and apoplexy). We demonstrated the proof of concept of disease detection by analyzing leaf samples from healthy plants and from symptomatic and symptomless shoots in diseased plants. The final symptomatic outcome of ESCA disease later in the season was used as the final benchmark.

Results

Leaves from diseased and healthy grapevines of Marzemino cultivar were sampled and analyzed 24 hrs after collection by Raman spectroscopy. Two types of spectroscopic system were used zfor investigation, a micro-Raman modular system by Horiba, with 532 nm excitation and 50x long working distance objective, and a portable Raman spectrometer (BWTek) equipped with 785 nm excitation and optical fiber attachment. The tested portable system can eventually be used for future applications in field. With both excitation sources, the fluorescence of chlorophylls is a competing signal to Raman spectroscopy which should be removed prior to signal analysis. For 532 nm light, a small detection time (2 s) was used to avoid leaves deterioration due to light absorption. For 785 nm excitation the detection time was increased to 10*s* as no

deterioration of the leaves was noticed. The data were acquired from leaves taken from different vines that are healthy or are infected. From the infected plants, symptomatic and asymptomatic leaves were tested.

The visual inspection of leaves does not allow to distinguish healthy from infected/asymptomatic vines. The spectra of grapevine leaves (Fig. 1) showed vibrational bands assigned to carotenoids, polyphenols and chlorophylls [9][10]. The typical spectra are similar for different classes with only minimal changes, thus indicating that a data analysis is necessary to extract information from the data. For this purpose, spectral data were elaborated using a classification method, namely partial least squares (PLS) algorithm-discriminant analysis (PLS-DA), which combines dimensionality reduction and discriminant analysis into one algorithm and is especially applicable to modeling high dimensional (HD) and collinear data as produced by RS.

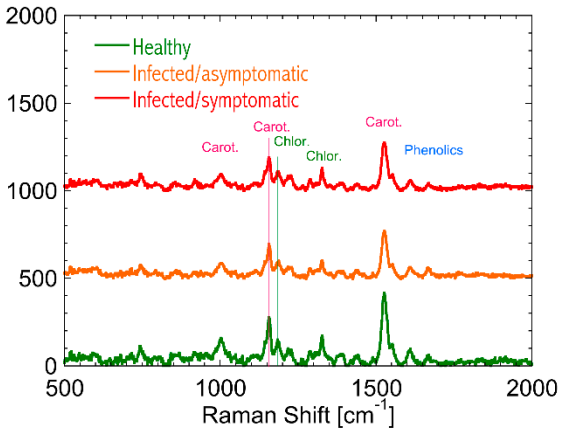

Fig. 1. Example of Raman spectra collected from healthy and Infected (symptomatic and asymptomatic) leaves.

Table 1 report the confusion matrix of the test dataset resulting from PLS-DA analyses when using 532nm laser is shown in Tab. 1. Regarding the prediction from the chemometrics analysis, each row corresponds to a predicted class, each column to an actual class. The classification accuracy (the ratio of correct predictions to total predictions made) is equal to 97%.

real/predicted	Infected	Healthy	not assigned
Infected	147	3	0
Healthy	4	96	0

Table 1: confusion matrix of the test dataset prediction resulting from PLS-DA.

Conclusions

The outcomes of this preliminary investigation showed that we can identify symptomless leaves in ESCA-affected vines as belonging to a diseased vine by measuring a change in spectroscopic properties by RS. A very good classification accuracy was obtained by preliminary tests.

References

[1] C. Bertsch *et al.*, *Plant Pathol.*, vol. 62, no. 2, pp. 243–265, 2013, doi: 10.1111/j.1365-3059.2012.02674.x.

[2] V. Hofstetter, B. Buyck, D. Croll, O. Viret, A. Couloux, and K. Gindro,*Fungal Divers.*, vol. 54, pp. 51–67, 2012, doi: 10.1007/s13225-012-0171-z.

[3] G. Surico, L. Mugnai, and G. Marchi, *Phytopathol. Mediterr.*, vol. 45, no. SUPPL. 1, pp. 68–86, 2006, doi: 10.14601/Phytopathol_Mediterr-1847.

[4] S. Yeturu, P. Vargas Jentzsch, V. CiobotĂ, R. Guerrero, P. Garrido, and L. A. Ramos, *Anal. Methods*, vol. 8, no. 17, pp. 3450–3457, 2016, doi: 10.1039/c6ay00381h.

[5] N. Altangerel *et al.*, *Proc. Natl. Acad. Sci. U. S. A.*, vol. 114, no. 13, pp. 3393–3396, 2017, doi: 10.1073/pnas.1701328114.

[6] A. A. Gitelson and M. N. Merzlyak, *J. Plant Physiol.*, vol. 148, no. 3–4, pp. 494–500, 1996, doi: 10.1016/S0176-1617(96)80284-7.

[7] A. H. Elmetwalli and A. N. Tyler, *Agric. Water Manag.*, vol. 242, no. March, p. 106413, 2020, doi: 10.1016/j.agwat.2020.106413.

[8] J. K. et al H. M. Kalaji, K. Bosa, *Omi. J. Integr. Biol.*, vol. 15, no. 12, pp. 925–934, 2011.

[9] C. Baratto, G. Ambrosio, G. Faglia, and M. Turina, *IEEE Sens. J.*, vol. PP, no. Xx, p. 1, 2022, doi: 10.1109/JSEN.2022.3211616.

[10] L. Mandrile, A. M. Giovannozzi, A. M. Rossi, G. Gambino, E. Noris, and A. M. Rossi, " vol. 13, no. June, 2022, doi: 10.3389/fpls.2022.917226.

DOI 10.5162/SMSI2023/D3.3

How can Raman spectroscopy support optical detection systems for plastic identification in complex recycling streams?

Andréa de Lima Ribeiro[1], Margret C. Fuchs[1], Sandra Lorenz[1], Christian Röder[2], Nadine Schüler[3], Johannes Heitmann[2], Richard Gloaguen[1]
[1] Helmholtz-Zentrum Dresden-Rossendorf, Helmholtz Institute Freiberg for Resource Technology, Freiberg, Germany,
[2] Technische Universität Bergakademie Freiberg, Institute of Applied Physics, Faculty of Chemistry and Physics, Freiberg, Germany
[3] Freiberg Instruments, Freiberg, Germany
a.ribeiro@hzdr.de

Summary:
Binary sorting between ABS and PS polymers is a challenge for the recycling industry, particularly when black pigments are present. We propose the sequential application of a hyperspectral sensor in the short-wave infrared (HSI-SWIR) and a Raman sensor unit (532 nm excitation). HSI-SWIR created maps which allowed for initial spectral and spatial assessment of the material stream and Raman point measurements enabled specific identification of ABS (white and black) and PS. The operationalisation of this sensor network requires advanced solutions for fast data acquisition, processing and classification.

Keywords: polymer, hyperspectral imaging, electronic waste, ABS, PS

Background and Experimental Context

In plastic recycling operations, the accurate identification of polymer types is essential to increase efficiency and particularly quality of recycling products. In complex waste streams, such as waste from electronic and electric equipment (WEEE), the distinction between Polystyrene (PS), Acrylonitrile butadiene styrene (ABS) and the presence of black pigments poses additional challenges to polymer identification by traditional optical methods [1].

Optical sensors aid sorting in recycling lines, and industrial operational requirements for such remote sensing technologies include: i) fast acquisition of spatial and spectral information (< 2 seconds); ii) compatibility with conveyor belt operations; and iii) robust identification of polymers in specific types, preventing downcycling. Polymer identification typically relies on diagnostic features in the visible to short-wave infrared spectral ranges that are recorded by fast hyperspectral sensors (HSI-SWIR, 970 – 2500 nm). The employment of HSI technology allows for instant mapping visualisation displaying spatial composition variations within the waste stream. Still, HSI-SWIR sensor applications are restricted to the identification of some transparent and light-coloured plastics, being unsuitable for identification of black plastics [2] and for fast differentiation between ABS and PS, which are the most common thermoplastics in WEEE [3].

In this contribution, we suggest the sequential employment of HSI-SWIR followed by acquisitions of Raman spectroscopic data. In order to operationalise this sequential sensing, fast data acquisition, process and fusion tools must be developed and integrated to the sensor network.

We selected the following polymer standards, of known composition, to highlight the capacities of each sensor in the proposed network to promote robust and improved recycling: transparent PS, white ABS and black ABS. We employed a HSI-SWIR sensor with acquisition speeds compatible with the recycling industry (SPECIM AisaFenix, @SWIR: 970 – 2500 nm, spectral resolution: 12 nm, spatial resolution: 1.6 mm, integration time: 4.5 ms). For Raman data acquisitions, we designed a custom-based sensor and performed measurements using the following specifications: excitation laser @ 532 nm, 100 mW (maximum laser power); spectrometer WP 532, Wasatch Photonics: 11 cm^{-1} spectral resolution; wavenumber range from 200 – 2500 cm^{-1}; maximum integration times per acquisition: 500 ms.

HSI data corrections for geometric distortions, reflectance calculations and continuum removal (hull correction) were performed using in-house

processing routines based on the Hylite toolbox [4]. We have calculated minimum wavelength (MWL) maps for each data cube indicating the strongest absorption feature for each pixel (from 1650 – 1750 nm). Raman spectra were corrected for background and fluorescence signals from 700 – 2500 cm^{-1}.

Results

Hyperspectral image analysis using the MWL method generated similar results for white ABS and transparent PS (see Fig 1, right). Both polymers exhibit minimum absorption features within the same range (1677 – 1689 nm) and close inspection reveals strong spectral similarities between these thermoplastics (Fig 1, left). The overlap of diagnostic features indicates the impossibility of discerning PS from ABS using this SWIR sensor relying solely on MWL analysis. Previous investigations have identified spectral differences between ABS/PS in the midwave-infrared (MWIR) range, however, the commercial availability of HSI-MWIR sensors is limited. Still, HSI-SWIR spectral information can be used for initial assessment and separation of ABS/PS from other polymers in recycling streams. Furthermore, our HSI-SWIR sensor was able to record the spatial homogeneity with minimum variations of fingerprint positions and hence, consistent with spectral behaviours of the given reference material (Fig 1, right).

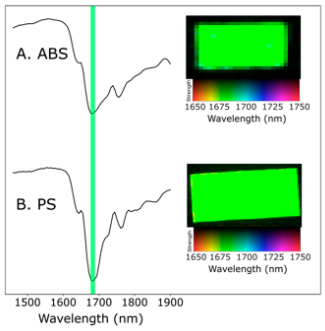

Fig 1. Left: Median spectra calculated for hyperspectral data. The spectral range of diagnostic features for selected polymers is indicated in green. Right: Minimum Wavelength Maps for hyperspectral data cubes (range: 1650 - 1750 nm). A) ABS; B) PS.

Characteristic Raman signals were obtained from all samples, including black ABS. Raman spectra for ABS and PS were marked by benzene ring vibrational modes at ~1001 cm^{-1}. An additional Raman peak is present only on ABS, linked to the butadiene stretching vibrational mode, and allows for clear distinction between ABS and PS polymers, including black ABS. Nevertheless, Raman data acquisitions are restricted to point measurements and do not allow for mapping and 2D digitalization of the recycling stream.

Sensor integration

We propose a sensor network benefitting from both HSI-reflectance and Raman spectroscopic sensors for identification of PS and ABS polymer types. HSI-SWIR provides information for initial classification. Depending on these results regions of the material stream will be selected, where additional validation is required by Raman measurements. The final material classification is updated and then up-scaled to the entire material stream by fast, AI-based algorithms relying on spectral libraries.

Conclusion

The integration of hyperspectral imaging sensors in the short-wave infrared and Raman scattering measurements has potential for solving binary sorting of ABS (including black ABS) and PS using optical methods. An integrated sensor network aiming towards this separation should apply both sensor types, operating with advanced mechanical tools (*e.g.* robots) and relying on advanced data processing strategies for ABS/PS classification based on spectral features.

Acknowledgments

This research was supported by EIT RawMaterials within the KAVA up-scaling project “RAMSES-4-CE” (KIC 19262). We thank The Helmholtz Institute Freiberg for Resource Technology for funding the AisaFENIX sensor.

References

[1] A. Vázquez-Guardado, M. Money, N. McKinney, D. Chanda, Multi-spectral infrared spectroscopy for robust plastic identification, *Applied Optics* 54(24), 7396 (2015); doi: 10.1364/ao.54.007396

[2] O. Rozenstein, E. Puckrin, J. Adamowski, Development of a new approach based on midwave infrared spectroscopy for post-consumer black plastic waste sorting in the recycling industry, *Waste Management* 68, 38–44 (2017); doi: 10.1016/j.wasman.2017.07.023

[3] G. Martinho, A. Pires, L. Saraiva, R. Ribeiro, Composition of plastics from waste electrical and electronic equipment (WEEE) by direct sampling, *Waste Management* 32(6), 1213–1217 (2012); doi: 10.1016/j.wasman.2012.02.010

[4] S. Thiele, S. Lorenz, M. Kirsch, I. C. Contreras Acosta, L. Tusa, E. Herrmann, R. Möckel, and R. Gloaguen, Multi-scale, multi-sensor data integration for automated 3-D geological mapping, *Ore Geology Reviews* 136 (2021); doi: 10.1016/j.oregeorev.2021.104252

DOI 10.5162/SMSI2023/D3.4

Flue gas analysis of wood combustion

Gunter Hagen[1], Thomas Wöhrl[1], Andreas Müller[1], Julia Herrmann[1], Ingo Hartmann[2], Ralf Moos[1]
[1] Department of Functional Materials, Zentrum für Energietechnik (ZET), University of Bayreuth, 95440 Bayreuth, Germany
[2] Deutsches Biomasseforschungszentrum (DBFZ), 04347 Leipzig, Germany
gunter.hagen@uni-bayreuth.de

Summary:
Energetic use of biomass by combustion of wood in log-fueled fireplaces becomes more and more attractive. In-situ sensor-based flue gas analysis could help to efficiently reduce emissions. Firing experiments were carried out with simultaneously collected data about flue gas composition. This includes FTIR gas analysis, particle emissions concerning amount and size distribution (particle spectrometer), several temperature sensors and a lambda probe to determine the residual oxygen concentration beside the data from an inhouse developed sensor, that is sensitive to combustible gases. The sensor results impressively follow the FTIR data. Further investigations and data analysis should focus on correlations between sensor (incl. secondary data) and particle analysis to clarify whether gas sensor data might hint on particle emissions.

Keywords: wood-log fueled batch firing, carbon monoxide gas sensor, flue gas analysis, particle spectrometer, FTIR gas analytics

Background

Actual discussion about energy availability and transformation to renewable sources include the question of biomass use. More and more households use wood-log fueled fireplaces. However, emissions concerning toxic gases like carbon monoxide (CO) or particulate matter (PM) could be immense as both the operation and the combustible material can be highly individual. Several scientific attempts show that automated operation by sensor-based control algorithm may significantly lower the pollutant concentration [1]. Goal of the present study is to demonstrate a possible sensor for flue gas analysis and to collect simultaneously several data during batch firing. For the first time, data from a particulate spectrometer were taken to evaluate number and size distribution of particulate matter continuously during burn-off.

Experimental Setup and Devices

Combustion was done in a LEDA UNIKA fireplace with natural ventilation chimney. Reproducible experiments were done as follows: Fire was started with lighting up four pieces of pine wood (in total 300 g). After a certain time (flame nearly burned down), two other pieces (in total 800 g) were added to the combustion chamber on top of the glow. Combustion air was set to a maximum during the whole burn-off. Gas analyses were carried out by a MKS FTIR system including IAG FLS system with integrated heated filter for probe sampling. All reducing components from the FTIR data were summed up to a CO equivalent value (CO^e). Additionally, a BOSCH LSU 4.9 lambda probe measured the residual oxygen concentration (ROC). Several thermocouple signals (type K) were logged to monitor the flue gas temperature at different positions in the chimney. Beside this, a self-made gas sensor was installed in the chimney. Its measuring principle is based on generated heat by exothermic reactions of reducing gases at a catalytically activated film (details in [2]). The temperature gradient between this activated area and an inert region within the sensor tip is recorded as a thermovoltage signal U_{th}. Particle data were received utilizing a CAMBUSTION DMS 500 particulate spectrometer. Herein, a particle-loaded gas sample is diluted directly after sampling, and particles are charged by a high voltage electrode and analyzed continuously in a column by several electrometer rings.

Results

One exemplary burn-off experiment (cold start) is described in figure 1. Starting the fire causes steeply rising flue gas temperatures. In general, in terms of good combustion, the oxygen content decreases, resulting in kind of a curve that behaves inversely to the flue gas temperature (fig. 1a). Strong changes in temperature and $p(O_2)$ in the range before 1000 s indicate opening the furnace and stoke the fire with wood. Particle analysis shows higher particle concen-

tration during the phase of lighting up with larger particles (high fluctuations). During the second phase of the experiment, particles are below 50 nm with numbers of about $1 \cdot 10^8$ (fig. 1b).

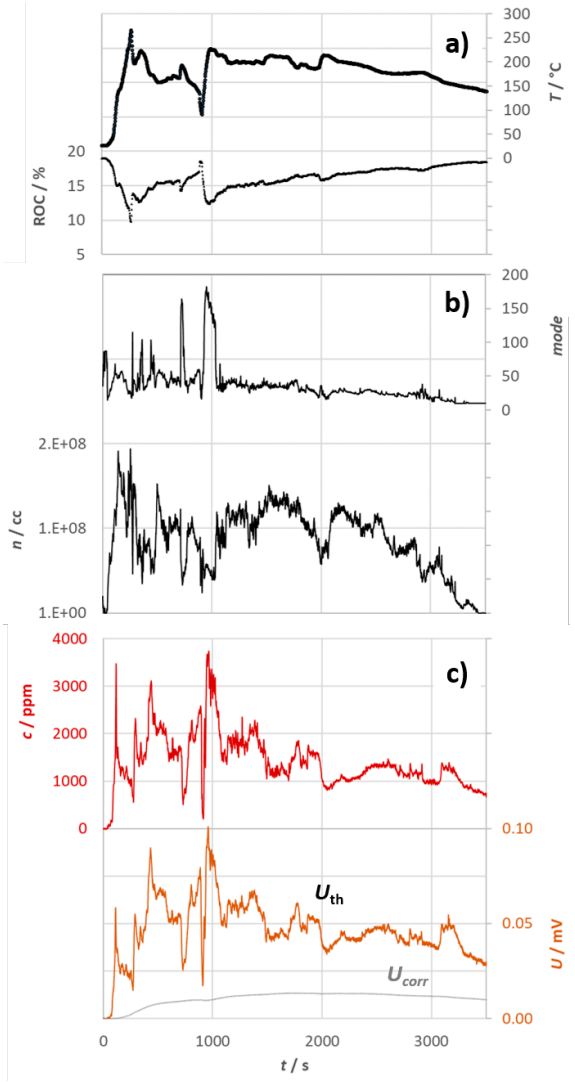

Fig. 1. Several measures during burn-off: a) flue gas temperature at sensors position (T/°C) and residual oxygen concentration p(O_2)/%); b) particulate size mode (maximum of monomodal size distribution in nm) and particulate number value (n/cm³); c) sum of reducing gases (as CO^e equivalent value in ppm) from FTIR analysis, sensor raw signal U_{th} and changing offset voltage U_{corr} from temperature-based coupling effects with respect to the sensor housing to be subtracted.

The gas analysis (FTIR data) shows also higher values during the first phase of the experiment (fig. 1c). Here also, good combustion should result in lower pollutants concentrations. However, the wood-log fueled combustion is highly individual. Fig. 1c also shows the sensor raw data U_{th} (set to zero at t = 0) with its fast response behavior. The signal is slightly cross-sensitive to changing temperatures in the sensor housing, resulting in a variable offset-voltage. This drawback is overcome as follows: An offset-correction value (U_{corr}) was derived from simultaneously taken temperature data ($T_{housing}$ is the temperature at the flange outside the chimney, where the sensor is installed) after equation (1), in which c denotes a constant coupling factor (here: 0.00023 mV/°C).

$$U_{corr} = T_{housing} \cdot c \quad (1)$$

The now corrected sensor signal (U_{th} – U_{corr}) was processed with the sensor's sensitivity (slope of the linear characteristic curve with 25 µV / 1000 ppm CO, which is a typical value achieved in lab measurement with synthetic gas) to a ppm value. Both data are plotted against each other to show their impressive correlation (fig. 2).

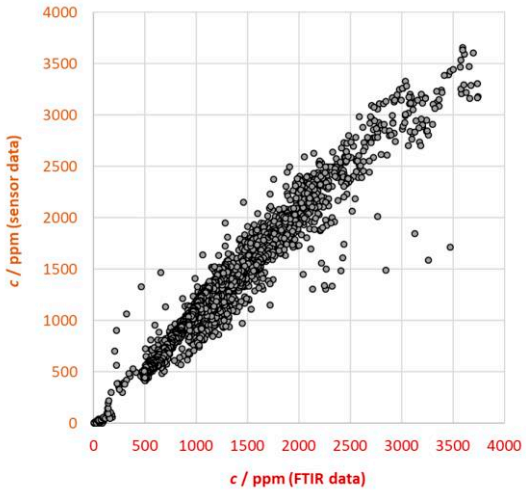

Fig. 2. Sensor data vs. FTIR gas analysis of real exhaust flue gas analysis. Details see text.

Outlook

Highly individual flue gas composition during wood burning in a single room fireplace was analyzed by different devices and methods. Results from a developed thermoelectric gas sensor correlate well with FTIR analytics. Together with several secondary data, correlations might also be found to deduce from gas sensor results to particle formation.

References

[1] P. Butschbach, F. Hammer, H. Kohler, A. Potreck, T. Trautmann, Extensive reduction of toxic gas emissions of firewood-fueled low power fireplaces by improved in situ gas sensorics and catalytic treatment of the exhaust gas, *Sensors and Actuators B* 137(1), 32-41 (2009); doi: 10.1016/j.snb.2008.12.007

[2] S. Wiegärtner, G. Hagen, J. Kita, W. Reitmeier, M. Hien, P. Grass, R. Moos, Thermoelectric hydrocarbon sensor in thick-film technology for on-board-diagnostics of a diesel oxidation catalyst, *Sensors and Actuators B* 214, 234–240 (2015); doi: 10.1016/j.snb.2015.02.083

DOI 10.5162/SMSI2023/D4.1

The Contribution of Sensors of Haptic Feedback in Robotic Hand Control and Teleoperation

Jonas Fischer[1], Daniel Andreas[1], Anany Dwivedi[1], Philipp Beckerle[1,2]
[1] Chair of Autonomous Systems and Mechatronics, Department of Electrical Engineering, Friedrich-Alexander-Universität Erlangen-Nürnberg, Erlangen, Germany,
[2] Department of Artificial Intelligence in Biomedical Engineering, Friedrich-Alexander-Universität Erlangen-Nürnberg, Erlangen, Germany
daniel.andreas@fau.de

Summary:
This paper investigates the importance of sensory feedback for a vibrotactile haptic interface. We propose our initial design with first functional tests using a bidirectional robotic hand. Finally, opportunities to improve the interface with the integration of additional sensors are outlined.

Keywords: haptic feedback, vibrotactile feedback, robotic hand, human-machine interfaces, force sensing

Introduction

The advancements in computing technology over the past decades has led to an increased presence of robotic devices in our everyday life, ranging from vacuum cleaning robots to robotic assistants. These robotic agents can be teleoperated from a distance, leading to applications in the field of tele-presence, tele-medicine, space exploration, and search and rescue operations etc. [1].

In the case of teleoperated robots, it is important for the operator to be aware of their environment for interacting in an efficient manner. The sense of touch is responsible for proprioception of the body (ability to sense movement, action, and limb location) leading to a feeling of presence in the environment [2].

In this work, we propose a wearable haptic feedback armband for bidirectional human-machine interaction with robotic devices that heavily relies on sensory data. To do this, we employ a wearable sensor glove to teleoperate a robotic hand (equipped with fingertip tactile sensing and an inertial measurement unit (IMU)), and using the haptic feedback armband, the operator can receive information regarding the forces exerted during the interactions or weight of the objects.

Background

Vibrotactile feedback is based on vibration motors that change their intensity proportional to the force typically measured at the fingertips. A study by Nabeel et al. [3] claims an improved performance in distinguishing different weights while using vibrational feedback. Seiler et al. [4] investigated the phantom tactile sensation with a vibrotactile interface. The study shows that two closely spaced actuators on the skin produce vibrations which are perceived as one single vibration in between. They found out that it is possible to distinguish between more than 32 different haptic sensations on the upper arm. Vibrotactile feedback is one of the most promising feedback systems so far [3] and is thus within the focus of this work.

Within another study, Clemente et al. [5] presented a device that is able to deliver short-lasting vibrotactile feedback to transradial amputees using commercially available myoelectric hands. By using the proposed feedback system participants improved significantly in handling fragile objects.

Beckerle et al. [6] conducted a study to investigate, which design solutions would increase embodiment during interactions with robotic anthropomorphic hands. Experts in robotic hand design and control systems were asked to develop a design concept for robotic hands as well as for their opinion on haptic feedback and feedback control. Most of the experts (84.62%) agree that the combination of feed forward and feedback control is the best choice. Finally, 76.92% of the experts agreed that force/torque is the quantity that should be controlled.

Sensor-Supported Haptic Feedback

Our system includes a 3D-printed robotic hand which is based on the model of the open-source project "exiii hackberry" by Mission ARM Japan

[7] with added force sensing in all five fingertips. These force sensors not only provide the necessary data for the haptic feedback interface but also allow force control. The robotic hand is controlled by a data glove that contains flex sensors to measure the joint angle of each finger and an IMU.

The vibrotactile feedback system is adapted from Seiler et al. [4]. Linear Resonant Actuators (LRA) are used which can modulate vibration intensity by changing the amplitude rather than frequency. The armband consists of five 3D printed modules, each containing one LRA. These modules are connected through an elastic cord, cables and a toggle drawstring to fit the armband to any arm circumference. Each LRA changes its vibration intensity individually according to the applied force on the corresponding fingertip. To assess the effectiveness of the armband, two studies are proposed. First study focuses on estimation of the weight of the objects being lifted by the robotic hand and the second study focuses on identifying the fingers of the robotic hand which touches the object.

First functional tests with the proposed vibrotactile feedback armband show the general functionality of the system. These tests indicate the possibility to localize vibration of individual modules correctly and thus the affiliation to the respective fingers which is in line with the findings of the study by Seiler et al. [4]. Initial findings also include the possibility to perceive different vibration intensities, depending on the applied force on the fingertips of the robotic hand, which partially matches the results by Nabeel et al. [3].

Conclusion and Outlook

The proposed haptic feedback system could help in distinguishing between different force levels applied on the fingertips of the robotic hand and provides the user, information on the localisation of the stimulation on the robotic hand. However, further large-scale user studies are necessary to draw firm conclusions.

The tightness of the armband affects the performance of the haptic feedback armband. This challenge could be overcome with the integration of FSRs to measure the force between the skin and each of the vibration modules to ensure a determined tightness of the interface. This could make the vibrotactile feedback more reliable across users and less prone to artefacts caused by displacements through motion. The sensory data could allow automatic user-based calibration and inform the user about the ideal tightness. With additional force measurements from the palm of the robotic hand to provide a feedback to the user, a higher dexterity could be achieved by assessing the grasp stability. Furthermore, in the future design we plan to include an IMU to the feedback armband. In combination with the IMU of the data glove, this would allow to control a robotic hand mounted to a robotic arm for teleoperation, while providing the user useful feedback about the applied force on objects.

Haptic interfaces are always reliant on sensory data. This goes beyond the sensory-based localization and intensity of the feedback and includes potential ways to improve the reliability and personalization of the system as well as the ability to control robotic arm/hand systems. These interfaces can be employed not only in case of providing feedback during the use of robotic control, but also with limb prostheses, where persons with limb amputations can receive feedback regarding the interactions for making the control more effective, intuitive, and embodied.

References

[1] A. Dwivedi, G. Gorjup, Y. Kwon, M. Liarokapis, Combining electro-myography and fiducial marker based tracking for intuitive telemanipulation with a robot arm hand system, *28th IEEE International Conference on Robot and Human Interactive Communication (RO-MAN)* 1-6, IEEE (2019); doi: 10.1109/RO-MAN46459.2019.8956456

[2] I. S. MacKenzie, Human-computer interaction: An empirical research perspective. computer interaction. Pearson Education India. (2012)

[3] M. Nabeel, K. Aqeel, M. Ashraf, M. Awan, M. Khurram: Vibrotactile stimulation for 3D printed prosthetic hand, *2nd International Conference on Robotics and Artificial Intelligence (ICRAI)* 2016, S. 202–207 (2016); doi: 10.1109/ICRAI.2016.7791254

[4] J. Seiler, N. Schäfer, B. Latsch, R. Chadda, M. Hessinger, P. Beckerle, M. Kupnik: Wearable Vibrotactile Interface Using Phantom Tactile Sensation for Human-Robot Interaction, *Haptics: Science, Technology, Applications, Springer International Publishing* S. 380–388 (2020), doi: 10.1007/978-3-030-58147-3_42

[5] F. Clemente, M. D'Alonzo, M. Controzzi, B. Edin, C. Cipriani: Non-Invasive, Temporally Discrete Feedback of Object Contact and Release Improves Grasp Control of Closed-Loop Myoelectric Transradial Prostheses, *IEEE Transactions on Neural Systems and Rehabilitation Engineering* 24, 12, S. 1314–1322 (2016); doi: 10.1109/TNSRE.2015.2500586–ISSN 15344320

[6] P. Beckerle, M. Bianchi, C Castellini, G. Salvietti: Mechatronic designs for a robotic hand to explore human body experience and sensory-motor skills: a Delphi study, *Advanced Robotics* 32, S. 670–680 (2018); doi: 10.1080/01691864.2018.148937

[7] Mission Arm Japan: *EXIII-Hackberry*. http://exiii-hackberry.com/. Version: 2022

DOI 10.5162/SMSI2023/D4.2

Zero Signal Determination for Torque Measurement Under Rotation in Test Benches

Paula Weidinger[1], Zihang Song[1], Hongkun Zhang[2], Maximilian Zweiffel[3], Rafael Soares de Oliveira[4]
[1] Physikalisch-Technische Bundesanstalt PTB, Bundesallee 100, 38116 Braunschweig, Germany
[2] Fraunhofer IWES DyNaLab, Am Luneort 100, 27572 Bremerhaven, Germany
[3] Chair for Wind Power Drives CWD, Campus Boulevard 61, 52074 Aachen, Germany
[4] INMETRO, Av Nossa Senhora das Graças, 50, 25650020, Duque de Caxias, Brazil
Paula.Weidinger@ptb.de

Summary:
This paper discusses the problem of determining the zero point when measuring torque under rotation. Two approaches are presented and analysed: static zero signal determination, which should be used for efficiency calculation, and rotational zero signal determination, which should be used for test bench torque calibration under rotation.

Keywords: zero signal determination, offset determination, torque measurement, torque under rotation, torque in test benches

Introduction

Torque transducers that use strain gauges to sense the applied torque characteristically feature an offset signal. This offset signal, called the zero signal, is caused by pre-loads that arise when strain gauges are applied. For correct torque measurement, the zero signal must be determined prior to measurement and used to tare the measurement signal. For static measurements and calibrations, the zero signal is determined as a single value at the beginning of a load sequence. By contrast, a single value for determining the zero signal is not sufficient for measurements under rotation. When measuring under rotation and in a horizontal position, misalignment errors (such as eccentricity, non-parallelism, and tilting in the drive train) and the dead weight of the transducer affect the torque output signal. Under rotation, such dead weight and misalignments can lead to periodic effects. In the following, different approaches are presented for taking these problems into account when determining the zero signal in test benches.

Established approaches

In static torque calibration, the signal in the unloaded condition at the beginning of each load cycle is tared to zero, or it is treated mathematically as zero in the evaluation of the subsequent measurements. [1]

In most test benches, the zero signal is usually defined as just a single value after the torque transducer is installed in the drive train, but in some cases as the mean value of two measurements at different positions. This value is saved and remains valid until the next calibration or until a significant variance in the zero signal is observed.

Zero signal determination in test benches

For zero signal determination in test benches, two options are available: i) static zero signal determination and ii) rotational zero signal determination. [2]

i) Static zero signal determination
The zero signal is measured in equally spaced steps over one full revolution of the drive train. In this work, 30° steps were used for a total of 12 measurement positions. Per position, the signal is averaged over 20 s after a dwell time of 30 s to let the system settle. The static zero signal is then the mean of these averaged signals for all positions over one full revolution.

ii) Rotational zero signal determination
The rotational zero signal is determined at the beginning of each torque load cycle either at minimum or at prevailing rotational speed. Because this approach can be easily integrated into the load cycle, temperature influences are automatically taken into account. The zero signal is averaged over an integer number of full drive train revolutions.

Results

When not installed, the transducer showed a zero signal of 67.76 kN m prior to the measurements in a 10 MW nacelle test bench (NTB).

After these and before the measurements in a 4 MW NTB, the unmounted zero signal of the same transducer was 69.85 kN m.

In Fig. 1, the static zero signal of the torque transducer installed in the 10 MW NTB is plotted over one full revolution. A periodicity of the signal can be seen. This is caused by the dead weight, which was compensated to the greatest possible extent, of the heavy adapters required to install the transducer, the test bench's hexapod, and the drive train itself. In addition, misalignments can have a periodic impact.

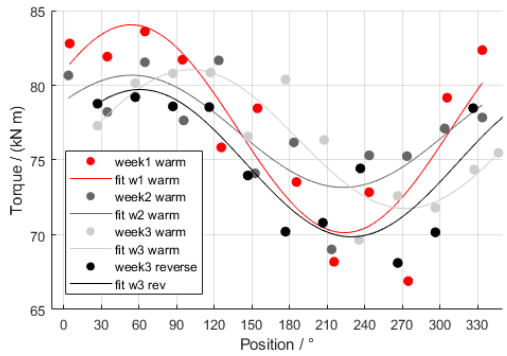

Fig. 1. Static zero signal in 10 MW NTB.

At 75.36 kN m, the average static zero signal on the test bench deviates by 7.60 kN m from the unmounted zero signal.

In the 4 MW NTB, the dead weight of the drive train is actively compensated by the non-torque load system. The averaged zero signals per angle position on different measurement days are randomly distributed; there is no recognisable position-dependent connection (Fig. 2). With an averaged zero signal of 75.31 kN m, the static zero signal in the 4 MW NTB deviates by 5.46 kN m from the non-installed signal.

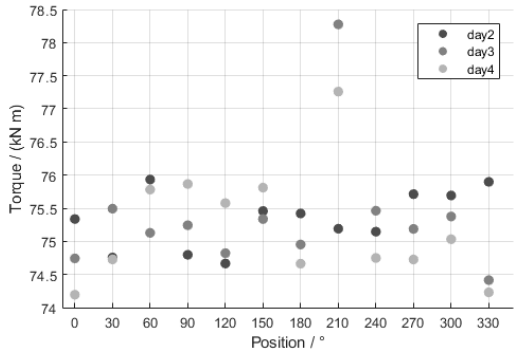

Fig. 2. Static zero signal in 4 MW NTB.

Because of the need to factor in frictional torque as a form of drive train power loss, the static zero signal should be used when determining the efficiency of drive trains on test benches.

The rotational zero signal determined under rotation at different rotational speeds in the 4 MW NTB is depicted in Fig. 3. Here again, the dead weight is actively compensated.

When the converter is switched off, the coherence between torque and rotational speed increases linearly. The increase in torque is caused by the rotational speed dependent friction in the bearings and the cogging torque of the generator. This influence is compensated by the test bench control, as can be seen by the light grey measurement points in Fig. 3. The unloaded signal at the beginning of a load cycle should, as with static torque calibration, also be used for torque calibration under rotation in a test bench. The calibration should be carried out at different rotational speeds, meaning that the zero signal must likewise be determined at different rotational speeds under the same conditions as the subsequent load cycle with control. Here, the quality of the "controlled zero" is not critical for the calibration as the signals for both transducers are tared under the same conditions.

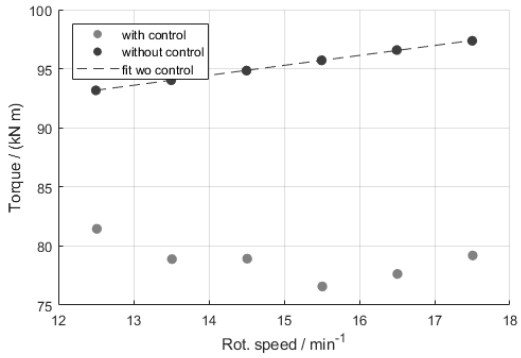

Fig. 3 Rotational zero signal with and without converter and, therefore, DUT control (4 MW NTB).

Conclusion and outlook

When torque measurement under rotation in test benches is done to determine the drive train efficiency, the zero signal should be determined statically over one full revolution. For the calibration of test bench torque under rotation, however, rotational zero point determination at different rotational speeds is the preferred method.

Acknowledgements

Project 19ENG08 has received funding from the EMPIR programme co-financed by the Participating States from the European Union's Horizon 2020 research and innovation programme.

References

[1] *DIN 51309: 2013-09 Material testing machines - calibration of static torque measuring devices.*

[2] P. Weidinger and G. Foyer, "Traceable torque measurement under rotation in nacelle test benches," 2019.

DOI 10.5162/SMSI2023/D4.3

3D Bin Picking with an innovative powder filled gripper and a torque controlled collaborative robot

Fabian Kirner[1], Prof. Dr.-Ing. Thomas Wendt[1], Nikolai Hangst[1]
[1] Hochschule Offenburg, Max-Planck-Straße 1 77656 Offenburg, Deutschland,
Fkirner@stud.hs-offenburg.de

Abstract

A new and innovative powder filled gripper concept will be introduced to a process to pick parts out of a box without the use of a camera system which guides the robot to the part. The gripper is a combination of an inflatable skin, and a powder inside. In the unjammed condition, the powder is soft and can adjust to the geometry of the part which will be handled. By applying a vacuum to the inflatable skin, the powder gets jammed and transforms to a solid shaped form in which the gripper was brought before applying the vacuum. This physical principle is used to pick parts. The flexible skin of the gripper adjusts to all kinds of shapes, and therefore, can be used to realize 3D bin picking. With the help of a force controlled robot, the gripper can be pushed with a consistent force on flexible positions depending of the filling level of the box. A Kuka LBR iiwa with joint torque sensors in all of its seven axis' was used to achieve a constant contact pressure. This is the basic criteria to achieve a robust picking process.

Keywords: Powder filled gripper, vacuum, 3D bin picking, force controlled robot, joint torque sensors

Introduction

Robot based bin picking is a rising topic in the field of fully automated assembly. Traditional feeding methods like bowl feeders and presenting parts to the assembly robot in a tray drive up costs in automation projects. The more unique components there are in an assembly, the more feeding systems are needed to present the parts in proper orientation for the assembly robot. Very often, the costs for feeding systems exceed the costs for robots in an assembly project. Therefore, new concepts are needed to increase the economic efficiency of assembly cells. One of these concepts is bin picking. The idea is to present a box filled with components to the robot and the robot picks the parts out of the box.

State of the art

Common bin picking systems described in the literature, use a high performance camera system which guides the robot to a part in the box. Both, the position and the orientation of the parts needs to be guided by the camera [1] [2]. Despite 3D bin picking being a popular research topic for years, it hasn't been developed in practice. There are many issues which stop companies from using this technology. On the one side, 3D objects have different appearances, illumination, and occlusion when seen from different viewpoints [3]. Many more issues occur in practice, depending on the geometry, the surface, and the material of the parts which should be handled. These problems often lead to unreliable image recognition which, in turn, lead to unsuccessful picking results.

Powder filled vacuum gripper

In this article, a gripper with an inflatable skin filled with powder is being used to pick the parts out of the box. No camera is needed. The function of the gripper is quite simple. In the unstressed condition, the powder in the gripper is soft and enables the possibility to adjust to any contour of the part which has to be picked. Once the gripper forms around the part, a vacuum generator creates a vacuum in the inside of the inflatable skin. The applied vacuum forces the powder inside the inflatable skin to become solid. A combination of form, fit, traction, and adhesion, is causal that the part sticks at the gripper [4]. For the inflatable skin, many known materials, such as a balloon and latex bag, were tested. It turned out that the finger of a rubber glove gives a very good compromise between resistance and adjustability.

Coffee powder was used for the filling, as it is light, and gets very soft in the un-jammed condition [4]. The part used was a gear with sharp edges which should be handled with the gripper. The sharp edges of the gear require a high wear resistance and a high puncturing of the skin.

Bin Picking with a sensitive robot

In the test, a box filled with gears was emptied by a sensitive robot with a powder filled gripper. A Kuka LBR iiwa 7 R800 robot was selected as an adequate robot. It can handle a payload of 7 kg and is equipped with joint torque sensors in all seven of its axis.

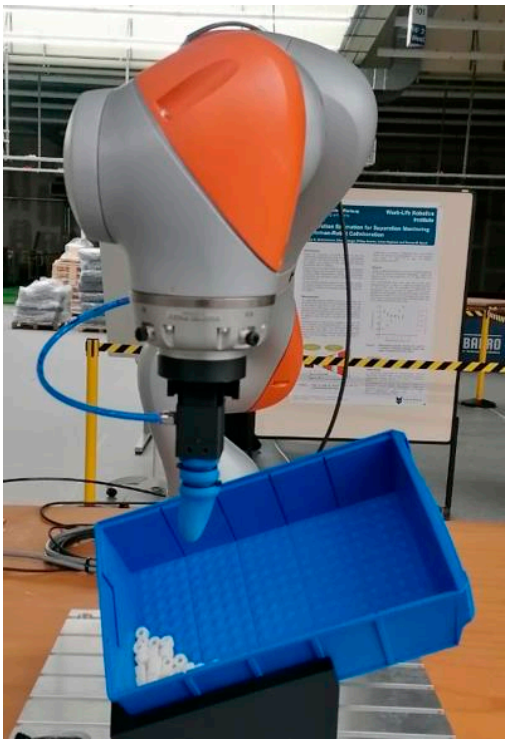

Figure 1: Kuka iiwa LBR 7 R800 robot with a powder filled gripper

These joint torque sensors enable to operate the robot force controlled. The accuracy of those sensors in each axis is 2% of the max torque [5]. The high performance controller also enables force and torque controlled movements in all of its seven axis, as well as along and around the Cartesian axis. It can measure the weight and the center of gravity of its end of arm tool automatically. The use of joint torque sensors provides the opportunity to make the end of arm tool flexible in the required axis. Additionally, it provides the opportunity to simulate a spring with the robot arm and move the robot arm until a specified force is applied on the end of arm tool. The robot is collaborative because of its lightweight design and its joint torque sensors. Also, the gripper doesn`t have any moving parts which means it can be seen as collaborative. Before pushing the gripper on the gears, the gripper gets applied with a positive pressure of 0.2 bar to ensure a soft powder. If the pressure is less than 0.2 bar the gripper doesn`t lose the coffee powder properly. If the pressure is increased above 0.2 bar the gripper inflates. The possibility to move the end of arm tool until a specified force is met on the end of arm tool is used to empty the boxes filled with gears. In a series of tests, it was determined that the optimal force, with which the gripper has to be pressed on the gears in the box, is 40 N. The robot was programmed to move in Z-direction until it measures a counter force of 40 N. It then stops the movement. Once this occurs, the powder filled gripper is applied around one or more gears in this area. Then the vacuum gets applied on the gripper and the parts stick on the gripper. These parts can then be placed in a centering fixture or on a plate where the next robot can pick the part. The force control is important since the filling level in the box changes. This feature enables to compensate the changing pick up height.

To avoid areas without parts in the box it should be placed tilted (see figure 1). In case a situation occurs which leads to a couple of unsuccessful gripping, knocking on the box changes the order of the gears in the box and allows further picking.

Conclusion and Outlook

In this work, a new concept for bin picking has been successfully demonstrated. A force controlled robot with a powder filled gripper does make sense when an automation has more than one component to be picked out of the box. As a next step, the lifetime of the gripper needs to be validated. To orientate the gears in a specified orientation an alignment station could be created.

References

[1] C. Martinez, R. Boca, B. Zhang, H. Chen, S. Nidamarthi, Automated Bin Picking System for randomly located industrial parts, *2015 IEEE International Conference on Technologies for practical Robot Applications (TePRA), (2015);* doi: 10.1109/TePRA.2015.7219656

[2] M. Berger, G. Bachler, S. Scherer, Vision Guided Bin Picking and Mounting in a Flexible Assembly Cell, *Intelligent Problem Solving. Methodologies and Approaches, 109-117* (2003); doi: 10.1007/3-540-45049-1_14

[3] C. Zhuang, Z. Wang, H. Zhao, H. Ding, Semantic part segmentation method based 3D object pose estimation with RGB-D images for bin-picking *Robotics and Computer-Integrated Manufacturing Volume 68* (2021); doi 10.1016/j.rcim.2020.102086

[4] J. Amend, E. Brown, N. Rodenberg, H. Jaeger, H. Lipson, A Positive Universal Gripper Based on the Jamming of Granular Material, *IEE Transactions on Robotics Volume 28 341 – 350* (2012); DOI: 10.1109/TRO.2011.2171093

[5] Kuka, Datasheet for LBR iiwa 7 R800 (2022)

DOI 10.5162/SMSI2023/D4.4

Innovative and cost-effective Measurement Setup to determine Robot Accuracy

Thomas M. Wendt[1], Markus Gapp[1], Anke Fischer[1]
[1] Offenburg University of Applied Sciences, Badstraße 24, 77652 Offenburg, Germany,
markus.gapp@hs-offenburg.de

Summary
Established robot manufacturers have developed methods to determine and optimize the accuracy of their robots. These methods vary from robot manufacturers to their competitors. Due to the lack of published data, a comparison of robot performance is difficult. The aim of this article is to find methods to evaluate important characteristics of a robot with an accurate and cost-effective setup. A laser triangulation sensor and geometric referenced spheres were used as a base to compare the robot performance.

Keywords: accuracy, laser triangulation, measurement, repeatability, robotics

Introduction

Robot accuracy is crucial in current industrial applications with needed deviations smaller than 0.2 mm [1]. Beneath the pose accuracy often stated by manufacturers, other criteria are far more essential for many applications, e.g. the path accuracy or the distance for relative programming [2]. These are listed in ISO 9283 among several other criteria for pose and path accuracy [3]. A complete set of the characteristics needed for comparison between robots are often not given. For accuracy critical processes such as assembly or laser related operations it is essential to have the robot performance in advance.

In the beginning theodolites were used for measurement and calibration of robotic kinematics [4]. Nowadays camera-based units and laser interferometer are preferred [5]. A disadvantage of all systems is the effort in use and the costs.

This work provides a solution to derive with simple equipment two criteria of the above mentioned ISO 9283 in order to estimate the performance of the robot for individual use in one's own production.

Methods

The path accuracy and the pose repeatability were measured as a feasibility test for the set-up. An edge is used to derive the path accuracy which is measured while the robot is moving along a given linear path. A board with four spheres and a diameter of 32 mm was used for the pose repeatability test. This board is a geometric reference with defined positions to each other as seen in **Figure 1**. The center of one sphere is used to trace back the position of the robot. The setup was a laser triangulation sensor (ECCO75.100, SmartRay) mounted at a 6-DoF robot (RA605-710-K, HIWIN) and the set-up board. The sensor data were given as distances of a 2D-line measured between sensor and board.

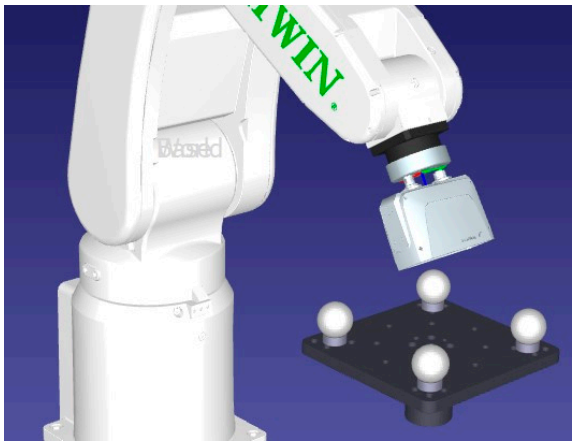

Figure 1 Robot and geometric setup (example), Picture was generated with RoboDK library [6].

As stated in ISO 9283 thirty measurements were repeated to evaluate the repeatability of pose. One data set was recorded for the path accuracy. The measured circle section was used to calculate x- and y-coordinates of the center. The radius was determined with a circle fit method [7]. The resulting errors were calculated as stated in ISO 9283.

Results

The data sheet specifies the pose repeatability as ±0,02 mm. The calculated robot pose re-

peatability results in ±0,031 mm. **Figure 2** shows the distribution of the pose repeatability according to Reinhart et al. [1]. The distribution results in measurement standard deviation of 6.5 µm.

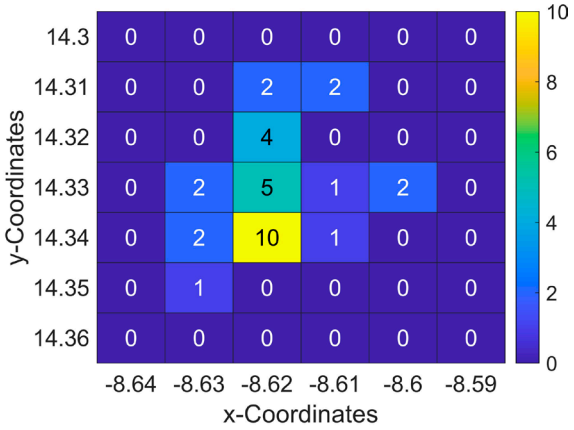

Figure 2 Distribution of sphere centers in pose repeatability measurements. The numbers show the distribution of the respective calculated coordinates.

The robot movement was parallel to a metal edge. While moving with 32 mm/s, the sensor measured with a sample rate of 50 Hz.

The base level of the start and end position was estimated by using the average of ten samples at the beginning and end of the predefined trajectory. The calculated nominal values of the line were used to derive the error along the 415 mm path resulting in maximum errors of 66 µm in x-, 656 µm in y- and 1.610 mm in z-direction (data in sensor coordinate system). This is shown in **Figure 3**.

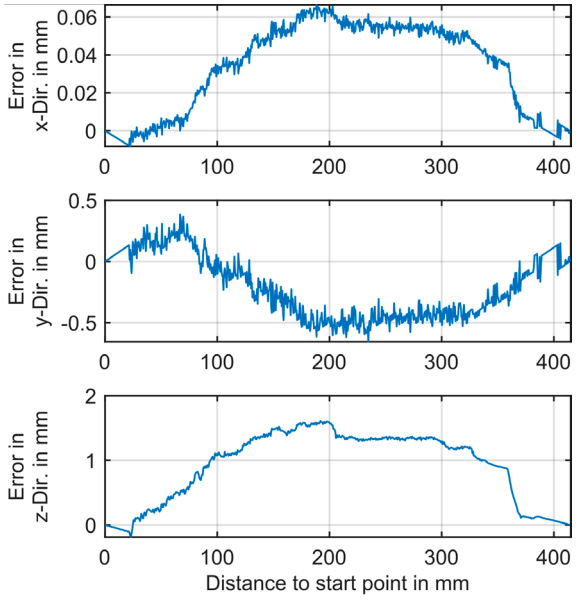

Figure 3 Path error, x, y and z error are shown separately.

Discussion

The setup is an accurate and low-cost solution to measure a robot on self-defined tasks. It is hypothesized that the exceeding errors occur due to inhomogeneous reflections on the spheres. The errors in z-direction are partly caused by shifts in x-direction since the 2-dimensional measurement is not capable to distinguish these errors.

On the path there can be reflections due to disturbances on the surface seen as peaks in **Figure 3**. These may have an influence in the maximum values. Also, the angle needs to be considered between the surface and the sensor. It has to be in the range of 40° to 60° in order the get a signal from both sides of the edge.

Conclusion

It has been shown that both characteristics, pose repeatability and path accuracy, could be derived with the inexpensive ECCO75.100 sensor. This setup can help to compare different robots in order to estimate the usability in certain applications, especially for the small size robot series up to 10 kg load.

Investigations need to be done in filtering the data, angle (object to sensor) optimization and implementing further criteria.

References

[1] Gunther Reinhart, Alejandro Magaña Flores, Carola Zwicker, Industrieroboter, Ed.1, *Vogel*, Würzburg, 23-24 (2018); ISBN-10:3834334014

[2] Andeas Pott, Thomas Dietz, Industrielle Robotersysteme, *Springer Vieweg*, Wiesbaden, 28-30 (2019), doi:10.1007/978-3-658-25345-5

[3] ISO:9283:1998 Manipulating industrial robots – performance criteria and related test methods, 1998

[4] Z. Roth, B. Mooring and B. Ravani, An overview of robot calibration, *IEEE Journal on Robotics and Automation*, 3(5), 377-385 (1987), doi: 10.1109/JRA.1987.1087124

[5] Z. Li, S. Li and X. Luo, "An Overview of Calibration Technology of Industrial Robots," *IEEE/CAA J. Autom. Sinica*, 8(1), 23-36 (2021) doi: 10.1109/JAS.2020.1003381

[6] RoboDK library, https://robodk.com/library, 2022

[7] Nikolai Chernov (2022). Circle Fit (Pratt method), https://www.mathworks.com/matlabcentral/fileexchange/22643-circle-fit-pratt-method, *MATLAB Central File Exchange*. Retrieved October 15, 2022.

DOI 10.5162/SMSI2023/D5.0

Compressed Sensing Spectral Photoluminescence Imaging of Wide Bandgap Semiconductor Materials for Power Electronics Applications

George Koutsourakis, Andrew Thompson, James C. Blakesley, and Sebastian Wood
National Physical Laboratory, Hampton Road, Teddington, Middlesex, TW11 0LW, UK
sebastian.wood@npl.co.uk

Summary:
A compressed sensing approach has been adopted for spectral photoluminescence imaging measurements at NPL. The features and performance of the proposed methodology is initially studied with simulations, which looked at the requirements for a measurement system implementation. Simulation results are presented for a typical homoepitaxial 4H-SiC defect, while an experimental implementation is proposed. Compressed sensing can offer a higher signal to noise ratio and faster measurement acquisition for spectral PL measurements than conventional techniques.

Keywords: spectral photoluminescence, compressed sensing, semiconductor metrology, power electronics, silicon carbide

Introduction

Wide bandgap (WBG) semiconductors such as silicon carbide (SiC) and gallium nitride (GaN) exhibit higher critical (breakdown) electric field strength, higher electron mobility, and better thermal properties than silicon (Si) [1][2]. Such attributes make them highly attractive for high-power and high-temperature applications for electronic devices, such as power electronics. A major challenge for high quality SiC and GaN production has been the elimination of defects that can affect device performance, such as stacking faults, edge dislocations, screw dislocations, polytype inclusions, and basal plane dislocations. Photoluminescence (PL) imaging spectroscopy is a useful method to detect defects, using PL spectroscopy with a 325 nm laser.

In this work, a novel spectral PL imaging method for WBG materials is presented. The methodology is based on compressed sensing, an advanced sampling methodology that can allow single pixel imaging, higher signal to noise ratio and increased measurement speed compared to a point-by-point scan. The method is validated through simulations and the experimental implementation is discussed.

Compressed sensing methodology

Compressed sensing (CS) refers to a methodology to solve inverse problems, where signals are reconstructed from incomplete or inaccurate measurements [3]. Reconstruction from undersampled datasets is possible by carefully designed measurements using assumptions about signal structure (sparsity).

For compressed sensing, a series of patterns is projected on the sample under test, instead of a point-by-point scan, with a measurement applied for each pattern. In this work the Walsh-Hadamard Transform (WHT) is used to generate patterns, wavelets are used as the sparsifying transform and the SPGL1 algorithm (Spectral Projected Gradient for $\ell 1$ minimization) [4] is used to reconstruct high resolution images in a few seconds on a conventional computer.

Simulation results

In order to investigate the application of CS for spectrally and spatially resolved photoluminescence measurements on WBG materials, a real spectral photoluminescence dataset was used. The dataset is from measurements of a polytype inclusion in homoepitaxial 4H-SiC. The initial PL map was acquired using a scanning spectral PL microscopy system with a 325 nm excitation laser, to provide the data cube for the simulations. In order to apply CS on this dataset, a smaller 64 × 64 area of the dataset was selected. The area corresponds approximately to a 50 µm × 50 µm area of the SiC wafer, around the centre of the defect. A series of binary structured patterns were projected on the selected area, with the total spectral profile for each pattern recorded, as presented in Fig. 1. Only contributions from pixels that correspond with unmasked areas of the pattern are taken

into account, and their sum is calculated for each wavelength.

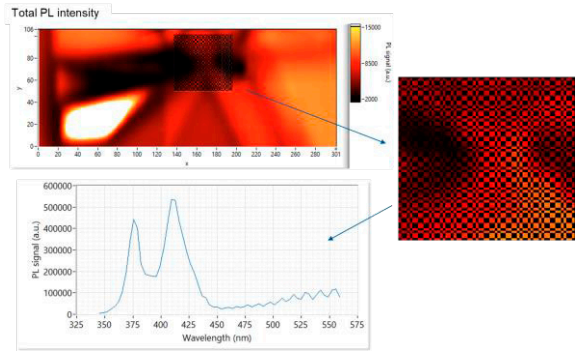

Fig. 1. The sampling process for the CS simulations. An area of the PL map is selected, a series of patterns is applied on this area.

The sampled data were then used to reconstruct a spectral map for each wavelength through the optimisation algorithm. Fewer samples than the pixels of the map (64 × 64 = 4096) are required for reconstruction, which means the final dataset can be acquired with undersampled datasets. Distinctive PL peaks are clearly observed corresponding to emission from polytypes with reduced bandgap.

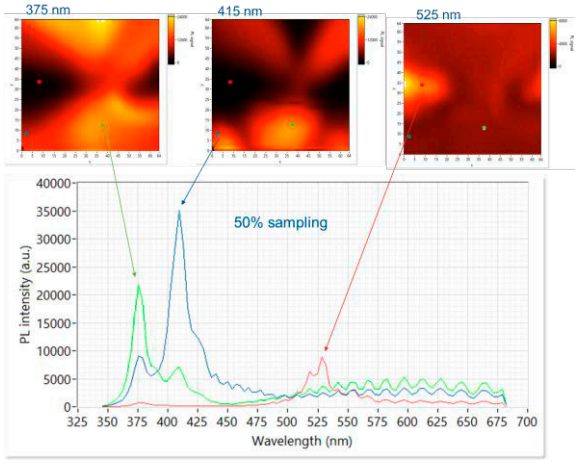

Fig. 2. Reconstruction results at 50% undersampling, for the three different PL emission peaks, along with the spectra of the selected points (red, green, blue spots) on the maps for each reconstruction case.

In order to get a more realistic understanding of the application of compressed sensing for spectral PL mapping, noise has been added in the sampling process. Noise levels from 0.1 % up to 1 % were tested, with the changes being apparent when higher levels of noise are added. The results are presented in Table 1, for the 410 nm reconstructed map at 50 % sampling, with different noise levels. Reconstruction results with noise higher than 0.5% of measured signal are significantly degraded.

Table 1. Correlation coefficient between initial and reconstructed PL image for different noise levels.

SAMPLING LEVELS / GAUSSIAN NOISE	25%	50%	75%
0.10%	0.990	0.992	0.996
0.20%	0.986	0.988	0.986
0.50%	0.961	0.943	0.923
1%	0.873	0.810	0.745

Experimental implementation

A simplified schematic of the experimental implementation is presented in Fig 3. A digital micromirror device (DMD) is used for pattern generation and a 325 nm UV laser for excitation. The spectrum for each pattern is measured using a spectrometer.

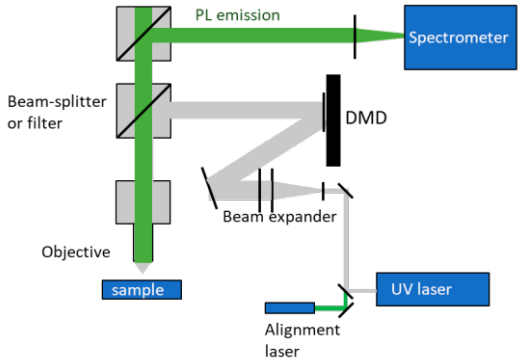

Fig. 2. Schematic of the CS spectral PL experimental setup of this work.

Conclusions

Compressed sensing has been demonstrated for spectral PL imaging measurements at NPL, through a simulation process using real measurement data. The potential for faster measurements due to undersampling has been observed and the noise requirements for the experimental implementation have been defined.

References

[1] T. Kimoto, “Bulk and epitaxial growth of silicon carbide,” *Prog. Cryst. Growth Charact. Mater.*, vol. 62, no. 2, pp. 329–351, Jun. 2016, doi: 10.1016/j.pcrysgrow.2016.04.018.

[2] X. Ding, Y. Zhou, and J. Cheng, “A review of gallium nitride power device and its applications in motor drive,” *CES Trans. Electr. Mach. Syst.*, vol. 3, no. 1, pp. 54–64, Mar. 2019, doi: 10.30941/CESTEMS.2019.00008.

[3] D. Donoho, “Compressed sensing,” *IEEE Trans. Inf. Theory*, vol. 52, no. 4, pp. 1289–1306, Apr. 2006, doi: 10.1109/TIT.2006.871582.

[4] E. van den Berg and M. P. Friedlander, “Probing the Pareto Frontier for Basis Pursuit Solutions,” *SIAM J. Sci. Comput.*, vol. 31, no. 2, pp. 890–912, Jan. 2009, doi: 10.1137/080714488.

DOI 10.5162/SMSI2023/D5.1

Compressed nano-FTIR Hyperspectral Imaging for Characterizing Defects in Semiconductors

Dario Siebenkotten[1], Arne Hoehl[1], Manuel Marschall[1], Gerd Wübbeler[1], Clemens Elster[1], Eckart Rühl[2], Sebastian Wood[3], Bernd Kästner[1]
[1] Physikalisch-Technische Bundesanstalt, Abbestr. 2-12, 10587 Berlin,
[2] Physikalische Chemie, Freie Universität Berlin, Arminallee 22, 14195 Berlin, Germany
[3] National Physical Laboratory, Hampton Road, Teddington, TW11 0LW, UK
bernd.kaestner@ptb.de

Summary:
In the field of power electronics, the ongoing development of wide-bandgap compound semiconductors is limited by material defects, which compromise device performance and reliability. New metrological tools are required with high sensitivity to local material properties, such as noninvasive nano-FTIR hyperspectral imaging to map properties such as: crystal structure, carrier density, or strain on the nanoscale. However, full spatio-spectral imaging is constrained by long measurement times. Here we discuss a compression method that allows us to reduce the measurement time by up to 90%.

Keywords: power electronics, semiconductor defects, nano-FTIR, compressed spectroscopy, low-rank matrix reconstruction.

Introduction

In infrared (IR) hyperspectral imaging (HSI) a spectrum is recorded at each pixel of a 2D specimen. It is a powerful tool for contactless material characterization utilized in analytical chemistry [1], microelectronics [2] and for novel functional materials [3]. In this work, we consider HSI with nanoscale spatial resolution using nano-FTIR [4]. However, HSI results in large data sets which are acquired in long, often unfeasible acquisition times. We therefore discuss a compression strategy to be employed at the measurement stage to image defects in the wide-bandgap semiconductor 4H-SiC which is particularly relevant for applications in the field of power electronics. We show that the amount of measured data can be reduced by up to 90% while keeping the information relevant for defect characterization in the reconstructed data.

Method

Nano-FTIR is a scanning-based technique which combines Fourier transform infrared spectroscopy (FTIR) and scattering-type scanning near-field optical microscopy. In nano-FTIR spectroscopy is realized by passing broadband IR radiation through an asymmetric Michelson interferometer containing a metallized tip of an atomic force microscope (AFM) in close proximity to the sample in one of the arms while the length of the reference arm is defined by a movable mirror. Here we employ a NeaSNOM instrument from Attocube GmbH operated using wideband synchrotron radiation [9]. For single-frequency imaging a quantum cascade laser is employed. The compression strategy was based on a low-rank matrix reconstruction method that was previously developed in Ref. [5] for FTIR measurements. It couples the spatial domain and the interferometer axis by reconstructing the most significant factorized basis elements. An additional incorporation of spatial smoothness using a Tikhonov regularization enhances our treatment and an L-curve criterion adapts the additional parameter.

Nearfield imaging of a triangular SiC defect

We demonstrate our method by imaging a triangular defect, which typically exhibits a polytype inclusion within a homoepitaxial layer of 4H-SiC layer. The inset of Fig. 1 shows an IR nearfield phase image of a defect-section recorded at 940 cm^{-1}. While there is clear contrast the interpretation is ambiguous since it can be caused by several factors.

A simulation of the nearfield phase for varying doping and polytype is shown in Fig. 1, both of which may vary spatially around defects. Therefore, it is not sufficient to image at a single frequency but to record the complete spectrum at each pixel.

Compressed nano-FTIR imaging

The same defect has also been imaged using the nano-FTIR method. Interferograms are recorded by continuous movement of the reference

mirror. They contain information about both, the phase and amplitude of the radiation scattered from the AFM tip. This means that the interferograms are measured directly while the spectrum is obtained by Fourier transformation. The phase spectrum can then be compared to the diagrams in Fig. 1.

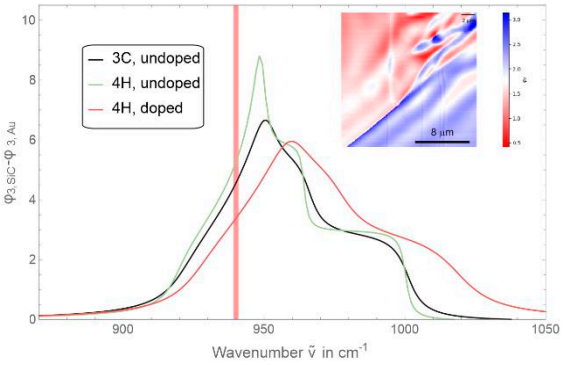

Fig. 1. Simulated phase spectra for 3C and 4H SiC polytypes and different doping; inset: nearfield phase image measured at 940 cm^{-1}.

The topography of the imaged defect is shown in the atomic force microscopy image in the inset of Fig. 2. The measurement time of each spectrum was 14 s. For demonstration purposes the spatial resolution was limited to 13x13 pixels within the red square marked in the topography image resulting in a total measurement time of 40 minutes.

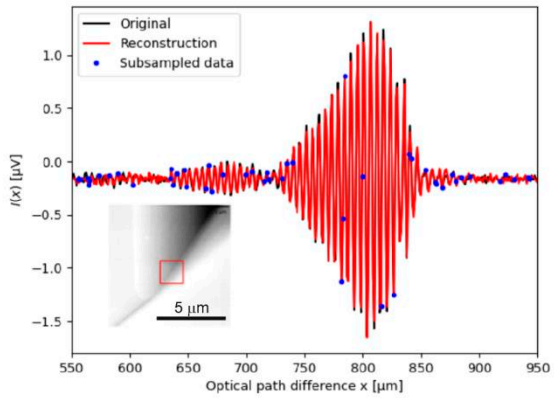

Fig. 2. Measured and reconstructed interferograms and topography of the defect-section.

Fig. 2 shows an example-interferogram from which the nearfield phase spectrum can be calculated. To illustrate that the amount of data can be reduced while keeping the relevant spectral information we randomly selected only 10% of the measurement points (blue dots). When applying the reconstruction algorithm of Ref. [5] the remaining 90% of the datapoints have been mathematically reconstructed. The reconstructed curve is plotted in red over the original curve in black. Note that the reconstruction algorithm relies on the ensemble of subsampled interferograms.

Conclusion and Outlook

We have shown that the amount of data in nano-FTIR hyperspectral imaging can be significantly reduced by considering the example of a triangular polytype defect in 4H-SiC. Depending on spectral properties such as sparsity and further prior knowledge about the sample alternative algorithms [6] or extensions [7] may be employed. The random selection of data may lead to idle times during the measurement when transferring between different datapoints. This issue has been discussed in Ref [8] where specific continuous measurement routes have been suggested which do not significantly affect the reconstruction quality using the low-rank algorithm. This will facilitate hardware implementations in commercially available instruments, such as the one employed in this work.

Acknowledgement

The work was partially funded within the project 20IND09 PowerElec from the EMPIR programme co-financed by the Participating States and from the European Union's Horizon 2020 research and innovation programme. We acknowledge financial support by Deutsche Forschungsgemeinschaft (Grants EL 492/1-1, RU 420/13-1).

References

[1] R. Salzer & H. W. Siesler, "Infrared and Raman Spectroscopic Imaging," (Wiley, 2009).

[2] W. S. Lau, "Infrared Characterization for Microelectronics," (World Scientific Publishing, 1999).

[3] J. Barnett, et al., *Adv. Funct. Mater*. 30, 2004767 (2020); doi: 10.1002/adfm.202004767

[4] F. Huth, et al., *Nano Letters*, 12, 3973–3978 (2012); doi: 10.1021/nl301159v

[5] M. Marschall, et al., *Optics Express*, 28, 38762 (2020); doi:10.1364/OE. 404959

[6] B. Kästner, et al., *Optics Express*, 26, 18115 (2018); doi:10.1364/OE. 26.018115

[7] G. Wübbeler, et al., *Measurement Science and Technology*, 33, 035402 (2022); doi: 10.1088/1361-6501/ac407a

[8] S. Metzner, et al., *IEEE Transactions on Instrumentation and Measurement*, 71, 1–8 (2022); doi: 10.1109/TIM.2022.3204072

[9] P. Hermann, et al., *Optics Express*, 21, 2913 (2013); doi: 10.1364/OE.21.002913

DOI 10.5162/SMSI2023/D5.2

Optical and Tactile Measurements on SiC Sample Defects

Jana Grundmann[1], Elena Ermilova[2], Andreas Hertwig[2], Petr Klapetek[3], Silvania F. Pereira[4], Jila Rafighdoost[4], Bernd Bodermann[1]
[1] Physikalisch-Technische Bundesanstalt (PTB), Bundesallee 100, 38116 Braunschweig, Germany,
[2] Bundesanstalt für Materialforschung und -prüfung (BAM), Division 6.1 Surface Analysis and Interfacial Chemistry, Unter den Eichen 44-46, 12203 Berlin, Germany,
[3] Cesky Meteorologicky Institut (CMI), Okružní 31, 638 00 Brno, Czech Republic,
[4] Delft University of Technology, Faculty of Applied Sciences, Imaging Physics Department, Lorentzweg 1, 2628 CJ Delft, Netherlands
jana.grundmann@ptb.de

Summary:
The different defect types on SiC samples are measured with various measurement methods including optical and tactile methods. The defect types investigated include particles, carrots and triangles and they are analyzed with imaging ellipsometry, coherent Fourier scatterometry and atomic force microscopy. Each of these methods measures different properties of the defects and they all together contribute to a complete analysis.

Keywords: defects, silicon carbide, imaging ellipsometry, coherent Fourier scatterometry, atomic force microscopy

Introduction

Power electronics is a key technology in many areas of our daily lives, such as intelligent energy distribution or electromobility. It is currently dominated by silicon technology. However, there is an increasing transition to wide bandgap compound semiconductors, which also include gallium nitride and silicon carbide (SiC). These compound semiconductors offer many advantages over silicon as they can operate at higher temperature, switching frequency and voltage [1]. However, material defects can affect the long-term stability of these materials. During the manufacturing processes, it is difficult to identify and characterize these defects with existing techniques. For this reason, novel methods will be developed to make this possible. There are several approaches, all of which have in common that they are non-destructive. Imaging ellipsometry and coherent Fourier scatterometry are the optical methods used and atomic force microscopy is the tactile method used.

In the following, the different types of defects on SiC layers epitaxially grown on SiC substrates will be discussed as well as the measurement methods used and their respective measurements.

The SiC epitaxial wafers used for the measurements were grown in an AIXTRON Planetary Reactor®.

Defect types

Defects on SiC are distinguished between crystallographic defects within the wafer and surface defects. Crystallographic defects can expand onto the wafer surface during epitaxial growth and thus form the surface defects [2]. Various surface defects are found on the samples studied here, the most common being particles, carrots and triangles (see Fig. 1).

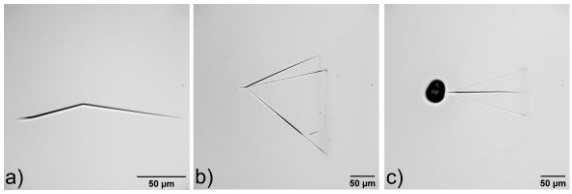

Fig. 1. Microscope images of the SiC defects. a) carrot defect; b) triangle defect; c) particle with triangle defect

Imaging Ellipsometry

An imaging ellipsometer combines classical ellipsometry with microscopy. In ellipsometry, changes in the polarization of light are detected after reflection or transmission at the sample. For the imaging setup, the data is evaluated for each pixel of the camera instead of being integrated over the entire illumination spot size as in the case of classical ellipsometry. This makes it possible to measure polarization features locally on the sample, areas much smaller than the illumination spot size and even non-periodic structures. However, it is an indirect

method and requires numerical simulations to reconstruct structure parameters and to solve the inverse diffraction problem. [3]

Both Mueller matrix and Psi and Delta images are used for the data evaluation. Psi and Delta are the measured ellipsometric transfer quantities. The dielectric properties and the thickness of thin transparent and semi-transparent layers can be determined from them. The Mueller matrix is a 4 by 4 matrix with dimensionless values between -1 and 1 and represents the change in the polarization. Each matrix element consists of an image in which each pixel represents the value of the corresponding matrix element (see Fig. 2b)).

Coherent Fourier Scatterometry

Coherent Fourier scatterometry (CFS) is a measurement method based on scatterometry, where coherent light is focused on the sample and the scattered light is collected in the far field on a split detector. The data is collected by scanning the sample in a raster scan mode and recording the differential photocurrent of the split detector for each scan point. The scattered maps reveal all asymmetries in the scattered field and is thus sensitive to the presence of isolated defects on the sample. This technique has been applied for the detection of isolated spherical nanoparticles [4] and in this work we show that it can also be used for the detection of non-spherical defects as shown in Fig. 2c).

Atomic Force Microscopy

Atomic force microscopy (AFM) is a high-resolution tactile scanning method and is used for the measurement of the surface topography. It can be used for the mapping of the defects at different spatial scales, up to individual atomic plane resolution and it can include both the local defects and overall statistical parameters, like roughness.

Measurements

Different areas within the complex structure of SiC defects could be detected and analyzed by means of the imaging ellipsometer EP4 from Accurion. An ellipsometric microscope image is shown in Fig. 2a), a Mueller matrix image in Fig. 2b) and a CFS scattered map in Fig. 2c). These optical measurements show the ability of imaging ellipsometry and CFS to identify the surface defects with high contrast. In the Muller matrix image, a change in the polarization state is visible in some matrix elements, which simplifies the detection of these defects.

In Fig. 2d) an AFM measurement of a triangle defect is shown. Its surface topography can be clearly seen, and the dimensions of the defect can be derived from the topography. In this way, the AFM measurement supports the analysis of the SiC defects, which can be detected using the optical methods.

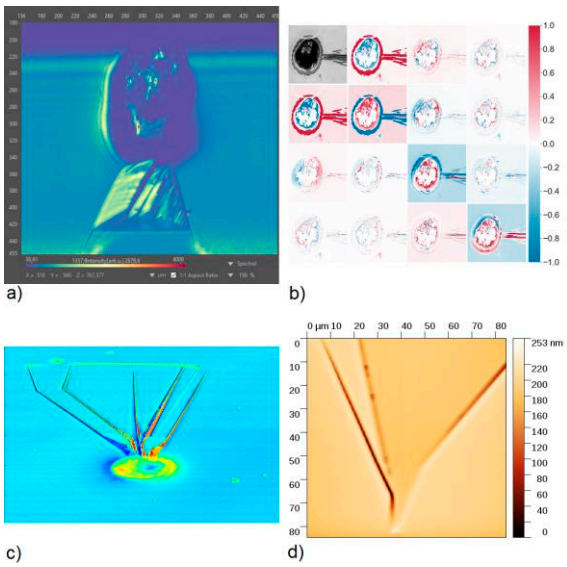

Fig. 2. Measurements on SiC defects. a) ellipsometric microscope image of a particle with triangle defect, 10x magnification; b) Mueller matrix image of a particle with triangle defect, 20x magnification; c) CFS scattered map of a particle with triangle defect; d) AFM measurement of a triangle defect

References

[1] N. Kaminaki, State of the art and the future of wide band-gap devices, *2009 13th European Conference on Power Electronics and Applications*, 1-9 (2009)

[2] H. Song, T. S. Sudarshan, Basal plane dislocation conversion near the epilayer/substrate interface in epitaxial growth of 4° off-axis 4H-SiC, *Journal of Crystal Growth* 371, 94-101 (2013); doi: 10.1016/j.jcrysgro.2013.02.011

[3] S. Liu, W. Du, X. Chen, H. Jiang, C. Zhang, Mueller matrix imaging ellipsometry for nanostructure metrology, *Opt. Express 23*, 17316-17329 (2015); doi: 10.1364/OE.23.017316

[4] S. Roy, A. C. Assafrão, S. F. Pereira, H. P. Urbach, Coherent Fourier scatterometry for detection of nanometer-sized particles on a planar substrate surface, *Opt. Express 22*, 13250-13262 (2014); doi: 10.1364/OE.22.013250

Acknowledgement

This project 20IND09 PowerElec has received funding from the EMPIR programme co-financed by the Participating States and from the European Union's Horizon 2020 research and innovation programme.

DOI 10.5162/SMSI2023/D5.3

Electrical Characterization of the SiO_2/4H-SiC Interface

Chezhiyan Nanjappan[1], Georg Pfusterschmied[1], Ulrich Schmid[1]
[1] Institute of Sensor and Actuator Systems, Gußhausstraße 27-29, 1040 Wien, Austria,
Corresponding Author's e-mail address: chezhiyan.nanjappan@tuwien.ac.at

Summary:
The interface trap density D_{it} is an important parameter to characterize the quality of the oxide/semiconductor interface. The low channel mobility (20 cm^2/Vs for dry thermal oxidation) in silicon carbide-based MOS devices is mostly attributed to the high amount of interface traps. To attain high mobilities (>80 cm^2/Vs), it is required to reduce the D_{it} to the range of 10^{10} $cm^{-2}eV^{-1}$ or below. Post oxidation annealing under nitrogen-based gaseous environment is known to reduce D_{it}, but still there is the requirement to reduce the D_{it} to reach those values of standard silicon/silicon-dioxide interfaces (10^{10} – 10^{11} $cm^{-2}eV^{-1}$). Oxides on SiC formed by plasma oxidation process instead of dry oxidation represents a promising technology, as it is known for exhibiting lower D_{it} values in the range of 10^{10} – 10^{11} $cm^{-2}eV^{-1}$. However, the physics behind the plasma oxidation of 4H-SiC is not yet completely understood. In this work, we report first results about the enhanced oxidation rate and improved electrical characteristics when an oxygen plasma pre-treatment is implemented before the standard dry oxidation of 4H-SiC.

Keywords: Siliconcarbide, thermal oxidation, plasma oxidation, TEOS, interface, defect density.

Introduction

Hexagonal silicon carbide (4H-SiC) has gathered considerable interest in the recent decades due to its superior material properties compared to silicon (Si). The high band gap of 3.26 eV, a high thermal conductivity of 450 W/mK and a high breakdown field of 2.4 MV/cm makes this compound semiconductor a promising candidate especially for power electronics. A bottleneck of SiC-based devices is the low inversion channel mobility (n-channel mobility ~40 cm^2/Vs for TEOS deposited oxide), while their Si counterparts exhibiting a mobility of ~360 cm^2/Vs [1-3].

Dry thermal oxidation is the most widely used method for the oxidation of SiC. On the SiC surface, oxygen reacts with silicon and forms amorphous SiO_2 at temperatures above 1000°C. The remaining carbon from the SiC crystal lattice either outgasses as carbon oxides (CO or CO_2) or remains in the oxide or at the interface as structural defects (SiO_xC_y) [4]. As the latter are electronically active, SiO_xC_y species are regarded to reduce substantially both the oxide quality and the transition region at the interface, thus negatively impacting the channel mobility. Moreover, it is a time-consuming process (for example, obtaining 100 nm thermal oxide on the Si-face of 4H-SiC it takes about 20 hours at 1200°C [5]) with the requirement of a high thermal budget [4-8].

Plasma oxidation on SiC is facilitated by exposing the substrate to highly active oxygen plasma. Compared to dry thermal oxides, plasma oxides have reduced concentration of the carbon species (SiO_xC_y) because the highly active oxygen atoms (O_2^*) react with these carbon species to form SiO_2 and CO or CO_2 is outgassed as shown in eq. (1). This results in a reduced number of the interface state density D_{it} (10^{10} – 10^{11} $cm^{-2}eV^{-1}$) compared to dry oxidation with D_{it} values in the range of 10^{12} – 10^{14} $cm^{-2}eV^{-1}$ [3, 4].

$$SiO_xC_y + O_2^*(\text{plasma}) \rightarrow SiO_2 + CO(g)/CO_2(g) \quad (1)$$

In plasma oxidation, it is the diffusion of high active oxygen atoms (O_2^*) through the interface while in thermal oxidation it is mostly O_2 molecule that migrate to the SiC/SiO_2 interface [4].

Another technique of oxide formation on SiC is oxide deposition from tetraethyl orthosilicate (TEOS). A bubbler-system in combination with argon (Ar) as carrier gas is used to hydrolyze TEOS. The hydrolyzed TEOS-Ar gas mixture is introduced to a process chamber where SiO_2 is deposited on the SiC substrate at low pressure levels of < 1 Torr and temperatures of about 700°C. Since this technique does not consume the substrate, there is no incorporation of carbon atoms into the oxide or any accumulation of carbon at the interface (D_{it} -10^{11} -10^{12} $cm^{-2}eV^{-1}$) [3]. Also, the deposition rate is high (~15 nm min^{-1}) compared to the previous methods and does not show any thickness dependencies. Main drawback of TEOS oxides is that they suffer from

increased gate leakage, which is likely due to the presence of structural defects and trapped charges originating from dangling bonds predominantly at the interface [3, 11].

Experimental details

MOS capacitors were fabricated with commercial n-type 4H-SiC substrates with a 5 µm thick epilayer on top. The doping concentration of the epilayer was ~$2 \cdot 10^{16}$ cm^{-3}. Wafer was first cut into 1 cm x 1 cm squared sample snippets. All samples were cleaned using standard RCA (Radio Corporation of America) cleaning procedure before further processing.

For this study three samples have been investigated. Sample #1 was thermally oxidized at 1100°C in pure O_2 atmosphere at 760 Torr pressure for 34 hours. Sample #2 was pre-treated with an oxygen plasma before thermal oxidation (same process as sample #1). On sample #3 the oxide layer was deposited using TEOS. The fabrication of sample #3 was conducted by an external service provider and can be considered as an industry reference standard. A SiO_2 layer thickness of around 100 nm was achieved on all three samples. Next all samples underwent post oxidation annealing in nitrous oxide (N_2O) environment at 1100°C which facilitates nitridation of the interface, thereby reducing D_{it}.

For electrical characterization, Titanium (Ti) and Platinum (Pt) were sputtered on the bottom sides of the substrate. Then the samples were subjected to rapid thermal annealing at 1000°C for 1 minute to obtain a good ohmic contact. Aluminum (Al) was evaporated for the gate electrode. An array of circular metal pads with a diameter of 500 µm are patterned by wet etching.

Results

The oxide thickness of sample #1, #2 and #3 were 118 nm, 135 nm and 100 nm, showing that the enhanced oxidation rate during thermal oxidation by about 14 % when plasma pre-treatment was applied. The oxide layers were characterized using AFM, SEM and TEM.

Capacitance-voltage (C-V) and conductance-voltage (G-V) measurements were done simultaneously to evaluate the quality of the MOS capacitors. From C-V curves, the doping concentration (Sample #1 and #2 - $8.1 \cdot 10^{16}$ cm^{-3}, #3 – $1 \cdot 10^{16}$ cm^{-3}) of the epi layer was obtained by plotting $1/C^2$ vs V. From G-V measurement, the flatband voltage (Sample #1 – 3.4 V, #2 – 0.4 V, #3 – 0.9 V) was obtained. Next, the ideal CV curve was calculated with the determined flatband voltage and doping concentration. Then the D_{it} is calculated with the Terman method [10].

From the results (see Fig. 1), we can clearly see that the plasma pre-treatment reduces the D_{it}, but needs further research efforts to reach the industry standard D_{it} values from TEOS oxides on 4H-SiC.

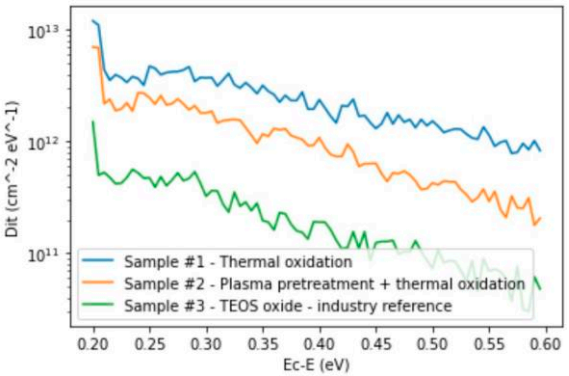

Fig. 1. Interface state density values of industry reference TEOS oxide, thermal oxide and plasma pretreated thermal oxide.

Conclusion

We investigated thermal oxidation on 4H-SiC substrate with an additional plasma pre-treatment step. We observed that the plasma pretreatment results in increased oxide rate and also improves the electrical properties of the MOS capacitor. In the near future, the reason for this improved oxide quality when applying this plasma pretreatment has to be studied, so that better quality oxides can be fabricated with this approach.

References

[1] Advancing Silicon Carbide Electronics Technology II. Materials Research Forum LLC, 2020. doi: 10.21741/9781644900673.

[2] Y. Zhang, IOP Conf. Ser.: Mater. Sci. Eng. 738, 012004 (2020). doi: 10.1088/1757-899x/738/1/012004.

[3] D.-K. Kim, K.-S. Jeong, Y.-S. Kang, H.-K. Kang, S.W. Cho, S.-O. Kim, D. Suh, S. Kim, and M.-H. Cho, Sci Rep 6, (2016). doi: 10.1038/srep34945.

[4] T. Yamamoto, Y. Hijikata, H. Yaguchi, and S. Yoshida, MSF 600–603, 667 (2008). doi: 10.4028/www.scientific.net/msf.600-603.667.

[5] Benfdila, A., & Zekentes, K. (2010). On silicon carbide thermal oxidation. The African Review of Physics, 4.

[6] X. Liu, J. Hao, N. You, Y. Bai, and S. Wang, AIP Advances 9, 125150 (2019). doi: 10.1063/1.5115538.

[7] P. Fiorenza and V. Raineri, Appl. Phys. Lett. 88, 212112 (2006). doi: 10.1063/1.2207991.

[8] A. Siddiqui, R.Y. Khosa, and M. Usman, J. Mater. Chem. C 9, 5055 (2021). doi: 10.1039/d0tc05008c.

[9] Y. Hijikata, S. Yagi, H. Yaguchi, and S. Yoshi, Physics and Technology of Silicon Carbide Devices (2012). doi: 10.5772/50748.

[10] D.K. Schroder, Semiconductor Material and Device Characterization (John Wiley & Sons, Inc., 2005). doi: 10.1002/0471749095.

[11] J.H. Moon, I.H. Kang, H.W. Kim, O. Seok, W. Bahng, and M.-W. Ha, Current Applied Physics 20, 1386 (2020). doi: 10.1016/j.cap.2020.09.003.

DOI 10.5162/SMSI2023/D5.4

Compressed Sensing Time Resolved Photoluminescence Imaging for Semiconductor Characterisation

Aidas Baltušis[1,2], *George Koutsourakis*[2], *Sebastian Wood*[2], *Stephen Sweeney*[3]
[1]*Advanced Technology Institute, University of Surrey, Guildford, GU2 7XH, UK*
[2]*National Physical Laboratory, Hampton Road, Teddington, Middlesex, TW11 0LW, UK*
[3]*James Watt School of Engineering, University of Glasgow, Glasgow, G12 8LT, UK*
aidas.baltusis@npl.co.uk

Summary:
Compressed sensing has been applied to time-resolved photoluminescence measurements for semiconductor device and material characterisation. This novel approach has the potential to achieve charge carrier lifetime imaging of semiconductor samples with shorter measurement times, higher repeatability and increased signal to noise ratio. The feasibility of the approach is investigated through simulations and an order of magnitude improvement in measurement acquisition speed over scanning approaches is demonstrated in this work. A proof-of-concept experimental system is presented, with initial measurements confirming the feasibility of this method.

Keywords: Compressed sensing, photoluminescence, semiconductor characterisation, signal processing, TCSPC

Introduction

The recent emergence of single pixel imaging techniques via compressed sensing [1] has led to implementations in various types of measurements. It is particularly useful in novel imaging applications where standard CMOS/CCD sensors cannot be used. It allows for images to be accurately acquired using a single-point detector, such as a photomultiplier tube (PMT) without requiring any mechanical movement of samples. Instead, digital light processing with a series of measurement patterns is used, and the image information is later reconstructed.

For semiconductor devices, this approach has been reported in the past for photocurrent mapping [2]. Another established but more complex measurement technique in semiconductor material and device characterisation is time-resolved photoluminescence (TRPL) [3]. The optical nature of the measurement is particularly useful because no contacts are required, and the method is non-destructive. The sample is excited using a laser pulse, resulting in photoluminescence (PL) emission. PL emission is detected with a single pixel detector such as a PMT, with high temporal resolution, allowing determination of the decay time of the signal and the charge carrier lifetimes. The lifetime probes the radiative and non-radiative recombination processes happening within the material [4].

In this work, a time correlated single photon counting (TCSPC) prototype system is demonstrated which can acquire maps of TRPL signal across a sample by applying compressed sensing methods. The process of the method is presented, along with feasibility experimental results and limitations of the prototype system.

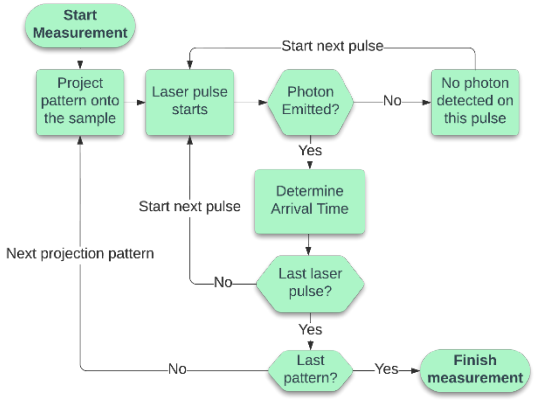

Figure 1. A diagram of the compressed sensing TRPL process. After projecting each pattern, the TRPL response is gathered from the excited area. The final measurements are TRPL responses for each pattern.

Methodology

In previous work, we have demonstrated the computational model for implementing compressed sensing TRPL imaging. Based on that, a proof-of-concept experimental setup has been developed. The measurement system is built similarly to a standard time-resolved photoluminescence setup. A digital micromirror device (DMD) [5] was added into the optical path and

the laser beam expanded to overfill the DMD area. This allows for compressed sensing patterns to be projected onto the measured sample. A typical measurement process is shown in Figure 1. After projecting each sampling pattern onto the sample, the combined TRPL response of the excited area is acquired. PL images for each bin of the decay curve are then reconstructed using a modified convex optimization algorithm SPGL1 (spectral projection gradient L1 minimisation algorithm) [6].

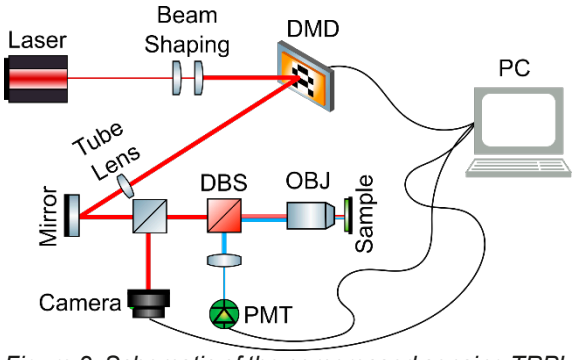

Figure 2. Schematic of the compressed sensing TRPL system of this work.

Results

Results from Cadmium Indium Gallium Selenide (CIGS) solar cell sample are presented in this work. Figure 3 (a) shows a photocurrent map of the measured sample area. This is used as a reference image, against which reconstructed photoluminescence maps were compared, although we do not expect the photocurrent map to correspond directly to the PL images. In subfigure (b) the total reconstructed photoluminescence map is shown. PL map at the peak of TRPL decay and 1.2 ns after the peak are shown in (c) and (d) respectively. In (c) the PL illumination is more evenly distributed across the measured area, with a low-intensity corner remaining in the top-left part of the sample, where a contact is located. In (d) the recombination is more unevenly distributed, as carriers diffuse and recombine. The extended defects in the sample show up as darker areas in the image.

The current limitations of the prototype system are its sensitivity to any non-uniformities in the laser beam profile as well as noise sources in the measurements. The non-uniform beam profile of the laser used shows up as higher or lower intensity regions in the reconstructed images, convoluted with any variations of the sample structure. Furthermore, drift in the sample response and fluctuations in laser power result in the reconstruction algorithm being less efficient and so introduce random noise to the images.

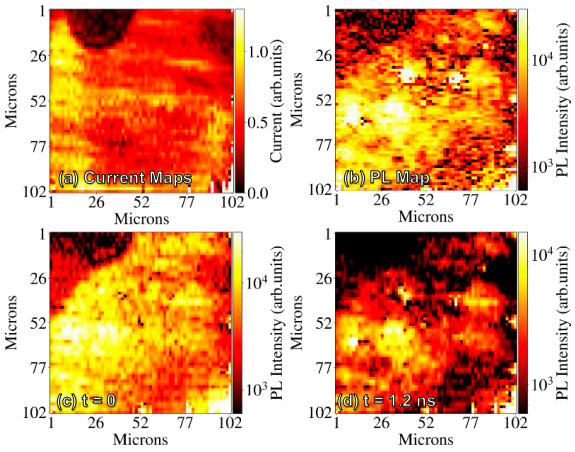

Figure 3. a) Photocurrent response map of a CIGS sample, 64x64 px resolution. The dark area in the top left is a piece of electrical contact, the rest is active material. (b) PL map after compressed sensing process of the same area. (c) and (d) present PL intensity maps at the peak of TRPL and 1.2 ns after the peak.

Conclusions

We have developed a prototype system and methodology for TRPL imaging without using a raster scanning approach. The use of projection patterns increases the measurement acquisition speed. The system can be further optimised by using a higher power laser with a uniform beam profile. Similar measurement methods can potentially be implemented to different types of measurements such as spectrally resolved photoluminescence.

References

[1] M. F. Duarte *et al.*, “Single-pixel imaging via compressive sampling” *IEEE Signal Process. Mag.*, vol. 25, no. 2, pp. 83–91, 2008, doi: 10.1109/MSP.2007.914730.

[2] G. Koutsourakis, A. Thompson, and J. C. Blakesley, “Toward Megapixel Resolution Compressed Sensing Current Mapping of Photovoltaic Devices Using Digital Light Processing,” *Sol. RRL*, vol. 2100467, pp. 1–8, 2021, doi: 10.1002/solr.202100467.

[3] T. Trupke, B. Mitchell, J. W. Weber, W. McMillan, R. A. Bardos, and R. Kroeze, “Photoluminescence imaging for photovoltaic applications,” *Energy Procedia*, vol. 15, no. 2011, pp. 135–146, Jan. 2012, doi: 10.1016/j.egypro.2012.02.016.

[4] M. Maiberg and R. Scheer, “Theoretical study of time-resolved luminescence in semiconductors. I. Decay from the steady state,” *J. Appl. Phys.*, vol. 116, no. 12, 2014, doi: 10.1063/1.4896483.

[5] L. J. Hornbeck, “The DMD™ Projection Display Chip: A MEMS-Based Technology,” *MRS Bull.*, vol. 26, no. 4, pp. 325–327, 2001, doi: 10.1557/mrs2001.72.

[6] E. van den Berg and M. P. Friedlander, “Probing the Pareto frontier for basis pursuit solutions,” *SIAM J. Sci. Comput.*, vol. 31, no. 2, pp. 890–912, 2008, doi: 10.1137/080714488.

DOI 10.5162/SMSI2023/D6.1

Multiplexing interferometers to provide novel capabilities for nanometrology

Thomas Kissinger
Institute of Process Measurement and Sensor Technology, Technical University of Ilmenau, Germany
thomas.kissinger@tu-ilmenau.de

Summary:
Multiplexing interferometers within a single beam, based on their optical path difference, using laser wavelength-modulated signal processing techniques such as the range-resolved interferometry method, allows for interesting new capabilities in precision interferometry. For example, these include single-beam differential interferometry or position encoders with multiple degrees-of-freedoms using only a single fibre-coupled access port.

Keywords: optical interferometry, interferometer multiplexing, pseudo-heterodyne interferometry, range-resolved interferometry, nanometrology

Introduction

The ability to spatially resolve and synchronously demodulate the interferometric phase at multiple locations along a single beam, based on the optical path difference (OPD) of each individual interferometer, allows new, innovative uses in precision interferometry. This is possible using new variants of laser wavelength-modulated (pseudo-heterodyne) interferometric signal processing techniques, such as the range-resolved interferometry (RRI) [1] technique. Here, a sinusoidal modulation of the laser wavelength introduces a unique carrier signal for each interferometer dependent on the respective OPD that can be used for phase demodulation of that interferometer.

General advantages of pseudo-heterodyne signal processing techniques are that interferometric phase demodulation can be achieved, unlike in most homodyne or heterodyne techniques, without the need for polarization-optical components or other methods of beam separation. Furthermore, using diode lasers, wavelength modulation can be achieved by simple injection current modulation, minimizing component complexity. Numerous pseudo-heterodyne techniques have been proposed in the past. These include techniques with linear (sawtooth or triangular) modulation waveform, such as the original pseudo-heterodyne scheme [2]. While linear techniques are conceptually simple, they pose practical difficulties because of the difficulty in keeping a linear sweep waveform stable owing to the many harmonics present in the modulation waveform. A second class of pseudo-heterodyne schemes uses sinusoidal modulation waveforms. These include the phase generated carrier [3], and the deep frequency modulation [4] methods. Similar techniques are also widely used in commercially available Fabry-Perot interferometers [5].

Multiplexing Interferometers

Prior approaches, with the exception of some specialized schemes [6], generally only allow demodulation of the phase of a single interferometer at a single OPD. Therefore, no multiplexing is possible and furthermore, the presence of multiple interferometric signal components, which could also be unintentionally introduced by multiple or parasitic reflections, can cause nonlinearity problems. In contrast to most schemes, the RRI approach uses very strong wavelength modulation of the laser diode. This allows the separation of multiple signals in the recorded interferogram based on their OPD-dependent fringe rate. In contrast to prior art [6], this is not restricted to a specified OPD grid, but OPDs of constituent interferometers can be continuously variable once a minimum separation, dependent on the laser wavelength modulation excursion, is exceeded.

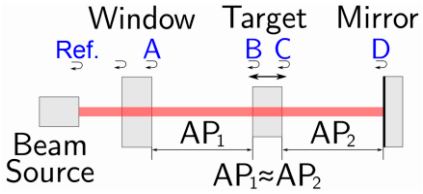

Fig. 1. Setup of the single-beam differential interferometry approach, with the movement of a semi-transparent target being measured by computing the difference between two nominally equal air path lengths AP1 and AP2 from four reflections A to D.

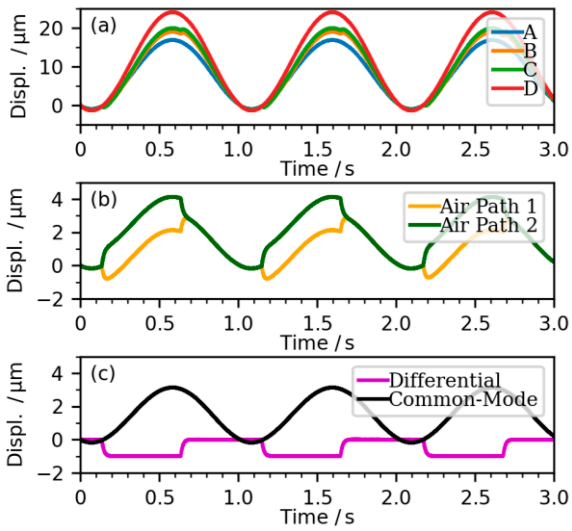

Fig. 2. Example measurement where the target step movement can be cleanly separated from an intentionally introduced sinusoidal wavelength disturbance.

One interesting example of the usefulness of multiplexing interferometers is single-beam differential interferometry [7]. The general principle of this approach is shown in Fig. 1. Here, four interferometers are spanned between the reference, obtained from the fibre tip reflection at the fibre collimator, interfering with the four respective window/mirror surfaces marked A to D. The aim of this approach is to measure the movement of a semitransparent target window. This is being measured by evaluating the difference between the phase signals corresponding to the two air paths AP1 (B-A) and AP2 (D-C). Because the two airpaths are nominally of similar length, calculating their difference reduces the effective dead path to near zero, strongly suppressing common-mode influences, such as air refractive index changes, laser wavelength drift or homogeneous thermal expansion. Fig. 2 shows an example measurement, where a 1 µm step movement is measured in the presence of an intentionally introduced sinusoidal disturbance of the laser wavelength of ±45 ppm amplitude. Here, Fig. 2(a) shows the phase signals that are directly measured for the four reflections A to D. Fig. 2(b) then plots the signals for the computed air paths, while Fig. 2(c) illustrates clean separation of the step movement from the common-mode disturbance.

A further example of multiplexing interferometers is described in detail in [8]. Using a single laser, a single photodetector and a single fibre coupled access port, a total of three interferometers are multiplexed, enabling use of this configuration as a 3D stage encoder. Multiplexing several interferometers onto only one access fibre is especially interesting for vacuum or cryogenic environments, where such an arrangement reduces the number of fibre feedthroughs required. For example, the multiplexing of interferometers using RRI has recently been demonstrated by Christiansen et al. [9] in a cryogenic environment, ultimately intended for space use.

Conclusion

The ability to multiplex interferometers has many potential applications, some of which are discussed above. In addition, these approaches also leverage on the availability of cost-effective yet highly coherent monolithic laser diodes and associated fibre components, originally developed for the telecoms industry. Therefore, range-resolved signal processing techniques open up novel solutions to existing measurement problems in precision engineering.

References

[1] T. Kissinger, T.O.H. Charrett, and R.P. Tatam, Range-resolved interferometric signal processing using sinusoidal optical frequency modulation, *Opt Express* 23.7, 9415-9431 (2015); doi: 10.1364/OE.23.009415

[2] D. A. Jackson et al., Pseudoheterodyne detection scheme for optical interferometers, *Electronics letters* 25.18, 1081-1083, (1982); doi: 10.1049/el:19820740

[3] A. Dandridge, A.B. Tveten, and T.G. Giallorenzi, Homodyne demodulation scheme for fiber optic sensors using phase generated carrier, *Trans. Microw. Theory Tech.* 30.10, 1635-1641, (1982); doi: 10.1049/el:19820740

[4] O. Gerberding, Deep frequency modulation interferometry, *Opt Express* 23.11,14753-14762, (2015); doi: 10.1364/OE.23.014753

[5] K. Thurner et al., Fiber-based distance sensing interferometry, *Appl. Opt.*, 54.10, 3051-3063, (2015); doi: 10.1364/AO.54.003051

[6] I. Sakai, R. Youngquist, and G. Parry, Multiplexing of optical fiber sensors using a frequency-modulated source and gated output, *J. Lightwave Technol.* 5(7), 932–940, (1987); doi: 10.1109/JLT.1987.1075586

[7] T. Kissinger and R. P. Tatam, Differential displacement measurements along a single beam using range-resolved interferometry, In *SPIE Optical Metrology 2019, Munich, Germany, Proc SPIE* 11056, 76-81, 2019; doi: 10.1117/12.2524009

[8] K.B. Wiseman, T. Kissinger and R.P. Tatam, Three-dimensional interferometric stage encoder using a single access port, *Opt. Lasers Eng.* 137, 106342, (2021); doi: 10.1016/j.optlaseng.2020.106342

[9] A.J. Christiansen, D.A. Naylor, A.M. Anderson and B.G. Gom, A cryogenic FMCW range-resolved laser interferometer: challenges and applications, In *SPIE OPTO, 2022, San Francisco, USA, Proc SPIE* 12008, 25-38, (2022); doi: 10.1117/12.2607894

DOI 10.5162/SMSI2023/D6.2

Measuring sub nanoradian angles

Andrew Yacoot[1], Simon Alcock[2], Rabia Ince[2], and Hiten Patel[2]
[1] National Physical Laboratory, Hampton Road, Teddington Middlesex TW11 0LW UK,
[2] Diamond Light Source, Harwell Science & Innovation Campus, Didcot, Oxfordshire OX11 0DE UK
Corresponding Author: andrew.yacoot@npl.co.uk

Summary:
This paper describes the application of optical interferometry for high accuracy angle metrology to characterize the performance of Diamond Light Source's small angle generator NANGO that is used to support testing of x-ray optics. The optical interferometer offers a higher resolution and bandwidth than is achievable with commercially available autocollimators and was used to measure traceably nanoradian steps and sub nanoradian oscillations generated by NANGO.

Keywords: optical interferometry, angle metrology, traceability, picoradians, nanometrology

Introduction

Optical interferometry is an essential link in the traceability chain for length metrology [1]. Small angles are usually measured using autocollimators, however, since angle measurement is really a measurement of two distances, optical interferometry lends itself to angle measurement. In recent years there have been significant advances in the fields of small (nanoradian) angle metrology to support a range of applications [2,3]. One of the most demanding applications for angle metrology focuses on the metrology of X-ray optics where nanoradian metrology is routinely required.

Angle metrology at Diamond

Diamond Light Source is the UK's synchrotron light facility serving the UK's academic and industrial research communities. Nanoradian angle metrology is required both to position components in front of X-ray beams emerging from the particle accelerators and for the quality assessment of X-ray optics.

To meet the requirements for angle metrology, Diamond constructed NANGO [4], a flexure-based, small angle generator designed to provide angle metrology. Although NANGO has an internal encoder, independent verification of its performance was required.

NPL angle interferometer

The NPL angle interferometer is a homodyne interferometer that was originally designed as a one axis, high-resolution interferometer for measuring angular errors (pitch and yaw, depending on the orientation of the interferometer) in nanopositioning stages. A schematic diagram is shown in Figure 1. It comprises two components; a fixed part, and a moving part that sits on the rotating device, NANGO. The main components in the fixed part are two Kösters prisms that are cemented together. Prior to cementing the faces, a phase quadrature metal coating [5] was deposited onto one of the faces in order to form a beamsplitter to generate a phase difference between the transmitted and reflected beams. The design of the interferometer is symmetric. In the path of the interferometer, light emerges from the Kösters prism and is incident on a roof prism on the moving component. The light is reflected back to the fixed body and then re-reflected back to the roof prism at a lower level. The light is then reflected back into the Kösters prism before recombining with light at the beamsplitter that had passed through the other side of the interferometer. The returned reflected and transmitted beams are in approximate phase quadrature (i.e. 90° phase difference) allowing for bi-directional counting of displacement.

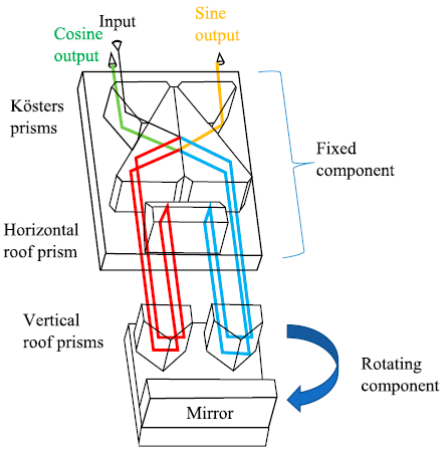

Fig. 1 The NPL angle interferometer

The interferometer design is such that as the moving component rotates, there are changes in the length of the two interferometer beam paths. If the separation of the two roof prisms is known, the angle of rotation can be calculated *i.e.,* the optical equivalent of a sine bar. The interferometer design is such that one optical fringe (158 nm) corresponds to ~ 4.8 µradians (1 arc second). This is dependent on the roof prisms' separation. A mirror is mounted on the back of the moving part to enable an autocollimator to directly determine the angle corresponding to one optical fringe.

Measurements of NANGO

Figure 2 shows the output from the optical interferometer when NANGO was commanded to generate 1.0 nanoradian steps. This represented the limit of NANGO's performance in closed loop due to the resolution of the control system for the actuators in NANGO.

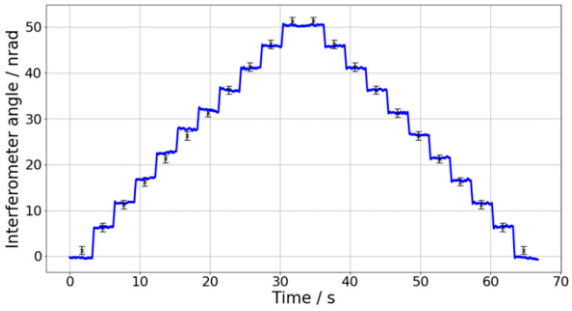

Figure 2: The interferometer output when NANGO was commanded to make 1.0 nanoradian steps

The higher bandwidth of the interferometer electronics (200 kHz) in comparison to the autocollimator (25 Hz) enabled the dynamic performance of NANGO to be investigated. Figure 3 shows the interferometer measurements of NANGO's rotation when NANGO was commanded to make a 300 nanoradian step.

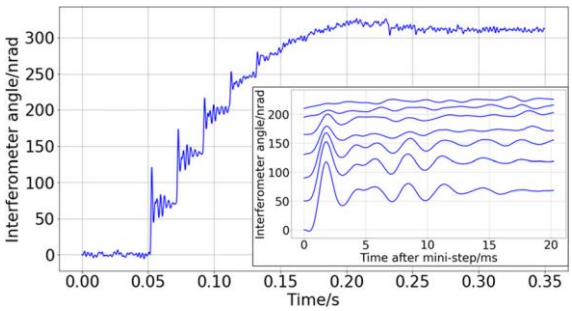

Figure 3: The dynamic behaviour of NANGO when making a 300 nanoradian step.

The step comprises a series of successively smaller steps, each slightly overshooting the target position. Sub nanoradian performance of NANGO was investigated in open loop; angular displacements were generated by applying a sinusoidal signal to the actuator. This had the advantages that smaller steps be generated and Fourier filtering could be used without any rounding to the signal.

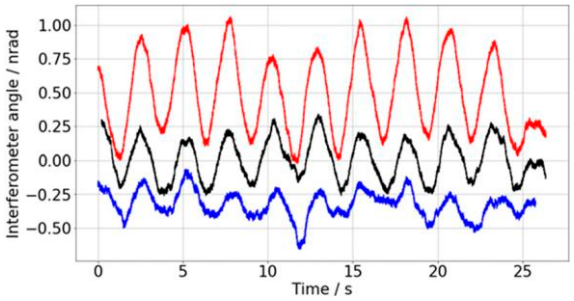

Figure 4. The interferometer signals as voltages were applied to NANGO's actuator to generate 500 picoradian, 250 picoradian or 125 picoradian steps. Note signals displaced vertically for clarity

Figure 4 shows the interferometer output when driving signals were applied to NANGO to generate nominal 500 picoradian, 250 picoradian 125 picoradians oscillations.

Conclusions

The NPL interferometer has validated the performance of NANGO at the nano- and sub nanoradian level. This enhances the metrological capability at Diamond for the evaluation of rotation stages and X-ray optics. Through this work, we have identified areas for improvement both in NANGO and the interferometer. Further details of this work together with an uncertainty budget can be found [6].

Acknowledgements

IOP publishing are thanked for permission to reproduce figures from [6] and the Department for Business Energy and Industry Strategy UK is thanked for funding.

References

[1] Schödel R, Yacoot A and Lewis A 2021 The new mise en pratique for the metre—a review of approaches for the practical realization of traceable length metrology from 10^{-11} m to10^{13} m *Metrologia* 58 052002

[2] European Metrology Research Program (EMRP) Proj.SIB58 ANGLES http://anglemetrology.com/

[3] Celik M, *et al*. 2016 Application of the differential Fabry–Perot interferometer in angle metrology *Meas. Sci. Technol*. 27 035201

[4] Alcock S G *et al*.2015 A novel instrument for generating angular increments of 1 nanoradian *Rev. Sci. Inst.* 86 125108 doi: 10.1063/1.4937352

[5] Raine K W and Downs M J 2010 Beam-splitter coatings for producing phase quadrature interferometer outputs *Opt. Acta* 25 549–58

[6] Alcock S G, Yacoot A, Ince R and Patel H, Generating and measuring pico-radian angles Metrologia 59 (2022) 064002 (17pp)

DOI 10.5162/SMSI2023/D6.3

Recent progress on AFM techniques for traceable 3D nanometrology at PTB

Gaoliang Dai [1], Jan Thiesler [1], Johannes Degenhardt[1], Rainer Tutsch[2]*
[1] Physikalisch-Technische Bundesanstalt, Bundesallee 100, 38116 Braunschweig, Germany
[2] Technische Universität Braunschweig, IPROM, Schleinitzstraße 20, 38106 Braunschweig, Germany
**) corresponding author: Gaoliang.Dai@ptb.de*

Summary:
This paper presents an overview on recent research progress achieved at PTB for reference 3D nanometrology: (1) development of a new low noise 3D-AFM, which has combined measurement modes of CD-AFM and tilting-AFM in one instrument; (2) accurate calibration of the tip form with a new traceability route using the silicon lattice parameter which is suggested by the *Mise en pratique* for the realisation of the *Metre* in nanometrology; (3) development of a novel true 3D AFM probe, referred to as a 3D-Nanoprobe, which has quasi-isotropic stiffness in three directions and is thus more powerful for detecting 3D tip-sample interaction forces in AFM measurements.

Keywords: Atomic Force Microscopy, dimensional nanometrology, traceability, calibration, critical dimension (CD), tilting AFM, tip characterization, 3D-AFM probe

Background and motivation

Progressive developments in nanomanufacturing, particularly in the nanoelectronic industry, pose increasing challenges in measuring nanostructures with ever smaller size and more complex three dimensional (3D) shape. Traceable metrology of nanostructures including measurands such as e.g. feature width, sidewall angle, line edge/width roughness (LER/LWR), corner rounding are essential tasks for quality assurance of process developments and process control in nano-manufacturing.

This paper will provide an overview of recent research progress achieved at PTB for reference 3D nanometrology.

Progress

The *first* progress concerns the development of a new low noise 3D-AFM, as shown in figure 1(a). The AFM offers two combined measurement modes in one instrument, referred to as the CD-AFM and tilting-AFM. When it is operated in the CD-AFM mode, a flared AFM tip which has an extension at the free tip end is applied. Such a flared AFM tip allows direct probing of vertical sidewalls or even undercuts in a single measurement. However, due to the complex shape of the flared AFM tip, it is difficult to measure dense nanopatterns. To solve this problem, the tilting-AFM mode is realized, as shown in figure 1(b). Using this technique, a nanostructure is measured by an AFM tip tilted in different angles, where the obtained AFM images will then be fused to derive the real 3D topography of the nanostructure. Owing to the sharp AFM tip applicable in the tilting AFM, it has the capability to measure patterns of high density, however, the uncertainty in data fusion will impact the measurement accuracy. The complementary application of two measurement modes thus offers an optimized solution for reference 3D nanometrology.

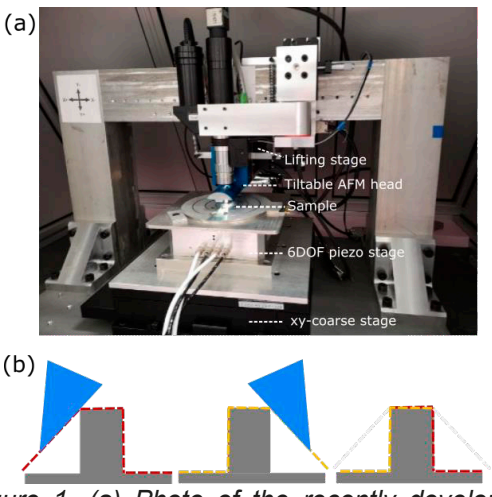

Figure 1. (a) Photo of the recently developed low noise 3D-AFM at the PTB; (b) schematic diagram showing the principle of the tilting AFM for true 3D metrology of complex nanostructures.

The *second* progress concerns the accurate calibration of the tip form. A fundamental concern in AFM measurements is the influence of the AFM tip geometry on the measurement results. The tip-sample interaction represents the most critical challenge of AFM measurements. From the morphological point of view, the profile measured by an AFM is the dilated result of the real structure by the so-called effective tip geometry. At PTB, a new method for accurately characterizing the tip geometry has been developed. A sample type IVPS100-PTB whose line features have vertical sidewalls, round corners with a radius of approx. 5~6 nm and very low surface roughness has been applied as the tip characterizer. The geometry of the line features has been accurately and traceably calibrated to the lattice constant of crystal silicon. Detailed measurement strategies and data evaluation algorithms have been developed, particularly concerning several important influence factors such as the line width roughness of the tip characterizer, measurement noise, measurement point density, and the calculation of the averaged tip geometry. Thorough experimental studies have been carried out, indicating sub-nm measurement accuracy of the developed method. An example is shown in figure 2.

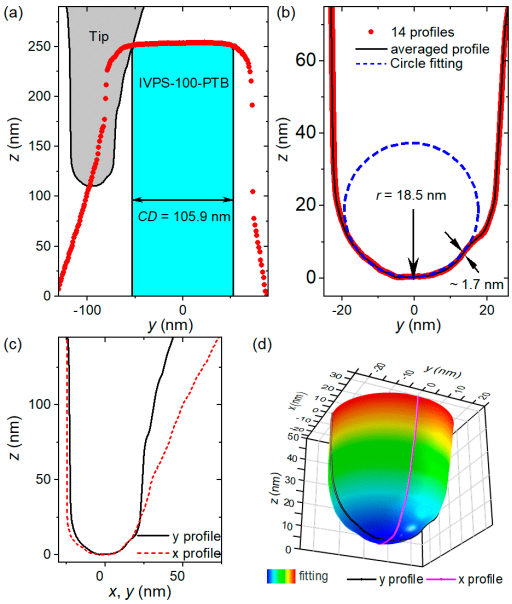

Figure 2. (a) a measured AFM profile (in red) together with the geometry of reference line feature of IVPS100-PTB standard. (b) 14 reconstructed tip profiles along the y-axis (red) and the averaged profile (black) of the tip. The blue dashed line denotes the fitting circle of the tip apex; (c) the averaged tip profiles along the x (red) and y (black) direction, respectively; (d) 3d fitting geometry of the tip according to reconstructed profiles.

The *third* progress concerns the development of a novel true 3D AFM probe, referred to as a 3D-Nanoprobe. Such a probe is realized by introducing flexure hinge structures to the cantilever of a conventional CD-AFM probe. It has quasi-isotropic stiffness in three directions and is thus more powerful for detecting 3D tip-sample interaction forces in AFM measurements. In addition, the stiffness of the 3D-Nanoprobe is balanced to the bending stiffness of slender CD-AFM tips, offering improved 3D sensitivity. In our study, a design example of a 3D-Nanoprobe based on a CD-AFM probe with a nominal tip diameter of 70 nm will be presented. The design parameters are optimized via theoretical modelling and finite element analysis (FEA) method. The simulation results indicate that the designed 3D-Nanoprobe has much better performance than that of the original CD-AFM probe, for instance, its stiffness' anisotropy ratio (including the tip contribution) has been improved from 7:7:1 (x, y, z) to 0.7:0.8:1 (x, y, z). The probing sensitivity is improved by a factor of more than 84, 128 and 1.5 in x-, y- and z-direction, respectively. In addition, the designed 3D-Nanoprobe has the first bending mode eigenfrequency of 46 kHz and the first torsional mode eigenfrequency of 177,6 kHz. The 3D-Nanoprobe has been manufactured by applying a focused ion beam (FIB) tool. Finally, to detect the full 3D interaction forces by the 3D-Nanoprobe, a new AFM-head prototype which consists of a dual optical lever and two differentially working interferometers has been developed.

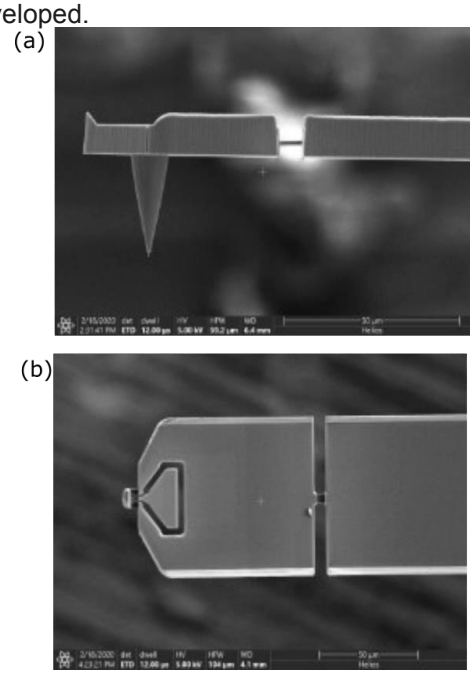

Figure 3. SEM image of developed 3D-Nanoprobe, shown as (a) a side view and (b) a top-down view.

DOI 10.5162/SMSI2023/D6.4

Current Advances in 3D Tip- and Laser-based Nanofabrication in Extended Working Areas

Ingo Ortlepp[1]
[1] *Research Training Group (RTG) NanoFab, Technische Universität Ilmenau, Ehrenbergstraße 29, 98693 Ilmenau, www.tu-ilmenau.de/nanofab*
ingo.ortlepp@tu-ilmenau.de

Summary:
Nanotechnology is affecting almost all areas of life, from semiconductor industry to optics, medicine and agriculture. Classical methods for sensing, measuring and fabricating on the nanoscale are faced with new challenges: features are getting smaller and the variety of structures and materials is increasing. Thus, many new techniques are developed in this field. Research at the Technische Universität Ilmenau aims to support transferring these new technologies to industrial scale for future application. The focus is on tip- and laser-based processes together with devices for nanometer positioning.

Keywords: nanomeasuring, nanomanufacturing, scale-spanning, tip-based, laser-based

Introduction and Motivation

Classical optical lithography was and still is the main technology for fabricating structures in the nanometer range. However, with the trend to ever smaller structures, complex 3D features and large processing areas [1], the necessary effort has become huge, making this technology expensive and inflexible with respect to design changes [2]. On the other side, nanotechnology can give the answer to many questions in almost all areas of live from energy to environment and climate [3] and many more. In this fields, many new technologies for measuring, structuring and sensing in the nanometer range are developed [4]. However, these technologies are often only investigated in lab scale, leaving the question of their suitability for large scale application unanswered. To bring these new technologies to larger scale, it is necessary to provide a flexible technological framework which is capable of nanomeasuring, nanopositioning and nanofabrication in the range of several square centimeters. For that purpose, the research training group (RTG) *NanoFab* at the Technische Universität Ilmenau is aiming to combine their nanopositioning and nanomeasuring machines (NPMMs) [5] with new nanofabrication technologies to close the gap between lab scale proof-of-concepts and industrial application [6].

Methods

Basic devices for research in our RTG are the NPMMs which have been developed at the Technische Universität Ilmenau since two decades. They offer highly accurate, high dynamic, reproducible and long-term stable nanometer positioning in a large working range between 25 x 25 x 5 mm^3 [5] and 200 x 200 x 25 mm^3 [5] or a 2D area of Ø100 mm [7]. This makes them perfectly suitable for the challenges in current alternative nanofabrication technologies. Based on these NPMMs, several research topics are currently investigated in the RTG *NanoFab*, including tip-based and laser-based processes as well as solutions for curved surfaces, nanooptical systems, measuring of small forces and future nanopositioning systems [6].

Results

In the field of tip-based fabrication, current research in our RTG is on the combination of atomic force microscopy (AFM) with field-emission scanning probe lithography (FE-SPL) which can be used for resistless structuring of 2D materials by a defined electron exposure dose [8]. With this technique, sub-20 nm resolution nanolithography can be performed on different materials, including graphene, semiconductors, semimetals and topological insulators. This tool combination is also used for long-range exposure of Calixarene-coated samples. Using the NFM-100 for positioning, gap-less and stitching-less FE-SPL [9] (see Fig. 1) and nanometer-resolution AFM measurements [10] (see Fig. 2) over several millimeters can be performed. To enhance the position uncertainty and stability of the NPMMs, these machines are constantly developed further. In addition to the investigation of alternative measuring systems [12], focus is on new concepts for the control system [13] to further enhance the positioning performance. For that purpose, a control con-

cept for a pneumatic gravity compensation was developed to reduce heat dissipation in the vertical drive axes of NPMMs (see Fig. 3).

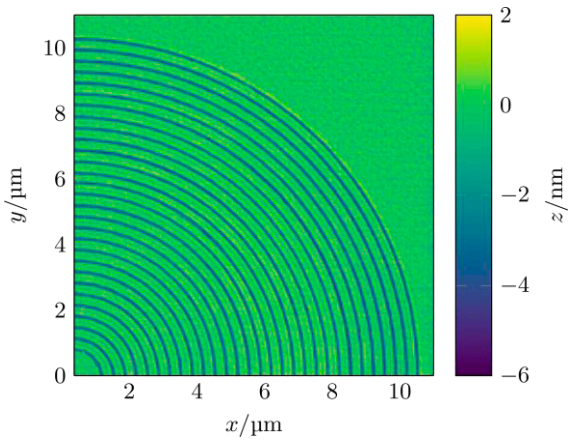

Fig. 1. Detail of a 1 mm FE-SPL line in spiral trajectory seamlessly written with the NFM-100. [11]

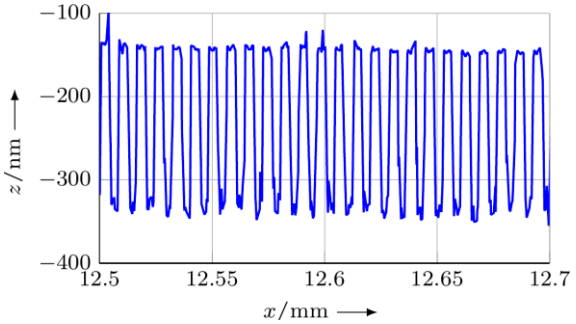

Fig. 2. Detail of a seamless 50 mm AFM scan of a periodic grating using the NFM-100. [10]

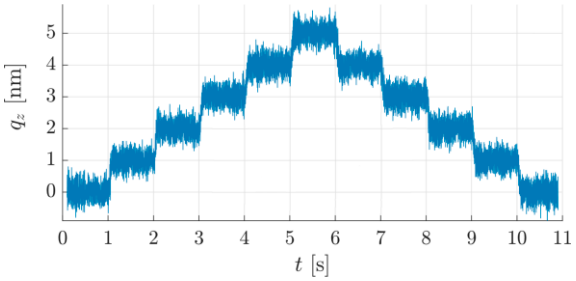

Fig. 3. Vertical positioning of a 4 kg payload with nanometer accuracy. Due to pneumatic gravity compensation, heat dissipation is only 54 nW. [13]

Besides the tools for fabrication, devices for measuring in the nanometer range are investigated, as pre- and post-inspection of the manufactured structures is an important link in the complete toolchain. Where lateral resolution is of lower priority, optical principles are preferred due to their neglectable interaction with the sample and the achievable measuring speed. For ensuring nanometer depth-accuracy, the influence of the measured surface has to be exactly modeled and compensated [14].

Conclusion

Nanopositioning and nanomeasuring in large working areas is required for bringing alternative technologies from lab scale to industrial scale. In the RTG *NanoFab*, a broad spectrum of the resulting challenges in the fields of tip- and laser-based fabrication processes, measurement technology and control theory is addressed.

References

[1] IEEE: International Roadmap for Devices and Systems, 2022

[2] Fritze, M. et al.: Post-Moore: prospects for novel patterning of low volume ICs, *Novel Patterning Technologies*, SPIE, 2021, 11610

[3] Diallo, M. S. et al.: Nanotechnology for sustainable development: retrospective and outlook, *Nanotechnology for Sustainable Development*, 2014

[4] Chen, Y. et al.: Sub-10 nm fabrication: methods and applications, *International Journal of Extreme Manufacturing*, 2021, 3, 032002

[5] Manske, E. et al.: Progress of nanopositioning and nanomeasuring machines for cross-scale measurement with sub-nanometre precision *Measurement Science and Technology*, 2020, 31, 085005

[6] Ortlepp, I. et al.: Tip- and Laser-based 3D Nanofabrication in Extended Macroscopic Working Areas, *Nanomanufacturing and Metrology*, 2021

[7] Stauffenberg, J. et al.: Measurement Precision of a Planar Nanopositioning Machine with a Range of Motion of 100 mm, *Applied Sciences*, 2022, 12

[8] Reuter, C. et al.: Resistless Nanopatterning of 2D Materials by Field Electron Emission Scanning Probe Lithography, *Graphene*, 2022

[9] Stauffenberg, J. et al.: Tip-based nanofabrication down to 40 nm combined with a nanopositioning machine with a range of motion of ø 100 mm, submitted to *Micro and Nanoengineering*

[10] Ortlepp, I. et al.: Processing and Analysis of Long-Range Scans with an atomic force microscope (AFM) in Combination with Nanopositioning and Nanomeasuring Technology for Defect Detection and Quality Control, *Sensors*, 2021, 21

[11] Ortlepp, I. et al.: Nanofabrication and -metrology by using the nanofabrication machine (NFM-100), *Novel Patterning Technologies*, SPIE, 2022

[12] Straube, G. et al.: A Heterodyne Interferometer with Separated Beam Paths for High-Precision Displacement and Angular Measurements, *Nanomanufacturing and Metrology*, 2021

[13] Huaman, A. S. et al.: Robust Tracking Control with L1 Adaptive Augmentation for a Long-Stroke Vertical Nanopositioning System, *Conference on Control Technology and Applications*, 2022

[14] Belkner, J. et al.: Compensating aberration induced error in differential confocal microscopy, *Optical Measurement Systems for Industrial Inspection XII*, SPIE, 2021, 11782, 137 - 146

DOI 10.5162/SMSI2023/D7.1

D7.1 Continually Learning Deep Machines that Understand What They Don’t Know

M. Mundt, Technische Universität Darmstadt, Darmstadt (Germany)

The short paper of this contribution is not available

DOI 10.5162/SMSI2023/D7.1

D7.1 Continually Learning Deep Machines that Understand What They Don’t Know

M. Mundt, Technische Universität Darmstadt, Darmstadt (Germany)

Summary:

Please describe briefly the highlights of your work. The summary of max. 6 lines should be typed across both columns. Please do not leave any spaces between the short paper and the title of your first section and please do not use symbols in the summary. (style “SMSI_Conference_Bodytext”)

Keywords: List five descriptive words, separated by a comma (e.g. printing, type style, titles, illustrations, references). These will be included in the index of keywords in the electronic conference volume. (style “SMSI_Conference_Keywords”)

DOI 10.5162/SMSI2023/D7.2

Arc Welding Process Monitoring Using Neural Networks and Audio Signal Analysis

Saichand Gourishetti[1], Jaydeep Chauhan[1], Sascha Grollmisch[1], Maximilian Rohe[2], Martin Sennewald[2], Dr. Jörg Hildebrand[2], Prof. Jean Pierre Bergmann[2]
[1] Fraunhofer IDMT, Ilmenau, Germany
[2] Technische Universität Ilmenau, Germany
saichand.gourishetti@idmt.fraunhofer.de

Summary:
This paper investigates the potential of airborne sound analysis in the human hearing range for automatic defect classification in the arc welding process. We propose a novel sensor setup using microphones and perform several recording sessions under different process conditions. The proposed quality monitoring method using convolutional neural networks achieves 80.5% accuracy in detecting deviations in the arc welding process. This confirms the suitability of airborne analysis and leaves room for improvement in future work.

Keywords: Deep learning, industrial sound analysis, GMAW, WAAM, DED-Arc

Arc welding Process and Recording Setup

Fig. 1. Illustration of arc welding piece (left) and layer pattern (right).

Additive manufacturing techniques such as arc welding gain importance in the producing industry and quality monitoring plays a vital role in the welding process to ensure the quality of the outcome. Fluctuations in the process parameters such as speed, power, shielding gas rate, and oil contamination can lead to pores in the arc welding seams and thus to poor quality [1]. To generate an appropriate dataset for our analysis, additive-manufactured Aluminium walls with 50 layers were produced. Direct energy deposition was used as the manufacturing process. With a 1.2 mm AlMg4.5 wire, structures were built up layer by layer, as shown in Fig. 1. To prevent exposure of the molten weld pool to atmospheric gases, shielding gas is used. The shielding gas rate was randomly changed for every layer from 15 L/min to 7.5 L/min. Also, oil was randomly applied on the surface of the previous welded layer to simulate the anomalies in the arc welding process.

Layers with 15 L/min shielding gas and with no oil are labeled as *io*. All other layers were labelled as *gasX*, where *X* denotes the rate of shielding gas in L/min. The welds were performed with a Fronius TPS 500i as welding machine and a kuka KR60 as a handling system. Welding speed was fixed to 0.4 m/min. As welding program, the Cold Metal Transfer mix was used with a wire feed rate of 8 m/min and a contact tube to workpiece distance (CTWD) of 12 mm. The produced walls have a length of 150 mm. To ensure a constant sound pressure level the sensors were mounted on a special fixture with a fixed distance to the arc. To reduce the impact of environmental sounds, an acoustic chamber was constructed around the process with molleton as an absorber. The experimental setup can be seen in Fig. 2.

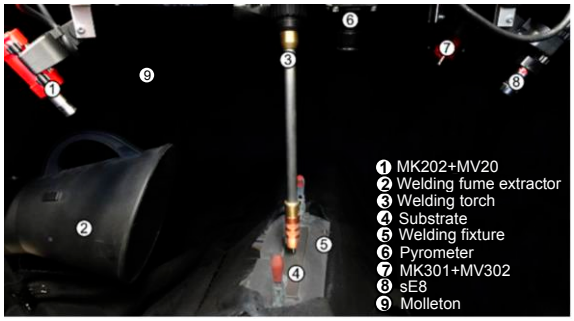

Fig. 2. Experimental setup with microphones and welding equipment.

Dataset Properties

With this recording setup, we produced 11 different wall structures with different arc welding parameters. The number of classes and files per class can be seen in Table 1, and each file is a 15 second long recording of a single welding layer.

Tab. 1: Number of files for each of the different process parameters

io	oil	gas7.5	gas10.5	gas12.0	gas13.5
133	80	64	73	68	70

In this work, we focus on the human hearing range up to 20 kHz for our analysis. To investigate the stability of the recording process, the statistical distribution of the RMS level of the acoustic signals was examined, and no significant difference regarding the process parameters was found.

Neural Network-based pipeline

Based on our previous work [2], we use a convolutional neural network (CNN) for automatic classification. The proposed processing pipeline is shown in Fig. 3. The log power spectrogram is

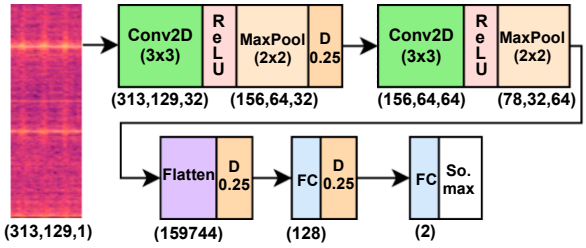

Fig. 3. CNN architecture with 2 convolution layers, rectified linear unit (ReLU) activation, Dropout (D), flatten layer, 2 fully connected (FC) layer, and a final Softmax (So. max) classification layer.

used as a feature representation, computed using the Short-time Fourier transform (STFT) with a window size of 256 and a hop size of 128 samples. The spectrograms are normalized to zero mean and unit variance per frequency bin. Further, we used the mix-up data augmentation technique [3] to improve the robustness of the network. We train the CNN model using the Adam optimizer with a batch size of 16 with categorical cross-entropy loss for 150 epochs and a learning rate of 1e-3.

Experiments and Results

We split the dataset into train and test sets with 5-fold cross-validation and a split ratio of 80% and 20%, respectively. Splits are done on a wall basis to remove any potential biases from the recording sessions itself. In addition, the dataset is balanced by applying the up-sampling technique. First, binary classification is performed, where all *gas* and *oil* classes are considered as *nio*, which results in 80.5% mean file-wise accuracy on the test dataset. Second, we perform a multiclass classification for a more detailed classification where *gas7.5* and *oil* are considered as separate classes. Here, our model yielded a mean file-wise accuracy of 75.4% on the test dataset. The confusion matrices for binary and multiclass classification are shown in Figure 4. One can clearly see which the misclassification between *io* and *nio*. A possible reason for this misclassification could be that the differences in the welding process between *gas* and *io* are too small as compared to *gas7.5*. Furthermore, detailed annotations on anomalies in addition to process parameters and also model hyperparameters tuning could significantly improve the classification results.

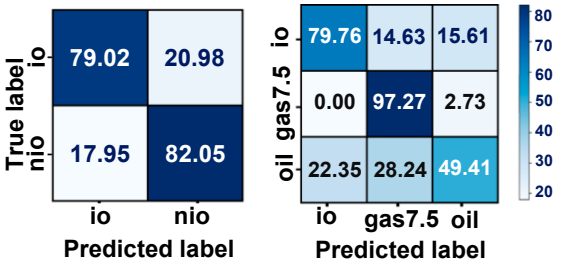

Fig. 4. Confusion matrices for binary (left) and multiclass (right) classification.

Conclusion

In this work, we analyze the potential of analyzing airborne acoustic emissions using artificial neural networks for the arc welding process for quality inspection. Our results demonstrate that acoustic emissions provide useful information for detecting different process parameters which directly influences the arc welding quality. Specifically, this is the case when there is a lack of shielding gas or contamination by oil on the layers. In future work, we want to improve this proposed method by recording more diverse dataset. Furthermore, hyperparameter optimization or better feature representations might improve these results. Also, a more detailed annotation is required to measure when and where pores exactly happened.

References

[1] M. Rohe, B. Stollt, J. Hildebrand, J. Reimann, J. Bergmann. “Detecting Process Anomalies in the GMAW Process by Acoustic Sensing with a Convolutional Neural Network (CNN) for Classification,”. *Journal of Manufacturing and Materials Processing.* 5. 10.3390/jmmp5040135, 2021.

[2] S. Grollmisch, et al., “Plastic Material Classification using Neural Network based Audio Signal Analysis,” in *SMSI*, Nürnberg, 2020.

[3] H. Zhang, M. Cisse, Y. N. Dauphin, & D. Lopez-Paz, “mixup: Beyond empirical risk minimization,” in *ICLR* 2018.

This work has been funded by Federal Ministry for Education and Research (code 01IS20001E (Projekt AkoS). The responsibility for the content of this publication lies with the authors.

DOI 10.5162/SMSI2023/D7.3

Evaluation of the bi-wave method for ultrasound preload determination in the field with machine learning

Simon Herter[1,2], Sarah C.L. Fischer[1], Michael M. Becker[1]
[1] Fraunhofer IZFP Institute for Nondestructive Testing,
Campus E3.1, 66123 Saarbrücken, Germany,
[2]Universität des Saarlandes,
Campus, 66123 Saarbrücken,
simon.herter@izfp.fraunhofer.de

Summary:
Preload determination in bolts via ultrasound measurements is still a challenging task. Effects like scattering, interference and mode conversion produce signal distortion, which can cause invalid time-of-flight measurements and yield unreliable preload determination. There are different methods to detect invalid signals and eliminate them from the data analysis. However they have mostly been applied on controlled laboratory scale data sets. This paper evaluates the extension of these methods to more complex data collected on a wind turbine shaft.

Keywords: Ultrasound, Time-of-flight measurement, Preload determination in bolts, Machine Learning, Non-destructive evaluation 4.0

Introduction

Preload determination during the bolting process and the life cycle of bolted joints is an important topic to ensure defined and safe connection between different mechanical parts. Common methods like the torque or pressure measurements allow an indirect measurement of the preload during to the bolting process.

An alternative approach is to use ultrasound to evaluate the preload in bolts. Ultrasound measurements allow a direct determination of the preload, because the time-of-flight change directly correlates with the stresses in the bolts. Ultrasound offers two possible methods two measure the preload.

One-wave method

The one-wave method is well described and is already established for industrial applications. This method only utilizes the longitudinal wave mode to calculate the time-of-flight change compared to the unloaded state. The measured time-of-flight change allows calculating the preload directly via the acousto-elastic material constant, as described by Murnaghan, Huges and Kelly. [1][2]

The one-wave method requires a reference measurement of the time-of-flight in the unloaded state, which is its biggest limitation as it is not always available in the field, like for already build in bolts.

Bi-wave method

In contrast to the one-wave method, the bi-wave method enables the determination of the preload without referencing to the unloaded state by combining time-of-flight measurements for both longitudinal and transversal waves. The quotient of the two time-of-flight values provides the so-called Q_0 factor (see eq.1) which only depends on the Poisson's ratio of the material. [3]

$$Q_0 = t_{0trans}/t_{0long} = \mathrm{sqrt}((2*(1- v))/(1-2*v)) \quad (1)$$

$$Q = t_{trans}/t_{long} \quad (2)$$

The Q factor, see eq. 2, correlates linearly with the uniaxial stress and therefore enables the preload determination in bolts without a reference state. For using the bi-wave method in field applications, the unloaded Q factor can be determined on equivalent bolts and used for all bolts of the same material and geometry.

Problem

Due to the complex geometric structure of bolts the ultrasonic signals are highly influenced by interference and mode conversion. The high precision time-of-flight measurement, which is mandatory for preload determination, becomes a challenging task. The above-mentioned effects results in time-of-flight shifts, which limit

the application of the bi-wave method to laboratory environments. [4]

Preload Measurements

In the current work, ultrasonic preload measurements were performed on a wind turbine shaft. In total 78 M42 bolts with a length of 670 mm were investigated. All bolts were measured with the two wave modes in the unloaded and in the loaded state. Additional monitoring measurements during the life cycle of the shaft were carried out.

During the initial tightening process, the time-of-flight change of the longitudinal waves is recorded to track the preload, see Figure 1. These preload curves can be the basis of an automatic labelling procedure for the longitudinal wave data.

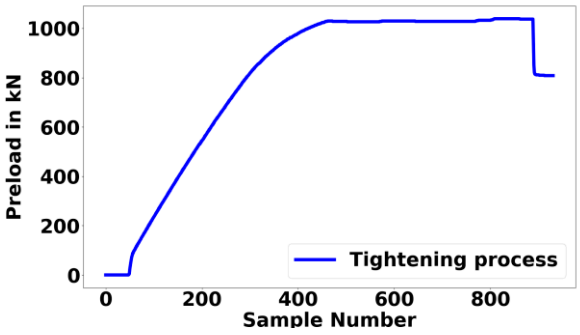

Figure 1: Preload curve during the tightening process of a bolt over the number of recorded A-Scans.

A comparison of the calculated preload value after finishing the tightening process between the one-wave and bi-wave method is displayed in Figure 2.

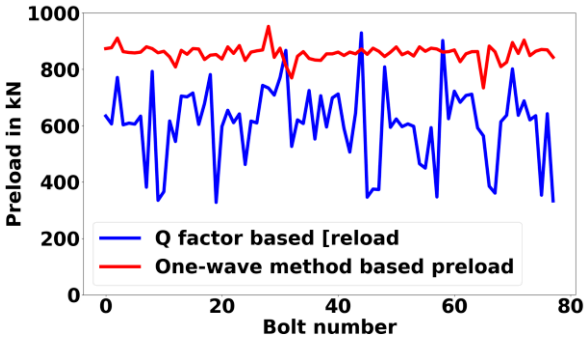

Figure 2: Calculated preload based on the one-wave method (red) compared to the bi-wave method (blue) without any signal validation.

The time-of-flight change calculation of the one-wave method is performed with the autocorrelation function of the first backwall signal to ensure valid and stable results. For the bi-wave method, the cross correlation function is used to determine the time-of-flight, because commonly for the bi-wave method the reference signal is not necessary.

The difference of the two preload curves is caused by different effects like material properties, slightly different bolting conditions, but also due to phase shifts in the time-of-flight measurement of both wave types.

In current work, the different influences are investigated. Especially the phase shifts occurring during the ultrasonic measurements will be addressed during the processing and analyzing of the signals. The aim is to build an artificial intelligence model capable of detecting phase shifts. With such a model the invalid signals could be eliminated and the failure in the calculation of the time-of-flight values can be avoided, by which the accuracy and reliability of the bi-wave method increases.

Moreover, an AI model would contribute significantly to bring the advantages of the bi-wave method closer to the application in field because a parametric model would ensure the validity of the ultrasonic signals and no advanced user knowledge would be necessary for an ultrasound-based preload detection.

Acknowledgements

The authors thank their colleagues from the Fraunhofer IWES for the possibility to conduct the measurements.

References

[1]: F. D. Murnaghan, Finite Deformation of an Elastic Solid, New York: John Wiley and Sons, Inc., 1951.

[2]: D. S. Hughes und J. L. Kelly, „Second Order Elastic Deformation of Solids," Physical Review, Bd. 92, Nr. 5, pp. 1145-1149, 1953.

[3]: Becker, Michael, Nadja Groß, and Rüdiger Herzer. "Determination of preload in bolts by ultrasound without referencing in unloaded state." *Proc. 19th World Conference on Non-Destructive Testing*. 2016.

[4]: Herter, S.; Youssef, S.; Michael, M.B.; Fischer, S.C.L. Machine Learning Based Preprocessing to Ensure Validity of Cross-Correlated Ultrasound Signals for Time-of-Flight Measurements. J. Nondestruct. Eval. 2021, 40, 1–9.

DOI 10.5162/SMSI2023/D7.4

Creating Synthetic Training Datasets for Inspection in Machine Vision Quality Gates in Manufacturing

Iris Gräßler[1], Michael Hieb[1],
[1] University of Paderborn, Heinz-Nixdorf-Institute, Faculty of Product Creation,
33102 Paderborn, Germany
[1]{iris.graessler, michael.hieb}@hni.upb.de

Summary:
Manufacturing companies face the challenge of reaching required quality standards. Using optical sensors and deep learning might help. However, training deep learning algorithms require large amounts of visual training data. Using domain randomization to generate synthetic image data can alleviate this bottleneck. This paper presents the application of synthetic image training data for optical quality inspections using visual sensor technology. The results show synthetically generated training data are appropriate for visual quality inspections.

Keywords: synthetic training data, machine vision quality gates, deep learning, automated inspection and quality control, production control

Introduction

Quality controls are essential in manufacturing. In general, quality controls represent a measuring point within the manufacturing process that ensures the required quality-relevant product properties. Often, quality controls are visual inspections by trained personnel using a product-related checklist. Although quality controls are essential, manual inspections are time-consuming and labor-intensive. In addition, inspections are characterized by a high degree of monotony and susceptibility to errors [1]. Especially automated visual inspections using deep learning algorithms offer a high potential for automation. Machine vision quality gates generally consist of one or more cameras, light source(s), trigger, production line control and image processing software (e.g., MVTec Halcon) able to deploy deep learning methods [2]. The basis for the implementation of deep learning algorithms for quality inspections is high-quality annotated training data. In particular, data acquisition, data preparation, and data annotation of real image data are considered being time-consuming and costly. Synthetically generated training data can mitigate these steps. Using rendering software, CAD, and the domain randomization approach, annotated training datasets (DS) can be generated within minutes. Using synthetic training data can reduce time and cost by 80% [3]. The goal of this work is to generate and use synthetically generated training data for machine vision quality gates. For this purpose, one assembly step of the open-source jointed-arm robot "Zortrax" [4], which is manufactured in the Smart Automation Laboratory of the Heinz Nixdorf Institute [1], is used as a validation example. Therefore, three training datasets are generated: 1) baseline with real image data; 2) hybrid dataset with 5% real image data and 95% synthetic image data; 3) fully synthetic training dataset. All approaches are tested and validated with collected real image data. Precision, Recall and F1-Score are used as validation criteria for comparison. This research contributes to evaluate the use of synthetically generated image data for machine vision quality gates.

State of the Art

Synthetic training image data is mostly used within the scope of computer vision. Generating synthetic training image is dominated by the approaches of generative adversarial networks (GAN), vector quantized variational autoencoders (VQ-VAE) and domain randomization (DR) [3]. Especially the approach of DR is promising in the field of machine vision since no real image data is required. DR is considered most promising for transfer learning from synthetic-to-real data [3]. First introduced in the 1990s [5], DR has undergone serval improvements. Generally, DR is a random approach using a 3D environment to create 2D images. Therefore, three virtual layers are created. The first layer is the occluding layer, the second layer the relevant object(s) and the third layer is the background layer. The first and third layer are used as noise layers generating variation to

improve the focus towards the relevant object(s). Additionally, every object is randomly positioned and textured.

Pipeline to Generate Synthetic Image Data

The basis to create synthetic image data is the approach of DR. Basically, the approach requires three steps: (1) generate/collect CAD, (2) build synthetic environment (three layers) and (3) set parameters and randomly generate image data (see Fig.1). The used software tool to generate synthetic images is the rendering software Blender.

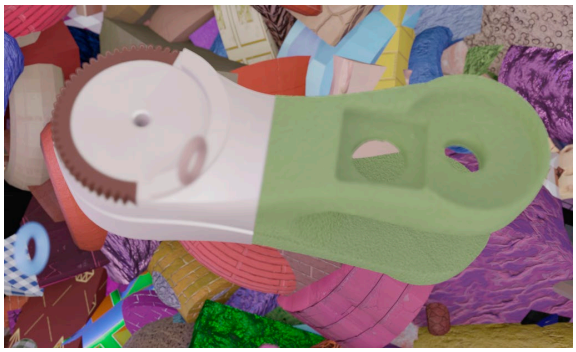

Fig. 1. Synthetic generated training image

Validation Setting

The aim of the validation is to properly classify the correct assembly of the second assembly step (AS) of the jointed-arm robot Zortrax using a machine vision quality gate. That assembly step requires the proper alignment and connection of the arm-1-lower and arm-1-upper (see Fig. 2). The possible error is to wrongly turn one of the arms forming a binary classification problem. Therefore, two classes (wrong and correct assembly) are formed with corresponding datasets. All training sets contain 2000 training, 200 test and 200 validation images. The trained deep learning model is the Xception model with 60 epochs, 0,001 learning rate and a RGB 1024 x1024 target size. The model is evaluated using the key performance indicators Precision (P), Recall (R) and F1-Score (F1).

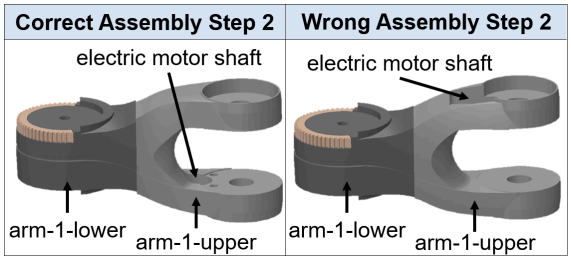

Fig. 2. Classification problem of assembly step2

Results

The results indicated high performance distinguishing the correct- and wrong assembly. Training merely on synthetic image training data reaches lower key performances.

Tab. 1: Summary of training results (Macro Average)

AS	Dataset	P	R	F1
2	Real	0.92	0.91	0.90
	Hybrid	0.90	0.89	0.88
	Synthetic	0.87	0.86	0.85

Discussion

Comparing the results of the baseline containing only real image data with the hybrid and synthetic datasets, it is supported that synthetic datasets are appropriate to inspect the quality of the second assembly step. When using models trained solely on synthetic image data, a slight domain gap between real and synthetic data is apparent. In further studies, the amount of synthetic image data used will be increased to improve the results. Also, other deep learning models should be evaluated. Finally, it is shown that using small amounts of real data improves the performance (see Tab.1 hybrid). Thus, using real data from similar assembly steps continuously recorded by optical sensors improves the results in the future.

Summary

In summary, the results show that synthetically generated training datasets are generally suitable to be used in machine vision quality gates using optical sensors. The approach offers great potential to simplify the training process for deep learning models in optical sensor quality inspection. Especially in the field of mass customization with a high number of product variants, synthetically generated image data seems promising. In future studies, different scenarios for generating synthetic image data can be explored.

References

[1] I. Gräßler and A. Pöhler, Human-centric design of cyber-physical production systems, *Procedia CIRP*, vol. 84, pp. 251–256, 2019. doi: 10.1016/j.procir.2019.04.199

[2] C. Steger, M. Ulrich, and C. Wiedemann, Machine Vision Algorithms and Applications, Weinheim, Germany, 2018 ISBN-13: 978-3527407347

[3] S. Nikolenko, Synthetic Data for Deep Learning, Springer, 2021, ISBN-13: 978-3-030-75178-4.

[4] Zortrax Robotik Arm, https://library.zortrax.com/project/zortrax-robotic-arm/, 2022.

[5] Jakobi, N., Husbands, P., Harvey, I.: Noise and the reality gap: The use of simulation in evolutionary robotics. In: Morán, F., Moreno, A., Merelo, J.J., Chacón, P. (eds.) Advances in Artificial Life, pp. 704–720. Springer, Berlin, Heidelberg, 1995.

DOI 10.5162/SMSI2023/E5.1

The power of temperature sensors in EV-charging applications

Christoph Nick, Tobias Holz, Martin Bleifuss
Heraeus Nexensos GmbH, Reinhard-Heraeus-Ring 23, Kleinostheim, Germany
Tobias.holz@heraeus.com

Summary:
In this work the importance of temperature measurements in the EV-charging infrastructure is explained and requirements for temperature sensors for this specific application are derived. Typical sensors being applied in such environments include platinum-based sensors (Pt-RTDs) and thermistors with a negative temperature coefficient (NTCs). The performance of these two types of sensors is compared focusing on the crucial parameters response time and accuracy over lifetime (stability of the sensor).

Keywords: temperature sensors, Platinum RTD, EV-charging, charging infrastructure, power control

Background, Motivation an Objective

Measuring the correct temperature is crucial for many applications such as exhaust gas treatment, in the medical and lab environment or in other applications enabling a temperature compensation. Also, in the growing field of e-mobility and its charging infrastructure having the right temperature signal is very important.

In charging applications measuring the peak temperature is a necessary safety requirement: The battery needs to be charged as fast as possible without causing overheating in the system, since such an overheating might cause a significant reduction of battery lifetime, a higher wear of components such as connectors and higher maintenance cost. In extreme cases overheating of the battery can cause a system failure leading ultimately to fire, damage of property and in the worst case even injuries of passengers.

It is thus important to closely control the temperature by limiting the power during the charging cycle as it is depicted in figure 1. The temperature at different locations in the charging infrastructure increases steadily with the start of inrushing current. Locations might be the connector pins on the vehicle side or on the station side, power electronics or even the battery. When a certain peak temperature is reached, that is slightly below the critical value the current and with that the power is limited causing the temperature to decrease and thus avoiding an overshoot above a critical value. Obviously charging time shall be limited for the ease of use and at the same time it should happen at a relatively low temperature to ensure safety. Here measuring the temperature as accurately and without any delay is of utmost importance to shorten the charging time as much as possible and at the same time staying away from critical system conditions [1].

Fig. 1. Typical charging cycle showing the increase of temperature in the system starting with the inrush of current. Applied power is then limited once a certain threshold in temperature is reached to ensure safety and avoiding any critical conditions [according to a presentation by Phoenix GmbH].

Widely applied temperature sensors include:

- Platinum based RTDs (resistance temperature detectors)
- NTCs (Negative temperature coefficient)
- Thermocouples
- Semiconductor based sensors

For each if these types of sensors advantages and disadvantages can be found, also depending on the application and the requirements.

In this paper a comparison of the most prominent types, Pt-RTDs and NTCs shall be done, referring to the already mentioned system requirements in charging applications.

Requirements and Methods

Requirements of sensors detecting the temperature in the charging infrastructure such as the charging pins include:

- Accuracy

  The detected signal must be as close to the real value as possible. This is typically indicated with the potential error of the sensor at 0°C.

- Repeatability

  Due to the high amount of measuring points in the global charging infrastructure a repeatable signal is necessary, meaning that one sensor behaves the same way as other sensors independent of manufacturing batch or even sensor provider.

- Stability

  The signal of the sensor and its accuracy must remain the same over the entire lifetime of the application without showing any drift. Typically, this is proven by validating the sensor with accelerated life-time tests such as temperature endurance tests, temperature cycle tests, temperature shock tests or vibration tests.

- Fast response time

  The sensor signal must follow and detect a presented change in temperature ideally in real-time with the delay being as short as possible. The response time is typically given as a T0.5-value and a T0.9-value, referring to the time elapsed to respond to 50% or 90% of a temperature step. It is measured either by presenting a temperature step in moving air or moving water with clearly defined temperatures and velocities.

- High dielectric strength

  With voltage being as high as during charging cycles, the sensor obviously must be electrically robust for being applied in such conditions.

Results

In this study a comparison between two prominent temperature sensors, Pt-sensors and NTCs has been done, focusing on response time and lifetime stability.

As depicted in figure 2 it can be shown that Pt sensor elements have a significantly shorter response time when presented to a temperature step. Comparing the median value of 50 measurements each the T0.5-value is up to six times faster for Pt-elements compared to the value of different NTCs.

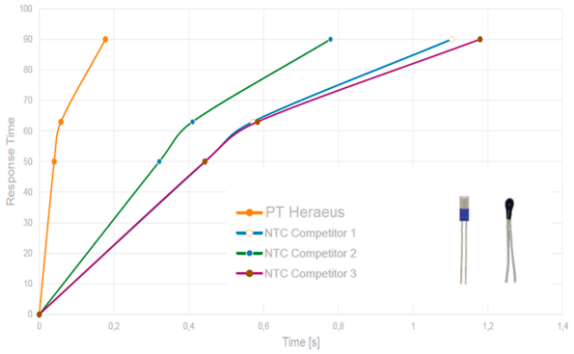

Fig. 2. Comparison of the response time between a Platinum temperature sensor and three different NTC-sensor elements. The superiority of the Pt-sensor can clearly be seen with the response time being up to six times faster.

Comparing the performance of the sensor after temperature cycle tests results show a significantly lower deviation in signals for primary housed Pt sensors as depicted in figure 3.

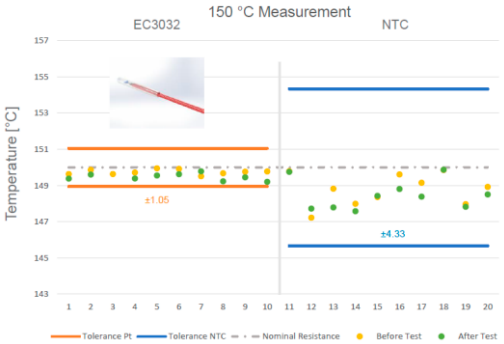

Fig. 3. Comparison of signal accuracy at 150°C after 1000 temperature cycles (-40°C – 150°C).

Conclusion

In this study the performance aiming at the application in the EV-charging infrastructure of Pt-based temperature sensors and NTCs was compared, showing the superior performance of Pt-based sensors in lifetime stability (accuracy) and response time.

References

[1] T. Stanczyk, L. Hyb, Technological and organizational challenges for e-mobility, *The Archives of Automotive Engineering*, Vol. 84, No. 2, (2019)

DOI 10.5162/SMSI2023/E5.2

Integration of a High-Precision 3D Sensor into a 3D Thermography System

Miguel Méndez[1], Sebastian Schramm[1], Robert Schmoll[1], Andreas Kroll[1]
[1] University of Kassel, Department of Measurement and Control
Mönchebergstraße 7, 34109 Kassel, Germany
miguel.mendez@mrt.uni-kassel.de

Summary:
In this paper, the integration of an industrial high-precision 3D sensor into a 3D Thermography System is presented. A large size object was recorded using the previous and the new system. The obtained point cloud geometry was evaluated by means of a non-referenced point cloud quality assessment approach. The implementation showed an improvement of the local curvature and anisotropy.

Keywords: 3D Thermography, Sensor Data Fusion, No-Reference Point Cloud Quality Assessment.

Introduction

The capability of energy loss detection and quantification is one of the most relevant industrial sustainability challenges. The development of fast response and reliable thermal inspection methodologies is gaining importance, addressing topics such as infrared thermography and sensor data fusion. A 3D Thermography System (3DTS) enables the creation of a live 3D model, which eases the interpretation and analysis of results, compared with 2D thermal images.

A 3DTS was developed by [1] and compared with the obtained system by [2], where the capability of the concept for measuring large size objects was extended. For both cases, an infrared camera was used in conjunction with a relative low-cost depth and RGB sensor. In this work, the improvement of the reconstructed model geometry by the implementation of an industrial high-precision 3D sensor (MotionCam-3D (MC3D) by Photoneo) for the depth measurement task is presented.

3D Thermography System

The improved system consists of a long-wave infrared (LWIR) camera, a structured light sensor MC3D and a RGB camera (see Fig. 1). The processing tasks are performed by a developed C++ (CUDA) executable. It exploits the hardware capabilities of a high-end graphics card laptop (GeForce GTX 980M, 4 GB VRAM) by implementing multithreading computations. These computations range from the unification of the three camera coordinate systems to the point cloud fusion, by means of an extended processing algorithm from [3], as described in [2].

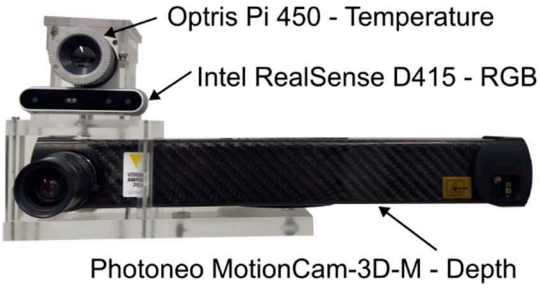

Fig. 1: Assembled 3D Thermography System.

Two main problems had to be solved for the integration of the MC3D. The first one was the perturbation of the RGB model texture caused by the red-light pattern of the MC3D, which was solved by the suppression of the red component from the color vector. The second one was the temporal synchronization of the three sensor frames. As the post-processing features of the MC3D introduce a time delay of the depth frames, the system must search backwards in the temperature and color buffers for the respective frames, which match the last depth measurement in time. When the three images are temporally quasi-aligned, they are processed by the extended Elastic Fusion algorithm.

3DTS evaluation

A flow measurement test bench (see Fig. 2) was investigated using the previous and the new 3DTS. The obtained point cloud (PC) was assessed following the approach suggested by [4], since it is not dependent on a reference point cloud. Each point was grouped in a neighborhood with the 9 closest points (10 members), using the Euclidean distance metric.

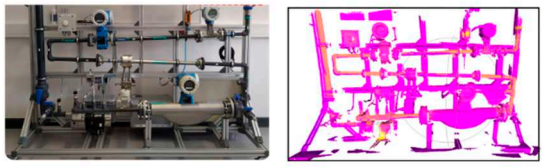

Fig. 2: Flow measurement test bench (left) and an example of the 3D Thermogram (right).

For each point, the surface variation could be approximated to the covariance matrix C_i [5]:

$$C_i = \frac{1}{10}\sum_{j=1}^{10}(p_j - \hat{p})(p_j - \hat{p})^T \quad (1)$$

Where p_j and $\hat{p}$ are cartesian coordinate vectors and represent the j-th member and the centroid of the neighborhood, respectively. Formulating the eigenvector problem:

$$C_i \cdot v_l = \lambda_l \cdot v_l, l \in \{1,2,3\} \quad (2)$$

With the eigenvectors (v_1, v_2, v_3) and the corresponding eigenvalues ($\lambda_1 > \lambda_2 > \lambda_3$), the variation of the p_i along the direction of v_l are represented by λ_l [6]. The curvature:

$$Cur(p_i) = \frac{\lambda_3}{\lambda_1+\lambda_2+\lambda_3} \quad (3)$$

and the anisotropy:

$$A(p_i) = \frac{\lambda_1-\lambda_3}{\lambda_1} \quad (4)$$

formulations were chosen, since they represent the local roughness and the geometrical variation, respectively. These metrics are important for the thermographic data fusion due to the emissivity dependency with the surface normal angle [1].

Results and discussion

One exemplary detail of the obtained PCs is presented in Fig. 3. A visual improvement on the geometry quality is observed with the MC3D. The system extension provides for straighter lines and flatter surfaces, in addition to a diminution of the number of aleatory points around the recorded objects. This is visible in the proposed indicators (see Fig. 4), where the local curvature is reduced, and the neighborhoods are more aligned in a single direction, as the anisotropy indicates. Less dispersion is also remarkable with the MC3D, indicating an overall impact for the complete geometry.

Conclusions

An industrial MC3D was integrated into a 3DTS. The quality of the new model was compared to respective one of the previous system. The results showed a significant improvement of the analyzed local curvature and anisotropy.

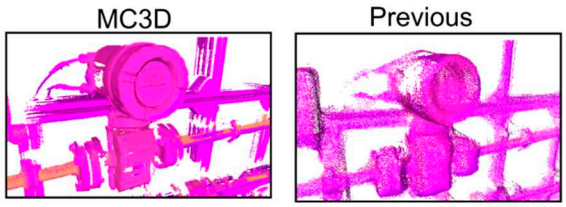

Fig. 3: Detail of the PCs obtained with both systems.

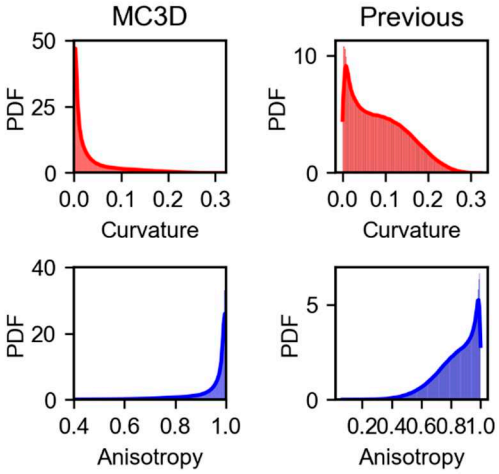

Fig. 4: Obtained normalized Probability Density Function (PDF) for the curvature and the anisotropy features.

References

[1] A. Ordonez Muller and A. Kroll, "Generating High Fidelity 3-D Thermograms with a Handheld Real-Time Thermal Imaging System," *IEEE Sens J*, vol. 17, no. 3, pp. 774–783, Feb. 2017, doi: 10.1109/JSEN.2016.2621166.

[2] S. Schramm, P. Osterhold, R. Schmoll, and A. Kroll, "Generation of Large-Scale 3D Thermograms in Real-Time Using Depth and Infrared Cameras," *15th Quantitative Infrared Thermography*, Dec. 2020. doi: 10.21611/qirt.2020.008.

[3] T. Whelan, S. Leutenegger, R. F. Salas-Moreno, B. Glocker, and A. J. Davison, "ElasticFusion: Dense SLAM Without A Pose Graph." *Robotics: Science and Systems*, 2015, doi:10.15607/RSS.2015.XI.001.

[4] Z. Zhang, W. Sun, X. Min, T. Wang, W. Lu, and G. Zhai, "No-Reference Quality Assessment for 3D Colored Point Cloud and Mesh Models," *IEEE Transactions on Circuits and Systems for Video Technology*, 2022, doi: 10.1109/TCSVT.2022.3186894.

[5] R. Rusu, "Semantic 3D Object Maps for Everyday Manipulation in Human Living Environments," *KI-Künst Intell* 24, 345 -348 (2010), doi: 10.1007/s13218-010-0059-6

[6] M. Pauly, M. Gross, L. P. Kobbelt, E. Zürich, and R. Aachen, "Efficient Simplification of Point-Sampled Surface." *Proceedings of the IEEE Visualization Conference*. 1. 163 – 170, doi: 10.1109/VISUAL.2002.1183771.

DOI 10.5162/SMSI2023/E5.3

Suitability of ECT for Non-invasive Temperature Monitoring in Fixed-bed Reactors

Michael Weiss[1, 2], *Gerhard Fischerauer*[1], *Andreas Jess*[2]
[1] *Chair of Measurement and Control Systems, Center of Energy Technology, Universität Bayreuth*
[2] *Chair of Chemical Engineering, Center of Energy Technology, Universität Bayreuth*
Universitätsstraße 30, 95447 Bayreuth, Germany
mrt@uni-bayreuth.de

Summary:
We characterize the temperature-dependent effective permittivities of two-phase materials (glass beads, hydrogenation catalyst) by means of electrical impedance measurements in a temperature range from about 25 °C to 240 °C. Measurements with the same materials using a commercial electrical capacitance tomography (ECT) system are carried out while the temperature of the fixed bed is changed. The images show that the measurement method is able to detect temperature gradients in a fixed bed, even though further efforts are needed to improve the quality of the results.

Keywords: ECT, temperature, fixed bed, material characterization, impedance measurement

Introduction

Many chemical reactions in fixed-bed reactors are exothermic. It is then essential for safe and economically optimal reactor operation to know the heat and mass transfer and the temperature distribution within the fixed bed. By the state of the art, this is measured with temperature probes in a localized and invasive way. Mathematical models are then used to derive the conditions in the entire reactor based on these measurements [1]. The results obtained are uncertain and the method produces measurement errors due to the influences of the packed bed structure and the heat transport.

It is desirable to have alternative measurement methods that can determine temperatures within packed beds non-invasively. One method that could be capable of doing this is electrical capacitance tomography (ECT) [2].

Electrical Capacitance Tomography

ECT is a non-invasive and non-intrusive imaging method based on the measurement of the capacitances of pairs of electrodes mounted on the surface of a volume to be investigated, e. g., a pipe. The region of interest (ROI) within the pipe is considered as being made up of discrete pixels for inverse computation. A reconstruction algorithm computes a normalized permittivity for each pixel from the measured capacitances. This results in an estimated permittivity distribution for the entire pipe cross-section. Using known permittivity-temperature relations for the materials in the ROI, the temperature distribution $\vartheta(\vec{r})$ is derived from the reconstructed permittivity distribution $\varepsilon_r(\vec{r})$.

The method has already been investigated in the context of temperature measurement in the production of plastic pellets and in a polymer extrusion machine [3, 4]. In the field of reaction engineering, the method has already been used to identify flow regimes in fluidized beds [5]. As far as the authors are aware, the use of ECT for temperature monitoring in fixed-bed reactors is still completely unexplored.

Temperature-dependent Material Characterization by Measuring Electrical Impedance

To establish the mentioned permittivity-temperature relations, a cylindrical measuring cell was used, see Fig. 1(a). The cell was filled with the material under test (MUT) and the complex-valued electrical impedance between the inner and outer electrodes was then measured at 1 MHz (the excitation frequency of the ECT system used) with an impedance analyzer. The measuring cell was heated in a furnace from room temperature up to 240 °C in steps of 40 °C. At each temperature, the impedance was measured ten times, each measurement comprising the mean value of 200 readings. During a measurement (for about 1 min), the heating current was switched off to minimize noise interference. To avoid a significant temperature drop, the furnace was reheated for at least two minutes between measurements.

By the equivalent circuit of Fig. 1(b), the effective relative permittivity of the bulk material is

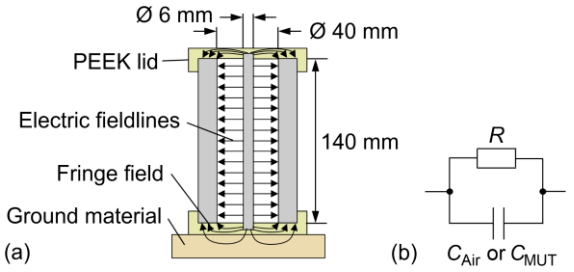

Fig. 1. Measuring cell. (a) Schematic cross-section. (b) Assumed equivalent circuit.

$$\varepsilon_{r,\mathrm{eff}} = \frac{C_{MUT} - C_{FE}}{C_{Air} - C_{FE}} . \qquad (1)$$

Here, C_{Air} and C_{MUT} are the capacitances of the empty and the filled capacitor, respectively. C_{FE} is the capacitance due to the fringe effects at the top and bottom ends of the cylinder.

Fig. 2 shows the calculated effective permittivity for packs of soda lime glass beads or of rod-shaped particles made of a commercially available nickel catalyst which had been oxidized before the measurements. The catalyst permittivity clearly exhibits a stronger temperature dependence than the glass permittivity.

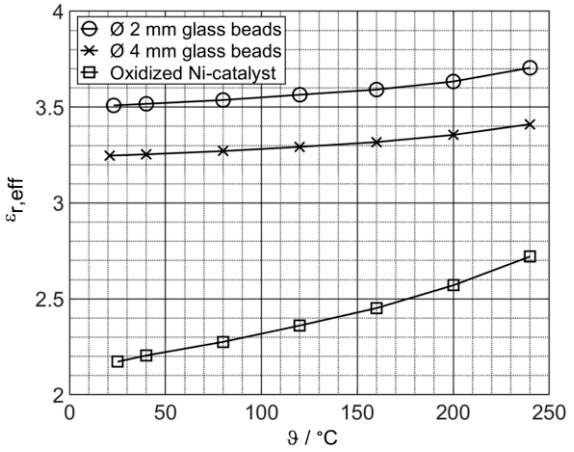

Fig. 2. Effective permittivities calculated from measured impedances as functions of temperature. The MUTs were packs of either glass beads or rod-shaped particles of oxidized nickel catalyst.

ECT Measurements

With the same materials, experiments were carried out with a commercially available ECT system. The setup consisted of a gas-tight sealable tube made of polyether-ether-ketone (PEEK) with two rings of twelve measuring electrodes. The tube was connected to an external compressed-air supply via gas lines. The measuring fixture was located in a convection oven constantly heated to 200 °C. The heated bulk material was then exposed to a cold compressed-air stream, resulting in the progression of a temperature front through the tube.

Fig. 3 shows tomograms obtained in an experiment involving 4-mm glass beads. The reconstructed permittivity has been converted to temperature by Fig. 2 with limits of 100 °C and 200 °C, respectively, known from thermocouple measurements. The inferred temperature in the plane further away from the cool-gas inlet (Fig. 3(b)) drops visibly later than the temperature in the plane near the gas inlet (Fig. 3(a)) — as one would expect. Measurements with the oxidized-catalyst rods led to analogous results.

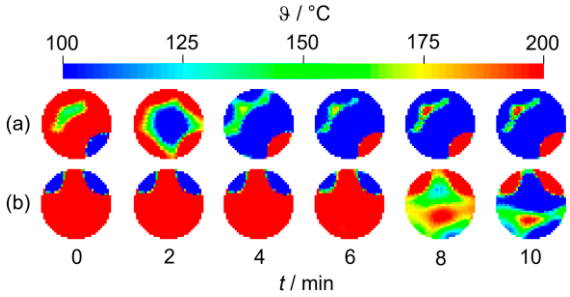

Fig. 3. Reconstructed temperature inside a heated tube filled with a pack of 4-mm glass beads when a cold compressed air stream is injected into the tube for t > 0. (a) Cross-sectional plane closer to the gas inlet. (b) Plane further away from the gas inlet.

Conclusion

It was demonstrated that temperatures inside fixed bed can be estimated by ECT in principle. Issues such as data quality and measurement uncertainty need to be explored in more detail.

Acknowledgement

The authors acknowledge financial support by the Bavarian State Ministry of Science and the Arts within the framework Graduiertenkolleg Energieautarke Gebäude of the Techologieallianz Oberfranken (TAO).

References

[1] J. Shen et al., Experimental and simulation study of the temperature distribution in a bench-scale fixed bed Fischer-Tropsch reactor, *AIChE J* 67 (5), 1–14 (2021); doi: 10.1002/aic.17145.

[2] E. Barsoukov, J. R. Macdonald, Impedance Spectroscopy. Wiley, Hoboken, NJ, 2005.

[3] Y. Hirose et al., Noninvasive real-time 2D imaging of temperature distribution during the plastic pellet cooling process by using electrical capacitance tomography, *Meas. Sci. Technol.* 27, 015403 (2016); doi: 10.1088/0957-0233/27/1/015403.

[4] Y. Yang et al., Temperature Distribution Measurement and Control of Extrusion Process by Tomography, *Proc. IEEE Int'l Workshop Imaging Syst. Techn. (IST)*, 170–174 (2008); doi: 10.1109/IST.2008.4659963.

[5] K. Huang et al., High-temperature electrical capacitance tomography for gas-solid fluidised beds, *Meas. Sci. Technol.* 29, 104002 (2018); doi: 10.1088/1361-6501/aad64.

DOI 10.5162/SMSI2023/E5.4

Material-integrated Temperature Sensors for Wireless Monitoring of Infusion and Curing in Composite Production

Lukas Bertram[1], *Michael Brink*[2], *Walter Lang*[1]
[1] *Institute for Microsensors, -actuators and -systems, University of Bremen, Bremen, Germany,*
[2] *BIBA - Bremer Institut für Produktion und Logistik GmbH, Bremen, Germany*
lbertram@imsas.uni-bremen.de

This work was supported by the German Federal Ministry for Economic Affairs and Climate Action based on a resolution of the German Bundestag, (Nr. 20941 N).

Summary:
This paper presents a novel sensor node for wireless monitoring of local laminate temperature for production of fibre reinforced plastic (FRP) composites. The sensor is realized as a battery-less, flexible RFID tag for material integration and therefore usable throughout the whole composite life cycle. Measurement results are reported for a case study of an eight-layer glass fiber composite production, allowing for flow front monitoring during infusion, and giving information about curing progress.

Keywords: wireless, temperature, sensor, composite, infusion, curing

Introduction

Rising production volumes and number of use cases for FRP components demand for increasingly efficient production processes. A major part of production time and cost is polymer curing, which is strongly dependent on temperature [1]. This is why local matrix temperature data contains information about reaction rates of the material and therefore about curing progress [2]. Also, temperature influences resin viscosity and therefore flow, distribution and impregnation throughout the fibre lay-up during infusion [2].

Consequently, measurement of local temperature is one of the basic ways to get information about both infusion and curing processes. To precisely estimate cure state, surface measurements are often too indirect, especially for thicker layer structures. To circumvent this, temperature sensors can be integrated into the laminate structure prior to infusion. Conventionally, wired sensors are used, creating several problems in turn. Apart from significantly complicating FRP production by impeding build-up of the vacuum foils and seals, protruding wires are prone to breakage during component application.

This paper presents results of integration tests for wirelessly monitoring matrix temperature. The sensor measures local temperature inside the laminate, both during production and later usage of the composite part.

State of the Art

Resin flow monitoring during FRP production has been subject of several publications. [3] successfully integrated wired pressure sensors for flow front and impregnation monitoring. Similarly, [4] used wired pressure sensors in wind turbine blade manufacturing. [5] and [6] integrated off-the-shelf RFID transponders to monitor production, thereby showing that embedding wireless sensors into FRP is generally feasible. Both [7] and [8] have presented work on wireless temperature and pressure monitoring for flow front observation and prevention of local voids. The sensors worked well during infusion but dropped out as temperature increased during cure. In order to monitor cure, [9] successfully used material-integrated temperature sensors and showed that outside measurement was not able to give the same information.

Sensor Design

The sensor [10] used for the presented experiments is realized as flexible printed circuit board. It operates fully passively, harvesting all power from the reader-supplied electromagnetic field via its spiral antenna and RFID chip [11]. For temperature sensing, a *TMP117* [12] is utilized, as it is a small, pre-calibrated, high precision sensor with very low power consumption.

Experiments and Setup

For validation of the process monitoring functionality, two FRP boards were fabricated, containing three sensor tags each. This was done with a vacuum assisted resin infusion setup on a heated table surface (see Fig. 1). To fix the tags in position on the textile and ensure good adhesion, they were cleaned, degreased, and attached with special glue [13].

Prior to infusion, table temperature (T_R) was set to 40 °C and the resin reservoir was heated to 30 °C. The experiment was started by opening

the infusion valves. As the vacuum foils etc. were transparent, process stages could be recorded visually for later-on correlation (see Fig. 2). After 17 minutes, the whole mould was visibly filled. To ensure complete fill-up, the resin inlet valve was closed three minutes later. At 22 minutes, the whole setup was covered with an insulating fleece to reduce heat dissipation at the surface and thereby accomplish a more homogeneous temperature distribution.

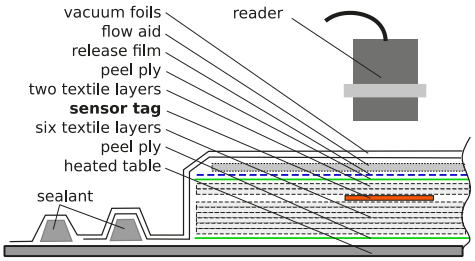

Figure 1: Schematic cross-section of layer stack-up

For curing, T_R was increased in three stages. First, it was set to 55 °C to initiate the curing reaction. After 2:12 h, T_R was set to 65 °C, and again increased to 75 °C at 2:42 h The sensors were read out continuously with three readers mounted above each tag, respectively.

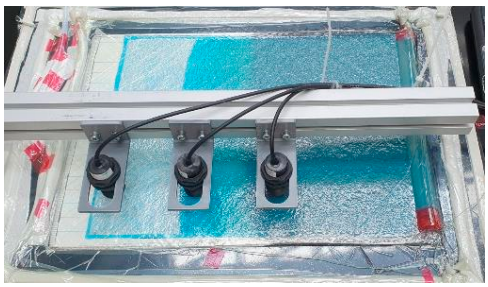

Figure 2: Experiment setup (top view)

Results

Measurement data for infusion and curing is displayed in Fig. 3 and 4. All sensors stayed functional until and after the end of the experiment. Results show a maximum deviation between sensor temperatures of approximately 1.9 °C for board one and 2.1 °C for board two, respectively. For both boards, maximum deviation was observable for the two tags positioned at greatest relative distance, supporting the conclusion that deviations were mostly due to inhomogeneous heating via the table surface. This could later be confirmed by thermal imaging.

During infusion, advancement of the flow front through the lay-up was reflected in the sensor values. In Fig. 3, a close correlation between visual arrival times of the resin at the tag positions is visible. This is indicated by a distinct drop in temperature, caused by the cooler resin, and a distinct rise in temperature briefly after. The latter can be attributed to increased heat flow from the table surface to the tags by better thermal conductivity of the fluid resin.

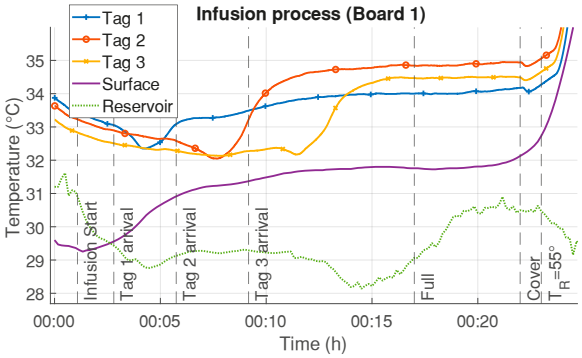

Figure 3:Sensor measurements during infusion, visual arrival times at sensors tags indicated (dashed lines)

During the first phase of heating, the exothermic nature of the curing reaction is visibly reflected in the measured values: Even though surface temperature stays nearly constant (ca. 2 °C drift), temperature inside the material shows a distinct local maximum, marking the exothermic peak of the curing reaction (see Fig. 4).

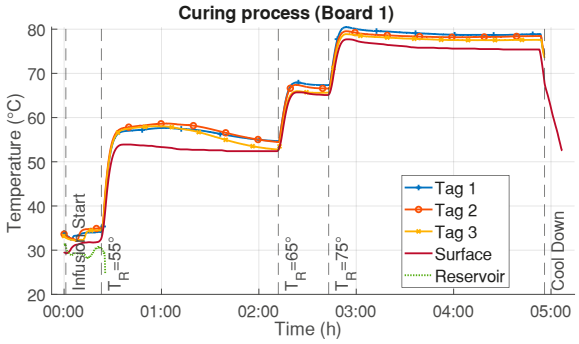

Figure 4: Overview of the production process for board 1. Change of heating targets indicated (T_R)

Apart from this, sensor tag data closely follows the values of the reference sensor located at the surface of the top vacuum foil, with the temperature inside the laminate being slightly higher, probably due to heat dissipation. During the second and third heating phase, inside temperatures follow surface temperature much more closely, indicating reduced heat generation of the curing reaction, thereby reflecting further progression of cure.

Conclusions and Outlook

This paper shows that wireless, material-integrated monitoring of the infusion process and flow front advancement is possible with the presented approach for temperature measurement. Also, progression of the curing reaction was deducible from the measured values. As for the impact of the sensor tags on structural integrity of the resulting FRP material, mechanical tests have yet to be conducted, the results of which will be subject of a future publication.

References

[1] M. J. Lodeiro and D. R. Mulligan, ‘Cure Monitoring Techniques for Polymer Composites, Adhesives and Coatings’. National Physical Laboratory Teddington, Middlesex, United Kingdom, TW11 0LW, 2005. [Online]. Available: https://www.npl.co.uk/special-pages/guides/mgpg75.aspx?ext=.pdf

[2] S. Konstantopoulos, E. Fauster, and R. Schledjewski, ‘Monitoring the production of FRP composites: A review of in-line sensing methods’, *Express Polym. Lett.*, vol. 8, no. 11, pp. 823–840, 2014, doi: 10.3144/expresspolymlett.2014.84.

[3] M. K. Moghaddam, A. Breede, C. Brauner, and W. Lang, ‘Embedding Piezoresistive Pressure Sensors to Obtain Online Pressure Profiles Inside Fiber Composite Laminates’, *Sensors*, vol. 15, no. 4, Art. no. 4, Apr. 2015, doi: 10.3390/s150407499.

[4] A. Dimassi, M. G. Vargas Gleason, M. Hübner, A. S. Herrmann, and W. Lang, ‘Using piezoresistive pressure sensors for resin flow monitoring in wind turbine blades’, *Materials Today: Proceedings*, p. S2214785320305988, Feb. 2020, doi: 10.1016/j.matpr.2020.01.493.

[5] M. Veigt, E. Hardi, M. Koerdt, A. S. Herrmann, and M. Freitag, ‘Curing Transponder – Integrating RFID transponder into glass fiber-reinforced composites to monitor the curing of the component’, *Procedia Manufacturing*, vol. 24, pp. 94–99, 2018, doi: 10.1016/j.promfg.2018.06.014.

[6] E. Hardi, M. Veigt, M. Koerdt, A. S. Herrmann, and M. Freitag, ‘Monitoring of the vacuum infusion process by integrated RFID transponder’, *Procedia Manufacturing*, vol. 52, pp. 20–25, 2020, doi: 10.1016/j.promfg.2020.11.005.

[7] M. G. Vargas Gleason, R. Jedermann, A. Dimassi, and W. Lang, ‘Embedded Wireless Sensor Systems for Resin Flow Monitoring in Glass and Carbon Fiber Composites’, *IEEE Sensors J.*, vol. 19, no. 22, pp. 10654–10661, Nov. 2019, doi: 10.1109/JSEN.2019.2928635.

[8] M. G. V. Gleason, R. Jedermann, A. Dimassi, and W. Lang, ‘Wireless Piezoresistive Pressure Sensors Used for Quality Control in Glass Fiber Composite Laminates’, in *2018 IEEE SENSORS*, Oct. 2018, pp. 1–4. doi: 10.1109/ICSENS.2018.8589933.

[9] M. Hübner and W. Lang, ‘Online Monitoring of Composites with a Miniaturized Flexible Combined Dielectric and Temperature Sensor’, in *Proceedings of Eurosensors 2017, Paris, France, 3–6 September 2017*, Aug. 2017, p. 627. doi: 10.3390/proceedings1040627.

[10] L. Bertram, M. Brink, K.-D. Thoben, and W. Lang, ‘A Passive, Wireless Sensor Node for Material-Integrated Strain and Temperature Measurements in Glass Fiber Reinforced Composites’, 2022, pp. 182–193. doi: 10.1007/978-3-031-16281-7_18.

[11] ‘NHS 3152 - Therapy adherence resistive monitor’. NXP Semiconductors B.V., 2021. [Online]. Available: https://www.nxp.com/docs/en/data-sheet/NHS3152.pdf

[12] ‘TMP117 High-Accuracy, Low-Power, Digital Temperature Sensor With SMBus™- and I2C-Compatible Interface’. Texas Instruments Inc., Apr. 2021. [Online]. Available: https://www.ti.com/lit/ds/symlink/tmp117.pdf

[13] SAERTEX GmbH, ‘SAERfix®EP // SAERfix®UP KLEBEMATERIALIEN - Produktflyer’. 2022. [Online]. Available: https://www.saertex.com/de/service/downloads/saerfix/file/3a01f3af1d97f092dedccf5256905b94/0143-14-066_SAERTEX_Produktflyer_SAERfix_DEU.pdf

DOI 10.5162/SMSI2023/E6.1

Hierarchical Digital Offset Voltage Trimming of Fully-Differential Amplifiers in Self-X Sensor Electronics

Senan Alraho[1], Qummar Zaman[1], Andreas König[1]
[1]Lehrstuhl Kognitive Integrierte Sensorsysteme (KISE), TU Kaiserslautern Deutschland,
aube@eit.uni-kl.de

Summary:
This paper presents an improved approach to the digital offset voltage calibration scheme of fully differential amplifiers by splitting the adaptation process into two levels using separated coarse and fine digital-to-analog (DAC) current steering converters. The key feature is to avoid the matching complexity of using a single high-resolution DAC. Furthermore, the dynamic offset trimming process can be repeated based on the second DAC only, leading to a reduction in the calibration time. The achieved results based on Monte Carlo simulation show the ability to calibrate the offset voltage of the fully-differential instrumentation amplifier (In-Amp) below 100 µV for tackling offset voltage around ± 9 mV. The circuit is designed using XFAB 0.35 µm technology and verified with Cadence Virtuoso tools.

Keywords: Infield optimization, Self-X properties, Instrumentation amplifier, digital offset calibration.

Background, Motivation and Objective

The presence of the input offset voltage (V_{OS}) defines the amplifier resolution for detecting minimum input voltage in the sensor readout circuit. Furthermore, depending on the V_{OS} absolute value, it can drive the amplifier toward the output saturation region, thus reducing the output dynamic range when a high closed-loop gain is required. Several circuit-level solutions [1, 2, 3] are followed to tackle both the static and dynamic source of V_{OS} , avoiding the use of expensive and maybe not affordable wafer-level static approaches in the standard CMOS technology, e.g, laser trimming [4]. Digital offset trimming [5, 6] is a common dynamic technique owing to the advantages of simplicity and compatibility to the continuous- time signal processing circuits. However, the minimum V_{OS} is proportional to the resolution of the used digital-to-analogue converter. This abstract aims to use a higher resolution DAC with less matching constraints and to reduce the calibration time, which allows running the calibration period at a higher rate to support the principle of smart sensors with self-X properties (self-calibration, self-healing) [7,8].

Description of the Proposed Methodology

The block diagram of the proposed approach is depicted in Fig. 1. The calibration scheme is used to null the input offset voltage of the fully differential instrumentation amplifier (In-Amp) [9]. During the calibration time, the In-Amp is set to the maximum closed loop gain of 128 to subdivide the inherent offset voltage of the hysteresis comparator, while the In-Amp inputs are shorted to the common mode voltage (V_{CM}). Also, the configurable compensation capacitor is set to the minimum value to improve the settling time of the In-Amp without affecting the stability condition. The adaptation is split into two separate levels, in the first level a 6-bit segmented current steering (CS) DAC with 4-bit binary-weighted bits and 2 bits with thermometer coding to improve the matching on the top two MSB bits. In the second level, an 8-bit M3M CS DAC [10] is employed to fine-tune the VOS outcome from the first level.

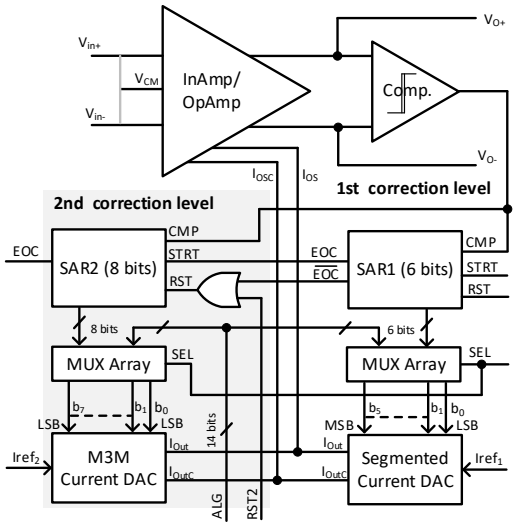

Fig. 1. Block diagram of the proposed digital V_{OS} calibration.

The two separated DACs do not need to match together as compared to a single 14-bit DAC.

Nevertheless, with this scheme, it is possible to iterate the calibration using the second level only, reducing the calibration time when tackling dynamic V_{OS} drift due to temperature and supply voltage fluctuations. Whilst both levels are only required at the chip startup. To enhance the calibration flexibility when used in smart sensory electronic systems, the inputs to the DACs are multiplexed to allow reading calibration data from the optimization algorithm performed on the digital-processing unit, which allows for infield adaptation concurrently during the measurement operation.

Results

To verify the circuit performance, both the In-Amp and the calibration circuit are simulated together to extract the V_{OS} using Monte Carlo (MC) with a large number of samples (1000 samples) per temperature and supply voltage corners (V_{DD}=3.3±10%, -40 ≤ T ≤ 85 ºC). This is important to count the offset voltage due to the DACs output currents mismatches and the residual offset of the comparator. The process variation of 6 σ with Gaussian distribution MC type is selected to emulate more realistic conditions of device fabrication. The worst-case result is found at T=-40 ºC and V_{DD}=3 V. Then the MC is again repeated with 1000 sample around the last corner to have a dense distribution at the worst corner. As shown in Fig. 2, most of the samples fall between V_{OS} = ± 9 mV with a steady deviation of 2.623 mV from the typical mean value.

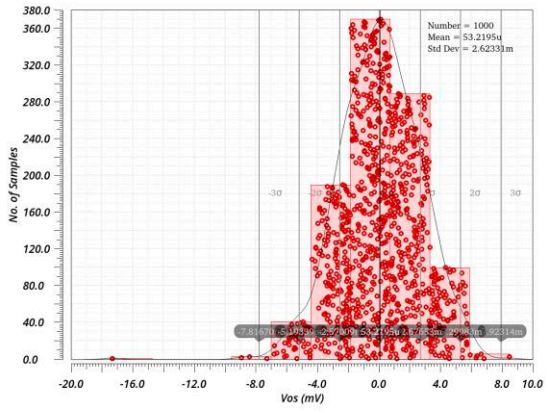

Fig. 2. MC simulation result at the worst-case corner.

The two maximum absolute V_{OS} is back annotated as a statistical corner from the MC sample batch to run the optimization scheme over it in the next step. Fig. 3 demonstrates how the calibrated V_{OS} is reduced below 100 µV in either case. A clock frequency of 100 kHz is used in this simulation test to drive the successive approximation registers (SAR). The estimated design area is 0.75 mm^2 and the power consumption of the optimization loop is about 140 µW.

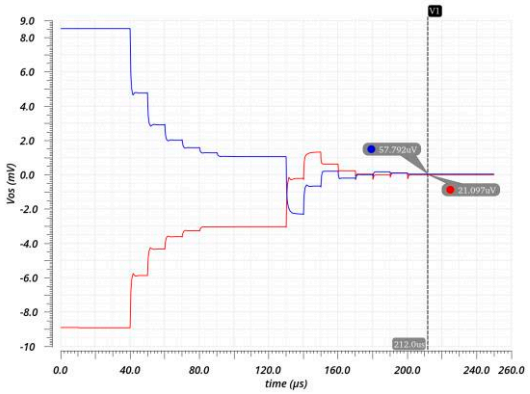

Fig. 3. Optimization run against maximum absolute extracted V_{OS} .

References

[1] Freier, R., Braun, S., & Koenig, A. (2014, June). Reconfigurable precision instrumentation amplifier for universal sensor interface. In Sensors and Measuring Systems 2014; 17. ITG/GMA Symposium VDE.

[2] C. C. Enz and G. C. Temes, “Circuit techniques for reducing the effects of op-amp imperfections: autozeroing, correlated double sampling, and chopper stabilization,” Proc. IEEE, 1996.

[3] Meijer, G., Pertijs, M., & Makinwa, K. (2014). Smart sensor systems: Emerging technologies and applications. Wiley Publishing.

[4] Magri, J., Grech, I., Casha, O., Gatt, E., & Micallef, J. (2016, December). Design of CMOS front-end circuitry for the acquisition of biopotential signals. In 2016 IEEE ICECS.

[5] C.-G. Yu and R. L. Geiger, “An automatic offset compensation scheme with ping-pong control for CMOS operational amplifiers,” IEEE J. Solid-State Circuits, vol. 29, no. 5, pp. 601–610, 1994.

[6] M. Šovčík, V. Stopjaková, D. Arbet, and M. Potočný, “Autonomous On-Chip Digital Calibration for Analog ICs in Nanotechnologies,” in 2020 30th International Conference Radioelektronika (RADIOELEKTRONIKA), 2020, pp. 1–5.

[7] König, Andreas. "Integrated sensor electronics with self-x capabilities for advanced sensory systems as a baseline for industry 4.0." Sensors and Measuring Systems; 19th ITG/GMA-Symposium. VDE, 2018.

[8] Alraho, Senan, Qummar Zaman, Hamam Abd, and Andreas König. "Integrated Sensor Electron-ic Front-Ends with Self-X Capabilities." Chips 1, no. 2 (2022): 83-120.

[9] Zaman, Qummar, Senan Alraho, and Andreas König. "Efficient transient testing procedure us-ing a novel experience replay particle swarm op-timizer for THD-based robust design and optimi-zation of self-X sensory electronics in industry 4.0." Journal of Sensors and Sensor Systems 10, no. 2 (2021): 193-206

[10] Pastre, M., & Kayal, M. (2006). Methodology for the digital calibration of analog circuits and systems: with case studies (Vol. 870). Springer Science & Business Media.

DOI 10.5162/SMSI2023/E6.2

Compensation of Zero-Flow-Offset due to Electronics and Transducers Mismatch

Friedrich Bahnmüller, Tarek Elrifai, Tuyen Nguyen
Sciosense Germany GmbH, Friedrich-List-Strasse 4, 76297 Stutensee
friedrich.bahnmueller@sciosense.com

Summary:
Ultrasonic flow meters are widely used in industry for water and gas flow measurements. In practice, those flow meters tend to show a zero-flow error in the time of flight (ToF) measurement that can be suppressed by matching the downstream and upstream transducers in the system. In this work, the effect of mismatch on the ToF measurement is demonstrated for various ultrasonic flow meters under different conditions.

Keywords: Ultrasonic flow meters, flow measurement, zero-flow error, Time of flight measurements, downstream and upstream transducer.

Introduction

The ultrasonic flow meters measure water and gas flow for a wide range of applications. They have the advantage of not having moving parts in the flow, which in turn minimizes the maintenance needs and costs over time. The ultrasonic flow meters are time of flight (ToF) based meters where the transit time difference between the upstream and downstream flow is used to measure the flow velocity. As per [1], ultrasonic flow meters are reciprocal systems, and the only non-reciprocal part of the system is the flow itself. Therefore, in the absence of flow, ideally, the measured time difference should be zero in reciprocal operation [3]. But practically a zero-flow offset is often measured. This offset results in a phase difference between the upstream and downstream measurements. This offset is introduced due to the available mismatch between the up and downstream transducers and simultaneously mismatch in the transducer electronics.

Background, Motivation

The reciprocal operation principle allows for a negligible zero-flow offset measurements [2]. It states that the flow system consisting of piezoelectric transducers, electronics and spool-piece responds same at one side when driven from the other side and vice versa resulting in a small difference in ToF measurement (diff-ToF). For the system to maintain this property, either the impedances of the transducers pair or the impedances of the electronics at both sides need to be matched. This can be analyzed as a two-port network, where the voltage transfer function downstream and upstream can be represented by eq. (1) respectively [3],

$$\frac{V_I^{(2)}}{V_{II}^{(1)}} = \frac{I_I^{(2)}}{I_{II}^{(1)}} = \frac{\left(Z_S + Z_I\right)}{\left(Z_S + Z_{II}\right)} \frac{\left(Z_L + Z_{II}\right)}{\left(Z_L + Z_I\right)} \quad (1)$$

Where Z_r, Z_s are the impedance from the electronics in down and up transducer cases.

It is obvious that the voltage transfer functions up- and downstream are identical, when all impedances Z_r, Z_s are identical. In that case, it is important to deduce that the transducer's impedance Z-parameters do not need to be matched as well for the zero-flow offset to be minimized.

Measurement Setup

An ultrasonic flow transducer is placed on the up- and down-stream side of a DN20 water spool piece. An integrated circuit (IC) is added to read out the data and calculate the diff-ToF. The first measurement set is the zero-flow offset in water over a temperature range from 10 to 60 degrees Celsius when there is no flow. The data is averaged over 200 points. The second measurement set is performed by creating a mismatch between the transducer pair by adding a parallel capacitor to either the up- or the downstream transducer which changes its total impedance. The range of capacitance used is from 0 to 220pF, this accounts for 20% of the transducer's self-capacitance which is approximately 1nF. These measurements are performed using the TDC-GP30 board and a competitor board.

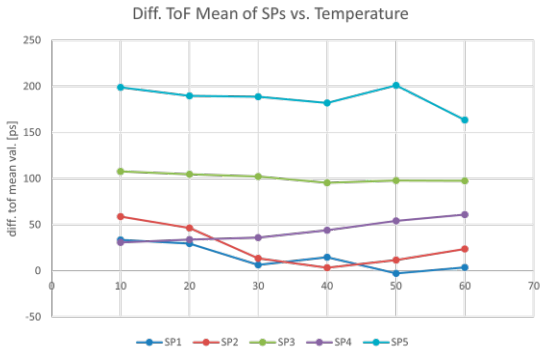

Fig. 1. Diff-ToF measurements with GP30 over the temperature range 10-60°C using different spool pieces.

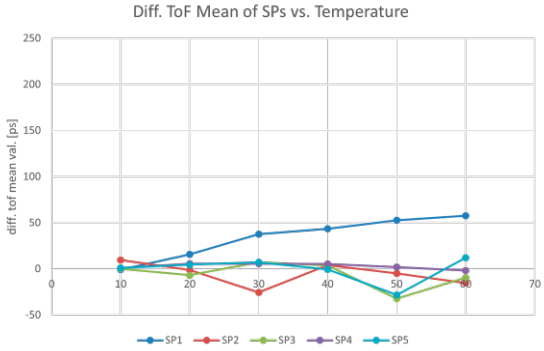

Fig. 2. Diff-ToF measurements with a competitor board over the temperature range 10-60°C using different spool pieces.

Results and discussion

Fig.1. shows the diff-ToF measurements over temperature with GP30. The resulting temperature drift is observed in the diff-ToF values over the different spool pieces, the mean diff-ToF for each spool piece is shown in Table 1. Its minimum and maximum are 12ps and 55ps respectively. Fig. 2. shows measurements on same spoolpieces using a competitor's IC. The span in temperature drift defined as difference in maximal and minimal value of diff-ToF is represented in Table 1. Its minimum and maximum diff-ToF are 7ps and 58ps respectively. The mean part of the offset, which is constant over temperature, is of only of minor importance for application. With compensation in post processing, the offset can be set to zero for both devices. The second measurement is depicted in Fig.3. where both measurements with capacitor on up- and downstream transducers are added using GP30 and competitors' IC. It is performed at room temperature using two spool pieces. When no capacitor is added, the diff-ToF offset is only due to the IC being used which can be compensated as in the first measurement. Then as we add capacitors, the mismatch effect is more pronounced.

Table 1. Span in Temperature Drift

	TDC-GP30 (ps)	Competitor's(ps)
SP1	36.46	58.57
SP2	55.60	35.22
SP3	12.27	39.55
SP4	30.15	7.45
SP5	37.51	40.33

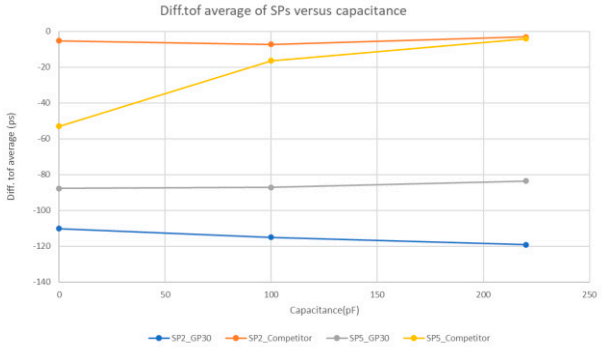

Fig. 3. Mismatch between transducers due to added parallel capacitors from 0 to 220pF.

This effect can be seen using GP30 where the offset is between 4ps and 18ps for both spool pieces. As for the competitor's IC the offset is between 1ps and 48ps with both spool pieces. It can be deduced that the added strong mismatch has only an effect in picosecond range on the intrinsic offset of the chips.

Conclusion

In this work, the zero-flow drift in GP30 and a competitor's IC are presented. It is highlighted that this drift is comparable for both products and is less than 60ps in all cases. This is important for the application. Moreover, in applications with mismatched spool pieces, the effect on the diff-ToF is less noticeable for GP30 with a maximum offset of 18ps compared to the competitor's IC with a maximum offset of 48ps.

References

[1] J.Hemp, Flowmeters and reciprocity, *The Quarterly Journal of Mechanics and Applied Mathematics*, vol 41, no. 4, pp. 503-520, 1988.

[2] P. Lunde, M. Vestrheim, R. Bo, S. Smorgrav and A. K. Abrahamsen, 5D-4 Reciprocal Operation of Ultrasonic Flow Meters: Criteria and Applications, *2007 IEEE Ultrasonics Symposium Proceedings*, 2007, pp. 381-386, doi: 10.1109/ULTSYM.2007.105.

[3] P.Lunde, M. Vestrheim, R.Bo, S.Smorgrav and A.K. Abrahamsen, Reciprocity and its utilization in ultrasonic flow meters. *2005 23rd International North Sea Flow Measurement Workshop.*

DOI 10.5162/SMSI2023/E6.3

Integrated Signal Amplification and Conditioning of Pyroelectric Sensor Elements

Robin Lehmkau[1]
[1] *InfraTec GmbH, Gostritzer Str. 61-63, 01217 Dresden (Germany), r.lehmkau@infratec.de*

Summary:
The signal conditioning of sub-pA pyroelectric currents with a monolithic circuit is a challenging task. A switched capacitor enables the emulation of high-ohmic resistance values in the GΩ-range for a high amplification on a small chip area. Different circuit topologies are simulated and measured whereby the realized digital detector achieves a specific detectivity of 2.5 · 10^8 cm√Hz/W at 10 Hz.

Keywords: Switched capacitor, Transimpedance amplifier, ASIC, SPICE, Pyroelectrical detector

Motivation

Pyroelectrical detectors are used in numerous applications like high-performance gas analysis, contactless temperature measurement and fast flame detection. Miniaturization and digitization are important subjects of current research. One aim is to increase the integration density, e.g. by including the signal conditioning inside the detector. This is possible by using an application-specific integrated circuit (ASIC), which combines a lot of different functions on a small silicon chip. Until now, mostly circuits with discrete resistors in the GΩ-range are used to amplify the pyroelectric current. These resistance values would cover large chip area on a wafer, which is why other circuit approaches need to be implemented [1].

The contribution of this paper are the simulations and measurements of circuit topologies for the integrated amplification of pyroelectric signals.

Circuit Topologies

The crucial part of the readout circuit is the high-ohmic resistance. Figure 1 illustrates a typical single supply transimpedance amplifier (TIA), continuously converting the pyroelectric current I_{pyro} to an output voltage V_{out}.

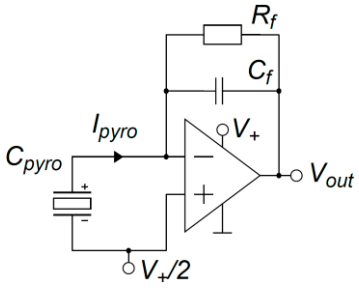

Fig. 1: Analog single supply TIA with a feedback resistor R_f and capacitor C_f.

The demand to achieve very high resistance values on a small silicon area is examined in several publications, e.g. for large time constants of electrical filters or current amplifications [1] [2]. A common approach is to replace the ohmic resistor with a switched capacitor (SC). Two adapted principles to discretely convert the pyroelectric current are shown in Fig. 2. The charge-voltage (QU)-converter in Fig. 2(a) integrates the input current on C_{int} and is reset periodically to return to the working point of the operational amplifier. Shortly before the reset, the output voltage is sampled. Figure 2(b) behaves like an analog TIA where the resistor is replaced by the stray insensitive circuit built by C_{sw} and four switches S_x resulting in an effective resistance of:

$$R = \frac{1}{f_{sw} \cdot \boldsymbol{C_{sw}}} \quad \text{Eq. (1)}$$

with the switching frequency f_{sw}. Afterwards the output signal is low pass filtered with the corner frequency f_c to smooth the switching transients.

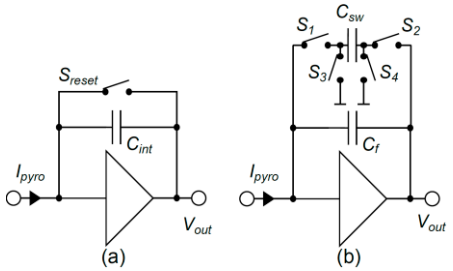

Fig. 2: Topology of the (a) QU-converter and the (b) SC-TIA as analog frontend of the ASIC.

Circuit Simulations

For a comparison, the circuits are simulated with *LTSpice*. A rectangular input current I_{pyro} (±1 pA, 50 % duty cycle, 10 Hz) is chosen. The capacitors C_{int} = C_{sw} = 100 fF with a switching frequency of f_{sw} = 1 kHz lead to an effective

R_f = 10 GΩ. Figure 3 shows the output voltage of the analyzed circuits for different off resistances $S_{x\,off}$ of the switches and C_f = 200 fF.

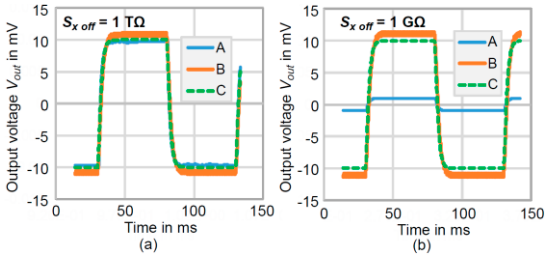

Fig. 3: Low pass filtered (f_c = 200 Hz) output signal in the time domain of A…QU-Converter, B…SC-TIA and C…discrete TIA for (a) 1 TΩ and (b) 1 GΩ off switch resistance.

The signal of the SC-TIA (B) is nearly insensitive to the off resistance of the switch but has a small voltage ripple compared to the analog counterpart (C), which can be further smoothed by a larger spacing between f_c and f_{sw}. The signal of the QU-converter (A) highly depends on the switch properties of S_{reset}. With $S_{x\,off}$ = 1 GΩ the capacitor C_{int} discharges faster and the output amplitude decreases in Fig. 3(b). Moreover, non-ideal behavior like charge injection, clock feed-through and noise folding effects due to the switches have a negative impact on the noise behavior in the frequency domain. Some techniques like correlated double sampling (CDS) or the use of dummy switches can minimize those effects. A profound noise analysis for a discrete-time integrated amplifier can be found in [3].

For a first run, the SC-TIA of Fig. 2(b) is realized, because it is stray insensitive, it needs no reset, and it is better suited for low-frequency pyroelectric applications with lower switch requirements.

Measurements

An overview of the whole developed ASIC is shown in Fig. 4. The analog part amplifies and filters the pyroelectric current of up to four parallel sensor elements.

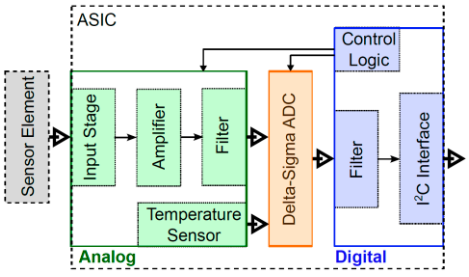

Fig. 4: Main components of the realized ASIC.

Afterwards the voltage is fed into a 16-bit delta-sigma converter and the digitized counts can be read via a I²C communication interface (FM+). A huge advantage compared to a discrete setup is the flexible configuration of the input stage, because the emulated feedback resistance and capacitance can be adjusted over a wide range of 2 GΩ … 1 TΩ and 50 fF … 6400 fF, respectively. That is why the measured responsivity of the detector in Fig. 4 can be adjusted over more than two decades, in comparison to the fixed responsivity of the commercial detector LRM-244.

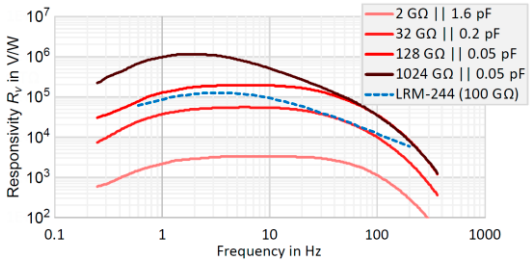

Fig. 5: Responsivity of the digital detector for different feedback configurations in the frequency domain.

The output noise densities of the discrete TIA and the SC-TIA theoretically are the same because the noise folding effects of the SC circuit result in a white noise corresponding to the realized resistance value R_f at low frequencies. Measurements show that the noise density of the SC-TIA is ≈ 180 µV/√Hz (128 GΩ, 10 Hz) and higher than for a discrete R_f, due to several other impacts like the current and voltage noise of the operational amplifier or the specific implementation of the switches. In total, a specific detectivity of 2.5 · 10^8 cm√Hz/W (10 Hz, 500 K) could be achieved with the integrated SC-TIA.

Conclusion

An ASIC for the signal conditioning and digitization of sub-pA currents was successfully integrated in a pyroelectrical detector to minimize the external hardware effort. The input stage is realized as TIA in which the discrete high-ohmic resistor is replaced by a switched capacitor. This leads to a similar signal behavior for low frequencies and much less chip area is needed for the monolithic circuit. But the measured noise density of the whole digital detector is higher than for state-of-the-art analog pyroelectrical detectors with identical setup. This is for example due to different operational amplifiers, leakage currents and the integrated switches. Still, the digital detector achieves a high specific detectivity of 2.5 · 10^8 cm√Hz/W and offers a lot a flexibility for different applications.

References

[1] R. Gregorian, K. Martin, G. Temes: „Switched-Capacitor Circuit Design“, *Proc. IEEE Vol. 71 (1983)* DOI: 10.1109/PROC.1983.12700

[2] M. Crescentini et al.: “Noise Limits of CMOS Current Interfaces for Biosensors: A Review”, *IEEE Trans. on Biomedical Circuits and Systems Vol. 8* (2014) DOI: 10.1109/TBCAS.2013.2262998

[3] M. Crescentini et al.: “A noise model for full characterization of discrete-time current sensing”, *6th Ph.D. Research in Microelectronics & Electronics Conf.* (2010)

DOI 10.5162/SMSI2023/E6.4

Biological Neural Coding for Adaptive Spiking Analog to Digital Conversion

Hamam Abd[1], *Andreas König*[1]
[1] *Institute of Cognitive Integrated Sensor Systems (KISE), TU Kaiserslautern Deutschland,*
abd@eit.uni-kl.de

Summary:
A conventional ADC in leading-edge integration technologies faces numerous challenges due to manufacturing deviations, signal swings, noise, etc. Designers of ADCs are shifting to the time domain and digital design techniques to manage these challenges. Consequently, we aim to design a novel self-adaptive spiking neural ADC (SN-ADC) with promising properties, e.g., low-voltage operation, technology scaling issues, noise-robust conditioning, and low power. In this work, we focus on designing one building block of our concept, a decoder that converts place coding to digital code.

Keywords: Spike-domain information presentation, Biological neural coding, Industry 4.0.

Background, Motivation and Objective

The number and diversity of sensors increase with the progress in integration technologies due to the rapid progress of machine learning and artificial intelligence in the internet of things (IoT) and Industry 4.0 [1]. The performance of the smart sensor faces many problems due to dynamic and static divergence. These problems are effectively addressed by utilizing reconfigurable structures with self-X (self-optimization, self-monitoring, self-calibration, and self-healing) properties [2]. However, reconfigurable structures use amplitude representation that faces problems with leading-edge technologies. These advocates transition to spike domain representation with self-X properties.

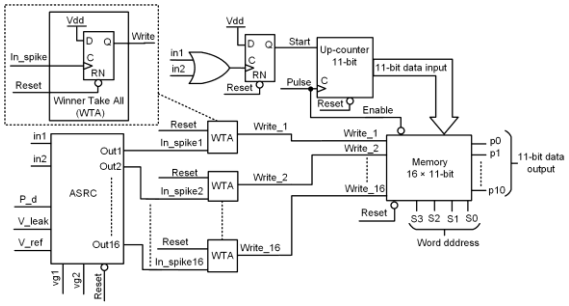

Fig. 1. Proposed schematic of place coding to digital code.

In our previous work, we proposed a self-adaptive spiking neural ADC (SN-ADC) system [1]. It is built on based rank order coding. It consumes a massive area and needs a high conversion time for the 14-bits. The required number of neurons and synapses is 16384 and 32768, respectively. Additionally, it needed 16384 cells of WTA. These advocated designing the SN-ADC based on another biological neural coding to decrease the consume area and increase the speed for the high resolution, e.g., 14-bits. Many coding schemes for biological neural transmission can be divided into density coding, rank order coding, and place coding [3]. In this work, we design a novel decoder that converts the place coding to digital code with promising features, e.g., high resolution, low area consumption, high speed, and low power consumption.

Proposed Methodology

In this work, we design a circuit that converts the place coding to a digital number (see Fig. 1). Every output of adaptive spike-to-rank coding (ASRC) is connected to one cell in the WTA circuit. The outputs of the WTA circuit are connected to the memory. There is a location in memory for each cell of WTA to save its place in the observation window. The outputs of the WTA write the counter output on their location on the memory when they convert from zero to one. The output of the OR gate is connected to the D-flip-flop clock, and flip-flop output is connected to the counter start. The counter is started increasing when the in1 or in2 input is presented. The 11-bit counter is used to divide the observation window into 2048 sub-windows. In our previous work [1], we designed the ASRC with 16 outputs. Therefore, in the current work, we implement memory with the 16 locations (see Fig. 2). Every location is set for one output of the ASRC to save its position. The proposed work needs 16 neurons and 32 synapses for the 14-bits. It used 16 cells of WTA. The proposed design is implemented using X-

FAB 0.35 µm CMOS technology and Cadence tools.

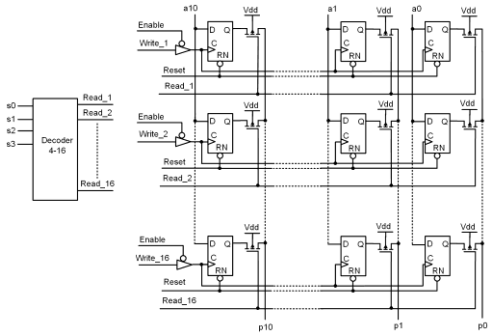

Fig. 2. Schematic of the memory.

Results

Figure 3 shows the ASRC outputs when two pulses are presented to the ASRC inputs with a difference of 3 ns between in1 and in2.

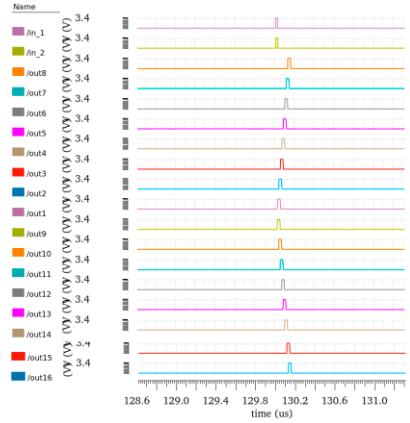

Fig. 3. Simulation of the ASRC, with a difference of 3 ns between in1 and in2

The ASRC outputs from out1 to out16 are shown in Figure 3 go to the inputs In_spike1 to In_spike16 of the WTA cells, respectively (see Fig. 1). The WTA cells generate pulses that are used to write the counter's output to the memory (see Fig. 4). The time difference steps between in1 and in2 are from −8044 to 8044 ns in steps of 1 ns, as shown in Table 1.

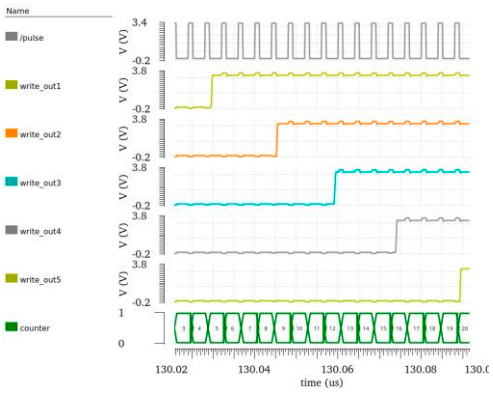

Fig. 4. Simulation of WTA outputs and counter,

Tab. 1: Place code outputs of the memory

In2-in1 (ns)	-8044	-8043	….	8043	8044
out1	5	5	….	2015	2016
out2	9	9	….	2020	2020
out3	13	13	….	2024	2025
out4	18	18	….	2028	2029
out5	22	22	….	2033	2033
out6	27	27	….	2037	2038
out7	31	31	….	2042	2042
out8	36	36	….	2046	2047
out9	2016	2015	….	5	5
out10	2020	2020	….	9	9
out11	2025	2024	….	14	14
out12	2029	2029	….	18	18
out13	2033	2033	….	22	22
out14	2038	2038	….	27	27
out15	2042	2042	….	31	31
out16	2047	2046	….	36	36

It obtains up to 16087 different output place codes representing 13.97 bits in the binary code. From the speed perspective, the conversion time is 8.142 us. From the energy consumption perspective, the energy consumption of circuits ASRC, WTA, counter, and memory is 103.3 pJ per 1 µs when there is no spike. They consume 1.24 nJ per spike when there is a spike. While in previous work [1], for 14-bit, the conversion time was 368.640 us, and the energy consumption was 91.56 nJ per 1 µs when there was no spike and 1.238 µJ per spike when there was a spike.

References

[1] H. Abd, and A. König. "Design of a CMOS memristor emulator-based, self-adaptive spiking analog-to-digital data conversion as the lowest level of a self-x hierarchy." Journal of Sensors and Sensor Systems https://doi.org/10.5194/jsss-11-233-2022,

[2] S. Alraho, Q. Zaman, H. Abd, and A. König.. "Integrated Sensor Electronic Front-Ends with Self-X Capabilities." Chips 1.2 (2022): https://doi.org/10.3390/chips1020008.

[3] S. Thorpe, A. Delorme, and R. Van Rullen. "Spike-based strategies for rapid processing." Neural networks 14.6-7 (2001): https://doi.org/10.1016/S0893-6080(01)00083-1.

DOI 10.5162/SMSI2023/E7.1

Miniaturized SMD-Reflow-Capable Photoacoustic CO_2-Sensor Using a Dual-Chamber Approach

Simon Gassner [1,2], Simon Essing [3], David Tumpold [2], Katrin Schmitt [1,4], Jürgen Wöllenstein [1,4]
[1] University of Freiburg, Department of Microsystems Engineering (IMTEK), 79085 Freiburg
[2] Infineon Technologies AG, 85579 Neubiberg
[3] Technical University of Munich, Department of Electrical and Computer Engineering, 80333 Munich
[4] Fraunhofer IPM, 79110 Freiburg
Corresponding author: simon.gassner@infineon.com

Summary:
The increasing interest in monitoring indoor air quality has led to a growing demand for simple and small-scale gas sensors. We present a miniaturized photoacoustic dual chamber sensor module that includes an infrared hotplate emitter and a wafer-level manufactured photoacoustic detector. The sensor module was controlled by a PSoC 4200M microcontroller and is capable of being soldered in a SMD reflow soldering process. The sensor prototype achieves a 3-sigma noise level of 138 ppm CO_2, which is suitable for most consumer applications.

Keywords: photoacoustic, gas sensor, wafer-level, CO_2, MEMS

Introduction

Interest in measuring air quality has increased significantly over the past three years. The publication of studies showing a correlation between bad air quality and viral load spurred the demand for small and simple sensor solutions [1]. The most commonly used marker for bad indoor air quality is an increased concentration of carbon dioxide (CO_2) in the air [2].

The first commercially available optical gas sensors were relatively large and mechanically complex. However, sensor technology has improved over the years, allowing for the manufacturing of smaller, more cost-efficient devices. Recent trends have shown a movement towards reducing the sensor size even further and the introduction of surface mounted device (SMD) reflow capability as an assembly feature. The latest generation of CO_2 sensors uses the photoacoustic effect to determine the CO_2 concentration in air. However, such sensors work with a spectral filter and only one photoacoustic cell [3]. Therefore, this approach has a limited selectivity towards the target gas and is sensitive to acoustic interference.

In another approach, the so called "dual-chamber approach", two sensor cells are used: one exposed to ambient air and a second cell containing the microphone and filled with the target analyte. In this concept, the filling gas acts as a spectral filter and makes the sensor selective only to the target gas [4].

We present a miniaturized sensor based on this dual-chamber approach, measuring only 9 x 13 x 7.8 mm³ (L x W x H). To our knowledge, this is the smallest dual-chamber concept photoacoustic sensor module reported to date.

Methods

The sensor module consists of a micro-electrical-mechanical system (MEMS) microphone membrane, which we encapsulated on both sides using wafer bonding technology. During the encapsulation process, the device was exposed to a 100% CO_2-atmosphere, which effectively trapped the CO_2 in the cavities above and below the microphone membrane. This microphone was placed on a thin substrate circuit board and connected to an application specific integrated circuit (ASIC) which features an integrated temperature sensor and digital signal filter for preprocessing of the acoustic data. The microphone assembly was soldered together with a ceramics-packaged MEMS infrared (IR) emitter module onto a component carrier circuit board. Both components were covered by a gold-plated and reflective metal lid. This lid acted as a protective housing and at the same time as a reflector for the IR radiation. The module was contacted using castellated hole side contacts. A photograph of the sensor module without the attached reflector lid can be seen in Fig. 1. The module was connected to an Infineon PSoC 4200M microcontroller-based motherboard which carried voltage supply circuitry, a MOSFET for driving the IR-emitter as a low side

switch and a USB-UART bridge was used for communicating with the microcontroller.

During operation, the IR-emitter is driven in a sequence of 18 square-wave pulses at a frequency of 40 Hz. The acoustic signal of the microphone is recorded by the microcontroller and sent to a host-computer after each pulse sequence for post-processing and evaluation.

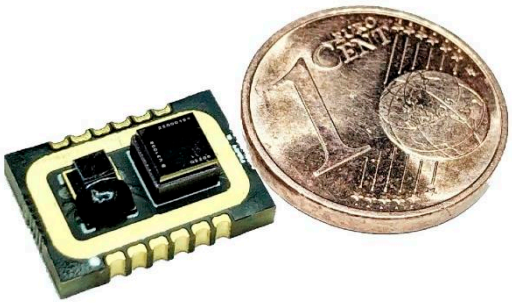

Fig. 1. Developed sensor module with MEMS-detector (left), and IR-emitter (right) (without lid) and a eurocent coin as a size reference.

In post-processing, the microphone signal is bandpass filtered and the RMS value of the signal pulses is determined. The measurement is triggered once every second. To enhance stability, a moving average filter with a window size of 20 seconds is applied. Before each pulse sequence, the integrated temperature sensor is read out. A linear compensation algorithm corrects the slight temperature-dependent influence on the baseline.

Results

In a laboratory gas measurement setup, the sensor module was exposed to a constant gas flow of 500 sccm per minute with varying CO_2 concentrations in the range from 0 to 5000 ppm.

The gas concentration, as well as air temperature, humidity and pressure, were monitored using reference sensors. Fig. 2 depicts the sensor output of our prototype together with the data of the CO_2-reference sensor (GMP343, Vaisala Oyi).

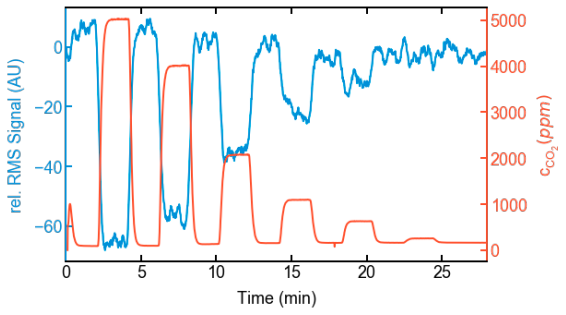

Fig. 2. Averaged RMS signal of our sensor prototype (left) vs. the CO_2 concentration taken from reference sensor (right)

The measurement routine began with a flushing step at zero ppm CO_2 for a duration of two minutes, followed by different concentrations of CO_2 ranging from 5000 ppm to 100 ppm. Each step was held for two minutes and followed by a flushing step with synthetic air for another two minutes.

The sensor sensitivity was determined by evaluating the signal at regions with stable CO_2 concentrations (see Fig. 3).

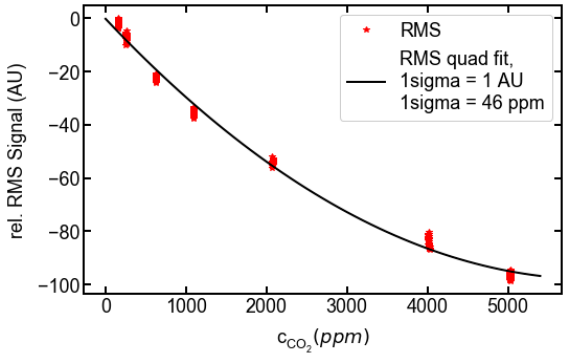

Fig. 3. RMS signal vs. CO_2-concentration for seven different concentrations and quadratic fit curve

Despite the small size of the sensor prototype, we achieve a 3σ-noise level of 138 ppm. The one σ-noise level is 46 ppm. This level of accuracy is appropriate for applications such as the measurement and regulation of indoor air quality.

Acknowledgements

This project received funding from the German Federal Ministry of Education and Research (BMBF) within the research project PASiC under No. 03XP0276A.

References

[1] R. K. Bhagat, M. S. Davies Wykes, S. B. Dalziel, and P. F. Linden, Effects of ventilation on the indoor spread of COVID-19. *Journal of Fluid Mechanics* 903 (2020); doi: 10.1017/jfm.2020.720

[2] M. von Pettenkofer, Über den Luftwechsel in Wohngebäuden (1859); doi: 10.11588/diglit.41379.6

[3] C. Carbonelli, A. Hollenbach, W. Furtner, and D. Tumpold, System Level Simulations of an Open Photo-Acoustic Gas Sensor. Eurosensors 2018, 773 (2018); doi: 10.3390/proceedings2130773

[4] J. Huber, J. Wöllenstein, S. Kolb, A. Dehé, and F. Jost, E6.3 - Miniaturized Photoacoustic CO2 Sensors for Consumer Applications. AMA Conferences 2015, 688–692 (2015); doi: 10.5162/sensor2015/E6.3

DOI 10.5162/SMSI2023/E7.2

Cutout as Augmentation in Constrative Learning for Detecting Burn Marks in Plastic Granules

Muen Jin, Michael Heizmann
Karlsruhe Institute of Technology, Institute of Industrial Information Technology, Hertzstraße 16A, 76187 Karlsruhe, Germany
muen.jin@kit.edu

Summary:
Burn marks in plastic granules are formed during the plastic injection process. The granules with burn marks are not acceptable for use in industrial application and should be filtered out in a sorting process. AI-based anomaly detection approaches are widely used in area of visual-based sorting due to the high accuracy and the low requirement of expert knowledge. In this contribution, we show that using cutout, a simple data augmentation strategy, can improve the accuracy of a contrastive learning-based anomaly detection method. In this work, synthetic image data are used due to the lack of real data.

Keywords: Data Augmentation, Contrastive Learning, Anomaly Detection, Image Synthesis

Background

In the plastic injection process of plastic granules, burn marks caused by either excessive heating or too fast injection speed can be identified as black dots on the surface. In extreme case, the whole granule surface could be burnt. Burn marks are not merely visual defect, moreover, they indicate the degradation of both physical and chemical properties of the corresponding parts compared to the intact parts. Plastic granules with burn marks should be identified and filtered out by a sorting system.

Due to the limited amount of data and the lack of reliable ground truth labels of corresponding data, we modelled the granules by using the rendering software Blender. We modelled multiple granule instances for each rendering to simulate the practical sorting process (Fig. 1a). With the embedded Python interpreter, both the precise location of plastic granules in the rendered image and the ground truth label of each granule are accessible without manual effort. Single plastic granule will then be cropped from the rendered image and be labelled for subsequent processing, e.g., classification and anomaly detection. (Fig. 1b).

In practical sorting process, large amount of nominal plastic granules images can be accessed using methods such as blob detection. Under this assumption, cropped synthetic images of nominal plastic granules can be leveraged to pretrain a neural network in an unsupervised manner using contrastive learning method, as contrastive representation shows state-of-the-art performance on visual recognition tasks [1]. In common contrastive learning settings, data augmentations like color jittering and random crop are applied on images. Neural networks are trained to learn features in image by judging if two augmented images are from same original image.

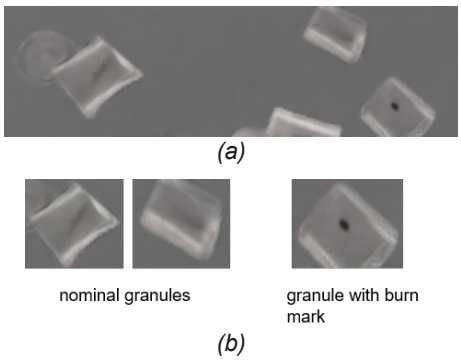

Fig. 1. Rendered image of synthetic plastic granules (a) and examples of automatically labelled crops of single granule for classification (b).

Method

Our work is based on the distribution-augmented contrastive learning for one-class classification [2], while one class classification and anomaly detection are viewed functionally equal in our context. This method builds a two-stage classifier. The first stage is pretrained with nominal data using self-supervised contrastive learning, while the learned representation is used for training a one-class classifier in the second stage. In this method, the intro-

duced distribution augmentation applies rotation as geometric transformations on images. The distribution augmentation is disjoint from data augmentation. By applying data augmentation on original image and on corresponding distribution-augmented image, a negative pair instead of a positive pair for self-supervised learning is generated. The distribution augmentation is proved to make distribution of nominal data in embedding space compacter to better distinguish anomalies. For burn mark detection, we apply cutout [3] instead of rotation as our distribution augmentation. This is inspired by the visual similarity between burn marks and masked-out sections after cutout operation (Fig. 2).

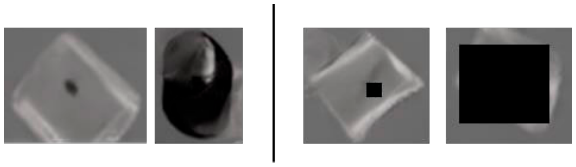

Fig. 2. Granules with burn marks (left) and cutout-augmented nominal granules (right).

In our experiments, a ResNet-18 [4] is used as feature extractor as in [2]. The depth of multilayer perceptron (MLP) head on ResNet-18 for representation learning is reduced to 3. After the self-supervised pretraining, the MLP head is replaced with a kernel density estimation (KDE) model for classifying granules with burn marks. Used data augmentations include crop-and-resize, horizontal flip, random grayscale and random blur. No image augmentation is applied for the training of KDE model. All images are resized to 32×32. Models are trained 200 epochs with momentum (0.9) SGD and a single cycle cosine learning rate decay.

Results

We run experiments 5 times with different random seeds and report the mean and standard deviations of area under the receiver operating characteristic (AUROC). The performance of applying rotation and/or cutout as distribution augmentation method is shown in Table 1. The results indicate that by replacing rotation with cutout, the learned representations of nominal granules and of granules with burn marks are further apart in embedding space and thus increase the accuracy of anomaly detection. Besides, using both augmentations at the same time leads to a worse classification performance.

To explain the improvement by applying cutout for representation learning, we choose the fixed threshold, which corresponds to the highest accuracy at test time, for the trained KDE model and use the model to again classify the test image of nominal granules, but this time applied with cutout. In this case, 66.8% of these images are identified as anomalies. This result implies that the effect of cutout differs from that of rotation as distribution augmentation for contrastive learning, in that the cutout to some degree simulates the burn marks and therefore implicitly enables the learned representation for classification, while applying rotation only makes the representation of nominal images compacter.

Table. 1:Anomaly detection performance (AUROC) on test synthetic data.

Distribution augmentation method	AUROC
None	80.7±1.6
Rotation	86.7±1.2
Cutout	90.7±0.3
Rotation+Cutout	83.3±0.4

Summary

This article shows that cutout is a better choice than rotation as distribution augmentation method in contrastive learning for burn mark detection. In future studies, other defects and corresponding augmentations should be analyzed (e.g., surface blur on granules and local blurring as distribution augmentation). On this basis, a more general analysis of augmentations which generate anomaly-like data and their influence in the self-supervised contrastive learning could be conducted.

References

[1] T. Chen, et.al., A simple framework for contrastive learning of visual representations, *International Conference on Machine Learning. PMLR,* 2020; doi: 10.48550/arXiv.2002.05709

[2] K. Sohn, et al., Learning and evaluating representations for deep one-class classification, *International Conference on Learning Representation (ICLR)* 2021; doi: 10.48550/arXiv.2011.02578

[3] T. DeVries, G. Taylor, Improved Regularization of Convolutional Neural Networks with Cutout, *arXiv preprint;* doi: 10.48550/arXiv.1708.04552

[4] K. He, et.al., Deep residual learning for image recognition, *Proceedings of the IEEE conference on computer vision and pattern recognition*. 2016; doi: 10.1109/CVPR.2016.90

DOI 10.5162/SMSI2023/E7.3

Development of a Chromatic Confocal Sensor Model Dedicated to Investigating Object-Dependent Effects

Dan Linnert[1], Manuel Stavridis[2], Ulrich Neuschaefer-Rube[1]
[1] Physikalisch-Technische Bundesanstalt (PTB), Bundesallee 100 38116 Brunswick, Germany
[2] Physikalisch-Technische Bundesanstalt (PTB), Abbestraße 2-12 10587 Berlin, Germany
Corresponding Author's e-mail address: dan.linnert@ptb.de

Summary:
In optical dimensional metrology object-dependent systematic effects significantly influence measurements and limit traceability. With the aim to describe and if possible correct systematic effects and estimate task-specific measurement uncertainties, PTB developed a virtual instrument that allows to consider the influence of the specimen. Early simulations show such effects.

Keywords: digital twin, chromatic confocal sensor, ray tracing, traceability, optical metrology

Introduction

The benefits of optical metrology are in demand from many different industries. However, optical dimensional and 3D roughness measurements still suffer from limited traceability causing a lack of confidence in their results and therefore preventing an even wider application.

A great challenge is the complexity of the light-matter-interaction. Although the physics accurately describes the scattering of light, it might either be too computationally expensive, or not all constraints regarding the measured surface are known. Additionally, the resulting systematic effects strongly depend on the applied instrument – there are not only fundamental differences among the many measuring principles but even among instruments of the same batch significant differences can occur, e.g., because of small differences in the adjustments of the respective imaging systems.

In order to approach this topic, PTB has initiated the joint research project TracOptic. Characterizing multiple confocal microscopes, coherence scanning interferometers, focus variation microscopes and optical distance sensors regarding workpiece influences, we aim to set up virtual instruments capable to correct or predict systematic effects. Hence, we will be able to use those models to estimate task-specific measurement uncertainties.

In this article we will present our approach to model a commercial chromatic confocal probe (CFP) [1], describe early implementations and show early simulation results.

General Description of the Virtual Instrument

We are using the SimOptDevice-Toolbox [2] which is an in-house development of PTB to model optical experiments to simulate the light propagation based on geometrical optic theory, i.e., ray tracing. It provides us full accessibility to all algorithms and has already proven itself in various other use cases [3].

A software-package dedicated to model all aspects of the measurement system relevant to us had been set up recently. It includes the illumination, scattering at the specimen, the detection as well as algorithms for confocal peak evaluation. Also, the axes of the associated CMM are included although our current research focuses on an accurate simulation of single point measurements assuming an ideal CMM.

We reached a state where we can run and present full simulations of measurements of easy to describe surfaces.

As of right now, a major limitation is that only ideal specular and diffuse (Lambertian) reflection are implemented. However, we can already survey first systematic effects introduced by the measured object while measures to simulate more realistic reflection characteristics are currently being developed by partners in TracOptic.

Simulation Results

We expect that the most significant systematic effects are caused by the instrument's response to surface slope, curvature, and reflection characteristic. Therefore, we ran two simulations in

which we varied slope and curvature, respectively.

Each simulation returns an intensity distribution over a section of wavelengths – the confocal peak. Such peaks are evaluated using dedicated algorithms to return a single wavelength λ_m describing the location of that peak. The following results were achieved applying a center of gravity algorithm using intensity values of 50 % and more relative to the corresponding maximum value.

As a first case we set up a plane specimen and varied its orientation relative to the instrument's optical axis. Fig. 1 shows in case of a specular reflection a peak to valley deviation of approximately 0.8 nm which – depending on the operating distance – translates to a difference of a height measurement of about 800 nm for the modeled sensor. As expected, there is no significant influence of surface tilt when measuring Lambertian surfaces. However, such measurements might suffer from a reduced SNR when measuring higher slopes which is currently not captured by our model. The results for specular reflection show some mild outliers due to higher slopes causing rays to miss the instruments aperture.

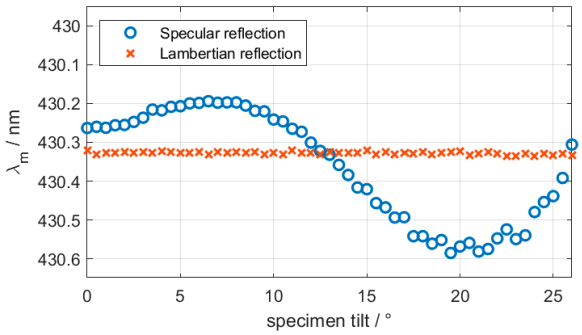

Fig. 1. Simulated focal wavelength λ_m for different surface slopes.

In the second case the measurement of a spherical specimen was simulated (Fig. 2). The radius was varied between 0.1 mm and 1 mm with negative values describing a convex surface and positive values describing a concave surface. The spot-size of the modeled sensor is specified to be 5 µm in diameter. The measured point is located at the pole, so the distance to the sensor remained constant. In addition, the results for a flat sample are represented by an infinite radius of curvature.

Fig. 2 shows a less distinct influence of surface curvature compared to tilt. At least on a macroscopic scale curvature seems to be less significant. However, the results suggest that this effect might cause large errors when smaller radii of curvature are present, e.g., introduced by certain manufacturing techniques or surface defects. The general characteristic matches previous findings regarding self-imaging effect in confocal microscopy [4].

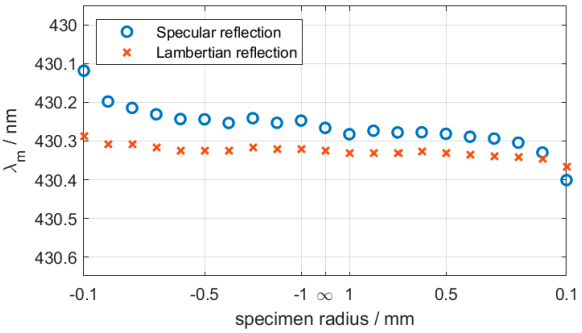

Fig. 2. Simulated focal wavelength λ_m for different surface curvatures.

Summary and Outlook

We have developed a ray-tracing model capable of simulating the measurement process of a CFP. While there is a lot of work to be done, simulations already show that object-dependent measurement errors are significant and need to be addressed to achieve traceable measurements.

Future work will focus on including realistic reflection characteristics, e.g., by introducing BRDF-data (bidirectional reflection distribution function) to our model. Further, we will investigate the influence of diffraction and noise. We will also compare our simulations to measurements in particular to measurements of a specifically designed material standard, we are currently working on.

Acknowledgement

The 20IND07 TracOptic project has received funding from the EMPIR programme co-financed by the Participating States and from the European Union's Horizon 2020 research and innovation programme.

References

[1] M.A. Browne et al., Confocal Surface Profiling Utilizing Chromatic Aberration, Scanning, vol. 14, 145–153 (1992); doi: 10.1002/SCA.4950140304

[2] R: Schachtschneider et al., SimOptDevice: a library for virtual optical experiments, J. Sens. Sens. Syst., vol. 8, no. 1, 105–110 (2019); doi: 10.5194/jsss-8-105-2019

[3] M. Schenker et al., Effects of misalignments on the modulation transferfunction measurement of camera lenses analyzed in optomechanical simulations, Opt. Eng., vol 59, no. 3, 034101 (2020); doi: 10.1117/1.OE.59.3.034101

[4] F. Mauch et al., Improved signal model for confocal sensors accounting for object depending artifacts, Opt. Express, vol. 20, 19936-19945 (2012); doi: 10.1364/OE.20.019936

DOI 10.5162/SMSI2023/E7.4

Magnetic field measurement as an essential part of quality control

Sebastian Rivera[1], Benjamin Wenzel[2], Arvind Mohanr[1]
[1] TK Dr. Kassen GmbH, Beim Eberacker 3, D-35633, Lahnau, s.rivera@itknet.de
[2] Matesy GmbH, Löbstedter Straße 101-103, D-07749, Jena, b.wenzel@matesy.de

Summary:
There is an increasing demand for magnets, driven primarily by the move to electromobility and renewable energy. Magnets are needed for both sensors, such as encoders, as well as for electric motors. Magnetic encoder systems for precision applications depend greatly on the quality of the magnetic scale. While the magnetization process itself is often based on empirical data, the measurement processes and used measurement devices for the magnetic scales and pole rings are selected in a best-practice manner. This paper focuses on the design and development of the 3D magnetic mapper to describe a standardized protocol for measuring and quality control of magnetic scales, pole rings and magnet assemblies for motor applications.

Keywords: Magnets, magnetic field mapping, accuracy, precision, calibration

Introduction

The rise in the popularity of electromobility and renewable energy is resulting in increasing demand of magnets, which are used in both sensors and electric motors.

Magnets in the form of magnetic scales and pole rings, as part of encoder systems, are produced in-house on various levels within the supply chain. In some cases, even the Tier-1 within the B2B supply chain produces the scales. Due to the varied manufacturing processes and the fact that the magnetic measurement processes are based on best-practice methods, the quality control and characterization of magnetic scales and pole rings differs across the entire supply chain. Unifying the needs for more standardized measuring protocols led to the development of the DIN SPEC 91479 standard “Characterization of scales for magnetic length and angle measurement systems”, for which the consortium has just recently started. Both Matesy and ITK are members of the consortium.

Magnetic assemblies for motor applications are of similar focus, however the reason for magnetic measurements differ. It is common practice to perform functional tests with electric motors where magnetic errors of the rotor are likely to be identified. Sensors however are in many cases not tested together with the scale used in the application.

This increase in demand of magnets along with the varied manufacturing processes, is consequently leading to the need of accurate 3D magnetic mapping systems for quality control and characterization of magnetic systems and subassemblies. This paper will describe the design and development of a highly dynamic and accurate 3D magnetic mapper.

3D Magnetic Mapper

3D magnetic mappers (3DMM) serve several applications such as inspection of magnetic components, sub-assemblies and generation of magnetic stray field data used in calibration of finite element models and empirical models. The ever-increasing application of magnets also leads to making the requirements of 3DMM more complex and demanding. To match smaller and more complex magnetic applications, 3DMM must have high spatial resolution, high repeatability and absolute accuracy while maintaining high speed for improved productivity. To ensure high accuracy of the measured magnetic fields, the 3DMM must be designed to have a low stray field affecting the magnetic measurements.

Realization of 3DMM

In cooperation ITK Dr. Kassen GmbH and Matesy GmbH have jointly developed a highly dynamic and accurate 3DMM as seen in Fig 1. The developed 3DMM is based on the PT15 3-axis scanning platform, a high-speed scanning system utilized in the semiconductor and life science sectors, with a resolution in the nanometer range, an absolute accuracy of sub-micrometer

level and a measurement range for any typical industrial motor design. The magnetic sensor is a calibrated Hall linear sensor array (MHLS – Matesy Hall Line Sensor) with 32 3-axis Hall sensors [1]. The sensor pitch is 2.5 mm in the longitudinal axis of the sensor line. Sample rate of the sensor is 200 S/s, the calibrated measurement range reaches between ±800mT within an accuracy of 0.5%.

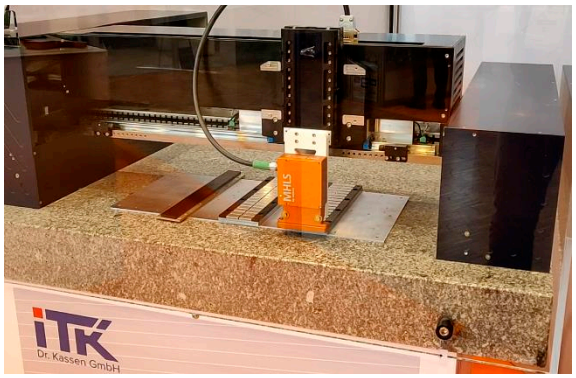

Figure 1: 3DMM

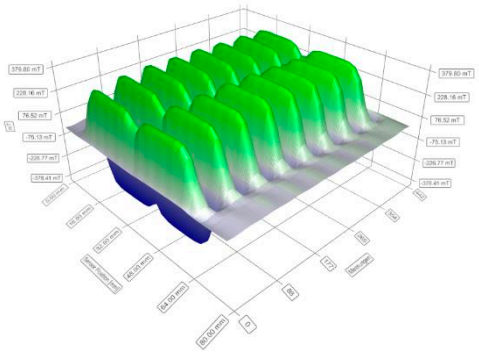

Figure 2: Measurement result magnetic stray field linear stator element

The development of this system consisted of 2 demanding design criteria:

- Optimization of the 3D scanner design to reduce the effect of stray fields of the scanner drive technology while being precise with high dynamic requirements
- Development and calibration of the magnetic sensor to enable fast measurements of the magnetic sub-assemblies

The presentation during SMSI will provide detailed information of stray field measurements in comparison to simulated stray fields. For this FE based simulations were compared to Magpylib, an analytical and therefore extremely fast magnetic simulation software.

Target applications will usually need different sizes and adapted 3DMM needs by each customer. Verification of stray field simulations is therefore the key to easily adapt system configurations.

Design Optimization of the 3DMM

The stray fields of the scanner drive system were simulated and verified against measurements. The sensor used to perform a magnetic mapping within the working of the scanner was a MMC5633NJL (3-axis AMR magnetic sensor) calibrated by Matesy. These stray field effects were taken into consideration and the 3D scanner system was adapted in order to optimize for low stray fields and high accuracy. The linear motors used within the 3DMM were a main point of concern, but experiments and simulation data (as shown in Fig 3 and 4) confirm that no significant influence on the magnetic measurement is given.

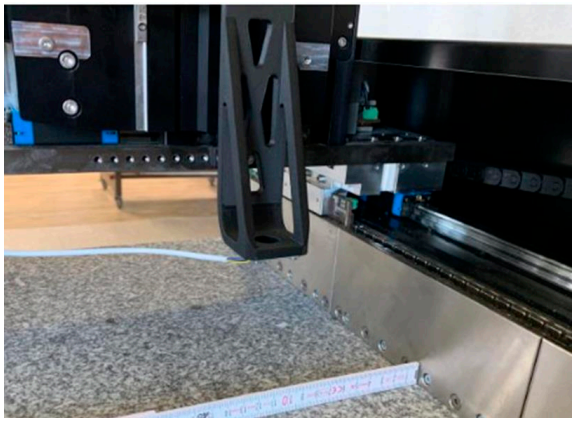

Figure 3: Experimental magnetic measurement

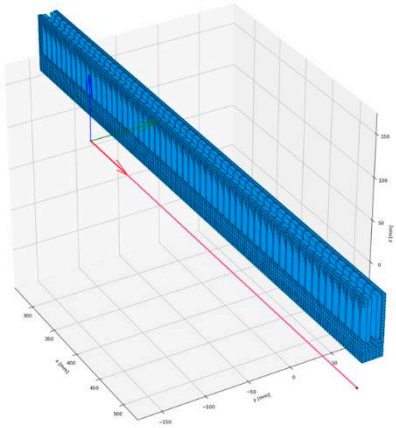

Figure 4: Simulation of linear motor

The magnetic field of the measuring area closest to the linear motor were measured and compared against simulation results. Both magnetic results were similar in trend and the magnitudes were determined to be too small to have a

significant influence on the magnetic measurements (Fig 5 and 6).

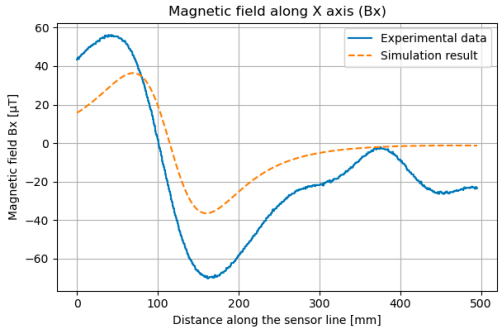

Figure 5: experimental vs. simulated magnetic field along x axis

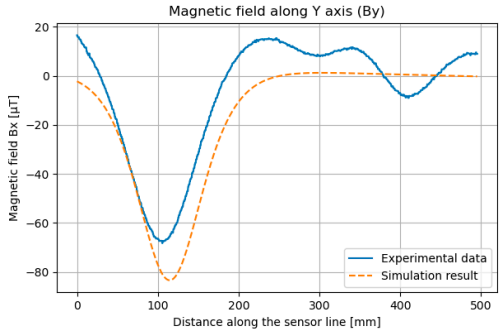

Figure 6:: experimental vs. simulated magnetic field along y axis

Calibration of the magnetic sensor

The Hall Line Sensor was calibrated at Matesy in all 3 directions in space. For this purpose, the system was positioned in a homogeneous area of an electromagnet and the corresponding magnetic fields were approached over the entire measuring range of ± 800 mT. The sensor alignment was previously referenced in a calibrated 3D Helmholtz coil to the reference surfaces on the housing. The correction function is stored directly in the sensor, so the sensor can be used immediately as a magnetometer.

Applications

The application examples of such a 3DMM are:

- Inspection of stator magnet sub-assemblies for linear motors: To avoid expensive replacement of defective magnet segments.
- Characterization of magnetic scales for magnetic linear encoders: Avoid unnecessary production delays that are caused due to late (or no-existent) magnetic field measurements.

By applying techniques such as MOIF (magneto-optical indicator film) in the future, the application of the 3DMM can be extended to gathering both the magnetic characteristics and the microstructure data using the same device.

Results

With the developed 3DMM end of line magnetic mapping has never been so fast and precise. With both partners being in the consortium of DIN SPEC 91479 the 3DMM will consequently be developed to be used as a calibrated measurement tool for and industrial company with magnetic assemblies. From material incoming inspection to sub-assembly testing, the 3DMM provides important data to make magnetic quality assurance more transparent and cost effective.

References

List and number all bibliographical references at the end of the paper. When referenced within the text, enclose the citation number in square brackets, i.e. [1]

[1] M. Schmidt, 100% Quality Control of Permanent Magnets for Industrial Applications, Magnetics Conference 2022, Orlando FL

Poster

DOI 10.5162/SMSI2023/P01

Non-Overlap Image Registration

Stefan Siemens[1], *Markus Kästner*[1], *Eduard Reithmeier*[1]
[1] *Institute of Measurement and Automatic Control, An der Universität 1, 30823 Garbsen, Germany, stefan.siemens@imr.uni-hannover.de*

Summary:
This work aims to predict the relative position of non-overlapping image pairs consisting of a moving and a fixed image. For this purpose, a modified VGG16 convolutional neural network is proposed. The network is trained on a large dataset with microtopographic measurement data of different materials and processing methods. The proposed method shows a high prediction accuracy on the test data and the potential for developing non-overlap registration algorithms.

Keywords: Image Registration, Surface Metrology, Convolutional Neural Networks, Machine Learning, Jigsaw Puzzle Problem

Background

Optical measurement methods are an essential tool in the research and development of technical components. They allow for a fast, accurate, and non-damaging acquisition of the component's micro-topography and its subsequent characterization [1]. Measuring with a high lateral resolution, e. g. being able to resolve small structures, leads to a significant decrease in the field of view and, therefore, the statistical significance of the characterization based on a single measurement. A solution to this problem is given by image registration. It is a widely used tool to find the geometric relation between multiple measurements to unify them into a single coordinate system. Use cases range from consumer tech, like generating panoramic photographs, to metrological use cases. Here they enable capturing surfaces with a high spatial resolution and a large spatial extent simultaneously.

Motivation and Objective

Traditionally, intensity- and feature-based registration algorithms have been used, with the latter still widely used today [2]. However, these traditional approaches are often lacking with today's requirements. In recent years deep learning and convolutional neural networks have achieved impressive results in many disciplines concerning computer vision or audio and text processing. Learning-based approaches have also shown promising results in image registration, where they often outperform traditional methods [3]. However, if the images to be acquired do not have any shared visual content, i.e., if they do not overlap, both classical and learning-based approaches cannot be used [4]. Therefore, this work aims to investigate a method to find the geometric correspondence of an image pair if they do not overlap or even if there is a gap. This problem is simplified by limiting the registration to a classification problem of nine classes, e. g. a center image and its 8-connected neighbors. The problem shows similarities with the jigsaw puzzle problem [5]. However, no inference can be made based on the image's shape. In addition, the images are not directly adjacent to each other but have gaps.

Methods and Data

In order to estimate the relative position of two images, a VGG16 Net with batch normalization is modified and trained in a supervised manner. The VGG Net is a convolutional neural network introduced by Simonyan and Zisserman [6]. The architecture is shown in Fig. 1. The input layer consists of the image pair. It is followed by a feature extractor, e. g. alternating convolutional and pooling layers.

Fig. 1. Architecture of the modified VGG16 Net.

The extractor is followed by a classificator, consisting of three fully connected layers with 25088, 4096, and 9 neurons, respectively. The network outputs the estimated class, e. g. the position of the moving image in relation to the fixed image (the center image). The cross-entropy loss, and the Adam optimizer were used with a batch size of eight. The learning rate was scheduled with an initial value of 0.0001, patience of 5 epochs, and a decay factor of 0.1. Each input pair consist of a moving and a fixed image. The fixed image is always the center image (class

C5), while the moving image is either an image patch from the 8-connected neighbors or the center patch (classes C1-C9). These nine patches are cropped from microtopographic measurements of different surfaces, see Fig. 2.

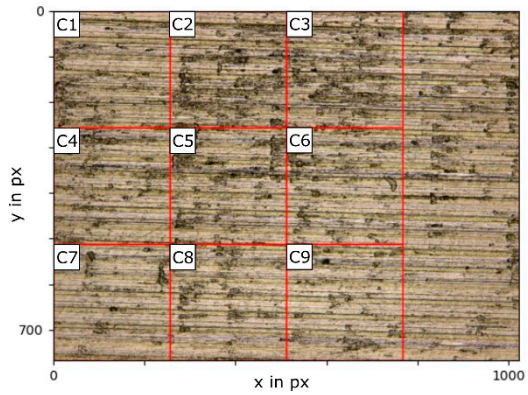

Fig. 2. Cropping of the nine patches from a microscopic image (5x magnification) of a horizontally milled Nickel alloy surface with R_a=6,3 µm and R_z=32 µm.

In total, surfaces with 23 different processing methods were measured. Many processing methods were manufactured with different roughnesses, for example, Ra=0.55 µm, 1.0 µm, 1.6 µm, 3.0 µm, 6.0 µm, and 10 µm for flat ground specimens. Tab. 1 shows five exemplary processing methods from the dataset.

Tab. 1: Examples of materials and processes used in the dataset.

Material	Manufacturing Process
Al_2O_3	Thermal Spraying
Nickel Alloy	Flat lapping
Nickel Alloy	Polishing
Nickel Alloy	Spark erosion
Rubber	Foam

The images were acquired using the two confocal laser scanning microscopes (CLSM) Keyence VK-X210 & Keyence VK-X3000. Objective lenses with 2.5x, 5x, 10x, 20x and 50x magnification were used. The sensors of both microscopes have a resolution of 1024x768 px. Each measurement contains a 2.5D height map, a laser-intensity image, an RGB image, and a combination of the latter two. For this work, combined laser-intensity-RGB images were used. In total, 55.210 measurements were taken. From these measurements, 306.603 patches were cropped and used for training, 101.826 patches for validating, and 102.735 for testing the network. The patches have a size of 256x256 px. From each patch, 240x240 px are randomly cropped, so there is a gap between 0 px and 45 px or 0-18% of the patches' side length.

Results

Fig 3. shows the result after 50 epochs of training. It can be seen that the mean accuracy for the validation set is 97.35% and 96.85 % for the test set, respectively. The highest accuracy was achieved for the center class. This result is in line with the expectation, as there is no movement between the fixed and moving image in this case. The other classes are predicted with an accuracy between 95.48 % and 97.31%.

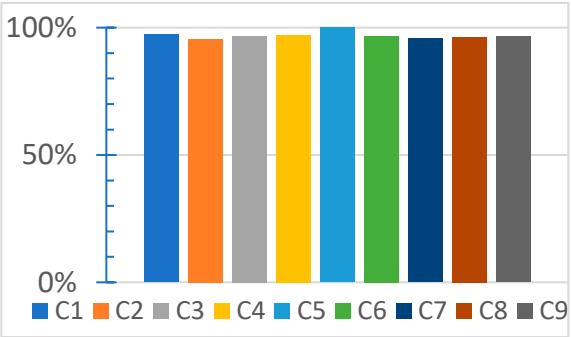

Fig. 3. Percentage of correct predictions on the test dataset for each class.

Conclusion

This work shows that learning-based algorithms can be used to predict the relative position between two images. The predictions have very high accuracy and are robust for many surface types and gaps between the images. The results offer much potential for future work in which, for example, the prediction of homographies for non-overlapping images could be investigated.

References

[1] X. Jiang, et al., Paradigm shifts in surface metrology. Part II, Proceedings of the Royal Society A 463, 2071-2099 (2007); doi: 10.1098/rspa.2007.1873

[2] S. Paul, U.C. Pati, A comprehensive review on remote sensing image registration, International Journal of Remote Sensing 42, 5396-5432 (2021); doi: 10.1080/01431161.2021.1906985

[3] N.J. Tustison et al., Learning image-based spatial transformations via convolutional neural networks: A review, Magnetic Resonance Imaging 64, 142-153 (2019); doi: 10.1016/j.mri.2019.05.037

[4] C. Guérin et al., Detection of comic books twin pages with a non-overlapping stitching method, MANPU 16 (2016); doi: 10.1145/3011549.3011550

[5] S. Markaki, C. Panagiotakis, Jigsaw puzzle solving techniques and applications: a survey, The Visual Computer, (2022); doi: 10.1007/s00371-022-02598-9

[6] K. Simonyan, A. Zisserman, Very Deep Convolutional Networks for Large-Scale Image Recognition, ICLR 2015 (2015); arXiv:1409.1556v6

DOI 10.5162/SMSI2023/P02

Simulation, Manufacturing and Evaluation of a Transformer Eddy-Current Sensor for Deep-Drawing Processes

Sara Kamrani, Rico Ottermann, Folke Dencker, Marc Christopher Wurz
Institute of Micro Production Technology, Leibniz University Hannover, Garbsen, Germany
kamrani@impt.uni-hannover.de

Summary:
This article shows the manufacturing and evaluation of an eddy current sensor based on the transformer principle for monitoring a deep drawing process. First, the optimized parameters of two inductive sensor coils were determined by 2D-finite-element simulation (conductive path width, number of turns, measurement frequency) concerning the resulting output voltage. Then, the sensor was fabricated according to the simulation using thin film technology processes. Finally, the sensor is evaluated and a comparison with the simulation is shown.

Keywords: deep drawing, eddy current sensor, inductive sensor, thin film technology, transformer

Introduction

For monitoring the material flow of the deep-drawing process, the use of eddy current sensors is one of the most suitable choices due to their non-contact measurement method. Two types of eddy current sensors can be used, one consisting of only one coil (parametric principle) and the other consisting of two coils (transformer principle). Recent work already presented a parametric micro planar sensor coil on a stainless-steel substrate using thin film technology [1]. Since the substrate is used to protect the coils by installing the sensor upside down, the sensitivity of the sensor decreases [1]. To improve the induced output signal, the optimized sensor parameters should be determined by means of an electromagnetic simulation. Thereafter, certain modifications of the thin film manufacturing process are required. In this article, a transformer is used, due to its simplification of the measurement and evaluation of the induced voltage compared to the inductance in the parametric principle [2]. Finally, the sensor is evaluated against simulation results.

Simulation-based Design

The 2D models applied for finite-element simulation with the software Ansys Electronics are depicted in Fig. 1. Two opposing planar coils (excitation and measuring coil) with the same outer d_o and inner d_i diameters – for optimal interconnection of the coils while forming the flux – were chosen. z_1 and z_2 are the insulating layers between the substrate and the secondary coil and the secondary and primary coils, which are 25 µm and 10 µm, respectively. z_3 represents the distance between the substrate and the sheet which is 10 mm, due to the anti-wear layer and lubricants used in the deep drawing process. The model depth in z-direction is determined to 55 mm. When a constant current (0.5 A) is applied to the excitation coil (primary coil), the induced voltage is read on the measuring coil (secondary coil) during deep drawing.

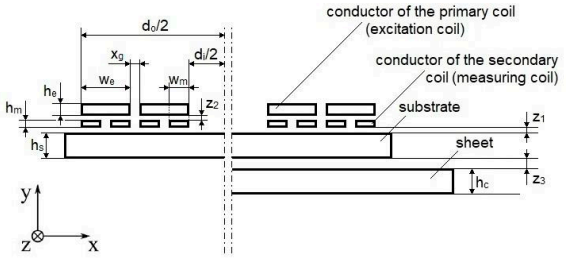

Fig. 1. 2D-illustration of the sensor used for simulation without (left) and with (right) sheet

To conclude the sensor sensitivity, the ratio between U_S and U_0 should be determined, where U_S is the voltage induced on the secondary coil fully covered with the sheet and U_0 is its induced voltage without any sheet. For higher sensor sensitivity, the ratio U_S/U_0 should deviate as much as possible from 1. Therefore, the influencing parameters to maximize the signal are investigated. According to the simulation, an increase in the number of turns of the primary coil leads to an increase in the voltage induced on the secondary coil, while U_S/U_0 remains constant. The number of turns of the secondary coil is kept at 25 (based on previous work [1]). 5 is chosen as the number of turns of the primary coil. Furthermore, if the difference between the outer and inner diameter of the coils is decreased, resulting in a denser ar-

rangement of the conductors, the absolute change of induced voltage is increased [1]. Therefore, the distance between the conductors x_g is reduced to 50 µm to have denser coils with the same number of turns. Lengthening the coils outer diameter d_o increases the absolute change of the induced voltage [1]. However, to measure narrow areas accurately, d_o should be as small as possible without significantly decreasing the sensitivity. Therefore, a compromise should be made. In this case, we decided for more precision and decreased d_o to 15 mm, while d_i is 5.1 mm. Other selected parameters are presented in Table 1.

Tab. 1: Parameters of the optimized transformer sensor based on simulation (see Fig. 1)

Symbol	Value	Symbol	Value
h_e	15 µm	h_c	1 mm
h_m	5 µm	w_e	150 µm
h_s	1 mm	w_m	950 µm

Sensor Fabrication

A 25 µm insulating layer z_1 of photosensitive polyimide LTC 9320 (Fujifilm) is spin-coated onto a 1 mm thick 4” stainless steel (1.4301) wafer. For galvanic deposition of the conductors, a seed layer is sputtered consisting of 50 nm chromium as an adhesion promoter and 200 nm copper. The 5 µm thick copper conductors h_m of the secondary coil are electroplated onto the seed layer using a photomask and the resist AZ® 10xt. Then the 10 µm thick VIAs of the coil are further electroplated. Afterwards, the photomask is removed and the seed layer is eliminated by ion beam etching and the conductors and VIAs are embedded in a 15 µm thick polyimide. Thereafter, all the processes are repeated for the primary coil, where the thickness of the conductors h_e is now 15 µm and therefore the polyimide embedding thickness is 25 µm. The VIAs of the secondary coil are further electroplated in each subsequent step. Finally, conductive connections to 4 VIAs are made by 10 µm thick copper electroplating, and the entire sensor is protected by embedding in a 25 µm thick polyimide layer. The processed sensor has a size of about 65 mm x 15 mm and is shown in Fig. 2.

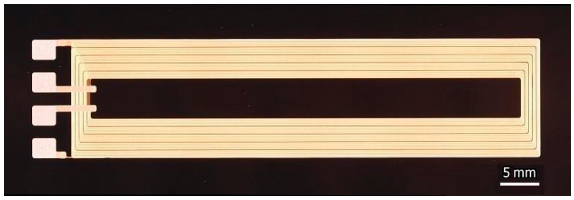

Fig. 2. Top view of the fabricated microsensor in transformer configuration

Measurement Results

To test the manufactured sensor and evaluate its sensitivity, the induced voltage on the secondary coil by applying a current of 0.5 A to the primary coil was measured at different frequencies, once U_0 and once U_S with an austenitic 1 mm thick steel sheet. To compare the measurement results with the simulation results, the ratio U_S/U_0 for simulation and measurement was plotted in Fig. 3. Both graphs are almost parallel and have a maximum sensitivity of 19 % at a frequency of 40 kHz, with the ratio U_S/U_0 showing a lower sensitivity in the experiment. The difference between the results of the simulation and the experiment could be due to the simplified model of the simulation e.g., the missing coil ends.

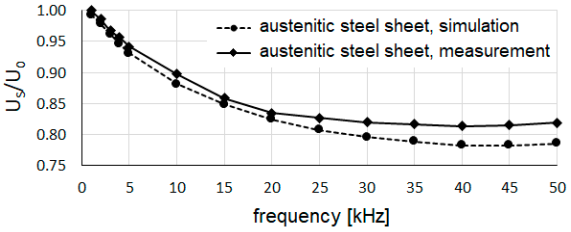

Fig. 3. Comparison of simulated and measured U_S/U_0-curves

Conclusion

An eddy current sensor for monitoring of the deep-drawing process based on the transformer principle was designed and manufactured according to optimized parameters based on 2D-finite-element simulation. The sensor was fabricated using photolithography, electrodeposition of copper and polyimide embedding. It was evaluated for two extreme cases (completely covered with an austenitic steel sheet and a completely free sensor) with different frequencies. The ratio between the induced voltage of the two measured cases showed a maximum sensitivity of 19 % at a frequency of 40 kHz. Furthermore, a comparison between the simulation and measurement results showed a similar course. Further investigations include other sheet materials and sensor protection against wear to use multiple sensors simultaneously in a deep-drawing machine.

References

[1] M. Arndt, F. Dencker and M. C. Wurz, Novel Eddy-Current Sensor for Industrial Deep-Drawing Applications, *IEEE Sensors* (2019); doi: 10.1109/SENSORS43011.2019.8956948

[2] V. Seidemann, S. Buttgenbach, Closely Coupled Micro Coils with Integrated Flux Guidance: Fabrication Technology and Application to Proximity and Magnetoelastic Force Sensors, *IEEE Sensors Journal* 3, 615-621 (2003); doi: 10.1109/JSEN.2003.817172

DOI 10.5162/SMSI2023/P03

Unveiling charge carrier dynamics of GaN-based materials through a combined Cathodoluminescence and Kelvin Probe Force Microscopy under variable illumination protocol

P. González-Izquierdo[1], D. Zoccarato[1], N. Rochat[1], J. Simon[1], P. Le Maitre[1], M. Volpert[1], M. Charles[1] and Ł. Borowik[1]

[1]*Univ. Grenoble Alpes, CEA, Leti, F-38000 Grenoble, France*

*email: palmerina.gonzalezizquierdo@cea.fr

In this study, we developed a method combining cathodoluminescence (CL) and KPFM under variable illumination to study GaN-based materials, by showing two case studies: n.i.d. GaN-on-Si and GaN/InGaN MQW mesa structures. These two techniques were chosen for their complementarity (CL has access to the radiative recombination and KPFM to radiative and non-radiative recombination) and their nanometric spatial resolution (well suited to study dislocations).

Kelvin Probe Force Microscopy (KPFM) is a relatively widespread technique that permits to map the Contact Potential Difference (CPD) between a probing tip and the sample with nanometric resolution. By measuring the CPD in darkness and under illumination, we can map the Surface Photo-Voltage (SPV), defined as the change in the surface potential induced by the reorganization of the photo-generated carriers. The SPV, therefore, can shed light onto the different processes of charge transport, recombination and trapping in the material. The measurement protocol (see Fig. 1) consists on dividing the sample surface to study into a grid of pixels and measure simultaneously the topography (by AFM) and the CPD as a function of the laser power used to illuminate the sample. During the measurement, the laser is turned on, its power is increased linearly until arriving to a plateau of the CPD and, finally, the laser is switched off, measuring until the CPD comes back to the initial state in darkness. This method allows us to follow the SPV during the generation and recombination of charges, giving us information about the charge transfer dynamics on the system rather than a static picture. Furthermore, we performed these measurements at low temperatures in order to see the effect of this parameter on the material's surface potential.
Regarding CL, we developed a protocol to measure the same sample area at different temperatures, in order to obtain an estimation of the internal quantum efficiency (IQE), and different electron beam energies, to probe different depths of the sample.

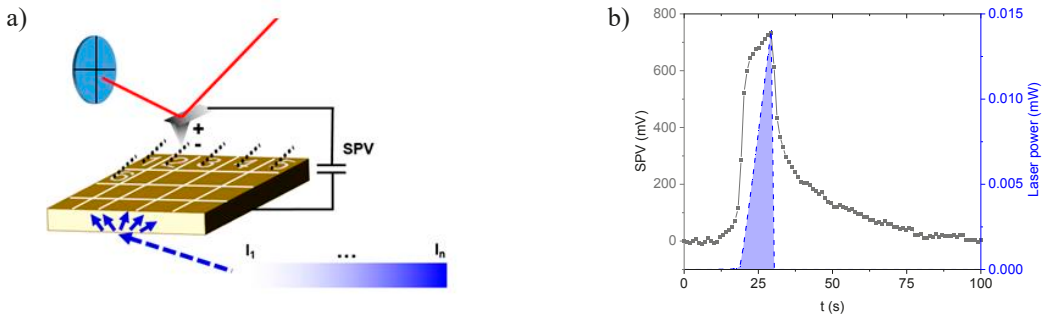

Figure 1: a) Scheme of the KPFM under variable illumination protocol. b) Example of the SPV curve (gray squares) respect to the laser power (blue dashed line) obtained in one pixel of a MQW GaN/InGaN LED illuminated with a laser with 405 nm emission.

For both studied samples, we found a considerably long decay time (around 70 s), compared to the carrier lifetimes reported on bibliography, on the order of ns or ps. These data suggest that the observed slow decay does not correspond to the recombination of carriers but to de-trapping from deep defect energy levels. Regarding this sample, we measured longer time decay constants around dislocation pits (Fig. 2.c), identified by AFM (Fig. 2.a), which indicates more trapping of negative charges on dislocations. This is also in agreement with the lower SPV signal found around pits (Fig. 2.b). Furthermore, the low temperature measurements reveal two different components contributing to the SPV with different sign (Fig. 2.d). We propose a hypothesis for this behavior, attributing the positive contribution to the SPV to the transfer and trapping of holes to surface states due to the upwards surface

band bending, and the negative signal to the trapping of electrons on dislocation-related defect levels. The CL measurements showed less light emission from dislocations. Therefore, from these two techniques combined, we can conclude that the trapping of charges on dislocations decreases the radiative recombination activity.

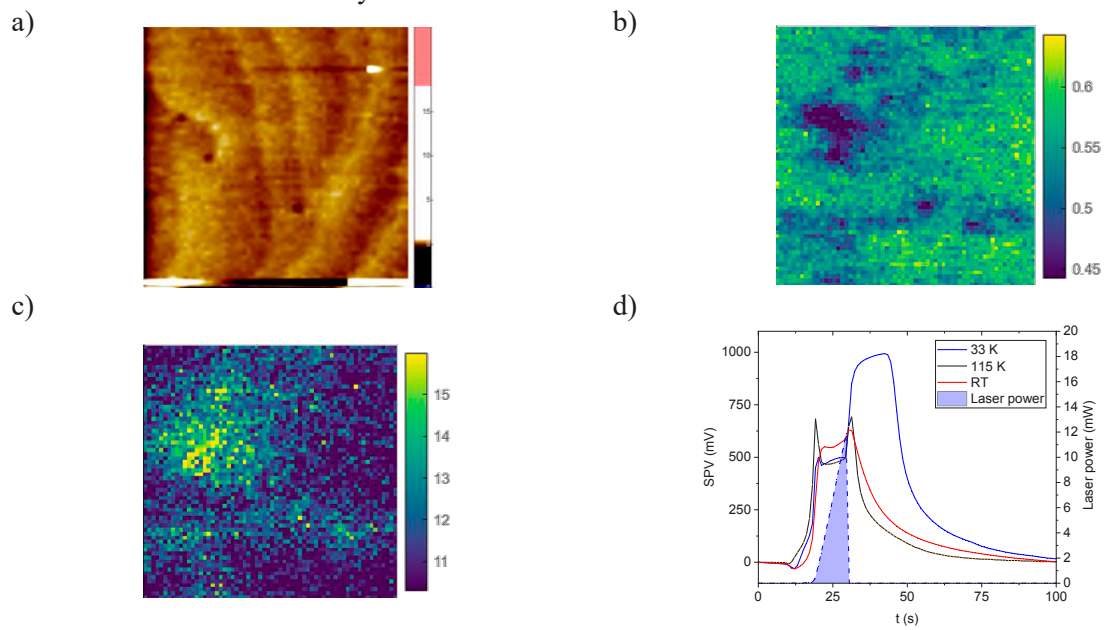

Figure 2: 800 x 800 nm^2, 64 x 64 px^2 image on GaN-on-Si: a) topography (AFM) in nm, b) SPV at maximum illumination in mV, c) time decay constant map from the fit in each pixel in seconds and d) SPV vs. time as a function of laser power at three different temperatures.

With respect to the GaN/InGan MQW mesas, we also observed long decay of the SPV, however, in this case, this decay could be better described by a double exponential, indicating the presence of at least two different dynamics on the de-trapping process with the same sign. By CL, we observed a reduction of the light MQW emitting efficiency on the border of the mesas, known to be a problem for the miniaturization of LEDs. However, no border effect was observed through KPFM, from which we can conclude that the well reported border effect on LEDs is not caused by trapping of charges but by other mechanism.

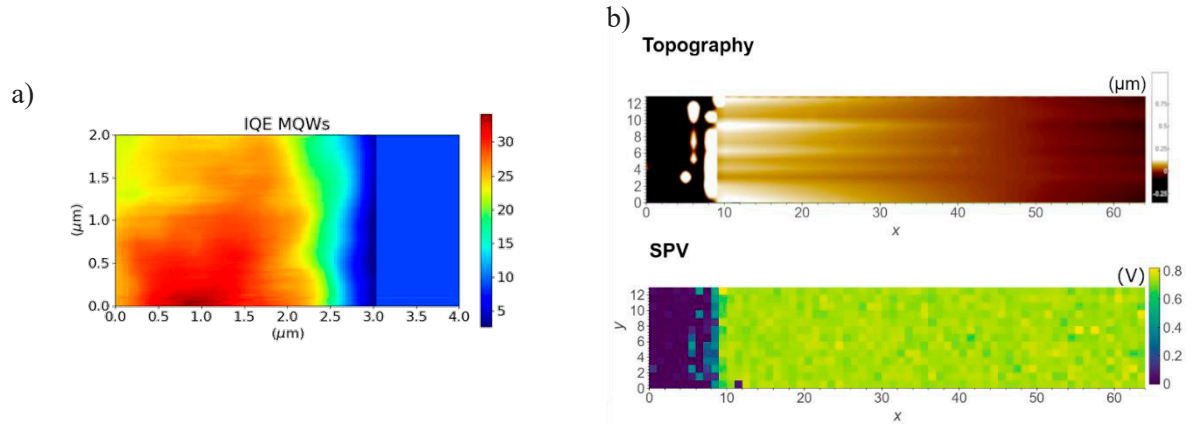

Figure 3: a) Internal quantum efficiency map (obtained from dividing the maps measured at room temperature and low temperature) and b) topography and SPV under maximum illumination maps (4 x 0.8 µm^2, 64 x 13 px^2) on the border of a 1 x 1 mm^2 mesa.

This work, performed on CEA's NanoCharacterization PlatForm (PFNC), was supported by the "Recherches Technologiques de Base" programme, the French Agency for National Research (ANR) via Carnot funding, as well as by PowerElec project, which has received funding from the EMPIR programme.

DOI 10.5162/SMSI2023/P04

Stress Analysis in Drivers Using Wavelet Analysis

Christoph Heidemann[1], Martin Bussas[2]
[1/2] Trout GmbH, Parkstraße 28, 34119 Kassel, Germany
go@trout-gmbh.de

Abstract:

The ability to acquire vital parameters and classify cognitive conditions opens doors to new technologies in diverse areas such as medical technology, automation, aerospace, fitness/wellness and security. For the statistical analysis of the measured ECG data, correlation coefficients and various hypothesis tests were used, which provide information about the correspondence between vital parameters and stress level. Furthermore, the theory of Krawchouk polynomials and the wavelet analysis based on it have been successfully applied.

Keywords: stress level, Baevsky's index, wavelet analysis, Krawchouk polynomials

Introduction

The monitoring and analysis of the stress level of people is used in many areas, such as space travel, autonomous driving and medical technology. Analysing the heart rate variability using an electrocardiogram ECG has proven useful for this purpose. The changes in the duration of cardiac cycles are measured, which guarantee the adaptability of the organism to external factors.

Since the beginning of space history, the widely accepted method to categorize the state of stress has been Baevsky's index. It is also used here to determine stress levels. Furthermore, the theory of Krawchouk polynomials and the wavelet analysis based on it are used.

Fig. 1. Driving Simulator

In the course of the new approach, ECG data sets were collected from a person in a driving simulator (Fig. 1), whereby the demands on the driver increased from test drive to test drive.

Motivation

The analysis of heart rate variability HRV starts at the beginning of space history. When Yuri Gagarin left earth, only breath and ECG were recorded as vital signs transmitted back to the ground control from the astronaut. To get a glimpse of his condition the ECG was examined.

Analysis of HRV during the first space flights have shown that during the launch of the rocket, which is the most stressful phase of the space flight, the HRV dropped significantly. Which means that the heartbeats occurred at equal intervals. In the following period, during orbital flight, the HRV increased again.

Roman Markovich Baevsky is a co-founder of space cardiology and was directly involved in planning and supervising the first human spaceflights in what was then the Soviet Union. The method described here is based on Baevsky's index SI. [1]

$$SI = \frac{AMo}{2\ Mo \times VR}$$

AMo (mode amplitude) is based on the number of RR intervals occurring at the mode. It is divided by the total number of RR intervals (see next chapter, Medical Background).

Mo (mode) denotes the most frequently occurring RR interval value of the measured series.

VR (variation range) describes the range of variation of the measured RR intervals by calculating the difference between the largest and the smallest RR interval.

Medical Background

The heart rate variability describes the changing durations of heart cycles and is used to calculate the stress level. A cardiac cycle is the process from the beginning of one heartbeat to the beginning of the next. This period can be read from the pulse or from the electrical voltages that run through the heart, where the electrical voltages provide a more accurate measurement result.

The impulse for a heartbeat comes from the sinus node. It controls the frequency and intensity of heart beats. The sinus node is in the right atrium of the heart and is made up of muscle tissue and nerves. It sends electrical impulses to the rest of the heart and thus ensures that the muscle contracts and blood flows through the body. The strength of these impulses can be measured on the skin, resulting in an electrocardiogram.

To determine heart rate variability, the intervals between heartbeats are measured and their change is observed. Algorithms calculate these by using the time between two R-waves. This is called the RR interval.

Heart rate and HRV are controlled by the sympathetic and parasympathetic part of the nervous system. These two parts of the autonomic nervous system are predominantly antagonistic to each other. The sympathetic part is activated through external stimuli such as stress. It increases the heart rate by increasing the rate at which the sinus node releases electrical impulses. It also lowers HRV. The parasympathetic part of the nervous system is activated during internal processes such as the working of organs, but also through active exercise in the fresh air and progressive muscle relaxation. It lowers heart rate and increases HRV.

Wavelet Analysis

Similar to spectral analysis, wavelet analysis involves the expansion of functions in terms of a set of base functions.

In this approach, the Krawtchouk functions are used as the set of base functions for the wavelet analysis for the following reasons:

In contrast to Fourier analysis, wavelets are used to expand signals instead of trigonometric functions. They are based on a mother wavelet and are localized in time and space [2].

Krawtchouk functions as wavelets are suitable for denoising signals [3]. Noise is at most a hindrance to analysis of signals.

Krawtchouk polynomials are discrete orthogonal polynomials associated with the binomial distribution. They were introduced by Mikhail Krawtchouk in 1929 [4].

Results

With the help of common methods using correlation coefficients and hypothesis tests, the various indices of a data set, collected with the driving simulator have been examined for correspondence.

Furthermore, the various test drives have been checked for interrelationships.

The different frequencies of the mother wavelet have different degrees of goodness of fit with the signals. The linear connection of these with the SI has successfully been proven.

The highest values of the correlation coefficient between the wavelet analysis and indices are found at the lower frequencies of the Krawtchouk function. VR_D1-1 shows the highest linear correlation to the stress index.

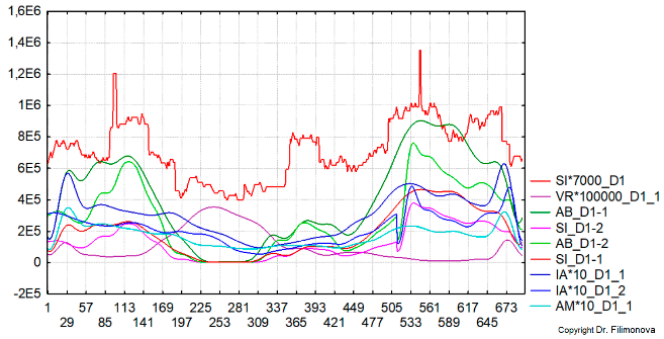

Fig. 2. Stress Level (red) against the wavelets

When looking at the frequencies of the wavelet analysis, we observed that some of them may produce a better model of the stress state than the original stress curve, which is why we are pursuing this approach in a follow-up project.

To do this, we want to collect data as part of test drives in public road traffic.

References

[1] RM Baevsky und AP Berseneva. „Use of kardivar system for determination of the stress level and estimation of the body adaptability“. In: Methodical recommendations. Standards of measurements and physiological interpretation. Moscow-Prague (2008).

[2] Daniel TL Lee und Akio Yamamoto. „Wavelet analysis: theory and applications“. In: Hewlett Packard journal 45 (1994), S. 44

[3] P-T Yap, Raveendran Paramesran und Seng-Huat Ong. „Image analysis by Krawtchouk moments“. In: IEEE Transactions on image processing 12.11 (2003), S. 1367–1377

[4] M Krawchouk. „Sur une généralization des polynomes d'hermite“. In: Comptes Rendus de l'Académie des Sciences 189 (1929), S. 620–622.

DOI 10.5162/SMSI2023/P05

Flood Prediction using High-Precision GNSS

Biswas; Jeet[1], Prof. Dr. Haid; Markus[2], Ehrhard; Jasmin[2], Hennemann, Lukas[2]; Deegener Alexander[2]; Lemke Sebastian[3]; Engelhardt; Stephan[3]
[1,2] University of Applied Science Darmstadt, Schöfferstraße 3, 64295 Darmstadt, Germany
[3] eRay Europa GmbH, Hilpertstraße 31, 64295 Darmstadt, Germany
jeet.biswas@ccass.de

Summary:
Globally, climate change has accelerated extreme weather and floods have become more frequent. The traditional water level measuring stations are old, invasive and have limited capability in terms of telemetry. Because of the unavailability of a proper warning system, the floods have caused numerous deaths. WAMO 300 provides an innovative and non-invasive way of measuring water levels that uses Navigation satellites such as GPS or Galileo to provide real-time warnings to the various stakeholders.

Keywords: GNSS, RTK, Flood, Water level monitoring, Environmental monitoring

FLOOD PREDICTION USING HIGH-PRECISION GNSS

Background, Motivation and Objective

In mid-July 2021, climate change-related flood disasters occurred in Germany, with North Rhine-Westphalia and Rhineland-Palatinate the worst affected. During the night, the rain caused massive flooding, leading to socio-economic impacts, which amount to up to 180 presumed deaths and infrastructure damage in the billions [1].
Despite sufficient warning systems, such as a nationwide system of precipitation radar stations, the disasters occurred due to a lack of measures and equipment in civil protection [1].
WAMO-300-system (Water Monitoring) is the first all-in-one real-time surface water assessment platform that will provide real-time monitoring and timely alerts to the various stakeholders such as water authorities, firefighters and the common people that will help take timely action and reduce losses.

Satellite Navigation System

When satellite constellations are used for positioning or time service, it is called a Navigation satellite system. Based on the coverage, they can be classified as either GNSS (Global navigation satellite system) or RNSS (Regional Navigation Satellite Service) for regional coverage [3].

D-GNSS and RTK

As the signal travels from space, various factors, e.g. ionospheric delay or multipath, might result in errors. To reduce it, various techniques are used, such as WAAS (Wide Area Augmentation System), GBAS (Ground Based Augmentation System), EGNOS (European Geostationary Navigation Overlay Service) or D-GNSS (Differential-GNSS). D-GNSS uses a reference station whose position is fixed and known. So when the satellite signal reaches the base station, it knows the error in calculated pseudo-ranges. It then broadcasts this correction locally, and a receiver station may correct its calculations by this amount.

The accuracy of the resulting range measurement is essentially a function of the ability of the receiver's electronics to accurately process signals from the satellite. To avoid this, RTK (Real Time Kinematic) uses the satellite signal's carrier wave as its signal, ignoring the information contained within.

The base station re-broadcasts the phase of the carrier that it observes, and the mobile units compare their own phase measurements with the one received from the base station. The range of a satellite is essentially calculated by multiplying the carrier wavelength times the number of whole cycles between the satellite and the rover and adding the phase difference. Thus, providing up to centimetre-level accuracy [3].

The WAMO 300 system

WAMO 300 is a self-sustainable movable floating platform with a GNSS receiver connected to it, which allows us to calculate the water level. The usage of the U-Blox C94-M8P RTK-based sensor for water level monitoring is

the innovation point. As soon as the rover receives a correction message, it changes to RTK Float mode. In this state, the accuracy is at the decimeter level. When the Dilution of Precision is below 100, the rover enters RTK Fixed mode. In this state, the accuracy is at the centimeter level.

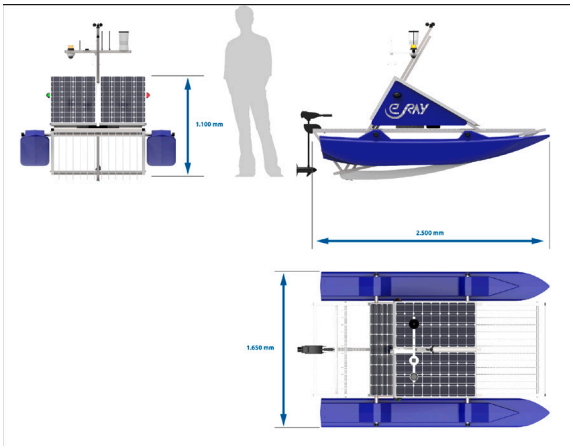

Fig. 1: Different viewpoints of WAMO 300, measurements: 2500 mm x 1650 mm x 1100 mm

The power supply is composed of three 100-120 W solar PV modules that provide power autonomy and have an energy management system with 3.8 - 24 V DC/AC, wired in the marine standard for on-board safety. The communication system offers the options GSM, LTE, LoRa, Wi-Fi, as well as Satellite Communication such as SWARM Technologies Two GNSS receivers with RTK capability are used in base-rover pair to measure water level with centimeter precision (± 2500 mm).

Furthermore, the device allows the integration of other sensors, such as temperature sensors, to record atmospheric and water temperature as well as the internal system temperature. It also measures the parameters of the built-in battery management system (BMS) for safety measures.

The innovative design allows fast integration, flexible installation and easy maintenance.

Experiment Setup and Goal

The tests took place in the Woog lake in Darmstadt, in partnership with the Darmstadt city authority. The experiment's goal was to demonstrate the system's capability in a near-real-life scenario and to demonstrate the availability of the system over a long period. The observations during this period would be used to improve the further functionality of the system.

Observation

Total number of days - 79

Total readings - 107929

Tab. 1: Real Time Kinematic availability rate

RTK Status	Total count	Relative amount of counts [%]
RTK Fixed	92177	85.4
RTK Float	8078	7.5
No RTK	7674	7.1

As can be seen in the table above, The system was in RTK Fixed mode for 85.4% of the time. Further, RTK Float mode availability increases the uptime to 92.9 %. The No RTK mode was observed because of electrical faults in the base station. It can be mitigated by proper electrical installation and thus increasing the availability further.

Prospect

The next step involves developing algorithms to predict floods based on real-time data provided by WAMO.

In the future, the WAMO 300 platform will be further developed. Usage of Dual Band GNSS chips such as C099-F9P may further increase the accuracy of measurements in RTK Float mode or even when there is no RTK message.

The flexibility of the system to accommodate additional sensors further increases the system's potential. WAMO's measurements can be used to establish models for understanding potential changes in water quality and monitoring surface water conditions.

References

[1] Bundeszentrale für politische Bildung; Jahrhunderthochwasser 2021 in Deutschland; 2021; online: https://www.bpb.de/kurz-knapp/hintergrund-aktuell/337277/jahrhunderthochwasser-2021-in-deutschland/

[2] EPA; Climate Impact on Water Utilities; 2022; online: https://www.epa.gov/arc-x/climate-impacts-water-utilities

[3] Dodel, H., Häupler, D.; Die Satelliten-navigation, Springer, Berlin, Heidelberg, 2019; doi: https://doi.org/10.1007/978-3-540-79444-8

DOI 10.5162/SMSI2023/P06

Low Power Wearable sensing system for the Monitoring of Knee Joint Instabilities

Karthika Sheeja Prakash, Vicky Chantal von Einem, Sabari Kannan Muthulagu, Priyank Agarwal, Peter Woias, Laura Maria Comella*
Department of Microsystems Engineering – IMTEK, University of Freiburg, Germany
*karthikasprakash@gmail.com**

Summary:
The anterior cruciate ligament tear causes instability to the knee joint, and it is very common among young adults. The diagnosis in many cases are subjective because it is exclusively based on the physical examination methods of the attending physician. Also, certified instruments exist. However, they are bulky and uncomfortable for the patient. For this reason, a flexible, capacitive sensor has been developed along with the wireless front-end electronic system. Both the stretchable sensor and the flexible board adhere to the leg like a patch, being comfortable to wear and light to carry. The whole sensor unit has been tested with a knee simulator, proving that it is suitable for everyday clinical use.

Keywords: ACL rupture diagnosis, strain gauge, microcontroller, Bluetooth, wearable sensors.

Introduction

Currently, the diagnosis for anterior cruciate ligament (ACL) injury is done using a bulky and uncomfortable system that is difficult to operate [1, 3] and it is operator dependent. A full analysis of the pathological changes due to an ACL rupture requires an accurate measurement system that is reproducible and repeatable [5] and is till today, a challenge. Additionally, the sensing system should be wearable, lightweight, comfortable for the patients to wear and for the doctors to use. To achieve this goal, in this paper we describe (1) a newly developed flexible capacitive strain gauge sensor [4] and 2) An electronic front-end integrating the sensor optimized for this application. The battery powered system acquires data, process it and, send the data wirelessly via Bluetooth to a receiver. The overall system is tested on a knee simulator to analyze its functionality and reliability.

Electronic System Overview

To make the system suitable for clinical use, the device must be (1) light weight and wearable, (2) must allow wireless data transfer, and (3) permit a long battery life. The system overview is shown in Fig. 1:

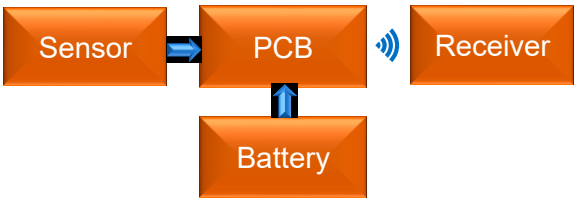

Fig. 1. System Overview.

Capacitive Sensor: Design & Fabrication: The sensor is a stretchable capacitive strain gauge. It consists of a polydimethylsiloxane (PDMS) layer substrate and a carbon black layer obtained by doping PDMS (Neukasil® RTV-23 and RTV-17) with carbon particles (ENSACO® 250 P from TIMCAL Ltd., Bodio, Switzerland). The carbon black layer is laser patterned to obtain an interdigital structure consisting of 279 fingers [4] as shown in Fig. 2:

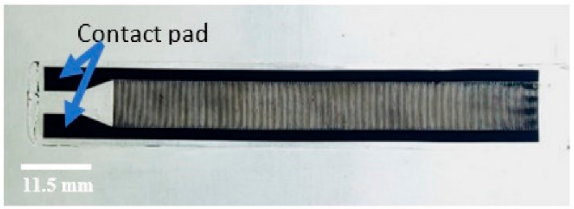

Fig. 2. Capacitive strain gauge sensor. [4]

The sensors obtained are reproducible [4]. The capacitive strain gauge sensor is connected to the electronic board using screws.

PCB: The microcontroller CC2652R1 (Texas Instruments) is chosen for the electronic data acquisition and processing, the properties of which satisfy the system requirements. The microcontroller is powered by a battery. A battery protection circuit is used to prevent over charging. The capacitance is measured using the time to digital (TDC) converter integrated into the CC2652R1. The internal electronics charge the sensor with a constant current of 4.5 µA, while the real-time clock counts the charging time. Hence, the CC2652R1 measures how many clock periods (clock ticks) are necessary to charge the

capacitance. The number of clock ticks is proportional to the capacitance size.

Measurement Setup

The sensor system was tested on the knee simulator developed in [5] to validate the measurement system in a lab environment, which also replicates the knee movements of a person.

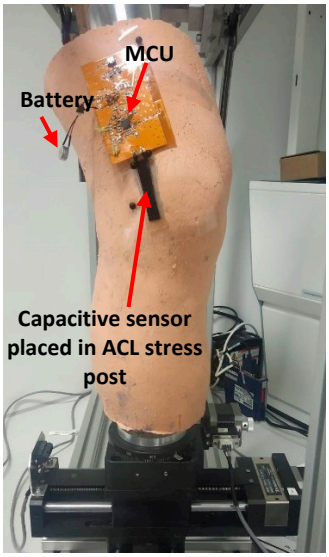

Fig. 3. Knee Simulator Setup

The whole sensor and the electronic are attached to the robotic leg in along the line of the anterolateral ligament [2] as shown in Fig. 3. The knee simulator is rotated from 10° to 45° in-steps of 5° each. The degree of rotation is comparable to the real knee rotation scenario in a clinical setup.

The sensor measurements are taken for 3 cycles of rotation and the results are compared.

Results

The sensor is subjected to 3 cycles of motion. The measurements in each cycle have a good correspondence and are fitted with a second-order polynomial equation. The slight deviation in the curve towards larger angles is due to the disruption of the simulator when rotating. The R-square value of 0.993 is close to 1 which also proves a good correspondence of all the data with the fitting model. The data plots are shown in Fig. 4:

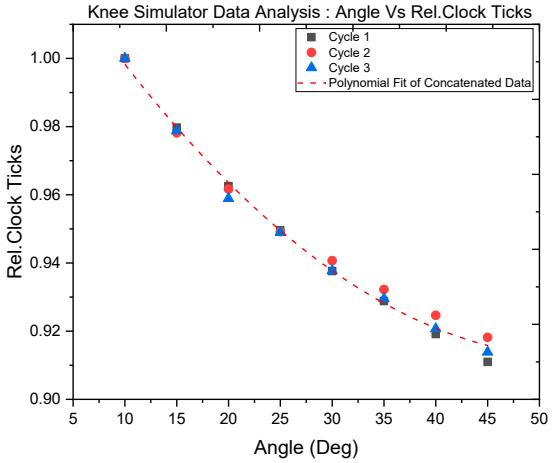

Fig. 4.Knee simulator data analysis.

From the data analysis, the sensor produces a reliable measurement along with the electronics.

The developed system satisfies the requirements of wearability, reproducible and repeatable. Therefore, this validation of data with the knee simulator paves the way towards clinical trials on patients with ligament instabilities.

References

[1] Mattias Ahldén, Kristian Samuelsson, Freddie H Fu, Volker Musahl, and Jón Karlsson. 2013. Rotatory Knee Laxity. *Clinics in Sports Medicine* 32, 1 (Jan. 2013), 37–46. DOI: https://doi.org/10.1016/j.csm.2012.08.005.

[2] Hermann O. Mayr, Anna Hoell, Anke Bernstein, Robert Hube, Claudius Zeiler, Thomas Kalteis, Norbert P. Suedkamp, and Amelie Stoehr. 2011. Validation of a measurement device for instrumented quantification of anterior translation and rotational assessment of the knee. *Arthroscopy: the journal of arthroscopic & related surgery: official publication of the Arthroscopy Association of North America and the International Arthroscopy Association* 27, 8, 1096–1104. DOI: https://doi.org/10.1016/j.arthro.2011.02.034.

[3] Hermann. O. Mayr and A. Stöhr. 2010. *Aktueller Stand der instrumentellen Messung der Knielaxität. Arthroskopie 23(1):56-61*.

[4] Karthika Sheeja Prakash, Hermann O. Mayr, Prachi Agrawal, Priyank Agarwal, Michael Seidenstuecker, Nikolaus Rosenstiel, Peter Woias, and Laura M. Comella. 2022. Batch Fabrication of a Polydimethylsiloxane Based Stretchable Capacitive Strain Gauge Sensor for Orthopedics. *Polymers* 14, 12. DOI: https://doi.org/10.3390/polym14122326.

[5] Martin Zens, Philipp Niemeyer, Anke Bernstein, Matthias J. Feucht, Jan Kühle, Norbert P. Südkamp, Peter Woias, and Herrmann O. Mayr. 2015. Novel approach to dynamic knee laxity measurement using capacitive strain gauges. *Knee Surg Sports Traumatol Arthrosc* 23, 10, 2868–2875. DOI: https://doi.org/10.1109/MeMeA.2014.6860064.

DOI 10.5162/SMSI2023/P07

Development of a Miniaturized Combined DSC and TGA Sensor

Johanna Distler[1], Robin Werner[1], Michael Gerlach[2], Michael Gollner[2], Florian Linseis[2], Jaroslaw Kita[1], Ralf Moos[1]
[1] University of Bayreuth, Department of Functional Materials, 95440 Bayreuth, Germany,
[2] Linseis Thermal Analysis, Vielitzer Straße 43, 95100 Selb, Germany
functional.materials@uni-bayreuth.de

Summary:
A miniaturized sensor with both, differential scanning calorimetry (DSC) and combined thermogravimetric analysis (TGA) functionality is presented. The ceramic sensor with integrated heater features high heating and cooling rates and enables the analysis of aggressive materials. The working principle based on the mass-dependent frequency change of the chip as a vibrating cantilever is described. The analysis of copper sulfate pentahydrate ($CuSO_4 \cdot 5\ H_2O$, an often-used reference substance) proves that DSC and TGA measurements can be carried out simultaneously under real conditions.

Keywords: DSC, Calorimetry, Thermogravimetry, Chip-DSC, LTCC.

Introduction

A differential scanning calorimeter (DSC) measures the difference in heat flow between a sample and a reference during a controlled temperature program. This important thermal analysis method is used to characterize phase changes, glass transitions, decomposition, recrystallisation or chemical reactions. Conventional DSC devices are complex apparatuses with an external furnace, which significantly increases the size and cost of such a device. As an alternative to conventional DSC devices, a miniaturized ceramic DSC chip with integrated heater was developed. The sensor is manufactured in Low Temperature Cofired Ceramics (LTCC) technology and is shown in Fig. 1. The small thermal mass of the sensor allows high heating and cooling rates and an excellent temperature control. In addition, materials can be analyzed that form aggressive gases and would damage or destroy conventional apparatuses. Detailed information about the design, manufacturing and proof of functionality is given in [1-4].

Integrating a Weighing Device

So far, the sample mass, which is required to obtain material parameters such as enthalpies or specific heat capacities, must be determined using an external laboratory balance. By integrating a weighing device directly into the DSC chip, not only the initial sample mass can be measured, but also small mass changes during thermal analysis. This development results in a completely new miniaturized device for thermogravimetric analysis (TGA) and combined simultaneous thermal analysis (STA), which enables more detailed correlation between gravimetric and caloric effects.

First steps of integrating a weighing device into the DSC chip were already described in [5]. On this basis, this contribution presents new and promising results with a combined DSC and TGA sensor.

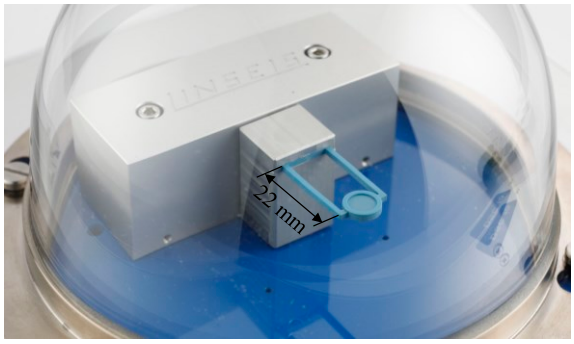

Fig. 1. Miniaturized ceramic differential scanning calorimeter chip.

Working Principle

The setup and working principle of the already existing DSC chip can be obtained from [1-4]. To introduce the functionality of the weighing device some theoretical considerations are briefly described. The working principle is based on the mass-dependent frequency change of a vibrating cantilever. As the sensor vibrates, the resonant frequency of the chip correlates with the mass load.

In the case of a periodic excitation with a continuous sinusoidal force, the chip oscillates at the excitation frequency. As the excitation frequency approaches the resonance frequency, the amplitude of oscillation increases and becomes maximum in the area of resonance. To obtain the resonance frequency, a frequency sweep is performed, and the maximum amplitude is evaluated. After calibrating the sensor, the frequency change can be converted into a mass change.

Measurement Results

Copper sulphate pentahydrate ($CuSO_4 \cdot 5\ H_2O$, an often-used reference substance) loses water of crystallization in three steps when heated [6]. As it shows a defined mass loss in three temperature ranges, dehydration of copper sulphate pentahydrate is measured to characterize the weighing functionality of the sensor chip.

Fig. 2 shows the simultaneously obtained DSC and TGA curves of three chip measurements in comparison with the TGA curve of a conventional TGA device. All measurements were taken at a heating rate of 10 K/min. The DSC curves illustrate the mass loss steps as endothermic peaks in the heat flux. The TGA curves are given as a percentage of the initial sample mass and show good reproducibility of the weighing functionality of the miniaturized chip. In addition, the onset temperatures of the mass loss steps obtained from the simultaneous DSC and TGA measurements agree very well. The comparison with the TGA curve of the conventional device demonstrates a good agreement in the height of the steps and proves the functionality of the mass measurement of the miniaturized DSC-TGA chip. A sensitivity of -1.18 Hz/mg is obtained by comparing with the reference measurement.

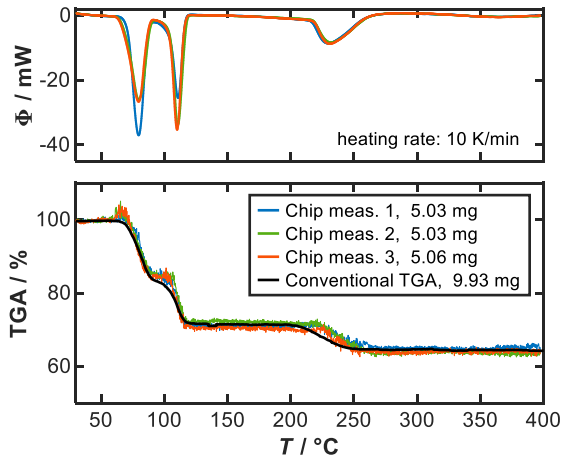

Fig. 2. Analysis of copper sulfate pentahydrate: heat flux measured with the DSC-TGA chip and TGA curve measured with the DSC-TGA chip in comparison with a conventional TGA. All measurements were performed at a heating rate of 10 K/min.

Conclusion

A miniaturized sensor with both, DSC functionality and combined TGA functionality was designed and manufactured. The principle of mass determination by obtaining the change in the resonant frequency of the sensor chip was proven for measurements under real circumstances. The simultaneous DSC and TGA measurements of the dehydration of copper sulphate pentahydrate show promising results and confirm the usability of the new combined chip.

Acknowledgements

The authors would like to thank the Bavarian Research Foundation (Bayerische Forschungsstiftung, BFS) for funding (grant AZ-1346-18).

References

[1] W. Missal, J. Kita, E. Wappler, F. Gora, A. Kipka, T. Bartnitzek, F. Bechtold, D. Schabbel, B. Pawlowski, R. Moos: Miniaturized Ceramic Differential Scanning Calorimeter with Integrated Oven and Crucible in LTCC Technology, *Sensors and Actuators A:* Physical, 172, 21–26 (2011); doi: 10.1016/j.sna.2011.01.025.articles

[2] W. Missal, J. Kita, E. Wappler, F. Bechtold, R. Moos: Calorimetric Sensitivity and Thermal Resolution of a Novel Miniaturized Ceramic DSC Chip in LTCC Technology, *Thermochimica Acta*, 543, 142–149 (2012); doi: 10.1016/j.tca.2012.05.019

[3] J. Kita, W. Missal, E. Wappler, F. Bechtold, R. Moos: Development of a Miniaturized Ceramic Differential Calorimeter Device in LTCC Technology, *Journal of Ceramic Science and Technology*, 4, 137–144 (2013); doi: 10.4416/JCST2013-00008

[4] A. Brandenburg, E. Wappler, J. Kita, R. Moos: Miniaturized ceramic DSC device with strain gauge-based mass detection - First steps to realize a fully integrated DSC/TGA device, *Sensors and Actuators A: Physical*, 241, 145–151 (2016); doi: 10.1016/j.sna.2016.02.011

[5] J. Distler, T. Wöhrl, R. Werner, R. Moos, J. Kita, M. Gerlach, M. Gollner, V. Linseis, F. Linseis: Miniaturized differential scanning calorimeter with integrated mass sensing system: First steps, *Journal of Sensors and Sensor Systems: Special issue: Sensors and Measurement Systems 2022*, under review

[6] L. Cheng, W. Li, Y. Li, Y. Yang, Y. Li, Y. Cheng, D. Song: Thermal analysis and decomposition kinetics of the dehydration of copper sulfate pentahydrate, *Journal of Thermal Analysis and Calorimetry*, 135, 2697-2703 (2019); doi: 10.1007/s10973-018-7595-y

DOI 10.5162/SMSI2023/P08

Detection of the ammonia storage of vanadia-based SCR-catalysts by a radio-frequency method

Thomas Wöhrl[1], Thomas Ritter[2], Gunter Hagen[1], Ralf Moos[1]
[1] Department of Functional Materials, University of Bayreuth, Bayreuth, Germany,
[2] H+H Engineering & Service GmbH, Sonnefeld, Germany
E-Mail: Functional.Materials@uni-bayreuth.de

Summary:
Stricter regulations for nitrogen oxide emissions require an aftertreatment of exhaust gases from biomass combustion plants, such as biogas cogeneration plants. For this reason, SCR systems are used in these applications and their functionality should permanently be monitored during operation to ensure sufficient efficiency at lowest operating costs. The radio-frequency-based state diagnosis of catalytic converters is suitable for this purpose and has already been extensively tested for three-way catalytic converters (TWC) or NO_x storage catalysts (LNT) in the automotive sector.

Keywords: Selective catalytic reduction (SCR), ammonia loading, vanadium-based catalyst (VWT), cavity resonator, radio-frequency

Motivation

After the emissions of nitrogen oxides (NO_x) from vehicles have been increasingly regulated by law in recent years, the exhaust gases from biomass combustion plants, such as pellet heating systems, are now also affected. Therefore, the use of efficient systems for the selective catalytic reduction (SCR) of NO_x becomes more relevant in the future [1].

In the SCR process, ammonia (NH_3), bound in an aqueous urea or NH_3 solution, serves as a reducing agent for the nitrogen oxides, which are converted to nitrogen (N_2) and water (H_2O) on a catalyst. Before the SCR reactions can take place, a previous adsorption of ammonia at the catalyst is essential. For this reason, the catalyst has the property to store a certain amount of ammonia [2].

Therefore, the control of the exhaust gas aftertreatment in many automotive applications is based on the loading status of the catalyst, which is calculated by means of different sensors up- and downstream the catalyst and on the basis of various models [3].

Since biomass combustion systems are usually individual setups, the effort to determine suitable models would be too complex. Accordingly, the direct NH_3 load monitoring of the catalyst by means of radio-frequency technology is a less extensive and complicated alternative compared to the usual techniques.

Methods and Setup

In the radio-frequency-based state diagnosis, the catalyst itself operates as a sensor. For this purpose, the catalyst housing is regarded as a cavity resonator. The catalyst inside of the metallic housing serves as a dielectric material. It changes its complex permittivity due to NH_3 loading [4]. In addition, the housing contains two openings for the installation of two coupling elements (antennas). The schematic structure is shown in Fig. 1.

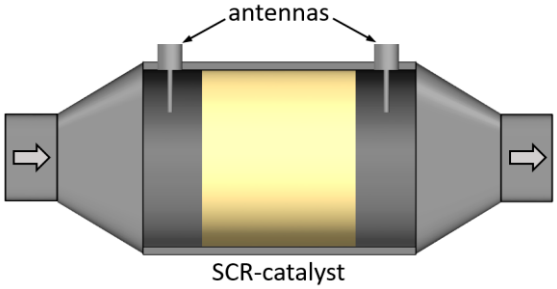

Fig. 1. Schematic design of the catalyst housing as a cavity resonator with built-in antennas

A vector network analyzer is used to couple electromagnetic waves into the catalyst housing via the antennas. Standing electromagnetic waves can be excited at specific frequencies.

The scattering parameters S_{ij}, which represent the reflection and transmission behavior of the catalyst, are used as the measured variable. Depending on the NH_3 loading of the catalyst, its radio-frequency properties change, which results in a shift in the resonance frequency f_{res} and a change in the quality factor Q [5].

Results and Discussion

The following measurements were carried out with a vanadia-tungsten-titanium-based catalyst (VWT; catalyst with 1.7 wt% V_2O_5) at a mixing unit for synthetic exhaust gases (5 % O_2, 5 % H_2O in N_2), while the catalyst was heated to an operating temperature of approx. 400 °C. Meanwhile, the SCR catalyst was loaded with 300 ppm ammonia in the exhaust gas at constant flow rate and unloaded as soon as the maximum was reached. The following investigations refer to the transmission factor S_{21}.

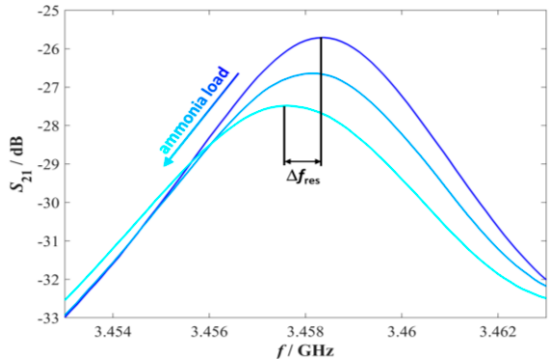

Fig. 2. Scattering parameter S_{21} as a function of frequency for different ammonia loadings of the catalyst at 400 °C

Fig. 2 shows the curves of three transmission spectra at different loading states of the catalyst. The loading of the catalyst with ammonia leads to changes in the electrical properties, including the permeability ε_r and the conductivity σ, which in turn influence the radio-frequency behavior [6]. The measured signal shows a decrease of the resonance frequency f_{res} with increasing ammonia loading.

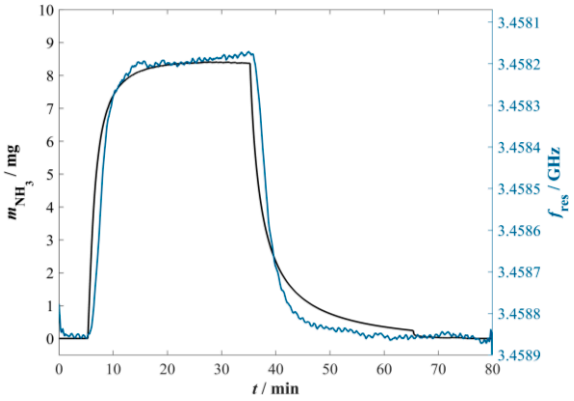

Fig. 3. Comparison of the calculated mass loading m_{NH3} of the catalyst with the measured resonance frequency f_{res} at 400 °C

Using the ammonia concentration up- and downstream of the catalyst determined by an FTIR spectrometer, the amount of stored ammonia can be calculated from the difference and compared with the resonance frequency determined from Fig. 2.

The results (see Fig. 3) show that the two measured values correlate. During loading at the beginning of the measurement, a clear drop in the resonance frequency can be observed (inverted axis) and reaches an almost constant value as soon as the catalyst is fully loaded. After unloading, the resonant frequency returns to its initial value.

Summary and Outlook

It is possible to determine the ammonia loading of catalysts directly by evaluating the resonance frequency of a cavity resonator with a built-in SCR catalyst. The functionality of this simple system was tested primarily during measurements at a gas mixing unit.

Future measurements will be carried out on a real SCR system for the exhaust gas aftertreatment of a biogas cogeneration plant. Here, it is important to investigate further information on the cross-sensitivities of this system.

References

[1] S. Ozgen, S. Cernushi, S. Caserini, An overview of nitrogen oxides emissions from biomass combustion for domestic heat production, *Renewable and Sustainable Energy Reviews 135,* 1 – 9 (2021); doi: 10.1016/j.rser.2020.110113

[2] I. Nova, E. Tronconi, *Urea-SCR Technology for deNOx After Treatment of Diesel Exhausts*, 10 – 26 (2014); doi: 10.1007/978-1-4899-8071-7

[3] T.V. Johnson, Review of diesel emissions and control, *Internal Journal of Engine Research 10*, 275 – 285 (2009); doi: 10.1243/14680874JER04009

[4] R. Moos, Microwave-Based Catalyst State Diagnosis - State of the Art and Future Perspectives, *SAE International Journal of Engines 8*, 1240 – 1245 (2015); doi: 10.4271/2015-01-1042

[5] R. Moos, G. Beulertz, S. Reiß, G. Hagen, G. Fischerauer, M. Votsmeier, J. Gieshoff, Overview: Status of the Microwave-Based Automotive Catalyst State Diagnosis, *Topics in Catalysis 56*, 358 – 364 (2013); doi: 10.1007/s11244-013-9980-x

[6] M. Dietrich, C. Steiner, G. Hagen, R. Moos, Radio-Frequency-Based Urea Dosing Control for Diesel Engines with Ammonia SCR catalysts, *SAE International Journal of Engines 10*, 1638 – 1645 (2017); doi: 10.4271/2017-01-0945

Acknowledgement

Special thanks to the Federal Ministry for Economic Affairs and Climate Change and Project Management Jülich for the funding of the project (FKZ: 03EI5435B), as well as to the DBFZ, H+H Engineering & Service and CPK Automotive for the good cooperation.

DOI 10.5162/SMSI2023/P09

Characterization and Modeling of Thermal MEMS for Selective Determination of Gas Properties

Philipp Raimann[1], *Frank Hedrich*[1], *Sophie Billat*[1], *Alfons Dehé*[1,2]
[1] *Hahn-Schickard, 78052 Villingen-Schwenningen, Germany,*
[2] *Department of Microsystems Engineering, University of Freiburg, 79110 Freiburg, Germany*
Philipp.Raimann@Hahn-Schickard.de

Summary:
This work presents the characterization and modeling of thermal MEMS for the determination of gas properties. The sensor consists of thermopiles arranged on a membrane, which allow the determination of the gas property-dependent temperature response of an electrically excited heating element. Experimental data are used to demonstrate the applicability of a lumped-model for the modeling of a thermoelectric gas property sensor. The calculated sensor's sensitivity for small quantities of hydrogen in nitrogen is about 0.7mV per % H_2 at a heating power of 6 mW.

Keywords: MEMS, Thermal gas sensor, Thermal modeling, Lock-in amplifier techniques, Gas analysis.

Background and Motivation

Measurements of gas properties are becoming increasingly important in industrial and environmental applications to clarify process-related and safety-relevant issues [1]. Here, thermal MEMS have decisive advantages over other measurement principles due to low-cost manufacturing, non-consumable operation, wide measurement range, fast response times and low power consumption. Often thermal conductivity sensors with thin metal wires made of platinum [2] or tungsten [3] are used, which also act as detector elements. However, in order to distinguish specific gases or unknown components in gas mixtures, an independent determination of further gas properties is necessary. For example, the thermal conductivity of argon is only 7% higher than that of carbon dioxide, while the volumetric heat capacity of argon is about half that of carbon dioxide (see Tab. 1).

Tab. 1: Thermal conductivity k (mW m^{-1} K^{-1}) and volumetric heat capacity cv (kJ m^{-3} K^{-1}) of different gases at 293 K and 1 bar [4].

Gas	Ar	CO_2	N_2	He	H_2
k	17,50	16,25	25,47	153,5	183,4
cv	0,855	1,536	1,197	0,852	1,181

In this paper, the thermal response ΔT of a heater structure with different gases is analyzed using an equivalent model and the applicability of the model for the optimization of future thermal gas property sensors is demonstrated.

Description of the System

The direct heat transfer of a polysilicon heater to the surrounding gas is measured with polysilicon/aluminum thermopiles with their hot junctions located close to the heater (see Fig. 1). In contrast to the measurement of the temperature-dependent heater resistance R, this approach allows higher sensitivity in addition to galvanic isolation.

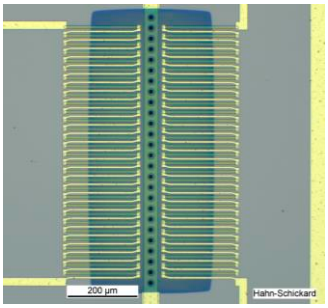

Fig. 1. MEMS thermal gas property sensor.

For detection of gas properties, the perforated heater is periodically excited with an electrical voltage U and the resulting response signal of the thermocouples U_{TP} is measured with a lock-in amplifier.

Lumped-Element-Model

An equivalent circuit composed of discrete components [2] describes the temperature response ΔT of the heater caused by Joule heating (see Fig. 2).The thermal equivalent parameters are of the form (1) and (2) and depend on the characteristic length L_i, the cross-sectional

area A_i, the volume V_i and the thermal properties k_i and cv_i.

$$R_{th,i} = L_i / (k_i \bullet A_i) \quad (1)$$

$$C_{th,i} = cv_i \bullet V_i \quad (2)$$

These formulas apply to the parasitic heat transfer through thin film structures (e.g. membrane, heater) and to the surrounding gas.

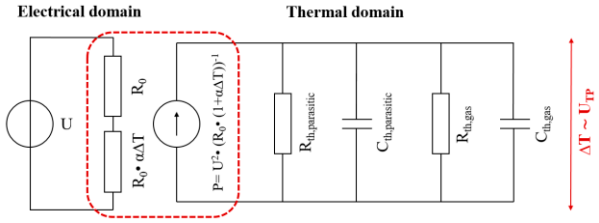

Fig. 2. Lumped model of the thermoelectric sensor.

Results and Outlook

Since a low excitation power P is chosen, the effect of the heater's temperature coefficient of resistance (TCR) is neglected. Thus, the measured thermopile signal is proportional to the thermal impedance of the system (see Fig. 3). Fitting the obtained signals to the RC-low pass model yield the respective fit parameters X_1 and X_2, which are proportional to the thermal impedances R_{th} (K/W) and C_{th} (J/K), respectively.

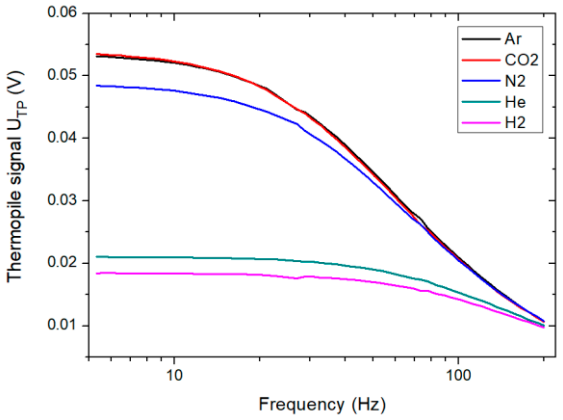

Fig. 3. Single-sided thermopile signal measured for different gases. This signal is fitted with the model function U_{TP}= ((1/X1)^2+(2•π•f•X2)^2)^-0.5 to derive the thermal equivalent parameters X_1 and X_2.

The resulting fit parameters can be described in both cases as a function of the gas properties using the formulas (1) and (2). Figure 4 shows that X_1 decreases with increasing thermal conductivity of the gas. The highest sensitivity is achieved at low thermal conductivities (e.g. small amounts of H_2 in N_2). Figure 5 depicts the linear dependence of X_2 with volumetric heat capacity. Since the volumetric heat capacity depends on the density, X_2 varies with pressure. X_1, on the other hand, is unaffected by pressure in a first approximation.

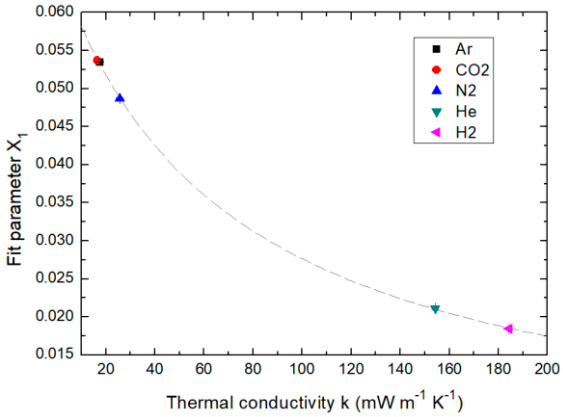

Fig. 4. Dependency of the fit parameter X_1 on the thermal conductivity of the surrounding gas.

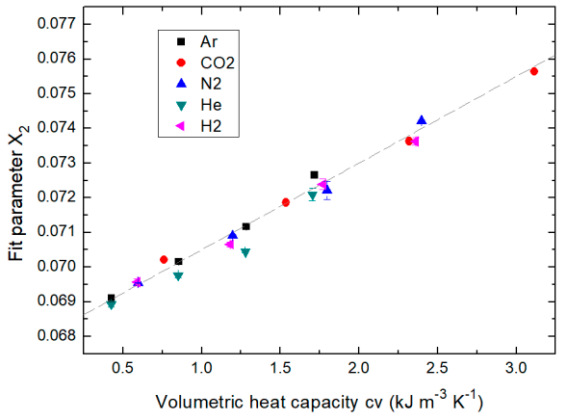

Fig. 5. Dependency of the fit parameter X_2 on the volumetric heat capacity of the surrounding gas. For additional changes of the volumetric heat capacity, pressure variations are used.

Based on this knowledge, miniaturized gas property sensors with a high selectivity towards individual properties are to be developed and combined with thermal flow sensors to address novel applications in the field of hydrogen technologies, smart grid, domotics or medicine.

References

[1] M.I.A. Asri et al., MEMS Gas Sensors: A Review, *IEEE Sensors Journal* 21, 18381-18397 (2021); doi: 10.1109/JSEN.2021.3091854

[2] A. Lofti, M. Navaei, P.J. Hesketh, A Platinum Cantilever-Based Thermal Conductivity Detector for Ammonia Sensing Using the 3-Omega Technique, ECS Journal of Solid State Science and Technology 8, Q126 (2019); doi: 10.1149/2.0231906jss

[3] D. Berndt et al., A Robust Miniaturized Gas Sensor for H_2 and CO_2 Detection Based on the 3w Method, *Sensors* 22, 485 (2022); doi: 10.3390/s22020485

[4] E.W. Lemmon et al., NIST Standard Reference Database 23: Reference Fluid Thermodynamic and Transport Properties-REFPROP, Version 10.0, National Institute of Standards and Technology, Standard Reference Data Program, Gaithersburg (2018)

DOI 10.5162/SMSI2023/P10

Solder Joint Examination and Characterization by using the 3ω-Method

Ralf E. Bernhardsgrütter[1], Yannick Barb[1], Julia Schläpfer[1], Rainer Schädler[1], Christoph Hepp[1]
[1] Innovative Sensor Technology IST AG, Ebnat-Kappel, Switzerland
ralf.bernhardsgruetter@ist-ag.com

Summary:
Solder joint quality strongly depends on the size and number of voids and cracks in it. The check of the quality of these solder joints (e.g. X-ray or photomicrography) is often complex and time-consuming. This paper presents a new approach to examine the solder joint quality of soldered platinum elements by using the 3ω-method. The results show high reliability and are compared to results of photomicrographs and thermal contact measurements using constant temperature anemometry. The presented method enables an automated 100 % validation to increase the solder joint quality.

Keywords: solder joint examination, 3ω-method, platinum thin film technology, thermal contact, thermal sensor

Motivation and Background

Soldering of sensor elements on the area of interest is a crucial assembly and packaging technology in many fields, e.g., for temperature sensors, thermal flow sensors and others. For such applications the quality of the soldering joint is critical. Today, the screening of soldering joints is often done by optical techniques, e.g., X-ray or photomicrography [1, 2]. Such techniques are time-consuming and depend partially on the subjective validation of the operator.

An automated, purely electrical validation is preferred. The validation criteria of such a method are operator independent. The presented validation is based on the 3ω-method and is applicable for resistive elements having a defined and finite temperature coefficient of resistance (TCR).

Method

The claims of this paper are: (1) The 3ω-method can be used to validate the solder joint of a resistive element having a defined and finite TCR. It is shown for a thermal sensor element based on platinum thin film technology. (2) The method is purely electrical, and no operator validation is needed. (3) The method can be used to compare different joining techniques.

The 3ω-method is a well-known method to measure thermal properties of solids, liquids, and gases [3,4]. It is based on a metallic resistive structure with a defined TCR. The resistor is driven by an AC-current with the frequency ω which heats it up due to Joule heating. The resulting temperature oscillation has an AC-component with the frequency 2ω which acts as a thermal wave. The propagation of this wave depends on the thermal properties of the resistor's surrounding. Due the resistor's TCR, the resistor is also modulated with the frequency 2ω. Therefore, the voltage across the resistor contains an AC-component with the frequency 3ω which is the signal of interest.

Due to different thermal properties of the solder layer including voids or cracks, the quality of the soldering joint can be characterized by the 3ω-method.

Experiment and Results

The solder joint validation using the 3ω-method is investigated by using a thermal sensor (see figure 1). The sensor is based on a platinum thin film element which soldered on a stainless-steel surface. The resistor is designed as a 50 Ω at 0 °C resistance with a temperature-to-resistance coefficient of 3850 ppm/K.

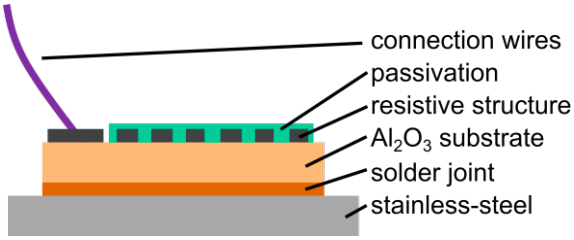

Fig. 1: Sensor cross section: Platinum thin film element on a Al_2O_3 substrate. The resistor has a resistance of 50 Ohm at 0 °C with a temperature-to-resistance coefficient of 3850 ppm/K.

The setup for the 3ω-method is based on a digital lock-in amplifier. The drive frequency was set to 1 Hz and the current amplitude to 50 mA for the presented results. In addition to the electronical measurements, photomicrography and heat transfer measurements using constant temperature anemometry (CTA) act as reference validation techniques.

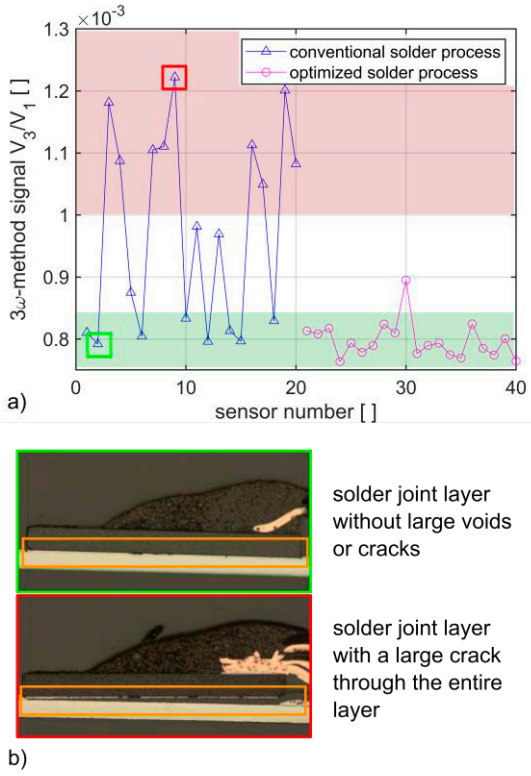

Fig. 2.: Comparison between the signal of the 3ω-method and optical inspection using photomicrography. a) The signal of the 3ω-method of 20 sensors. A signal of around 0.8x10^{-3} (green background) indicates solder joints without large voids and cracks. Signals larger than 1.0x10^{-3} (red background) indicates solder joints with large voids and cracks. b) Examples of solder joint with no large voids and cracks (green frame) and with large voids and cracks (red frame).

In a first step, the signals of 40 solder joints are investigated by the 3ω-method and by photomicrography. Figure 2 shows its result. One could show that the signal of the 3ω-method can be correlated with findings in the photomicrograph of the corresponding solder joints. The lower the signal of the 3ω-method, the less voids and cracks are observed in the photomicrograph. Theoretical considerations confirm this finding. The better solder joint is, the higher the thermal contact to the area of interest. Therefore, the heat wave of the 3ω-method can better propagate through the solder joint meaning that the heat is less confined, and the corresponding signal is lower. The signals around 0.8x10^{-3} correspond to be the lowest signal for this sensor structure and indicates a proper solder joint.

In a second step, the solder joints of 70 sensors are tested by investigating the thermal contact using the 3ω-method and CTA as a reference. Both methods are independent of the operator. Therefore, a purely objective comparison is possible. The CTA is done by using a water flow below the stainless-steel layer with a velocity of 0.26 m/s. Furthermore, the temperature difference between the element and the ambient temperature is set to 8 K. The 3ω-method signal as a function of the signal of CTA is shown in figure 3. The signal of the 3ω-method correlates with the CTA power. This correlation can be approximated by a linear behavior.

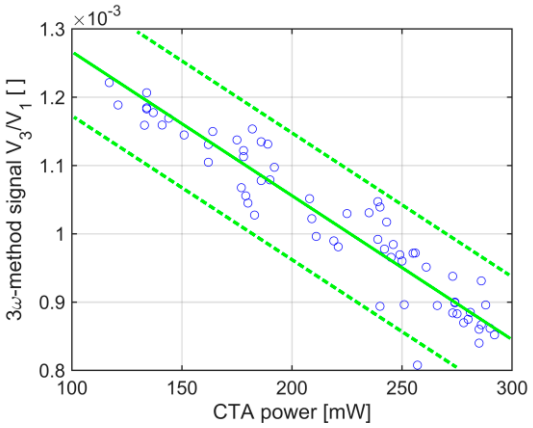

Fig. 3: Comparison between the signal of the 3ω-method and the heat transfer measurement. A linear correlation between the signal of these two methods can be seen.

This experiment verifies that the 3ω-method is an excellent method to characterize the quality of solder joint. Especially for higher volume serial products this method is interesting. Such an electronical test enables an automated 100 % validation. Furthermore, no complex measurement setup or time-consuming sample preparation are needed. In fact, this method can also support the optimization of new solder process because of its simplicity (see figure 2).

References

[1] Y. K. Ry and H. S. Cho, New optical measuring system for solder joint inspection, *Optics and Lasers in Engineering* 26 (6), 487-514 (1997); doi: 10.1016/0143-8166(95)00118-2

[2] L. Su, et al., Defect inspection of flip chip solder joints based on non-destructive methods: A review, *Microelectronics Reliability* 110, 113657 (2020); doi: 10.1016/j.microrel.2020.113657

[3] D. G. Cahill, Thermal conductivity measurement from 30 to 750 K: the 3ω method, *Rev. Sci. Instrum.* 61, 802-808 (1990); doi: 10.1063/1.1141498

[4] R.E. Bernhardsgrütter et. al., Towards a robust thin film sensor for distinguishing fluids using the 3ω-method, *Sens. Actuators A: Phys* 321, 112419 (2021); doi: 10.1016/j.sna.2020.112419

DOI 10.5162/SMSI2023/P11

Indirect Measurement Method Using Reconfigurable Non-intrusive Sensors for Integrated Sensory Electronics

Qummar Zaman[1], Senan Alraho[1], Andreas König[1]
[1]Lehrstuhl Kognitive Integrierte Sensorsysteme (KISE), TU Kaiserslautern Deutschland,
aube@eit.uni-kl.de

Summary:
This paper presents a new approach for indirect measurement methods (IMs) by using reconfigurable non-intrusive sensors (NS) for the infield optimization of the reconfigurable integrated circuit with self-x properties. The typical IMs approach of using the regression model for the device under test (DUT) performance prediction is integrated with a metaheuristic optimization algorithm for the reconfigurable non-intrusive sensors. The novelty of this work comes from running the optimization algorithm on the NS by copying the same tuning knobs of the DUT, which allows for indirectly optimizing the DUT performance without interrupting its operation. Additionally, the infield optimization will be based on low-cost measurement of the embedded sensors. The achieved correlation performance metrics for the regression task is 90.13%. The DUT circuit is designed using XFAB 0.35 µm technology.

Keywords: Indirect measurements, Non-intrusive sensors, Infield optimization, Self-x properties, Metaheuristic optimization algorithm, Reconfigurable integrated circuit.

Background, Motivation and Objective

The integration of machine learning (ML) and artificial intelligence (AI) with other emerging technologies, such as cyber-physical systems and edge computing, is initiating the most profound transformation in the industrial domain known as industry 4.0 [1,2]. The smart sensory electronics systems (SSES) perform the essential part of the data generation in this domain. However, the performance of SSES is normally deviated with time [3]. To tackle the aging and process variations effects, analog ICs are commonly overdesigned, leading to more power and or larger chip area. Nevertheless, with the introduction of ML and AI, the reconfigurable hardware structure of the SSES enables the self-X (self-healing, self-calibration, self-learning, etc.) properties [4][5]. In order to support self-X properties, the analog ICs is designed with controllable tuning knobs and performance evaluation set-up [6] for chip performance monitoring. The primary objective of this work is to replace and reduce the number of real expensive chip measurements with a simple and cost-effective indirect performance evaluation method (RIMs) for SSE

Description of the Proposed Methodology

The block diagram of the proposed methodology is shown in Fig. 1. The reconfigurable non-intrusive sensors (NS) are integrated in close proximity to the main design under test (DUT) to face the same operating conditions imposed on the DUT, that is, PVT variations (process, voltage, temperature). In this work, the reconfigurability is introduced in the NS for the first time and the whole optimization is performed by utilizing the tuning knobs of NS rather than tuning knobs of the DUT with the help of the pre-trained regression model (RM). A wide tunable range low pass filter (LPF) is used to present this concept. The DUT and NS share similar TK values to reduce the search space complexity and ease the ML regression task. This feature also allows the online performance optimization of the DUT without interrupting its operation.

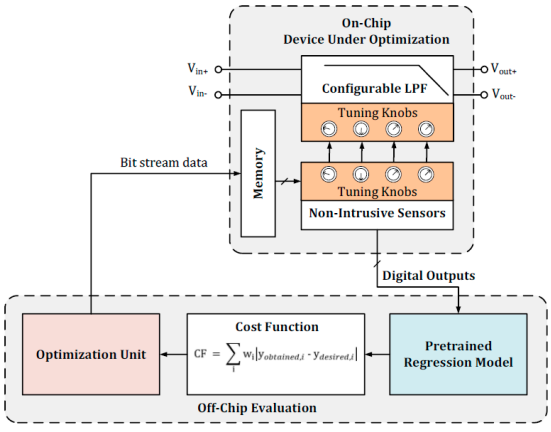

Fig. 1. Block diagram of the proposed IMs method.

The TK values are copied to the main DUT after the completion of the optimization process. Random forest regressor (RFR) is used to create an accurate regression model between the

NS outputs, TK, and DUT performance. The RFR helps to simplify the estimation of the DUT performance indirectly based on the low-cost measurement of the quasi-digital output frequency of the NS. The flow diagram of the proposed approach is depicted in Fig. 2.

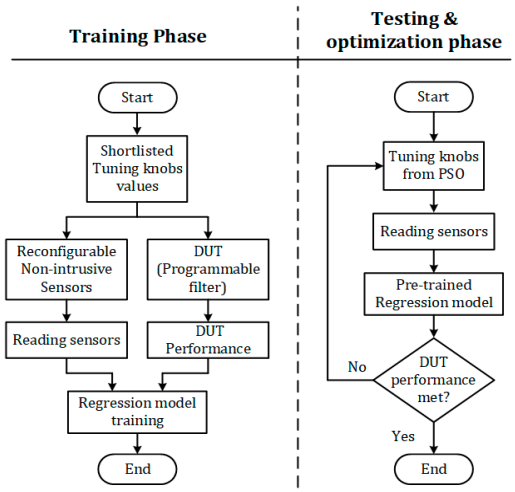

Fig. 2. Flow chart of the proposed IMs approach

First, different TK values are shortlisted for the training phase from the optimization search space to minimize the training data set and evaluation time. In the next step, the output of the NS and performance of the DUT are simulated and subjected to similar PVT conditions. 80% of data set are randomly used for the training of the RFR while the residual 20% are selected to assess its performance. During the testing phase, the particle swarm optimizer (PSO) determines the TK values which will be applied to the NS. The output response of the NS is provided as input to the pre-trained RFR along with the current TK values to indirectly predict the DUT performance. Based on the output response of the RFR the PSO decides the respective TK values for the next iteration.

Results

For this experiment, a fully differential fourth-order tunable continuous-time active low pass filter based on the Sallen–Key structure with Butterworth approximation is used as a test vehicle [7]. The digitized MOS resistor is used as a TK of the filter to determine the cutoff frequency. We used a total of 1000 estimators with mean squared error as a criterion for the RFR. The performance of the RFR is graphically illustrated Fig. 3. The adjusted R squared value (ARS) of the RFR is 90.13%. The details about the metaheuristic parameters of the PSO can be found in our previous work [8]. This experiment is performed using 10 particles and 100 iterations. The experiment is repeated five different times, and the averaged optimization results are summarized in Table 1. The maximum estimation error of the optimization result is roughly 9% for the 1 kHz but can be minimized by increasing the training data set around this region. Our institute already submitted the chip prototyping for fabrication to prove the concept practically with real measurements.

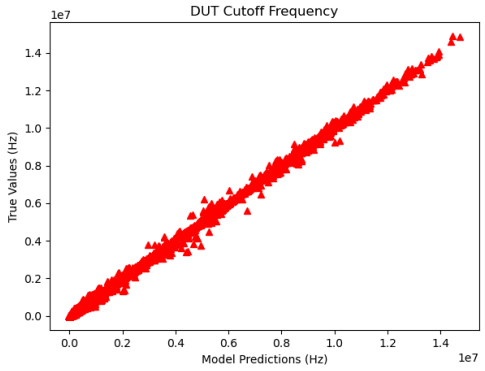

Fig. 3. Scatter plot of the predicted and true values.

Tab. 1. Optimization results of the DUT.

DUT Characteristic	Targetted	Achieved
3 dB cutt off frequency	5 MHz	4.95 MHz
	1 MHz	1.03 MHz
	100 kHz	94.37 kHz
	10 kHz	9.56 kHz
	1 kHz	1.09 kHz

References

[1] Kagermann, Henning. "Recommendations for implementing the strategic initiative INDUSTRIE 4.0." (2013).

[2] Diez-Olivan, A., Del Ser, J., Galar, D., & Sierra, B. (2019). Data fusion and machine learning for industrial prognosis: Trends and perspectives towards Industry 4.0. Information Fusion, 50.

[3] Lee, S., Shi, C., Wang, J., Sanabria, A., Osman, H., Hu, J., & Sánchez-Sinencio, E. (2018). A built-in self-test and in situ analog circuit optimization platform. IEEE TCAS-I.

[4] König, Andreas. "Integrated sensor electronics with self-x capabilities for advanced sensory systems as a baseline for industry 4.0." Sensors and Measuring Systems; 19th ITG/GMA-Symposium. VDE, 2018.

[5] "Self-learning AI smart sensor: BHI260AP", 2022 (accessed 2022). URL https://www.bosch-sensortec.com/products/smart-sensors/bhi260ap/

[6] Andraud, Martin, Haralampos-G. Stratigopoulos, and Emmanuel Simeu. "One-shot non-intrusive calibration against process variations for analog/RF circuits." IEEE TCAS-I (2016).

[7] Alraho, Senan, Qummar Zaman, Hamam Abd, and Andreas König. "Integrated Sensor Electronic Front-Ends with Self-X Capabilities." Chips 1, no. 2 (2022): 83-120.

[8] Zaman, Qummar, Senan Alraho, and Andreas König. "Efficient transient testing procedure using a novel experience replay particle swarm optimizer for THD-based robust design and optimization of self-X sensory electronics in industry 4.0." Journal of Sensors and Sensor Systems 10, no. 2 (2021): 193-206.

DOI 10.5162/SMSI2023/P13

SI Traceable Non-Laboratory Humidity Measurements – How to Minimize Measurement Uncertainty

Hannu Sairanen, Vuokko Lantz
Vaisala Oyj, Vanha Nurmijärventie 21, Finland
hannu.sairanen@vaisala.com

Summary:
SI traceability forms a baseline for high quality measurements. In case of humidity measurements, the traceability is usually established through temperature and dew point temperature calibrations. However, when the measurements are taken out from laboratories, new uncertainty sources are introduced. Naturally, environments, both process and ambient, are not as stable as in a laboratory, stabilization times are minimized, and it is not always possible to carry the best instrument for the specific measurement to the field. In this work, these topics are discussed and potential solutions introduced.

Keywords: SI traceability, measurement uncertainty, humidity, capacitive humidity sensor

Introduction

In industry, humidity measurements are typically carried out to optimize processes, to improve energy efficiency and to improve end-product quality. Thus, they cover wide range of applications from extremely dry applications to extremely humid, from cold to hot, up to high pressure and from clean to dirty environments. Therefore, laboratory calibrations may not be presentative and other uncertainty sources should be taken into account. For example, outdoor humidity measurements are always carried out in chancing temperature: slope is usually slower when night turns into day but more rapid when bright day turns into thunder. This problem of non-static environments has already been recognized by humidity metrology community [1].

Primary measurand of a capacitive humidity sensor is typically relative humidity [e.g. 2]. Also, temperature is normally measured to enable humidity conversions from one unit to another. However, if the probe around the humidity sensor is large, it may have a heat flux ruining temperature representativity and thus ruining humidity measurement. Also, heavier probes have longer stabilization times especially in terms of temperature.

In practice the additional uncertainty sources of a field humidity measurement instrument can put in the following categories:

- Short-term uncertainty sources
- Long-term uncertainty sources
- High humidity or condensate

Short-term uncertainty sources include e.g. long stabilization times i.e. temperature changes during humidity measurement (see Fig. 1) or long thermal stabilization of massive probes [3]. This is often a problem in field when the measurement needs to be completed as quickly as possible without long enough stabilization time.

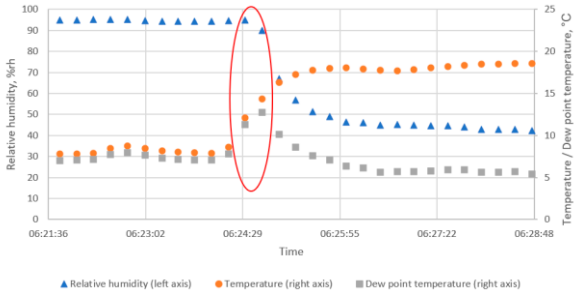

Fig. 1. An example measurement with Vaisala's HMP9 humidity probe. The probe reacts to increasing temperature, although humidity sensor has not yet reacted. Thus, the calculated dew point temperature increases for few data points although in this test the dew point temperature should be almost constant.

Long-term uncertainty sources include e.g. bad representativity of the humidity probe. This could be caused by significant temperature gradient over the probe. Hence, the measured temperature and thus relative humidity do not represent the targeted environment. More severe problem would be if the probe measures process humidity at higher dew point temperature than the ambient temperature. In those cases, condensation may take place at the sensor causing sensor failure or significant drift. Similarly, drift can be caused by exposing the sensor on harmful chemicals.

Third category includes exposure of a humidity sensor to high humidity or even condensate. Some capacitive humidity sensors never recover after high humidity exposure and liquid water on a sensor is even worse. In these cases, it is hard or even impossible to know when and how much the probe has drifted without calibration.

Short-term uncertainties

Stability related uncertainties are usually caused by non-ideal instrumentation. Naturally, service personnel cannot bring all kind of instruments on site and therefore measurements are completed with the instruments on hand. This is especially a problem when high accuracy is a requirement. In general, smaller thermal mass probes are faster and thus reaches stability faster. If a larger probe is not thermally stabilized it can easily add from 2 %rh to 5 %rh error to the indicated value [3]. Also filtering of data might be useful, although that would increase response time, which is typically unwanted in field measurements.

If a probe is thermally controlled, the probe overreacts significantly less. In Fig. 2 Vaisala's HMP7 was tested in a heat chamber without humidity control when temperature is increased from 20 °C to 30 °C. The result clearly indicates that the dew-point temperature drop in the beginning is significantly less when the probe is thermally controlled.

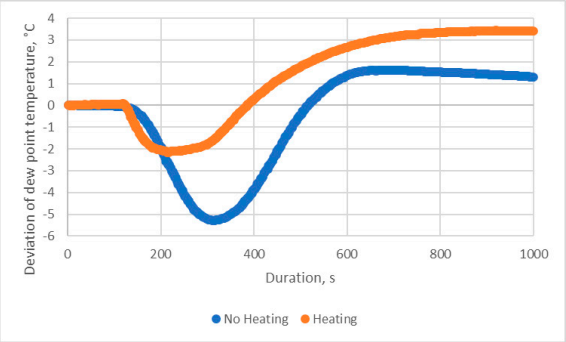

Fig. 2. Vaisala's HMP7 dew-point temperature response to temperature change from 20 °C to 30 °C. During the test dew-point temperature was not controlled resulting difference to the ends of measurements.

However, one thing that must be considered on field is that the probes used have to be robust enough. Otherwise, there might be some sort of mechanical failure which can rise as a small and not obvious drift.

Long-term uncertainties

In a third-party humidity laboratory Vaisala's HMP9 was tested in a non-standard way. Before each measurement point purge function was performed and the hysteresis was almost completely removed (see Table 1). Vaisala designed the purge function initially to prevent humidity sensor drifting due to chemicals.

Table 1: Drift and repeatability of Vaisala's HMP9 with active purge usage resulting 0.0 %rh error in repeatability and 0.1 %rh error in hysteresis.

Relative humidity, %rh	10	50	90	50	10	50
Error, %rh		0.0		0.1		0.0

Back in the old days climatic chambers used psychrometric wicks and temperature sensors for humidity measurements. The problem with the capacitive humidity sensors was poor tolerance of high humidity exposure. This is still the problem with many sensor types and manufacturers, but significant development steps have been taken by manufacturers.

Recovery from condensate

Especially humidity sensors that measures outdoor weather are exposed to wide range and significant variations of humidity and temperature conditions. One way to tackle this issue is to build a shield or cover on the probe. However, there is still chance that condensation occurs. In addition of this external protection, some manufacturers have introduced protective warming systems. This way the maximum relative humidity the sensors are exposed is reduced and the sensors measures rather dew point temperature than relative humidity.

Conclusions

As pointed out in [3], transient conditions may increase measurement inaccuracy significantly. Thus, it is important to understand requirements for the specific measurement and to specify the need to the instrument supplier.

Vaisala's solution is to offer handheld instruments with wide range of probe types and features for different environments and applications to enable quick, repeatable, and reliable measurements.

References

[1] EURAMET, "Publishable Summary for 14IND11 HIT Metrology for humidity at high temperatures and transient conditions," The European Association of National Metrology Institutes, http://www.euramet.org, 2018

[2] Vaisala, "Vaisala HUMICAP® Technology," https://www.vaisala.com/en/vaisala-humicapr-technology

[3] H. Sairanen, Errors in Relative Humidity Measurements Due to Slow Temperature Response, SMSI 2020-Sensors and Instrumentation (2020); doi: 10.5162/SMSI2020/P1.10

DOI 10.5162/SMSI2023/P14

Ongoing MEMS-based FAIMS-Research for VOC-Detection

Alexander Graf[1], Nils Funke[2], Olaf R. Hild[1]
[1] Fraunhofer Institute for Photonic Microsystems IPMS, Maria-Reiche-Str. 2, 01109 Dresden, Germany
[2] Fraunhofer Center Microelectronic and Optical Systems for Biomedicine, Herman-Hollerith-Str. 3, 99099 Erfurt, Germany
alexander.graf@ipms.fraunhofer.de

Summary:
Subject of the development is a miniaturized chip-based device that uses ion mobility spectrometry (IMS) for detecting low concentrated volatile organic compounds e. g. in environmental sensing. Focus from preceding development was the fabrication process of the IMS chip with field asymmetric ion mobility (FAIMS) as ion filter. The required electronics were combined with the IMS chip and a demonstrator system has been developed. The measured spectra of exemplary ketones (acetone, 2-hexanone) show typical behavior. This proof of function enables ongoing development towards specific applications.

Keywords: ion mobility spectrometry, volatile organic compounds, miniaturized, MEMS, chip device

Introduction

A wide range of applications in environmental sensing makes use of the detection of volatile organic compounds (VOCs). VOCs are harmful even in low ppb concentrations. This results in an urgent need for portable devices at the point of interest. VOCs can also be used for diagnosis of diseases. It is known that infections have an impact on the VOC footprint of breath gas, urine, blood and saliva. A fast and easy-to-use point of care device for diagnosis or monitoring would open up a large market. Low concentrated analyte gases, varying conditions and interfering substances result in a demanding development of an easy-to-use system. The current development focuses on a miniaturized sensor element that enables a selective detection of common ketones.

FAIMS-Chip as Miniaturized IMS

Ion mobility spectrometry (IMS) is an established method to detect gaseous analytes like VOCs under ambient conditions [1]. Therefore, IMS allows an easy integration into a measurement system. Ionized molecules are filtered according to their specific ion mobility K. This value depends on the ion mass, collision cross section and background gas. The ion trajectories and hence the filtering is done using electric fields in which the ions move with the drift velocity v_D

$$v_D = K\,E. \qquad (1)$$

With regard to a miniaturized sensor component that can be manufactured by means of microtechnologies, common time of flight ion filters are unsuitable. In contrast, field asymmetric ion mobility (FAIMS) shows a good downscaling. High electrical field strengths are used, which have an impact on cluster and collision processes and hence the ion mobility K(E) itself. In addition, special shaped signals are applied to the filter with high field and low field conditions. Thus, the ions move on specific ion trajectories and only ions with an appropriate K(E)-behavior pass the ion filter and reach the ion detector. An additional compensation voltage CV changes the filter parameters and enables other ions to reach the detector. A CV sweep leads to a single spectrum with peaks that represents one kind of ion. An additional sweep of the maximum field strength E_{Filter} lead to FAIMS typical spectra. The CV shift of the peak maximum is characteristic for the ion [1].

Demonstrator System and Measurements

The developed demonstrator uses a miniaturized IMS Chip with FAIMS ion filter, that is already described in [2] and [3], and also comprises necessary electronic components. This new system according to Fig. 1 allows measurements of spectra and hence the proof of function of the IMS chip. An UV discharge lamp was used for atmospheric pressure photoionization (APPI).

Exemplary measurements according to Fig. 2 show the expected and typical FAIMS spectra, namely a decrease of peak intensity with increasing field strength E_{Filter} and changes in the location of the peak maxima on the compensation voltage axis. Differences of these two peak

properties can be observed in the spectra for acetone and 2-hexanone.

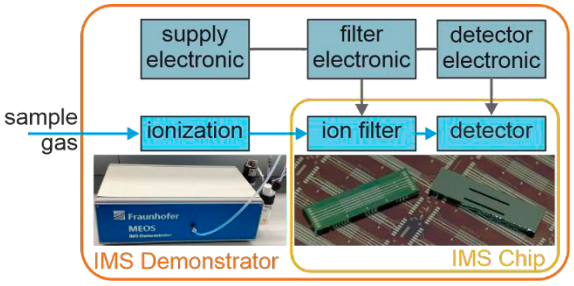

Fig. 1. Schematic overview of the developed IMS demonstrator with IMS chip that includes ion filter and detector, ionization source and basic electronic components

The CV shift of acetone firstly becomes positive, then negative for increasing dispersion voltages. For 2-hexanone the measurements show a negative shift of the CV. The observed trends agree with results from literature [4]. However, the absolute CV displacement is lower than expected.

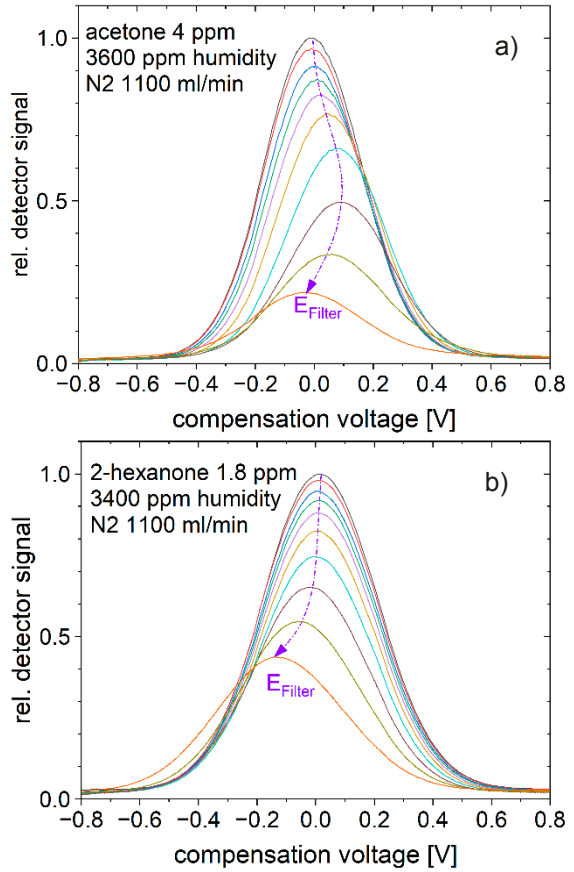

Fig. 2. Typical FAIMS spectra with a) positive CV shift and b) negative CV shift of the peak position with increasing filter field strength E_{Filter}.

According to [5], high humidity and atmospheric pressure chemical ionization (APCI) lead to water clusters $H^+(H_2O)_m$ that are not related to the analyte molecule. FAIMS spectra show a pronounced displacement towards positive CV due to strong clustering effect. Measurements with the given setup and APPI show the same effect. (Fig. 3)

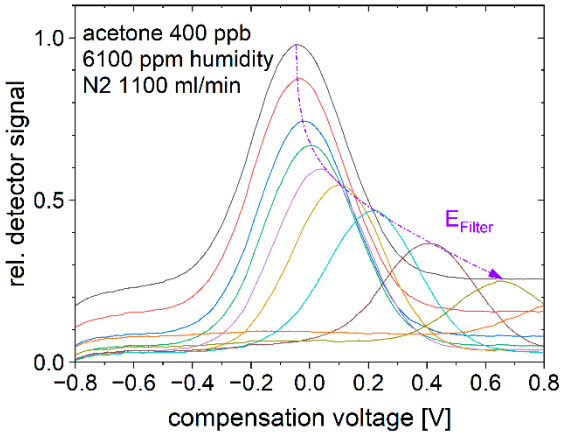

Fig. 3. Typical FAIMS spectra with a relatively large positive CV shift at high humidity conditions (approx. 22% rel. humidity at 22°C)

Summary and Outlook

Measurements were performed with the developed demonstrator and the integrated IMS chip with FAIMS ion filter. Results are in agreement with comparable FAIMS data. This provides the basic proof of function. Further focus must be placed on understanding and accurately analyzing the spectra obtained. This can be done in combination with mass spectrometry and other laboratory methods. The deeper knowledge about the measurements and dependencies are a basis for addressing new applications.

References

[1] G.A. Eiceman, Z. Karpas, H.H. Hill Jr., *Ion Mobility Spectrometry*, 3. ed. Boca Raton : CRC Press, 2014

[2] A. Graf, R. Stübner, C. Kunath, S. Meyer, H. Schenk, Miniaturized sensor for the detection of environmental pollutants, *Proceedings International Conference on Sensors and Measurement Technology (SENSOR)* (2017)

[3] A. Graf, N. Funke, O.R. Hild, Extended concept for a MEMS and IMS based ion filter, *Proceedings MikroSystemTechnik Congress 2021*, 539-542 (2021)

[4] E. Krylov, E. G. Nazarov, R. A. Miller, B. Tadjikov, and G. A. Eiceman, Field Dependence of Mobilities for Gas-Phase-Protonated Monomers and Proton-Bound Dimers of Ketones by Planar Field Asymmetric Waveform Ion Mobility Spectrometer (PFAIMS). J. Phys. Chem. A 106, 5437-5444 (2002); doi: 10.1021/jp020009i

[5] Z. Safaei, G.A. Eiceman, J. Puton, J.A. Stone, M Nasirikheirabadi, O. Anttalainen, M. Sillanpää, Differential Mobility Spectrometry of Ketones in Air at Extreme Levels of Moisture. *Scientific reports* 9, 5593 (2019); doi: 10.1038/s41598-019-41485-7

DOI 10.5162/SMSI2023/P15

Limitations of the fluorescence lifetime measurement from green plants using FD-FLIM to monitor plant health due to prolonged laser exposure

Maximilian Wohlschläger[1], Martin Löder[2], Marti Versen[1], Christian Laforsch[2]
[1] Rosenheim Technical University of Applied Sciences, 83024 Rosenheim, Germany
[2] University Bayreuth, 95447 Bayreuth, Germany
maximilian.wohlschlaeger@th-rosenheim.de

Summary:
Remote monitoring of plant health is essential for environmental research and agriculture. In this contribution, we demonstrate how FD-FLIM is used to measure the effect of prolonged laser exposure on the fluorescence lifetime of chlorophyll from a dandelion leaf, an oak leaf and grass. We describe the limitations of FD-FLIM and propose further experiments to monitor the plant's health status.

Keywords: chlorophyll, plant health monitoring, fluorescence lifetime, FD-FLIM, remote sensing

Introduction

Living plants have sensitive optical signatures, which are advantageous to monitor plants' health, which is affected by a wide range of contaminants. As a result, plant diseases caused by bacteria [1], fungi [2] or other contaminants such as microplastics [3] are getting more and more attention in research.

Currently, standard methods to determine plant functions are near-infrared (NIR) spectroscopy [5], leaf reflectance spectroscopy [6], pulse-amplitude modulated fluorescence [7] and solar-induced fluorescence spectroscopy [8]. Several factors limit the analysis using the four methods directly in the environment. Sunlight, humidity and the distance of the measurement system to the sample affect the measurement. In [4], a promising method was introduced: measuring the fluorescence lifetime at high distances using a high-intensity, ultra-short pulsed laser to gather plant information.

The results in [4] were auspicious, and thus we conducted experiments using frequency-domain fluorescence lifetime imaging microscopy (FD-FLIM) to determine the effects of prolonged laser exposure on the chlorophyll fluorescence lifetime of plants. Therefore, we intentionally damaged the plants by using the highest excitation power and by exposing the plants to laser light for five durations to investigate the effects of prolonged light exposure on the fluorescence lifetime of the plants. In the end, a way is proposed how the fluorescence lifetime could be used to determine the health status of a plant.

Materials and Methods

In frequency-domain fluorimetry, the samples are excited by a sinusoidally or rectangularly excitation laser source. The fluorescence signal caused by the excitation follows the harmonic excitation phase shifted, amplitude damped, and equivalent shifted [9]. A phase-dependent (PD) fluorescence lifetime can be calculated using the measured phase shift by dividing the tangent of the phase shift by the modulation frequency. FD-FLIM adapts the measurement principle of FD fluorimetry but allows an areal measurement of the PD fluorescence lifetime. The fluorescence lifetime is obtained using an FD-FLIM camera, a laser diode having an excitation wavelength of 488 nm and a laser power of 200mW (both from Excelitas PCO GmbH), a PSM1000 microscope from Motic and two optical filters: a band-pass filter in the excitation path and long pass filter in the emission path. Using this setup, 1008x1008 location-dependent PD fluorescence lifetimes of the plant samples are determined in one measurement. The measurement data is evaluated by a Gaussian analysis resulting in expectation values and standard deviation of the areal PD fluorescence lifetimes.

To investigate the effect of prolonged light exposure, the fluorescence lifetime of a dandelion leaf, an oak leaf and grass are investigated. The FD-FLIM measurements are taken after the laser has radiated for t_1 = 0s, t_2 = 2s, t_3 = 4s, t_4 = 6s and t_5 = 8s the measurement spot of the sample surface.

Results

The measured FD-FLIM data is evaluated using the described methods. In Fig. 1, the PD fluorescence lifetimes are plotted against the measurements time t_i.

Fig. 1 shows that the fluorescence lifetime becomes smaller the longer the laser radiates onto the sample surface. Additionally, it can be obtained that laser irradiation results in an exponential decrease in the fluorescence decay time.

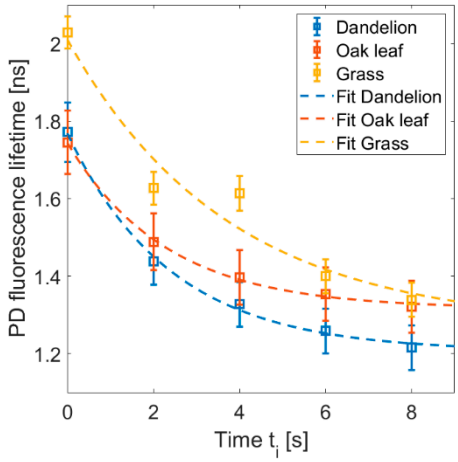

Fig. 1. PD fluorescence lifetime against the time of measurement t_i for the dandelion, oak leaf and grass samples and the corresponding fits.

The exponential model, shown in eq. (1) is fitted to the measurement data, and the parameters for $a\ [ns/s]$, $b\ [ns]$, $c\ [ns]$ and the goodness-of-fit value R^2 are determined and shown in Tab 1.

$$\tau = a \cdot e^{-\frac{t_i}{b}} + c \quad (1)$$

Tab. 1: Obtained values for a, b, c and R^2

Sample	$a\ [ns/s]$	$b\ [ns]$	$c\ [ns]$	R^2
Dandelion	0.56	2.40	1.21	0.99
Oak leaf	0.43	2.29	1.32	0.99
Grass	0.74	3.72	1.27	0.95

The exponential fit shows R^2 values that are larger or equal to 95% which means that the fitted models match the measured fluorescence lifetimes very well. Furthermore, the measured fluorescence lifetimes converge towards a limit value of $c\ [ns] = 1.27 \pm 0.06\ ns$ for long exposure times for the three fitting models. The dandelion and oak leaf show similar values for the parameters $a\ [ns/s]$ and $b\ [ns]$, indicating that they have similar ingredients and chlorophyll content compositions. On the other hand, the values of $a\ [ns/s]$ and $b\ [ns]$ of grass are significantly higher than those of dandelion and the oak leaf, indicating other compounds that influence the fluorescence signal of chlorophyll.

In conclusion, the study showed the exponential decrease of the PD fluorescence lifetime when the leaves are exposed to a prolonged laser light, also known as irreparable photobleaching. The exponential decrease was modelled using the exponential model in eq. (1). A convergence of the PD fluorescence lifetime to $1.27 \pm 0.06\ ns$ is observed for long light exposure times.

Using a high-power laser leads to non-reversible photobleaching of chlorophyll, it is hardly possible to determine the health status of plants. Further experiments must be conducted in which the laser power is reduced so much that no photobleaching occurs. If the inspection of plants is possible without photobleaching effects, the fluorescence lifetime could be a candidate to detect early-stage plant diseases due to the change in chlorophyll and, thus, the fluorescence lifetime.

References

[1] S.G. Borkar, R.A. Yumlembam, Bacterial Diseases of Crop Plants, *CRC Press*, (2016); doi: 10.1201/9781315367972

[2] R. Dean, *et al.*, The Top 10 fungal pathogens in molecular plant pathology, *Molecular Plant Pathology* 13, 414-430 (2012); doi: 10.1111/j.1364-3703.2011.00783.x

[3] S. Piehl, *et al.*, Identification and quantification of macro- and microplastics on an agricultural farmland. *Sci. Rep.* 8, (2018); doi: 10.1038/s41598-018-36172-y

[4] L.A. Finney, *et al.*, Ultrafast laser filament-induced fluorescence for detecting uranium stress in Chlamydomonas reinhardtii, *Sci. Rep.* 12, (2022); doi: 10.1038/s41598-022-21404-z

[5] J.A. Prananto, *et al.*, Chapter One - Near-infrared (NIR) spectroscopy as a rapid and cost-effective method for nutrient analysis of plant leaf tissues, *Advances in Agronomy* 164, Pages 1-49 (2020); doi: 10.1016/bs.agron.2020.06.001 .

[6] S.L. Ustin, *et al.*, Retrieval of foliar information about plant pigment systems from high resolution spectroscopy, *Remote Sensing of Environment* 113, Pages S67-S77 (2009); doi: 10.1016/j.rse.2008.10.019 .

[7] G.H. Mohammed, *et al.*, Remote sensing of solar-induced chlorophyll fluorescence (SIF) in vegetation: 50 years of progress, *Remote Sensing of Environment* 231, (2019); doi: 10.1016/j.rse.2019.04.030 .

[8] E.H. Murchie, T. Lawson, Chlorophyll fluorescence analysis: a guide to good practice and understanding some new applications, Journal of Experimental Botany 64, 3983–3998 (2013); doi: 10.1093/jxb/ert208

[9] J.R. Lakowicz, Principles of Fluorescence Spectroscopy, Springer Science+Business Media, (2006); ISBN: 978-0-387-46312-4

DOI 10.5162/SMSI2023/P16

Material Characterization by Ignition Spark Excited Lamb Waves

Jan Lützelberger[1], Alexander Backer[1], Sandro Krempel[1], Klaus Stefan Drese[1]
[1] Institute of Sensor and Actuator Technology (ISAT), Coburg University of Applied Sciences and Arts, Am Hofbräuhaus 1b, 96450 Coburg, Germany
jan.luetzelberger@stud.hs-coburg.de

Summary:
Material characterization using contactless excited and detected guided acoustic waves is a well proven, but overall expensive approach, since a cheap method of excitation is missing so far. Ignition-spark-excitation of Lamb waves could be such a method but has not shown to be suitable for material characterization yet. Covering various thicknesses and materials of metal plates, systematic dependencies of the spectral amplitude of the ignition-spark-excited Lamb waves are presented in this work. This enables the approach to be an alternative for exciting Lamb waves for material characterization.

Keywords: contactless excitation, Lamb waves, electric spark, non-destructive testing, material characterization

Background and motivation

For several decades, the use of Lamb waves as a type of guided acoustic waves (GAW) promised to be a useful approach for characterizing material properties [1,2]. However, if a contactless and non-destructive technique of excitation is required, the only common choices are laser-based excitation and measurement [3] as well as electromagnetic acoustic transducers (EMAT) [4]. As this comes along with a high financial effort, a cheaper technique for contactless and non-destructive Lamb wave generation is desired. Krempel et al. [5] presented such a technique using a very basic ignition coil - spark plug design. With this, they successfully excited the antisymmetric Lamb A0 mode in a metal plate at a broad and low frequency range up to 200 kHz with a maximum at about 30 kHz. However, the potential of using the so generated Lamb waves for material analysis, was still unclear.

Therefore, in this work, the setup of [5] is adapted to investigate the possibility of material characterization with the excited Lamb waves.

Methodology

The experimental setup is shown in Fig. 1. A suppressed spark plug of type NGK Iridium CR7HIX (1) with removed counter electrode, supplied by a non-suppressed ignition coil Jinan Qingqi QM50QT-6(A), was connected with a self-made electronic switchbox (2). The box was powered by a 30 V DC power supply Tenma 72-7245 and was controlled by a periodic pulse from a function generator of type Agilent 33521B with 200 µs pulse width and a repetition rate of 33.3 Hz. Every time the current was interrupted by the switch, the spark plug generated an electric spark on a metal plate (3) serving as the counter electrode (distance between metal plate and spark plug was 1.4 mm). This spark caused electromagnetic interferences which could be captured via an oscilloscope LeCroy HDO6034.

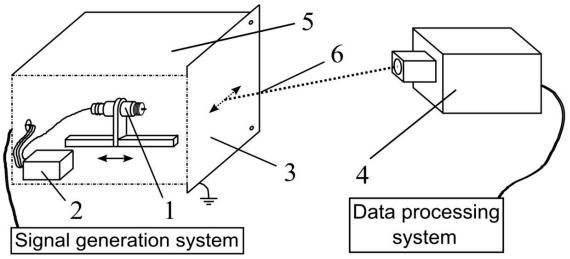

Fig. 1. Illustration of the experimental setup

Out of this, it then generated a trigger signal which was transmitted to the control unit of a laser scanning vibrometer of type Polytec PSV-400-M (4). For reasons of electromagnetic compatibility, the spark plug as well as the ignition coil and the switchbox were installed in a stainless steel box (5). To analyze the propagation of the Lamb waves generated by the electric sparkover, a horizontal line (6) on the outer surface of the metal plate was scanned by the vibrometer. For each of the 316 scanning points (0.44 mm distance) in this line, the surface deflection of the metal plate was captured for 500 µs (10.24 MHz sample frequency). Further

data processing especially included the performance of one- and two-dimensional Fourier transforms for characterizing the resulting Lamb wave in the frequency domain.

During the experiments six different plate thicknesses as well as three different materials were investigated to evaluate whether they cause remarkable changes in the signal.

Results

The amplitude spectrum for using a range of 1 mm thick metal plates is shown in Fig. 2.

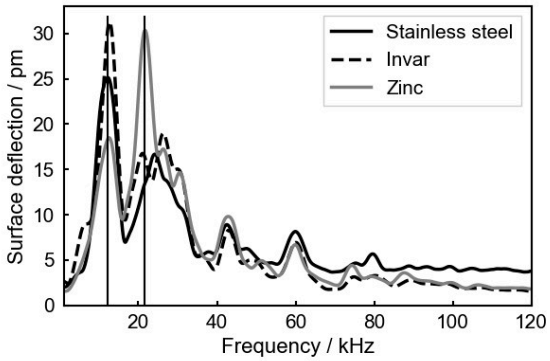

Fig. 2. Surface deflection vs frequency for different plate materials including main peaks (vertical lines)

At about 12 kHz, Invar shows the highest spectral amplitude followed by stainless steel and Zinc. Whereas at 21.5 kHz, Zinc shows a much higher amplitude than Invar and stainless steel.

Having the same material - stainless steel - but different thicknesses, has an even stronger effect on the location of the spectral main peak. When decreasing the plate thickness, the peaks are shifted towards lower frequencies and lower wavenumbers. Depicting the phase velocity with respect to the product of central frequency (maximal amplitude) and thickness gives a progression which is well represented by a linear relation (Fig. 3.).

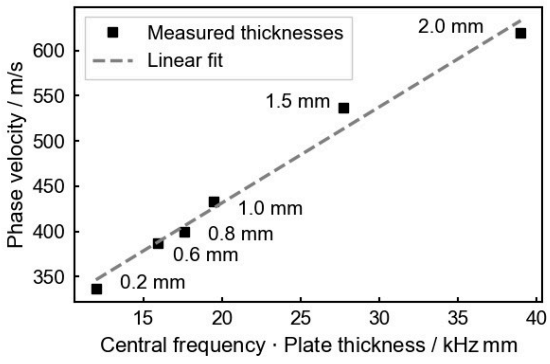

Fig. 3. Phase velocity vs frequency-thickness-product for different stainless steel plate thicknesses

Consequently, this approach enables to distinguish between different plate materials and thicknesses with the generated Lamb waves.

Repeatability measurements showed that related changes in the amplitude spectrum were small compared with those of different materials and thicknesses. Besides, various distances between the spark plug electrode and the plate surface demonstrated to change the absolute spectral amplitude only, but not the peak locations or ratios. In addition, microscopic investigations revealed no noticeable damage of the plate surfaces, so it is reasonable to call it a non-destructive approach.

Conclusions and outlook

Summarizing the results of the presented investigation, the spark-excited Lamb waves show systematic dependencies on plate thickness and material properties. Since repeatability measurements confirm the results, the so excited Lamb waves offer a possibility for being used for distinguishing between different plate thicknesses and materials. This opens the potential for the presented approach to be a low-cost alternative for contactless excitation of Lamb waves. Going beyond the presented results there are strong indications for a pressure wave as the dominating physical reason (over thermal expansion) for the Lamb wave excitation. This must be investigated further in order to completely understand the physical processes happening when exciting Lamb waves using ignition sparks.

Acknowledgements

The authors thank the various supporters of the project at ISAT, especially Sabrina Tietze, Florian Dötzer, Jürgen Fahrenberger, and the European Fund of Regional Development (EFRE) within the project "InnoTerm".

References

[1] D.C. Worlton, Experimental Confirmation of Lamb Waves at Megacycle Frequencies, *Journal of Applied Physics* 32.6, 967-971 (1961); doi: 10.1063/1.1736196

[2] Z. Su, L. Ye, Y. Lu, Guided Lamb Waves for Identification of Damage in Composite Structures: A Review, *Journal of Sound and Vibration* 295, 753-780 (2006); doi: 10.1016/j.jsv.2006.01.020

[3] H. Nakano, S. Nagai, Laser generation of anti-symmetric Lamb waves in thin plates, *Ultrasonics* 29.3, 230-234 (1991); doi: 10.1016/0041-624X(91)90061-C

[4] Z. Guo, J.D. Achenbach, S. Krishnaswamy, EMAT generation and laser detection of single lamb wave modes, *Ultrasonics* 35.6, 423-429 (1997); doi: 1.0.1016/S0041-624X(97)00024-3

[5] S. Krempel, A. Backer, F. Dötzer, K. Drese, Excitation of Guided Acoustic Waves Using Ignition Sparks, *SMSI 2021-Sensors and Instrumentation*, 97-98 (2021); doi: 10.5162/SMSI2021/A9.1

DOI 10.5162/SMSI2023/P17

Setting up a pressure sensor with flush membrane and without oil filling

Th. Frank, St. Hermann, A. Grün, D. Hanig, M. Kermann.
CiS Forschungsinstitut für Mikrosensorik, Konrad-Zuse-Straße 14, 99099 Erfurt, Deutschland
tfrank@cismst.de

Summary:
For high -pressure applications over 70 MPa, thin layer technology is mainly used on steel. With this technology, sensors with a front -bundle connection can only be realized with great effort. This paper contains a technology for a sensor with a front -bundle media connection and strict separation to the electrical side. Use are used for cross-no-sensitive SI-DMS. These are added to the media facing the media using a glass frit.

Various technologies and measurement principles are used to manufacture pressure sensors. The piezoresistive measurement principle is most widespread. To implement the measuring resistors, thick layer or thin-layer but also implanted measurement resistors are used in silicon. The deformation body for the thick layer or thin layer technology is made of ceramic or steel. The structure is largely standardized. In the case of silicon -based pressure sensors, there is a wide range of constructions.

A requirement is similar in all principles, the separation from the electrical side and the media.

The electrical side includes both the measuring resistances and the electrical connections with signal processing.

In silicon -based sensors, this is done with an oil filling and a separating membrane. In many cases, a flush front surface is advantageous, since there is no dead volume in the tube.

The steel and ceramic sensors are operated from the back. The measurement resistances are mandatory on the planar front. Different pressure sensors and a flush front surface cannot be realized.

The goal of arranging the measurement resistances is a full bridge. For this purpose, similar measurement resistors are placed on the deformation body in areas of negative and positive mechanical tension.

For high pressures from 700 bar, steel is primarily used as a deformation body. Due to the prevailing technology, the geometric size is limited downwards. Even a flush front area can only be implemented with great effort.

There is essentially a demand for the following properties:

- Small, flush front surface <Ø 5 mm
- Temperature range up to 200 ° C, injection molding tool
- Pressure range> 700 bar.

These requirements can be easily met if the measuring resistances can be positioned in the middle of the bending plate on the back. This is how the flush front area represents the media side. For a technological solution, the challenges at different positions lie:

- Severe accessibility of the back, lithography and screen printing are not possible
- The edge area is not accessible to position the measuring resistances, only a half -bridge is possible
- Isotropic stress field in the middle of the plate, measurement resistances with very low cross -quality sensitivity are required.

Fig. 1 shows the simulation of a deformation body with a load of 100 MPa from above. The line graph of the mechanical voltage on the underside and the top of the plate is shown in Fig. 3 and Fig. 4. The use of measuring resistors would be on the edge of the plate and in the middle for the well -accessible top. A position in the middle, since there is an isotropic stress field, requires measurement resistances with low sensitivity to cross. If this is not the case, the effect is greatly reduced. For assembly on the back, only the heavily accessible center is eligible, since the edge is practically not accessible. The solution is based on a Si-Strain Gauge, which is placed on the back by a glass frit connection and in the middle of the plate. The measurement resistances have a minimal a cross-stretch sensitivity. A split deformation body is used. After electrical contact, this is added by a welding process.

Fig. 2 and Fig. 5 show the plate from the back with a added Si Strain Gauge, as a half bridge.

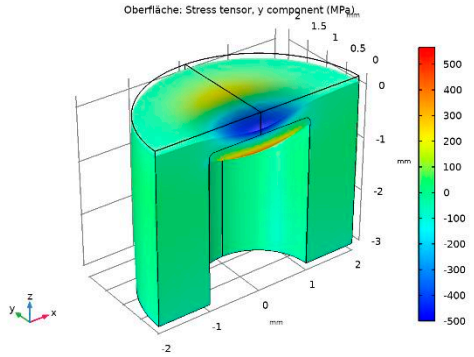

Fig. 1. Simulation deformation body, 100 MPa load from above

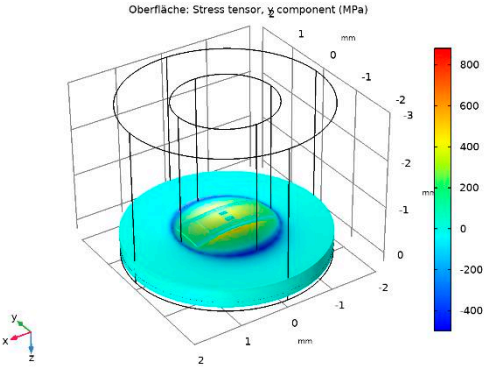

Fig. 2. .Pressure sensor with a cross-stretch insensitive Si-Strain Gauge

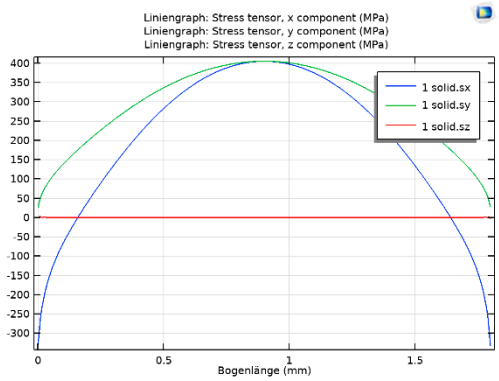

Fig. 3. Line graph of the mechanical stress on the underside of the plate.

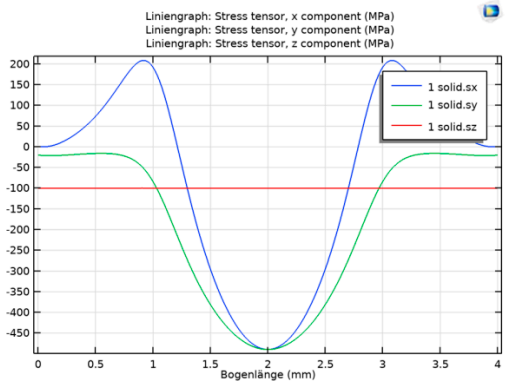

Fig. 4. Line graph of the mechanical stress on the top of the plate.

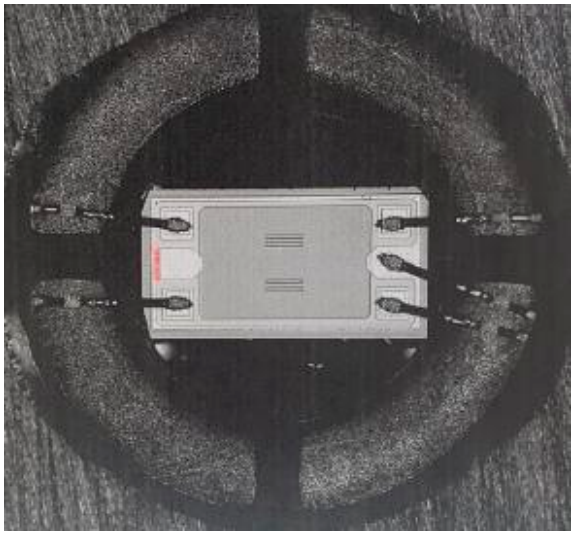

Fig. 5. Pressure sensor with a cross-stretch insensitive Si-Strain Gauge

DOI 10.5162/SMSI2023/P18

Multi-pass Laser Raman Spectroscopy for Combustion Diagnostic

Riccardo Dal Moro[1,2], Lorenzo Cocola[2], Fabio Melison[2], Luca Poletto[2]
[1] University of Padova, CISAS "G.Colombo", Via Venezia 15, 35131 Padova, Italy,
[2] CNR – IFN, via Trasea 7, 35131 Padova, Italy
riccardo.dalmoro@pd.ifn.cnr.it

Summary:
In this paper is proposed a laser-based system to perform a real time Raman spectroscopy applied to in-line combustion diagnostic. This approach is widely used for solid and liquid analysis; the problem related to gas samples is the low density since the amount of Raman scattering is proportional to the quantity of molecules in the matter-light interaction region. Our setup is based on a multi-pass cell (designed to increase the collected signal) that allows high-frequency acquisitions.

Keywords: combustion, diagnostic, Raman, spectroscopy, laser

Background, Motivation and Objective

Solutions to improve combustion efficiency have experienced a considerable growth in the last years. Such analysis can lead to substantial cost reductions, paving the way towards more sustainable policies regarding air pollution. In order to fully understand the dynamic of industrial combustion, new tools and diagnostic techniques need to be developed.

Optical analysis techniques represent an excellent choice as they are capable to provide high data sampling rate and non-specific sample preparation is required. In addition they are non-destructive and contactless analysis. The main optical techniques are IR absorption spectroscopy, such as FT-IR or tunable diode laser (TDLAS) approach, and Raman spectroscopy.

Raman spectroscopy is based on the phenomena of radiation scattering. The sample molecules are excited using a laser source and part of the scattered light will have a wavelength characteristic of the molecule that emitted it. The use of a monochromatic radiation allows to observe different gases with a single source. In addition, as we operate in the visible light range, the use of infrared detectors is not required. The problem related to gas analysis is the low density since the amount of Raman scattering is proportional to the quantity of molecules in the matter-light interaction region.

As demonstrated by these studies [1][2], it is possible to use the Raman technique to effectively study gaseous samples.

Our setup is based on a multi-pass cell (designed to increase the collected signal) that allows high-frequency acquisitions.

Method

Through a dispersion grating spectrometer (coupled with a CMOS camera), we collect the Raman scattering produced inside a windowed cell were a Nd:YAG 532 nm CW laser is focused into the gaseous stream. The interaction cell is coupled to a system of spherical mirrors in order to perform 16 reflections of the laser beam back to the focal plane (i.e.17 passages). This design increases the optical power density in the light-matter interaction region in a way to boost the amount of collected signal.

In Figure 1 is reported the multi-pass setup with its main components: 532 nm CW laser source (1), spherical mirrors (2a, 2b),windowed gas cell (3) and spectrometer (4).

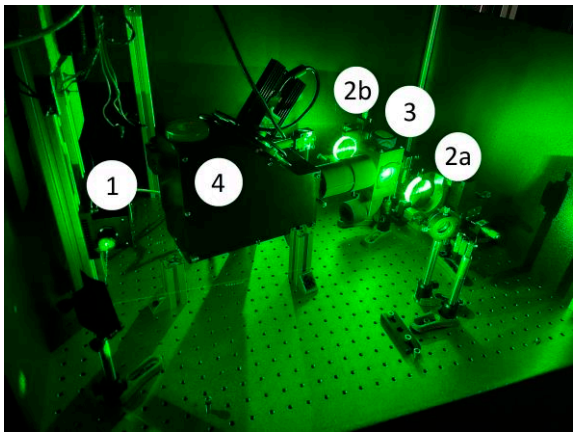

Fig. 1. Multi-pass laser beam setup.

This design is tailored to improve the amount of collected Raman scattered signal in order to minimize the acquisition integration time by maintaining high spectral performance. Figure 2 shows a comparison between the raw spectrum of ambient air collected with the mono-pass and

the multi-pass set up (with the same integration time). A sensitivity increase is clearly visible (appearance of water peak not visible in mono-pass setup) at the expense of an increase in background diffused light, that has been subtracted using a polynomial 3-rd-order fit.

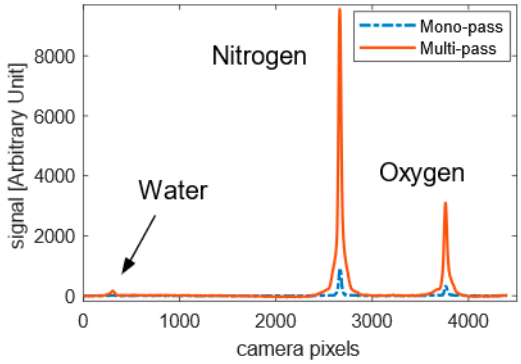

Fig. 2. Ambient air spectrum for the mono-pass system compared with the same for the multi-pass configuration.

The addition of a spherical mirror (feedback mirror) opposed to the spectrometer has also been evaluated. Such implementation reflects the Raman scattering on this side into the spectrometer reaching a further doubling of signal.

Starting from each acquisition frame we compute the spectrum as elaboration of pixel's intensity, then we perform the quantitative analysis using a non-linear least square approach based on the reference gas calibrations.

The application is focused on combustion diagnostic, but as previously mentioned Raman spectroscopy allows to observe the presence of many gases simultaneously. It is therefore possible to extend the analysis to a large group of gases.

Results

In terms of signal intensity, the multi-pass setup reaches a x16 magnification effect compared to the mono-pass system (evaluated on the air Nitrogen integral signal). The presence of the feedback mirror increases the magnification factor up to about x30. These factors are computed from the ambient air analysis without the gas cell. The presence of the cell induces a progressive loss in the laser beam power, in this case we reach a signal magnification of about x14.5 times the single passage (without the presence of the feedback mirror). The system performs analysis with 0.15 seconds per acquisition, which is a significant achievement in Raman spectroscopy on gaseous samples.

An example of a qualitative combustion analysis of a 4-stroke gasoline engine is reported in Figure 2. As we can see the trend of different gasses is recorded by the system, in this case we focused the analysis on N_2, H_2O, O_2, CO, CO_2 and exceeding combustible gas (HC).

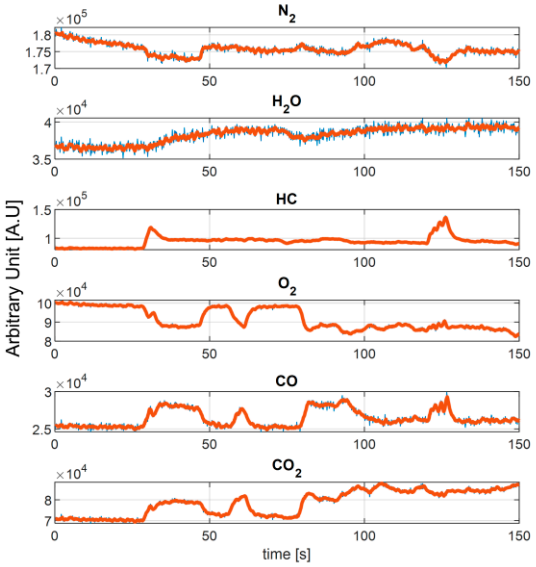

Fig. 3. : Example of qualitative diagnostic of a 4-stroke gasoline engine combustion (0.15 seconds of integration time).

Conclusion

Our research demonstrated that a Raman spectroscopy approach meets the main requirements of combustion diagnostic since it is capable to follow the time scale of the process. Future studies will be focused on further increase in performance. The system will be redesigned in order to get a compact prototype.

Particular attention will be put to increase the reliability of the alignment and to the miniaturization of the system. The goal is to create a portable instrument in order to perform combustion diagnostic in harsh conditions.

Acknowledgements

The authors acknowledge the support from the Project PiPe4.0, part of ATTRACT that has received funding from the European Union's Horizon 2020 Research and Innovation Programme.

References

[1] L. Cocola, F. Melison, N. Scarabottolo, G.Tondello, L. Poletto, Diode-based Raman sensor for fuel gas analysis, Proc. SPIE 11354, Optical Sensing and Detection VI, 113541A (2020).

[2] M. A. Buldakov, V. A. Korolkov, I. I. Matrosov, D. V. Petrov, A. A. Tikhomirov, and B. V. Korolev, "Analyzing natural gas by spontaneous Raman scattering spectroscopy," J. Opt. Technol. 80, 426-430 (2013)

DOI 10.5162/SMSI2023/P19

Investigation of the shape deviation for gas pores measured with X-ray computed tomography

Benjamin Baumgärtner[1], *Tino Hausotte*[1]
[1]*Friedrich-Alexander-Universität Erlangen-Nürnberg, Chair of Manufacturing Metrology (FMT), Nägelsbachstr. 25 91052 Erlangen, Germany*
benjamin.baumgaertner@fmt.fau.de

Summary:
The component porosity is a quality attribute in additive manufacturing (AM). One way for a non-destructive three-dimensional determination of the porosity or the shape of pores is X-ray computed tomography (CT), which enables to investigate the influence of AM process parameters on the appearance and characteristics of pores. Due to the lack of a porosity standard for CT, a traceable measurement uncertainty determination is not possible. To investigate the capability of CT for porosity analysis, measurements of an optically measurable glass specimen that contains highly spherical pores are used to validate results from a digital twin of the CT system. The influence of a fixed gray value threshold for the porosity analysis algorithm and the deviation of the surface determination are investigated.

Keywords: computed tomography, porosity measurement, sphericity, silica glass, additive manufacturing

Introduction and Method

One of the main challenges in additive manufacturing is to achieve dense components. The correlation between the process related parameters such as the deposited energy or the hatch distance and the resulting pores is therefore of interest [1]. CT is a nondestructive method, which can be used to determine the shape, size und volume of inner defects. However, due to missing porosity standards for CT, there is no possibility to determine the measurement uncertainty. Furthermore, the CT porosity measurement is not traceable and reliable conclusions are difficult. This work investigates the validity of CT porosity measurements using a silica glass specimen with optical accessible gas pores. One main advantage of this material is the possibility of reference measurements with a dark-field microscope. In addition, gas pores generally have a high sphericity, so that the geometric properties can easily be reproduced with a computer-aided design (CAD) model. Such a model can be used for simulating CT measurements by means of a digital twin of the CT system and is a useful reference to determine deviations of the size, shape and position of pores. For the investigation, the sphericity (1) has been used to determine the mismatch.

$$\psi = \frac{A_{\mathrm{sphere}}}{A_{\mathrm{defect}}} \qquad (1)$$

This criterion compares the detected surface of a pore A_{defect} with the surface of a sphere with identical volume A_{sphere}. Values near 100 % are expected for round gas pores. Significant lower values can be caused by measurement deviations for A_{defect}, by a pore shape that is less spherical than assumed. A comparison with results from CT simulation reveal actual causes.

Experimental

The investigated silica glass specimen has a wedge shape with outer dimensions of (12.5 x 21.8 x 6) mm³. For the CT simulation using the software aRTist 2.10 (BAM, Germany), a CAD model is used that is roughly adjusted to the real part. It contains ideally spherical gas pores with diameters from 48 µm up to 208 µm with steps of 16 µm. Real measurements were performed using the CT system Metrotom 1500 (Zeiss IMT, Germany) for a validation of the CT simulation. The resulting gray value volume data are analyzed using VGStudio MAX Version 2022.3 (Volume Graphics, Germany). A local adaptive surface determination is applied and the porosity analysis is performed with the algorithm VGDefX and a threshold of the deviation of -1 standard deviation of the material peak in respect of [2].

Results and Discussion

The sphericity of the pores obtained experimentally (orange) and by simulation (blue) are shown in Fig. 1 in dependence of the pore diameter. In comparison, the simulation can reproduce the behavior of real gas pores in glass very sufficient. Both data are almost invariant with respect

to the pore size, which corresponds to the expectation of high spherical pores. However, both do not obtain 100 % sphericity. To determine whether the CT parameters or CT artefacts have an impact on the measured shape, CT measurements under idealized conditions with a minimum of CT artefacts and noise have been performed and are displayed in Fig. 1 (yellow).

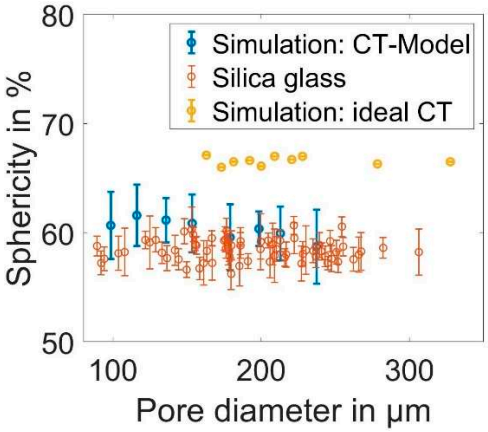

Fig. 1: CT measurement results of the sphericity of gas pores in glass (orange) and ideal pores in CT simulation (CT mode: blue) (ideal CT: yellow).

Although there is an influence of the CT parameters in the CT model, which is basically caused by the focal spot size and the related geometric blur, the sphericity is only slightly increased by the ideal CT. From Eq. (1), it is likely that there is an increase of A_{defect} in form of different shape. In order to distinguish whether the form itself is deformed because a sphericity of 60% is equal to a tetrahedron or the surface is enlarged by noise threw minor deviations like a golf ball, the pore size is compared with a reference value. The deviation of the difference can be calculated using the diameter of the CAD-model for the CT simulation and the dark-field microscopy for glass and compares it with a Gaussian fit of a sphere on the surface data points. The result is plotted in Fig. 2a) for the real (orange) and the simulated (blue). There is a minor negative difference of the diameter of the simulated pores, which does not indicate that the pore shape is preserved. Though there is a under scale of the pore size, which will lead to a smaller detectable volume, this will not affect the sphericity due to the definition in Eq. (1). The standard deviation of the surface points with respect to the fitted sphere can be calculated with a maximum value of 2 µm. In relation to the sensitivity of Eq. (1), a noisy surface of the pores can have the impact to increase A_{defect}. Furthermore, this could also affect the porosity analysis, since the threshold is defined according to the surface determination of a pore [2]. In this research, the threshold/ analyzing area is optimized for a pore with a diameter of 180 µm. The difference of the CAD-model and the calculated data of the algorithm is plotted in Fig. 2b). The deviation increases beside the optimized point, which can be explained with the correlation of the gray value, pore size and a static threshold value and will lead to over- and undersized pores. Considering the constant behavior of the sphericity even for pores on the optimized point, the scaling of the algorithm has no or a minor effect but will affects the compactness as a volume criterion [2], which is not discussed here. The sphericity criterion on spherical pore seems to be very sensitive on noisy influences but quite robust against scaling effects.

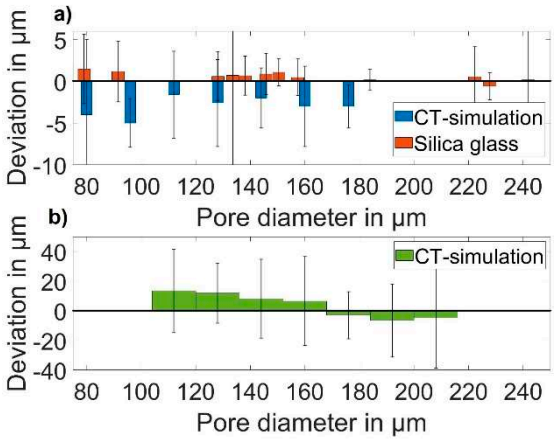

Fig. 2: a) Difference of the surface determination diameter and the CAD-model for CT Simulation (blue) and the dark-field-pore-diameter for the glass (orange). b) Difference of the CAD-model and the calculated diameter of the porosity analysis algorithm for the CT simulation (green).

Conclusion

The question whether CT is able to perform a shape constant image of gas pores cannot fully be answered without a calibrated standard. Nevertheless, the investigation with CT simulation shows that the deviation of the sphericity of ideal pores is mainly caused by noise. There is a high probability that gas pores in glass will not be recognized as such by using the CT. How this could affect materials of AM might be topic of a future research.

Acknowledgements

This study has been funded by the Deutsche Forschungsgemeinschaft (DFG, German Research Foundation) -Project-ID 61375930-SFB814, Subproject C4.

References

[1] R. Snell, S. Tammas-Williams, S. Chechik: Methods for Rapid Pore Classifications in Metal Additive Manufacturing, JOM 72,101-109 (2020); doi: 10.1007/s11837-019-03761-9

[2] Bundesverband der Deutschen Gießerei-Industrie e.V BDG, P203-Richtlinie (2019)

DOI 10.5162/SMSI2023/P20

A Method for In-Field Calibration for Periodical Technical Inspections Particle Counter Devices

Helmut Krasa[1], *Martin Kupper*[1], *Mario A. Schriefl*[1,2], *Alexander Bergmann*[1]
[1] *Institute of Electrical Measurement and Sensor Systems, Graz University of Technology, Graz, Austria,*
[2] *Emission Measurement Department, AVL DiTEST GmbH, Graz, Austria*
helmut.krasa@tugraz.at

Summary:
The introduction of particle number (PN) emission limits in periodical technical inspection for passenger cars leads to the need of PN measurements for any individual car. Besides the need for measurement devices, a fast and simple PN calibration method to allow for high-throughput calibration is key. In this work we present such a calibration method to evaluate the linearity and the plateau counting efficiency region of a PN counter is on-site.

Keywords: Particles, Number Concentration, Vehicle Emission, Periodical Technical Inspections

Introduction

The introduction of particle number (PN) limits for vehicle homologation in the European Union led to a decrease in particle emission levels in urban environment [1]. A sample survey by Burtscher et al showed that 10% of the highest emitting vehicles are responsible for 85% of the PN emission [2].

In order to identify those high emitters, Germany introduces PN emission limits for Euro 6 diesel vehicles as part of the periodic technical inspection (PTI) starting in 2023. This will increase the number of PN counters in use manifold. Calibration of PN counters for usage in homologation measurements must be performed according to ISO 27891, which is of high effort and requires an appropriately equipped lab. Additional efforts are added by ISO 17025 to ensure traceability including a reference counter, mass flow controllers and a differential mobility analyzer to select monodisperse particles as well as a rigid procedure.

Since around 35,000 PN counters will have to be calibrated for PTI per year in Germany alone from 2023 onwards, and the requirements for PTI devices are less stringent than for approval devices, a faster and simpler calibration procedure is needed.

PN counter calibration addresses two quantities. First, the counting efficiency (CE), which is defined as the ratio of number concentration of particles counted divided by a reference number concentration. The CE must be calibrated in the transition regime for particles smaller than 50 nm and at the efficiency plateau for bigger sizes. A typical PN counter CE curve with calibration limits for PTI devices is shown in Fig. 1. As can be seen, the CE is heavily impacted by the particles' chemical composition. Secondly, the counter must show a linear response over the whole particle concentration range.

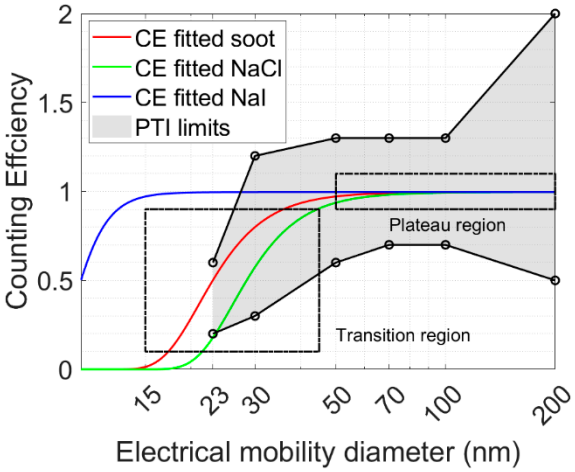

Fig. 1: Graph of fitted CE curves for three particle types of a PN counter curve and the required limits for calibration

In this work, we present a method that allows for in-field calibration of the linearity and plateau efficiency.

Methods and Results

Particles were generated with an atomizer that creates droplets from aqueous salt solutions. The droplets are then dried, leaving airborne salt particles. The setup is shown in Fig 2. We used NaI, which shows CEs bigger than 50% down to

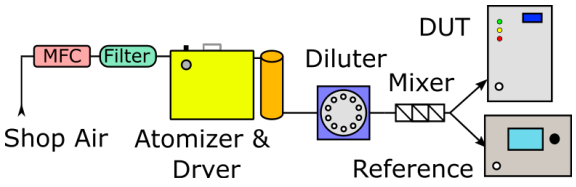

Fig. 2: Measurement Setup to evaluate the plateau CE, consisting of a particle source, a diluter, a mixer, a reference counter and the device under test (DUT).

18 nm, unlike the commonly used NaCl (Fig 1) [3]. The mean particle size changes with the salt concentration. Compared to other methods of particle generation, the atomizer has reduced tuning options, but is easy to use, portable and only requires pressurized air and an appropriate salt solution. Two size distributions for different salt concentrations of NaI are shown in Fig. 3. NaI shows a high CE at small sizes and the particle size distribution shows low concentrations below 15 nm. This means, that all particles generated by the atomizer are counted. For NaI, it is therefore possible to perform calibration without using monodisperse particles. Thus, the use of a differential mobility analyzer can be avoided, which makes the setup suitable for field use.

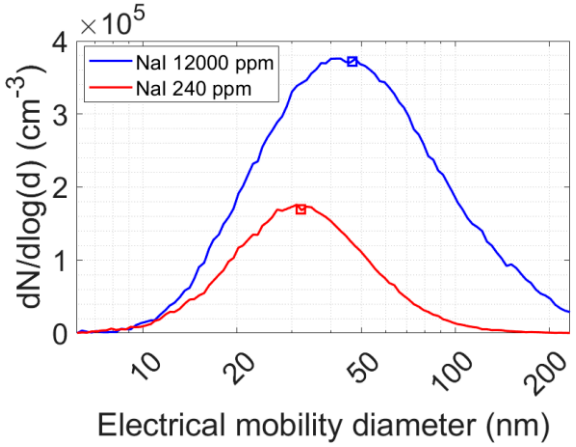

Fig. 3. Particle size distribution and their geometric mean diameter of NaI for two concentrations. Mean diameters were 46.8 and 32.1 nm.

Results

At first, we evaluated the CE for monodisperse particles at sizes in the plateau region. The respective data can be seen in Table 1.

Table. 1: CE of monodisperse NaI particles

Size / nm	Counts Refence / cm^{-3}	Counts DUT / cm^{-3}	CE
30	1170	1250	1.068
50	1950	2100	1.077
75	2520	2750	1.091
100	2250	2450	1.088
Average			1.085

The CE was then evaluated for polydisperse NaI (high concentration). The PN concentrations were between 80 cm^{-3} and 30 000 cm^{-3}. Typically, linear regressions are used, however the fitted CE is then primarily determined by the value at the highest concentration [4]. Instead, we used the averaged CE and fitted it for the polydisperse measurement, as can be seen in Fig 4. Good linearity was observed over the whole concentration range. The mean CE of 1.079 agrees within 1 % with the monodisperse measurement of 1.086.

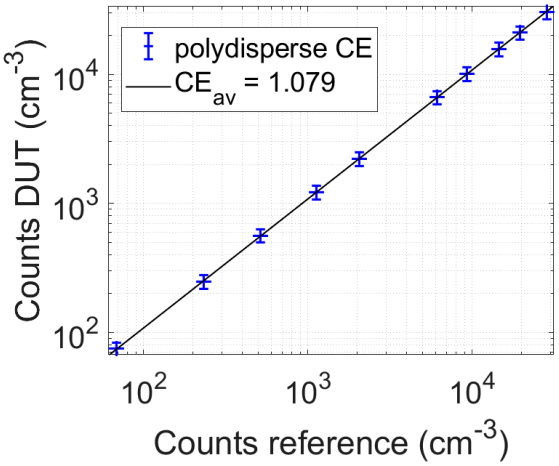

Fig. 4: Linearity test for polydisperse NaI between 80 cm^{-3} and 30 000 cm^{-3}.

Conclusion and Outlook

The plateau efficiency of a PN counter was successfully calibrated with polydisperse, atomized NaI particles. This method does not need a differential mobility analyzer and allows for in-field calibration, only requiring a compact atomizer, pressurized air and a reference counter. A portable calibration method for the CE of the transition regime using polystyrene latex is subject of current investigations.

References

[1] Font, A.; Guiseppin, L.; Blangiardo, M.; Ghersi, V.; Fuller, G.W. A Tale of Two Cities: Is Air Pollution Improving in Paris and London? *Environ. Pollut.*, 249, 1–12 (2019); doi: 10.1016/j.envpol.2019.01.040

[2] Burtscher, H.; Lutz, T.; Mayer, A. A New Periodic Technical Inspection for Particle Emissions of Vehicles. *Emiss. Control Sci. Technol.*, 5, 279–287 (2019); doi: 10.1007/s40825-019-00128-z

[3] Krasa, H; Kupper, M., Schriefl, M.A; Bergmann, A Towards a Simplified Calibration Method for 23 nm Automotive Particle Counters using atomized inorganic salt particles [Manuscript submitted for publication]

[4] Giechaskiel, B., & Stilianakis, N. I. A note on the comparison of particle number counters. *Measurement Science and Technology*, *20*(7) (2009); doi: 10.1088/0957-0233/20/7/077003

DOI 10.5162/SMSI2023/P21

Contactless torque measurement in BTA/STS deep hole drilling by using the Villari effect – a first proof of concept

Schwersenz, A.[1]; Nawal, K.[1]; Erli, R.[1]; Schmidt, R. [2]; Michel, S.[2]; Wiesweg, L.[2]; Biermann, D.[2]
[1] Magnetic Sense GmbH Zeilbaumweg 18, 74613 Öhringen Germany
[2] Institute of Machining Technology TU Dortmund University, Baroperstr 303 44227, Germany
Corresponding Author's e-mail address: Anatol.Schwersenz@magnetic-sense.de

Summary:
Based on a contactless torque sensor for pedelec application, the first exemplary tests were carried out on BTA/STS deep hole drilling machines at the TU Dortmund to verify the general functional principle in use with machine tools. Initial data show direct proportionality to reference data from the strain gauge, confirming that torque can be reliably measured with the contactless sensor. The following describes the basic principles of contactless magnetic torque measurement, its application on BTA/STS deep hole drilling machines and presents some of the results of the associated proof of concept.

Keywords: Torque Measurement, Contactless Measurement, BTA/STS deep hole drilling, Villari effect, Micromagnetic method

Introduction

Nowadays, various processes are used in manufacturing to produce precise and deep bores. The high metal removal rate, the quality of the bores and the achievable surface qualities show that this is a very economical process. In particular, the BTA (Boring and Trepanning Association) deep hole drilling process fulfills these characteristics for larger bore diameters (D ≥ 30 mm) [1]. Figure 1 a) shows a schematic sketch of a BTA/STS deep hole drilling machine with a total length of approx. L ~ 12 m.

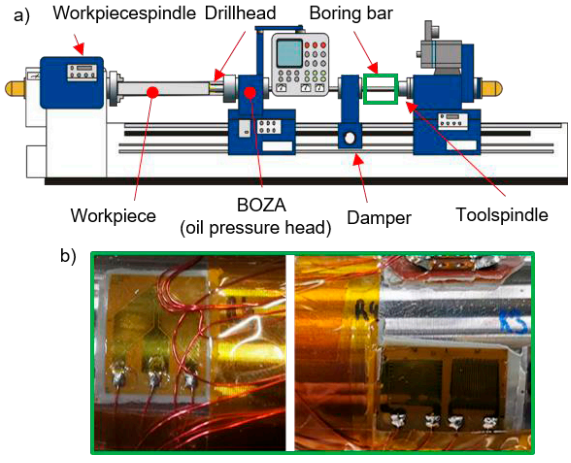

Fig. 1. a) The BTA deep hole drilling machine Guiseppe Giana GBB 560. b) Strain gauges applied to the boring bar

Due to the two spindles, it is possible to rotate either the tool, the workpiece or both sides, which increases the flexibility of the process. The bore moment and the thrust force of the process are often measured at the boring bar to obtain information about the cutting forces at the drill head and the dynamic state of the process. Therefore, strain gauges are applied to the boring bar as shown in Fig 1 b). Due to the cables from the strain gauges, the boring bar cannot rotate which reduces the flexibility of the process. However, there are techniques to use strain gauges with a rotating tool. These techniques either use a sensible telemetric transmission unit or integrate the measurement equipment and the power supply inside the tool spindle. Both techniques still rely on strain gauges, which require careful preparation of the boring bar before application and are not suitable for usage outside of the laboratory.

Description of the measurement principle

The relative permeability of ferromagnetic materials changes when mechanical load is applied. This effect is called inverse magnetostriction or Villari effect [3].

By exploiting the inverse magnetostriction, it is possible to electrically detect the change in the magnetic properties of a shaft under mechanical load.

For this purpose, the sensor imprints an alternating magnetic field into a shaft via generator coils. When applying torque, the material of the shaft is compressed and stretched at the same time, as shown in Fig. 2. This causes a change of relative permeability in the two depicted directions. These changes are then detected by measuring

the change in amplitude of the magnetic flux coupled with the four sensor coils. The simultaneous evaluation of the signals in the directions of compressive and tensile stress allows a statement on the torque direction.

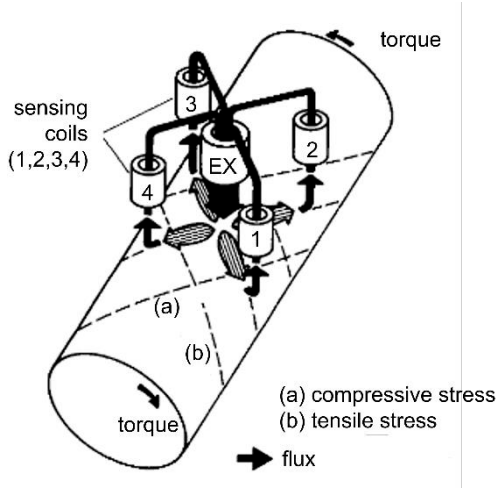

Fig. 2. Schematic representation of the basic principle [3]

Description of the Proof of Concept

For the proof of concept, strain gauges were applied onto the boring bar of a BTA deep hole drilling machine as shown in Fig.1 (b). At the same time, the contactless torque sensor is positioned around the boring bar with an adapter as shown in Fig.3. Subsequently, a defined torque is applied at the drill head and into the boring bar to measure, evaluate and compare both signals.

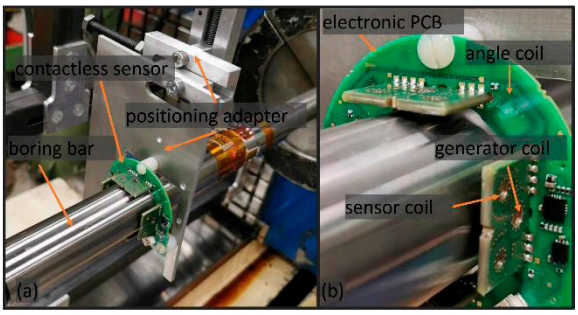

Fig. 3. a) Test setup with strain gauges b) and contactless torque sensor

Results of the Proof of Concept

In Fig. 4 the measurement signals of both methods are shown. The diagrams show a proportional relationship between the introduced torque and the measured signal in both measuring methods is visible. In the case of the strain gauge, a strain is measured and compared to the applied torque. The contactless torque sensor, on the other hand, outputs an electrical voltage value in V. Both output values must be converted into torque via a material-specific proportionality constant.

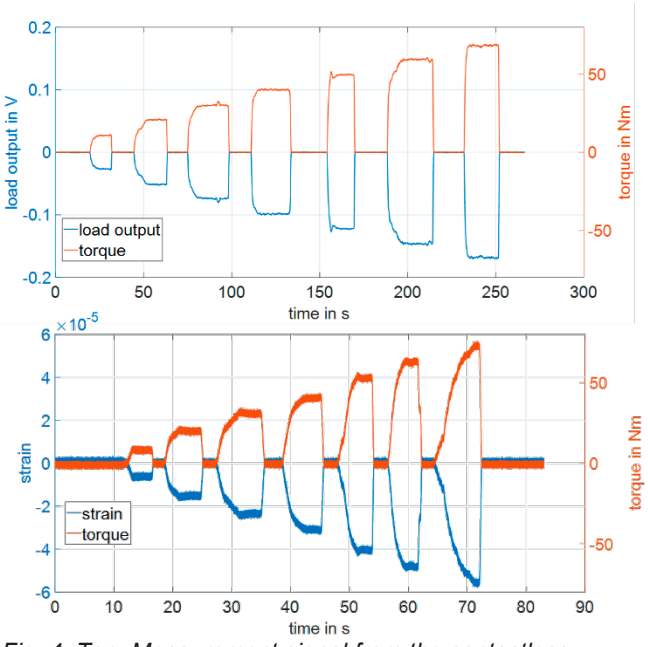

Fig. 4. Top: Measurement signal from the contactless sensor; Bottom: Measurement signal from the strain gauges

Conclusion

The proof of concept was successful. The contactless torque sensor measures at a similar level of linearity and precision as strain gauges while offering additional functions such as:

- Measurement of additional parameters and forces should be possible
- Increased flexibility of the process due to contactless measurement
- Variable placement of the sensor and operator-friendly setup

In future investigations measurements while drilling with a rotating workpiece and rotating tool will be carried out. Here the influence of the process dynamic on the contactless torque sensor will be investigated.

References

[1] Biermann, D.; Bleicher, F.; Heisel, U.; Klocke, F.; Moehring, C.; Shih, A.: Deep hole drilling, CIRP Annals 67, 2 (2018) 673–694. https://doi.org/10.1016/j.cirp.2018.05.007

[2] Magnetic Sensors, Volume 5, Sensors A Comprehensive Survey by Richard Boll, Kenneth J. Overshott

[3] Fleming, W. J., Engine Sensors: State of the Art, SAE Congress, Detroit, MZ, 1982 Paper 820904 97-113

DOI 10.5162/SMSI2023/P22

Validation of an inside sensor system for deformation measurements on bionic lightweight gears

Marina Terlau[1], *Marc Pillarz*[1], *Axel von Freyberg*[1], *Andreas Fischer*[1]
[1] *University of Bremen, Bremen Institute for Metrology, Automation and Quality Science (BIMAQ), Linzer Str. 13, 28359 Bremen, Germany*
m.terlau@bimaq.de

Summary:
To validate design guidelines of bionic, holistic lightweight gears with integrated load monitoring, an inside sensor system will be used to continuously record the deformation behavior under dynamic load. Strain gauges based on thin-film technology and metal substrate are used as sensors for this purpose. Measurements on a gear show that, during the entire tooth meshing, the deformation behavior of each tooth can continuously be measured with the implemented inside sensor system and that the various tooth meshing zones can also be detected.

Keywords: bionic lightweight gear, inside sensor system, deformation measurements, dynamic load

Introduction

Due to steadily increasing dimensions of wind turbines (WT), the trend of an increasing resource consumption for gears in WT gearboxes is emerging. To conserve resources, design guidelines for bionic, holistic lightweight gears with an integrated load monitoring are designed and validated. For the real-time load monitoring in the future and for the validation of the design guidelines, an inside sensor system is required. The inside sensor system directly characterizes the deformation behavior of the lightweight gears in operation, which is unknown, especially in the case of dynamic loads and, thus, enables load monitoring to predict material failure.

Due to the unknown deformation behavior, the bionic, holistic lightweight gears cannot be validated and observed with conventional condition monitoring systems [1, 2] when used in wind turbine gearboxes, because they do not record the deformations and loads directly at the gears. Conventional methods for recording forces and deformations are based on strain gauges, but so far, they lack robustness against adverse environmental conditions for long-term measurements [3]. Also, tactile and optical gear measuring systems [4, 5] are generally suitable for direct deformation measurement on gears, but not during dynamic loads. Indeed, the current studies have not yet addressed the detectability of deformations on bionic, holistic lightweight gears and of load peaks for real-time load monitoring.

Therefore, the aim of this work is to validate an inside sensor system for measuring the tooth deformation of lightweight gears under dynamic load conditions. The research question to be answered is whether the implemented inside sensor system can be used to continuously measure the deformation behavior of all teeth, i. e. the entire tooth mesh of all teeth.

Methodology and experimental setup

An inside sensor system is used to measure the mechanical stress states and the resulting deformations of dynamically loaded gears. Due to handling and compatibility with the test environment, the inside sensor system is first characterized on medium straight-toothed classical gears with involute profile. The gears have a pitch diameter of 120 mm, a module of 8 mm and 15 teeth each. The contact ratio of the gear teeth is approx. 1.3, so that alternating one pair of teeth is in single mesh and two pairs of teeth are in double mesh. The gears are made of case-hardened steel 16MnCr5.

The sensors used in the inside sensor system are 4.5 mm x 9.5 mm strain gauges from Siegert TFT, based on thin-film technology and metal substrate. Four sensor elements are each designed as meander-shaped measuring grids and arranged at 90° angles to each other. The interconnection is based on the principle of a Wheatstone's measuring bridge in the configuration of a full bridge. The strain gauges are welded directly to the gear. To identify the appropriate sensor position and orientation, FEM simulations localized the maximum stress concentration and stress directions on a loaded tooth in the area of the tooth root. To validate the measurability of the entire tooth mesh, three strain

gauges are each welded to adjacent teeth. According to the contact ratio of the gears, the measurement signals of the successive strain gauges are expected to have temporal overlaps.

The measured strain is initially output in µV/V and can be converted to mm in the future. In order to record the measurement signals of the strain gauge bridge in real time, a telemetry system from imc Test & Measurement, rotating on the shaft, is used for data transmission.

For the validation of the sensor system, the gears are integrated in a shaft test rig and dynamically loaded. The experimental setup is illustrated in Fig. 1.

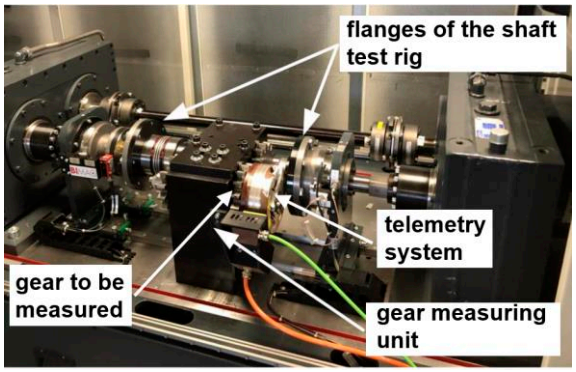

Fig. 1: Experimental setup for dynamically testing the inside sensor system to detect the entire tooth mesh.

Results

The focus of the observation is the measurability of the entire tooth mesh in order to characterize the deformation behavior of loaded teeth of lightweight gears and real-time load monitoring in future. According to a first gearbox stage of a wind turbine, a speed of $n = 15\ \text{min}^{-1}$ is initially set within the scope of the validation of the inside sensor system. The load is set to 100 Nm.

The results of the measurements demonstrate a signal overlap of the successive strain gauges, which is consistent with the expectation (cf. Fig. 2). In addition, the experimentally determined average gear meshing time for 15 min^{-1} is 0.287 s, which agrees well with a theoretically calculated gear meshing time of 0.284 s. As a result, the measurements validate that the total tooth meshing can be measured with the implemented inside sensor system.

Furthermore, the different meshing zones, single meshing and double meshing can also be distinguished in the signal curve of the strain gauges. At the start of meshing (A), the measurement signal initially increases abruptly. At this point, the signal curve overlaps with the measurement signal of the previous tooth, which decreases abruptly. It is hypothesized that the gear teeth are in double meshing in this state. When the double meshing is finished (B), the tooth meshing changes into a single meshing (B-D) and the slope of the signal curve changes abruptly. As soon as the next pair of teeth begins to mesh with each other, the gear is again in a double meshing (D-E).

In summary, the experiments validate the inside sensor system for measuring the deformation behavior of gears under dynamic load. With the selected sensor position and alignment, the entire mesh of a tooth can be measured with only one sensor.

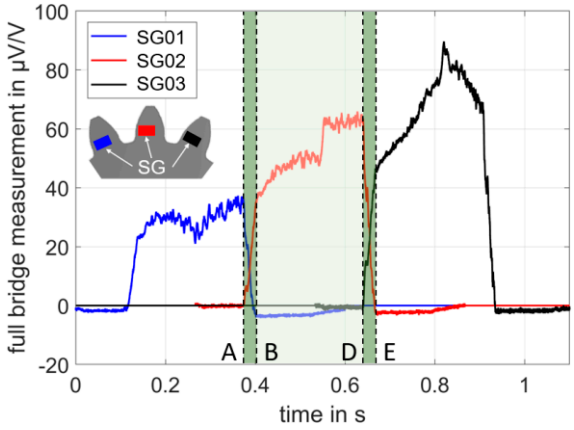

Fig. 2: Strains measured with the strain gauges (SG) of the inside sensor system during tooth meshing. A to E indicate different tooth meshing conditions. Note that the amplitudes of the strain gauges vary due to deviations in the alignment of the gears, but this does not affect the evaluation of the inside sensor system in terms of the measurability of the entire tooth mesh.

Funding: This research was funded by the German Federal Ministry for Economic Affairs and Climate Action (BMWK) within the project FlexGear, Grant Number 03LB1000A.

References

[1] J. P. Salameh, S. Cauet, E. Etien, A. Sakout, L. Rambault, Gearbox condition monitoring in wind turbines: A review, Mechanical Systems and Signal Processing 111, 251–264 (2018), doi.org/10.1016/j.ymssp.2018.03.052

[2] H. Luo, C. Hatch, M. Kalb, J. Hanna, A. Weiss, S. Sheng, Effective and accurate approaches for wind turbine gearbox condition monitoring, Wind Energy, 17:715–728 (2014), doi:10.1002/we.1595

[3] G. Goch, W. Knapp, F. Härtig, Precision engineering for wind energy systems, CIRP Annals – Manufacturing Technology, 61, 611-634 (2014)

[4] M. M. Auerswald, A. von Freyberg, A Fischer, Laser line triangulation for fast 3D measurements on large gears, The International Journal of Advanced Manufacturing Technology, 100, 2423–2433 (2019); doi: 10.1007/s00170-018-2636-z

[5] M. Pillarz, A. von Freyberg, A. Fischer, Determination of the mean base circle radius of gears by optical multi-distance measurements, Journal of Sensors and Sensor Systems 9(2):273–282 (2020), doi.org/10.5194/jsss-9-273-2020

DOI 10.5162/SMSI2023/P23

Special requirements of the design of new transfer artefacts for the calibration of mass standards

Katharina Lehrmann
Physikalisch-Technische-Bundesanstalt, Braunschweig, Germany
katharina.lehrmann@ptb.de

Abstract:
The harmonised modelling of new types of transfer artefacts made of monocrystalline silicon provides the necessary basis for highly accurate calibrations of mass standards with a nominal mass of one kilogram under atmospheric conditions. The special requirements for a material-independent design are investigated. All significant physical parameters as well as the requirements for user-friendly handling are taken into account.

Keywords: Transfer artefacts, buoyancy artefacts, sorption artefact, duplex artefact, inlay artefact, silicon sphere, mass, kilogram, mass calibration

Taxometry

Transfer artefacts can be used for mass comparison measurements. The measurements in vacuum and under atmospheric conditions allow conclusions to be drawn about the surface coverage by water or hydrocarbons and systematic effects due to air buoyancy, for example. The transfer artefacts discussed refer to a 1 kg silicon sphere as a reference standard. The surface of the reference sphere represents the minimum surface. The newly created term taxometry is composed of the definition for classification into systematic categories (taxonomy) and the subject area (metrology).

The transfer artefacts are classified into three different categories: a) sorption artefacts, b) duplex artefacts, c) buoyancy artefacts. Two sorption artefacts and two buoyancy artefacts are used as a pair. All test artefacts have the same nominal mass and surface properties (especially with regard to roughness) as the reference (reference sphere). In the following, designs with cylindrical artefacts whose surfaces differ as much as possible in terms of area must be determined for sorption artefacts. This results in 2-disc, 3-disc and 8-disc artefacts.

The described sorption artefacts are uniform in mass and density, which is realised by a disc-shaped assembly. Two variants of buoyancy artefacts can be used to determine the (air) buoyancy correction. Unlike the sorption artefacts, their nominal area is the same, but their density is different. For the greatest possible volume difference between the buoyancy artefacts, a artefact with hollow space (hollow artefact) and an artefact with an enclosed core of a denser material (inlay artefact) are designed.

Another category of transfer artefacts are so-called duplex artefacts. Due to their properties, these can be used to determine both sorption effects and buoyancy effects. Nominal mass and surface properties are similar to all other artefacts, including the reference. Duplex artefacts have the same nominal volume as sorption artefacts with a multiple of the surface area of the reference.

Limitations

Uniform installation dimensions are demanded for all transfer artefacts, due to the vacuum mass comparators used. The maximum radius of a cylinder is 0.045 m due to the housing geometry. The maximum usable installation height is 0.105 m. Due to the complex handling in the comparator, however, a maximum height of 0.1 m is pursued. Due to the mounting geometry, a minimum disc height of 0.015 m is recommended. The following densities apply:

Silicon 2 328.8 kg/m³ [1], Tungsten 19 250.0 kg/m³ [2] and Air 1.2041 kg/m³ [3, 4]. The surface roughness of all artefacts should be in the range of 10^{-9} m, analogous to the reference standard. The geometry of the chamfers to be designed describes straight chamfers with an angle of 45° and a leg dimension of 0.000 5 m. The calculation accuracy is 10^{-12} kg/m³. The accuracy of the calculation is set at 10^{-12}.

A uniform basic geometry of disc artefacts is used for all transfer artefacts, which enhances the development of a uniform calculation ap-

proach and simplified manufacturing. A transfer artefact is made up of at least one disc artefact, a straight circumferential chamfer and a number of spherical spacers, so-called coupling spheres. Via the latter, a six-point bearing is obtained, which serves as a kinematic coupling [5, 6] and connects the individual disc artefacts with a defined gap height. The stability for the assembly of the individual disc artefacts, as well as the tilting stability during the placement of the comparators and during the weighing process, was determined experimentally for an angle of inclination of up to 20° [7]. The reproducible dismountability of the disc stacks enables efficient and comparable cleaning [8] to the reference. If a transfer artefact consists of more than one disc artefact, a distinction is made between top, middle and base disc(s) for the disc stack.

Special requirements

Transfer artefacts enable the correction of systematic deviations and the calculation of a measurement uncertainty contribution during the substitution calibration of mass standards of different density [9]. The objective is the determination of environmental influences. High-quality 1 kg silicon spheres are used as a reference.

The following physical properties and handling conditions must be fulfilled for all transfer artefacts:

- same nominal mass as the reference
- same material and surface quality as the reference, natural monocrystalline silicon, if possible without amorphous surfaces
- nominal surface ratios of transfer artefact to reference should ideally be designed as whole numbers (this supports the descriptive assessment of sorption effects)
- Geometrical specifications of the measuring chambers within the mass comparators, variable parameters: Number, height and radius of the transfer artefact discs
- practice-oriented placement taking into account the mounting geometry (minimum height) within the comparators, this requires a special design of the base disc
- Simple dismantling of the transfer artefact discs for efficient cleaning
- Kinematic coupling by frictional connection of the transfer artefact discs to be stacked
- High tilt stability of the transfer artefact discs for transport and assembly of the comparators.

The transfer artefacts are used both under atmospheric conditions and under vacuum in mass comparators.

References

[1] PTB internal density measurement via hydrostatic weighing at 20 °C, May 2020

[2] N. Greenwood, A. Earnshaw, Chemie der Elemente, Edition 1, VCH, Weinheim, ISBN 3-527-26169-9, S. 1291, 1988

[3] M. Gläser, R. Schwartz, M. Mecke, Experimental determination of air density using a 1 kg mass comparator in vacuum, Metrologia 28 (1991) 45–50

[4] A. Picard et al., Revised formula for the density of moist air (CIPM-2007), Metrologia 45 (2008) 149, doi:10.1088/0026-1394/45/2/004

[5] PTB, Inventor Härtig, Frank; Hirsch Jürgen; Stein, Martin; Lin Hu: Präzisionsaufnahme; internal inventor information, 0454218DE1, 2014

[6] Wiemann, Ann-Kathrin; Stein, Martin, Kniel, Karin; Traceable metrology for large involute gears, Precision Engineering, Volume 55, January 2019, Pages 330-338, doi.org/10.1016/j.precisioneng.2018.10.001

[7] K. Lehrmann, Internal experimental tilt stability investigation with variable stacking of differently arranged spherical spacers, May 2020

[8] J. W. Chung, V. Görlitz, M. Vogtmann, E. Beyer, F. Härtig, The PTB Cleaning Procedure for Silicon Spheres, Version 1.01, Juni 20, 2016

[9] OIML 2004 Recommendation R111-1 Weights of classes E1, E2, F1, F2, M1, M1–2, M2, M2–3 and M3 (Paris, France: BIML),

DOI 10.5162/SMSI2023/P24

In-Situ Monitoring for Fused Filament Fabrication by means of Multi-Electrode Resistance Measurements

Alexander Dijkshoorn, Patrick Neuvel, Heime Jonkers, Stefano Stramigioli, Gijs Krijnen
Robotics and Mechatronics Group, University of Twente, Enschede, the Netherlands
Corresponding author: a.p.dijkshoorn@utwente.nl

Summary:
This work demonstrates in-situ monitoring of additive manufacturing through Fused Filament Fabrication with multi-electrode resistance measurements as an alternative to thermal and optical monitoring methods. Measurements are performed through the means of a resistive filament in combination with multiplexed nozzle to bed electrodes. When printing a beam, measurements show the addition of layers as well as nozzle x-position. Furthermore effects of the electrode placement, size and loss of nozzle contact can be measured. Future work will focus on measurements with a higher number of electrodes and more complex sample geometries.

Keywords: Process Monitoring, In-Situ, 3D-Printing, Fused Filament Fabrication, Electrical Resistance

Introduction

One of the main challenges in Fused Filament Fabrication (FFF) is dealing with uncertainties in the equipment and process. Therefore in-situ monitoring of the process is an important step towards understanding the process and improving its quality and efficiency [1, 2]. Research in this field is quickly developing and is considered fundamental for the industry [2, 3]. Thermal and optical imaging are the most common monitoring methods and have been used successfully for defect detection and closed-loop control purposes [2, 3]. Despite these advances, there is still a lack of effective and cheap in-situ monitoring techniques for non-destructive structural fault detection. Especially of those that can easily be incorporated into 3D-printers [1, 3], since the surface-based optical methods give very limited information on adhesion and bonding quality. In-situ electrical resistance measurements with conductive filament are able to measure bonding quality, part geometry, print temperature and presence of defects. Previous work applied measurements between two bed electrodes [4] and between a bed electrode and the nozzle [5], generating limited information in complex geometries. This work aims to extend the methodology by multiplexing the measurement path between multiple bed electrodes and the nozzle. The following sections demonstrate the methodology and implementation of in-situ multi-electrode measurements.

This work was developed within the Printing Electro-Tomography project, funded by the European Research Council under Grant Agreement No. 966668.

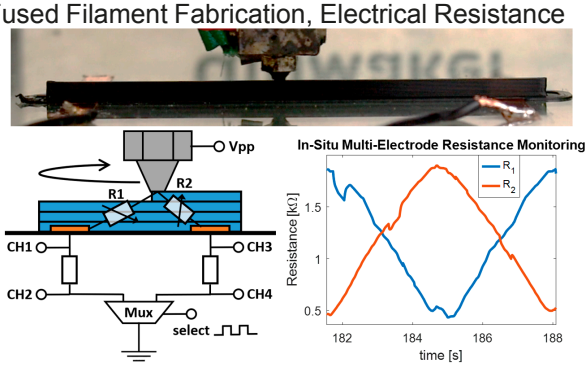

Fig. 1: Setup with the electrodes on the left and right side of the beam (top), schematic of the multiplexed setup (left) and typical data for printing from right to left and back (right).

Methods

Our novel in-situ measurement principle is based on electrical resistance measurements during printing with a resistive filament. By studying the changes in electrical resistance with added layers, the bonding between layers and the effect of printing parameters can be derived. The usage of additional electrodes with multiplexing allows for measurement of multiple resistive paths (R_1 forming the left and R_2 the right resistive path), Fig. 1. In this experiment a beam is printed across two bed electrodes, where the resistance to the nozzle typically increases and decreases as a result of the sideways movement of the printhead, fig. 1 (lower right). A long, thin sample is used to achieve a low thermal time constant, reducing the effect of the temperature-dependent electrical resistivity [4]. The setup consists of a customised Ultimaker 2

printer with a BondTech Bowden extruder and an E3D 0.8 mm stainless steel nozzle. The resistive filament of choice is carbon black filled Polylactic Acid (PLA) by Protopasta [6], which is printed at $30\,\mathrm{mm\,s^{-1}}$ with a $210\,^{\circ}$C nozzle temperature and a $50\,^{\circ}$C bed temperature. The beam has a length of 100 mm, a width of 3.2 mm and a height of 4 mm, and is printed with 0.25 mm layer height and a two track skirt. Copper tape with a width of 6.35 mm and a thickness of 66 µm is used to form the bed electrodes. Measurements are performed through voltage dividers, with $3422\,\Omega$ and $3243\,\Omega$ resistors and $V_{\mathrm{pp}} = 24$ V DC. The 2-to-1 mux circuit (2x BS170 NMOS) is triggered by a square wave at 10 kHz (Siglent SDG1032X) and sampled by an oscilloscope (Rigol DS1054Z). Signals are post-processed in MATLAB with an envelope function and a moving average filter to remove switching effects and provide noise reduction respectively. A 2D FEM simulation for a single printline is performed in COMSOL using the Electric Currents module with same sample geometry and a resistivity of $\rho = 0.2\,\Omega$m. The nozzle position is swept over the sample length to simulate the printing.

Results

The measurement data for the first layers is shown in fig. 2. The resistance decreases with added layers and opposing changes of R_1 and R_2 correlate with the nozzle x-position. After several layers, the relative change in resistance reduces with the number of layers N, given $R \propto 1/N$. The placement and size of the highly conductive electrodes influences the measurement and FEM data. The beam extends over the electrodes, increasing resistance when the nozzle extends past the electrodes to the outer positions. Additionally the electrodes act as equipotential, resulting in a small decrease in resistance when the nozzle passes over the electrodes. At the end of the print the nozzle is oozing after which it is pulled away from the part, with the blob being detected by both electrodes as well as the disconnect.

Discussion and Conclusion

In this work in-situ monitoring through multi-electrode resistance measurements is demonstrated. A clear correlation between nozzle position and resistance is shown, with the total resistance decreasing with the number of layers. Furthermore the effects of the electrode size, their location and loss of nozzle contact are observable in the data. The observed $1/R$ curve is not perfect, which can be explained by the parallel resistance of the skirt across the electrodes as well as the presence of thermal effects,

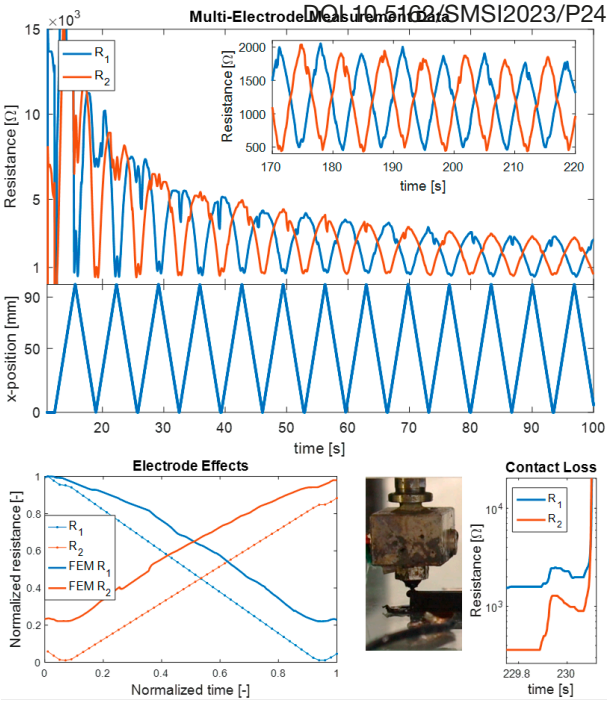

Fig. 2: The resistance data with a close-up at a later time (top), the nozzle x-position (center), the effects of electrode placement and non-zero width (bottom left) and loss of nozzle contact (bottom right).

despite the beam geometry. The geometrical resistance is expected to be linear with nozzle position as simulated, whereas measurements show a curvature for the first layers. Additionally the resolution and noise of the setup could be improved by grounding the nozzle and applying dedicated measurement equipment. Future work will focus towards complex geometries and a scaled number of electrodes, where machine learning could aid in data interpretation [7].

References

[1] J. Pellegrino *et al.*, "Measurement science roadmap for polymer-based additive manufacturing," Tech. Rep., Dec. 2016, National Institute of Standards and Technology.

[2] A. Oleff *et al.*, "Process monitoring for material extrusion additive manufacturing: a state-of-the-art review," *Progress in Additive Manufacturing*, vol. 6, no. 4, pp. 705–730, May 2021.

[3] Y. Fu *et al.*, "In situ monitoring for fused filament fabrication process: A review," *Additive Manufacturing*, vol. 38, p. 101749, 2021.

[4] A. Dijkshoorn *et al.*, "In-situ monitoring of layer-wise fabrication by electrical resistance measurements in 3d printing," in *2020 IEEE SENSORS*, 2020, pp. 1–4.

[5] H. Parker *et al.*, "In-situ print characterization and defect monitoring of 3d printing via conductive filament and ohm's law," *Procedia Manufacturing*, vol. 53, pp. 417–426, 2021, 49th SME North American Manufacturing Research Conference (NAMRC 49, 2021).

[6] ProtoPlant, makers of Proto-pasta. Composite PLA - Electrically Conductive Graphite. Accessed: 31-01-2017. [Online]. Available: https://www.proto-pasta.com/

[7] J. Qin *et al.*, "Research and application of machine learning for additive manufacturing," *Additive Manufacturing*, vol. 52, p. 102691, 2022.

DOI 10.5162/SMSI2023/P25

Resistive Sensor for Online Assessment of the Insulation Condition of High Voltage Capacitive Bushings

Marcos V. H. Rambo[1], Aguinaldo G. de Melo[1], Daniel Benetti[1],
Ivan J. Chueiri[2], Vóldi C. Zambenedetti[2], Edgard Jamhour[2]
[1] COPEL Geração e Transmissão S.A. (COPEL GeT), Brazil,
[2] Pontifícia Universidade Católica do Paraná (PUC-PR), Brazil
marcos.rambo@copel.com

Summary:
The main purpose of this work is to present a new resistive sensor for online assessment of the insulation condition of high voltage capacitive bushings. Capacitive bushings are one of the most critical components of power transformers and online monitoring can prevent explosions, that may result in damages ang power outages. The proposed sensor can online determine the absolute values of the capacitance with absolute errors that enable a qualitative analysis. Future studies may use this sensor to also determine the resulting sum of currents through three phase sensors and the insulations' power factor.

Keywords: High voltage capacitive bushings, capacitance, power factor, resistive sensor.

Introduction

High voltage capacitive bushings are the third most common source (17%) of failures of power transformers [1]. Bushings' insulation is degraded as consequence of aging and thermal, electrical, and mechanical stresses, and can cause catastrophic events, such as explosions, damages to adjacent equipment and power outages. One of the biggest power outages in Brazilian electrical grid, in the last years, was originated from a bushing failure [2]. Therefore, power utilities have invested in online monitoring of bushings' insulation [3]. Offline assessment is more accurate but must switch off the power transformers and may not identify insulation failures that develop quickly. In this way, this paper presents a new resistive sensor, which is installed in a 230/138 kV autotransformer.

Capacitive Bushings Equivalent Impedance

High voltage bushings are mainly capacitive due to their structure in layers. Each layer is made of insulation paper, impregnated with insulation oil, and have a conductive foil to promote a better distribution of the electric field along the insulation. Thus, the bushings impedance may be represented as a set of capacitors in series (see Fig. 1). Dielectric losses may be represented as resistors in parallel to the equivalent capacitances. Since the testing tap must be grounded, when the power transformer is operating, C_2 may be neglected.

The bushings' insulation capacitance (C_1) state may be labeled according to Tab. 1.

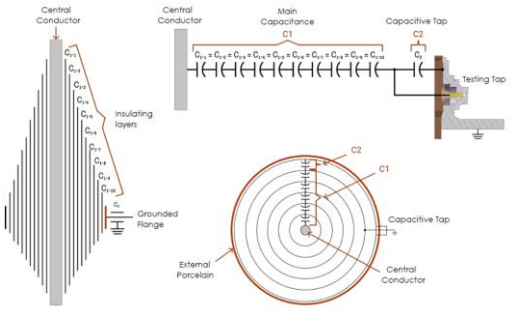

Fig. 1. Equivalent main capacitance (C_1) and tap capacitance (C_2) of high voltage bushings.

Tab. 1: Bushings' state, where C_p and PF_p denotate the nominal capacitance and power factor values [4].

State	Capacitance (C)	Power Factor (PF)
Good	$C_p \le C < 1.05 \cdot C_p$	$PF_p \le PF < 2 \cdot PF_p$
Alert	$1.05 \cdot C_p \le C < 1.1 \cdot C_p$	$2 \cdot PF_p \le PF < 3 \cdot PF_p$
Replacement	$C \ge 1.1 \cdot C_p$	$PF \ge 3 \cdot PF_p$

Nominal values of Power Factor are in the range of 0,3 to 0,4% [5], thus C_1 may be measured neglecting the current flowing throw the dielectric losses, i.e., the absolute current circulating through the sensor may be considered as the current that flows through C_1.

Proposed Bushing Sensor

The electrical schematic of the proposed sensor is presented in Fig. 2 (a). It is encapsulated in an aluminum casing that must be connected to the testing tap of high voltage capacitive bushings (see Fig. 2(b)).

Six sensors were installed at the bushings of a 150MVA 230/138kV power transformer in Bateias Substation of COPEL GeT.

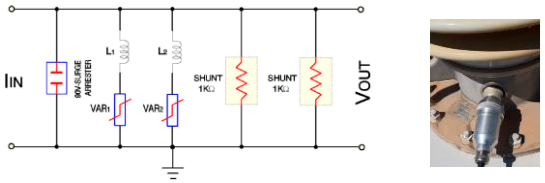

Fig. 2. Proposed resistive sensor. (a) Electrical schematic. (b) Sensor installed at Bateias Substation.

Results

The equivalent impedances of the resistive sensors were measured using a Keysight LCR Meter, model E4980A (see Tab. 2).

Tab. 2: Measured Impedance of the resistive sensors, where H is used for the sensors that were installed at 230kV level and X for 138kV.

Voltage level-Phase	Absolute value (|Z|) [Ω]	Phase [°]
H-A	496.68	0.11
H-B	496.33	0.10
H-C	496.85	0.10
X-A	496.24	0.11
X-B	496.47	0.11
X-C	496.33	0.11

Prior to sensors installation, the bushings insulations parameters were measured with Omicron CPC 100 (see Tab. 3).

Tab. 3: Nominal values (C_p and PF_p) and values measured with Omicron CPC 100 (C_o and PF_o) for C_1.

Bushing	C_p [pF]	C_o [pF]	PF_p [%]	PF [%]
H-A	277	271.11	0.35	0.3827
H-B	296	289.77	0.39	0.3989
H-C	290	283.72	0.36	0.3760
X-A	231	229.19	0.46	0.3999
X-B	230	227.01	0.37	0.3721
X-C	230	226.36	0.46	0.3597

After energization of the power transformer, the resulting voltages (*Vout*) at the sensors' outputs were acquired with a Tektronix TPS 2014 Oscilloscope (see Fig. 3).

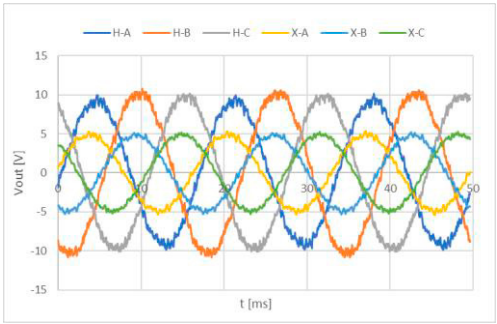

Fig. 3. Voltage signals at the resistive sensors' outputs.

The voltage signals of Fig 3 were filtered by a bandpass 256 tap FIR filter using MatLab, to preserve only the fundamental frequency (60Hz), and the root mean square (RMS) value of each filtered signal was calculated ($Vout_{RMS}$). The current (Ic_{RMS}) through C_1 was then calculated by dividing $Vout_{RMS}$ by the resistance of the sensor (|Z| in Tab. 2). The phase voltages at the bushings' main conductors (V_{MRMS}) were obtained from the substation Supervisory Control and Data Acquisition (SCADA). The voltage drop at the resistive sensors were not considered when calculating C_1, because the capacitive reactance (X_C) is higher than MΩ for the six bushings. The measured capacitances (C_M) were finally obtained from I_{CRMS} and V_{MRMS} (see Tab. 4).

Tab. 4: Currents and voltages at bushings' C_1 and their determined value (C_M). Relative errors E_1 and E_2 are related to C_p and C_o (see Tab. 3), respectively,

Bushing	$\|Ic_{RMS}\|$ [mA]	$\|V_{MRMS}\|$ [kV]	C_M [pF]	E_1 [%]	E_2 [%]
H-A	13.21	135.4	258.8	6.56	4,53
H-B	14.77	135.5	289.2	2,29	0,19
H-C	14.01	134.6	276.1	4,80	2,69
X-A	7.01	80.7	230.4	0,25	0,53
X-B	6.99	81.1	228.7	0,59	0,72
X-C	7.04	80.7	231.3	0,55	2,17

Conclusions

The preliminary results of Tab. 4 indicate that the proposed resistive sensor can be used to determine the state of capacitive bushings' insulation using a qualitative analysis. Further investigation with the sensor of H-A bushing must be conducted. Its errors are close to the thresholds of Tab. 1. If they are constant and enable the assessment of the capacitances changes, they may be compensated by the data acquisition system. Finally, the proposed sensor may also be used in future studies to determine the sum of currents through three phase sensors and to measure the power factor together with the synchronized measurement of the bus-bar voltages using potential transformers.

Acknowledgment

The present work was financed by the R&D Program of the Brazilian National Electric Energy Agency (ANEEL) - code PD 6491-0373/2015.

References

[1] CIGRE Brochure 755, WG A2-43, "Transformer Reliability Survey" (2019); ISBN 978-2-85873-457-3

[2] BRANDÃO, Marcelo; LEAL, Aline. "Apagão no Amapá não foi provocado por raio, diz laudo: Incêndio no transformador foi provocado por superaquecimento" (2020); <https://agenciabrasil.ebc.com.br/geral/noticia/2020-11/apagao-no-amapa-nao-foi-provocado-por-raio-diz-laudo>.

[3] M. Koch and M. Krüger, "A new method for online monitoring of bushings and partial discharges of power transformers", *IEEE International Conference on Condition Monitoring and Diagnosis* (2012): doi: 10.1109/CMD.2012.6416378.

[4] I. E. Comission, "Insulated bushings for alternating voltages above 1000 V" IEC 60137 Edition 6.0 (2008).

[5] Institute of Electrical and Electronic Engineers, "IEEE C57.19.01 – Standard for performance characteristics and dimension for power transformer and reactor bushing" (2017).

DOI 10.5162/SMSI2023/P26

Evaluation of microheaters for stationary miniaturized PCR thermocyclers

P. Bamerni[1], L. Mistry[1], J. König[1,2], K. Bartholomé[1,2], J. Wöllenstein[1,2], K. Schmitt[1,2]
[1] Department of Microsystems Engineering-IMTEK, Laboratory for Gas Sensors, University of Freiburg, Georges-Köhler-Allee 102, 79110, Freiburg, Germany
[2] Fraunhofer Institute for Physical Measurement Techniques IPM, Georges-Köhler-Allee 301, 79110 Freiburg, Germany
Passar.Bamerni@imtek.uni-freiburg.de

Summary:
PCR, as a very important and basic method in microbiology, is used to amplify DNA sequences and is applied worldwide, especially for the detection of diseases and viruses. Today, PCR devices are in most cases still laboratory-based, complex instruments. We present the use of microheaters with the aim to miniaturize PCR devices, making them faster, more energy efficient, mobile and cost-efficient.

Keywords: PCR, simulation, microheater, thermocycler, thermodynamics

Motivation

Polymerase **C**hain **R**eaction (PCR) has been a method used for decades to amplify nucleic acids (DNA and RNA) for the detection of hereditary diseases or viral infections. In PCR, a periodic repetition of three reaction steps is usually performed: A denaturation step to separate the two DNA strands at 92-96 °C (1. stage), primer hybridization at 55-68 °C (2. stage), and an amplification step at ~72 °C (3. stage), as outlined in Figure 1. The basic requirement for efficient amplification is a rapid heat transfer or heat dissipation into or out of the sample. Consequently, a heating element with low heat capacity and high thermal conductivity is desirable. In most traditional stationary PCR instruments, the heating and cooling rates of the heating elements used are relatively low due to components with a large thermal mass (cf. Figure 1). Miniaturization of conventional PCR instruments using novel heating elements could significantly accelerate the amplification reaction and also save reagents [1].

Our aim is to develop a thermal cycler for PCR devices that is faster, more energy efficient and smaller than previous conventional thermal cyclers, essentially by reducing the thermal mass. For this purpose, a new heating element technology for micro-PCR is evaluated. These novel heating elements have a great potential to perform PCR reactions in a small space without the need for Peltier or other coolers, thus minimizing the disadvantages of the currently available solutions for PCR.

Microheater

The most frequently used heater metallization in microsystems technology is platinum. There are several reasons in favor of platinum. The material enables a simple realization of heater structures and has a low tendency to oxidation. Platinum exhibits a linear temperature dependence of electrical conductivity and can therefore be used not only as a heater but also as a temperature sensor. The microheater is manufactured by depositing platinum on its carrier substrate, e.g. Al_2O_3, by vapor deposition or sputtering over the entire surface of the substrate. Subsequent patterning is usually done with aqua regia using a photoresist mask or alternatively with ion beam etching [2, 3].

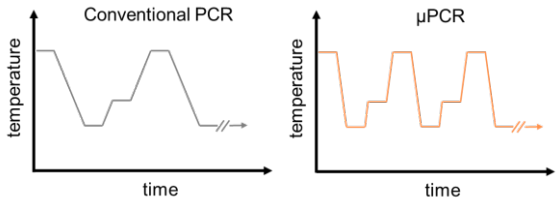

Fig. 1. PCR is based on cyclic repeating steps: Denaturation at 92°C – 96°C, hybridization at 55°C – 68°C, and polymerization at 72°C. This procedure is repeated several times. On the left, the temperature curve of a conventional PCR device with slow heating and cooling rates is shown. On the right, the µPCR is shown with faster heating and cooling rates.

Figure 2 shows the simulation of a microheater which consists of a 2.1 x 1.3 x 0.4 mm aluminum oxide substrate and a 2 mm thick platinum meander structure between two platinum pads lying on the substrate. The line width of the meander

structure is 56 µm, while the gaps between them are 15 µm. The substrate including the platinum structure is passivated with 15 µm thick borosilicate glass to prevent chemical reactions with the environment. The resistance of the microheater is 14.75 Ω. When an electrical voltage is applied to the pads, a current flows through the platinum meander structure.

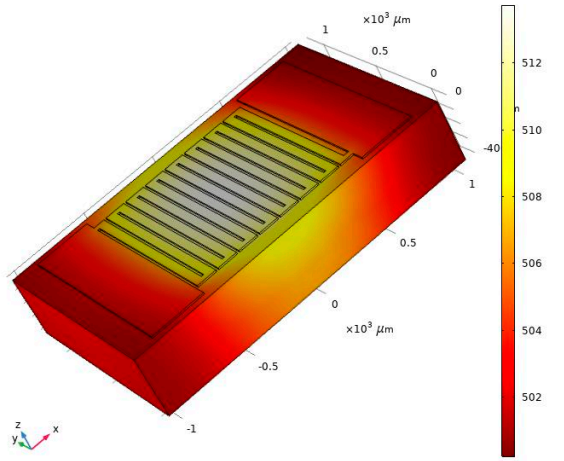

Fig. 2. The microheater consists of an aluminum oxide substrate and a meander structure made of platinum. The temperature distribution is shown in color.

The resulting Joule heating describes the conversion of electrical energy into thermal energy due to the ohmic resistance of the conducting material. Figure 2 shows the temperature distribution of the microheater in color, with maximum temperatures of over 500 K being reached at the meander structures for a voltage of 5 V.

PCR chamber

The chamber (Figure 3) is used to heat the DNA sample, which is located on the upper borosilicate glass layer of the microheater with a cylindrical volume of 10.6 µl. Compared to conventional thermal cyclers, this has the advantages that the contact resistance between heater and chamber is minimal, less energy is required for temperature cycling, and expensive reagents can be saved. The comparison of different chamber materials shows that especially metals such as aluminum allow a homogeneous temperature distribution within the chamber. This is due to the better thermal conductivity of metals with electrons as the dominant heat carrier in the particle model. Aluminum (237 W/mK) has for example a much better thermal conductivity than common ceramics such as Alumina (30 W/mK), where heat is mainly transferred via lattice vibrations. In addition, heating rates of over 20 K per second are possible with conductive metals, which is faster than commercially available thermal cyclers [4-6].

Conclusion

The use of microheaters in PCR offers new set-up possibilities. By reducing the thermal capacity and sample volume, low voltages are sufficient to generate high temperatures. The simulations confirm these assumptions. Materials as well as

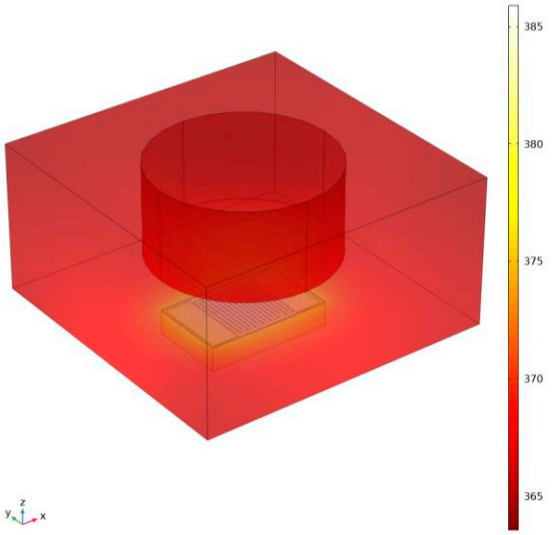

Fig. 3. The cylindrical sample chamber is placed on the microheater and has a volume of 10.6 µl.

reagents can be saved and enable cost-effective production and operation of thermal cyclers. The simulations serve as the basis for a possible battery-powered PCR solution, which enables the mobile design of thermal cyclers.

References

[1] Saiki RK, Enzymatic amplification of beta-globin genomic sequences and restriction site analysis for diagnosis of sickle cell anemia. Science. 1985 Dec 20;230(4732):1350-4. doi: 10.1126/science.2999980. PMID: 2999980.

[2] R. Zengerle, “Mikrosystemtechnik – Schichtabtragung durch Ätzen”, Script MEMS, Albert-Ludwigs-Universität Freiburg, 2015

[3] H. Frey, “Ionenstrahlgestützte Halbleitertechnologie”, VDI-Verlag, Düsseldorf, 1992.

[4] Makinson, R. (1938). The thermal conductivity of metals. Mathematical Proceedings of the Cambridge Philosophical Society, 34(3), 474-497. doi:10.1017/S0305004100020442

[5] A. Griesinger: Thermische Analyse in der Elektronik – Innovative Mess- und Simulationsmethoden für ein optimiertes thermisches Design, Cooling-Days, 23. Okt. 2013, Würzburg, Vogel Verlag.

[6] Oliveira, F. et al. A low-cost PCR instrument for molecular disease diagnostics based on customized printed circuit board heaters. Biomed Microdevices 23, 24 (2021). https://doi.org/10.1007/s10544-021-00563-2

DOI 10.5162/SMSI2023/P27

Air Quality (AQ) Sensors for Early Warning of Wildfires

J.R. Stetter[1,2], M.W. Findlay[1], D. Peaslee[2], T. Russ[2], V. Patel[1], B. Meulendyk[1], E.F. Stetter[1,2]
[1] KWJ Engineering, Inc., 8430 Central Avenue Suite C, 94560 Newark, CA, USA
[2] SPEC Sensors LLC, 8430 Central Avenue Suite D, 94560 Newark, CA, USA
Corresponding Author: jrstetter@gmail.com

Summary:

Over the past few decades, the number of wildfires and the damage caused by them has steadily increased throughout the world. The loss of lives and the cost in damages could be avoided by using low-cost, low-power, tiny but sensitive AQ sensor arrays capable to detect the environmental changes induced by wildfires. Here we report the use of such an array built from selective electrochemical sensors to detect these changes in AQ related to fires. We describe the calibration and field data for electrochemical and other AQ sensors in widespread networks for early warning systems for wildfires.

Keywords: wildfire detection, environmental sensors, electrochemical sensors, CO, particulate matter

Background, Motivation and Objective

According to the National Oceanic and Atmospheric Administration, the U.S. has suffered $553 billion in damage in weather and climate disasters since 2015. These damages were partially amassed during 79 billion-dollar disasters, 10 of which happened in California resulting in up to $100 billion in damages in California alone. Wildfires were the cause for half of these billion-dollar disasters [1]. In 2021, a total of 58,985 wildfires was recorded that caused roughly $11.2 billion in damages not accounting for the loss of life or personal traumas in affected communities and families [2]. According to the Insurance Information Institute, wildfires caused $20.8 billion in economic losses in 2021 [3]. The constant increase in number of wildfires (+223 % since 1983 [2]) and the damages caused by them led the Investor-Owned Utilities to spend $11 billion for mitigation strategies in 2021 and 2022 to prevent wildfires [4]. While the mitigation strategies are important to prevent fires from happening and to stop them once started, a system is needed additionally to detect wildfires early on when they are small and can sometimes be stopped before causing vast damage. Current methods of wildfire detection include satellite imaging, ranger eyesight and reports by civilians. Satellite imaging requires expensive instrumentation, especially with the suggested improvement discussed by the NOAA [5] where satellites rotate with the earth so they can stay focused on the most endangered parts of the earth (continuous imaging from the same area to be able to detect changes right away). Reports by civilians are chance-detections and somewhat unreliable. Similar issues are observed with detection by ranger eyesight. Rangers constantly check for fires; however, a fire often must spread before rangers are able to observe it if it started in areas that are not easily accessible for the rangers.

Since wildfires produce several different gaseous species like NO_x, CO, VOCs in addition to particulate matter [6], environmental sensors should be able to detect wildfires in their vicinity. Satellite data from 2018 has shown a severe increase in CO in areas with wildfires [7]. The same is true for PM2.5, particulate matter of 2.5 µm and smaller [5]. In a recent study, we were able to show that environmental sensors can indeed be used to detect wildfires [8]. Furthermore, we found that a mini array consisting of a CO sensor and a particulate matter sensor for PM2.5 are sufficient to obtain information on wildfires in their vicinity [8]. Data from the multiple burn events over a two-week period using a variety of wood fuels, loadings and moisture contents were monitored [8] and evaluations provided confirmation of our hypothesis that AQ changes do occur and can be detected from very small burnings at some distance, It may be possible to build effective networks with AQ sensors for early wildfire detection. The following results show some additional interpretations of the data set that reveal correlations between CO, PM2.5 and the presence of fires as well as possibilities to improve selectivity and obtain a practical deployment strategy

However, we also realized that there are several issues that need to be addressed before this technology can be used as an actual early warning system for wildfires. First, the sensors must

be connected to nodes that can communicate continuous status of the background pollutants. Second, the nodes have to be very low-cost and low-power so they can be deployed in large quantities to cover areas prone to fires. Third, sensitivity must allow for low-level detection since dilution of the fire's emissions will produce only small changes above AQ background levels in early stages of fire. We will describe the development of sensor nodes based on electrochemical sensors for the detection of wildfires, and what we have learned from their deployment including their advantages and their shortcomings. Further, the benefit of combining electrochemical sensors with a particulate matter sensor is discussed for increased selectivity, reduction of potential false alarms.

Experimental Methods

An array of electrochemical sensors (CO, SO_2, NO_2, O_3, …) and a particulate matter sensor (PM2.5) was packaged in a device (Thingy, LLC [9]) and used together with pollutant and local weather station data from nearby EPA monitoring stations. The data was analyzed to show how fires are followed using AQ measurements.

Results

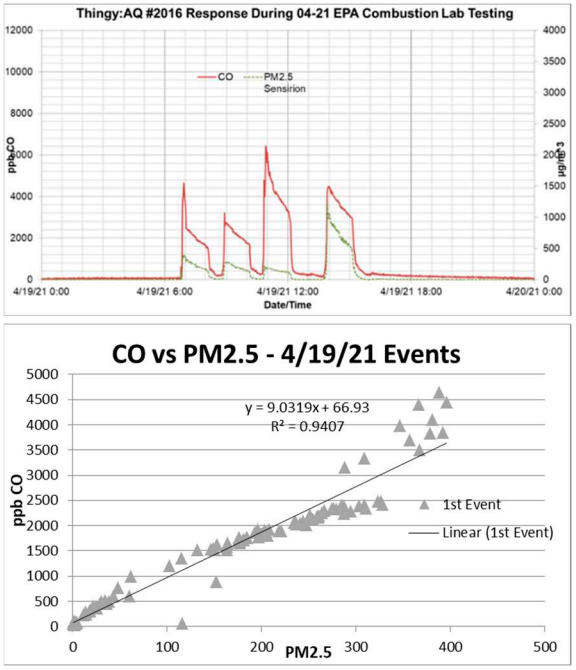

Figure 1: top: output of the respective sensors (CO: red; PM2.5: green) in four subsequent test events. Bottom: output of the CO sensor plotted against the output of the PM2.5 sensor during the first of four events shown at the top.

Figure 1a (top) shows the raw data of a particulate matter sensor (PM2.5) overlain on data from a CO sensor, Figure 1b (bottom) illustrates the linear correlation between the CO and PM2.5 for the first simulated fire event.

The comparison of the sensor data of the mini array with the reference sensors revealed: 1] while virtually all AQ parameters [T, P, RH, CO_2, CO, PM, SO_2, NO_2, O_3] varies during test burns, a single CO sensor and PM2.5 sensor could be sufficient for unambiguous detection wildfires; and 2] AQ readings from the sensor nodes were correlated to the local EPA measurements from 1- 4 miles away. This data analysis, together with the low cost of the nodes, support the hypothesis that sensor-based early detection of wildfires may be cost effective since prevention of just one big fire could save significant suffering/cost.

References

[1] https://sd27.senate.ca.gov/news/20200925-california-must-prepare-financial-fallout-cost-climate-emergency-threatens-drain, 11/21/2022. (n.d.).

[2] https://www.bankrate.com/insurance/homeowners-insurance/wildfire-statistics/#fire-damage-restoration, 11/21/2022. (n.d.).

[3] https://www.iii.org/article/background-on-wildfires, 21/11/2022. (n.d.).

[4] https://www.utilitydive.com/news/california-ious-plan-to-spend-11b-on-wildfire-prevention-in-2021-and-2022/594823/, 11/21/2022. (n.d.).

[5] https://www.nesdis.noaa.gov/news/noaa-satellites-improve-estimates-of-wildfire-smoke-air-quality-predictions, 11/22/2022. (n.d.).

[6] S.P. Urbanski, W.M. Hao, S. Baker, Chapter 4 - Chemical Composition of Wildland Fire Emissions, in: A. Bytnerowicz, M. Arbaugh, A. Riebau, C. Andersen (Eds.), Developments in Environmental Science, 2009 Elsevier B.V., 2008: pp. 79–107. https://doi.org/10.1016/S1474-8177(08)00004-1.

[7] https://climate.nasa.gov/news/2781/carbon-monoxide-from-california-wildfires-drifts-east/#:~:text=California%20is%20being%20plagued%20by,carbon%20monoxide%20into%20the%20atmosphere., 11/22/2022. (n.d.).

[8] M. Findlay, D. Peaslee, J.R. Stetter, S. Waller, A. Smallridge, Distributed Sensors for Wildfire Early Warnings, J Electrochem Soc. 169 (2022) 020553. https://doi.org/10.1149/1945-7111/ac5344.

[9] https://thingy.us/wlf/, (n.d.).

DOI 10.5162/SMSI2023/P28

Ring Magnet Optimization for Magnetic Angle Measurement

Florian Slanovc[1], Stefan Herzog[2], Michael Ortner[1]
[1] Silicon Austria Labs (SAL), Europastraße 12, 9524 Villach, Austria,
[2] ZF Friedrichshafen AG, Graf-von-Soden-Platz 1, 88046 Friedrichshafen, Germany
florian.slanovc@silicon-austria.com

Summary:
We present an optimization method for diametrically magnetized ring magnets, which are often used in magnetic angle measurement applications. For such magnet geometries, fast analytical models fail due to the strong material feedback. To address the latter, the Magnetostatic Method of Moments is implemented based on recently found analytical solutions for cylindrical rings and ring segments. The implementation is efficient enough to allow geometry optimization using standard methods.

Keywords: magnet optimization, method of moments, analytical field calculation, cylinder ring/segment/tile, magnetic angle measurement

Background and Motivation

Magnetic angle sensor systems are often realized with ring magnets with diametrical magnetization. The sensor is located inside the rotating ring (see Fig. 1), where the magnetic field is very homogeneous, so that the sensor system is quite robust against mechanical sensor displacements [1].

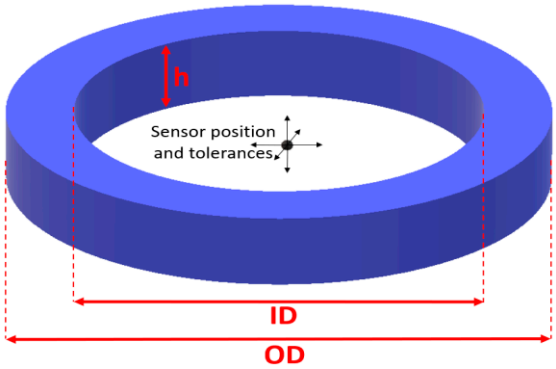

Fig. 1. Sketch of the cylinder ring with the geometrical parameters and the sensor in its center.

Recent work has shown that the Magnetostatic Method of Moments (MoM) can be used to simulate material interactions of magnetic bodies [2]. This method is particularly efficient when the region of interest is outside the magnetic material itself, which means that only a few cells are required, and when the calculation of the interaction is computationally efficient.

The open-source Python package Magpylib provides a fast and numerically stable calculation of the magnetic field of uniformly magnetized geometries based on analytical expressions from the literature [3]. The latest version 4.1.2 also includes the recently published full analytical solution for cylindrical ring segment geometries [4].

In the following, we show that it is possible to combine the analytical calculations of Magpylib with the MoM to calculate the behavior of materials in cylindrical geometries. The efficiency of the computation allows to solve system layout optimization problems with complex cost functions that are difficult to treat otherwise. With numerical methods, like finite element, it is practically impossible to solve global optimization problems in higher dimensions.

Computation Method

Our implementation of the MoM is based on point matching, which means that the cell interaction is approximated by the field at the barycenter. We choose a discretization of the cylindrical ring into ~50 elements (see Fig. 2) and a linear material response described by the susceptibility χ.

Optimization Problem

The cost function to be minimized considers the sensor displacement and the minimum field amplitude. We assume a possible mechanical tolerance of ±1 mm in the sensor position (in radial and axial directions) and want to accept a maximum angular error of 0.1° (based on a 2D field measurement, see [1]) and a minimum field amplitude of 25mT over the entire 360° rotation, regardless of the tolerances (see Fig. 1). To guarantee enough space for the sensor, we further assume ID≥10mm. With these constraints, we aim to minimize the magnetic material. It is assumed to have a magnetic remanence polarization of 500mT, a common value for bonded magnets.

Varying the inner and outer diameters ID, OD, and the height h of the cylindrical ring in Fig. 1 leads to an optimization problem in three dimensions. The objective function to be minimized is the volume of the cylindrical ring. The bounds for the angular error and the field amplitude can be included via penalty terms. This optimization can be performed with several different algorithms, e.g. differential evolution in scipy.optimize [5].

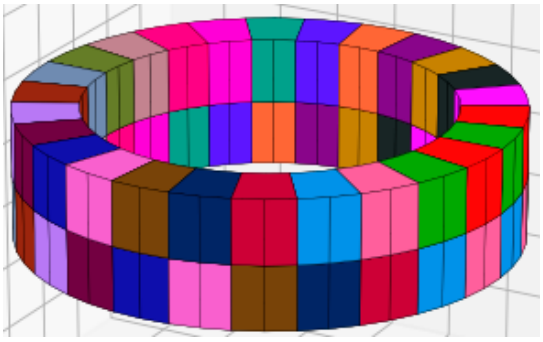

Fig. 2. Sketch of the discretized cylinder ring with ~50 cylinder cell elements. The demagnetization effect can be calculated via the interaction between the individual cells.

Results

In Fig. 3 we show that the method we use leads to a reasonable accuracy compared to the simulation with the finite element method in ANSYS for a cylindrical ring with χ=0.2 (OD=19mm, ID=14mm, h=10mm). We note that near the center we can achieve relative errors below 3% even with very few cells (see Fig. 3).

We solve the described optimization problem with three different assumptions: perfect hard magnetic material with χ=0, high quality neodymium magnets with χ=0.05 and bonded magnets with $\chi \geq 0.2$. The found optimum values for different permeabilities are shown in Tab. 1.

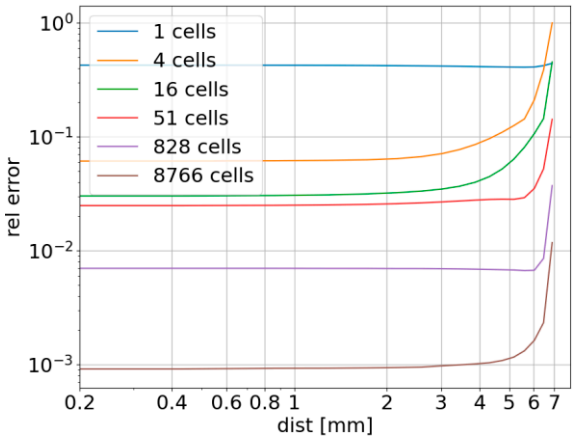

Fig. 3. Error of MoM and point matching with the analytical solution, compared with a finite element method. The maximum relative amplitude error of the field at different distances from the center is given for different numbers of cells.

Tab. 1: Results of the optimization

χ	ID [mm]	OD [mm]	h [mm]	V [mm³]
0	10.00	13.56	12.95	851.69
0.05	10.00	14.00	13.00	981.72
0.2	10.00	15.48	13.26	1454.94
0.5	10.00	18.41	13.84	2596.81

Conclusion

Using the example of angle measurement with cylindrical ring magnets, we have shown how the Magnetostatic Method of Moments can be used in combination with the analytical solution of cylindrical tiles for solving optimization problems including material response.

We have demonstrated that different susceptibility values result in different geometric optima. It is interesting to observe how strongly the required magnet volume increases with the susceptibility.

In conclusion, we have presented a good example, where optimization without consideration of material response leads to results far from the actual optimum.

References

[1] Y. Y. Lee, R.-H. Wu, S.T. Xu, Applications of Linear Hall-Effect Sensors on Angular Measurement, *2011 IEEE International Conference on Control Applications (CCA),* pp. 479-482 (2011); doi: 10.1109/CCA.2011.6044465

[2] O. Chadebec, J.-L. Coulomb, F. Janet. A review of magnetostatic moment method, *IEEE Transactions on magnetics*, 42(4):515–520 (2006); doi: 10.1109/TMAG.2006.870929

[3] M. Ortner, L. G. C. Bandeira. Magpylib: A free python package for magnetic field computation. *SoftwareX,* 11:100466, 1 (2020); doi: 10.1016/j.softx.2020.100466

[4] F. Slanovc, M. Ortner, M. Moridi, C. Abert, D. Suess. Full analytical solution for the magnetic field of uniformly magnetized cylinder tiles, *Journal of Magnetism and Magnetic Materials,* 559:169482, 10 (2022); doi: 10.1016/j.jmmm.2022.169482

[5] R. Storn, K. Price. Differential evolution – a simple and efficient heuristic for global optimization over continuous spaces. *Journal of Global Optimization,* 11:341–359 (1997); doi: 10.1023/A:1008202821328

DOI 10.5162/SMSI2023/P29

Zinc Oxide Dosimeter-type NO_2 Sensor Prepared by Discontinuous Powder Aerosol Deposition

Daniela Schönauer-Kamin[1], Mario Linz[1], Marc Herzing[1], Ralf Moos[1]
[1] Department of Functional Materials, University of Bayreuth, 95447 Bayreuth, Germany
Funktionsmaterialien@uni-bayreuth.de

Summary:
NO_2 dosimeters operated at room temperature provide an opportunity to detect the NO_2 concentration in ambient air and, specifically, directly mean values NO_2. It is evaluated whether the functional material, Al-doped zinc oxide, can also be applied by a room temperature process, the discontinuous powder aerosol deposition. The sensors are subsequently characterized with respect to their NO_2 dosimeter behavior at room temperature. Additionally, the influence of a low temperature annealing step of the DPAD-films on the NO_2-dosimeter characteristics is investigated.

Keywords: dosimeter-type sensor, NO_2 detection, zinc oxide, powder aerosol deposition, room temperature device

Dosimeter-type NO_2-sensor

NO_2 detection in ambient air is still challenging, especially concentrations in the range of ppb. For air quality control the detection of the hourly mean values or the total amount (dose) of NO_2 over a certain time interval are important. The working principle of a dosimeter-type NO_2 sensor operating at room temperature is described in [1] and [2]. The gas dosimeter detects the total dose of NO_2, i.e., the timely integration of the concentration over a certain time span, directly. The impedimetric device is based on sol-gel-synthesized Alumina-doped Zinc oxide (Al:ZnO) as functional material applied in thick-film technology [3]. During the first operation phase, the sorption phase, the NO_2 molecules are sorbed and the measured resistance changes almost linearly with the sorbed NO_2 amount. In absence of NO_2, the resistance remains constant. After reaching a certain loading state, which means that the adsorption sites are occupied, an UV-initiated regeneration phase follows. It releases all sorbed NO_2-species. Afterwards, a new loading cycle starts. The dosimeter allows for the detection of NO_2 at ppb-levels and therefore also the resulting hourly mean values.

Discontinuous Powder Aerosol Deposition

In contrast to the preparation of screen-printed thick films with consequent sintering steps at higher temperatures, the (discontinuous) powder aerosol deposition ((D)PAD) allows to prepare ceramic films at room temperature [4]. The ceramic powders are aerosolized by a carrier gas flow and accelerated into a vacuum chamber by a pressure gradient (Fig. 1). The impact of the particles leads, depending on the kinetic energy of the particles, to the formation of dense ceramic films on the substrates. Powder quantities below 100 mg can be deposited by DPAD. The nanocrystalline structure with many grain boundaries and the distorted lattice of the as deposited film lead to a high resistance of the film. Mild annealing (far below the sintering temperature) allows for restoring the reduced electric conductivity close to bulk values again [4,5].

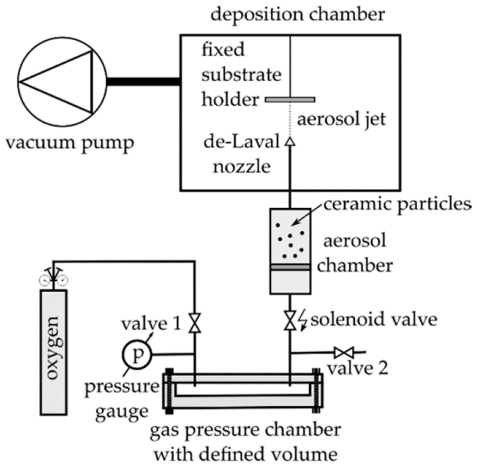

Fig. 1. Scheme of discontinuous powder aerosol deposition DPAD [4]

For a room temperature sensor device like a Al:ZnO-NO_2 dosimeter, a preparation technology working at room temperature would be advantageous. Therefore, sol-gel synthesized Al:ZnO-powders were deposited as sensing layers by DPAD and the dosimeter-type sensing characteristics of the films were investigated.

Experimental

Al:ZnO powder with 5% Al was synthesized as descried in [3]. The powder is then deposited by DPAD on top of platinum-interdigitated electrodes (IDE). To cover the IDE-area, three circular shaped films of Al:ZnO are applied. The resulting sensor device consists of a platinum heating structure on an alumina substrate and the Pt-IDE covered with the Al:ZnO-film.

The sensor behavior was investigated in dry synthetic air with NO_2 concentrations between 0 and 200 ppb at a constant flow rate. The impedance of the sensors was measured (U_{eff} = 100 mV, f = 1 Hz) and the resistance was calculated assuming an $R||C$ equivalent circuit. Before and after each measurement, the sensor was regenerated by UV-light exposure (385 nm). Additionally, the influence of thermal annealing of the Al:ZnO-films from 100 to 400 °C on the dosimeter signal (measured at RT) was characterized.

Results and Discussion

The relative resistance change $(R\text{-}R_0)/R_0$ (R_0: resistance in base gas; R: resistance with NO_2), measured at room temperature, during exposure to four NO_2 pulses are shown in Fig. 3. Indicated are the thermal annealing temperatures that are applied to the films. The sensor signal increases linearly for all annealing temperatures during NO_2 exposure and remains constant during NO_2-pauses. The sensor shows typical dosimeter-type behavior. An influence of the annealing temperature on the dosimeter behavior can be observed.

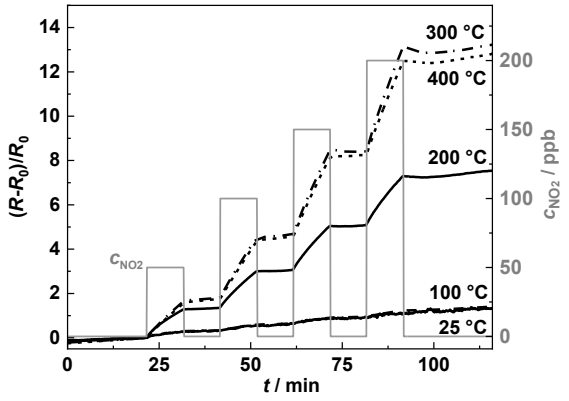

Fig. 3. Dependence of the relative resistance change $(R\text{-}R_0)/R_0$ on the NO_2-amount and the annealing temperature measured at room temperature

Fig: 4 shows the characteristic dosimeter curves, $(R\text{-}R_0)/R_0$ versus the calculated NO_2-dosis (in ppb s). Compared to screen-printed films, as expected, the DPAD-films show a lower NO_2-sensitivity. A linear relationship is visible, and the sensitivity increases with increasing annealing temperature. It is expected that the observed sensitivity increase is due to occurring oxygen desorption processes and additionally effects due to the thermal annealing of the film (relaxation of stresses, morphology changes). These processes will be investigated more in detail.

Conclusion

The work shows, that DPAD-deposited Al:ZnO films are sensitive to NO_2 at room temperature and provide dosimeter-type behavior. An influence of a thermal annealing on the dosimeter properties is observed which will be investigated in the future. Additionally, the effect of humidity needs to be addressed.

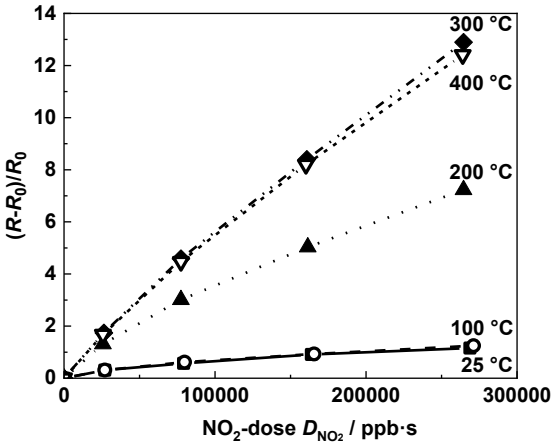

Fig. 4. Relative resistance change $(R\text{-}R_0)/R_0$ versus calculated dose of NO_x in dependence of sensor annealing temperature

References

[1] R. Wagner, D. Schönauer-Kamin, R. Moos, Novel Operation Strategy to Obtain a Fast Gas Sensor for Continuous ppb-Level NO_2 Detection at Room Temperature Using ZnO - A Concept Study with Experimental Proof, *Sensors*, 19, 4104 (2019); doi: 10.3390/s19194104

[2] R. Wagner, D. Schönauer-Kamin, R. Moos, Influence of Humidity and Different Gases on a Resistive Room Temperature NO_2 Gas Dosimeter Based on Al-Doped ZnO for ppb-Concentration Detection, *Journal of The Electrochemical Society* 167, 167516 (2020); doi: 10.1149/1945-7111/abcb65

[3] L. Vogel, R. Wagner, R. Moos, D. Schönauer-Kamin, Investigations on the crystal growth mechanism of one-pot-synthesized Al-doped ZnO and its UV-enhanced room temperature NO_2 gas sensing characteristics, *Functional Materials Letters*, 11, 1850087 (2018), doi: 10.1142/S179360471850087X

[4] M. Linz, J. Exner, J. Kita, F. Bühner, M. Seipenbusch, R. Moos, Discontinuous Powder Aerosol Deposition: An Approach to Prepare Films Using Smallest Powder Quantities, *Coatings* 11, 844 (2021); doi: 10.3390/coatings11070844

[5] Exner, T. Nazarenus, D. Hanft, J. Kita, R. Moos: What Happens during Thermal Post-Treatment of Powder Aerosol Deposited Functional Ceramic Films? Explanations Based on an Experiment-Enhanced Literature Survey, *Advanced Materials* 32,1908104 (2020), doi: 10.1002/adma.20190810

DOI 10.5162/SMSI2023/P30

Near-process Indirect Surface Geometry and Temperature Measurement for Laser Chemical Machining (LCM)

Merlin Mikulewitsch[1], Yasmine Bouraoui[3], Tim Radel[3], Dirk Stöbener[1,2], Andreas Fischer[1,2]
[1]University of Bremen, Bremen Institute for Metrology, Automation & Quality Science, Linzer Str. 13, 28359 Bremen, Germany. [2]MAPEX Center for Materials and Processes, P. O. Box 330 440, 28334 Bremen, Germany. [3]BIAS - Bremer Institut für angewandte Strahltechnik GmbH, Klagenfurter Straße 5, 28359 Bremen, Germany. Contact: m.mikulewitsch@bimaq.de

Summary:

Laser chemical machining (LCM) is intentionally limited in its removal rate to avoid disturbing boiling bubbles in the process fluid. To overcome this limitation, an enhanced material removal model is required based on surface geometry and temperature in-process data. For this purpose, fluorescence measurements and confocal microscopy are combined to enable in-process experiments in LCM environment. Derived from fluorescence effects, the geometry and surface temperature are indirectly determined under LCM-equivalent conditions such as thick fluid layers and gas bubbles in the beam path.

Keywords: Geometry measurement, in-process measurement, signal modeling, laser chemical machining, confocal fluorescence microscopy

Introduction

Compared to micro-manufacturing processes such as micro-milling, laser chemical machining (LCM) achieves higher dimensional accuracy at acute edge angles and small edge radii [1]. However, its manufacturing speed is significantly lower since the process energy, or removal rate respectively, supplied by a focused laser is severely limited to avoid the creation of disturbing boiling bubbles in the process fluid when the induced surface temperature reaches the boiling point. The influence of boiling bubbles on the material removal rate can be reduced by adjustments of the laser beam and fluid properties (e.g. beam shape or fluid viscosity). However, to achieve an increased removal rate while maintaining removal quality, the current understanding of removal mechanisms must be fundamentally expanded. In this context, comprehensive LCM process modeling that incorporates the boiling bubble influence is only possible through in-process measurements of the surface geometry, the surface temperature, and the boiling bubbles in the removal zone. With the complex fluid environment, the gas bubbles occurring during removal, and the measurement requirements for the manufactured cavities, no suitable in-process measurement technique exists for the cavity geometry or the process-relevant surface temperature. Due to various aspects, conventional optical geometry measurement methods are unsuitable for a near-process application in the LCM environment. Refractive index variations in the process fluid prevent the use of interferometric methods and steep edge angles produce unavoidable artifacts due to unwanted reflections in measurements using confocal microscopy [3]. In contrast, an indirect geometry measurement using confocal fluorescence microscopy is not subject to these interferences. The method has already been successfully applied close to the process in manufacturing environments with fluid layers as thin as 120 µm [4] and in situ in fluid layers several millimeters thick [5]. However, no near-process application of the indirect measurement approach has been performed in the LCM process environment to date. Thus, it is of fundamental interest to investigate whether removal geometry and temperature can in principle be measured in the LCM process environment with thick fluid layers, interfering gas bubbles, or particles in the beam path.

Measurement principle

The indirect measurement technique is based on a conventional confocal fluorescence microscope with a model-based evaluation of the fluorescence signal to measure the micro-geometry and temperature in the mm-thick fluid layers present in LCM [5]. In contrast to conventional methods, which use the light scattered from the surface, the indirect principle determines the fluid boundary layer to the workpiece by detecting the fluorescence light emitted by the fluid, from which the geometry and temperature of the

workpiece are inferred. Since light is detected even at angles > 75° to the surface normal, samples with steep edges can also be measured [2]. The detection of the fluorescence signal is limited to a confocal volume around the focal plane of the objective. If the confocal volume moves in z-direction through the fluid, a characteristic fluorescence signal S is generated, which can be modeled as follows:

$$S(x,y,z) = S_0 \cdot \left(\operatorname{erf}\left(\frac{z - z_0(x,y)}{2\Xi} + \epsilon\Xi \right) - \operatorname{erf}\left(\frac{z - z_1}{2\Xi} + \epsilon\Xi \right) \right) \cdot \mathrm{e}^{\epsilon(z - z_1)} \quad (1)$$

Here, $S_0 = f(T(x,y,z),\epsilon)$ represents a parameter of the total fluorescence intensity that is dependent on the temperature and the concentration dependent absorption parameter ϵ while Ξ describes the properties of the confocal volume, and z_1 the position of the fluid surface. From the pointwise measured fluorescence signal $S(x,y,z)$, eq. (1) the surface geometry $z_0(x,y)$ and temperature distribution $T(x,y,z)$ is determined by a least squares approximation.

Results

The result of an indirect in-situ geometry measurement under LCM-equivalent environmental conditions, i.e. gas bubbles generated during material removal contaminating the fluid, is shown in Fig. 1a. It turns out that the presence of gas bubbles in the fluid directly above the measured object, does not hinder the determination of a surface position but leads to an increased measurement uncertainty that correlates with the gas bubble density. The model-based evaluation of the indirect measurement of the fluorescence intensity signal enables the indirect measurement approach to compensate for the signal noise resulting from the presence of interfering gas bubbles in the beam path by considering the total signal data in the least squares optimization. As a result, the indirect geometry measurement approach is shown to cope with realistic process conditions such as contaminated fluids while also enabling measurements of steep surface geometries and in thick fluid layers, as required for use in the LCM environment. In order to demonstrate the capabilities of the indirect measurement approach with regard to near-surface temperature measurements, a metal foil submerged in a fluorescent solution is heated on the bottom side by a gaussian laser profile. At the same time, the fluorescence intensity on the top side of the foil surface is measured confocally at a constant distance close to the surface. The lateral temperature profile resulting from the temperature-dependent fluorescence signal is shown in Fig. 1b. While this intensity-based measurement required calibration to yield quantitative results, it highlights the potential for simultaneous temperature and geometry measurements when the temperature is considered in the fluorescence signal model (see eq. 1).

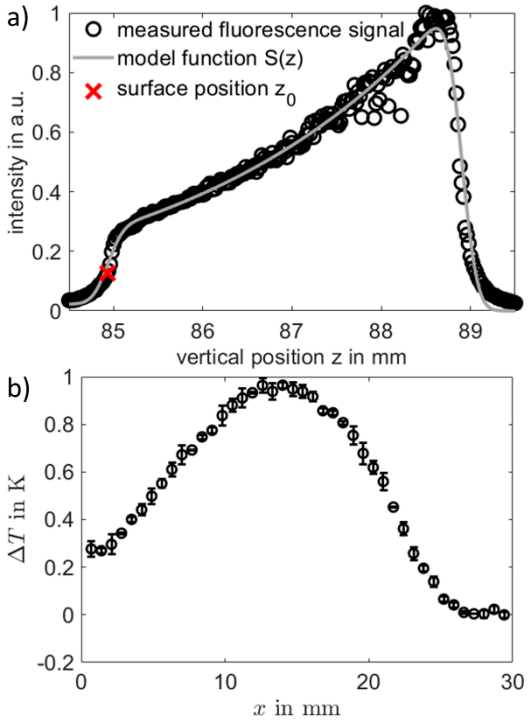

Fig. 1: a) Fluorescence signal and surface position z_0 resulting from model-based evaluation in a fluid contaminated with gas bubbles. b) Temperature profile on the top side of a submerged metal foil heated on the bottom side by a laser, measured via fluorescence.

Financial support: Deutsche Forschungsgemeinschaft (DFG) project no. 451385285.

References

[1] Messaoudi, H., et al., Chances and Limitations in the Application of Laser Chemical Machining for the Manufacture of Micro Forming Dies, Proc. of the 5th Int. Conf. on New Form. Techn. ICNFT, 1-8 (2018); DOI: 10.1051/matecconf/201819015010

[2] J. Liu, C. Liu, J. Tan, et. al., Super-aperture metrology: Overcoming a fundamental limit in imaging smooth highly curved surfaces, J. of Microscopy 261, 300–306 (2016); DOI: 10.1111/jmi.12334

[3] K. Maruno, M. Michihata, et. al., Fundamental study on novel on-machine measurement method of a cutting tool edge profile with a fluorescent confocal microscopy, Int. J. Autom. Technol. 10, 106-113 (2016); DOI: 0.20965/ijat.2016.p0106

[4] Y. Takaya, K. Maruno, M. Michihata, Y. Mizutani, Measurement of a tool wear profile using confocal fluorescence microscopy of the cutting fluid layer, CIRP Annals 65, 467–470 (2016); DOI: 10.1016/j.cirp.2016.04.014

[5] A. Fischer, M. Mikulewitsch, D. Stöbener, Indirect fluorescence-based in situ geometry measurement for laser chemical machining, CIRP Annals 69, 481-484 (2020); DOI: 10.1016/j.cirp.2020.03

DOI 10.5162/SMSI2023/P31

Thin quartz resonators as detector element for thermal infrared sensors

A. Eydam[1], *V. Norkus*[1], *G. Gerlach*[1]
[1] *Technische Universität Dresden, Solid State Electronics Laboratory, 01062 Dresden, Germany*
agnes.eydam@tu-dresden.de

Summary:
In this work, we describe the technology and packaging of a quartz sensor with a thickness of 5 µm. The temperature dependence of the resonance frequency of quartz resonators can be used for thermal radiation sensors. The sensitive element in the form of a bowl or a cantilever is ion beam etched and must be able to vibrate freely. Impedance measurements show the vibration of the 5 µm thick resonators, however highly damped and with a low quality factor.

Keywords: quartz resonator, thermal infrared sensor, ion beam etching, packaging, impedance spectrum

Introduction

Thermal radiation sensors absorb infrared radiation which results in a temperature change in the responsive element. Depending on the used physical effect the change of a physical quantity is usually transformed in a signal voltage, i.e. in pyroelectric sensors.

Quartz resonators on the other hand use the temperature dependence of the resonance frequency of piezoelectric oscillators. Frequency can be measured with great accuracy. These sensors stand out by a high specific detectivity D^* whereby very small radiation fluxes can be detected. Quartz bulk sensors with Y-cut and a thickness of 7 µm achieved a value of $D^* = 9 \cdot 10^7$ cmHz$^{1/2}$W^{-1} [1].

Goal of this work is the improvement of sensor parameters which directly influence the sensitivity like quartz thickness decreasing, thermal conductance between sensor and environment and the absorption coefficient.

Here, we present a technological procedure for manufacturing quartz sensors with a thickness of 5 µm with both plate and beam-like structures.

Manufacturing Technology

Starting point for the fabrication of the resonator devices are quartz wafers with a size of (20 x 20) mm² and a thickness of 500 µm (Quarztechnik Daun GmbH, Daun, Germany). They are thinned down to a thickness of 20 µm by lapping and polishing and cut to chips with a size of (4 x 4) mm². The chips are structured by photolithography followed by depositing thin films or by removing material. Electrode films of NiCr and Au are deposited by thermal evaporation. Structures like bowl-like cavities and trenches are ion beam etched.

In a first step, sensors were build up with unstructured quartz chips after each technology step (lapping, polishing, etching) to investigate their influence on the vibration because the crystal structure may be damaged by processing its surface [2]. However, our measurements showed no influence on the vibration.

After that, two sensor layouts were implemented:

- In the first layout, the front and back electrode form a cross. The sensitive element is the overlapping part where a bowl with a thickness of 5 µm is etched in the chip (Fig. 1a). The sensors are build up on a TO8 holder. A substrate is glued on the holder and the quartz chip is put on silicon rods so that it can vibrate freely (Fig. 2a).
- The second layout consists of a 5 µm thin cantilever which is connected to the thicker frame by a narrow bridge (Fig. 1b). The trench between cantilever and frame keeps the sensitive element thermally isolated. Here, the frame is firmly fixed on a substrate with a deepening in the middle leaving the cantilever versatile (Fig. 2b). This layout has been used successfully for pyroelectric $LiTaO_3$ sensors [3].

Before the 5 µm thin quartz chips were manufactured, the technology had been tried out with 80 µm thick chips.

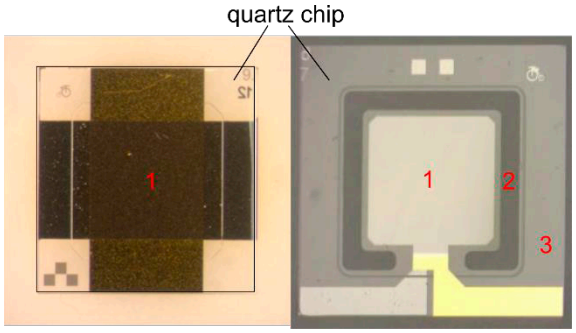

(a) (b)

Fig. 1. Two sensor layouts: a) sensitive element (1) as a bowl and (b) sensitive element (1) as a cantilever with trench (2) and frame (3).

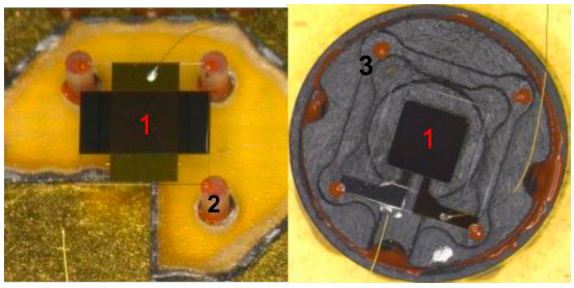

(a) (b)

Fig. 2. Sensor packaging for a) first layout with quartz chip (1) on silicon rods (2) and for b) second layout with quartz chip (1) fixed on substrate (3).

Measurement Results

The fundamental resonance frequency of a quartz crystal vibrating in thickness mode is determined by

$$f_r = \frac{1}{2d}\sqrt{\frac{c}{\rho}}, \qquad (1)$$

where *d* is the thickness of the quartz plate, *c* the Young's modulus and *ρ* the density [4].

Impedance measurements show the resonance frequency and the quartz parameters may be derived from them.

The following results refer to the first sensor layout with the bowl. The impedance spectrum of a sensor with a quartz resonator thickness of 80 µm shows a distinct peak at 25 MHz (Fig. 3a). The sensors with 5 µm thin sensitive elements which corresponds to a frequency of 370 MHz develop only a small and broad peak, however (Fig. 3b). In the latter case, the quartz crystal vibrates highly damped and with a low quality factor.

Measurements with the second sensor layout are going to follow which should improve the vibration amplitude.

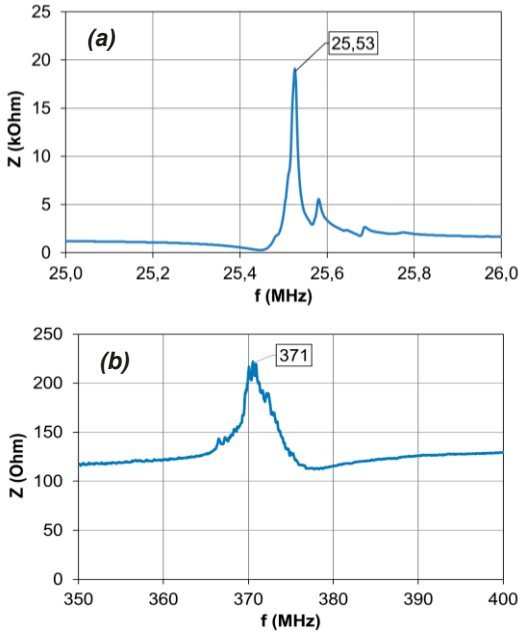

Fig. 3. Impedance spectrum (absolute value of the complex impedance Z) of a quartz resonator with a thickness of (a) 80 µm and (b) 5 µm.

Conclusions

Quartz chips were successfully thinned down to 5 µm by lapping, polishing and ion beam etching. Sensors with two different layouts were build up. 80 µm thick quartz resonators show a strong peak in their impedance spectrum, whereas the vibration of the thin crystals is highly damped. An optimized sensor layout and packaging should improve the vibration quality.

Acknowledgement

This research is supported by the Deutsche Forschungsgemeinschaft (DFG) in context of the project GE 779/44-1 "Schwingquarzsensoren zur hochauflösenden Detektion von infraroter Strahlung".

References

[1] K. Ren, M. B. Pisani, P. Kao and S. Tadigadapa, Micromachined quartz resonator-based high performance thermal sensors, *Sensors*, *2010 IEEE*, 2197-2201 (2010); doi: 10.1109/ICSENS.2010.5690612

[2] J. Danel und G. Delapierre, Quartz: a material for microdevices, *J Micromech Microeng* 1, 187-198 (1991); doi: 10.1088/0960-1317/1/4/001

[3] V. Norkus, M. Schossig, G. Gerlach, R. Köhler and G. Hofmann, Pyroelektrische Infrarotsensoren mit hoher spezifischer Detektivität, *TM* 81, 99-106 (2014); doi: 10.1515/teme-2014-1018

[4] J. Vig and R. Filler and Y. Kim, Uncooled IR imaging array based on quartz microresonators, *J Microelectromech Syst* 5, 131-137 (1996); doi: 10.1109/84.506201

DOI 10.5162/SMSI2023/P32

Homogeneous Soil Moisture Sensor with High Repeatability for Different Soil Depths.

Thomas Maier[1], *Lukas C. Kamm*[2], *Andreas W. Heckmann*[2], *Björn M. Eskofier*[1]
[1] *Department Artificial Intelligence in Biomedical Engineering, Friedrich-Alexander University Erlangen-Nuernberg, Erlangen, Germany,*
[2] *Agvolution GmbH, Philipp-Reis-Str. 2A 37075 Göttingen, Germany*
thomas.maier@FAU.de

Summary:
This paper presents a solution in measuring the moisture content of soil more reliably and more reproducibly. The sensor can detect moisture levels in different depths of the soil probed and in a more homogeneous way than comparable sensors that are commonly used. The repeatability of the measurement is also increased intrinsically because a larger soil volume is being sampled.

Keywords: Soil moisture sensor, FDR, Plate capacitor

Introduction

A lot of data generated by existing sensor systems has the problem of being very dependent on the installation process. Due to miniaturization of sensors and the heterogeneity of the soil volume probed, the latter is also often not contributing homogeneously to the measured values. A result is that many sensors that are currently used professionally have problems with repeatability and need to be calibrated. A thorough comparison of existing soil moisture sensor systems with different measurement principles is given in [1].

When examining the analyzed sensors in that paper, two things become clear. First, they only measure the soil moisture in a relatively small volume of around 600 ml. And second, they are all either using very punctual measurement probes or a highly non-homogeneous electrical field for their Frequency Domain Reflectometry (FDR) measurements. But soil itself can be very heterogeneous as presented in [2], which makes it unclear how well the sensed moisture values reflect the actual soil moisture content.

In order to avoid this, a solution is presented with improved performance and quantified sensor repeatability.

Approach

When using FDR probes with two rods as measuring electrodes, the non-linear behaviour of the electric field is causing problems. This is due to the fact that the electrodes generate an electric field similar to that of an infinite long line of charge, which can be described as follows [3]:

$$\vec{\mathbf{E}}_{\mathrm{line}}(\rho) = \frac{\lambda}{2\pi\epsilon_0\rho}\vec{\mathbf{e}}_{\rho} \qquad (1)$$

$\vec{\mathbf{E}}_{\mathrm{line}}(\rho)$: Electric field of line charge density at radius ρ
λ: Line charge density
ϵ_0: Dielectric constant
$\vec{\mathbf{e}}_{\rho}$: Unit vector in ρ direction

The electric field is inversely proportional to the distance from the electrodes and therefore strongest when close to the rods. If the rods are placed in the soil loosely or directly next to a big irregularity in the soil (e.g. stones or air pockets), the measured values differ very much. Water that accumulates directly on the sensor rod surfaces then also has a higher impact on the measured value. This effect was exploited in [4] for a specific measurement purpose but is generally not desired.

A solution for this problem is to use differently shaped electrodes. Instead of rods placed in the soil, two plates can be used. These imitate the electric field of a surface charge density with infinite surface as follows:

$$\vec{\mathbf{E}}_{\mathrm{surf}}(\mathrm{d}) = \frac{\sigma}{2\epsilon_0}\vec{\mathbf{e}}_{\mathrm{d}} \qquad (2)$$

$\vec{\mathbf{E}}_{\mathrm{surf}}(\mathrm{d})$: Electric field of surface charge density at distance d
σ: Surface charge density
$\vec{\mathbf{e}}_{\mathrm{d}}$: Unit vector in d direction

Equation (2) shows that the electric field strength between two plates is independent of the distance d from the plates. Therefore, this design is further evaluated.

Experimental Setup

In order to measure in different soil depths, 3 pairs of electrodes were realized on a printed circuit board (PCB). The capacitance between the electrodes was measured using the FDC2214 measurement chip [5]. The traces were shielded with ground potential with the 4-layer PCB structure to minimize external noise. The final sensor design can be seen in fig. 1.

Fig. 1. Sensor setup.

Installing the sensor in the soil can be accomplished by pre-punching the necessary slits in the soil with a hammer and a dummy sensor. This makes it possible to probe the soil almost in its original condition.

Results

First, the designed sensor was inserted into soil multiple times. The offset of the measured capacity was subtracted and normalized over the whole dynamic range. A histogram of the repetitions can be seen in fig. 2 for different heights.

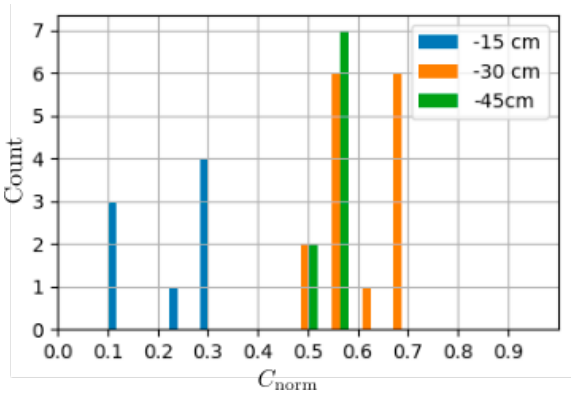

Fig. 2. Installation histogram with number of occurrence against normalized capacity.

For multiple insertions, the measured and normalized capacity is within 15 % of the total dynamic range, which is comparable to the sensors in [1]. The top sensor has a lower capacity because the soil is dryer on the surface.

In the next step, two latex balloons were filled with approximately 1.5 liters of air and water. These balloons were slightly squeezed between the different measurement levels. The measured capacities are shown in table 1. The volumetric sensitivity is calculated by subtracting the offset value of the air balloon from the water balloon and the completely submerged sensor value. The ratio between the water balloon between the sensor legs and the completely submerged sensor quantifies the contribution of water directly at the measurement point compared to the maximum possible value when the sensor is submerged. For two demo sensors the values lie within 50 % - 65 %.

Tab. 1: Volumetric sensitivity of two demo sensors

	$C_{\mathrm{b,a}}$	$C_{\mathrm{b,w}}$	C_{sub}	δ_{sen}
-10 cm	415 pF	457 pF	476 pF	68.8 %
	398 pF	428 pF	446 pF	62.5 %
-30 cm	350 pF	388 pF	413 pF	60.3 %
	334 pF	359 pF	387 pF	47.9 %
-45 cm	273 pF	311 pF	332 pF	64.4 %
	269 pF	297 pF	318 pF	57.1 %

$C_{\mathrm{b,a}}$: Capacity with air filled balloon
$C_{\mathrm{b,w}}$: Capacity with water filled balloon
C_{sub}: Capacity when submerged in water
δ_{sen}: Volumetric sensitivity

Conclusion and further work

The sensor design presented has a quantified installation sensitivity of around 15 % and volume sensitivity value of 50 % - 65 % in 1.5 liters of probe volume. It is therefore able to give a rough estimate of the soil moisture without calibration needs and a homogeneous measurement principle.

During the work it was noticed that the measured value is temperature sensitive and the thick sensing legs require heavy tools for the insertion. In future work the temperature sensitivity can be eliminated by implementing a differential measurement principle and the installation uncertainty can be improved by a thinner leg design because it is less invasive to the soil.

References

[1] C. Jackisch, K. Germer, et al, Soil moisture and matric potential – an open field comparison of sensor systems, *Earth System Science Data* 12, 683-697 (2020); doi: 10.5194/essd-12-683-2020

[2] O. Kanoun, A. Tetyuev, Bodenfeuchtemessung mittels Impedanzspektroskopie, *Technisches Messen* 71, 475-485 (2004); doi: 10.1524/teme.71.9.475.42751

[3] D. Fleischmann, Basiswissen Elektrotechnik, *Vogel Verlag Würzburg* 1st edition, 376-378 (1999); ISBN: 3-8023-1781-5

[4] T. Maier, L. Kamm, Moisture sensor for gravitation dependent plant watering, *International Astronautical Congress* 68, 1-7 (2017)

[5] Texas Instruments Inc., FDC2x1x EMI-Resistant Capacitance-to-Digital Converter, *Datasheet*, 1-62 (2015)

DOI 10.5162/SMSI2023/P33

Visualization of Magnetic Nanoparticles by Ultrasound Strain Imaging

Christian Marinus Huber[1,2], Karim El Aawar[2], Helmut Ermert[1], Ingrid Ullmann[2], Stefan Lyer[1]
[1] Department of Otorhinolaryngology, Head and Neck Surgery, Section of Experimental Oncology and Nanomedicine, Professorship of AI-controlled Nanomaterials, Universitätsklinikum Erlangen, Glückstraße 10a, 91054 Erlangen, Germany
[2] Institute of Microwave and Photonics, Friedrich-Alexander-Universität Erlangen-Nürnberg, Cauerstraße 9, 91058 Erlangen, Germany
Christian.Ch.Huber@fau.de

Summary:
In magnetic drug targeting, superparamagnetic nanoparticles are used as drug carriers. The local accumulation of these particles at the site of the tumor leads to a temporary change in the effective elastic tissue properties in this area. Therefore, mapping this change should allow visualization of the particle distribution. Ultrasound strain imaging is a method to map the local variation of elasticity. This method was tested using a polyvinyl alcohol ultrasound phantom with a magnetic nanoparticle inclusion. It was demonstrated, that this inclusion can be mapped in the proposed way.

Keywords: Ultrasound imaging, ultrasound elastography, magnetic nanoparticles, magnetic drug targeting

Introduction

The goal of modern chemotherapeutic treatment of cancer is dosing the drug in such a way that the tumor is treated efficiently, while the patient tolerates the dose and faces a minimum of side effects. However, these methods can cause damage to normal tissues or fail in eradicating the cancer completely. Magnetic drug targeting (MDT) using magnetic nanoparticles (MNP) as drug carriers has experimentally proven effective in the treatment of tumors for the direct and selective delivery of chemotherapeutic drugs to the tumor region [1]. Yet, real-time imaging of MNP distribution during the magnetically enhanced tumor treatment is still not fully realized. Ultrasound imaging would be a suitable tool for imaging MNP, but the particles' backscatter is too small for direct imaging. However, the accumulation of MNPs in the tumor area should lead to a temporal change in the mechanical properties of the particle-laden tissue. Mapping this change might allow for the detection of the MNPs. Therefore, ultrasound strain elastography was used in this work to map the MNP distribution. In addition, this method would allow performing MDT and MNP-imaging at the same time.

Ultrasound Strain Elastography

Ultrasound strain elastography based imaging allows for the qualitative assessment of tissue elasticity [2]. It provides a noninvasive method through mechanical stress to detect differences in tissue elasticity based on the changes in tissue displacement. Strain images are generated by using the ultrasound transducer to apply minimal pressure to the tissue. The subsequent tissue displacement is tracked between pairs of RF echo frames and the strain is calculated from the axial gradient of the displacement (see Figure 1).

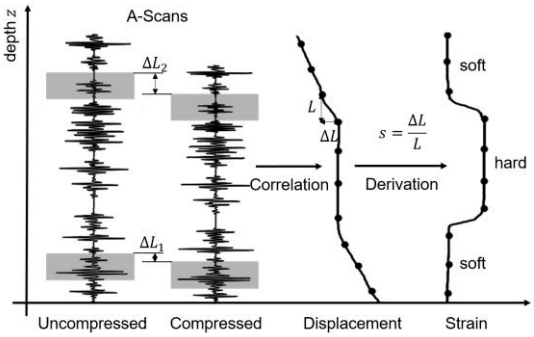

Fig. 1. Determination of local strain obtained from the uncompressed and compressed A-scan/RF-Data.

In the axial derivation

$$s = \frac{\Delta L}{L}, \qquad (1)$$

ΔL is the displacement between pre- and post-compression RF echo frames and L is the size of one frame. The frame size is adjusted according to the mechanical displacement of the transducer. It is four times larger than the induced displacement, to ensure that the displaced echo is

still within the frame. Now, the cross-correlation function of the two RF echo frames is computed:

$$\hat{R}_{xy}(m) = \begin{cases} \sum_{n=0}^{N-m-1} x_{n+m} y_n^*, & m \geq 0, \\ \hat{R}_{xy}(m), & m < 0. \end{cases} \quad (2)$$

N is the frame size and m the delay between the two RF-signals x_n, y_n. The displacement is then calculated from the delay m of the maximum correlation value:

$$\Delta L = \max_m \{\hat{R}_{xy}(m)\} \cdot z_S. \quad (3)$$

z_S is the sampling interval.

Experimental Setup

To investigate the imaging potential of the MNP with ultrasound strain elastography, ultrasound phantoms were created according to [3]. The material used here was polyvinyl alcohol (PVA). The PVA was filled in a mold with a centrally positioned cylindrical recess with a diameter of 20 mm. This opening was filled with PVA containing magnetic nanoparticles (SEON-Dex30) with an iron content of 15.84 mg/ml and a hydrodynamic diameter of 30.23 nm. Hardening of the PVA tissue phantoms was achieved by two overnight freeze-thaw cycles at -20° C.

Ultrasonic measurements were performed using the ultrasound research platform *Verasonics Vantage 64LE* and a linear array transducer (L11-5v, 128 elements, 7.6 MHz center frequency). The transducer was fixed in a mechanical shift device for precise compression. The ultrasound phantom was placed below the transducer. Ultrasound gel ensured acoustic coupling of the transducer and the phantom. Two sets of ultrasound data were measured. One before and one after compression was applied with the transducer. These sets of data were then processed offline. No magnetic field was applied during the measurements.

Results

Four different compression levels (0.1 mm, 0.5 mm, 1 mm and 2 mm) were tested to evaluate the robustness and effectiveness of the elastography method in terms of MNP imaging (Fig. 2). As shown, the correlation-based elastography method was highly dependent on the induced compression. With lower compression (0.1 mm and 0.5 mm), the MNP-inclusion was clearly distinguishable from the surrounding phantom area, with the 0.5 mm compression giving the best results. The area of the stiffest region (yellow) matched the inclusion (dashed circle). Particle-laden tissue is stiffer due to the iron content of the MNPs. At higher degrees of compression, the method failed to find the correct displacement and corresponding strain. This is a typical problem of the correlation method [2].

Conclusion

In this work, imaging of a magnetic nanoparticle inclusion within a PVA ultrasound phantom was presented. Based on a temporal ultrasound strain elastography algorithm the MNP inclusion was mapped. Ultrasound A-Scans were compared frame-wise before and after compression. The displacement between two frames was then computed and used as a measure of strain. This method can help to map the magnetic nanoparticle distribution in context of magnetic drug targeting. Future goals are to enhance the resolution and sensitivity using more sophisticated displacement estimation methods. Additionally, this method will also be tested during magnetic field exposition and under flow conditions.

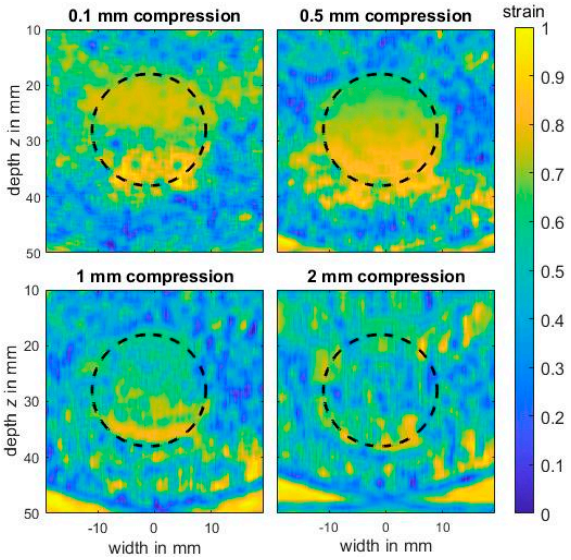

Fig. 2. Computed ultrasound strain images of PVA-phantoms with magnetic nanoparticle inclusion (black dashed circle) at different degrees of compression.

References

[1] R. Tietze, et al., Efficient drug-delivery using magnetic nanoparticles - biodistribution and therapeutic effects in tumour bearing rabbits, Nanomedicine: Nanotechnology, Biology and Medicine 9, 961-971 (2013); doi: 10.1016/j.nano.2013.05.001

[2] J. Ophir, et al., Elastography: ultrasonic estimation and imaging of the elastic properties of tissue, Journal of Engineering in Medicine 213, 203-233 (1999); doi: 10.1243/0954411991534933

[3] M. Fink, S. J. Rupitsch, S. Lyer and H. Ermert, Quantitative Determination of Local Density of Iron Oxide Nanoparticles Used for Drug Targeting Employing Inverse Magnetomotive Ultrasound, IEEE Transactions on Ultrasonics, Ferroelectrics, and Frequency Control 68, 2482-2495 (2021); doi: 10.1109/TUFFC.2021.3068791

DOI 10.5162/SMSI2023/P34

Microphone Based System for Visualization of Vibration Patterns

Artem Ivanov[1], *Arne Kulinna*[1]
[1] *Landshut University of Applied Sciences, Am Lurzenhof 1, 84036 Landshut, Germany*
Artem.Ivanov@haw-landshut.de

Summary:
An acoustic system for measurement and visualization of surface vibrations is described. Based on pressure gradient probes implemented with low-cost MEMS microphones, the system features highly parallel signal processing using low performance cores. Currently, the validation of the proposed method is ongoing. Presented results demonstrate the fundamental functionality of the system both for stationary and transient processes.

Keywords: contactless vibration visualization, microphone array

Introduction

Visualization of surface vibrations is of interest e.g. in structural health monitoring [1] or in investigations of musical instruments [2]. It can be accomplished in different ways, including Chladni powder patterns, speckle pattern interferometry and laser vibrometry to name a few. The methods have their own advantages and limitations and differ in the necessary instrumentation effort. The proposed visualization method targets applications where primarily the vibration pattern itself is of interest, whereas the absolute value of surface dislocation is secondary. It is based on acoustic measurement to allow a contactless acquisition of surface vibrations. The goal is to avoid sequential surface scanning and to be able to capture the propagating surface waves after a single excitation.

Near-Field Acoustic Holography (NAH) was shown to deliver surface vibration patterns in quasi stationary processes [3]. The method described here is based on the two-microphone technique [4], it differs from NAH in several basic aspects and potentially allows observing wave propagation. Two existing versions of system design feature parallel signal processing using microcontrollers, they rely on miniature MEMS microphones and target low hardware cost. Presently, the validation of the method is ongoing based on the system design described below. The current goals are the verification of the results and the defining the region of applicability of the method.

Measurement Principle and System Setup

The implemented system contains a number of measurement channels designed as pressure gradient probes with two closely spaced MEMS microphones (Fig. 1a). As the pressure gradient is proportional to the time derivative of particle velocity (Euler equation), its double integral leads to the particle displacement. Under the assumption that the object surface translates its motion into the motion of the air particles, the orthogonal component of the pressure gradient contains information about the surface motion. The approximation of the full vibration pattern is made by interpolating the measured surface displacements between the channel positions. This approach allows parallel processing of microphone signals up to the point where all data must be combined for visualization. Key advantages of the processing algorithm are simplicity and stability. The requirements on the single processing cores are drastically reduced on the cost of their number.

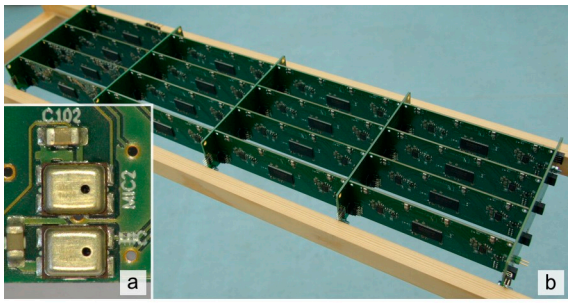

Fig. 1. (a) A close-up view of a measurement channel. Spacing between the microphone input ports is 3 mm. (b) The tested system with 64 channels.

The measurement system consists of identical sensor boards, several connector boards to set up a sensor array and a master board which controls the measurement process and transfers the results to a PC. Each sensor board

contains four measurement channels and a microcontroller to process the signals. The microphone pairs are mounted close to the PCB edge, which is directed towards the object surface during the measurement. The current design of the system targets measurements on more or less planar objects.

The results presented below were acquired with a 64-channel system arranged in a 16 by 4 matrix (30 mm channel spacing) covering a 450 × 90 mm² area (Fig. 1b). Each sensor board carries eight consumer-grade MEMS microphones and two audio ADC ICs. The AD conversion of the audio signals is performed with 16-bit resolution at 48 kSps. The boards can store measurement sequences of up to 43 s duration.

Results and Discussion

Selected results reproduced here originate from validation tests in stationary and transient cases. Fig. 2 shows a stationary situation, where the system was placed horizontally 10 mm above a shaker platform of 72 mm diameter which was driven with an amplitude of 5 µm in vertical direction by a sine signal with f = 500 Hz. For every channel (small black circles in Fig. 2) surface displacements are calculated and then interpolated by piecewise cubic Hermite polynomials. The three frames are taken from the continuous data stream with intervals of 500 µs to illustrate one half period of oscillation. A reasonable reproduction of the platform movement can be observed with an obvious restriction on minimum detectable features due to the sampling in space domain.

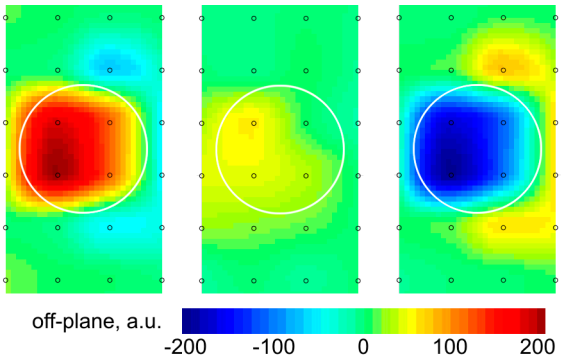

Fig. 2. Color coded off-plane displacements of a vibrating shaker platform (white circle). The black circles show positions of measurement channels.

In Fig. 3a the wave propagating in a carbon-fiber-reinforced polymer (CFRP) plate after a minor hit with a plastic pen in its center is shown. The plate (400 mm × 132 mm, 10 mm thick) was placed horizontally on two support rods spaced 200 mm apart as indicated in Fig. 3b, the measurement system was positioned 3 mm above the plate. The hereby used cubic spline interpolation provides extrapolated points outside the matrix of measurement channels.

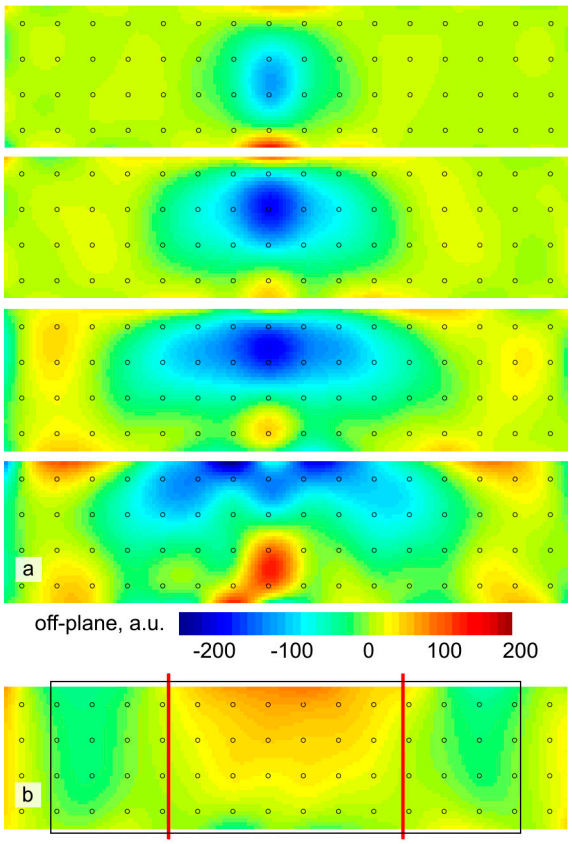

Fig. 3. (a) Data frames with interval 83 µs showing a wave propagating in a CFRP plate after a central hit. (b) A standing wave 85 ms later. Black rectangle indicates plate boundaries, red lines – support rods.

Fig. 3a reproduces every fourth frame of the data stream, giving an overview of the wave evolution during 250 µs after the excitation. The normal plate mode arising later is shown at 85 ms after the event (Fig. 3b).

As the next step the authors plan to perform a detailed comparison of the results with data of established vibration measurement methods.

References

[1] F. Riesberg, D. Felsl, S. Haase, N. Rümmler, Detektion von Strukturschäden in Faserverbundwerkstoffen mittels demontierbarer Sensorik, *Proc. Landshuter Symp. MST*, 147-154 (2016)

[2] H. Fleischer, Schwingungsuntersuchungen an der Violine. Beiträge zur Vibro- und Psychoakustik 1/10, UniBw und TU München (2010)

[3] J. Gomes, Y. Ishii, B. Ginn, Non-stationary Holography on Arbitrary Source Shapes, *Proc. Internoise* (2014)

[4] B. Forssen, M. J. Crocker, Estimation of acoustic velocity, surface velocity, and radiation efficiency by use of the two-microphone technique, *Journal of the Acoustical Society of America* 73, 1047 (1983); doi: 10.1121/1.389152

DOI 10.5162/SMSI2023/P35

Precision Time Synchronization Using NB-IoT for Locating Pipe Bursts in Freshwater Networks

M.Sc. Tim Scherer[1], Dr.-Ing. Stefan von Dosky[1], Dipl.-Ing. Stefan Klehr[1]
[1] Siemens AG, Karlsruhe

Summary:
Much effort has been put into developing algorithms for locating pipe bursts in freshwater networks. Such algorithms typically require a precision time-synchronization of all participating sensor nodes. The performance and efficiency of tight clock synchronization using Narrowband IoT (NB-IoT) has thereby rarely been characterized. The present work addresses this research gap by evaluating time-synchronization using NB-IoT enabled sensors. Multiple experiments showed that a relative time precision of 10 ms across the network compared to GNSS can be expected using a custom approach.

Keywords: Time-synchronization protocols, TSP, Internet of Things (IoT), NB-IoT, Burst detection

Background Motivation

Freshwater is vital for the survival of life on Earth, and water scarcity continues to be a major issue in various parts of the world. Apart from a proper water management in areas with high water stress, as proposed by Margolis et al. [1], it is also important to use advanced technological solutions to detect and locate pipe bursts. Much effort has been put into developing algorithms for accurately locating pipe bursts [2] [3]. These algorithms, however, require a precision time-synchronization to operate properly. It is generally accepted that relative timestamping is crucial in detecting the precise location of a burst. As the propagation speed of pressure waves in a pipe network is often greater than 1000 m/s, a timing difference of 1 ms between two sensor-nodes can already result in localization inaccuracy of 1 m. Due to reduced bandwidth and power availability, low power wide area networks (LPWANs) pose new challenges to synchronizing clocks. The present paper evaluates how time-synchronization can be performed using cellular NB-IoT radio technologies within a constrained industrial environment.

Problem Statement

Aside from naturally drifting clocks, synchronization of time via distributed networks is complicated by the fact that the propagation time of messages sent to synchronize them depends on several factors, such as down- and uplink as well as network buffering. This implies that IoT devices must be re-synchronized on a frequent basis to adapt time quickly and maintain a constant small offset. Both goals, however, contradict the desire to save energy as each synchronization is expensive in terms of power and data consumption. The question of how well state-of-the-art time synchronization protocols perform within constrained low-power NB-IoT networks arises.

Literature

In recent years, numerous protocols for time synchronization have been developed for a wide range of different transport media and application purposes. Tab 1 gives an overview of some of the most widely used protocols today. These protocols can be categorized in two signaling schemes: two-way message exchange and one-way message exchange [4]. The two-way message exchange approach is widespread and used on various transmission media. However, no information regarding time-synchronization over NB-IoT is found in literature.

Tab. 1: Overview of State-of-the-art time-synchronization protocols. PTP and SPoT need special hardware. Accuracy over internet as stated in [4] [5.]

Protocol	Accuracy	Example of use
NTP	~ 50 ms	Computer
SNTP	< NTP	Smartphones
PTP	sub-ms	Industry
SPoT	~ 10 ms	LoRaWAN IoT
Time	seconds	Computer

Schema:	One-Way	Two-Way

Other signaling schemas, such as Receiver-only and Receiver-receiver are not covered in this paper as they rely on a node-to-node communication which is not feasible in a cellular network structure.

Methodology

The presented results have undergone empirical analysis using quantitative techniques. The experiments were conducted with four SODAQ SFF N310 sensor-nodes in two distinct locations over multiple days. The SODAQ SFF N310 uses a SAMD21 µController and a u-blox SARA N310 communication module. A Raspberry Pi 3 is used as a ground-truth timeserver at another distinct place. The timeserver uses a GNSS satellite module to discipline its internal real-time clock with the Coordinated Universal Time (UTC) within ns precision. A custom application is installed on the Raspberry Pi 3 to discipline the time of each sensor-node with UTC accordingly. Because state-of-the-art protocols such as PTP and SPoT require special hardware, they are ineligible for the use with the available hardware. Furthermore, the high precision accuracy and low-power demand required by the burst detection algorithm would not be met by using NTP or SNTP; thus, a custom time-synchronization protocol (TSP) was developed. The accuracy of synchronization was measured using the time set by the built-in GNSS module and the PPS signal of each sensor-node.

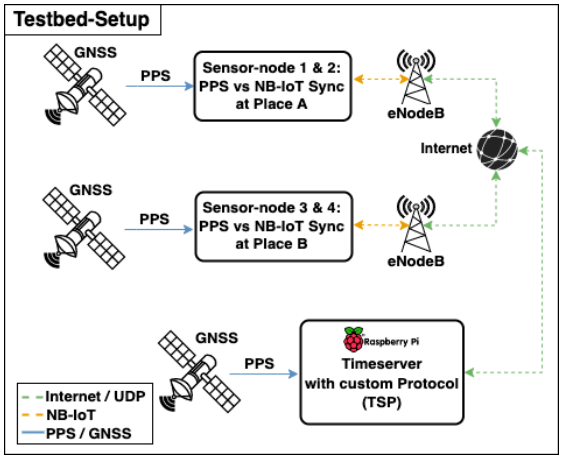

Fig. 1. The testbed consists of four exemplary sensor-nodes and a timeserver. Each node uses its own GNSS reference as ground-truth.

Solution

TSP is based on a two-way message exchange using unsolicited result codes of the u-blox communication module which enables the sensor-node to send a follow-up message with a corrected time, reflecting the real time upon transmission and reception. Using this approach, the synchronization accuracy can be increased towards ms precision. TSP yields optimal results when the delays between the sensor-node and timeserver are symmetric. TSP therefore tries to find those messages where the highest symmetry is available. This is accomplished using a custom bias-criteria algorithm that employs an estimation of the signal roundtrip time (RTT) in the NB-IoT cellular network infrastructure. Additionally, checking the NB-IoT signal quality has proven crucial in our tests. Reference Signal Received Power (RSRP) values better than -90 dBm turned out to be well suited.

Measurements and Conclusion

While excellent signal quality and bias-criteria are considered, a relative synchronization performance of 10 ms between all four sensor-nodes was found to be feasible in our test, as can be seen in Fig. 2. However, the origin of the roughly 50 ms systematic error remains unknown, and additional testing is advised. It was found out that RSRP values below -90 dBm result in significant asymmetries between the up- and downlink, to the point where reasonable ms-timing is no longer possible. This leads to the conclusion that under ideal conditions, burst detection algorithms employing NB-IoT and TSP are at least capable of detecting bursts within a radius of approximately 10 m. One advantage over existing GNSS-based time-synchronization is the fact that no additional GPS device with line-of-sight to satellites is required, allowing for easier installations in indoor and underground settings.

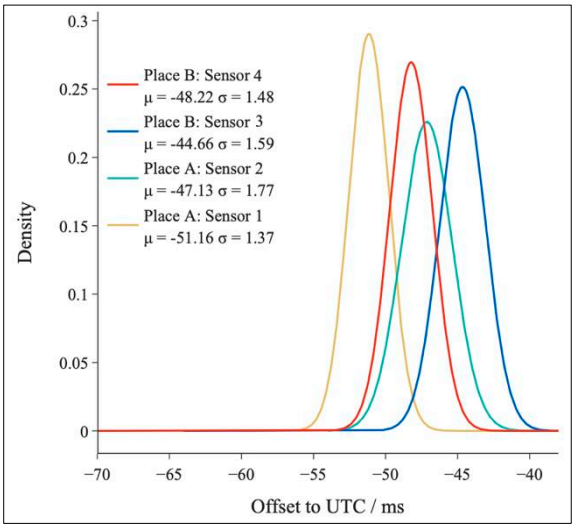

Fig. 2. Test-Result (Indoor) Relative synchronization accuracy using TSP in a NB-IoT cellular network structure.

References

[1] Liat Margolis, Aziza Chaouni, and Herbert Dreiseitl. Out of Water: Design Solutions for Arid Regions; ISBN: 978-3-03821- 006-1

[2] Menapace A, Zanfei A, Felicetti M, Avesani D, Righetti M, Gargano R. Burst Detection in Water Distribution Systems: The Issue of Dataset Collection, *Applied Sciences. 2020; 10(22):8219*; https://doi.org/10.3390/app10228219

[3] Advances in Modelling and Management of Urban Water Networks; MDPI AG, 2021; ISBN: 978-3-03943-789-4

[4] Yiğitler H, Badihi B, Jäntti R. Overview of Time Synchronization for IoT Deployments: Clock Discipline Algorithms and Protocols. Sensors. 2020; 20(20):5928; https://doi.org/10.3390/s20205928

[5] Sathiya Kumaran Mani, Ramakrishnan Durairajan, Paul Barford, Joel Sommers; A System for Clock Synchronization in an Internet of Things; https://doi.org/10.48550/arXiv.1806.02474

DOI 10.5162/SMSI2023/P36

Telemetric angle sensing using additively manufactured millimeter-wave metamaterial

Alexander Schossmann[1], Michael Töfferl[1], Christoph Schmidt[1], Christof Michenthaler[2], Dirk Hammerschmidt[2], Alexander Bergmann[1]
[1] Institute of Electrical Measurement and Sensor Systems, Graz University of Technology, Austria
[2]Infineon Technologies Austria AG, Villach, Austria
alexander.schossmann@tugraz.at

Summary:
We present a fully telemetric sensor concept for real-time end-of-shaft angle measurement. It is based on additively manufactured metamaterial consisting of out-of-plane oriented structures. The sensor effect is based on the angle-dependent coupling of linearly polarized electromagnetic waves into the fundamental resonance of the metamaterial. This allows to quantify the rotation angle as a function of the reflection amplitude.

Keywords: Angle measurement, metamaterial, millimeter-wave, telemetric sensor, end-of-shaft measurement

Introduction

Angle sensors are widely used in automotive and robotics applications [1]. Most sensor systems are based on the fundamental idea of sensing the change in the magnetic field, either through CMOS-scaled magnetic sensors [2] or Hall effect sensors [3]. Encoders based on sensing the magnetic field have proven to be reliable transducers, but still have relevant drawbacks. On the one hand the measuring distance between the shaft end and the sensor is limited to *1-3 mm* [3], on the other hand they are sensitive to interfering electromagnetic fields. We propose a fully telemetric approach to angle measurement using additive manufactured millimeter-wave metamaterial, insensitive to electromagnetic fields outside the bandwidth of the metamaterial resonance.

Sensor concept

Our sensor concept is based on the fundamental resonance of Electric-LC resonator (ELC) metamaterials [4]. The coupling to this fundamental resonance depends on their orientation to the electric field polarization. Based on that, the idea is to irradiate an ELC-array with linearly polarized millimeter-waves and trace the reflection signal as a function of the rotation angle. We used additive manufacturing (Nano Dimensions) to produce the metamaterial target as shown in Fig. 1 and Fig. 2. The ELC elements are printed using nanometric conductive ink (AgCite™ 90072 Silver) in a square lattice arrangement embedded in a circular disc of dielectric (DragonFly LDM 1092). This allows a high density of structures in the metamaterial. The bottom of the disc comprises a solid conductive layer using the same conductive ink.

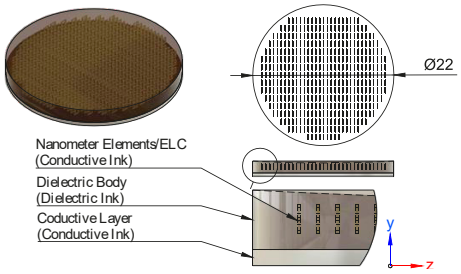

Fig. 1 Dimensions of the metamaterial (in mm)

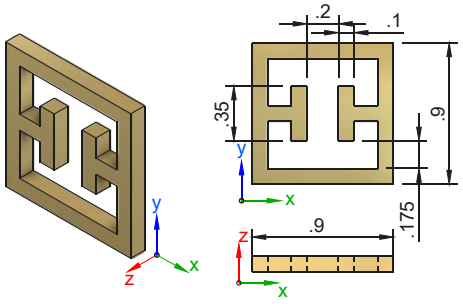

Fig. 2 Dimensions of the metamaterial elements (ELC) in mm

The geometrical parameters of the unit cell for a desired resonance at about $60\,\mathrm{GHz}$ were obtained from finite element simulations (COMSOL Multiphysics®). The linearly polarized millimeter-waves propagate along the *y*-direction. The coupling to the fundamental mode is maximized when the *E*-field is parallel to the *x*-direction.

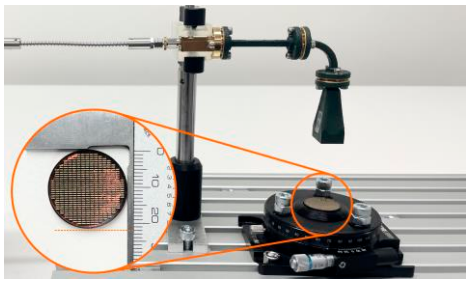

Fig. 3 The metamaterial mounted on a rotatable base plate.

Experimental results

We performed free-space measurements of the *S11* parameters using an *Anritsu MS4647B* vector network analyzer (VNA) with an external millimeter-wave test set and a *WR12* horn antenna. We conducted a calibration at the waveguide bend without the antenna. Thus, gating the data in time-domain in the postprocessing step was required. The metamaterial sample was mounted on a precision rotational stage (*Thorlabs PR01/M)* using a 3D printed adapter made from polylactide (PLA). The *S11*-spectra were recorded for various rotation angles and different distanced *d*. Fig. 4 illustrates the *S11*-spectra for a distance of $d = 38\ \mathrm{mm}$ between antenna and metamaterial sample. For a rotation of $90°$ the data shows a distinct minimum at about $78\ \mathrm{GHz}$ which arises from the characteristic resonant behavior of the metamaterial. The deviation from the simulated $60\ \mathrm{GHz}$ are most probably caused by manufacturing imperfections.

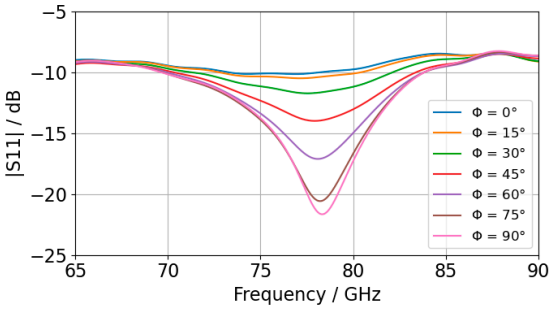

Fig. 4: VNA measurement of metamaterial, S11 spectra for different rotation angles, antenna distance d = 38 mm.

As expected, the data shows a decreasing minimum for increasing angles between the polarization of the *E*-field and the spatial orientation of the metamaterial. To check that this effect is independent of the measurement distance, we performed a measurement for three different distances between antenna and metamaterial (Tab. 1). From each obtained spectrum we evaluated the resonance minima in dB as a function of the rotation angle. Results are shown in Fig. 5.

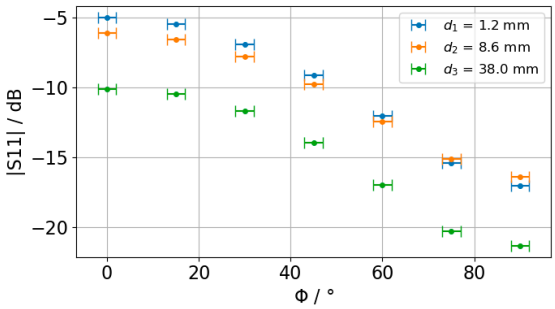

Fig. 5: Minima of measured S11 amplitude spectra as function of rotation angle.

The data shows the expected sensor effect for all three measurement distances: The reflection amplitude at the resonance frequency is changing as a function of the rotation angle. The curves only differ in an overall *S11*-amplitude offset. With larger distances, more surrounding objects are irradiated which leads to reflections that overlap with the reflections originating from the metamaterial. In order to assess the performance at different distances we quantified the observed minima by calculating the Q-factor at $\Phi = 90°$, using a Lorentzian fit.

Tab. 1: Q-factor for the measured distances

Distance/mm	1.2	8.6	38.0
Q-factor	11.6	11.0	9.8

Tab. 1 shows that the Q-factor only marginally decreases when the measurement distance is increased to $d = 38\ \mathrm{mm}$. Thus, our proposed sensor concept is suitable for a broad range of distances. Further work comprises the implementation of millimeter-wave chip technology for a compact sensor system.

References

[1] S.R. Ruocco, Robot sensors and transducers, *Open University Press Robotics Series,* ISBN: 978-94-011-6870-0

[2] K. Nakano, T. Takahashi and S. Kawahito, "A CMOS rotary encoder using magnetic sensor arrays,", *IEEE Sensors Journal*, vol. 5, no. 5, pp. 889-894, Oct. 2005, doi: 10.1109/JSEN.2005.853597.

[3] D. Rapos, C. Mechefske and M. Timusk, Dynamic sensor calibration: A comparative study of 2a Hall effect sensor and an incremental encoder for measuring shaft rotational position, *2016 IEEE International Conference on Prognostics and Health Management (ICPHM)*, 2016, pp. 1-5, doi: 10.1109/ICPHM.2016.7542858.

[4] D. Schurig, J. Mock, D. Smith, Electric-field-coupled resonators for negative permittivity metamaterials, *Applied Physics Letters, 88, 4 2006,* doi: 10.1063/1.2166681

DOI 10.5162/SMSI2023/P37

Detection of nm-Scale Displacements at Frequencies down to 1 mHz by Differential Laser Doppler Vibrometry

Dhyan Kohlmann[1], *Marvin Schewe*[2], *Hendrik Wulfmeier*[1], *Christian Rembe*[2], *Holger Fritze*[1]
[1] *TU Clausthal, Insitute of Energy Research and Physical Technologies, Am Stollen 19 B, 38640 Goslar, Germany*
[2] *TU Clausthal, Institute for Electrical Information Technology, Leibnizstraße 28, 38678 Clausthal-Zellerfeld, Germany*
dhyan.kohlmann@tu-clausthal.de

Summary: The displacement of the surface of a sample is detected contact-less by Differential Laser Doppler Vibrometry (D-LDV) at elevated temperatures. The time signal contains the phase difference of the measurement and reference laser beams, already greatly reducing noise from, e.g., length fluctuations, heat haze, and mechanical vibrations. In postprocessing of the data, anharmonic signal contributions are identified and extracted to show the correct thickness changes of thin films and related sample bending. The approach is demonstrated on a $Pr_{0.1}Ce_{0.9}O_{2-\delta}$ (PCO10) thin film sample.

Keywords: Laser Doppler Vibrometry, chemical expansion, thin films, SOFC materials, data processing

Introduction and Motivation

Many active materials which are exposed to varying chemical environments alter their stoichiometry, which is often accompanied by a change in lattice parameter called chemical expansion [1]. Chemical expansion of thin films is of great interest because materials in high-temperature applications such as sensors, fuel cells, and catalysts are often implemented as thin films [2]. The expansion of a thin film adhering to a non- or differently expanding substrate is constrained, which leads to the build-up of great mechanical stress, deformation and, ultimately, delamination or cracking, one of the main failure reasons [3]. Chemical expansion is coupled to the formation and diffusion of oxygen vacancies or interstitials, resulting in an oxygen non-stoichiometry δ. These are slow processes, often requiring long equilibration times. Therefore, new approaches are required to study this directly, especially when the expansion over time is not harmonic and information is partially stored in higher harmonics.

State of Research

When an oxide is exposed to reducing conditions, it exhibits an oxygen non-stoichiometry δ, that reflects the oxygen vacancy concentration $V_{\ddot{O}}$. In case of PCO, the relation at high oxygen partial pressure p_{O2} is [1]

$$[V_O^{\bullet\bullet}] \propto p_{O_2}^{-1/6} \qquad (1)$$

and becomes nearly constant at intermediate p_{O2} [4]. With the chemical expansion ε_C or strain ε being proportional to δ, it is also constant at intermediate p_{O2} [4]. In other words, the maximum strain is p_{O2} independent at intermediate p_{O2} ranging from about 10^{-17} to 10^{-5} bar. Therefore, Fig. 1 shows essentially the temperature dependent maximum stain provided that the samples reached nearly equilibrium and that the data evaluation adequately takes into account nonlinear effects. The former is fulfilled for slow (periodic) changes of p_{O2} in the mHz range. The latter, i. e. the correct consideration of nonlinear effects, is the main objective of this work.

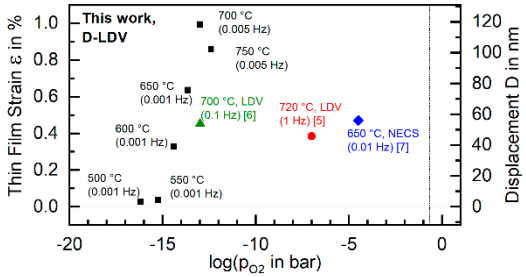

Fig. 1. Literature data and data from this work for the chemical strain in PCO10 thin films vs p_{O2}.

Experimental Procedure

The sample is comprised of an oxygen-ion conducting substrate [5–7] which acts as a pumping cell. On the substrate, a thin film of PCO10 is deposited. Electrodes are deposited on the film and the backside of the substrate. The sample is excited electrochemically by applying a sinusoidal voltage. According to (1), $V_{\ddot{O}}$ strives toward equilibrium with the effective oxygen partial pressure $p_{O2,eff}$ given by the Nernst relation (2). Here, $p_{O2,air}$ is the ambient p_{O2}, e_0 the elementary charge, k_B

Boltzmann's constant, and T the absolute temperature:

$$p_{O_2,\mathrm{eff}} = p_{O_2,\mathrm{air}}\, e^{-4\, e_0\, U / k_B\, T} \qquad (2)$$

By pumping the sample sinusoidally, the chemical expansion is driven, bending the sample [5–7]. The full displacement, which is the sum of the bending and film-thickness change, can be detected by D-LDV (developed by the authors), and its value extracted from the Fourier transform of the time signal [8]. When entering the range of constant nonstoichiometry, the displacement becomes constant for a portion of the excitation period. Here, some of the information is contained in higher harmonics at the multiples of the excitation frequency, which must be taken into account to extract the true displacement value.

Evaluation of the Data and Results

A fast Fourier Transform (FFT) [8] is done on the high-pass [9] filtered time signal, yielding the spectrum containing delta-shaped peaks at the multiples of the excitation frequency (Fig. 2).

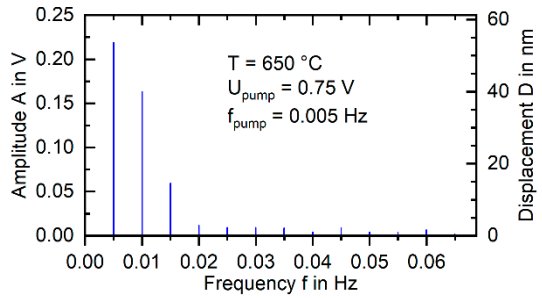

Fig. 2. The filtered spectrum for the inverse FFT.

Because the information is stored in these peaks only, the noise between them can be discarded before transforming the filtered spectrum back into a time signal, from which the displacement is extracted. It is taken as the difference between the minimum of the back transformed signal and the average of the constant range (Fig. 3).

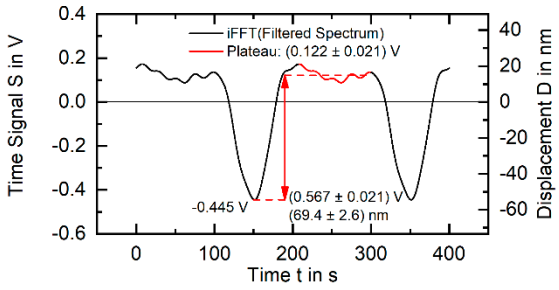

Fig. 3. The extraction of the full displacement.

Conclusions

The applicability of the method is confirmed by comparing two datasets acquired with different pumping voltages (Fig. 4). If higher harmonics taken into account as demonstrated here, the datasets are agreeable with one another, as the theory predicts. If only the first harmonic at the excitation frequency is evaluated, an increase in excitation voltage results in a decrease in displacement, which contradicts theory. The new evaluation method presented here is, therefore, considered as a valuable tool for the correct detection of chemical expansion.

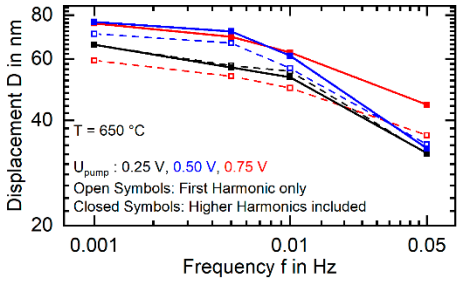

Fig. 4. Comparison of the displacements extracted from first harmonic only and from full spectrum.

References

[1] S.R. Bishop et al., Chemical Expansion, Implications for Electrochemical Energy Storage and Conversion, *Annual Review of Materials Research* 44, 205-239 (2014); doi: 10.1146/annurev-matsci-070813-113329

[2] E. Acosta, Properties and Applications, *A.E. Ares (Ed.): Thin Films* (2021); doi: 10.5772/intechopen.95527

[3] A. Atkinson, Solid Oxide Fuel Cell Electrolytes – Factors Influencing Lifetime, *N.P. Brandon, E. Riuz-Trejo, P. Boldrin (Eds.): Solid Oxide Fuel Cell Lifetime and Reliability* 19-34 (2017); doi: 10.1016/B978-0-08-101102-7.00002-7

[4] S.R. Bishop et al., Chemical expansion of nonstoichiometric $Pr_{0.1}Ce_{0.9}O_{2-\delta}$: correlation with defect equilibrium model, *Journal of the European Ceramic Society* 31 2351-2356 (2011); doi: 10.1016/j.jeurceramsoc.2011.05.034

[5] S. Schmidtchen et al., Chemical expansion of praseodymium-cerium oxide films at high temperatures by laser doppler vibrometry, *Solid State Ionics* 319 61-67 (2018); doi: 10.1016/j.ssi.2018.01.033

[6] H. Wulfmeier et al., Thin-film chemical expansion of ceria based solid solutions: laser vibrometry study, *Zeitschrift für Physikalische Chemie* 236, 1013-1053; doi: 10.1515/zpch-2021-3125

[7] J. Swallow et al., Dynamic chemical expansion of thin-film non-stoichiometric oxides at extreme temperatures, *Nature Materials*, 16, 749-755 (2017); doi: 10.1038/NMAT4898

[8] C.R. Harris et al., Array Programming with NumPy, *Nature* 585, 357–362 (2020); doi: 10.1038/s41586-020-2649-2. Used packages: numpy.fft.fft, numpy.fft.ifft, numpy.fft.fftfreq

[9] P. Virtanen et al., SciPy 1.0: Fundamental Algorithms for Scientific Computing in Python. *Nature Methods*, 17(3), 261-272; doi: 10.1038/s41592-019-0686-2. Used packages: scipy.signal.butter, scipy.signal.sosfilt

DOI 10.5162/SMSI2023/P38

Optimization of Micro-Hotplates for better Performance as infrared Emitters

A.T. Winzer[1], T. Schildhauer[1], J. Baldauf[1], and N. Thronicke[1]
*[1]**CiS** Forschungsinstitut für Mikrosensorik GmbH, Erfurt, Germany*

Summary:
The optimization process for a particular application of micro-hotplates as infrared emitters is considered. It starts with a baseline combination of technology and design. This combination yields a set of 5 performance parameters (radiant flux, manufacturing costs, modulation speed, power efficiency, and device lifetime). Changes of design or technology often affect more than one parameter in an intricate way. Numerical simulations, which have been verified by experimental data, allow a prediction of the outcome of changes and thus a time and resource saving device optimization.

Keywords: membrane, microheater, micro-hotplate, infrared emitter.

Introduction

There is an increasing need for micro-hotplates in sensor applications. Those micro-hotplates can be used as infrared emitters [1] in gas sensors [2]. There are other kinds of infrared emitters which are based on semiconductor diodes of the AlInSb-system. By preparing quantum wells with these materials with thicknesses from 2 to 6 nm, it is even possible fabricate a LED with different emission wavelengths from 3.4 to 4.2 µm [3]. However, the band gap of the antimonides and the deposition technology limit the maximal attainable wavelength to less than 6 µm which compromises applications for infrared transmission sensing on organic molecules.

In this work we look at a set of performance parameters for micro-hotplate infrared emitters in the course to optimize for a certain sensor application. We consider a simply design change for enhancing the spectral flux in a desired spectral region and demonstrate the impact onto the performance parameters.

Basic Technology and Design

The start of an optimization is a baseline solution, which is a given manufacturing technology and a sensor design. As a substrate a double-side polished silicon wafer has been used. The most important part of such a device is its free-standing membrane which contains a heating layer which can be TiN, $MoSi_2$, or Pt sandwiched between dielectric layers such as silicon nitride, silicon carbide or silicon oxide. In the membrane area, the silicon is etched away, so that the membrane is only supported a its edge by the bulk silicon. An example (type A) is shown in fig. 1. The chip has edge dimensions of 1 mm x 1 mm, a circular membrane and a tapered heater in the middle.

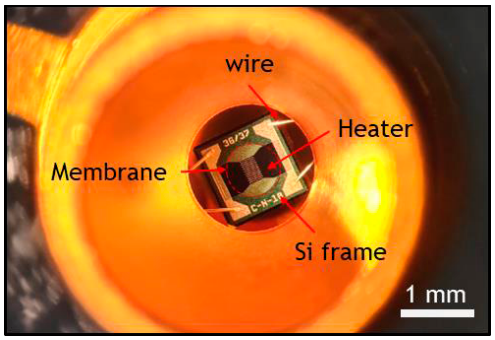

Fig. 1. Photograph of a micro-hotplate infrared emitter type A. The chip has been mounted and wire bonded on a transistor outline socket TO-39. On top of the socket a reflector cap has been placed to enhance the emission in forward direction.

Performance and Optimization Process

In order to discuss an optimization, we choose a set of performance parameters and give values for this chip. First of all, our presumed measurement task requires a certain spectral radiant intensity I_e at a wavelength of $\lambda = 6$ µm. Our type A emitter delivers I_e at $\lambda = 6$ µm of 0.24 mW/µm/sr. The costs of such a device are crucial in industrial applications. The chip manufacturing costs K vary approximately with the chip area. For the small type A chip, K is of the order of a few € per piece. K also scales with the number of produced parts. The next important parameter very often is the switching speed or the cutoff frequency f_c. We determined f_c by observing the radiant flux with a fast InAsSb photodiode while exciting the emitter with

square wave electrical modulation and taking the frequency at a decay down to 63% of the static flux. For type A f_c is 51 Hz. Device reliability plays an important role, too. Our devices shall have a mean time to failure *MTTF* of several years. For some applications, for instance when powered by a field bus, energy efficiency η as the ratio between the total radiant flux and the electrical input power has to be considered. Because the edge of the membrane is very close to the heated zone, heat can dissipate fast to the silicon frame and further to the socket, our type A emitter has an η of 5.7%.

All of these parameters are an outcome of a particular technology and a particular design. Any changes in design or technology may likely cause changes in the performance parameters, which is symbolized by figure 2.

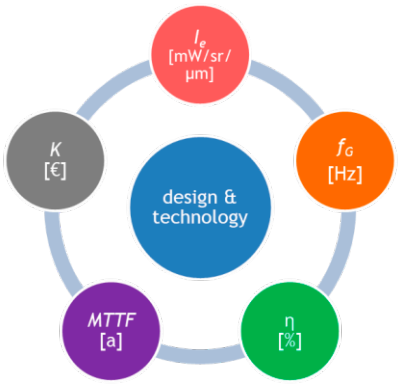

Fig. 2. The 5 main parameters of an infrared emitter are a result of a particular design and technology.

Increasing the radiant flux

For optimizing I_e of the type A emitter, several design or technology options are possible. The first very obvious one is to increase the emitting area, i.e. fabricate a larger chip, see figure 3. Compared to type A with 1 mm edge length, type B (2 mm) and C (3.6 mm) emit 4.7 times and 26 times more light at λ = 6 µm, with costs scaling by the chip area. The I_e increase scales above linearly with the membrane size, which is caused by a better thermal isolation between the heater and the silicon frame, increasing η to 6.3% and 19.3% !, respectively without much detrimental effect on the *MTTF*. On the other side, f_c decreases from 51 Hz down to 26 Hz and 7 Hz !, respectively.

Instead of measuring fabricated devices, with knowledge of the material parameters all three physical quantities I_e, f_c, and η can be calculated by numerical simulations. With a validated multiphysical model, this enables for a much faster optimization speed in comparison to experiments. Figure 4 shows one outcome of the electrical-thermal model for the type C emitter. The temperature distribution as well as temporal behavior were simulated by the model and are in close agreement to measurements.

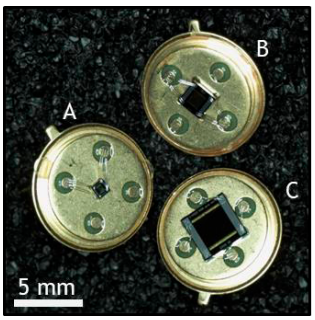

Fig. 3. Photograph of 3 chip types fabricated with similar technology.

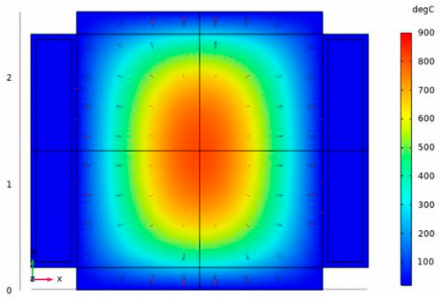

Fig. 4. Multiphysical thermal-electric simulation of the temperature distribution on the membrane of the type C emitter at 700 mW of electrical input power.

Summary

Changes of design or technology often affect more than one parameter in an intricate way. Numerical simulations, which have been verified by experiments, allow a time and resource saving device optimization.

Acknowledgments

We gratefully acknowledge the funding of parts of this work by the German Federal Ministry for Economic Affairs and Climate Action under the grants 49MF190034 and 49MF18072. We also value the fruitful discussions with Mr. Biermann of CMOS IR GmbH, Erfurt.

References

[1] J.F. Creemer, D. Briand, H.W. Zandbergen, W. van der Vlist, C.R. de Boer, N.F. de Rooij, P.M. Sarro, Sensors and Actuators A: Physical, 148, 416 (2008).

[2] H. R. Barnard, E. Zossimova, N. H. Mahlmeister, L. M. Lawton, I. J. Luxmoore, and G. R. Nasha, Appl. Phys. Lett. 108, (2016) 131110.

[3] M. Aziz, C. Xie, V. Pusino, A.Khalid, M. Steer, I.G. Thayne,D.R. Cumming. Applied Physics Letters, 111, (2017) 102102.

DOI 10.5162/SMSI2023/P39

Real-time Characterization of Inductive Position Sensors

Aldi Hoxha[1], Francesco Campagna[1,2], Ruben Specogna[1,2]
[1] EMCLab, University of Udine, via delle scienze 206, 33100 Udine, Italy,
[2] EMC Gems Srl, via Sondrio 2/M6, 33100 Udine, Italy,
ruben.specogna@uniud.it

Summary:
We propose a fast method to characterize inductive position sensors with zero physical prototypes. The technique is based on an in-house developed electromagnetic simulation tool which shows three orders of magnitude improvement with respect to the most widely used commercial software. This simulation software is used for producing synthetic data for training a machine learning surrogate model based on a neural network. In this way the characterization of a sensor takes just milliseconds.

Keywords: encoders, resolvers, inductive position sensors, electromagnetic simulation, machine learning

Introduction

Inductive position sensors (IPS) perform linear or angular position measurements [1-2]. Being contactless, low cost and immune to external magnetic field, dust and liquids they are preferred in those applications where the position measurements are performed in harsh environment. Furthermore, since the measured position derives from a ratiometric measurement they can operate in different thermal conditions.

An IPS consists of a transmitter (TX) coil (see Fig. 1) which, being driven by an alternate current, establishes a variable magnetic field inside the sensor. In this region two receiver coils RXsin and RXcos (see Fig. 1) measure induced voltages U_RXsin and U_RXcos.

When a conductive target is positioned above the sensor, eddy currents are generated inside it. These eddy currents shield the magnetic flux in such a way that the induced voltage on the RX coils depend on the target position with a sine and cosine spatial variation. The position of the target can be determined thanks the following formula

$$\theta_{mis} = atan\left(\frac{U_{rxsin}(\theta)}{U_{rxcos}(\theta)}\right). \qquad (1)$$

The main drawback of this type of sensors is that the linearity error in many cases can be too high. Hence, the prediction of this error by means of a simulation tool is of paramount importance for its characterization. In fact, in this way the linearity error can be estimated without realizing a physical prototype at all, saving time and resources.

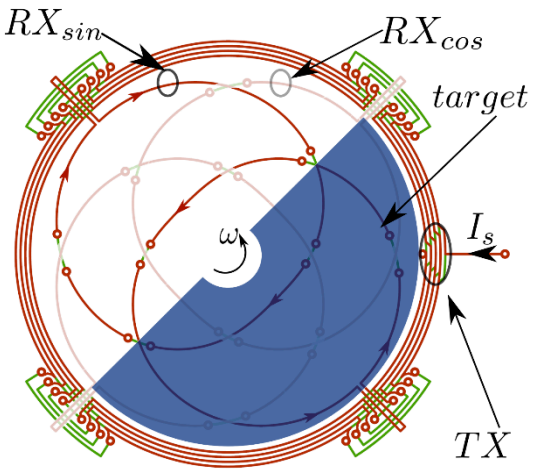

Fig. 1. An example of rotary inductive position sensor. The target is represented in blue.

Simulation tool

For the virtual prototyping of the sensor, there is the need to solve many eddy current problems by varying the position of the target (see Fig. 2). If Finite Elements tools are used, as implemented in most commercial software, the simulation speed is poor. In particular, when the target is moved, both the mesh and the simulation have to be recomputed from scratch.

A different strategy for IPS simulation uses the *surface integral method*. The main advantage of such a method is that only the conductors are meshed, whereas the insulators are not. Thus, this method is very efficient especially for modeling eddy currents with moving conductors since the remeshing is not needed.

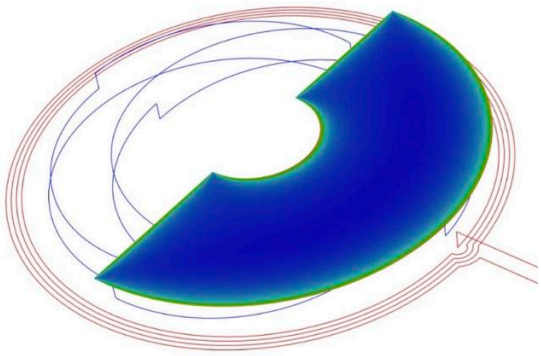

Fig. 2. Example of the simulated sensor with the surface integral method.

The surface integral method is not widely used because the produced matrix is full and its entries are difficult to compute accurately because their computation involves the evaluation of a singular integral. The use of surface integral method for inductive position sensors has been introduced in [3-4].

In this paper we propose a new method called SUPERO, which builds around novel basis functions recently introduced in [5] for a volume integral method. In place of using the standard Rao-Wilton-Glisson (RWG) or Raviart-Thomas basis functions, we designed new basis functions tailored for the surface integral method, which enable a very efficient and accurate construction of the system matrix. Moreover, the full matrix can be sparsified obtaining unprecedented simulation speed.

The results provided by SUPERO are very accurate and can be obtained 2500 faster than the most widely used commercial software.

Surrogate model

With the new tool SUPERO, the simulation of 101 positions of an inductive position sensor can be performed in about 30 seconds, in place of roughly 24 hours needed with a FEM software. Still, 30 seconds to assess the linearity error of a sensor are not acceptable for many applications we have in mind.

For this reason, we exploit the fast simulation tool SUPERO to produce many artificial data to be used for training a supervised machine learning method. The aim is to obtain a surrogate model which can estimate the error of a configuration in milliseconds.

Three methods to build the surrogate model will be compared:

1. Support vector machine (SVM);
2. Gaussian processes regression (GPR);
3. Neural network (NN).

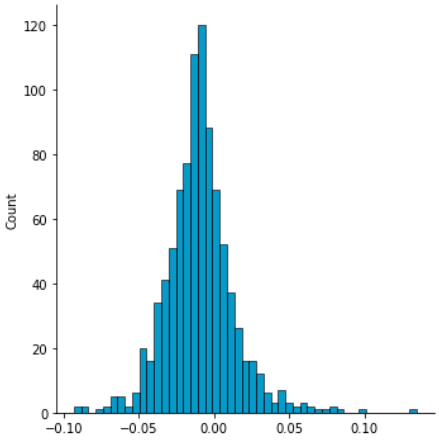

Fig. 3. Distribution of the discrepancy between the sensor linearity error provided by the simulation and the simulation error provided by the surrogate model based on a 3-layer neural network.

Results

We used 5 design variables: maximal radius of the TX coil, minimum and maximum radius of the RX coils, minimum and maximum radius of the target. 3000 designs have been used for training and 1000 for testing. The method that provides the best results both in terms of training and prediction time and forecasting accuracy is the neural network model (see Fig. 3).

Conclusions

By using the surrogate model, the characterization of the error of an inductive position sensor can be performed in milliseconds. This opens new possibilities of devising novel design support systems to guide the user in the design of the sensor.

References

[1] J. Fraden, “Handbook of Modern Sensors: Physics, Designs, and Applications, Fourth Edition”, p. 681.

[2] B. Aschenbrenner and B. G. Zagar, “Analysis and Validation of a Planar High-Frequency Contactless Absolute Inductive Position Sensor”, IEEE Transactions on Instrumentation and Measurement, vol. 64, no. 3, pp. 768–775, Mar. 2015

[3] M. Passarotto, G. Qama, and R. Specogna, ‘A Fast and Efficient Simulation Method for Inductive Position Sensors Design’, IEEE SENSORS, Montreal, QC, Canada, Oct. 2019

[4] A. Hoxha, M. Passarotto, G. Qama, and R. Specogna, “Design Optimization of PCB-Based Rotary-Inductive Position Sensors”, Sensors, vol. 22, no. 13, p. 4683, Jun. 2022

[5] M. Passarotto, S. Pitassi, and R. Specogna, “Foundations of volume integral methods for eddy current problems”, Computer Methods in Applied Mechanics and Engineering, vol. 392, p. 114626, 2022.

DOI 10.5162/SMSI2023/P40

Development of Conductive Molecularly Imprinted Polymer Blends for VOC Sensing

Adriana Feldner[1,2,3], Vincent Nussbaumer[1], Peter Lieberzeit[1], Philipp Fruhmann[3]
[1] University of Vienna, Faculty for Chemistry, Department of Physical Chemistry, Währingerstraße 42, 1090 Vienna, Austria
[2] University of Vienna, Vienna Doctoral School in Chemistry (DoSChem), Währinger Str. 42, 1090 Vienna, Austria
[3] Centre of Electrochemical Surface Technology, Viktor Kaplan-Straße 2, 2700 Wiener Neustadt, Austria
adriana.katharina.feldner@univie.ac.at, adriana.feldner@cest.at

Summary:
We synthesized molecularly imprinted polymers for the templates heptanal and 2-propanol. Blends of the polymers with the conductive polymer P3HT proved suitable as receptor layers on both QCM and chemiresistors. Both types of sensors provide concentration dependent signals for the respective analyte. In comparison the QCMs can detect lower concentrations than the chemiresistor.

Keywords: molecular imprinting, conductive polymers, quartz crystal microbalance, chemiresistor, volatile organic compounds

Background, Motivation an Objective

Molecularly imprinted polymers (MIPs) are synthetic materials that contain binding sites for selectively rebinding the target analyte. [1] Herein, conductive MIP blends serve as receptor layers on quartz crystal microbalance (QCM) sensors as well as chemiresistors. QCM is a mass-sensitive sensor based on the piezoelectric properties of quartz. [2] Chemiresistors can detect volatile organic compounds (VOCs) in the gas phase through thin conductive polymeric films. Adsorption of the analyte causes the films to swell which results in a change in electric resistance. [3] Conductive MIP blends have already proven useful sensor materials to detect limonene on QCMs and chemiresistors. [4] We now intend to extend the applications to other compounds. The analytes in this case are VOCs that have been identified as biomarkers in the exhaled air of breast cancer patients. [5] Those sensors could be preliminary work towards applications in non-invasive early detection of diseases via breath analysis. Alternatively, they could serve as a stepping stone to other conductive MIP systems for VOC monitoring purposes.

Description of the New Method or System

This short paper presents the results obtained with conductive MIPs as sensor materials for detecting heptanal and 2-propanol, respectively. For heptanal detection MIPs based on the functional monomer N,N-dimethylacrylamide (DMAA) and the crosslinker ethylene glycol dimethacrylate (EGDMA) were developed. MIPs for the detection of 2-propanol are based on polyurethane (PU) containing diphenylmethane 4,4'-diisocyanate, bisphenol A and phloroglucinol. Both are blended with the conductive polymer poly(3-hexylthiophene-2,5-diyl) (P3HT). One electrode of the dual-channel QCM sensors is coated with the imprinted conductive blend (MIP) via spin-coating. The second electrode is coated in the same way with the corresponding non-imprinted polymer (NIP) and acts as the reference. Both electrodes of the chemiresistors are coated with the MIP blends. The reference electrode is covered with a tape prior to the measurement. All sensors are tested in gas flows containing different concentrations of the respective analytes. Selectivity tests with other VOCs were performed.

Results

QCMs coated with the conductive polymer blends can detect heptanal in gas phase in a range of 250-1000 ppm (Figure 1). Blending the MIP with P3HT increases the average sensor response for 1000 ppm heptanal from 5 to 8 Hz/10 nm polymer layer compared to pure MIP. Selectivity tests with other volatile organic compounds suggest selectivity towards the desired analyte.

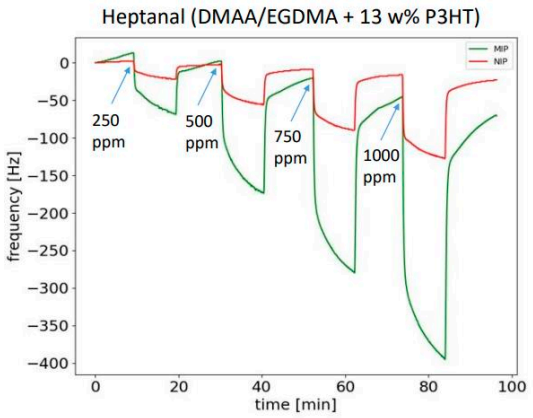

Fig. 1. QCM measurement at different heptanal concentrations. (DMAA/EGDMA containing 13 w% P3HT).

The blends also proved suitable for use in a chemiresistor (Figure 3). On average 1000 ppm heptanal leads to a reversible shift of 0.5% in the sensor response.

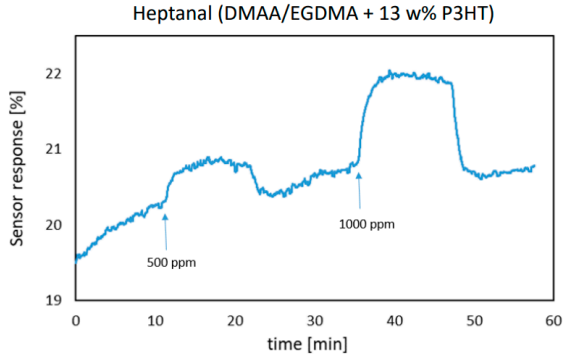

Fig. 2. Chemiresistor measurement at different heptanal concentrations. (DMAA/EGDMA containing 13 w% P3HT).

The conductive polyurethane blends can detect 2-propanol in the range 500-2000 ppm with similar signal intensities as the pure MIP. 1000 ppm 2-propanol lead to a reversible frequency shift of 1 Hz/10 nm polymer.

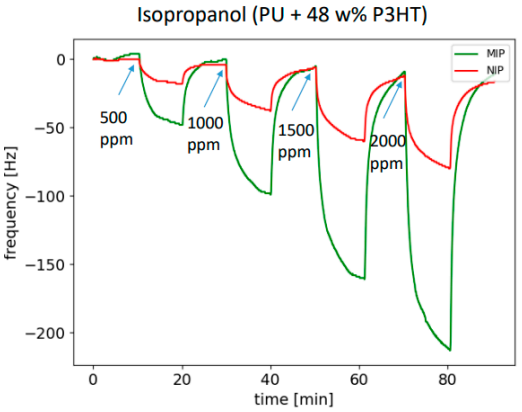

Fig. 3. QCM measurement at different 2-propanol concentrations. (PU containing 48 w% P3HT).

The chemiresistors coated with the polyurethane blends so far only react to concentrations above 1500 ppm (Figure 4). 2000 ppm of the analyte cause a sensor response of 0.1 %.

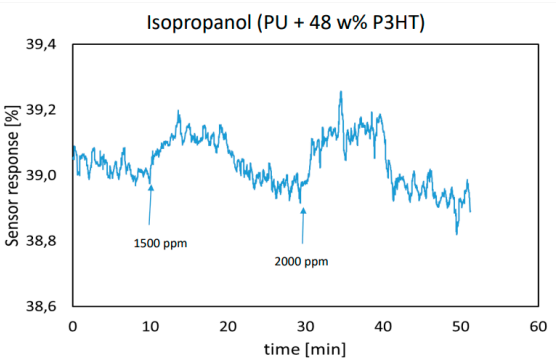

Fig. 4. Chemiresistor measurement at different 2-propanol concentrations. (PU containing 48 w% P3HT).

Based on this, our future focus will be the improvement of the signal intensity, as well as increasing the signal/noise ratio of our chemiresistor devices.

The combination of simple chemiresistors with conductive MIPs was proven successfully and bears huge potential with respect to the simplicity of the system and its broad applicability.

References

[1] K. Haupt, A. V. Linares, M Bompart, B. T. S. Bui, Molecularly Imprinted Polymers, *Molecular Imprinting. Topics in Current Chemistry 325*, 1-28 (2011); doi: 10.1007/128_2011_307

[2] A. Alassi, M. Benammar, D. Brett, Quartz Crystal Microbalance Electronic Interfacing Systems: A Review, *Sensors* 17, 2799 (2017); doi: 10.3390/s17122799

[3] S. Yan, J. Bintinger, S. Park, S. Jain, K. Alexandrou, P. Fruhmann, K. Besar, H. Katz und I. Kymissis, Inexpensive, Versatile and Robust USB-Driven Sensor Platform. *IEEE Sensors Letters* 1, 1-4 (2017); doi: 10.1109/LSENS.2017.2763989

[4] J. Völkle, K. Kumpf, A. Feldner, P. Lieberzeit, P. Fruhmann, Development of conductive molecularly imprinted polymers (cMIPs) for limonene to improve and interconnect QCM and chemiresistor sensing, *Sensors and Actuators B: Chemical* 356, 131293 (2022); doi: 10.1234/s10000

[5] M. Phillips, R. N. Cataneo, B. A. Ditkoff, P. Fisher, J. Greenberg, R. Gunawardena, C. S. Kwon, O. Tietje, C. Wong, Prediction of breast cancer using volatile biomarkers in the breath, *Breast Cancer Research and Treatment* 99, 19-21 (2006); doi: 10.1007/s10549-006-9176-1

DOI 10.5162/SMSI2023/P41

A MEMS micromachined low cost microheater platform for applications in thermal sensors

A. Laades[1], C. Heinze[1], L. Long[1], D. Karolewski[1], J. Baldauf[1], T. Klein[1] and T. Ortlepp[1]
*[1]**CiS** Forschungsinstitut für Mikrosensorik GmbH Erfurt*

Summary:
We developed a low-cost thin membrane based microheater platform (MHP) as scalable basic unit for thermal sensors. The MHP consisting of thin membranes supporting the microheater and temperature sensors is CMOS/MEMS compatible and features high performance characteristics such as controllable temperature distribution and low power consumption.

Keywords: membrane, microheater, thermal isolation trench, thermopile, microcalorimetric sensor.

Introduction

There is an increasing need for low cost microheater platforms (MHPs) for use in different thermal sensor systems such as gas sensors [1, 2, 3], thermal flow meters [4, 5], microreactors [6], radiation bolometers [7] as well as infrared emitters [8]. The focus of the work shown in this paper is to be develop a platform which is CMOS/MEMS-compatible and made of cost-effective materials for the carrier membrane, heating elements, temperature sensors and thermal insulation.

Sensor design

Preliminary simulation works yielded different approaches to chip design a selection of which is shown in Fig. 1. Based on these results, the design of the chips consisting of microheaters with different geometries and temperature sensors was derived and optimized.

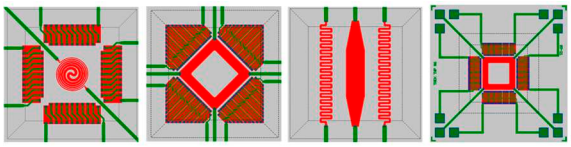

Fig. 1. Layouts of different microheater shapes, thermopiles, and thermistors for use as temperature sensors.

Simulations of the distribution of the heating voltage, current density and temperature show that our MHP have different thermoelectric properties that allow their use in diverse applications. The simulated temperature distribution on the membrane and the temperature profiles at the junction between the membrane and the silicon frame for two chips with two microheater geometries (square and spiral) are displayed in Fig. 2.

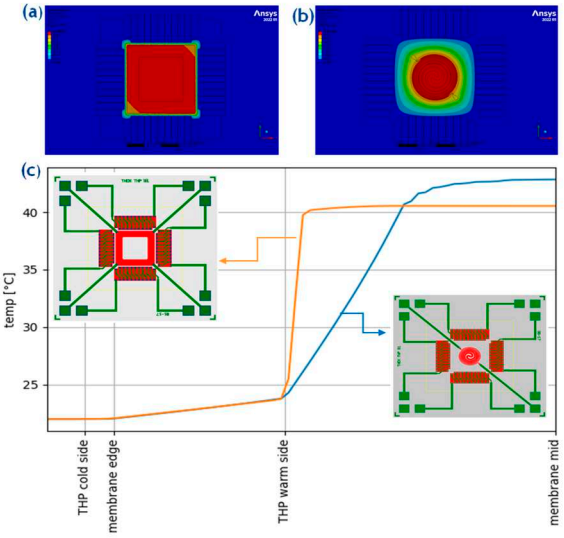

Fig. 2. Simulation of two MHPs with thermopiles and different heater geometries in terms of temperature distribution on the membrane and profiles at its edge.

Sensor fabrication and measurements

A technology for producing MHPs with closed as well as suspended membranes was developed. This is carried out with a process sequence consisting of the deposition of a dielectric layer stack made of silicon oxides and silicon nitrides, chemical vapor deposition of a polycrystalline silicon (Poly-Si) doped with phosphorus or boron, additional deposition of silicon nitride and silicon oxide layers, and magnetron sputter deposition of aluminum (containing 3% Si). Thermopiles and thermistors were chosen as temperature sensors because they have many advantages over other temperature sensors such as diodes [9].

Results

Fig. 1 shows some MHPs with suspended membranes.

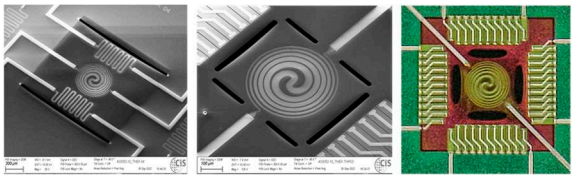

Fig. 3. Scanning electron microscope and 3D laser microscope pictures of the MHP showing isolation trenches.

The MHPs were characterized thermoelectrically at wafer level as well as using single chips mounted on PCBs. To determine the resistances and the corresponding temperature coefficients (TCR) of the heater and thermistors, calibration curves were determined upon varying the temperature. It was observed that, the heater resistance increases when the bias voltage changes from 0.1 to 10 V, which proves the Joule self-heating effect and thus the desired operation of the MHP. Regardless of the heater voltage, the heater resistance increases with the temperature, leading to TCR of 860 ppm/°C for the poly-Si used in our microheaters, thermistors and thermocouples. According to our measurements the Seebeck coefficients for the thermocouples made of poly-Si and Al (containing 3% Si), is about 100 to 103 µV/K.

The MHP was tested as calorimetric thermal flow sensor. Fig. 4 shows the thermoelectric voltage of four thermopile sensors (S1 to S4) symmetrically surrounding a square microheater in a diagonal arrangement (see inset) as a function of heating voltage. Fig. 4 (a) shows the output voltages depending on the heating voltage without air flow, causing the signals to overlap. This shows the existence of a symmetrical temperature field around the heater.

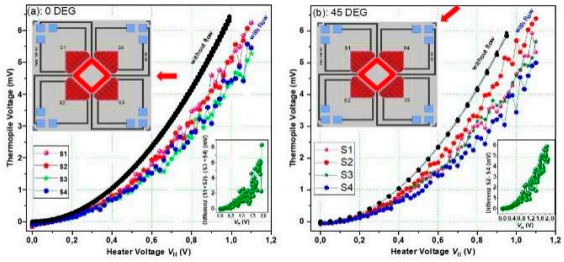

Fig. 4. Electrical self-Test applied to a microcalorimetric thermal flow consisting of a square heater and 4 thermopiles arranged diagonally to the heater. The arrows show the flow direction. The insets exhibit the difference between the downstream and upstream sensor signals.

When applying an air flow using pressurized air, the thermoelectric voltage of all four sensors decreases and the output voltage of the upstream sensors is weaker than the voltage of the downstream sensors. In Fig. 4 (b) it can be clearly seen that S4 is cooled down more than S2. This symmetry is thus disturbed. The resulting temperature difference serves as a measure for the flow velocity. Thus, the flow modulates the temperature distribution on the sensor membrane and demonstrating the calorimetric effect.

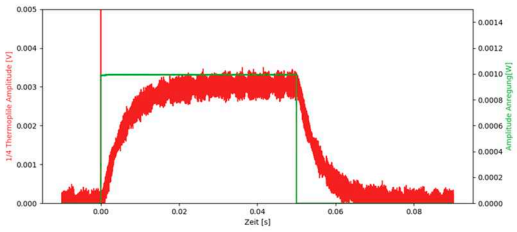

Fig. 5. Time response of electrically excited sensor.

Figure 5 shows the time response of a thermopile using power pulse of 1mW with a duration of 50ms. From this plot recorded directly from the measuring instrument, the heating time constant is about 8 ms. Thus, the MHP studied here achieves high heating power with a short response time.

Conclusion and outlook

Based on very extensive simulation and experimental work, low-cost and CMOS/MEMS compatible membrane-based microheater platforms with good performance could be designed and processed. Using the approach shown above MHPs for various applications can be fabricated.

References

[1] S. M. Majhi, A. Mirzaei, H. W. Kim, S. S. Kim, T. W. Kim, Nano Energy 79 (2021) 105369

[2] S. Bagga, J. Akhtar, S. Mishra, AIP Conference Proceedings (2020) 2294

[3] Y. Chen, M. Li, W. Yan, X. Z., K. W. Ng, X. Cheng, ACS Omega publication (2021)

[4] V. Balakrishnan, H.-P. Phan, T. Dinh, D.V. Dao, N.-T. Nguyen, Sensors 17 (2017) 2061

[5] M. Babaelahi, and S. Somayyeh, Metrology and Measurement Systems 29.1 (2022).

[6] J. F. Creemer, S. Helveg, P. J. Kooyman, A. M. Molenbroek, H. W. Zandbergen, and P. M. Sarro, J. Microelectromech. Syst. 19 (2010) 254

[7] H. Meister H. Langer, S. Schmitt, Fusion Eng. Des. 120, (2016) 21

[8] S. Biermann, A. Magi, P. Sachse, M. Hoffmann, K. Wedrich, L. Müller, R. Koppert, T. Ortlepp, J. Baldauf, Proc. SPIE 11279, Terahertz, RF, Millimeter, and Submillimeter-Wave Technology and Applications XIII (2000) 1127908

[9] B.W. van Oudheusden, Sensors and Actuators A 30 (1992) 5.

DOI 10.5162/SMSI2023/P42

PVDF SENSOR ARRAY FOR UNSTEADY WALL-PRESSURE MEASURMENTS IN SHOCKWAVE-BOUNDARY LAYER INTERACTIONS APPLICATION

Bei Wang[1], Cosimo Corsi[2], Julien Weiss[2], Zirui Pang[3], Ha Duong Ngo[1]
[1] University of Applied Sciences, Berlin, Germany
[2] Technical University, Berlin, Germany
[3] University of Applied Sciences, Tianjin, China
haduong.ngo@htw-berlin.de

Summary:

This paper presents the development and 3D integration of a PVDF piezo-film sensor array for unsteady wall-pressure measurements in a turbulent SBLI (Shockwave-boundary layer interactions). The sensor array is developed and tested inside the supersonic wind tunnel in an SBLI configuration. The sensor array is large and have no obstacles on the surface. The sensor system has been 3D integrated and no bond wires are needed. With this type of large area sensor array several local pointwise measurements can be taken without disturbing the flow field. The dynamic wall-pressure field of a turbulent SBLI at Mach 2 is measured and displayed. The obtained results show good agreement with other studies present in literature. The PVDF setup is compared with the standard state-of-the-art sensor used for unsteady pressure measurements, a reference piezoresistive transducer, highlighting the good qualities of the proposed sensor.

Keywords: PVDF Sensors, Sensorarray for unsteady wall-pressure measurements, 3D sensor integration

Background / Motivation

One of the most challenges in development of next engine generation (Geared Turbofan Engine – GTF Engine) is to provide a separation-free and stable flow over the whole range, especially at the edges. The next engine generation should achieve a fuel burn reduction of 11%. It's the goal in the EU climate-neutral aviation Clean Sky 2 program [1] to reduce the CO2 and noise emission in the year 2030 approximately 30%. To optimize the aircraft structure to reduce internal and external noise generated by TBL pressure fluctuations, high fidelity characterization of the wall pressure spectrum in spatial wavenumber space and in temporal frequency is needed. Existing sensor solutions in practice do not meet all the requirements. Up to now, bulky and expensive semiconductor-based pressure sensors such as silicon-based piezoresistive sensor solutions from company Kulite have been used [2]. They do not provide enough information about the interactions, and show limitations in resolution and frequence domain. To overcome the above mentioned limitations we have developed a new high performance wall mounted sensor array for surface unsteady pressure and wall shear stress measurements for future aircrafts.

Description of the New Method or System

In this paper we present a 3D piezoelectric sensor array setup for use in SBLI (the concept in shown in figure 1).

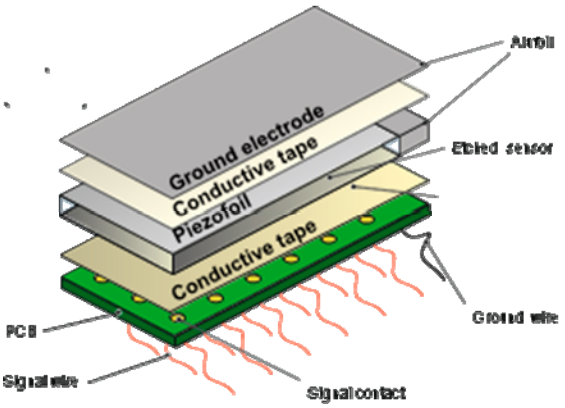

Fig. 1. Concept of the PVDF-based sensor array. The structured piezofoil has been embedded between two conductive tapes as electrical contact but also as shielding. In our system no bumps or wires are needed. The sensor surface is obstacle-free and so does not interfere with the flow.

We will focus on the sensor structuring technology, the electronics, the packaging and shielding concept in details. The sensor system does not need any bumps or bond wires for contacting, so it can be realized very small in size and compact. The electrical path is vertical and so can be very short. The sensor array has been realized using PVDF-foils [3]. This material has been used in a wide range of applications [4]. The foils are flexible and can be very thin (110µm in this project). The foils are based on the polymer polyvinylidenefluoride (PVDF). Metal layers (Ag, Al, Au) are deposited on both sides of the foil for electrical contacts. The metal layers (in this paper Ag-based) have been structured using different methods (laser etching, wet etching, milling) to form small electrodes for the piezoelectric sensors. The sensor setup can be seen in the figure below (figure 2).

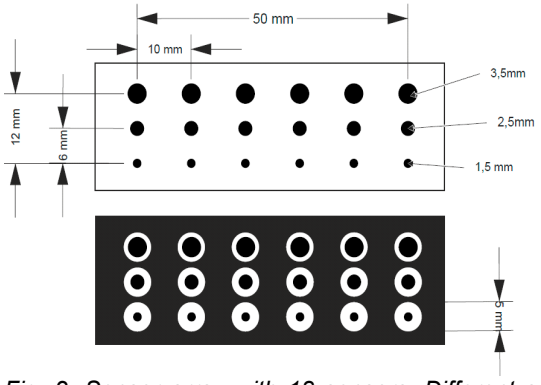

Fig. 2: Sensor array with 18 sensors. Different sensors layouts have been realized by using laser ablation, wet etching and mechanical milling. Laser ablation and milling provide the best sensor performance, whereas the wet etching is not really suitable due to the low selectivity. Black areas are the Ag-electrodes remaining.

The sensor array can be integrated on different surfaces, such as air foil**.**

Results

The sensor array with 18 and 48 sensors, electronics for signal acquisition and 3D packaging technology have been developed. The sensor system is flexible and can be integrated in all surfaces in aerospace. Tests in the supersonic wind tunnel (figure 3) with the developed sensor arrays and reference sensor system from Kulite have been conducted.

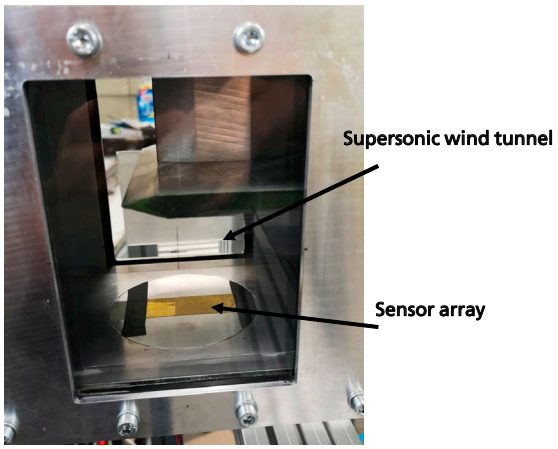

Fig. 3: View of the window in the supersonic wind tunnel and the sensor array.

It can be demonstrated (figure 4) that the new sensor system is able to match the reference sensor signal precisely.

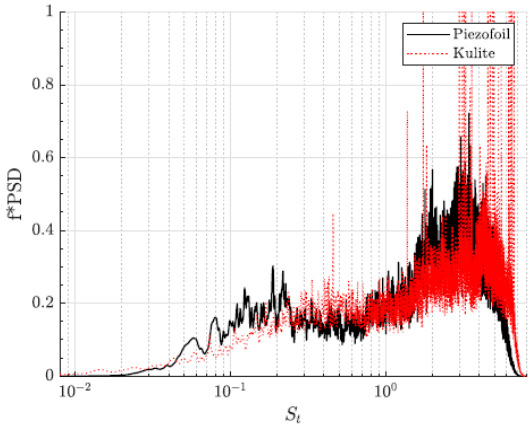

*Fig. 4: Comparison between piezofoil sensor (position 1) and reference sensor using f*PSD. Red – reference sensor, and back the piezosensor.*

[1] EU Clean Sky, *Roadmap to climate-neutral aviation*. 2021. https://clean-aviation.eu.

[2] C. Corsi at al. *Tech. Digest AIAA 2022*, pp. 2022-4135. https://doi.org/10.2514/6.2022-4135.

[3] Measurement Specialties, I. *Piezo film sensors technical manual*, 2008. https://doi.org/10.1148/100.2.415.

[4] F. Clemente et al., *A piezo-film-based measurement system for global haemodynamic assessment*. Physiological Measurement, Vol.31, No.5, 2010.

DOI 10.5162/SMSI2023/P43

Versatile impedance sensor for multiphase flow monitoring

Eduardo Nunes dos Santos[1], Natan S. Reginaldo[1], Dalton Bertoldi[1], Marco José da Silva[1,2], Rigoberto E. M. Morales[1]
[1] Multiphase Flow Research Center (NUEM) Federal University of Technology – Paraná (UTFPR), Curitiba, Brazil.
[2] Johannes Kepler Universitat, Linz, Austria.
ensantos@utfpr.edu.br

Summary:
This paper presents a versatile impedance sensor in a way that can be used in multiphase flow applications. The sensor measures the electrical parameters of flowing media. It can be deployed distributed along flowlines to perform real-time multiphase flow characterization. The sensor was evaluated against commercial references and further applied fluid-dynamics investigation.

Keywords: multiphase flow measurement, impedance sensor, distributed sensing

Introduction

Multiphase flow is a recurrent topic and is commonly founded in various industrial applications. For instance, in the oil and gas industry, fluids such as water, oil and gas stream typically in pipes or vessels, forming a multiphase flow mixture. For many years, scientists and engineers have extensively investigated the phenomena by performing experiments under controlled conditions to support the validation of flow models and provide data for validating computational fluid dynamic (CFD) codes, where pilot-plant studies are typically used for scaled-down flow simulation of large-scale circuits and components. However, new challenges emerged with the required energy transition, where carbon capture and sequestration (CCS) or geothermal source of energy, making further investigation necessary to understand a new type of phenomena, such as methane hydrate formation and flow at high concentrations of CO2, among others. Yet, all flow meter technologies have limitations, and most have a tough time with the multiphase flow. The fluid dynamic characteristics of the mixture are highly complex and, to a large degree, are still not characterized by modern-day fluid dynamic models [1].

Current-in-use equipment is based on measurement techniques such as electrical impedance, ultrasound, and ionic sensors (e.g., x-ray and ɣ-ray). However, none has universal applicability; some have considerable drawbacks and may fail in particular practical situations. Furthermore, installing many of them in small-scale experiments running at university laboratories and research centers is improbable due to the cost of equipment and infrastructure, making it even more challenging to access information. In this fashion, this work explores the development of versatile impedance sensors to achieve a broader application range compared to single modalities techniques, contributing to a more universal application than those currently in use. As a step towards the further development of sensor technology, we describe a dual-modality electronic being able to simultaneously evaluate the conductive and the capacitive component of the flowing media over a broad range of values and at high repetition rates in real-time.

Phase fraction measurement in fluids

Electrical impedance measurement is a common tool for characterizing the electrical properties of materials and substances. In process diagnostics, the measurement allows individual phases to be distinguished from each other based on their specific electrical properties (e.g., conductivity and permittivity).

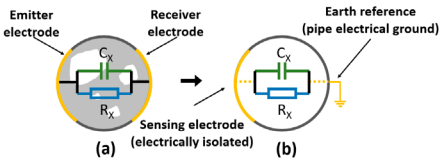

Fig. 1. Simplified electrical model for fluid mixture and capacitance and resistance measurement to earth ground reference.

Figure 1a depicts the equivalent low-frequency (up to a few MHz) circuits for a homogeneous mixture which is given by the parallel connection of a capacitor and a resistor between two electrodes (emitter and receiver). Fig 1b shows the connection topology considering a sensing electrode measuring the parameters to the common

ground electrode, which is very common for some types of sensor geometry.

The measurements are carried out with the help of a measuring cell or probe designed for a determined application. Thus, the phase fraction can be estimated using sensor calibration curves, electrical mixture models, and data fusion algorithms [2].

Dual Modality Impedance Sensor

In this work, the sensor was conceived to be low-cost and easy to handle, so a number of them can be installed along a flow loop to support fluid dynamics investigation.

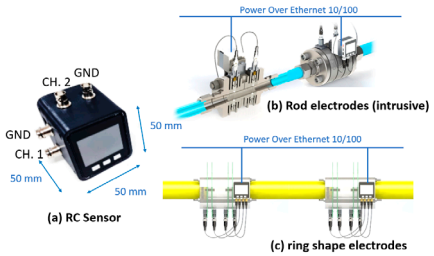

Fig. 2. (a) RC Impedance sensor; (B) distributed in a high-pressure system using intrusive electrodes; (b) distributed in flow lines using non-intrusive electrodes.

An embedded real-time system controls the sensor electronics (Fig. 2a). The sensor comprises two distinct circuits to measure capacitance and resistance parameters to the ground-earth reference. This topology was chosen to reduce the number of electrodes required because the sensor's body is made of metal to operate in conditions where the temperature and pressure are elevated (Fig. 2b). Different probes, such as rod sensors and non-intrusive ring shape electrodes, can be used (Fig. 2c). The sensor uses two channels to obtain flow velocity applying cross-correlation or specialized flow feature extraction algorithms.

The measurement type selection (R or C) is achieved by an analog switch that also commutes the measurement channel (Ch.1 or Ch.2). In addition, to investigate fast events that occur on the multiphase flow phenomena, it was designed to deliver high sensitivity at high-speed measurements. Therefore, the sensor can measure both R and C values in both channels at a repetition rate of 1000 samples per second/parameter/channel. The sensor acts like a server and continuously streams the data to the clients in a bidirectional communication through a WebSocket protocol, providing full-duplex communication channels over a single TCP connection. The sensor is powered along with data on twisted-pair Ethernet cabling. The information can be sent directly to a personal computer or a server containing services to process the data automatically and make the information available to many clients in real-time (Fig 3).

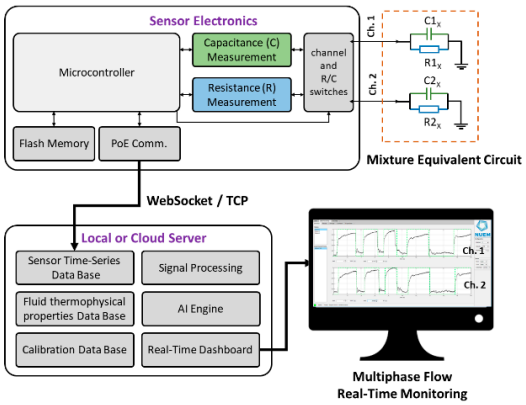

Fig. 3. Measurement components: Sensor electronics and cloud server.

Experimental Evaluation

In this work, the sensor was first evaluated by measuring commercial resistors and capacitors in a range of 0.5 ohms up to 1k ohm and 1.2 pF to 1 nF. The results show a deviation within 0.5% against reference values. As a second test, the sensor was applied to measure an oil-water mixing test. The pipe segment was filled with oil and water. An impeller mixed the phases for a short time, and the sensor monitored the separation process, as depicted in Fig. 4b.

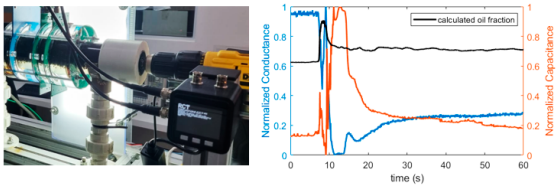

Fig. 4. (a) Experimental setup; (b) normalized conductance (blue), normalized capacitance, calculated oil fraction (black).

Conclusions

The sensor electronics were presented and evaluated. The system is able to simultaneously determine the capacitive and conductive components of fluids showing reasonable accuracy and fast response. Future work will further validate the phase fraction measurement based on resistance and capacitance measurements.

References

[1] G. Falcone, “Heavy Oil Metering Applications” in Multiphase Flow Metering: Principles and Applications, 1st ed., vol. 54, Elsevier Science, 2009, pp. 251–266.

[2] N. Libert, R. Morales, Capacitive measuring system for two-phase flow monitoring. Part 2: Simulation-based calibration, *Flow Measurement and Instrumentation*, 102-111 (2016); doi: 10.1016/j.flowmeasinst.2016.05.011

DOI 10.5162/SMSI2023/P44

Towards inline hydrates detection by electrical impedance measuring system

Gustavo Fraga Gehring[1], Natan S. Reginaldo[1], Jean Paulo Nakatu Longo[1], Marco José da Silva[1,2], Rigoberto E. M. Morales[1], Eduardo Nunes dos Santos[1]
[1] Multiphase Flow Research Center (NUEM) Federal University of Technology – Paraná (UTFPR), Curitiba, Brazil.
[2] Johannes Kepler Universitat, Linz, Austria.
ensantos@utfpr.edu.br

Summary:
Methane hydrates is a critical occurrence in the oil and gas industry because it can potentially interrupt the flow of pipelines. Monitoring the formation of hydrates is critical for decision-making leading to damage control of blockages. To date large safety margins are applied in hydrates management which could be optimized by proper monitoring, thus decreasing costs. Here we show that a straightforward impedance-based measuring system can detect fluctuations in conductance and capacitance and correlate them to the formation of ice in a tube. Ice has similar properties to hydrates and was therefore selected as model substance in this study.

Keywords: electrical impedance, capacitance and conductance, flow assurance, hydrates, ice formation.

Introduction

Hydrates blockages can be problematic in oil and gas facilities. The presence of hydrates can cause flow restrictions and permanent damage to pipelines. Current hydrates management strategies rely on large safety margins as well as remediation strategies such as thermal heating of pipelines of the injection of chemicals (so-called hydrated inhibitors) [1]. In that sense, detecting hydrates formation is essential for maintaining safe conditions and/or decreasing costs in oil and gas production. Since ice has similar properties to hydrates, it was therefore selected as model substance in this study.

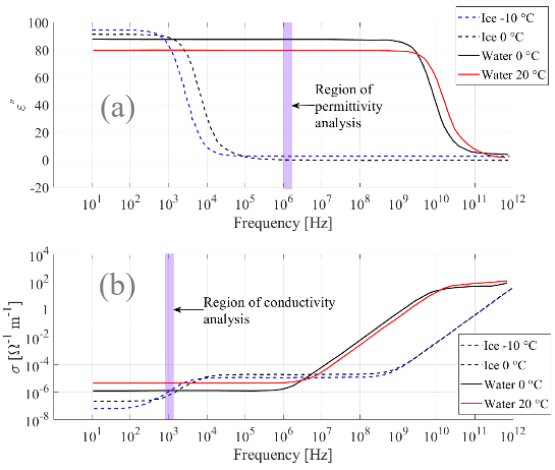

Fig. 1. Frequency-dependent (a) relative permittivity and (b) conductivity of water and ice [2].

The proposed measuring system works with the changes in conductivity and relative permittivity of water and ice to sense when solidification occurs. The frequency dependence of the relative permittivity and conductivity is shown in Fig. 1, which is generated based on the models given by [2]. Furthermore, some temperature dependencies of these electrical quantities can be seen. The region of analysis of relative permittivity was MHz, and conductivity was kHz.

Measuring system

The experimental setup depicted in Fig. 2(a) consists of a pipe section with four ring-shape sensors (1). The impedance-based measuring system (indicated by RC sensor) (3), was applied to measure the conductance and capacitance during ice formation. A computer (4) was used to monitor in real-time the electrical parameters measured by the sensor and temperature. The temperature sensor (5) was placed inside the pipe, and the control of temperature until the solidification of water was done by inserting the pipe inside a chiller (6).

A photograph of the system is shown in Fig. 2(b). The pipe was built as an apparatus consisting of a two-inch pipe (1); inside the pipe, it had two pairs of ring-shaped sensors with the same diameter. The sensors were placed to form a non-intrusive measurement. The ring-shaped is a pair of parallel electrodes with a ring geometry well-established to characterize flow patterns [3].

The electrodes support the RC sensor in sensing changes in electrical parameters (conductance and capacitance). The impedance-based measuring system has two independent circuits which determine conductance (by an opamp-based I-V method) and capacitance (by a capacitance-to-digital IC). To control and monitor the parameters of the RC sensor, a proprietary software was used (4) to display in real-time visualize the measurements. Furthermore, a temperature data logger was also applied based on the type K thermocouple. The precise temperature control was realized by the chiller.

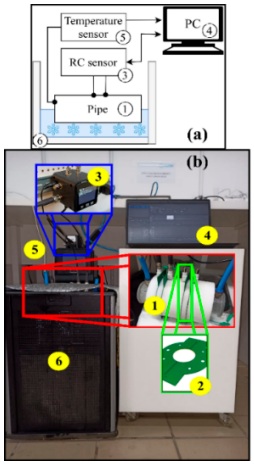

Fig. 2. Measurement system. (a) Experimental setup (b) photograph of the system.

Ice formation

The ice formation process (Fig. 3), with the pipe full of water, started when (t = 0 s) with setting the bath to -10 °C. At this time, the temperature inside the pipe was 7 °C (the thermocouple has a nominal uncertainty 1 °C tolerance). As the temperature of the water inside the pipe is higher than the temperature of the bath, heat is transferred from the water inside the pipe to the fluid in the bath; for that reason, the temperature inside the pipe starts to fall. As temperature decreases, changes in normalized conductance and normalized capacitance occur – this was expected for the dependency of these electrical parameters over temperature (see [4, 5]). The conductivity of water decreases with the temperature; this change in this parameter causes a decrease in the conductance measured.

On the other hand, the permittivity of the water increases as the temperature decay – as noted in Fig. 1(a). These higher permittivity values increase the capacitance measured. These behaviors are in good agreement with [2]. The temperature inside the pipe decreases until -3 °C. Although the freezing temperature of the water is close to 0 °C, the water rarely freezes when it hits this temperature; that is the well-known supercooling principle [5]. At the time t = 01:15:00, the temperature abruptly changes from -3 °C to 0 °C. This is when nucleation occurs, and that ice begins to form. A rising in temperature characterizes this stage due to latent heat being released by the ice crystal absorbed by water. When ice is formed, steep fluctuations in conductance and capacitance are noticed. Both normalized conductance and capacitance decrease due to the conductivity and relative permittivity of ice is lower than water, thus being a good indicator for ice formation.

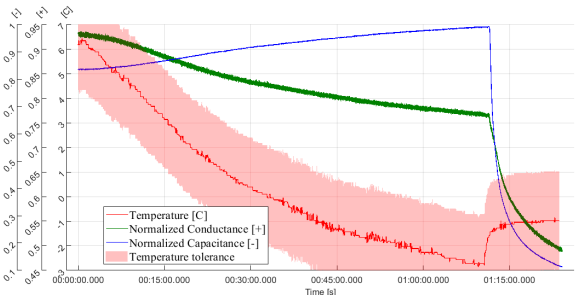

Fig. 3. Ice formation from fresh water.

Conclusion

An impedance-based measuring system was developed and tested to monitor the ice formation process. The system was capable of detecting conductance and capacitance variations that were correlated to the solidification of water. Hydrates is expected to behave similarly and will be studied in the next research phase.

References

[1] Makogon, T. Y. (2019). Handbook of multiphase flow assurance. Gulf Professional Publishing.

[2] Artemov, V. G., Ryzhkin, I. A., & Sinitsyn, V. V. (2015). Similarity of the dielectric relaxation processes and transport characteristics in water and ice. JETP Letters, 102(1), 41-45; doi:10.1134/S0021364015130020

[3] Shi, X., Tan, C., Dong, F., dos Santos, E. N., & da Silva, M. J. (2020). Conductance sensors for multiphase flow measurement: A review. IEEE Sensors Journal, 21(11), 12913-12925; doi: 10.1109/JSEN.2020.3042206

[4] Felsberger, R., Schweighofer, B., Flatscher, M., Rath, M., Grubmüller, M., & Wegleiter, H. (2018, June). Low power ice detection with capacitive and impedance spectroscopy-based measurements. In 2018 IEEE 27th international symposium on industrial electronics (ISIE) (pp. 809-813). IEEE; doi: 10.1109/ISIE.2018.8433765

[5] Gordon, J. R. (1996). An investigation into freezing and bursting water pipes in residential construction. Building Research Council. School of Architecture. College of Fine and Applied Arts. University of Illinois at Urbana-Champaign.

DOI 10.5162/SMSI2023/P46

Compact Gas and Aerosol Sensing based on Photothermal Interferometry

Manuel Tanzer[1], *Benjamin Lang*[1], *Alexander Bergmann*[1]
[1] *Institute of Electrical Measurement and Sensor Systems, Technical University of Graz, Inffeldgasse 33/I, 8010 Graz, Austria*
manuel.tanzer@tugraz.at

Summary:
An instrument for gas and aerosol sensing based on photothermal interferometry has been developed. Depending on the light source used for photothermal excitation, either gas or aerosol concentrations may be measured. A fabrication process for low-cost air-spaced Fabry-Pérot etalons, for the interferometric detection unit, is presented. Based on a demonstrator setup, an extensive scrutiny of all noise sources is being performed serving as a basis for the evaluation of the miniaturization potential of said sensor system. First measurements with water vapor were conducted, highlighting the sensor's potential.

Keywords: Photothermal Spectroscopy, Photothermal Interferometry, Fabry-Pérot Etalon, Gas Sensing, Aerosol Sensing

Introduction

Photothermal interferometry (PTI) has received a lot of scientific attention in recent years, due to outstanding sensitivities and selectivity. In PTI the target gas is periodically excited via laser irradiation, leading to a modulated local heating and, therefore, to a modulated change of the refractive index (RI). This change of RI can be detected interferometrically, e.g. by the use of a Fabry-Pérot etalon (FPE), allowing miniaturization, as the laser-gas interaction path can be reduced drastically. However, in the past, mostly complex and large bench-top systems have been developed [1]. It has also been shown, that a commercial all-optical microphone can be utilized for the detection of photothermal signals [2], with the downside of high costs. In order to demonstrate compact, reliable and efficient systems compatible with large-scale production, all components have to be evaluated with regard to miniaturization potential, noise contributions and cost. Selective and reliable measurement of gases like CO/CO_2 will greatly benefit areas like medical health monitoring (breath analysis), the automotive industry (cabin sensing), and environmental monitoring (greenhouse gases).

Methods

For the systematic analysis of all signal-limiting noise sources, a system model and a lab demonstrator have been developed and built. The setup is depicted in Fig. 1. The interferometer's light source (probe laser) is an ultra-low-noise (ULN) laser with exceptionally narrow linewidth (<100 *Hz*) and is controlled with the provided software. An isolator prevents back-reflections into the laser cavity and the subsequent 90/10 splitter divides the light into a signal- and a reference path, allowing the use of a balanced photodetector (BD). Thereby, common noise present in both light paths is electronically canceled, allowing measurements at the shot noise limit. Due to the FPE being present in just the signal path, laser phase noise, which gets converted by the FPE into amplitude noise, cannot be eliminated by the BD, highlighting the need for an ULN laser.

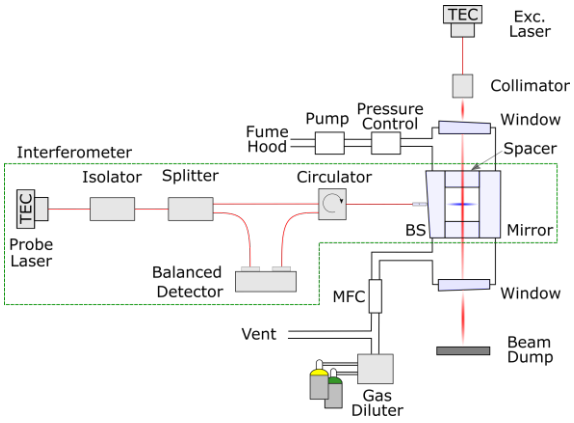

Fig. 1. Schematic of the optical PTI setup. The green frame indicates the interferometer. Fibers = solid red lines, free space excitation laser light = red beams, probe laser = blue beam, BS = beamsplitter, MFC = mass flow controller, TEC = thermo electric cooler.

Roughly 10 % of the light from the splitter is guided onto the reference photodiode of the BD and the rest is directed into the FPE via a circulator. The light reflected from the FPE is transmitted to the signal photodetector of the BD. As the system should be compact, rugged and low in cost, a custom-made air-spaced FPE is used as an interferometer. The FPE was built completely by standard, commercially available bulk-, as well as fiber-optic components. It is integrated into a gas-tight 3D-printed measurement cell. The bulk optic etalon consists of a 70 % semi-reflecting, as well as a highly-reflecting mirror, which are separated by 3 mm high-precision spacers. To maintain optical alignment during handling, the etalon is fiber-coupled via a GRIN lens, permanently mounted onto the backside of the semi-reflecting mirror. An alignment platform, consisting of translation and goniometric stages was assembled, to optimize the coupling between the fiber-coupled GRIN-lens collimator and the etalon. To maximize sensitivity, the operating point (OP) of the FPE has to be tuned to the inflection point of the reflectance function, where its first derivative has a maximum. For proof of principle measurements, the laser's wavelength is fixed at the OP via a constant driving current. Further, feedback-based, stabilization methods are subject of ongoing work. Water vapor was chosen for initial tests, as its strong absorption bands (e.g. at 1364.7 nm) can be targeted with low-cost telecom laser sources. Via a lens, the excitation laser is focused through the measurement cell, intersecting the probe beam perpendicularly inside the FPE. System control and data acquisition are implemented on a National Instruments FPGA-based system. The modulation frequency was set to be 125 Hz, well clear of disturbing 50 Hz harmonics.

Results

With the alignment setup, as well as the optical components described in the previous section, a fiber-coupled FPE with an effective finesse of ~15 could be fabricated and characterized. In Fig. 2, a rendering of the measurement cell with integrated FPE as well as the measured reflectance function is depicted.

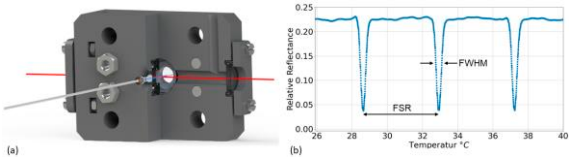

Fig. 2. The fiber-coupled bulk-optical FPE. (a) Rendering of the measurement cell with the integrated FPE. Red lines = excitation, blue lines = probe laser. (b) Temperature sweep over three free spectral ranges (FSR), with arrows indicating the full width at half maximum (FWHM).

For water vapor measurements, the cell is operated with open windows and exposed to ambient air with a concentration of 13 762 ppmV, as measured by a reference device (temperature = 21.4°C, pressure = 979.9 hPa, relative humidity = 52.2 %). The signal is extracted by means of a Fast Fourier Transform (FFT) and compared to the background signal with the excitation laser turned off (see Fig. 3). A signal to noise ratio (SNR) of more than 7000 can be obtained, corresponding to a limit of detection of approximately 5 ppmV (3σ).

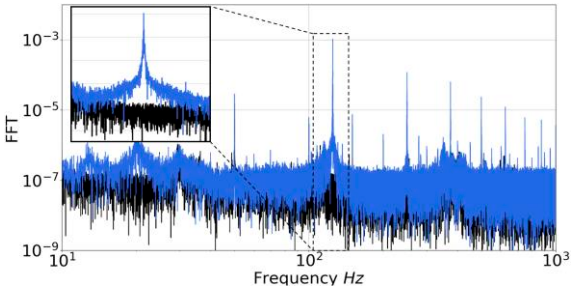

Fig. 3. FFT signal of two measurements. In blue, the modulated (125 Hz) excitation laser is turned on. The first (inset), as well as higher harmonics can clearly be distinguished from the background. In black, the background, with the excitation laser turned off, is shown.

Additional use of a Lock-In amplifier is expected to further increase the SNR.

Conclusion and Outlook

We have successfully developed and built a PTI system from ground up. A novel method to fabricate a low-cost air-spaced FPE from standard commercially available components has been established. First proof of principle experiments with water vapor were conducted and a SNR of more than 7000, for 13 762 ppmV, has been achieved. A custom developed ICL laser source in the 4 µm region [3] will be implemented as excitation source, enabling sensitive measurement of greenhouse gases like CO_2 at compact overall system sizes. Further optimization of the sensor system is in progress and is expected to improve performance significantly.

References

[1] J. Waclawek et al., Balanced-detection interferometric cavity-assisted photothermal spectroscopy employing an all-fiber-coupled probe laser configuration, Opt. Express 29, 7794-7808 (2021); doi: 10.1364/OE.416536

[2] P. Breitegger et al., Intensity Modulated Photothermal Measurements of NO_2 with a Compact Fiber-Coupled Fabry–Pérot Interferometer, Sensors. 19(15):3341(2019); doi: 10.3390/s19153341

[3] H. Knötig et al., Continous-wave operation of vertically emitting ring interband cascade lasers at room temperature, Appl. Phys. Lett. 116, 131101 (2020); doi: 10.1063/1.5139649

DOI 10.5162/SMSI2023/P47

Portable Raman sensor systems for life sciences and agri-photonics – from light sources to field measurements –

Bernd Sumpf, Marcel Braune, Jeannine Gleim, André Müller, Kay Sowoidnich, Marko Vastag, Lucas Wittenbecher, Thomas Filler, Neysha Lobo-Ploch, Martin Maiwald

Ferdinand-Braun-Institut, Leibniz-Institut für Höchstfrequenztechnik
Gustav-Kirchhoff-Str. 4, 12489 Berlin, Germany

Raman spectroscopy is a well-established non-invasive label-free optical measurement technique for the analysis of numerous substances in various application fields, e.g., process control, food safety and quality control, the detection of hazardous compounds, e.g., explosives, and narcotics, and the analysis of minerals. Finally, also the application in medicine, e.g., for point-of-care diagnostics, is promising.
Nevertheless, in several fields, when disturbing signals like fluorescence from the sample itself occurs or background light from the sun or artificial light sources cannot be avoided, the weak Raman signals are obscured. Beside mathematical techniques to simulate the disturbing signals and subtract the obtained background spectra from the measured signals, physical approaches have the advantage of a direct separation of desired and interfering spectral contributions. Here, beside the selection of the excitation wavelength or the utilization of the different temporal behavior of fluorescence and Raman signals, several methods using multiple laser wavelengths within a narrow spectral range for the excitation of the Raman effect can be implemented. The underlying effect in this case is that the Raman signals follow the change in the excitation wavelength whereas the background signals remain mainly constant.
Shifted excitation Raman difference spectroscopy (SERDS) uses two excitation lines typically with a spectral distance of about the full-width at half-maximum of the Raman signals under study. For solids and liquids this value amounts to 10 cm^{-1} and it corresponds to a spectral distance of 0.25 nm at a commonly used excitation wavelength like 488 nm, whereas the value at 785 nm excitation is 0.60 nm. Lasers based on atomic transitions like the Argon-ion laser cannot be tuned over such spectral distances and solid-state lasers with a broader gain profile like Ti:sapphire lasers require moving mechanical parts to adjust the respective wavelengths. Here, diode lasers and diode laser based light sources with implemented wavelength stabilization and the option for spectral tuning provide a compact and robust solution, e.g. with respect to portable instruments for field deployment.
In this contribution, compact dual-wavelength diode lasers and diode laser based light sources developed for SERDS will be presented together with their implementation into portable Raman sensor systems widely usable from measurements on agricultural fields to applications in hospital environments, e.g., for point-of-care measurements or therapy monitoring.
The light sources used for SERDS in the red and near-infrared spectral range are based on monolithic dual-wavelength diode lasers. The dual-wavelength operation is realized using two implanted Bragg gratings and respective ridge waveguide (RW) branches which were coupled using a Y-branch coupler followed by a common output section. The switching between the two wavelengths can be performed directly by applying an injection current to the respective RW-section. Herewith, a fast switching up to the kHz-range is easily possible. The spectral distances between the two wavelengths can be adjusted by implemented resistor heaters located above the gratings. Using this concept, one-chip diode lasers with emission wavelengths of 671 nm and 785 nm were realized with output powers up to 200 mW.
Devices for the green and blue spectral range are developed based on frequency doubling of the laser emission of distributed feedback or distributed Bragg reflector RW-lasers. Here, light sources at 488 nm, 515 nm, and 532 nm with output powers up to 50 mW were realized. Due to the fact, that the temperature-related spectral tuning of the grating wavelength and the phase-matching wavelength of typically used Li:NbO_3-crystals are comparable, the tuning can be performed by changing the temperature of the whole device.
The above-described laser devices were implemented into in-house developed and manufactured turn-key-systems, that provide the necessary heat removal, temperature control, and injection and heater currents for laser operation. The emitted laser radiation can be transmitted into the Raman setup either by using free space optics or fiber coupling. The control of the whole system is realized via a standard USB interface and a graphical user interface based on in-house developed software.

Such a turn-key-system equipped with a 785 nm dual-wavelength Y-branch DBR-RW-laser was implemented into a measurement system inside a rugged housing dedicated for Raman measurements on soils in the field. Via a fiber coupler, the light was transferred into a commercial transfer optic from InPhotonics (Raman probe II^{TM}), which is designed for a 180° backscattering geometry. The probe contains the necessary optical filters for the suppression of spontaneous emission from the diode laser and the Anti-Stokes shifted Raman photons as well as Rayleigh scattered light. The Stokes-shifted Raman photons are coupled into a 300 µm optical fiber and transferred to a compact Raman spectrometer. All assemblies are supplied by means of a rechargeable battery with a nominal voltage of 12 V and a capacity of 20 Ah. With this system, successful measurement campaigns on agricultural fields were performed showing the potential to detect carbonates and soil organic matter.
A similar system was manufactured to measure carotenoids using resonance Raman enhancement at an excitation wavelength of 488 nm. Here, the target was to monitor the antioxidant level of human skin in vivo to gain data on human health status and provide diagnostic information during medical treatments and accompanying medical therapies. Again, the light source was implemented into a turn-key-system and the light was fiber coupled into an in-house developed optical transfer system. A calibration procedure using skin phantoms containing varying ß-carotene levels demonstrated a limit of detection of 0.03 nmol g^{-1}, which is well-below the typical concentration of carotenes in skin.
Beside the technical description, examples for field and clinical measurements will be presented. An outlook will be given with respect to other targets and applications and the potential to simplify the setup by implementing a filter-based detection concept.

References:

[1] A. P. Shreve, N. J. Cherepy, R. A. Mathies, "Effective rejection of fluorescence interference in Raman spectroscopy using shifted excitation difference technique", *Appl. Spectrosc.,* **46**, no. 4, p. 707-711, 1992.
[2] M. Maiwald, J. Fricke, A. Ginolas, J. Pohl, B. Sumpf, G. Erbert, G. Tränkle, "Dual-wavelength monolithic Y-branch distributed Bragg reflection diode laser at 671 nm suitable for shifted excitation Raman difference spectroscopy", *Laser Photonics Rev.,* **7**, no. 4, pp. L30-L33 (2013).
[3] B. Sumpf, M. Maiwald, A. Müller, J. Fricke, P. Ressel, F. Bugge, G. Erbert, G. Tränkle, "Comparison of two concepts for dual-wavelength DBR ridge waveguide diode lasers at 785 nm suitable for shifted excitation Raman difference spectroscopy", *Appl. Phys. B*, **120**, no. 2, pp. 261-269 (2015).
[4] M. Braune, M. Maiwald, B. Eppich, O. Brox, A. Ginolas, B. Sumpf, G. Tränkle, "Design and Realization of a Miniaturized DFB Diode Laser-Based SHG Light Source With a 2-nm Tunable Emission at 488 nm", *IEEE Trans. Compon. Packag. Manuf. Technol*., **7**, no. 5, pp. 720-725 (2017).
[5] B. Sumpf A. Müller, M. Braune, J. Gleim, N. Ruhnke, M. Vastag, M. Maiwald, "Diode laser based light sources for shifted excitation resonance Raman difference spectroscopy in the spectral range between 450 nm and 532 nm" *Proc. of SPIE, vol. 11978, Plasmonics in Biology and Medicine XIX, Photonics West, Hybrid Event, San Francisco, USA, Jan 22-27, 1197802 (2022).*
[6] M. Maiwald, K. Sowoidnich, B. Sumpf, "Portable shifted excitation Raman difference spectroscopy for on-site soil analysis", *J. Raman Spectrosc.*, **53**, no. 9, pp. 1560-1570 (2022).
[7] S. Jung, M.E. Darvin, J. Schleusener, G. Thiede, J. Lademann, M. Braune, M. Maiwald, B. Sumpf, G. Tränkle, D. Kutzer, F. Elban, H. Fuss, "In vivo detection of changes in cutaneous carotenoids after chemotherapy using shifted excitation resonance Raman difference and fluorescence spectroscopy", *Skin Res Technol.*, **26**, no. 2, pp. 301-307 (2020).

Acknowledgment:
This work was realized within the projects I4S-RaMBo (031A564C, 031B0513C), the projects Exasens (13N13858), Freshscan (16SV2334), and iCampus (16ES1132) funded by the Federal Ministry of Education and Research (BMBF) and it was supported by the Einstein Stiftung, Berlin, in the project Hautscan (A-2011-88). This work was also partly funded by the BMBF under the project reference number 16FMD02 (Research Fab Microelectronics Germany - FMD). Moreover, the work was supported by the European Commission in the project MIB (667933-2) and USER-PA (FKZ 2812ERA039).

DOI 10.5162/SMSI2023/P48

Study on Sensitivity and Accuracy of Piezoelectric Stack Actuators for Charge Self-Sensing

Sonja Müller[1,2], Stefan J. Rupitsch[1], Ulrich Mescheder[2]
[1] Freiburg University, Georges-Köhler-Allee 106, Freiburg, Germany
[2] Furtwangen University, Robert-Gerwig-Platz 1, Furtwangen, Germany
mso@hs-furtwangen.de

Summary:
The charge response of a force applied to piezoelectric stack actuators was characterized in the range of 0 N – 20 N for application in piezoelectric self-sensing. Results show linear behavior between applied force and collected charge for both actuators tested in this study. One actuator exhibits a 3.55 times higher sensitivity slope than the other related to its larger capacitance. An error analysis reveals a reduction of relative error in charge measurement with rising forces applied to the actuators.

Keywords: Piezoelectricity, linear stack actuator**,** self-sensing, charge measurement, miniaturization

Introduction

Piezoelectric self-sensing has shown to be of great potential when it comes to miniaturization of actuator systems [1]. Information about the displacement and force acting on the actuator can be gained without additional sensors. This information can further be used in a control loop or be collected to display the information about the state of the environment. Piezoelectric self-sensing has already been used in various research fields, for example vibration suppression [2] or force control [3].
The presented work focuses on the analysis of two linear piezoelectric actuators (PEA) under the influence of applied force by measuring the direct piezoelectric effect. A better understanding of the self-sensing response of each of the actuators should be achieved. We compare the differences of the sensing response of two actuators to investigate sensitivity and signal to noise ratio differences.

Methods

The two chosen PEAs for this study comprise the PA2JEW (Thorlabs, Inc.) and the PK2JA2P2 (Thorlabs, Inc.) stack actuator. The latter is composed of 4 PA2JEW actuators bonded together to form a longer stack and provide 4x larger stroke and capacitance. To measure the direct piezoelectric effect on the PEA, the actuator is inserted in a previously designed mechanical setup [4]. The force is applied by a screw pressing down on the actuator. A force sensor (adafruit, 4540) is placed below the PEA to determine the applied force.

The direct piezoelectric effect is sensed using an electrical circuit (Fig. 1). Electric current is measured flowing through an ammeter (Keysight B2981A) and integrated over time, giving information about the charge on the electrode surface of the PEA.

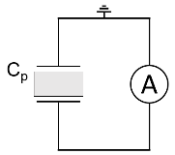

Fig. 1: Schematic of the electrical circuit to detect charge from the actuator surface. C_p: PEA

The charge resulting from applied force is detected for two PEAs, which both can be used in miniaturized inchworm actuators. Experiments are carried out with force of 5 N - 20 N, fitting to force occurring in the application of mandibular distractors [5]. The measurement at each force was repeated ten times. All experiments are done while the PEA is prestressed with a force of 0,3 N. The capacitance C of the PEAs can be calculated from Eq. (1) using the permittivity ε, the base area A, the distance d, and the number n of piezoelectric layers in each stack. The number of layers is obtained from Eq. (2) with the nominal stroke ΔL at an applied potential U and the dielectric constant d_{33}.

$$C = \frac{\varepsilon_0 * \varepsilon_r * A}{d} * n \quad (1)$$

$$n = \frac{\Delta L(U)}{d_{33} * U} \quad (2)$$

Results and Discussion

For PA2JEW, a capacitance of 185.48 nF is calculated, while the PK2JA2P2 has a capacitance of 741.9 nF. The calculated stack layers are 38 and 150, respectively. The capacitances deviate by more than 25 % from the manufacturer's specified capacitance. This can be explained by the uncertainties in layer thickness. The entire stack is assumed to contribute to the PEA, isolation layers are not considered. The results of the charge measurement at applied forces for both PEAs can be seen in Fig 2.

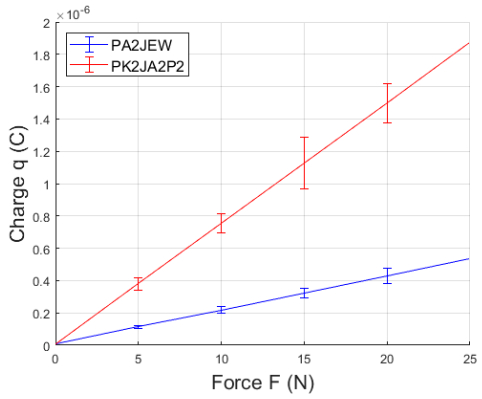

Fig. 2: Relationship between applied force and measured charge from the PEAs.

The results show that both measured piezoelectric stacks feature linear behavior between applied force and measured charge. The PK2JA2P2 has a slope 3.55 times higher than the slope from PA2JEW. Because the PK2JA2P2 is built of four blocks of the PA2JEW and shows a capacitance 4 times higher, the slope was expected to be four times higher.
This difference can have several reasons. The bonding layers between will be compressed by the acting force, thus reducing the total force acting on the piezoceramic layers. The PEAs both have an additional ceramic coating covering the sides of the PEAs, which might influence the force transmission. In addition, the PK2JA2K2 has a plastic wrapping, which might transfer some amount of force directly to the ground, bypassing the PEA.

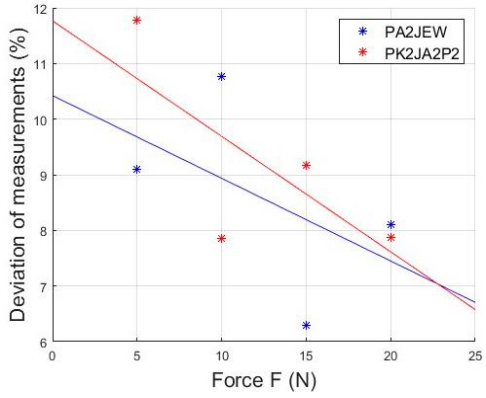

Fig. 3: Measurement error for charge measurement in percent with trend line

The relative error for each measured point is displayed in Fig. 3. It can be seen that with rising forces, the relative error gets smaller. This is due to noise in the system, which represents a smaller influence with larger measurement values. Additionally, the PA2JEW shows a better S/N ratio at low forces whereas at 20 N, the performance of both actuators is similar.

Conclusions

Different forces were applied to two PEAs and the resulting charge was measured to gather information about the number of accumulated charges at applied forces. Forces were applied in range that is expected to be observed in a medical application of piezoelectric self-sensing. Both PEAs show a linear behavior between applied force and collected charge. The range of error measurement is high but can be reduced with higher applied force due to noise reduction relative to the measurement.
The error in force measurement is lower for the PA2JEW at low forces up to 20 N and, therefore, more suitable for accurate force measurements.
In future work, the issue of errors in measuring charge at applied force needs to be addressed and reduced to make the stacks more feasible and measurements more accurate to use in any force sensing application. The measuring method can then be also adapted to work with actuation voltages on the PEA. The sensing circuit will need to be adapted accordingly.

References

[1] Kawamata, A et al (2008): Self-Sensing Piezoelectric Actuator using Permittivity Detection. In *Ferroelectrics* 368 (1), pp. 194–201. DOI: 10.1080/00150190802368495.

[2] Jansen, Bas; et al (2019): Active Damping of Dynamical Structures Using Piezo Self Sensing. In *IFAC-PapersOnLine* 52 (15), pp. 543–548. DOI: 10.1016/j.ifacol.2019.11.732.

[3] Badel, Adrien; et al (2008): Self-sensing force control of a piezoelectric actuator. In IEEE transactions on ultrasonics, ferroelectrics, and frequency control 55 (12), pp. 2571–2581. DOI: 10.1109/tuffc.2008.973.

[4] Mueller, Sonja et al (2022): Experimental characterisation of a piezoelectrically actuated force amplifier using optical and self-sensing methods. In : ACTUATOR 2022; International Conference and Exhibition on New Actuator Systems and Applications, pp. 1–4.

[5] Robinson, R. C. et al. (2001): Mandibular distraction force: laboratory data and clinical correlation. *J.of oral and maxillofacial surgery,* 59 (5), 539-44; discussion 544-5. DOI:10.1053/joms.2001.22688.

Acknowledgement: This work was funded by the BMBF project PersonaMed within the CoHMed project, project grant 13FH5I06IA.

DOI 10.5162/SMSI2023/P49

Using established microservices for data collection of distributed sensor systems

Henrik Lensch[1], Johannes Amann[1], Christian Bur[1], Andreas Schütze[1]
[1]Saarland University, Lab for Measurement Technology, Saarbrücken, Germany
h.lensch@lmt.uni-saarland.de

Summary:
In this work, a scalable capture and visualization setup for time series data of distributed field test systems is presented. As a data source various different commercially available metal oxide semiconductor (MOS) gas sensors with their on-chip sensor-integrated manufacturer evaluation models are used as well as own calibration models

Keywords: gas sensor, data storage, field test, calibration, IoT

Introduction

Recent trends in IoT technology and big data handling led to easy-to-use open source microservices that do not require extensive knowledge in programming. These services claim a high rate of automatization for handling data, especially long-term experiments [1]. It is only necessary to connect the needed services over preconfigured APIs and attach the experiment data output, e.g. files, automated scripts, to the data input of the database. Further interconnectivity is handled automatically once this is set up. This automatization enforces a standardized data format for different experiments, since uploading and querying the database must happen in a standardized format. This is a fundamental requirement for achieving findable and interoperable data [2].

As an example, to implement and test such a software stack, we chose a long-term measurement campaign, investigating the performance of different MOS sensors for indoor air quality monitoring and their manufacturer calibration against our own, more selective, calibration.

Hardware

To test the suggested software stack, time series data of four distributed field test systems consisting of various gas sensors is used. Each system holds ten sensors operating in manufacturer mode and additional five sensors using temperature cycled operation. All sensors are operated with a self-made hardware platform [3] connected to a Raspberry Pi [4]. Each sensor system was calibrated under lab conditions [5]. Based on this data, regression models are built by means of machine learning. Due to the various functionalities of a single sensor, several environmental variables (this highly depends on the sensor but such as humidity, total VOC, air quality index, ozone level, NOx, CO2 equivalent, etc.) are calculated already on chip and are provided together with the electrical resistance, i.e. raw data [6].

A total of four systems were set up in different locations. One is located at the Lab of Measurement Technology, one in a city flat, one in a flat in the countryside, and one in an office room of a local company. Specific events, like everyday processes in the flats such as cleaning or cooking, are recorded manually to correlate them to the sensor signals.

System Design

Since the systems are distributed across multiple locations and generating a large amount of data, a high degree of automatization is needed to transfer, store, and visualize data at a centralized location. This software stack should provide the following features:

- Display significant data instantly after initial setup with focus on a user with no expertise in databases.
- Annotation option to relate events at the site (cooking, cleaning, etc.) to a gas sensor signal.
- Queryable API to download data selectively for further evaluation with MATLAB, python, etc.
- Retroactively add, remove, and identify models based on lab-calibration data to the database and compare them with already existing models and manufacturer mode.
- Option to increase the number of field test systems easily.

- Automatic alerting mechanism if a field test system or the database malfunctions.

Results

The sensor data is saved and compressed in HDF5-files every hour. For transferring the raw data file to our storage server Syncthing is used. Syncthing is a peer-to-peer file synchronization tool avoiding transferring and storing data on a 3rd party's server. Additionally, no advanced configuration on the IT infrastructure is needed. The most important feature is that it automatically reconnects if the connection to the server is interrupted without disturbing the measurement software.

On our storage server, the HDF5 files of each system are extracted and reshaped for database upload and applying the machine learning models by a python script.

The raw data is fed through one or multiple automated machine learning toolchains based on the pre-trained calibration models. The model estimates together with on-chip calculated manufacturer models are pushed to an Influx timeseries database. This is one of the most popular databases for storing timeseries data because it is easy to set up and use without any knowledge of query languages thanks to its clickable query constructor [1].

This database is connected to a visualization dashboard, which can query the database and visualize the data in a browser. For the visualization system Grafana is used due to its popularity and excellent capability for handling timeseries data. Since it is impossible to constantly track the dataflow manually, an alerting system was configured to automatically send an email to notify the administrator if any system failure occurs. Thus, downtime of the software stack and the field test systems is minimized.

To add additional machine learning models, parameter files, containing the trained model parameters and a model name, can be placed in the synchronization folder by any client. This action is recognized by the python script which automatically applies these parameters retroactively to the raw data in the backup HDF5 files. Then, the new model estimates are uploaded to the database.

Fig 1 shows the dataflow from each site to the visualization system. The blue arrows represent internal dataflow whereas the yellow arrows represent standardized API calls to an interface. The asterisk on the python script indicates that this part of the toolchain is excluded from the "no expertise" policy because a basic understanding of python might be needed.

Conclusion

The suggested software stack was easy to set up and requires almost no knowledge in programming. The server operates in this form since June 2022 without failures, whereas connectivity losses to the clients through bad connection or software crashes of the client get reported immediately.

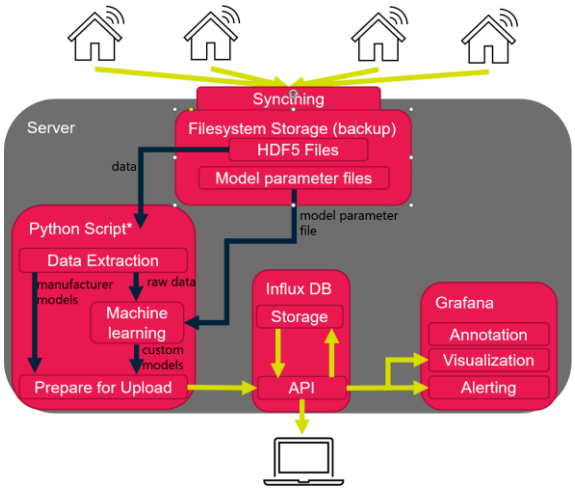

Figure 1 Schematic of the dataflow. Blue arrows indicate self-written code, whereas yellow arrows indicate standardized data transfer maintained by the tools.

References

[1] Nasar, M., et al.: "Suitability Of Influxdb Database For Iot Applications" International Journal of Innovative Technology and Exploring Engineering (2019).
[2] Wilkinson, M., et al.: "The FAIR Guiding Principles for scientific data management and stewardship." Sci Data 3, 160018 (2016).
[3] Fuchs C., et al.: "Concept and realization of a modular and versatile platform for metal oxide semiconductor gas sensors: A Versatile Platform to Measure Analog and Digital Gas Sensors" tm - Technisches Messen (2022).
[4] Amann J., et al.: "Monitoring Indoor Air Quality with low-cost Sensor Systems", Proceedings 16. Dresdner Sensor-Symposium (2022)
[5] Baur, T., et al.: "Random as mixtures for efficient gas sensor calibration" Journal of Sensors and Sensor Systems (2020).
[6] Baur, T., et al.: "Field study of metal oxide semiconductor gas sensors in temperature cycled operation for selective VOC monitoring in indoor air." Atmosphere (2021)

Acknowledgement

This research was partly performed within the project "VOC4IAQ" funded by the German Federal Ministry for Economic Affairs and Climate Action (BMWK) through the program Industrial Collective Research (AiF-iGF) under the grant number 22084N/1. The authors also thank the European Regional Development Fund (ERDF) for supporting our research within the project number 14.2.1.4-2019/1 and the German Research Foundation (DFG) for funding within project number 442146713.

DOI 10.5162/SMSI2023/P50

Research of Remote Measurement Based on the Robotic Mass Measurement System in NIM

Peng Cheng, Wang Jian, Zhong Ruilin, Wang Xiaolei, Hu Manhong*
NIM National Institute of Metrology, Beijing (P. R. China),
Corresponding Author: Wang Jian (wjian@nim.ac.cn)

Summary:
The raw data generated by the current robotic mass measurement system (RMMs) cannot be used as an effective record to meet the requirements of ISO/IEC 17025, manual work on data processing is still needed. Based on the RMMs, in this paper, a fully automated remote calibration system is designed with functions including data automatic processing (e.g., data splitting and recombination, data calculation and analysis, incomplete data processing, automatic generation of original records, and certificate reports) and remote control (e.g., online monitoring and remote calibration).

Keywords: Mass measurement, Remote measurement, Robotic mass comparators, Autonomous measurement system, Automatic certificate generating system.

Background, Motivation, and Objective

Across the world, some mass laboratories in national metrology institutes, NIMs, have been equipped with automatic mass comparators or the robotic mass measurement system (RMMs, for short) instead of manual measurement now [1]. Although the robotic mass measurement system has improved the efficiency of the weighing process, there are still some problems in actual use.

First, the raw data generated by the RMMs, only containing basic information (e.g., measurement time, weighing differences, weighing cycles, etc.), cannot directly generate a valid certificate report with comprehensive information as required in ISO/IEC 17025. Second, since the gap between the forks of the weights carries (about 1.5 mm~2 mm in width), the weight in a small mass value may easily drop off from the carriers during the weights multi-switching process, which leads to the interruption of the measurement task and the generating incomplete data, manual work still needed under the RMMs in this situation. Third, air density measurement is vital for air buoyancy corrections in high-accuracy mass measurements, some automatic mass measurement systems lack air density measurement devices, and others may be equipped with a built-in air density measurement module inside the RMMs (recalibrating each specific sensor individually is hard to realize). Forth, the calibration of the robotic mass comparators performed manually in many NIMs till now, customers need to transport the instruments to a qualified laboratory, and this calibration usually takes 15-20 working days. With a risk of shutdown (the recent pandemic COVID-19, for instance), the work related to this instrument in the customer laboratory will be suspended.

The latest computer communication technologies and IoT technologies enable a variety of applications in mass measurement and calibration fields, thus remote calibration in the mass measurement field has gradually become a necessity [2]. Since many of the available instruments are provided with some communication interfaces (RS-232, RS-495, USB) [3], remote calibration is rapidly developing in recent years, it is possible to create an actual remote functionality of the mass measuring systems, e.g., establishing the connection to national metrology institutes or other mass measurement laboratories to take the remote operation of the measuring instruments without local restriction.

Description of the Remote Measurement System

In this paper, we designed a remote measurement system that enables remote control and online monitoring. To sum up, the remote measurement system possesses the following functions:

a) Realize real-time air density collection and transmission of the environmental parameters and status.

b) Mass measurements data collection, processing, analysis, and calculation.

c) Realize the automatic generation of valid measurement records and certificate reports.

d) Transfer the measurement reports and upload them to the business system of the calibration institute automatically.

e) Realize the remote control of the measuring equipment, receive the instructions from the remote pc, and carry out the real-time monitoring of the measuring devices.

Results

To achieve the functions summarized above, the framework of the remote measurement system for the RMMs is designed in Figure.1.

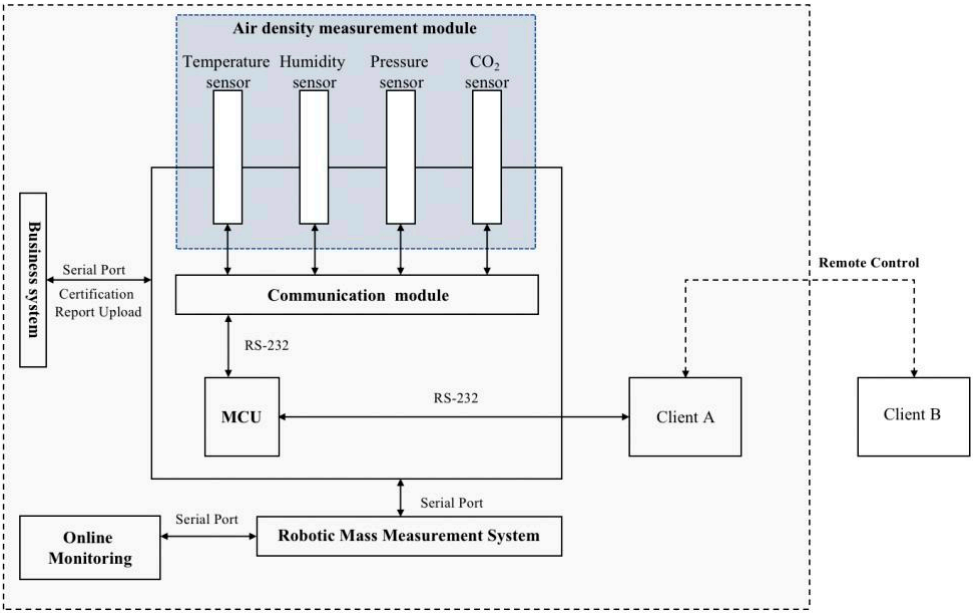

Fig. 1. The Framework of the remote measurement system (MCU represents the built-in microprogrammed control unit, Client A represents the PC installed inside the mass measurement laboratory, Client B represents any PC in a remote laboratory)

The remote measurement system mainly consists of two parts, one is the data processing and another is the remote control. The real-time ambient condition data can be collected by the sensors (e.g., Temperature sensor, Humidity sensor, Pressure sensor, and CO_2 sensor) through the 232 interface. Measurements data can be processed centrally through the built-in Microprogrammed Control Unit (MCU) to generate the raw record. The internet-connect to the business system, where a lot of information is saved (e.g., weights manufacturer, name of certificate unit, certificate report type, etc.), is established. Thus, the specific certificate report template can be downloaded, and the certificate report generated by the data processing module we designed can be directly uploaded. As for the remote control, we established the remote measurement based on the Client/Server (C/S) solution using the remote desktop protocol (RDP). Under the C/S architecture, measurement data computing task is logically distributed as the client and service side, which makes it possible to interoperate through network communication technology.

Based on the problems existing in data processing and original report and certificate generation of the automatic mass measurement system, this paper designs an automatic measurement data processing software to realize the measurement data splitting and recombination, air buoyancy correction calculation, and measurements record and the certificate reports automatic generation.

References

[1] Lee, W. G. Mass calibration designs for a robotic comparator loading three weights at most, *Measurement*,45 814-817 (2012); doi: 10.1016/j.measurement.2011.12.023

[2] Ivan A. Ershov, Oleg V. Stukach, Internet of Measurement development based on NI PXI Remote Calibration, *Institute of Electrical and Electronics Engineers,* 73-77 (2019); WOS:000525830900018

[3] Xiaoping Ren,Changqing Cai,Yi Li,Aibin Chen,etc. Mass Metrology Based on Robotic Mass Measurement System, Mouse, D. Duck, The Beagle Boys for President, *Springer-Verlag.Proceedings of 2013 Chinese intelligent automation conference*, 477-484 (2013); doi: 1 10.1007/978-3-642-38524-7_52

DOI 10.5162/SMSI2023/P51

Optimization of energy efficiency of an HPC cluster: On metrics, monitoring and digital twins

Alexander Kammeyer[1], *Florian Burger*[1], *Daniel Lübbert*[1], *Katinka Wolter*[2]
[1] *Physikalisch-Technische Bundesanstalt, Abbestraße 2-12, 10587 Berlin, Germany,*
[2] *Freie Universität Berlin, Takustraße 9, 14195 Berlin, Germany*
alexander.kammeyer@ptb.de

Summary:
In-depth monitoring together with a digital twin model allows to manage HPC clusters so that they can react to different external events. We shall use this information to improve operation of the cluster with respect to energy usage and cost of electricity, in order to maintain operation under reduced energy availability or to decrease the cluster's CO_2 footprint. Different additional external data sources together with system monitoring and modelling allow to adjust the HPC cluster to meet these goals.

Keywords: HPC, energy efficiency, energy supply, scheduling, digital twin, monitoring

Introduction

High Performance Computing (HPC) is the backbone of many research activities. The available compute performance has increased steadily over the last years. Despite of advances in energy efficiency of CPUs the total energy required continues to increase [1].

With the climate protection plan 2050 and climate protection program 2030 of the German federal government two initiatives exist that define goals for energy efficient data centres including the Blue Angel [2] certificate.

With energy becoming an increasingly limited resource and constant cooling becoming more and more difficult on record-breaking warm summer days, new ways of adapting an HPC cluster to such conditions are required.

The PTB operates an HPC cluster with a maximum power budget of approximately 30 kilowatts. This cluster is used by many research groups within PTB. Many other research facilities operate clusters of similar size. Lessons learned by this work can be applied to many other clusters as well.

This paper presents a new digital twin for an HPC system. It combines an in-depth monitoring system with additional external data to make cluster operation more dynamic using the digital twin and allows the system to react to events.

Efficiency metrics

Different energy metrics exist that cover different aspects of the HPC cluster. The four pillar framework [3] allows a classification of metrics and identifies which part of the data centre they cover.

Metrics, like Power Usage Effectiveness (PUE), focus on the whole data centre. Others, like Energy to Solution, focus more on the effectiveness of the hardware and software. The Blue Angel certificate uses the Energy Usage Effectiveness, a metric to be used at PTB.

Increasing effectiveness can also include reusing energy, as covered by the Energy Reuse Effectiveness metric. The Green Energy Coefficient describes how much green energy is used by the data centre. Similarly, CO_2 footprints can be quantified as described later.

Monitoring and documenting energy usage

In order to reduce energy consumption and classify energy reduction efforts, insight into the energy usage is necessary. The HPC cluster is to be fitted with a comprehensive energy monitoring. This allows to track energy usage, which is a requirement for the Blue Angel certificate and other metrics. The Blue Angel certificate requires a continuous, automatic monitoring not only of the energy but also cooling and system usage.

The monitoring can also be used to adjust the energy consumption, so that the consumption remains within defined bounds.

Digital twin

The operation of the HPC cluster is influenced by the operating system, scheduler and resource manager. A digital twin of the cluster helps these components to make predictions about the cluster in the future. This includes the available

energy and cost of the energy, expected energy consumptions of jobs and thermal load.

One possible use case is Power Aware Scheduling. With power aware scheduling, the system can be tuned to reduce overall power consumption [4]. Unused nodes can be turned off [1].

Demand Response

Demand response refers to a technique usually found in heavy industry. With a mutual agreement between the energy service provider (ESP) and consumer, the ESP notifies a consumer of an upcoming energy shortage and requests to lower the energy consumption. In return, the consumer receives a financial benefit or can remain operational as opposed to being cut from energy entirely.

This method can be adopted for HPC [5]. An HPC cluster offers many ways of reducing energy consumption. Possible ways are suspending running jobs, disabling idle compute nodes or reducing CPU frequency on the entire cluster. Even temporarily altering the scheduling behaviour, e.g. preventing new jobs from running, are conceivable. The digital twin model of the cluster helps to correctly predict the impact of the different methods and make the optimal decision.

CO_2 footprints

The energy in the energy grid consists of a mix of different energy sources like solar, wind and water but also gas, coal and nuclear energy. Each source has a different impact on the climate, most notably in terms of CO_2 emissions.

The current energy mix can be taken into account and allows to estimate the CO_2 footprint for the cluster. Jobs can be scheduled with the goal of reducing emissions and with the help of energy monitoring emissions can be tracked.

Cost of electricity

With energy becoming a more limited resource, companies might be required to buy energy packets on the so-called spot market to daily or even hourly changing rates.

If that is the case, it has a direct influence on the operating cost of the HPC cluster. This could be used to optimize the cost or make sure, that certain levels are not exceeded in times of high market prices. Jobs can be placed in times of lower prices or operation can be suspended if energy costs rise above a certain threshold.

Influence of weather conditions

The weather has an influence on the energy efficiency metrics because it directly influences the required energy for cooling. The metrics are therefore often averages over a year.

With the adaptation of a free cooling system, cooling becomes more efficient compared to a classic cooling machine but might not be feasible on extremely warm days. The HPC cluster needs to respond to such events of limited cooling. Using the comprehensive monitoring together with weather forecast data, the system scheduling can reduce the system load on predicted warm days when the outside temperature comes close to operational limits.

Summary

With the introduction of a comprehensive monitoring and the selection of metrics for energy efficiency, the energy optimization efforts for the HPC cluster at PTB can be measured and quantified.

With a digital twin for the HPC cluster, optimization efforts become easier as it combines different external data sources with the cluster monitoring. This combination allows the real system to adapt to different scenarios.

The monitoring and digital twin play an instrumental role when optimizing energy consumption, scheduling jobs during times of lower energy costs or outside extreme heat periods and help to operate the cluster within defined limits.

References

[1] Mämmelä, Olli et al., Energy-aware job scheduler for high-performance computing, *Computer Science - Research and Development 27*, 265-275 (2012); doi: 10.1007/s00450-011-0189-6

[2] RAL UMWELT, Energieeffizienter Rechenzentrumsbetrieb DE-UZ 161, 2 edition (2015)

[3] Wilde, Torsten et al., The 4 Pillar Framework for energy efficient HPC data centers, *Computer Science - Research and Development* 29, 241-251 (2014); doi: 10.1007/s00450-013-0244-6

[4] Bodas, Deva et al., Simple Power-Aware Scheduler to Limit Power Consumption by HPC System within a Budget, *2014 Energy Efficient Supercomputing Workshop*, 21-30 (2014); doi: 10.1109/E2SC.2014.8

[5] Ahmed, Kishwar et al., Enabling Demand Response for HPC systems through Power Capping and Node Scaling, *2018 IEEE 20th International Conference on High Performance Computing and Communications; IEEE 16th International Conference on Smart City; IEEE 4th International Conference on Data Science and Systems (HPCC/SmartCity/DSS)*, 789-796 (2018); doi: 10.1109/HPCC/SmartCity/DSS.2018.00133

DOI 10.5162/SMSI2023/P52

Importance of Traceability for Determining the Efficiency of wind turbine drive trains on test benches

Zihang Song[1], Paula Weidinger[1], Maximilian Zweiffel[2], Alexander Dubowik[1], Rafael Soares de Oliveira[3], Nijan Yogal[1], Christian Mester[4]
[1] Physikalisch-Technische Bundesanstalt (PTB), Bundesallee 100, 38116 Braunschweig, Germany
[2] Chair for Wind Power Drives CWD, Campus Boulevard 61, 52074 Aachen, Germany
[3] Instituto Nacional de Metrologia INMETRO, Av Nossa Senhora das Graças, 50, 25650020, Duque de Caxias, Brazil
[4] Eidgenössisches Institut für Metrologie METAS, Lindenweg 50, 3003 Bern-Wabern, Switzerland
Zihang.Song@ptb.de

Summary:
In this paper, the efficiency of a 2.75 MW nacelle is compared using calibrated and uncalibrated measurement devices. The results show that especially calibration of mechanical input is important, as the torque measurement is off by about 5 % and results in significantly lower system efficiencies.

Keywords: Calibration, efficiency determination, nacelle system test bench, mechanical input power, electrical output power

Introduction

In order to optimise the efficiency of wind turbine drive trains during the development process, measurements are carried out on nacelle system test benches (NTBs). A standardised method based on traceable mechanical and electrical power measurements is required for reliable and comparable efficiency measurements. Traceable measurements are possible either by installing additional calibrated high-precision measuring devices or by calibrating the existing measuring devices. In the given set-up, the calibration of the mechanical power measurement strongly influenced the resulting efficiency.

Measurement set-up

On the 4 MW NTB (see Fig. 1) at the Center for Wind Power Drives (CWD) of RWTH Aachen University in Aachen, Germany, onshore wind turbine drive trains can be tested. The low-speed prime mover operates the device under test (DUT) with up to 3.4 MN m and 30 rpm depending on the DUT. The DUT used for the measurements is a research nacelle of FVA (Forschungsvereinigung Antriebstechnik e. V.) with a nominal output of 2.75 MW and a rated torque of 1.55 MN m.

In the NTB, a non-torque loading unit (NTL) simulates wind loads by applying forces in three and bending moments in two degrees of freedom. The test bench's torque transducer is located between the prime mover and the NTL unit. In addition, a 5 MN m torque transducer from PTB, which is traced to national standards, was installed in the drive train directly on the rotor hub of the DUT. The mechanical input power was measured separately by these two torque transducers and a magnetic encoder for rotational speed measurement.

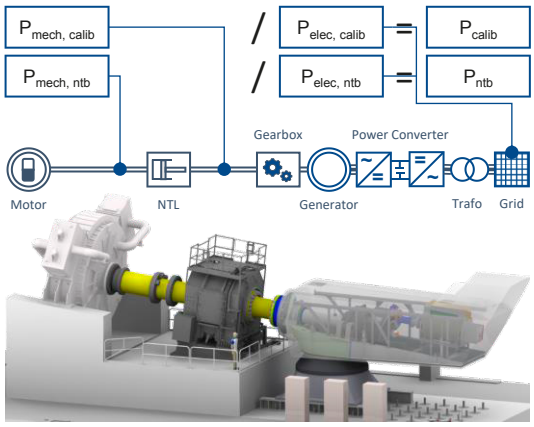

Fig. 1. 4 MW NTB at CWD of RWTH Aachen University including four measurement points for mechanical and electrical power measurement.

The electrical output power was measured by the test bench's current sensors and a voltage divider between the transformer and the middle voltage grid. For a traceable measurement of the electrical output power, three calibrated, high-precision current sensors and a high voltage divider traced to national standards were installed at the same point. All signals are gathered by separate data acquisition systems

(DAQs) which were synchronised via network time protocol (NTP). [1]

Measurement methodology

In general, the efficiency η of rotating electrical machines is the ratio of generated electrical power to total mechanical power in:

$$\eta = \frac{P_{\mathrm{el}}}{2\pi \cdot n \cdot M.} \qquad (1)$$

For torque measurement, signals are tared by the zero offset and averaged over six full rotations of the drive train. Detailed descriptions for measurement methodology and uncertainty analysis can be found in [2].

Results and analysis

The torque measured by the test bench's torque transducer before and after the calibration to the PTB torque reference is presented in Fig. 2.

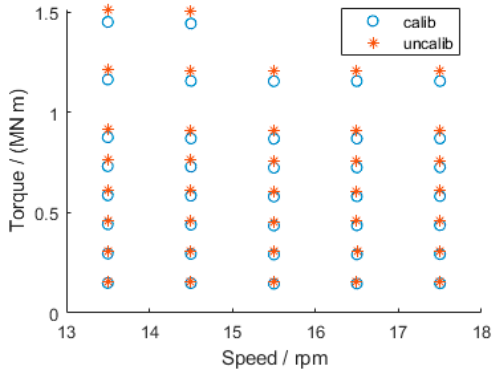

Fig. 2. Torque measurement before and after the calibration to the PTB torque transfer standard.

Without calibration, the test bench's torque measurement is off by about 5 %, as shown in Fig. 3.

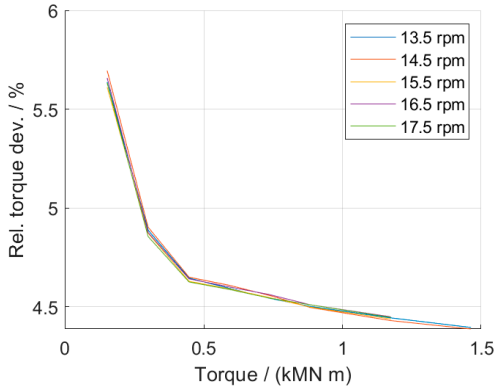

Fig. 3. The relative deviation of uncalibrated torque measurement.

For efficiency determination of the DUT, the efficiency results using uncalibrated and calibrated measurement devices are shown in Fig. 4. Without the calibrations, the efficiency of the DUT is measured significantly lower compared to the calibrated results. This is mainly due to the higher torque measured incorrectly.

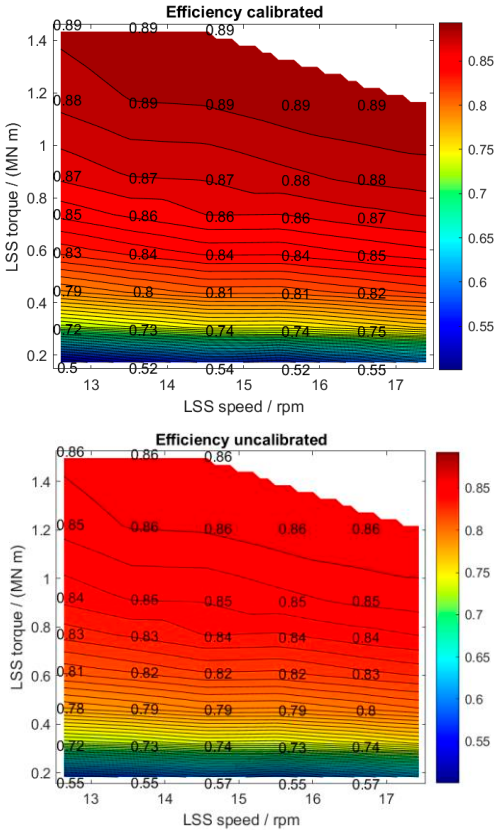

Fig. 4. Efficiency determination using calibrated and uncalibrated measurement devices.

Conclusion and outlook

In this paper, the efficiency of a 2.75 MW nacelle is compared using calibrated and uncalibrated measurement devices. The results show that especially calibration of mechanical input is important, as the torque measurement is off by about 5 % and results in significantly lower system efficiencies.

Acknowledgements

The project 19ENG08 – WindEFCY has received funding from the EMPIR programme co-financed by the Participating States from the European Union's Horizon 2020 research and innovation programme.

References

[1] P. Weidinger *et al.*, "Summary report describing the schedules for the three measurement campaigns to determine the efficiency of nacelles and their components on test benches with a target uncertainty of 1 % including pre-tests, measuring devices, and transfer standard specifi." Zenodo, 2022. doi: 10.5281/zenodo.7043161.

[2] Z. Song *et al.*, "Traceable efficiency determination of a 2.75 MW nacelle on a test bench". Manuscript submitted for publication.

DOI 10.5162/SMSI2023/P53

Concept for improving the form measurement results of aspheres and freeform surfaces in a Tilted-Wave Interferometer

Gregor Scholz[1], *Markus Schake*[1], *Michael Schulz*[1], *Ines Fortmeier*[1]
[1] *Physikalisch-Technische Bundesanstalt (PTB), Bundesallee 100, 38116 Braunschweig, Germany*
gregor.scholz@ptb.de

Summary:
Non-null-test interferometry, such as tilted-wave interferometry, has gained attention for accurate and flexible form measurement of aspherical and freeform surfaces. However, additional information is needed to improve the measurement results and distinguish between certain form errors and misalignment of the specimen. One way to achieve this is to improve the knowledge about the absolute measurement position of the specimen within the interferometer setup. In this work, we propose a method to measure the specimen-to-objective distance by utilizing a white light interferometer and a transparent test specimen.

Keywords: white light interferometry, distance measurement, tilted-wave interferometry, metrology, aspheres, freeforms, optical form measurement

Introduction

In the past decades, the usage of aspherical and freeform surfaces has become quite popular in optics. As a way of creating compact optical systems with low aberrations, they are now widely used both in consumer devices and professional applications. However, reliable fabrication of high-quality freeform surfaces is limited by the ability to accurately measure such surfaces. Measurement comparisons between different measurement methods show that the uncertainty of the determination of the spherical form error dominates in the form measurement of aspheres and freeform surfaces in both point-based and area-based measurement methods [1].

In interferometry, which belongs to the most accurate area-based measurement methods, different methods exist for the form measurement of such complex surfaces. For all these methods, it is difficult to distinguish between misalignment of the specimen and certain form errors [2]. The reason is that the (best-fit) radius of the test wavefront depends on its propagation distance, which depends on the position of the specimen within the measurement setup. This is also true for the tilted-wave interferometer (TWI, [3]), which is a promising non-null test method for the form of aspheres and freeform surfaces. Thus, to improve the measurement results of a TWI, additional information is needed. A solution is to improve the knowledge of the absolute measurement position of the specimen within the interferometer setup [4].

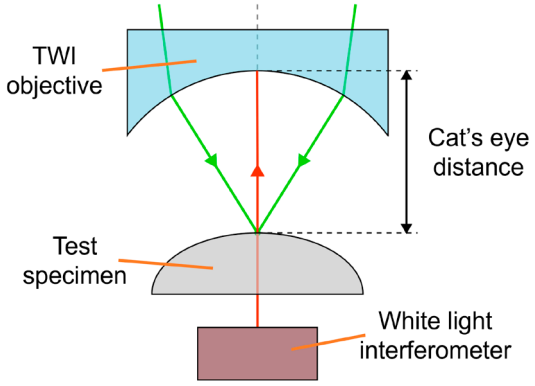

Fig. 1. Scheme of the measurement task. Measuring the distance between the surface of the test specimen and the surface of the TWI objective.

In this work, we investigate the concept of using a white light interferometer (WLI) to measure the absolute distance between a specimen surface in a reference position and the last surface of the TWI's objective.

Measurement task

To improve the knowledge about the absolute specimen position within the interferometer setup, a transparent test specimen is used. It is brought into a specified position in relation to the TWI's objective and the distance between the top surface of the specimen and the last surface of the objective is measured (Fig. 1).

As a fixed reference position, the cat's eye position of the objective is used. In this position the light from the TWI is reflected from a single spot on the crest of the specimen and therefore, the optical path length difference (OPLD) is unaffected by the surface structure. The alignment of the specimen in the reference position plays an important role and the accuracy of current alignment concepts will be investigated with the help of the setup developed in this work.

For the current TWI setup, the distance between the last surface of the objective lens and the cat's eye position is approximately 48 mm. In future work, the setup will be expanded to other objective lenses.

White light interferometer design

A white light interferometer based on a Michelson configuration can be used to measure the distance between different surfaces of transparent materials [5]. The proposed interferometer consists of a low coherent light source, a beam splitter, a measurement arm, which contains the objective and the specimen, a reference arm, an image detector and some optics for beam intensity control and focus. A scheme of such an interferometer is shown in Fig. 2.

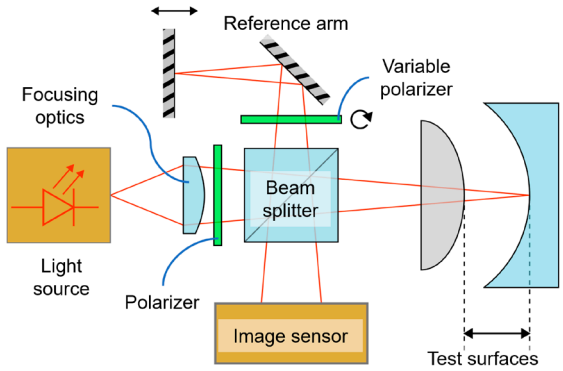

Fig. 2. Scheme of a white light interferometer for measuring the distance of two consecutive transparent specimens.

As light source a high-power LED with narrow spectral width of a few nanometers can be utilized. A resulting spectral coherence length of a few tens of micrometer is desirable. The interference pattern is recorded by an image sensor and the recording is analyzed by software employing envelope and phase evaluation.

Due to weak reflection from the transparent specimens' surfaces, intensity from the measurement arm is substantially decreased. However, to allow for a high interference contrast, the intensity from the reference arm should be equal to the measurement arm's intensity. Therefore, the reference beam intensity can be reduced by a variable polarization filter.

Measurement Procedure

In WLI, an interference pattern becomes visible on the sensor when the OPLD between a reflection in the measurement arm and the reference arm is within the coherence length of the light source. Further, its contrast is maximized when both lengths are equal. For multiple surfaces, each surface produces a local contrast maximum when reference and measurement arm length match. Since the medium between the two surfaces of interest and in the reference arm is ambient air, the measured distance based on the interference pattern contrasts directly translates into the distance between the surfaces along the measurement beam.

Conclusion

In this work we proposed an additional absolute distance measurement to improve the form measurement result of aspheres and freeform surfaces with a TWI. The proposed concept is based on a white light Michelson interferometer configuration. We have presented the basic ideas to improve the measurement results of a TWI by such a concept.

Acknowledgment

This research is funded by the Deutsche Forschungsgemeinschaft (DFG, German Research Foundation) – 496703792.

References

[1] I. Fortmeier, R. Schachtschneider, V. Ledl, O. Matousek, J. Siepmann, A. Harsch, R. Beisswanger, Y. Bitou, Y. Kondo, M. Schulz, C. Elster, Round robin comparison study on the form measurement of optical freeform surfaces. *J. Eur. Opt. Soc.-Rapid Publ*, 16(1), 2 (2020); doi: https://doi.org/10.1186/s41476-019-0124-1

[2] A. Gronle, C. Pruss, A. Herkommer, Misalignment of spheres, aspheres and freeforms in optical measurement systems. *Optics Express*, *30*(2), 797 (2022); doi: https://doi.org/10.1364/OE.443420

[3] G. Baer, J. Schindler, C. Pruss, J. Siepmann, W. Osten, Calibration of a non-null test interferometer for the measurement of aspheres and freeform surfaces. *Optics Express 22*(25), 31200 (2014); doi: 10.1364/OE.22.031200

[4] I. Fortmeier, M. Stavridis, A. Wiegmann, M. Schulz, W. Osten, C. Elster, Evaluation of absolute form measurements using a tilted-wave interferometer. *Optics Express 24*(4), 3393 (2016); doi: 10.1364/OE.24.003393

[5] P. Kühnhold, A. Nolvi, S. Tereschenko, I. Kassamakov, E. Hæggström, P. Lehmann, Transparent layer thickness measurement using low-coherence interference microscopy. *Proc. SPIE*, 95252F (2015); doi: https://doi.org/10.1117/12.2184011

DOI 10.5162/SMSI2023/P54

How Operating Pressure and Electric Field Strength Affect Sensitivity in High Kinetic Energy Ion Mobility Spectrometry

Florian Schlottmann[1], Ansgar T. Kirk[1], Leonardo Hermeling[1], Bert Ungethuem[2], Falko Ziegert-Kuehn[2], Andreas Walte[2], Stefan Zimmermann[1]
[1] Leibniz University Hannover, Institute of Electrical Engineering and Measurement Technology, Appelstr. 9a, 30167 Hannover, Germany
[2] AIRSENSE Analytics, Hagenower Str. 73, 19061 Schwerin, Germany
Schlottmann@geml.uni-hannover.de

Summary:
Currently, High Kinetic Energy Ion Mobility Spectrometers (HiKE-IMS) are under investigation regarding trace gas detection in field applications. Despite their low operating pressures between 20 and 60 mbar, previously reported limits of detection for compounds like benzene are in the single digit ppb_V-range [1]. However, even lower detection limits for a broad range of substances are required. To achieve this objective, we experiment with operating pressure and electric field strength to further improve the limits of detection of HiKE-IMS.

Keywords: trace gas detection, ion mobility spectrometry, low pressure, field-deployable HiKE-IMS, mass spectrometry

Introduction – Ion Mobility Spectrometers

Ion Mobility Spectrometers (IMS) are powerful tools for trace gas analysis in field applications capable of detecting hazardous substances in low concentrations of few parts-per-trillion (ppt_V) in mediums such as ambient air. Compared to large and heavy laboratory instruments like most mass spectrometers, IMS are available in small size and can be carried by a single person even wearing a hazmat suit. For most portable IMS systems, the gaseous samples are ionized via reactant ions, in most cases protonated ammonia or water clusters. Then, reactant and product ions are injected into a drift region where they are separated in an electric field. The degree of separation depends on the substance specific ion mobility, which is dependent on multiple properties including charge, mass, and ion-neutral collisional cross-section. At the end of the drift region, the separated ions reach a Faraday plate where they discharge and the current over time is recorded. The ion current is amplified with a transimpedance amplifier and the ion mobility spectrum results [2].

The previously described conventional ion mobility spectrometers have outstanding sensitivity and decent selectivity, but have three main issues: 1.) Non-polar, low proton affine substances, e.g. benzene, cannot be ionized through proton transfer reactions via water clusters or via adduct formation/ligand switching. Therefore, these substances are difficult or impossible to detect. 2) Quantitative analysis is difficult due to competing ionization reactions that can even lead to full discrimination of certain compounds in the presence of other compounds 3.) Different substances can have similar ion mobilities, resulting in overlapping peaks.

High Kinetic Energy IMS

In an effort to overcome the above mentioned issues of conventional IMS, the High Kinetic Energy Ion Mobility Spectrometer (HiKE-IMS) was developed [3]. The HiKE-IMS is operated at an absolute pressure of 20 - 60 mbar, which enables operation at high reduced electric field strengths ε of up to 120 Td where ε is defined as the electric field strength E divided through neutral gas density N. When operated at high reduced electric field strengths, protonated water cluster size can be reduced down to bare H_3O^+, which enables protonation of substances with low proton affinity like benzene, achieving limits of detection in the region of single digit ppb_V [1]. Furthermore, ionization is also possible with O_2^+, which enables charge transfer reactions with many substances. In order to further increase separation power the reduced electric field strength can be varied in both the reaction region and the drift region enabling (de)clustering of ions and/or exploring the field depended ion mobility.

Thus, we propose a new IMS design that can be switched from ambient pressure to low pressure to either have lowest limits of detection with decent resolving power (IMS mode) or less sensitivity but a broader spectrum of detectable substances, less chemical cross sensitivities and improved identification capabilities (HiKE-IMS mode).

Theoretical

A theoretical, and experimentally validated description of the sensitivity of HiKE-IMS was given in [1]. It was shown that the product ion concentration [S] depends on the square of the neutral gas density N and linearly on the reduced electric field strength ε. In this work, this relation is rearranged according to Equation (1), showing a linear dependence on the electric field strength E multiplied by the neutral gas density N. Thus, by increasing the pressure or electric field strength the sensitivity can be increased to significantly improve the limits of detection.

$$[S] \sim \varepsilon N^2 \sim E N \quad (1)$$

Therefore, we propose the above mentioned concept of varying operating pressure to operate the device in either IMS or HiKE-IMS mode.

Preliminary Data

Dimethyl methylphosphonate (DMMP) was used as a first test substance at constant concentration of 40 ppb_V in the clean, dry air (1.4 ppm_V water). The operating pressure and the reduced electric field strength were changed in factors of 2 at constant electric field strength, i.e. when operating at half the reduced electric field strength, pressure was doubled. First, reduced electric drift field strengths of 25, 50 and 100 Td were applied at a constant pressure of 50 mbar corresponding to electric field strengths of 33, 66 and 132 V/mm. The same electric field strengths were applied at 100, 200 and 400 mbar leading to reduced electric field strength of 12.5, 25 and 50 Td at 100 mbar, 6.25, 12.5 and 25 Td at 200 mbar and 3.125, 6.25 and 12.5 Td at 400 mbar. The resulting amplitudes of the DMMP product ion peak are shown in Figure 1. The expected linear relation between the amplitude and the electric field strength E is clearly visible for pressures 100, 200 and 400 mbar. However, the data set for 50 mbar shows a different behavior: At the highest electric field strength of 132 V/mm (100 Td) the signal amplitude decreases, which is caused by fragmentation of DMMP occurring for this substance at reduced electric field strengths above 90 Td. It should be noted that Equation 1 does not account for additional effects like fragmentation. If now looking at the slopes in Figure 1, the expected linear increase with increasing pressure is not visible. Since one pair of inlet capillaries was used as flow restrictions, changing the pressure also changes the sample flow rate into the (HiKE-)IMS and thus changes dilution of analytes. Hence, the measurements presented in Figure 1 need to be repeated with adjusted capillaries and also with other substances like benzene (non-polar) or methyl salicylate, to further validate the relationship between pressure and peak amplitude as a function of analyte class.

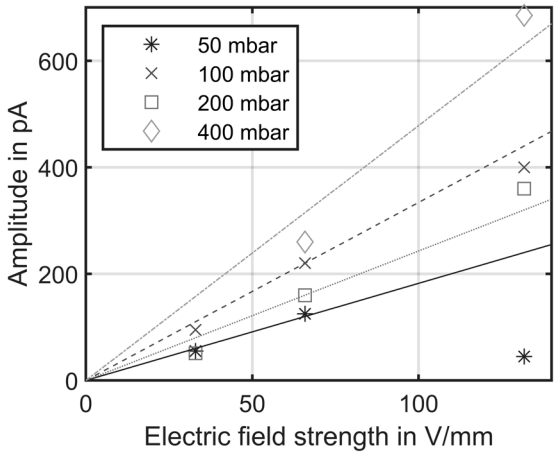

Fig. 1. Amplitude of the DMMP product ion peak (40 ppb_V DMMP in clean, dry air with 1.4 ppm_V water) in a (HiKE-)IMS operated at different pressures and electric drift field strengths. The (HiKE-)IMS temperature was constant at 40 °C.

Conclusion

As expected, the number of generated product ions and thus the sensitivity depends on the pressure and electric field strength, which explains the lower limits of detection in IMS compared to HiKE-IMS. Therefore, pressure should be variable according to the application to take advantage of either a HiKE-IMS or an IMS. This concept will be further investigated and presented at the SMSI in more detail.

Acknowledgements

Supported by the German Federal Ministry of Education and Research (BMBF) under the Grant 13N16007.

References

[1] F. Schlottmann, A. T. Kirk, M. Allers, A. Bohnhorst, S. Zimmermann, Journal of the American Society for Mass Spectrometry 31, 1536-1543 (2020); doi: 10.1021/jasms.0c00098

[2] G. A. Eiceman, Z. Karpas, H. H. Hill, ISBN 1439859973

[3] J. Langejürgen, M. Allers, J. Oermann, A. T. Kirk, S. Zimmermann, Analytical Chemistry 86, 7023-7032 (2014); doi: 10.1021/ac5011662

DOI 10.5162/SMSI2023/P55

Perspectives on Use of Resistive Force Sensing to Improve the Control and User Experience of Hand Prostheses

Daniel Andreas[1], *Mehmet Ege Cansev*[1], *Anany Dwivedi*[1], *Philipp Beckerle*[1,2]
[1] *Chair of Autonomous Systems and Mechatronics, Department of Electrical Engineering, Friedrich-Alexander-Universität Erlangen-Nürnberg, Erlangen, Germany,*
[2] *Department of Artificial Intelligence in Biomedical Engineering, Friedrich-Alexander-Universität Erlangen-Nürnberg, Erlangen, Germany*
daniel.andreas@fau.de

Summary:
Human hands help us to learn about the environment via haptic sensation and thus facilitating effortless interactions. A hand amputation can disrupt the life of persons with amputation in carrying out everyday tasks. In this paper, we provide our perspective on employing force sensing methods to improve the acceptance rate of the prosthetic limbs by providing haptic feedback.

Keywords: force sensing resistors, robotic prosthesis, affective touch, human-machine interface, data glove

Introduction

Humans learn about the environment by interacting with it. The human hand is a powerful tool that enables us to perform a wide range of tasks, from interacting with objects used in daily living to executing gestures in social activities. According to [1], approximately 540,000 persons with amputation suffer from upper limb loss in the US with the expected projections to be doubled by 2050. Europe approximately has 4.66 million persons with amputation, with up to 431,000 amputations performed each year [2]. The loss of a limb can have a detrimental effect on the quality of life, preventing people from performing critical activities of daily living [3].

The latest technological advancements have led to increasingly dexterous devices for persons with amputation. However, the use of such devices is still not widespread, as there are still challenges to be overcome. The control algorithms that utilize traditional biosignals-based sensing methods (e.g. electromyography) for control of prosthetic hands can be complicated as they require sophisticated electronics, frequent gelling on the skin electrodes to reduce noise, and can also be expensive [4]. Another challenge with prosthetic devices is that use of prosthetics is a cognitively intensive task due to absence of proprioception information, forcing the wearer to visually monitor the artificial limb [5]. For enhanced feeling of proprioception, researchers are exploring affective touch for integration of the prostheses into the bodily self of the wearer and to foster more natural interpersonal interactions [6].

In this paper, we present our perspective on the use of force sensing resistors (FSR) for improving the state-of-the-art of upper limb prosthetic devices by focusing on the above-mentioned challenges. To do this, we consider low-cost solutions for predicting the user intentions using alternate myography methods like an FSRs-based wearable glove and forcemyography (FMG) for acquisition of data for developing the decoding models. We also discuss employing affective touch methods to improve the feeling of proprioception leading to greater embodiment with the device and thus increasing the acceptability of the prosthesis.

Force Sensing based Data Acquisition

Acquiring ground truth data from persons with hand amputation to train machine/deep learning models to decode hand motions for prosthesis control is particularly difficult due to the missing limb [7]. Generally, there are two ways to overcome this challenge. The first option provides a simulated hand motion to guide the user through the movements to be performed [7,8]. Alternatively, people with hand amputation can perform tasks bilaterally while wearing a sensor glove on the intact limb to record ground truth data [7,8].

Such sensor gloves typically contain flex sensors that change their resistance while bending and thus work very similar to FSRs. The acquired signal can then be translated into finger

joint angles. We developed a sensor glove that contains eleven flex sensors with five additional FSRs mounted to the fingertips in order to measure the exerted force between the respective finger and the object. The added FSRs can be used as an additional input to improve the reliability of the decoder and to enable force control, given the hand prosthesis contains corresponding sensors.

FMG is a cost-effective alternative to electromyography (EMG) and is based around FSRs to measure muscle motion that result from hand movements. The acquired data can be used to decode finger and hand motions. In the past, decoding hand motions from FMG data outperformed EMG in many instances and is thus a promising way to acquire muscular activity [8].

Force Sensing for Enhanced Embodiment

In addition to physiological factors, psychological effects, e.g., embodiment, presence, pleasantness, and agency, play a critical role in acceptance of prosthetic devices. Although being a recently considered phenomenon in assistive and prosthetic robotics, affective touch has the potential to support the acceptance process [6].

To reveal the potential benefits of affective touch, we developed a prototype that stimulates either the lower or upper arm of a user so that it can be tested with different amputations [10]. Our design stimulates the mechanoreceptors on the skin in a realistic human-like manner as if fingers are touching the skin by using linear actuators and silicone coating. However, one of the most important factors that determines the realism of touch feeling is the contact force. Thus, we used FSRs to measure and control the contact forces to fit them into the suggested range of affective touch. Therefore, our design can be controlled by the sensor glove mentioned above to precisely apply the forces detected on the fingertips of the glove for further experiments.

Conclusion

Owing to the cost-effectiveness of the force sensitive resistors and flex sensors, they have found applications in various fields. In this paper, we present our perspective on the use of these sensors for development of an interface to acquire high quality data in a reliable way to decode hand motions from muscular activity. Future works could investigate the benefits of combining FMG with EMG in a single device for hand motion decoding. Furthermore, benefits of affective touch can be tested on persons with amputations by designing prosthetic sockets using modular linear actuators or vibration motors with force feedback to improve the user experience with robotic hand prostheses.

References

[1] K. Ziegler-Graham, E. J. MacKenzie, P. L. Ephraim, T. G. Travison, R. Brookmeyer, Estimating the prevalence of limb loss in the united states: 2005 to 2050, *Archives of physical medicine and rehabilitation*, 89, 3 (2008); doi: 10.1016/j.apmr.2007.11.005

[2] M. Bumbaširević, A. Lesic, T. Palibrk, D. Milovanovic, M. Zoka, T. Kravić-Stevović, S. Raspopovic, The current state of bionic limbs from the surgeon's viewpoint. *EFORT open reviews* 5 (2), 65-72 (2020); doi: 10.1302/2058-5241.5.180038

[3] M. C. Day, R. Wadey, S. Strike, Living with limb loss: everyday experiences of "good" and "bad" days in people with lower limb amputation, *Disability and Rehabilitation*, 41(20), 2433-2442 (2019); doi: 10.1080/09638288.2018.1467502

[4] C. Castellini, P. Artemiadis, M. Wininger, A. Ajoudani, M. Alimusaj, A. Bicchi, ... E. Scheme, Proceedings of the first workshop on peripheral machine interfaces: Going beyond traditional surface electromyography. *Frontiers in neurorobotics*, 8, 22 (2014); doi: 10.3389/fnbot.2014.00022

[5] A. Blank, A. M. Okamura, K. J. Kuchenbecker, Identifying the role of proprioception in upper-limb prosthesis control: Studies on targeted motion, *ACM Transactions on Applied Perception (TAP)*, 7(3), 1-23 (2008); doi: 10.1145/1773965.1773966

[6] P. Beckerle, R. Kõiva, E. A. Kirchner, R. Bekrater-Bodmann, S. Dosen, O. Christ, ... B. Lenggenhager, Feel-good robotics: requirements on touch for embodiment in assistive robotics, *Frontiers in neurorobotics*, 12, 84 (2018); doi: 10.3389/fnbot.2018.00084

[7] M. Atzori, A. Gijsberts, C. Castellini, B. Caputo, A. G. M. Hager, S. Elsig, ... H. Müller, Electromyography data for non-invasive naturally-controlled robotic hand prostheses, *Scientific data*, *1*(1), 1-13 (2014); doi: 10.1038/sdata.2014.53

[8] J. L. Nielsen, S. Holmgaard, N. Jiang, K. B. Englehart, D. Farina, P. A. Parker, Simultaneous and proportional force estimation for multifunction myoelectric prostheses using mirrored bilateral training, *IEEE Transactions on Biomedical Engineering*, *58*(3), 681-688 (2010); doi: 10.1109/TBME.2010.2068298

[9] J. Chapman, A. Dwivedi, M. Liarokapis, A Wearable, Open-Source, Lightweight Forcemyography Armband: On Intuitive, Robust Muscle-Machine Interfaces, *2021 IEEE/RSJ* International *Conference on Intelligent Robots and Systems (IROS)* (pp. 4138-4143). IEEE (2021); doi: 10.1109/IROS51168.2021.9636345

[10] N. Ferguson, M. E. Cansev, A. Dwivedi, P. Beckerle, Design of a Wearable Haptic Device to Mediate Affective Touch with a Matrix of Linear Actuators, *Advances in System-Integrated Intelligence*, SYSINT 2022, Lecture Notes in Networks and Systems, vol 546. Springer, Cham, 507-517. (2023) doi: 10.1007/978-3-031-16281-7_48

DOI 10.5162/SMSI2023/P56

2x2 factorial calibration of FBG sensors for simultaneous measurement of temperature and humidity in PEM fuel cells

K. Rostan[1], R. Kruglov[1], R. Engelbrecht[1]
[1] Polymer Optical Fiber Application Center (POF-AC), Technische Hochschule Nürnberg Georg Simon Ohm, Wassertorstraße 10, 90489 Nuremberg, Germany, rainer.engelbrecht@th-nuernberg.de

Summary:
Fiber Bragg grating (FBG) sensor technology is expected to make an important contribution to extending the lifetime of polymer electrolyte membrane (PEM) fuel cells. It allows accurate measurements of in-situ operating temperature and humidity, which is essential for an accurate control of both. For these applications an accurate and reliable calibration is crucial. This paper demonstrates the successful use of a 2x2 factorial calibration method for calibration of two standard FBGs for application in a PEM fuel cell. The calibrated low-cost FBG sensor allows temperature and humidity measurements with a RMS error (RMSE) of 0.45°C and 4.8 %RH, respectively.

Keywords: factorial design, fiber Bragg grating, calibration, temperature sensing, humidity sensing, PEM fuel cell

FBG sensors in PEM fuel cells

Polymer electrolyte membrane (PEM) fuel cells will contribute significantly to the mobility of the future. For an extension of the service life of the membrane as most critical component, it is necessary to precisely monitor and control the process temperature and humidity within the cell. Electronic sensors are of limited use in this harsh environment, whereas fiber Bragg grating (FBG) sensors are sufficiently small, chemically inert and do not generate an electrical short circuit. Characteristic for FBG sensors is the narrow wavelength band, which is reflected by the inscribed grating. It changes almost linear in response to the parameters to be measured. So far, FBG are mainly used for strain and temperature measurements. However, in [1] it was shown that FBG with polyimide coating can be used as humidity sensors. In [2], an FBG-based temperature and humidity sensor was successfully integrated into a PEM fuel cell. However, it required a complex production process, especially for the humidity measuring sensor requiring etching and coating with a specialty polymer. Therefore, in the present work simple FBG sensors are used for the same measurement task. Each FBG requires an initial calibration. Following [3], a 2x2 factorial design calibration is used. It allows to determine additional cross sensitivities between the quantities to be measured.

FBG sensor calibration by 2x2 factorial design

The used measurement setup is shown in Fig. 1. It relies on ordinary FBG sensors. One of the FBG has an acrylate coating and is therefore mainly sensitive to temperature changes, hereafter referred to as FBG_T. A second FBG with an ORMOCER coating (hereafter $FBG_{T,RH}$) is sensitive to both, temperature and humidity changes.

The FBG are placed in a climatic chamber and fed by a SLED Denselight DL-BP1-1501A broad-band light source, while the reflected signals are detected by an Ibsen I-MON USB 256 spectrometer serving as an interrogator.

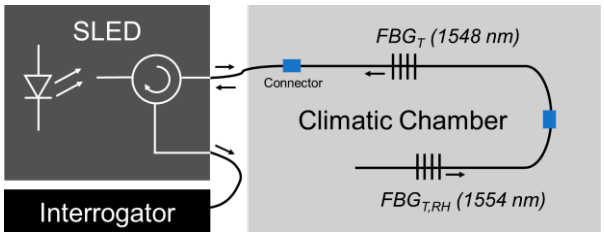

Fig. 1. Measurement setup for FBG sensor calibration.

A 2k factorial design calibration can be used when the parameter range to be covered is sufficiently small. For each calibration parameter *k* a measurement at an upper and a lower limit is to be performed. For two parameters, this results in 2^2=4 measuring points. A control point in the center is used for verification. Fig. 2 gives an overview of the parameter range used, which is typical for the targeted fuel cell. After successful calibration any combination of temperature and humidity that lies within the modelled square can be measured.

Each of the four measurement points defining the corner of the square forms a row in the equation system in Eq. (1). The reflected wavelength λ_i is

captured together with the temperature T_j and the relative humidity values RH_j for every point.

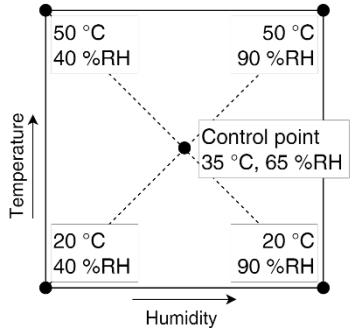

Fig. 2. Measurement square for calibration with 2x2 factorial design.

By solving the linear system of equations in Eq. (1), four calibration parameters are determined for each FBG: the fundamental wavelength λ_0, the temperature coefficient S_T, the humidity coefficient S_H and a mutual coefficient between temperature and humidity S_{TH}.

$$\begin{bmatrix}\lambda_1\\ \lambda_2\\ \lambda_3\\ \lambda_4\end{bmatrix} = \begin{bmatrix}1 & \Delta T_{low} & \Delta RH_{low} & \Delta T_{low}\Delta RH_{low}\\ 1 & \Delta T_{low} & \Delta RH_{high} & \Delta T_{low}\Delta RH_{high}\\ 1 & \Delta T_{high} & \Delta RH_{low} & \Delta T_{high}\Delta RH_{low}\\ 1 & \Delta T_{high} & \Delta RH_{high} & \Delta T_{high}\Delta RH_{high}\end{bmatrix} \times \begin{bmatrix}\lambda_0\\ S_T\\ S_H\\ S_{TH}\end{bmatrix} \quad (1)$$

Tab. 1 shows the determined coefficients for the two FBGs. It shows that FBG_T is as expected almost insensitive to humidity variations. For FBG_{TH} a 1°C temperature change results in a wavelength change that is almost equivalent to an approx. 5% change in relative humidity. In combination, both sensors allow a good temperature and humidity measurement. This is verified by a measurement of the control point showing an accuracy of -0.45 K and +1 %RH.

Tab. 1: Temperature and humidity sensitivities.

	FBG_T	$FBG_{T,RH}$
λ_0 [nm]	1548.815	1554.005
S_T [pm K^{-1}]	9.9	12.8
S_H [pm / %RH]	0.109	2.71
S_{TH} [pm / (K %RH)]	7.41 · 10^{-3}	- 1.58 · 10^{-2}

Results and Conclusion

Since the measurement environment in a PEM fuel cell is varying, a dynamic measurement cycle is used to check the measurement accuracy and precision of temperature and humidity values under close-to-real operating conditions. The internal temperature and humidity sensors of the climate chamber are used as a reference to calculate the RMSE.

As all possible parameter combinations are to be well covered by the model in Fig. 2, the dynamic test uses temperature plateaus in intervals of 10°C within the range between 20°C and 50°C. The humidity is varied linearly from 40 %RH to 90 %RH and back over a period of 4 hours to capture also possible hysteresis effects. Fig. 3 shows the temperature and humidity values as recorded by the climate chamber and the parallel measured Bragg wavelengths for the two FBGs. Since the two FBGs are installed in close proximity, they experience the same climatic conditions. From the Bragg wavelengths the temperature *T* and humidity *RH* can be calculated by solving the inverted equation system Eq. (1).

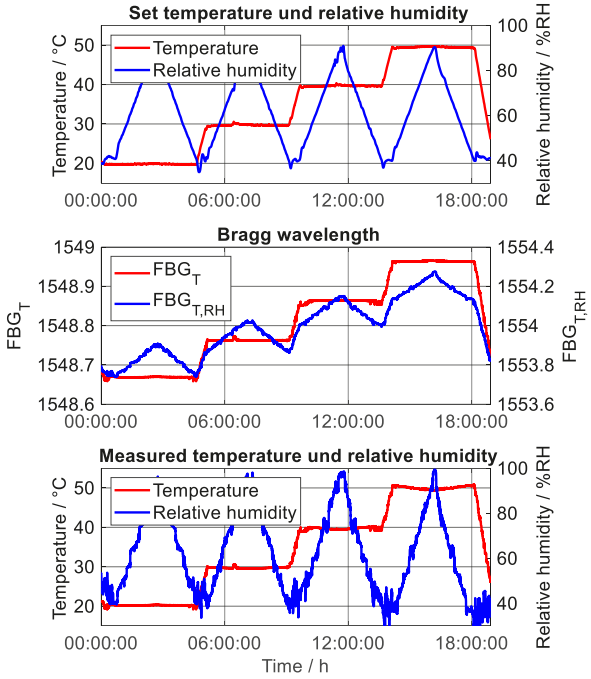

Fig. 3. Dynamic measurement cycle for verification.

With the presented set-up and a 2x2 factorial design calibration the temperature and the humidity can be measured with a RMSE of 0.45 °C and 4.8 %RH, respectively, with the internal climatic chamber sensors as reference. A part of the uncertainty of the RH measurement could be attributed to a limited precision of the climatic chamber, especially at high RH, and the low reflectivity of $FBG_{T,RH}$ of only 2.4 %. Thus, it has been demonstrated in this paper that it is possible to build a two-parameter measurement system for temperature and humidity based on ordinary and 'state of the art' FBG sensors.

References

[1] Y. Lin, Y. Gong, Y. Wu, H. Wu, Polyimide-coated fiber bragg grating for relative humidity sensing, *Photonic Sensors* 5 (1), 60-66 (2015)

[2] N. A. David, P. M. Wild, J. Hu, N. Djilali, In-fibre bragg grating sensors for distributed temperature measurement in a polymer electrolyte fuel cell, *J. of Power Sources* 192 (2), 376-380 (2009)

[3] N. S. Yazd, J. Kawakami, A. Izaddoost, P. Mégret, Effect of peak tracking methods on FBG calibration derived by factorial design of experiment, *Sensors* 21 (18), 6169 (2021)

DOI 10.5162/SMSI2023/P57

Piezoresistive Pressure Sensor Technology for Hydrogen Applications at High Temperatures

J. Gramich, O. Braun, M. Rohner, R. Rodrigo, T. Cadonau
Kistler Instrumente AG, Eulachstr. 22, 8408 Winterthur, Switzerland
joerg.gramich@kistler.com

Summary:
We report on a piezoresistive pressure sensor technology suited for pressure measurements in the ranges of 50 up to 1000 bar under 100% hydrogen gas in the emerging hydrogen economy. In contrast to existing solutions, the “dry” technology allows for measurements at elevated temperatures of 200°C and potentially above. The sensor is based on a silicon-on-insulator (SOI) block-type chip technology, with a steel membrane transferring the pressure to the sensing element. The proof-of-concept and stability of the technology could be demonstrated under 100% hydrogen up to 200°C.

Keywords: pressure sensor, hydrogen, high temperature, piezoresistive, SOI

Introduction

In today`s strive towards a future sustainable green energy society, hydrogen (H_2) is expected to play a key role as energy carrier [1]. To technologically and economically enable H_2 applications such as long-haul transportation, a whole “H_2 economy” with the corresponding production and infrastructure needs first to be developed [1]. In this economy, pressure sensors are a key element to monitor and control static and dynamic pressure changes during initial H_2 production, compression to higher pressures, storage, and distribution. Particularly, for the monitoring of static pressures, piezoresistive or thin-film strain gauge sensors are a well-established technology. But when exposed to H_2, technical challenges arise due to the potential embrittlement of H_2-exposed steel parts, as well as H_2 diffusion into the sensor interior [2]. These difficulties make many state-of-the-art static sensor concepts inherently unsuited for the long-term pressure monitoring (> 1yr) of 100% H_2. This is exemplarily shown in Fig. 1(a) for a classical oil-filled piezoresistive sensor, where H_2 can diffuse through the thin steel membrane into the oil filling and cavity of the silicon chip, leading to measurement errors and potential sensor failure [2]. While the sensor lifetime might be somewhat prolonged with additional coatings, the design flaw in the system is inherent. Similarly, standard Ni-Cr metal thin-film strain gauges bonded on a thin steel membrane are very sensitive to interaction with H_2 permeating into the sensor interior [3]. This becomes particularly important for future applications at high temperatures above 150°C, such as H_2 compression or SOFC fuel cells, where diffusion rates are increased. Here, only technologies without transmission fluids (“dry”) and cavity-based Si chips are suitable, and there is a strong need to find fitting high temperature sensor technologies.

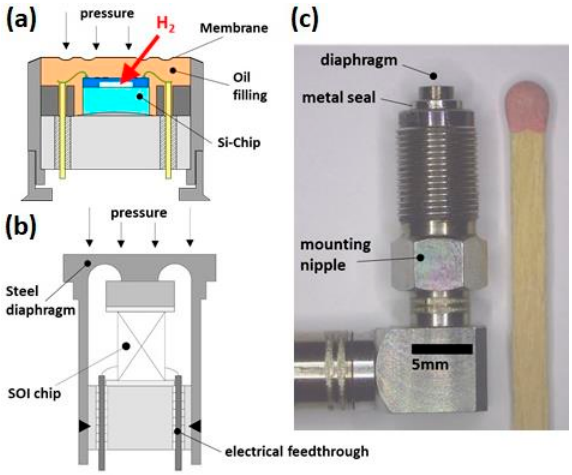

Fig. 1. (a) Typical oil-filled piezoresistive sensor: H_2 can diffuse through the thin membrane into the oil filling and silicon cavity, causing measurement errors. (b) Principle of “dry” block-type piezoresistive sensor technology [4]: pressure is transferred to stress in a SOI block-type chip, measured via piezoresistors on both sides of the chip. (c) Picture of the sensor prototypes, with a 3mm diameter diaphragm.

Sensor concept and testing approach

To allow for measurements under 100% H_2, pressure (p) ranges of 50-1000 bar and temperatures (T) up to 230°C, we use here a “dry” sensor concept [4] schematically shown in Fig. 1(b). Pressure is transferred via a flush-mounted ruggedized steel diaphragm as force on a piezoresistive silicon-on-insulator (SOI)-

based block-type bulk sensing chip. The piezoresistors on both sides of the high temperature capable SOI-chip are sensitive to the longitudinal and transverse strain experienced under load and connected to a full Wheatstone bridge. Depending on the application and p-range, various sensor sizes, membrane thicknesses and front diameters down to 3mm can be realized. For this proof-of-concept study, 14 prototype sensors have been built for a 500 bar p-range, with the design shown in Fig. 1(c). Special care has been taken to use a (flat) metal seal, no welds and only suitable materials in the H_2-exposed parts. Of the 14 prototype sensors, 11 have been tested under 100% H_2 exposure: first with a leakage test at -40°C, 23°C and 200°C, followed by 30'000 p-cycles between 1-500 bar at the respective 3 T's under recording of the p- and T-signals with an electronic amplifier, and finally all sensors were kept during 1 week at 200°C and 500 bar H_2. For comparison, similar p-cycles were performed under hydraulic oil on the 3 remaining reference sensors. All sensors were calibrated before and after the tests. To rule out any possible failure mechanisms (e.g. in the chip metallization) when H_2 permeates into the sensor, the chip alone (no housing) was also exposed to 100% H_2 at 1 bar and 175°C (to account for the T-gradient). For this purpose, a special setup was built to allow for the live chip signal measurement during H_2 exposure, and to compare the signal drifts with measurements under a neutral Argon gas.

Results

In Fig. 2(a), exemplary results of the chip-level drift characterization over 7 days under 100% H_2 at 175°C are shown. It is visible, that the pure chips drift less or similar in H_2 atmosphere than under the Ar gas reference, all on a small level mostly due to temperature effects. In the total H_2 exposure time of 360h measured at different T's, no effects due to H_2 could be detected: neither in the 7 live-measured samples nor in particular non-connected samples, that were optically, mechanically and electrically analyzed to rule out any possible failure mechanisms in the chip metallization stack or the chip bond. For the sensor prototypes, leak tightness could be achieved at all tested temperatures according to EC regulation EC79/2009. An exemplary evaluation of 30'000 temperature-stable p-cycles is shown in Fig. 2(b) for the 3 different T`s, showing pressure signal drifts at the lower cycling pressure of ~1 bar (~ZMO) of about 0.1%FSO. This is similar to what could be measured during hydraulic cycling without any H_2 influence. After a total H_2 exposure time of 600h, no influence of the H_2 could be detected and reference sensors behaved similarly, also during (re-)calibration.

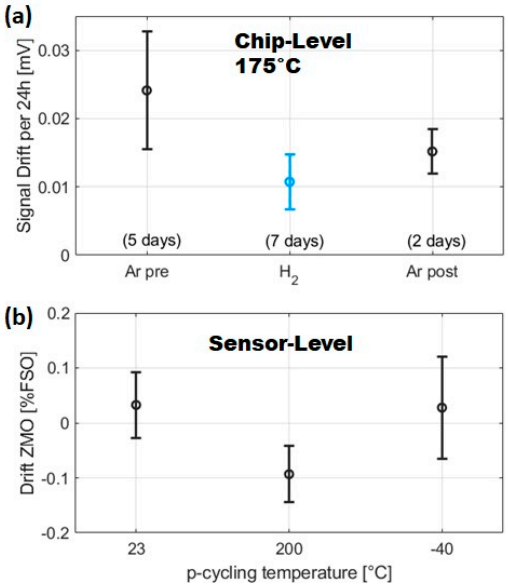

Fig. 2. Drift characterization at chip and sensor level: (a) Normalized and averaged drift signal of 7 chip samples under 100% H_2 compared to their prior and posterior drift under an Ar gas reference at 175°C. (b) Measured and averaged ZMO drift of each 3-4 sensor prototypes during 30'000 p-cycles (about 275h) between 1-500 bar at the indicated T's.

Conclusion

For the first time, based on a "dry" block-type SOI chip sensor technology, we have shown a technological proof-of-concept for the long-term monitoring of 100% H_2 pressures at 500 bar and elevated temperatures of about 200°C – a limit only due to the current test setup. In contrast to many existing solutions, there is no inherent design flaw such as a liquid filling, and the dry technology has the potential to work even up to 350°C [4]. Based on thorough tests, the sensor technology is expected to provide a robust and reliable solution particularly for future high temperature H_2 pressure measurement applications above 150°C.

References

[1] A.M. Oliveira, R.R. Beswick, Y. Yan, A green hydrogen economy for a renewable energy society, *Current Opinion in Chemical Engineering* 33, 100701 (2021), doi:10.1016/j.coche.2021.100701

[2] Karmjit S. Sidhu, Extreme pressure sensing, *Machine Design* Vol. 82 Mar 4-2010, 48-51 (2010)

[3] T. Matsuo, J. Yamabe, H. Furukawa, K. Seki, K. Shimizu, S. Watanabe, S. Matsuoka, Development of New Strain Gage for High-Pressure Hydrogen Gas Use, *Experimental Mechanics* 54, 431-442 (2014), doi:10.1007/s11340-013-9816-4

[4] J. von Berg, C. Sonderegger, S. Bollhalder, C. Cavalloni, Piezoresistive SOI-Pressure Sensor for High Pressure and High Temperature Applications, *Proc. of 12th Int. Conf. SENSOR* 2005, 33-38 (2005)

DOI 10.5162/SMSI2023/P58

Eddy current loss measurement with a focus on measurement sensors for permanent magnets (PM) in energy-efficient electrical machines

Nijan Yogal[1], Christian Lehrmann[1], Markus Henke[2]
[1] Explosion-protected electrical drive systems, Physikalisch-Technische Bundesanstalt (PTB), Bundesallee 100, 38116 Braunschweig, Germany
[2] Institute for electrical machines, traction and drives, Technische Universität Braunschweig, Hans-Sommer Str. 66, 38106 Braunschweig, Germany
nijan.yogal@ptb.de

Summary:
Permanent magnet synchronous machines (PMSMs) fed with frequency converter faces higher order harmonics signals which results higher eddy current losses in permanent magnets (PMs). This eddy current losses in the PMs leads to overheating causing irreversible demagnetization of PMs during the operation of the machines. One of the goals in machine design for the safe operation is to measure the total eddy current loss and minimize overheating of PMs. In this paper, measurement methods with a focus on measurement sensors and a finite element method (FEM) simulation for the eddy current loss (i.e. PM loss) of PMSMs are presented and compared.

Keywords: AC machine, Electrical machine, Eddy currents, loss measurement, permanent magnets, permanent magnet synchronous machines, rare earth metals, Measurement, Permanent magnet motor

Introduction, Motivation and Objective

In the last decades it has become clear that the demand for PM in various modern electrical and electronic applications has increased: the correct characterization of PM with eddy current losses urgently needs to be improved for use of PMSM (Fig. 1) in critical applications such as autonomous electric vehicles and medical applications. The accurate analytical analysis and measurement methods of PM loss with highly sensitive sensors can help PMSM designers to create robust PMSMs with high tolerances and higher energy efficiency at low manufacturing costs. In additions, the sensors should be easily implemented in all types, shapes and form of PM that are used in the PMSM as shown in Fig. 1. Various shape and forms of PM are used in SPMSM (surface permanent magnet synchronous motor), IPMSM (interior permanent magnet synchronous motor) and a SynRM (synchronous reluctance motor).

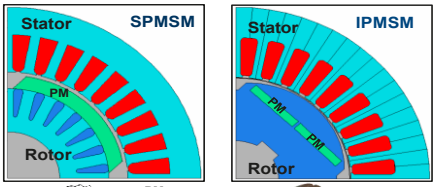

Fig. 1 Cross section (1/4 th view) of permanent magnet synchronous motors with surface mounted magnets (SPMSM - left) and interior magnets (IPMSM - right).

Experimental Measurement Setup Used to Measure Eddy Current Loss

As it can be seen in Fig. 2, the PM sample and the measurement coils available in the printed circuit board (PCB [1]) and matrix array sensors are exposed to the homogenous magnetic flux density (B_{ext}) generated via the PWM inverter signal through the excitation windings. Due to the eddy currents in the PM, the voltage is induced in the measurement coil (sensors). A compact data acquisitions unit (DAQ-FPGA) monitors both the induced voltages in the PCB and matrix sensors. The Matlab tool kit automatically reads the DAQ and the data is used to instantaneously calculate the magnetic field density B, magnetic field intensity H and eddy current loss P_{eddy} using Matlab.

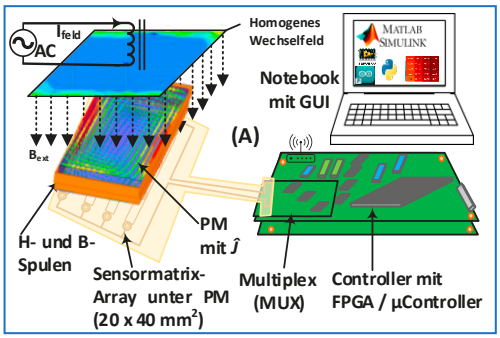

Fig. 2 Experimental measurement setup under inverter excitation current (I_{feld}) for eddy current loss measurement.

To validate the PM loss measurement with FEM simulation, rotor of SPMSM and IPMSM with the PM and the measurement matrix array sensors are created in ANSYS Maxwell software as shown in Fig. 3.

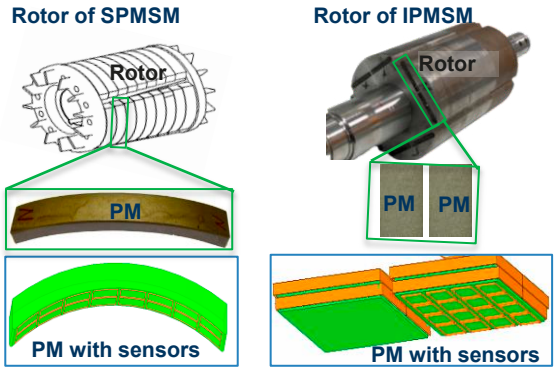

Fig. 3 3D FEM simulation model for PCB sensor and matrix sensor under PM for eddy current loss determination.

The eddy current loss per unit volume of the permanent magnet P_{eddy} is calculated using the integral (1) of the magnetic field strength *H* in the air gap and the magnetic flux density *B* from the permanent magnet.

$$P_{W\_Mess} = \frac{V_M}{T}\int_0^T \sum_{i=0}^{16} H_i \frac{d(\sum_{i=0}^{16} B_i)}{dt}\,dt \qquad (1)$$

The magnetic flux density of the two matrix sensors must be different due to the additional magnetic field generated and induced because of the eddy current inside the PM.

Results, Summary, Conclusion and Outlook

The eddy current loss with a non-sinusoidal signal such as a pulse width modulation signal generated by variable speed drives is of great interest, which is why it is investigated and presented in this paper. In addition, the analytical (FEM) investigation of the eddy current loss (i.e. PM loss) in PMs under sinusoidal and non-sinusoidal (PWM) external magnetic fields with higher frequency effects is also presented in this paper. The induced voltages (U_{air} and U_{PM}) are measured using the matrix array sensors as shown in Fig. 3. The measured induced voltages can be seen in Fig. 4. An expression of the change of the magnetic field strength *H* and the magnetic field density *B* of the magnet can be evaluated by integrating the induced voltage (U_{air} and U_{PM}) over time respectively.

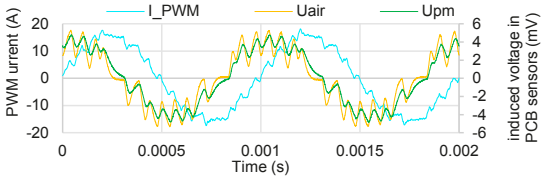

Fig. 4 The induced voltage in the coils under inverter excitation current (PWM) for eddy current loss measurement.

Furthermore, eddy current loss measurement at higher frequencies should be studied in more depth in future research and will be presented in the final paper The further study of the issue related to measurement uncertainty (MU) on induced voltage measurement using matrix sensors is a complex task and still has to be fulfilled. Therefore, the MU calculation of PM loss is not included in this paper although it is of great interest. The next stage of our research will be calibrating measurement matrix array sensors with MU in PM loss measurements. Further research on measurement matrix array sensors with higher external fields is desirable to understand the PM loss phenomena in PWM inverter fields

References

[1] N. Yogal, C. Lehrmann, and M. Henke, “Measurement of eddy current loss in permanent magnets with high-frequency effects of electrical machines for hazardous locations,” *in 22nd International Conference on Electrical Machines and Systems (ICEMS2019*), 2019, no. 6.

[2] N. Yogal, C. Lehrmann, and M. Henke, “Eddy Current Loss Measurement of Permanent Magnets Used in Permanent Magnet Synchronous Machines,” in *Proceedings of the International Conference on Power Electronics and Drive Systems*, 2019, vol. 2019, no. 17, pp. 3760–3765

DOI 10.5162/SMSI2023/P59

Improved determination of viscoelastic material parameters using a pulse-echo measurement setup

Dmitrij Dreiling [1], Dominik Itner [2], Tim Hetkämper [1], Carolin Birk [2], Hauke Gravenkamp [3], Bernd Henning [1]
[1] Measurement Engineering Group, Paderborn University, 33098 Paderborn, Germany
[2] Institute of Structural Analysis, University of Duisburg-Essen, 45141 Essen, Germany
[3] International Centre for Numerical Methods in Engineering (CIMNE), 08034 Barcelona, Spain
dreiling@emt.upb.de

Abstract:
Transmission measurements can be used to determine the frequency-dependent material parameters of polymers for simulative purposes. To achieve this goal, a hollow cylindrical sample is placed between two ultrasonic transducers. Hereafter, the material parameters are determined by ultrasound excitation in the MHz range and an inverse approach. However, the coupling conditions between the transducers and the sample is prone to uncertainties. Therefore, modeling of the setup for the inverse approach proves to be difficult. To reduce the uncertainties, this paper presents a measurement setup using a pulse-echo method in order to obtain frequency-dependent material parameters.

Keywords: ultrasonic transducer, pulse-echo method, material characterisation, polymers, scaled boundary finite element method.

Motivation

In order to keep production costs low, typical design processes rely on simulation-based approaches. For the simulations, the knowledge of the material behaviour is a central issue. Especially for polymers, reliable material parameters are only measured quasi-statically by the manufacturers. However, there is a demand for frequency dependent parameters for simulation purposes. In order to determine material parameters of polymers up to 2.5 MHz, a transmission measurement setup was introduced in [1].

Transmission measurement setup

The setup depicted in Fig. 1 consists of two transducers for transmitting and receiving acoustic waves through a hollow cylindrical polymer sample. Moreover, voltage gain amplifiers are used to amplify the electrical input and output signal. Otherwise, the received signals would be too small to evaluate, especially when investigating polymers with greater attenuation. By knowing both, the input and output, material parameters of a sample can be determined in an inverse approach by modelling the sample as a hollow cylindrical waveguide via an SBFE method [1, 2]. Previous studies of the measurement setup show a low sensitivity of the mechanical shear parameter μ_{L} due to the uniform full surface excitation of the transducers [1]. In order to increase the sensitivity of the measurement setup, a non-uniform, segmented excitation was investigated by means of numerical simulations in [3]. The simulation results show that the sensitivity can be increased by a segmented excitation. For this purpose, new ultrasonic transducers with 1-3 piezoelectric composites but structured electrodes were designed [4]. To apply these in the measurement setup and increase sensitivity and reproducibility, further modifications to the measurement setup are presented in this work.

Fig. 1. Two ultrasonic transducers (white) with a polymer sample in between.

Pulse-echo measurement setup

In the case of a full-surface excitation of a sample as in Fig. 1, results are insensitive to the exact position of the sample on the transducer's contact surface. Whereas a non-uniform excitation requires a perfect alignment of both transducers in order to match the waveguide simulations in

the inverse approach. For example, if a transducer with two sector-segments (half-half) is used for transmitting and another for receiving, it is difficult to place them on the sample and align the facing sectors of both transducers perfectly. Because of this difficult alignment, the uncertainty increases, and the reproducibility of a measurement decreases. One way to solve this problem is to use solely one transducer to transmit and receive the signal. The ultrasound transducers are developed for broadband use and are therefore suitable for transmitting and receiving. Due to the transition from polymer to air, the transmitted wave is reflected at the end face of the sample. The reflection occurs because of a large acoustic impedance difference. In addition, the forward model becomes simpler because only one transducer needs to be characterised and modeled.

Fig. 2 shows the concept for the new measurement setup. As already mentioned, voltage gain amplifiers are used to amplify the electrical signals. Due to the amplifiers, a direct connection between the transmit and receive path would lead to hardware damage. Therefore, a switch circuit is designed to prevent a short circuit between the transmitting amplifier A_1 and the receiving amplifier A_2. Due to a low contact resistance of $3.6\,\Omega$, the high symmetrical input voltage range of $\pm 15\,\mathrm{V}$ and the sufficient maximum current, the DG470 from Vishey is well suited for the presented switch-circuit.

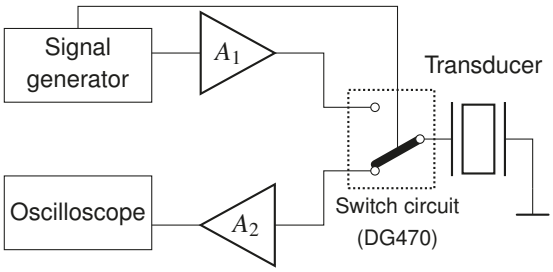

Fig. 2. The realised concept of the pulse-echo measurement setup.

Measurement results

Fig. 3 shows a result achieved with the pulse-echo measurement setup in comparison to a simulation via the SBFE method. In this measurement, a polyether ether ketone (PEEK) sample of $17\,\mathrm{mm}$ length and $18\,\mathrm{mm}$ outer diameter is investigated. Fig. 3 shows the typical three wave packets, resulting from mode conversion of the transmitted wave packet. While the time of arrival of the first packet mainly depends on the longitudinal velocity, the time of arrivals of the other wave packets are additionally depend on the transverse velocity. The simulation shows good agreement with the measurement. While the first wave packet is already in good agreement, the second and third wave packets show clearer differences. This is because the inverse method has not yet been tuned for the pulse-echo setup. The switch is not yet sufficiently represented in the model and the selected damping model has not been finally validated. This is particularly noticeable in the pulse-echo measurement method, where the sound wave has to travel twice the distance.

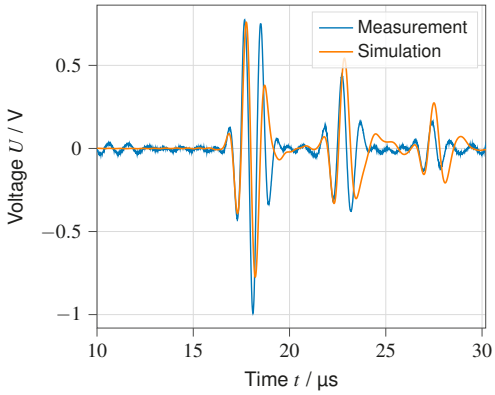

Fig. 3. Measurement result and simulation of a polyether ether ketone (PEEK) sample.

Conclusion

The modification of a transmission measurement setup to a pulse-echo setup is possible. By using a switching circuit, it is feasible to make comparable measurements, which can be used in an inverse approach to determine material parameters of polymer samples. Further investigations with regard to the chosen damping model and the reproducibility of the results have to be carried out.

Funding

The authors would like to thank the German Research Foundation (DFG, Deutsche Forschungsgemeinschaft) for financial support of the research project 409779252.

References

[1] F. Bause et al., Ultrasonic transmission measurements in the characterization of viscoelasticity utilizing polymeric waveguides, *Measurement Science and Technology 27*, no. 10 (2016); doi:10.1088/0957-0233/27/10/105601

[2] D. Itner, H. Gravenkamp, D. Dreiling, N. Feldmann and B. Henning, Efficient semi-analytical simulation of elastic guided waves in cylinders subject to arbitrary non-symmetric loads, *Ultrasonics 114*, (2021); doi: 10.1016/j.ultras.2021.106389

[3] D. Dreiling, D. T. Itner, N. Feldmann, H. Gravenkamp, and B. Henning, Increasing the sensitivity in the determination of material parameters by using arbitrary loads in ultrasonic transmission measurements, *SMSI 2020 - Measurement Science*, (2020); doi:10.5162/SMSI2020/D1.3

[4] D. Dreiling et al., Application and modelling of ultrasonic transducers using 1-3 piezoelectric composites with structured electrodes, *Fortschritte der Akustik - DAGA 2021*, (2021)

DOI 10.5162/SMSI2023/P60

A Novel Temperature Compensated Magnetic Field Sensor Based on the Magnetoelectric Effect

Manfred Wich[1], Florian Hubert[2], Jan Helmerich[1], Stefan J. Rupitsch[1]
[1] Department of Microsystems Engineering – IMTEK, University of Freiburg, Germany
[2] Chair of Sensor Technology, Friedrich-Alexander-Universität Erlangen-Nürnberg, Germany
manfred.wich@imtek.uni-freiburg.de

Summary:
This contribution presents a novel approach for a temperature compensated DC magnetic field sensor, based on the magnetoelectric effect. In utilizing two vibration modes of a rectangular cuboid magnetoelectric sample, we can determine the samples' temperature in addition to the magnetic flux density the sample is exposed to.

Keywords: Magnetoelectric, resonant magnetic field sensor, temperature compensation, delta-E effect, electromechanical vibration modes

Introduction

Magnetic field sensors, based on the magnetoelectric (ME) effect, are considered to become promising alternatives for conventional magnetic field sensors such as Hall probes and giant magnetoresistive devices [1]. Due to the direct ME effect, i.e., an electric polarization caused by a magnetic field, each ME device is in general capable of sensing magnetic fields [2]. However, only composite-based devices (mechanically coupled magnetostrictive and piezoelectric layers) are useful in practice, since they exhibit a significantly larger ME effect compared to single-phase materials [3]. These composite-based devices have made great progress in the detection of AC magnetic fields in recent years, but the detection of DC fields remains challenging [4,5]. Detecting low-frequency and DC magnetic fields in ME resonators is usually performed by evaluating the sensitivity of the Young's modulus to magnetic fields (delta-E effect) [6]. Our novel approach, utilizing the delta-E effect as well, is capable of sensing the ambient temperature in addition to the detection of DC magnetic fields. This enables a direct temperature compensation.

The resonance frequency of a resonator is determined by its geometry and material properties (such as Young's modulus and density) [7]. When a magnetostrictive material is exposed to an external magnetic field, its magnetic domains will align along the magnetic field, causing mechanical strain and a change in the Young's modulus of the material (delta-E effect) [1,2,6]. Thus, an external magnetic field causes a shift in the resonance frequency of a magnetoelectric device. Our novel approach utilizes two vibration modes (VM) instead of one only: (i) The VM along the length (VM-L, about 200 kHz in Fig. 1) and (ii) the VM along the width (VM-W, about 700 kHz in Fig. 1). Therefore, our sensor geometry features a rectangular cuboid shape (see Fig. 2).

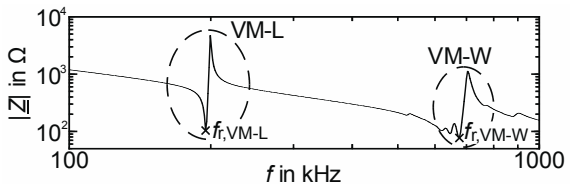

Fig. 1. Measured electric impedance spectrum |Z| of a magnetoelectric composite sample. The vibration modes in length (VM-L) and width (VM-W) direction are indicated by dashed ellipses. Their corresponding resonance frequencies ($f_{r,VM-L}$, $f_{r,VM-W}$) are marked by a cross (X).

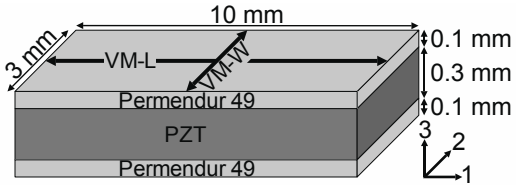

Fig. 2. Basic structure of the magnetoelectric composite samples.

Sample Preparation

The basic structure of the proposed sensor consists of three layers (cf. Fig. 2). A piezoelectric plate (PZT – PI Ceramic PIC 255, poled in 3-direction) is mechanically coupled with two magnetostrictive foils (Permendur 49). The mechanical coupling is realized by an adhesive. Two different types of adhesives were examined: We used cyanoacrylate for sample 1 and a 2-component epoxy adhesive for sample 2. A small area in the center of the contact surface is not covered with adhesive,

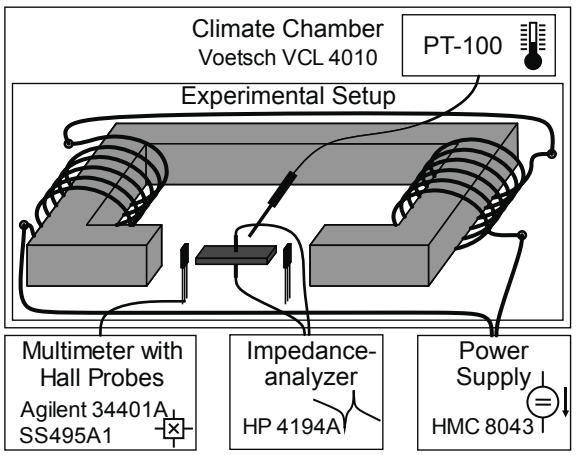

Fig. 3. Measurement setup.

but rather with silver conductive paint. This is to ensure electric conductivity between the magnetostrictive layer and the electrodes of the piezoelectric layer.

Measurement Setup

The measurement setup of Fig. 3 allowed for an evaluation of the shift in the frequencies f_r under variation of the ambient temperature and the DC magnetic flux density. The resonance frequencies ($f_{r,VM\text{-}L}$ and $f_{r,VM\text{-}W}$, respectively) of the two vibration modes (VM-L and VM-W) are determined by the measured electric impedance spectra (cf. Fig. 1). The experimental setup is placed in a climate chamber, where the ambient temperature is monitored by a PT-100 sensor placed near the sample and is stepwise increased by 5 °C from -20 °C to +25 °C. At each temperature step, the homogeneous DC magnetic flux density in the air gap of a ferrite core is reduced from +60 mT to -60 mT in 5 mT steps, while the electric impedance spectrum is measured for each set flux density. The magnetic flux density, to which the sample is exposed to, is measured by two Hall probes.

Results

The measurement results in Fig. 4 depict the sensitivities of the resonance frequencies f_r for each VM and its corresponding sample as a function of the magnetic flux density B and temperature T. Both VM show a clear decrease of the resonance frequency with an increasing temperature (Fig. 4 a-d). While the resonance frequency of VM-L is sensitive (up to 22.5 Hz/mT, Fig. 4 a, c) to the magnetic field, VM-W is almost independent from the magnetic field compared to the temperature (Fig. 4 b, d). Therefore, by utilizing $f_{r,VM\text{-}W}$, the sample's temperature can be determined by VM-W. This provides us with sufficient information on the temperature that allows us to derive the magnetic flux density from the resonance frequency of VM-L ($f_{r,VM\text{-}L}$).

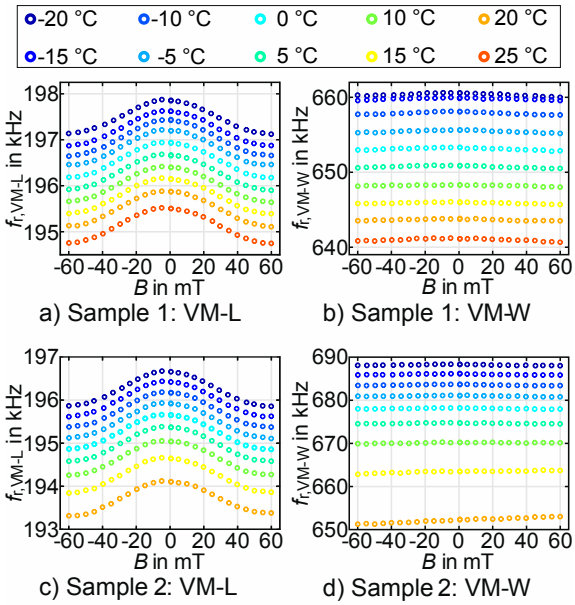

Fig. 4. Measured relationship between the resonance frequency f_r of VM-L or VM-W and the magnetic flux density B under variation of the ambient temperature T. The measurements were performed with two different samples.

Conclusion and Outlook

In this contribution we presented a novel approach for an electromagnetic sensor, which allows to measure both the magnetic field and the ambient temperature by utilizing different vibration modes. Further investigations on AC magnetic fields and sputtered layers are intended.

References

[1] D. Viehland et al., Magnetoelectric magnetic field sensors, *MRS Bulletin* 43, 834–840 (2018); doi: 10.1557/mrs.2018.261

[2] X. Liang et al., Roadmap on Magnetoelectric Materials and Devices, *IEEE Transactions on Magnetics*, vol. 57, no. 8, pp. 1-57 (2021); doi: 10.1109/TMAG.2021.3086635

[3] M. Bichurin et al., Magnetoelectric Magnetic Field Sensors: A Review, *Sensors*, vol. 21, no. 18, p. 6232 (2021); doi: 10.3390/s21186232

[4] R. Chen et al., Differential Configuration for Highly Sensitive DC Magnetic Field Sensing Based on Nonlinear Magnetoelectric Effect, *IEEE Sensors Journal*, vol. 22, no. 18, pp. 17754-17760 (2022); doi: 10.1109/JSEN.2022.3194142

[5] Y. Ren et al., Rotating Magnetoelectric Sensor for DC Magnetic Field Measurement, *IEEE Transactions on Magnetics*, vol. 54, no. 11, pp. 1-3 (2018); doi: 10.1109/TMAG.2018.2840823

[6] Y. Hui et al., High Resolution Magnetometer Based on a High Frequency Magnetoelectric MEMS-CMOS Oscillator, *Journal of Microelectromechanical Systems*, vol. 24, no. 1, pp. 134-143 (2015); doi: 10.1109/JMEMS.2014.2322012

[7] S. J. Rupitsch, Piezoelectric Sensors and Actuators: Fundamentals and Applications, *Springer Berlin Heidelberg* (2019)

DOI 10.5162/SMSI2023/P61

IMPROVED CALIBRATION CAPABILITIES FOR INFRARED RADIATION THERMOMETERS AND THERMAL IMAGERS IN THE RANGE FROM -60 °C TO 960 °C AT THE PHYSIKALISCH-TECHNISCHE BUNDESANSTALT

Ingmar Müller[1], Berndt Gutschwager[1], Albert Adibekyan[1], Elena Kononogova[1], Christoph F. Hemeling[2], and Christian Monte[1]
[1] Physikalisch-Technische Bundesanstalt, Berlin, Germany,
[2] Technische Universität Ilmenau, Ilmenau, Germany
ingmar.mueller@ptb.de

Summary:
At the Physikalisch-Technische Bundesanstalt (PTB), the national metrology institute of Germany, the calibration facility for thermal imager, infrared calibrators, and radiation thermometers has been updated to improve the calibration service. An additional cesium-heatpipe blackbody was installed to close the temperature gap from 270 °C to 500 °C and a new sodium-heatpipe blackbody was taken into operation. In addition, the precision of the positioning of the devices under test was improved and the new blackbodies were characterized and tested. The calibration facility now marks the state-of-the-art in terms of achievable uncertainties and automatization.

Keywords: metrology, radiation thermometry, infrared, calibration, uncertainty evaluation

Introduction

The main tasks of the department “Detector radiometry and radiation thermometry” of the Physikalisch-Technische Bundesanstalt (PTB), the national metrology institute of Germany, are non-contact temperature measurements (radiation thermometry) from -170 °C to 3000 °C and the quantitative measurement of electromagnetic radiation from the UV, to the visible and to the far infrared spectral range (THz radiation). This includes the realization, dissemination, and further development of the radiation temperature scale from -170 °C to 3000 °C by means of methods based on radiation thermometry and radiometry and the calibration of radiation temperature standards and radiation temperature devices [1]. The existing calibration facility for thermal imagers was enhanced to provide the calibration service for radiation temperature devices for the next 4 years as the current low temperature infrared calibration facility of PTB is going through a major revision.

The Thermal Imager Calibration Facility

The Thermal Imager Calibration Facility (TI-CF) (see Fig.1) of PTB provides radiation temperatures in the range from -60 °C up to 962 °C by means of four different heatpipe blackbodies [1]. Traceability to the ITS-90 is provided by standard platinum resistance thermometers (SPRTs) that measure the temperature of the heatpipe blackbodies very close to the bottom of the cavities (see schematic in Fig. 1). In addition to the existing ammonia- and water-heatpipe blackbodies, two new heatpipe blackbody cavities have been taken into operation.

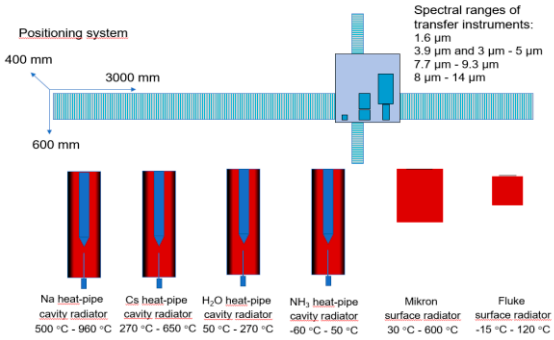

Fig. 1. Schematic of the TI-CF. The main components of the TI-CF are a high-precision positioning system, 6 different blackbodies and a set of radiation thermometers and thermal imagers as transfer instruments.

The new blackbody cavities are a Cs- and a Na-heatpipe blackbody. With the new blackbodies, the radiation temperature can be disseminated seamlessly from -60 °C up to 960 °C with uncertainties, that we believe, are among the smallest world-wide. Two surface radiators allow for the full illumination of FPA-Sensors in thermal imagers. A high-precision positioning

system enables controlled pixel-by-pixel movement of thermal imaging cameras. This is of utmost importance for the application of a non-uniformity correction method developed at PTB, which can also be used for non-uniform radiation sources [2].

Characterization of the heatpipe blackbodies

The blackbodies were characterized, and the corrections of the radiation temperature $t_{r,90}$ were determined following the guidelines published in [3]. The most important correction term accounts for the emissivity of the blackbodies. The calculation of the uncertainty components with respect to the emissivity was carried out for both isothermal and non-isothermal blackbody conditions. For the isothermal condition the emissivity of the surfaces of the blackbodies were measured at the emissivity measurement under air facility of PTB [4] by means of samples that have identical layer thickness of the paintings as the cavities (for the ammonia- and water heatpipes) or come from the same blanks as the material for Inconel cavities (Cs- and Na-heatpipes). As an example, the results for an Inconel 600 sample are shown in Fig. 2. With this information the effective emissivity of the cavities was calculated using Steep 321 [5].

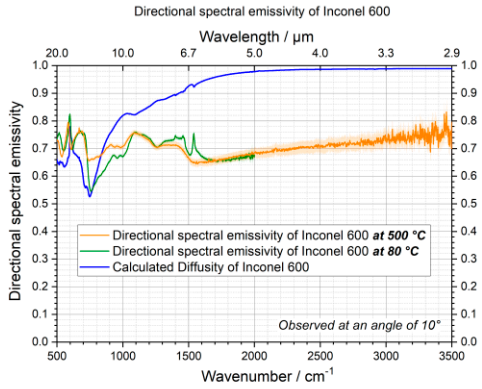

Fig. 2. Measured spectral emissivity of an Inconel 600 sample from the manufacturer of the Cs- and Na- heatpipe cavities and calculated diffusivity plotted over the wavelength.

To calculate the effective emissivity for non-isothermal blackbody conditions, the temperature profile along the cavity walls must be known. The temperature profiles were measured with a radiation thermometer and were compared with the results of the Steep 321 simulation. In an iterative process the temperature profiles in Steep 321 were adjusted until the measured and simulated temperature profiles matched. These measurements were performed at different temperatures. The difference of the isothermal and non-isothermal effective emissivity was included in the uncertainty budget. In addition, the radiation temperature corrections of the existing ammonia-heatpipe blackbody have been calculated accounting for the non-isothermal condition.

Results

Due to improved characterization methods in combination with Monte-Carlo-calculations of the effective emissivity, the uncertainties of the radiation temperature have been significantly reduced. This holds especially in the temperature range from 50 °C to 270 °C and temperatures between 270 °C and 350 °C where the uncertainties could be reduced up to a factor of 8 (see Fig. 3). The low temperature infrared calibration facility and the TC-IF have been compared by means of several transfer radiation thermometers at the wavelengths 1.6 µm and 3.9 µm and in the range from 8 µm to 14 µm and showed a very good agreement within the stated uncertainties.

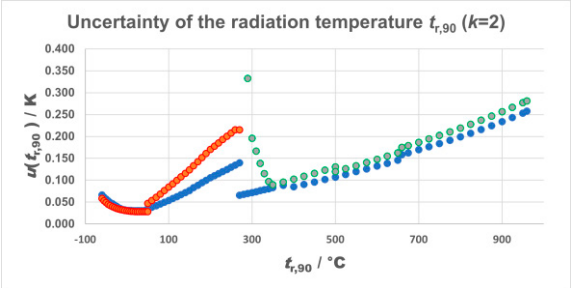

Fig. 3. Comparison of the uncertainties of the re-characterized TC-IF (blue dots) and the previous uncertainties of the ammonia- and water-heatpipe (red dots) and the Cs- and Na-blackbodies of the low temperature infrared calibration facility (green dots).

These results ensure that the calibration service can be maintained without any restrictions for customers in the coming years.

References

[1] I. Müller, et al., (2021) Non-contact temperature measurement at the Physikalisch-Technische Bundesanstalt (PTB), Quantitative InfraRed Thermography Journal, 18:3, 187-212, DOI: 10.1080/17686733.2020.1734392

[2] Berndt Gutschwager and Jörg Hollandt 2017 *Meas. Sci. Technol.* **28** 015401 DOI: 10.1088/1361-6501/28/1/015401

[3] Saunders, P., Fischer, J., Sadli, M. *et al.* Uncertainty Budgets for Calibration of Radiation Thermometers below the Silver Point. *Int J Thermophys* **29**, 1066–1083 (2008). https://doi.org/10.1007/s10765-008-0385-1

[4] C. Monte, J. Hollandt, The measurement of directional spectral emissivity in the temperature range from 80° C to 500° C at the Physikalisch-Technische Bundesanstalt. High Temp. High Press. **39**, 151–164 (2010)

[5] https://www.virial.com/

DOI 10.5162/SMSI2023/P62

An Optical Stokes Absolute Roll-angle Sensor with a Full Measurement Range of 360°

Chia-Wei Chen[1, 2], Matthias Hartrumpf[2], Thomas Längle[2], Jürgen Beyerer[1, 2]
[1] Vision and Fusion Laboratory (IES), Karlsruhe Institute of Technology (KIT), Haid-und-Neu-Str. 7, 76131 Karlsruhe, Germany
[2] Fraunhofer Institute of Optronics, System Technologies and Image Exploitation IOSB, Fraunhoferstraße 1, 76131 Karlsruhe, Germany
chia-wei.chen@kit.edu

Summary:
Angle measurements (roll, pitch, and yaw) are important parameters in many different fields. Roll angle is deemed the most challenging measurement quantity because the angular displacement of the roll angle is perpendicular to the probe beam. In this work, we proposed a Stokes roll-angle sensor whose measurement range can achieve 360° without ambiguity. The principle is based on the polarization change of a sensing unit (vortex retarder). Within the whole measuring range, the measurement errors are less than ±0.15° and the standard deviations are less than 0.09°.

Keywords: Roll angle, angle sensor, polarization sensor, Stokes polarimeter, angle measurement

Background and Motivation

Angle measurements (roll, pitch, and yaw angles) are important parameters in many different fields, e.g., remote sensing [1], navigation [2] and object tracking [3]. Roll angle is deemed the most challenging measurement quantity because the angular displacement of the roll angle is perpendicular to the probe beam. Most general methods for roll-angle measurements are variation of polarization states, rotary encoder, autocollimator, optoelectronic level, relative position shift of two parallel laser beams [4]. Nevertheless, only the first two methods can measure large angular displacement. The rest methods are limited to few degrees or few arcminutes. Compared to variation of polarization states, rotary encoders require a fixed distance between the optical head and the disk scale. This drawback decreases the feasibility of long-range measurements. The polarization-based measurements for the roll angle can be used for remote sensing but the range is limited to 180° [1,5,6].

In this work, we propose a Stokes roll-angle sensor whose measurement range can achieve 360° without ambiguity. The measurement principle is based on the special polarization characteristic of a vortex quarter-wave retarder (VR). The roll angle is acquired by measuring the change of the polarization states of linearly polarized light after passing the VR.

Description of the New Method

Figure 1 shows the schematic of the proposed roll-angle sensor. The light source passes a linear polarizer (LP) and a VR and the beam was received by a Stokes polarimeter.

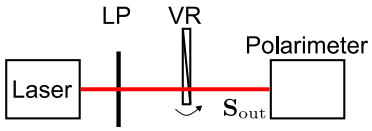

Fig. 1. The schematic of the proposed roll-angle sensor.

In the system, the VR is a sensing unit for the roll angle and the other components are fixed. There is an offset between the center of the VR and the light beam. The fast axis of the VR (first order) rotates continuously and its Mueller matrix is shown as

$$\mathbf{M}_{\mathrm{VR}} = \begin{bmatrix} 1 & 0 & 0 & 0 \\ 0 & \cos^2\phi & \frac{1}{2}\sin 2\phi & \sin\phi \\ 0 & \frac{1}{2}\sin 2\phi & \sin^2\phi & -\cos\phi \\ 0 & -\sin\phi & \cos\phi & 0 \end{bmatrix},$$

where ϕ is the orientation of the fast axis. If the axis of the LP is horizontal, the measured Stokes vector $\mathbf{S}_{\mathrm{out}}$ can be expressed as

$$\mathbf{S}_{\text{out}} = \begin{bmatrix} 1 & \cos^2\phi & \frac{1}{2}\sin 2\phi & -\sin\phi \end{bmatrix}^{\mathrm{T}}.$$

Figure 2 presents simulated Stokes parameters for the roll angle from 0° to 360°. It is obvious that the periods of s_1, s_2, and s_3 are 180°, 180° and 360°, separately. Therefore, the proposed sensor can measure roll angles with an unambiguous measurement range of 360°.

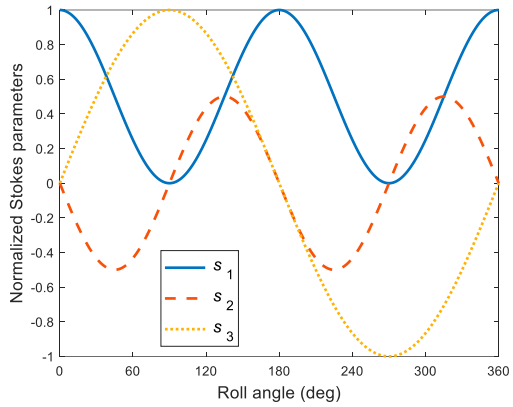

Fig. 2. Simulated Stokes parameters for the roll angle from 0° to 360°.

Results

In principle, the fast axis angle of the VR can be solved by the measured Stokes vector analytically. However, nonlinear errors existed in the measurement data. The reasons might be the alignment, uniformity of the retardance and manufacturing accuracy of the fast axis angle. In order to get more accurate results, we used a numerical fitting method in the following experiment. First, the VR was rotated by a stepper motor rotation mount with an absolute accuracy of 0.14° and unidirectional repeatability of ±60 µrad as an angle reference. Then a fitting model was established based on the measured data. Finally, the square error function can be written as

$$\chi^2 = \sum_{i=1}^{3}\left(s_i^{\text{Exp}} - s_i^{\text{Fit}}(\phi)\right)^2,$$

where the superscripts Exp and Fit indicate the experimental data and fitted models, respectively. Non-linear optimization method is applied to solve the fast axis angle of the VR. To verify the sensor, the sensing unit (VR) rotates five times from 0° to 360° with a step of 10°. Figure 3 shows the measurement results of the roll-angle sensor and the length of the error bars indicates the standard deviation of the measurements. Within the whole measuring range, the measurement errors are less than ±0.15° and the standard deviations are less than 0.09°. This experiment shows the proposed sensor has high accuracy and high precision. In addition, the construction of the roll-angle sensor is simple and the sensor can be easily set up for existing measurement systems because of the non-contact method and the simple design.

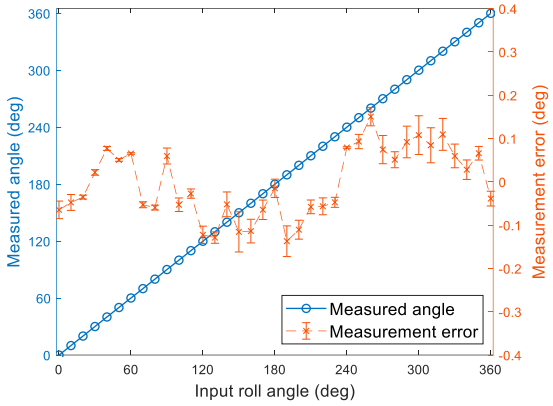

Fig. 3. Results of the measured roll angles compared with the values of a stepper motor rotation mount.

References

[1] X. Chen, J. Liao, H. Gu, C. Zhang, H. Jiang, S. Liu, Remote Absolute Roll-Angle Measurement in Range of 180° Based on Polarization Modulation, *Nanomanufacturing and Metrology* 3.3, 228-235 (2020); doi: 10.1007/s41871-020-00069-0

[2] D. Wang, H. Liang, H. Zhu, S. Zhang, A Bionic Camera-based Polarization Navigation Sensor, *Sensors* 14.7, 13006-13023 (2014); doi: 10.3390/s140713006

[3] H. B. Jeong, J. K. Park, D. Kim, K. N. Joo, Polarized Imaging Interpreter for Simultaneous Clocking Metrology of Multiple Objects, *Optics letters* 46.19, 4992-4995 (2021); doi: 10.1364/OL.439614

[4] Y. Shimizu, L.-C. Chen, D. W. Kim, X. Chen, X. Li, H. Matsukuma, An Insight into Optical Metrology in Manufacturing, *Measurement Science and Technology* 32.4. 042003 (2021); doi: 10.1088/1361-6501/abc578

[5] C.- W. Chen, M. Hartrumpf, T. Längle, J. Beyerer, Sensitivity Enhanced Roll-angle Sensor by Means of a Quarter-waveplate, *tm-Technisches Messen* 88.s1, s48-s52 (2021); doi: 10.1515/teme-2021-0069

[6] K.-H. Chen, J.-T. Tseng, C.-H. Yeh, J.-H. Chen, Alternative Method for Measuring the Phase Retardation and Fast Axis of a Wave Plate, *Optical Review* 26.6, 652-658 (2019); doi: 10.1007/s10043-019-00546-y

DOI 10.5162/SMSI2023/P63

Self-sensing properties of continuous carbon fiber reinforced, 3D-printed beams

Jonathan Schaaij, Alexander Dijkshoorn, Stefano Stramigioli, Gijs Krijnen
Robotics and Mechatronics Group, University of Twente, Enschede, the Netherlands
Corresponding author: a.p.dijkshoorn@utwente.nl

Summary:
This paper investigates self-sensing properties of continuous carbon fiber reinforced, 3D-printed beams as function of the number of reinforced perimeters. Samples containing various numbers of reinforced perimeters are tested for their stiffness and strain-dependent resistance using three-point bending tests. The mechanical properties are modelled using classical beam theory and the resistance can be estimated using the resistance of the fiber additive. Large resistance changes are measured during bending, which results in a high responsivity.

Keywords: 3D-Printing, continuous carbon fiber, self-sensing structures, strain gauge, piezoresistivity

Introduction

A novel method in fused filament fabrication (FFF) called composite fiber co-extrusion (CFC) enables to 3D-print continuous carbon fiber (CCF). Using this method a thermoplastic polymer is extruded around the fiber, embedding it inside the printed part [1]. The fiber provides excellent mechanical properties, crucial for making lightweight and stiff components. Additionally, CCF is electrically conductive and has piezoresistive properties, enabling the use of CCF for self-sensing structures in which fibers provide strength as well as sensing functionality [2, 3]. This offers numerous advantages over traditional separate sensors, such as a simplified manufacturing process and distributed sensing of large-scale structures. Luan et al. showed that such self-sensing structures can function as strain gauge measuring a linear reversible resistance increase for elastic deformation and also to measure structural damage [3]. To investigate the influence of the fiber count on the performance of the strain gauges, this work presents the electrical and mechanical characterization of 3D-printed self-sensing reinforced beams with various numbers of reinforced perimeters.

Methods

The tested samples are beams with a rectangular cross section containing CCF perimeters in top and bottom layers, where they provide maximum stiffness, fig. 1. Beam theory is used to determine the stiffness of the beams from a three-point bending test. The beam model is split into five layers with varying volume fractions to account for different materials. Using the rule of mixtures [3] the effective Young's moduli E_{eff} for each section can be determined and with the transformed section method the area moment of inertia I_{eff}. The center deflection y_{max} during a three-point bending test and the stiffness k of the samples can be calculated using [4]:

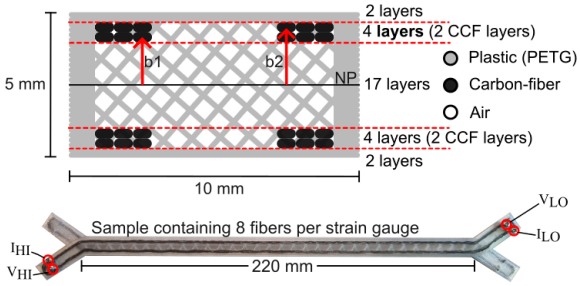

Fig. 1: Cross-section of the 3D-printed beams containing two strain gauges, made up of 2 fiber layers at distance b_1 and b_2 from the neutral plane (NP) and 3 reinforced perimeters (top). The 5 sections for the mechanical model are indicated by red lines. Topview of a beam with two CCF strain gauges (bottom)

$$y_{\text{max}} = \frac{FL^3}{48E_{\text{eff}}I_{\text{eff}}}, \quad k = \frac{F}{y_{\text{max}}} = \frac{48E_{\text{eff}}I_{\text{eff}}}{L^3} \quad (1)$$

where L the distance between supports and F is the applied force at $L/2$. The neutral electrical resistance is calculated from the resistance of a single filament and the number of fibers per beam, the piezoresistive responsivity K is defined as the relative resistance change per applied force:

$$R = \frac{R_{\text{fiber}}}{N_{\text{fiber}}} = \frac{R_{\text{fiber}}}{2N_{\text{layer}}N_{\text{perim.}}}, \; K = \frac{\Delta R/R_0}{F} \quad (2)$$

The test samples are printed on the Anisoprint

This work was developed within the PortWings project, funded by the European Research Council under Grant Agreement No. 787675.

DOI 10.5162/SMSI2023/P63

Composer A4 [1], an FFF 3D-Printer with a secondary extruder for CFC with CCF and Polyethylene terephthalate glycol (PETG) as materials. The layer height is set at 0.17 mm for PETG and 0.34 mm for CCF. The fibers are placed as reinforcing perimeter in top and bottom layers with different perimeter counts, either with one fiber layer on each side with 1 to 3 reinforcing perimeters or with two fiber layers with 1 to 4 reinforcing perimeters. Additional samples are printed without fibers and with a maximum number of fibers (120). Each sample has two outer perimeters of PETG, with 20 % triangular infill and the first two and last two layers with 100 % PETG. CCF is placed symmetrically at the top and bottom to ensure a centered neutral plane and to prevent warping caused by the different coefficients of thermal expansion of PETG and CCF. Stainless steel M2 bolts are used as electrical connection to the carbon fibers. A Keithley 2000 multi-meter is used to measure resistance with 4-terminal sensing. The samples are tested on a three-point bending setup with rounded supports ($r = 5$ mm) placed 200 mm apart. A load is applied at the center using a linear actuator in force control mode (SMAC LCA25-050-15F), while also measuring the displacement in compression and tension. A triangular load is applied from 0 N to 12 N with a period of 20 s for ten periods. Equations 1 and 2 are used to predict the stiffness and resistance.

Results

The force deflection curves for tension and compression show a linear trend with hysteresis, fig. 2. The resistance change for the sample with two fiber layers and 1 reinforcing perimeter during compression and tension can be seen in fig. 2. Large changes in resistance of up to 50 % are measured, exceeding previous research with changes of ≈1 % [3]. Like in previous research, the piezoresistive response is non-linear, showing a decreasing sensitivity for larger deflections. The stiffness of the sample with 120 fibers has been used to determine the Young's modulus of the printed CCF: $E_{\mathrm{CCF}} = 57.45$ GPa. The result is 43 % of the advertised CCF composite filament [1]. This result is confirmed by the model which matches the measured sample stiffness, fig. 2. Extrapolating the resistance of the unstrained, unprinted, CCF composite filament gives the expected neutral resistance in fig. 2. While most measured resistances are slightly higher than the expectation, there is a clear correlated trend. The resistance of the sample with two fibers is likely lower than the expected resistance as a result of inconsistent fiber placement. Due to unstable electrode connections under strain for the samples containing one fiber layer, the sensitivity is only determined for the two layered samples, fig. 2 bottom plot. It shows that the sensitivity of the CCF is higher in tension compared to compression. There is a negative correlation between the sensitivity and the fiber count, however, this is partly due to the relation between stiffness and fiber count.

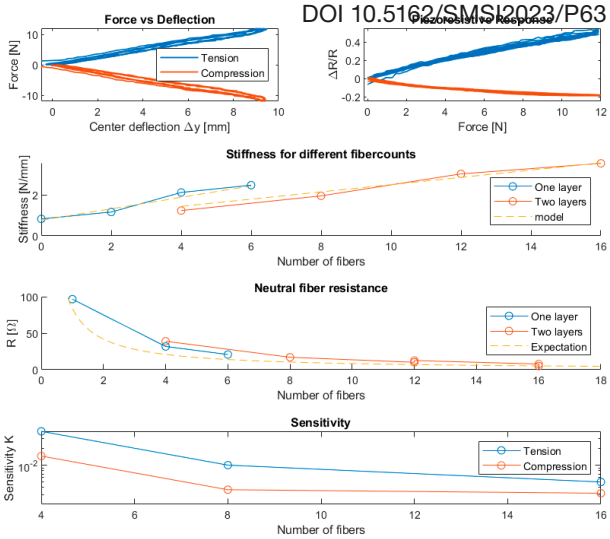

Fig. 2: Force deflection curve showing hysteresis (top left); Resistance response to tensile and compressive strain (top right); Measured stiffness (2nd row); Measured fiber resistance (3rd row) and Sensitivity for the two layered samples (bottom)

Discussion and Conclusion

This work demonstrates that resistance and stiffness of 3D printed continuous carbon fiber beams can be controlled by varying the perimeter count and can be predicted from theory. A high sensitivity of the strain gauges shows potential for sensitive CCF self-sensing structures, where the sensitivity is lower for compression compared to tension. More research is required to determine a correlation between the reinforcing perimeter count and the sensitivity of the self sensing structures. In future research the influence of other slicing settings, such as the fiber extrusion multipliers and plastic infill density, will be explored.

References

[1] Anisoprint, "Anisoprint Composer," https://anisoprint.com/solutions/desktop/, (accessed: 16.03.2022).

[2] P. Scholle *et al.*, "A review on the usage of continuous carbon fibers for piezoresistive self strain sensing fiber reinforced plastics," *Journal of Composites Science*, vol. 5, no. 4, 2021.

[3] C. Luan *et al.*, "Self-sensing of position-related loads in continuous carbon fibers-embedded 3d-printed polymer structures using electrical resistance measurement," *Sensors*, vol. 18, 2018.

[4] J. Hodgkinson, "7 - flexure," in *Mechanical Testing of Advanced Fibre Composites*. Woodhead Publishing, 2000.

DOI 10.5162/SMSI2023/P64

Conjugation of Molecularly Imprinted Polymer Nanoparticles with Metal Nanoparticles for Signal Enhancement in QCM-based Sensor Applications

Julia Völkle[1,2,3], Andrea Weiß[1, 3], Peter Lieberzeit[1], Philipp Fruhmann[3]
[1] University of Vienna, Faculty for Chemistry, Department of Physical Chemistry, Währinger Straße 42, 1090 Vienna, Austria
[2] University of Vienna, Vienna Doctoral School in Chemistry (DoSChem), Währinger Str. 42, 1090 Vienna, Austria
[3]Centre of Electrochemical Surface Technology, Viktor Kaplan-Straße 2, 2700 Wiener Neustadt, Austria
julia.voelkle@cest.at

Summary:
Solid phase synthesis of molecularly imprinted polymer nanoparticles (nanoMIPs) to detect the antibiotic vancomycin (VM) in a QCM-based assay format was established and optimized. To improve the limit of detection in gravimetric sensor setups, the nanoMIPs are designed to be further conjugated to metal nanoparticles for signal enhancement.

Keywords: QCM sensors, nanoMIPs, Signal Enhancement, Molecularly Imprinted Polymers, Biomimetic

Introduction

Molecular imprinting is a method used to obtain highly selective polymer materials that can offer some advantages over biological recognition units, such as an increased robustness against harsh, non-physiological conditions, long shelf life and reduced time and cost of production. Over the past decade, great focus has been put on nanosized imprinted particles (molecularly imprinted polymer nanoparticles, nanoMIPs) as promising materials for molecular recognition in the field of biosensors and assays. Obtained by a straightforward solid phase synthesis protocol, their high affinity, homogeneous binding sites and low non-specific binding yielded performances comparable to natural antibodies in ELISA, SPR and QCM-based assays.[1]–[3] However, limitations regarding achievable sensitivity in gravimetric detection are set by the low density of the polymer material.

This project focusses on the synthesis of nanoMIPs that can be conjugated to other, heavier nanoparticles (NPs), such as titanium dioxide-NPs. Binding of those nanoMIP-TiO_2NP conjugates would significantly increase the change of mass in a QCM-based sensor setup and therefore improve the limit of detection.

Methods

The solid phase synthesis of poly(n-isopropyl-acrylamide) (pNIPAM) based nanoparticles imprinted with the antibiotic vancomycin (VM) as a benchmark molecule was optimized. Special attention was paid to the choice of functional monomers. Here, not only the affinity towards the analyte, but also possible functional groups for further conjugation were considered when choosing the polymer composition. For that purpose, the functional monomer acrylic acid (AA) was added to the polymerization mixture of N-isopropyl-acrylamide (NIPAM) and N,N'-methylene-bis-acrylamide (BIS, crosslinker). For one, AA can introduce selective interaction sites with the analyte via hydrogen bonding. Moreover, it provides carboxylic groups within the polymer network, that can be used for further coupling via EDC/NHS crosslinking with amine-functionalized metal-NPs.

The nanoMIPs were characterized regarding their size, shape and polydispersity using dynamic light scattering and scanning electron microscopy. Fluorescence quenching and QCM-binding studies were used to assess the affinity between the analyte and the nanoMIPs as well as the nanoMIP crosslinking to an amine-bearing sensor surface.

Results

Fig. 1 shows both SEM and DLS characterization of pNIPAM-based nanoMIPs containing AA as functional monomer. Both SEM and DLS results indicate that the particles are of uniform,

spherical shape with an average diameter slightly below 100 nm. The PDI of 0.1 indicates a highly monodisperse size distribution of the nanoMIP suspension.

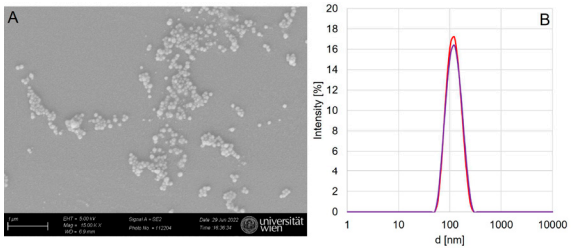

Fig. 1 A: SEM images of nanoMIPs, average diameter = 97.7 ± 0.5 nm, B: Size distribution of nanoMIP suspension in MQ H_2O measured by dynamic light scattering, d_h = 95.3 ± 15.4 nm, PDI = 0.1.

Fluorescence measurements show strong interaction between the imprinted particles and the analyte (Fig. 2). Mixing 250 ppm of VM with 25-250 ppm nanoMIPs results in concentration-dependent reduction of the VM-fluorescence by more than 80%; no such effect can be observed when adding non-imprinted reference particles with the same polymer composition. This indicates a significant increase in affinity between analyte and polymer due to imprinting.

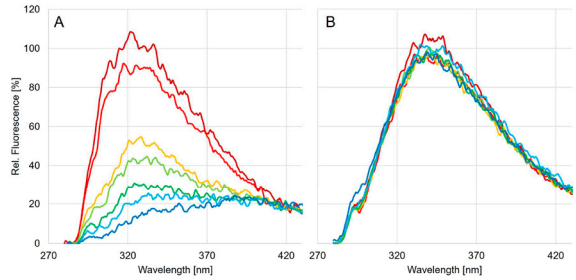

Fig. 2 Fluorescence signal of 250 ppm vancomycin in presence of 0-250 (red to blue) ppm of A) VM-imprinted nanoMIPs and B) non-imprinted reference NPs.

Affinity between the analyte and the nanoMIPs was also confirmed by QCM measurements (Fig. 3). A dual channel QCM was functionalized with VM on one electrode, while the other one was blocked with ethanolamine (EA). While the VM-functionalized channel shows a concentration-dependent frequency shift upon nanoMIP injection, the EA-electrode shows only small shifts at higher concentrations, indicating low non-specific binding of the nanoMIPs.

Lastly, QCM measurements to assess crosslinking between the carboxylic groups in the polymer network and an amine bearing compound were conducted. A cysteamine-functionalized QCM electrode was exposed to EDC/NHS activated nanoMIPs. As the measurement in Fig. 4 shows, the nanoMIPs bind to the QCM surface. Several washing steps with buffer did not remove the nanoMIPs, indicating covalent crosslinking to the cysteamine surface.

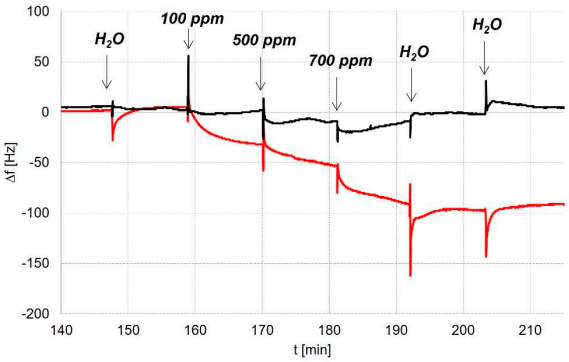

Fig. 3 Response towards varying nanoMIP concentrations of a dual channel QCM functionalized with VM on one channel (red) and ethanolamine on the other one (black).

As a next step, the nanoMIPs will be conjugated to APTES-functionalized TiO_2-NPs. The conjugates then can be used in a competitive assay format.

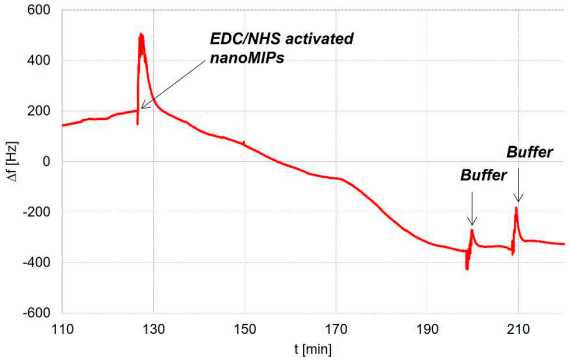

Fig. 4 Binding of AA-containing nanoMIPs activated by EDC/NHS to an amine-functionalized QCM electrode.

References

[1] L. Cenci, C. Piotto, P. Bettotti, and A. M. Bossi, “Study on molecularly imprinted nanoparticle modified microplates for pseudo-ELISA assays,” *Talanta*, vol. 178, no. October 2017, pp. 772–779, 2018, doi: 10.1016/j.talanta.2017.10.018.

[2] E. Moczko *et al.*, “Surface-modified multifunctional MIP nanoparticles,” *Nanoscale*, vol. 5, no. 9, pp. 3733–3741, 2013, doi: 10.1039/c3nr00354j.

[3] W. A. A. Sudjarwo, M. T. Dobler, and P. A. Lieberzeit, “QCM-based assay designs for human serum albumin,” *Anal. Bioanal. Chem.*, vol. 414, no. 1, pp. 731–741, 2022, doi: 10.1007/s00216-021-03771-0.

DOI 10.5162/SMSI2023/P65

Telemetric angle and position sensing using millimeter-wave metamaterial and a FMCW chip

Alexander Schossmann[1], Michael Töfferl[1], Christoph Schmidt[1], Christof Michenthaler[2], Dirk Hammerschmidt[2], Alexander Bergmann[1]
[1] Institute of Electrical Measurement and Sensor Systems, Graz University of Technology, Austria
[2]Infineon Technologies Austria AG, Villach, Austria
alexander.schossmann@tugraz.at

Summary:
A fully telemetric sensor concept is presented for real-time angle and position measurement using millimeter-wave metamaterials that exhibit Fano resonant behavior. The idea is to determine the angle of rotation from the reflection signals of a millimeter-wave transceiver chip. A metamaterial geometry exhibiting Fano resonance behavior has been designed and implemented on low-cost FR4 laminates. In addition, we show numerical and experimental analysis of the sensing effect and present the implementation with a frequency-modulated continuous wave (FMCW) chip.

Keywords: Angle measurement, position measurement, telemetric sensor, metamaterial, millimeter-wave

Introduction

Real-time position measurement, rotary as well as linear, is a fundamental quantity in powertrains and robotics. In this context, there is also a high demand for telemetric and contactless position sensors [1,2].

Sensor concept

It has been shown that planar metamaterials can exhibit Fano-type resonances that significantly determine their reflectivity [3]. The basic idea of our sensor concept is to exploit these Fano resonances which, due to their anisotropy, strongly depend on the orientation of the unit cell with respect to the polarization of the electric field. This results in an angle-dependent reflection of the metamaterial target, which can be used to determine the angle of rotation.

Numerical analysis

The metamaterial used in this work has a unit cell structure as shown in Fig. 1a. The metamaterial elements were fabricated on Panasonic R-1755M laminates with a thickness of 1.2 mm using standard PCB technology. We performed finite element simulations (FEM) in COMSOL Multiphysics®, extrapolating the material parameters of the laminate to the millimeter-wave range. The geometrical parameters were optimized to set the resonance frequency of the Fano type in the frequency range of the FMCW chip, which ranges from 58.0 GHz to 63.5 GHz.

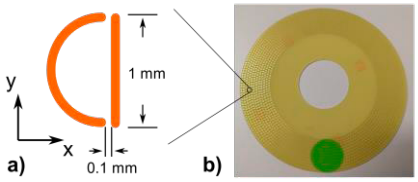

Fig. 1. Metamaterial. a: Sketch of unit cell. b: Array on FR4 disc. The dotted circle marks the illuminated area.

We simulated S11 amplitude spectra for various angles ϕ between the electric field polarization and the x-axis in Fig 1a. Results are shown in Fig 2 for ϕ in the range between $0°$ and $90°$.

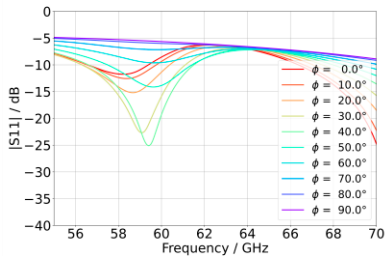

Fig. 2. Simulation of metamaterial S11 spectra.

Due to the symmetry of the unit cell, the curves in the range from $90°$ to $180°$ overlap with those from $0°$ to $90°$. The curve for $\phi = 40°$ shows a distinct minimum close to $60\ \mathrm{GHz}$ which comes from the Fano-type resonance. Thus, the coupling to this mode is maximum for $\phi = 40°$. Most importantly, the data shows that varying ϕ significantly changes the reflectance in the

frequency range close to the Fano resonance, which in turn allows to determine the rotation angle by measuring the reflectance.

VNA measurement results

The metamaterial is produced as a single layer on a 10 cm diameter disc in a circular arrangement (see Fig. 1b). All unit cells are aligned parallel to each other. The disk is mounted on an aluminum axis together with a degree disk for reading the angle of rotation. Reflectance measurements were performed using an Anritsu MS4647B vector network analyzer and a horn antenna. The measurement distance to the metamaterial was 1 cm. The area of the metamaterial array irradiated with this setup is outlined as a green circle in Fig. 1b. In a post-processing step, we performed time domain gating. Fig. 3 shows the measurement results.

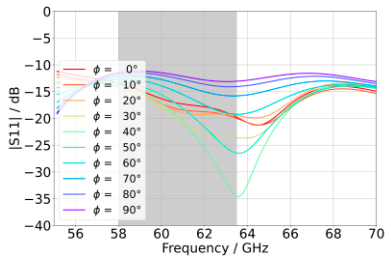

Fig. 3. VNA measurement of metamaterial S11 spectra. Grey area: Bandwidth of FMCW chip.

There is an overall horizontal shift of the curves compared to the simulation results (Fig 2). This indicates that the dielectric constant of the laminate is smaller than the value we extrapolated. In the range from $40°$ to $90°$ the change of the curves with increasing ϕ agrees well with the simulated ones. Furthermore, the coupling to the Fano-type resonance is maximum at $40°$. For ϕ between $0°$ and $30°$ the data in Fig 3 shows a shift of the minimum towards higher frequencies whereas the simulated curves show a shift towards lower frequencies. We explain this by the fact that in the FEM simulations plane wave incidence was assumed. Due to the small measurement distance, this is not strictly fulfilled in the experiment, which leads to a different coupling behavior for small values of ϕ. Nevertheless, the measured curves show the proposed sensor behavior for frequencies in the FMCW chip bandwidth (grey in Fig 3).

FMCW chip measurement results

We installed the FMCW chip at 3 cm distance to the metamaterial, considering the FMCW chirp bandwidth of 5.5 GHz. We calculated the amplitude spectra using the on-chip FFT routine and identified the peak that corresponds to the reflection from the metamaterial. Fig 4 shows the measured amplitude as a function of ϕ.

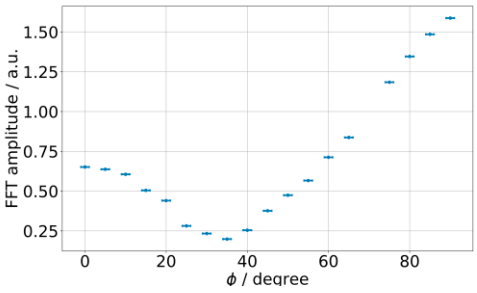

Fig. 4. Millimeter-wave transceiver: FFT amplitude as function of the rotation angle ϕ.

The horizontal error bars show the estimated reading error of the setup. The data clearly shows the angle-dependent change in the reflectance of the metamaterial. However, the curve in Fig 4 is not a bijective function over the whole range of ϕ. This is explained by the resonant behavior observed in simulations as well as measurements (Fig 2 and Fig 3) which show that the coupling to the Fano-type resonance is maximum at $\phi = 40°$. Our implementation can measure the rotation angle fully telemetric in the range from $40°$ to $90°$. However, the implementation of a sine encoder would be straightforward by varying the orientation of the unit cells in the metamaterial array such that the reflectance changes sinusoidally as a function of the sample's rotation angle or movement as sketched in Fig 5.

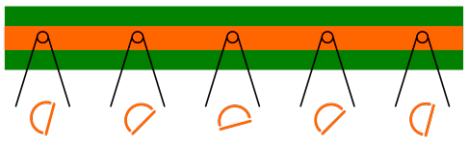

Fig. 5. Possible implementation of sine encoder

We are confident that our proposed sensor concept potentially paves the way toward a new angle and position sensor technology based on millimeter-wave metamaterials.

References

[1] S.R. Ruocco, Robot sensors and transducers, *Open University Press Robotics Series,* ISBN: 978-94-011-6870-0

[2] D. Nyce, Linear position sensors: theory and application. *John Wiley & Sons.,* ISBN: 978-0-471-23326-8

[3] V. Fedotov, M.Rose, S. Prosvirnin, et al., Sharp Trapped-Mode Resonances in Planar Metamaterials with a Broken Structural Symmetry, *Physical Review Letters, 99, 14 2007,* doi: 10.1103/PhysRevLett.99.147401

DOI 10.5162/SMSI2023/P66

Ultrasonic Sensor System for Water Localization in Fuel Cells: Investigation of Operational Conditions

Jakob Sablowski[1], *Christian Kupsch*[1]
[1] *Measurement, Sensor and Embedded System Laboratory (MSE Lab), Institute of Electrical Engineering, Technische Universität Bergakademie Freiberg, Winklerstrasse 5, 09599 Freiberg, Germany*
jakob.sablowski@et.tu-freiberg.de

Summary:
Water management is important for an efficient operation of proton exchange membrane fuel cells (PEMFCs). In particular, accumulation of liquid water in the flow channels must be prevented to ensure uniform distribution of the reactants and consequently high performance of the cell. It has been shown in ex-situ experiments, that liquid water drops on the flow field can be localized using ultrasonic guided waves. In this contribution, we show that temperature is the major influence on the measurement. We also demonstrate that the influence of temperature can be reduced by tracking the signal baseline with the temperature.

Keywords: ultrasound, guided waves, fuel cells, water management, temperature compensation

Introduction

Proton exchange membrane fuel cells (PEMFCs) are a key technology for hydrogen-based power generation. During operation, hydrogen is supplied on the anode side of the cell where it is catalytically split into protons and electrons. Protons permeate through the proton exchange membrane to the cathode side, where they react with oxygen and electrons from the outer electrical circuit to produce water. Due to operating temperature below 100 °C, the water can be liquid. Water management is necessary to prevent flooding of the oxygen flow channels on the bipolar plate as well as drying of the proton exchange membrane. Various techniques have been applied in this context to measure and visualize liquid water in PEMFCs [1]. These techniques typically require a large experimental effort and are limited in terms of integration in operating PEMFC stacks. Sensor systems based on ultrasonic guided waves could be beneficial in this regard. In this study, we investigate the influence of changing environmental and operational conditions on such a sensor system.

Sensor system for water detection based on ultrasonic guided waves

To detect and localize liquid water in a PEMFC, piezoelectric wafer active sensors (PWAS) can be used to excite ultrasonic guided waves within the bipolar plate of the PEMFC. The wave propagation through the bipolar plate and thus, the signals received at the PWAS are sensitive to the presence of liquid water on the bipolar plate. By comparing the received signals with a baseline signal, sessile water drops can be detected on the bipolar plate. Fig. 1 shows a scheme of the measurement principle.

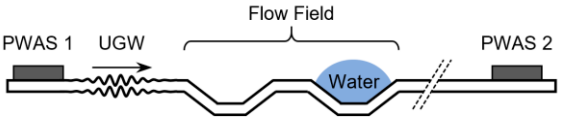

Fig. 1. Scheme of the measurement principle. Ultrasonic guided waves (UGW) are transmitted across the bipolar plate from PWAS 1 to PWAS 2. In the middle is the flow field with a water drop in one of the flow channels.

This measurement principle has been demonstrated in ex-situ experiments on a single bipolar plate in a temperature-controlled lab environment [2]. For an integration of the sensor system in an operating PEMFC, the changing environmental and operational conditions must be considered. Temperature changes affect the guided wave propagation and therefore the measurement signals. Additionally, the surface of the bipolar plate is in direct contact with the gas diffusion layer (GDL) when assembled in a PEMFC, which could potentially influence the measurements.

To investigate these influences, two piezoelectric wafer active sensors (PWAS, disc c255 o5 t0,5 wAg, *PI Ceramic*, Lederhose, Germany) are attached to a bipolar plate (Material No.: 1.4404, gold coating of 1 µm, sheet thickness: 100 µm, outer dimensions: 10 cm by 8 cm). In the center of the bipolar plate is a serpentine

flow field with eight flow channels (flow field design by *Hydrogen and Fuel Cell Center (ZBT GmbH)*, Duisburg, Germany). For the measurements, the bipolar plate is placed in a temperature-controlled test chamber. One of the PWAS is excited with a square wave signal (2 periods, center frequency: 4 MHz, peak-to-peak Voltage: 10 V). This leads to propagation of ultrasonic guided waves across the bipolar plate, which are received at the other PWAS. The *us4R-lite* platform (*us4us*, Warsaw, Poland) is used for data acquisition and to excite the PWAS.

Investigation of operational conditions

To quantify the change of the guided wave responses, the following signal processing is performed: averaging, selection of a region of interest, forward-backward filtering (4th-order Butterworth bandpass filter with cutoff frequencies of 3 MHz and 7 MHz). The baseline signal (measured at 25 °C without any water on the bipolar plate) is then subtracted from the measured signal. The resulting difference signal is divided into 500 windows before calculating the normalized signal energy E_d for each window. It has been shown that the resulting signal feature vector is suitable to localize single water drops on the bipolar plate using data-driven modelling [2]. Here, the same signal feature is used to quantify the influence of different conditions on the measurement. Measurements were performed under the same conditions, changing only one parameter: a) no change (same conditions as for the baseline signal), b) one water drop placed on the flow field, c) temperature change of 1 K, d) temperature change of 3 K, e) GDL placed on the flow field. Fig. 2 shows the resulting distributions of E_d.

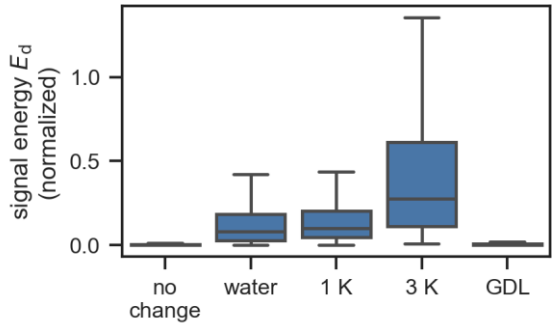

Fig. 2. Distribution of the normalized signal energy E_d for different measurement conditions (no change, added water drop, temperature changes of 1 K and 3 K, GDL placed on flow field). High values indicate a large influence on the guided wave response. Boxes indicate quartiles, whiskers indicate 1.5 interquartile range value.

Even small temperature changes of 1 K and 3 K influence the measurement to a similar or higher extend than the presence of a water drop on the flow field. The GDL on the other hand does not lead to any significant changes of the guided wave response as shown in fig. 2. It can be concluded that temperature changes have to be compensated to ensure accurate liquid water detection in an operating PEMFC. One method for compensation is the optimal baseline subtraction [3]. In fig. 3, the effect of temperature compensation is shown. It can be seen that, after temperature compensation, the effect of a water drop on the normalized signal energy E_d is similar for both temperatures.

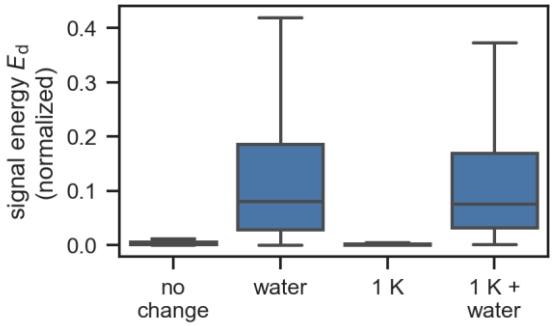

Fig. 3. Distribution of the normalized signal energy E_d with adjusted baseline to compensate for the temperature change of 1 K. Boxes indicate quartiles, whiskers indicate 1.5 interquartile range value.

Conclusion and Outlook

Sensor principles based on ultrasonic guided waves show a high potential for liquid water detection on complex plate-like structures and could provide valuable information on the water management in PEMFCs. The main challenge for the integration into an operating PEMFC stack is the high sensitivity of the sensor system towards temperature changes. It was found that a temperature change of 1 K affects the guided wave responses to a similar extent as the measuring effect used for water detection. Further research is needed to optimize temperature compensation strategies with consideration of the data-driven modelling that enables water localization on complex plate-like structures such as the bipolar plate.

References

[1] A. Bazylak, Liquid water visualization in PEM fuel cells: A review, *International journal of hydrogen energy* 34, 3845-3857 (2009); doi: 10.1016/j.ijhydene.2009.02.084.

[2] J. Sablowski, Z. Zhao, C. Kupsch, Ultrasonic Guided Waves for Liquid Water Localization in Fuel Cells: An Ex Situ Proof of Principle, *Sensors* 22, 8296 (2022); doi: 10.3390/s22218296.

[3] G. Konstantinidis, P. D. Wilcox, B. W. Drinkwater, An Investigation Into the Temperature Stability of a Guided Wave Structural Health Monitoring System Using Permanently Attached Sensors, *IEEE Sensors Journal* 7, 905-912 (2007); doi: 10.1109/JSEN.2007.894908.

DOI 10.5162/SMSI2023/P67

An Airborne Measurement System to Detect, Locate and Quantify Methane Emissions

Lars Kistner[1], Robert Schmoll[1], Andreas Kroll[1]
[1] University of Kassel, Department of Measurement and Control,
Mönchebergstraße 7, 34109 Kassel, Germany,
Lars.Kistner@mrt.uni-kassel.de

Summary:
An Airborne measurement system with onboard computer for data processing and recording with no need for constant radio communication for inspection and maintenance is presented that detects, locates and quantifies methane leaks.

Keywords: Leak Detection & Repair, Methane Mapping, Sensor Data Fusion, Remote Sensing, UAS

Introduction

The reduction of methane (CH4) emissions is important for environmental protection [1] and for operational safety in the energy sector, as gas mixtures with methane are potentially explosive. Methane is a major component of natural gas and biogas.

While earth observation satellites attempt to locate emissions on a facility scale [2], unmanned aerial systems (UAS) can find leaks at component level and provide maintenance staff with a more comprehensive view on leaks than regular ground-based inspections [3]. Based on experiences with a ground-based, portable system for detecting and quantifying [4] and a mobile robot system for localizing methane leaks [5], an UAS capable of remotely detect, locate and quantify methane leaks was developed.

Measurement System

The aerial inspection system consists of a measurement module, an onboard computer, a support box and a quadcopter drone, see Figure 1. The measuring module features a tunable diode laser absorption spectroscopy (TDLAS) sensor, two visual cameras and a laser rangefinder jointly mounted on a gimbal. The support box is used to safely accommodate additional PC components and the power distribution.

The onboard computer processes and stores both camera streams and all sensor signals from the measuring module and the drone. All data is simultaneously available on a ground station in real time. Due to the data processing and recording capabilities of the UAS, constant radio communication is not required during a mission. The drone allows to take measurements from different perspectives. In combination with a scanning gimbal full inspection of complex structures is possible. The position information is determined by the drone's real time kinematic (RTK) system. Knowledge of the drone's position, gimbal orientation and the measured range allow the system to locate each measurement point in a 3D coordinate system referenced in the global positioning system (GPS). The system utilizes the Robot Operating System (ROS), an established software framework for robot applications organized in microservices. All available sensor and actuator inputs are recorded, by default. All measurements are visualized live in a 3D viewport, see Figure 2, and can be exported as a point cloud file with extended information (wind speed, point of measurement, methane concentration, …) for post-processing tasks. The UAS does not have a sensor to measure the wind speed. Therefore, the wind speed is estimated from the drone's orientation as proposed in [6]. This circumvents the complicated mounting of

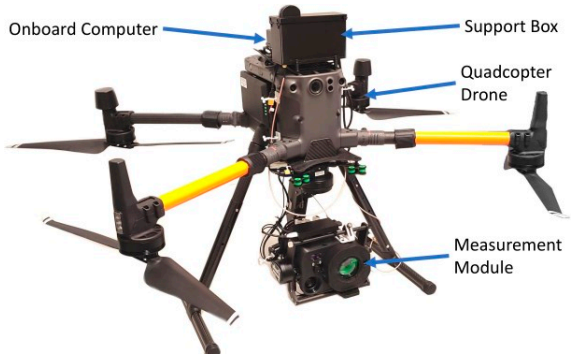

Fig. 1. UAS with cameras, laser rangefinder and TDLAS sensor to detect, locate and quantify methane leaks

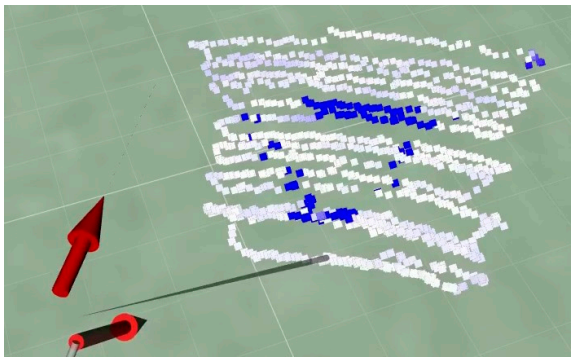

Fig. 2. Visualization of measurements from 0 ppm·m (white) to more than 300 ppm·m (blue) shown in the 3D viewport of the ground station. Arrows show drone's and gimbal's pose.

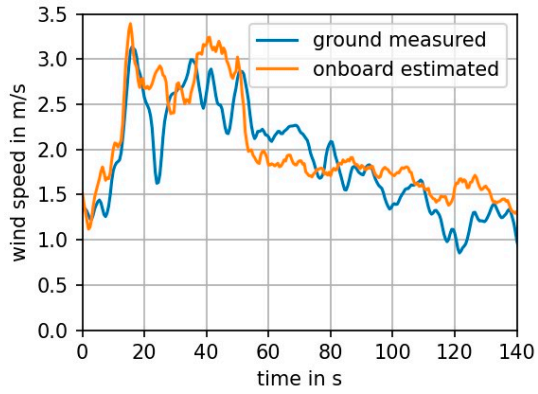

Fig. 3. Onboard estimated and ground measured windspeed for test data of 140 s.

an anemometer, such that it is not affected by the drone's own turbulences. Using methane concentration and wind speed allows estimating the amount of methane emitted [4].

Experimental evaluation

The UAS was evaluated in several field tests with methane-filled sample containers and mass flow controlled methane release under different weather conditions. The most important weather conditions are the level of cloud cover, as direct sunlight affects the TDLAS sensor and the wind speed, as this affects the methane dispersion and drone positioning. The results show that the drone can reliably hold its position and carry out measurements at windspeeds of at least 4 m/s. A sample container with a diameter of 0.2 m can be detected at a distance of 20 m. At a scan distance of approx. 10 m an area of 9.6 m²/min can be inspected. Figure 2 shows the result obtained for such scan speeds in the 3D viewport on the ground station. Regulated methane emissions of 43 g/h (approx. 60 l/h) can be located at ranges of over 10 m and wind speeds of at least 3 m/s. The wind speeds were measured with a 3D anemometer positioned close to the artificial leak and not at the drone's altitude. The wind speed measured on the ground is comparable with the wind speed estimated onboard the drone, see Figure 3. Under these conditions the estimated wind speed is sufficient to quantify methane leaks.

Summary and Outlook

Under normal wind conditions, the presented UAS is able to detect, from a technical point of view, small (approx. 60 l/h) methane leaks. It can inspect components and parts that are difficult to reach for ground-based inspections.

Acknowledgment

The authors would like to thank the German Environmental Foundation (DBU) for funding (Az.: 35407/01).

sponsored by
DBU
Deutsche Bundesstiftung Umwelt
www.dbu.de

References

[1] D. Bastviken et al., "Critical method needs in measuring greenhouse gas fluxes," Environmental Research Letters, vol. 17, no. 10, Sep. 2022.

[2] D. H. Cusworth et al., "Multisatellite Imaging of a Gas Well Blowout Enables Quantification of Total Methane Emissions," Geophysical Research Letters, vol. 48, no. 2, Jan. 2021.

[3] J. T. Shaw, A. Shah, H. Yong, and G. Allen, "Methods for quantifying methane emissions using unmanned aerial vehicles: a review," Phil. Trans. R. Soc. A, vol. 379, no. 2210, Sep. 2021.

[4] S. Dierks and A. Kroll, "Remote quantification of methane leaks in the laboratory and in biogas plants," International Journal of Remote Sensing, vol. 42 (20), pp. 7978-8003, Sep. 2021.

[5] G. Bonow and A. Kroll, "Gas leak localization in industrial environments using a TDLAS-based remote gas sensor and autonomous mobile robot with the Tri-Max method," in IEEE International Conference on Robotics and Automation (ICRA), Karlsruhe, Germany, May 2013.

[6] P. Neumann, S. Asadi, A. Lilienthal, M. Bartholmai, and J. Schiller, "Autonomous Gas-Sensitive Microdrone: Wind Vector Estimation and Gas Distribution Mapping," IEEE Robotics & Automation Magazine, vol. 19, no. 1, Mar. 2012.

DOI 10.5162/SMSI2023/P68

Characterization of Electrical Properties of Direct Ink Written Silver Ink

Heime Jonkers, Jelle Idzenga, Dimitrios Kosmas, Gijs Krijnen
Robotics and Mechatronics Group, University of Twente, Enschede, the Netherlands
Corresponding author: h.r.jonkers@utwente.nl

Summary:
Direct-Ink Written Silver-ink traces on top of thermoplastic polyurethane substrates produced by Fused-Filament-Fabrication were characterized in terms of electrical - and piezo resistivity. Low resistivity in the order of 52.8 µΩ cm was achieved with piezoresistive strain response being limited to strains below 1 % as a result of crack formation. Silver-ink traces are therefore deemed most suitable for interconnects.
Keywords: 3D Printed Sensors, Fused Deposition Modelling, Direct-ink writing, Silver ink, Strain gauge

Introduction

Multi material (MM) fused filament fabrication (FFF), with electrically conductive materials has shown potential in fabricating and integrating sensing mechanisms within a given structure [1]. FFF compatible thermoplastics doped with conductive particles are known to result in relatively high electrical resistivity and high anisotropy across traxels (track-elements) [2]. In direct-ink writing (DIW), a liquid ink with specific rheological properties [3] is extruded through a nozzle. Post printing, traces are cured by either heat or a UV treatment. Due to the layers not being fully solidified during the printing of subsequent layers, the inter-layer resistance will be comparable to the in-layer resistance and low anisotropy can be achieved [4].

In this work, silver ink (CI-1036 [5]) was characterized for use as interconnect as well as a piezoresistive sensor. This was achieved through analysis of its resistivity and the dependance thereof upon strain.

Theory

The volumetric resistivity of a material measured from a prismatic structure is given by eq. (1). ρ is resistivity in Ω m, R resistance in Ω, A area in m^2, and l the sample length in m.

$$\rho = \frac{R \cdot A}{l} \tag{1}$$

To ensure the validity of this formulation contact resistances have to be accounted for during measurement. This will be achieved with the use of the transfer length method (TLM) [6].

Design & Fabrication

Figure 1 provides the design for characterization of the resistivity. The side pads are used for current injection, the three contract pads (red) at the top can be used for 4 point measurements. Three separate measurements were performed across varying lengths of; 8.5 mm, 12 mm and 20.5 mm. For the characterization of the piezoresistivity, only the two side pads were included in the samples to be used as contact.

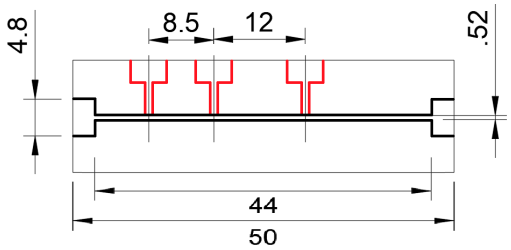

Fig. 1. Sample (black: strain, black&red: TLM)

Printing was performed on a Diabase H4 Pro MM 3D printer modified with an additional ViscoTec vipro-head 3 toolhead. This allows for both AM techniques to be performed intermittently, integrating silver-ink layers into the FFF structure. Post printing a thermal curing step was performed for 10 minutes at 120 °C in a convection oven (Memmert UF30) accelerating the evaporation of the ink solvent. All features were printed at a 100 % infill, with the substrate consisting of NinjaFlex TPU being printed at 220 °C and print speed of 25 mm s^{-1}. The silver-ink was deposited at a print speed of 4 mm s^{-1} at a layer height of 0.2 mm and a width of 0.514 mm.

Experimental Setup

Samples were clamped and mechanically loaded by a linear actuator (SMAC LCA25-050) operating under force control (figure 2). Piezore-

sistivity was evaluated by loading with a sine of 3 N amplitude at a frequency of 0.2 Hz. The resistance was measured through a micro-ohm meter (Keysight 34420A) at a sample frequency of 100 Hz.

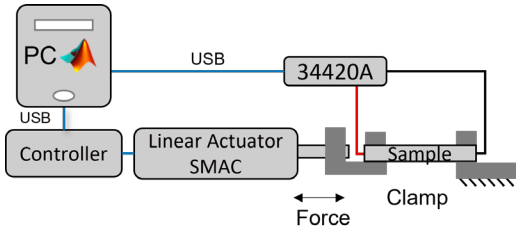

Fig. 2. Experimental measurement setup. (Blue: data transfer, red & black: 2-wire resistance measurement)

Results

Fabrication: Samples were manufactured by deposition of two layers of silver ink. Shrinkage was determined to be in the range of 70% after thermal curing, inline with the ink filler content of 66% [5].

Resistivity: Figure 3 shows the resistance as derived from the TLM method. Contact resistance was found to be in the order of 10.0 mΩ whilst providing a volume resistivity of 52.8 µΩ cm accounting for the volume shrinkage.

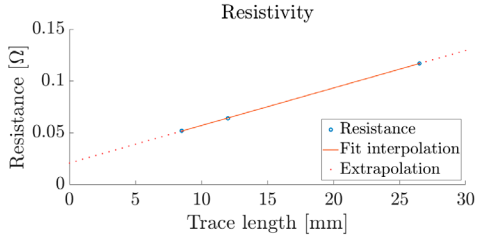

Fig. 3. Resistivity characterization

Piezoresistivity: Figure 5 and 4 show the response of the double ink layer sample to a sinusoidal force. Significant drift is observed in sensor resistance after repeated straining.

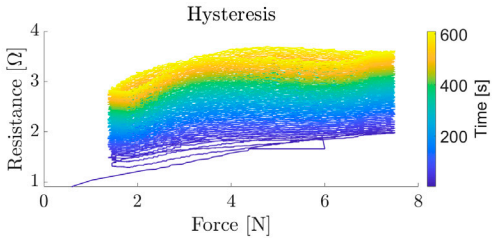

Fig. 4. Resistance vs force (2-layers)

A single cycle shows a reduction in sensitivity past ≈3.5 N, suggesting micro-crack formation in the silver ink. This crack formation was more

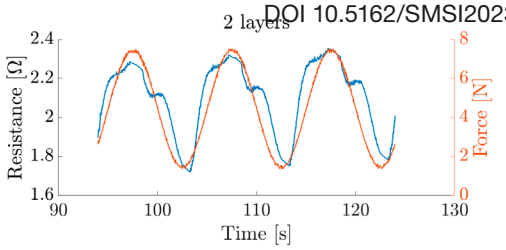

Fig. 5. Sinusoidal loading of (2-layer)

stongly observed for samples with a single layer of silver ink, as shown by figure 6.

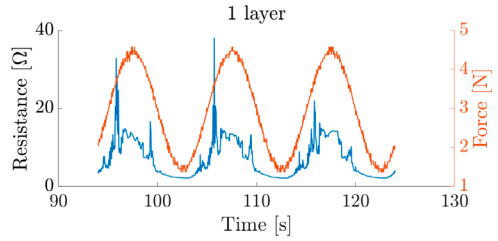

Fig. 6. Sinusoidal loading of (1-layer)

Discussion and Conclusions

In this work the application of printable silver-ink on top of a printed TPU substrate as a piezoelectric sensor was investigated. The silver-ink was shown to exhibit excellent electrical conductivity and a moderate resistance to strain, resulting from crack formation in the ink. Approximately linear strain sensing was found to be limited to 1%, resulting in a Gauge factor of 233. Modifying the design to only employ compressive strain of the silver ink might potentially extend this range.

References

[1] M. Schouten, G. Wolterink, A. Dijkshoorn, D. Kosmas, S. Stramigioli, and G. Krijnen, "A Review of Extrusion-Based 3D Printing for the Fabrication of Electro- A nd Biomechanical Sensors," *IEEE Sensors Journal*, vol. 21, no. 11, pp. 12 900–12 912, jun 2021.

[2] A. Dijkshoorn, P. Werkman, M. Welleweerd, G. Wolterink, B. Eijking, J. Delamare, R. Sanders, and G. J. Krijnen, "Embedded sensing: Integrating sensors in 3-D printed structures," *Journal of Sensors and Sensor Systems*, vol. 7, no. 1, pp. 169–181, mar 2018.

[3] L. Del-Mazo-Barbara and M. P. Ginebra, "Rheological characterisation of ceramic inks for 3D direct ink writing: A review," *Journal of the European Ceramic Society*, vol. 41, no. 16, pp. 18–33, dec 2021.

[4] J. K. Wilt, D. Gilmer, S. Kim, B. G. Compton, and T. Saito, "Direct ink writing techniques for in situ gelation and solidification," *MRS Communications*, vol. 11, no. 2, pp. 106–121, feb 2021.

[5] E. C. M. LLC, *Technical Data Sheet CI-1036, Highly Condcutive, Highly Flexible Silver Ink*, Engineered Conductive Materials LLC.

[6] D. K. Schroder, *Contact Resistance and Schottky Barriers*. John Wiley & Sons, Ltd, 2005, ch. 3, pp. 127–184. [Online]. Available: https://onlinelibrary.wiley.com/doi/abs/10.1002/0471749095.ch3

DOI 10.5162/SMSI2023/P69

Goodbye to the Non-SI unit dalton (Da) in the Digital-SI?

Joaquín Valdés[1]
[1] *Universidad Nacional de San Martín, 25 de Mayo y Francia, 1650 San Martín, Prov. Buenos Aires, Argentina*
jvaldes@unsam.edu.ar

Summary:
The need to develop an unambiguous digital version of the International System of units (SI) leads to a reconsideration of the status of the Non-SI units accepted for use with the SI. Here is considered the case of the Non-SI unit dalton that coexists with the kilogram in the field of atomic masses.

Keywords: metrology, kilogram, dalton (Da), digital SI, atom interferometry.

Atomic masses in Si and Non-SI units

The redefinition of the SI, the International System of units, ended with decades coexisting two systems of electrical units by fixing the values of the Planck constant h and the elementary charge e in the definitions of the kilogram and the ampere respectively. But we continue to live with two units of mass. For historical and technical reasons, the dalton is still used in atomic mass measurements instead of the kilogram. The dalton (Da) and the unified atomic mass unit (m_u) are alternative names for the same unit, equal to 1/12 of the mass of a free carbon 12 atom, at rest and in its ground state. The consequences of revising the SI for measurements in chemistry were analyzed in advance by IUPAC, the International Union of Pure and Applied Chemistry. A IUPAC technical report published in 2017 [1] stated that, since the masses of the nuclides are reported in the unified atomic mass unit, in the case of fixing the values of the Planck constant h and the Avogadro number N_A, as really occurred, the Atomic Mass Evaluations published at regular intervals by IUPAC would remain unaffected.

The kilogram is reaching the Dalton (Da)

The redefinition of the SI opened up improvements and new possibilities across the whole mass scale, especially in the range of atomic masses. Being the kilogram defined in terms of the Planck constant, the realization of mass can be achieved at any desired scale without the need to trace the measurements to a 1 kg mass. Employing atom interferometry, the measurement of the recoil velocity of an atom of mass m that absorbs a photon of momentum $\hbar k$, yields the ratio h/m ($\hbar = h/2\pi$ and $k = 2\pi/\lambda$, where λ is a laser wavelength). Because the value of the Planck constant h has been fixed in the new SI, the ratio h/m_u ensures the realization of the kilogram at the atomic scale. Furthermore, as the Avogadro constant has been also fixed, and the carbon molar mass $M(^{12}C)$ is no longer equal to 12g per mol, it is now determined from m_u. Before the redefinition of the SI the accuracy of atomic masses expressed in kg was in the order of 10^{-8}, well above the minor uncertainties reached in terms of the dalton. The last value recommended by CODATA at that time for the equivalence between kg and dalton was 1 Da = 1.660 539 040 × 10^{-27} kg, with a relative standard uncertainty of 1.2×10^{-8}. From the value of the ratio h/m_u, the uncertainty in the ratio dalton to kilogram just after fixing h was reduced in more than one order of magnitude.

Tab. 1: Evolution of the relative standard uncertainties of $h/m(^{133}Cs)$ and $h/m(^{88}Rb)$

Source	$h/m(^{133}Cs)$	$h/m(^{88}Rb)$	h/m_u
CODATA 2002	1.5×10^{-8}		6.7×10^{-9}
CODATA 2006	1.5×10^{-8}	1.3×10^{-8}	1.4×10^{-9}
CODATA 2010	1.5×10^{-8}	1.2×10^{-9}	7.0×10^{-10}
CODATA 2014	1.5×10^{-8}	1.2×10^{-9}	4.5×10^{-10}
Berkeley 2018	4.0×10^{-10}		
Paris 2020		**1.4×10^{-10}**	

The new SI is effective from 20 May 2019. Short after that date, some considerations on the future of the SI were already published [2], including last data showing how h/m(X) meas-

urements using atom interferometry were evolving from 2002, as recorded by CODATA. X may be ^{87}Rb atoms, as determined at the Laboratoire Kastler Brossel LKB in Paris, or ^{133}Cs atoms, as determined in the University of California in Berkeley. The 2022 CODATA adjustment of the fundamental constants is the next regularly scheduled adjustment, with a closing date of 31 December. Table 1 shows the evolution of *h/m* values, including now the last value obtained at LKB in Paris in December 2020 [3]. This value for $m(^{87}\mathrm{Rb})$ is the most accurate atomic mass measurement, reducing the uncertainty in the equivalence between kg and dalton to the 10^{-10} level.

Towards a digital system of units

Building confidence in the accuracy and global comparability of measurements requires the creation of a machine-actionable, unambiguous full digital representation of the SI. There are ontologies and unified codes including all units of measurement used in science, engineering, and business (e.g. QUDT, UCUM). Here we adress an existing Guide for the use of the metadata-format used in metrology for communication between machines using only SI-base units [4]. The document was developed within the framework of the EU-funded project SmartCom, ended in September 2021, with the support of international partners from science and industry. Several major National Metrology Institutes participated (PTB, NPL, etc.). Only non-SI units accepted for use with the SI stated in the SI Brochure [5] may be included, but only during a transition period. Metrological data are categorized into 5 quality classes of machine readability: platinum, gold “2030”, silver “2024”, bronze “2020” and “improvable”. Platinum corresponds to the strongest readability. The SI unit kilogram is classified platinum and the Non-SI unit dalton is classified silver, recommending the use of the kg. A significant highlight is the creation within the International Committee for Weights and Measures (CIPM) of a Task Group on the Digital-SI. The aim is to consider, develop and establish a world-wide uniform, unambiguous and secure data exchange format for use in IoT networks based on the SI described in the current SI Brochure.

Discussion

The coexistence of SI units with Non-SI units introduces ambiguities. The joint use for some of them has been admitted in the SI Brochure without any time limit. The new paradigm of the digital transformation now requires making decisions that were not on the agenda of different communities using Non-SI units. In the 2017 critical review the IUPAC report [1] showed no interest in expressing atomic masses in the SI unit kilogram. The removal of the Non-SI unit dalton opening the way to the use of the kilogram on the atomic mass scale would not have such a high negative impact as before the redefinition of the SI, since the experimental uncertainties achieved in the most precise cases are very close. In table 1 we observe how close is the relative standard uncertainty of the m_u value from that of the values of the atomic masses used in atom interferometry experiments, particularly from the mass of ^{88}Rb. Holger Müller’s group in Berkeley is also working on improvements, intending to produce new $h/m(^{133}\mathrm{Cs})$ results with uncertainties below 10^{-10} in the near future. The most precisely atomic and ion relative masses are known at the 10^{-11} level [6].

The transition period stated in the Guide D-SI [4] for quality class silver, also called 2024, should be reviewed in order to obtain wider consensus from other communities that use Non-SI units accepted for use with the SI. For example, the replacement by the unit 1 of the Non-SI units neper, bel and decibel, as identified in Table A.4 of the Guide D-SI, would not be as easy to adopt as the replacement of the dalton by the kg. That topic exceeds this short paper and deserves to be addressed in a more extensive one. Finally, the eventual decision to delete some Non-SI units in the SI Brochure will also require some time until a new version is published

References

[1] R. Marquardt et al. A critical review of the proposed definitions of fundamental chemical quantities and their impact on chemical communities (IUPAC Technicl Report). Pure Appl. Chem. 89(7), 951–981 (2017); doi: 10.1515/pac-2016-0808

[2] J. Valdés, Reviewing the Revised SI, AIEP 211, 121-186 (2019); https://doi.org/10.1016/bs.aiep.2019.05.001

[3] L. Morel et al. Determination of the fine-structure constant with an accuracy of 81 parts per trillion, Nature 588, 61-65 (2020); https://doi.org/10.1038/s41586-020-2964-7

[4] D. Hutzschenreuter et al. SmartCom Digital System of Units (D-SI), Guide for the use of the metadata-format used in metrology for the easy-to-use, safe, harmonized and unambiguous digital transfer of metrological data, Version D-SI 1.3 (2019); doi: 10.5281/zenodo.3522631

[5] BIPM – Brochure (2019). *The International System of Units (SI),* 9th edition (2019); https://bipm.org/en/publications/sibrochure

[6] Meng Wang et al. The Ame2020 atomic mass evaluation (II), Chinese Physics C, 45 – 3 (2021) 030003 1-512; doi: 10.1088/1674-1137/abddaf

DOI 10.5162/SMSI2023/P70

Virtual Test Scenarios for Human-Centered Design with Virtual Measurement Systems

Iris Gräßler[1], Daniel Roesmann[1], Marc Unverzagt[1], Jens Pottebaum[1]
[1] Heinz Nixdorf Institute, Paderborn University, Fürstenallee 11, 33102 Paderborn, Germany
marc.unverzagt@hni.upb.de

Summary:
The involvement of human workers is an essential part of the design of production systems. In this context, test scenarios in Virtual Reality are increasingly used to verify the fulfillment of requirements. This paper proposes a procedure for generating virtual test scenarios. The objective is to support human-centered design by means of virtual measurement systems. The procedure involves three steps: selecting relevant human factors in requirements, modeling the virtual test scenario, and carrying out the verification study. The goal is to advance the significance of testing outputs.

Keywords: virtual reality, virtual measurement systems, virtual test scenario, human-centered design

Introduction

One focus in the context of production systems in recent years has been on human-centered design. With the early consideration of human needs, the production system can be suitably designed. For this purpose, human factors requirements have to be met and verified during the design process. Verification is essential in established design methodologies that can be adopted for production systems such as the V-model of VDI/VDE 2206 [1]. Based on findings of verification activities, design change processes can be initiated. Virtual reality enables the assurance of production planning and control at design time. Due to immersion, the human-technology interaction in particular can be tested within the Virtual Reality. Based on human factors requirements, suitable test scenarios with measurement systems have to be defined. A virtual test scenario includes the virtual shape of the system under consideration, the definition of the environment and the definition of the data collection technique and its evaluation. Established measurement methods are only suitable to a limited extent in Virtual Reality and are time-consuming due to manual measurement. The aim of this paper is to develop a procedure for generating virtual test scenarios for human-centered design with virtual measurement systems that do not require time-consuming manual measurement.

Human Factors in Virtual Reality

Within future production systems of the future, the employee continues to be a decisive factor. Important design features are workplace design, work organization and time planning. The design features can either facilitate or hinder human work. Human factors design is concerned with the integration of human ergonomics, characteristics and capabilities into design problems. The aim is to improve productivity, safety and at the same time consider well-being of employees. Crucial within human factors design is the continuous verification of the system elements with regard to human factors requirements. Results from Lanzotti et al. [2] show that virtual reality offers an interactive possibility to verify human factors requirements. Buchholz et al. [3] develop a first initial testbench for human-centered requirements with virtual tools. According to Aromaa and Väänänen [4], the key factors concern modelling of the system (fidelity, virtuality, manipulation possibilities, etc.), modelling of the environment as well as data collection and analysis techniques. Studies [5] show a variety of applications and forms of these three factors in the verification of human design in virtual reality.

Virtual test scenarios for human-centered design with virtual measurement system

The procedure developed for generating test scenarios for human-centered design with virtual measurement systems basically consists of three steps (see Fig. 1). In the first step, specific human factors requirements are selected. Based on the traceability in the system model, associated functions, logical elements and system elements as well as behavioural properties are identified. In the second step, the virtual test scenario is modelled. Based on the results of step 1, the modelling of the system is first determined. System elements are realized with defined behaviour in Virtual Reality.

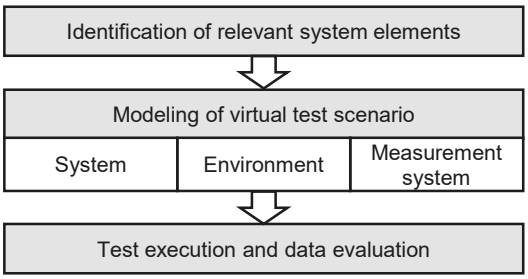

Fig. 1. Procedure for generating test scenarios

Furthermore, the environment is modelled. Depending on the requirements and the relevant human factors aspects (perceptual, mental, physical and psychosocial), the environment is modelled in a specific level of detail. For example, for perception-related aspect, the environment may have to be modelled in greater detail than for an ergonomic test. Finally, the virtual measurement system is selected. This is used for data collection. The selection is again based on human factors aspects. In the third step, the verification study is carried out. The test person is brought into the virtual environment with the help of VR goggles and carries out the defined test scenario with or without guidance.

Case example

Case example is the design of a manual assembly workstation in a flow assembly for linear actuators. For this purpose, requirements for the system were collected with stakeholders such as occupational safety. Tab. 1 shows an excerpt of the ergonomic requirements as a subset of human factors requirements for the workplace. Within a virtual test scenario, it is now to be verified whether the current design of the assembly workstation satisfies DIN ISO 14738.

Tab. 1: Excerpt of the ergonomic requirements of the DIN ISO 14738

#	Element	Requirement	Value
7.1	assembly table	Workspace depth	415 [mm]
7.7	assembly table	Viewpoint	30 [°]
…	…	…	…

Based on the system model of the assembly workstation, the assembly table with necessary accessories such as tools and containers are required. The workplace must have real physical properties. The tools are the only elements that can be manipulated in their position. As the requirement refers to ergonomic physical human factors aspects, the environment does not need to be explicitly modelled. The sensors on the HMD and controller as well as the use of "colliders" are selected as virtual measurement systems. Fig. 2 shows an excerpt from the implementation of the virtual test scenario in the VR-Software developed with Unity3D.

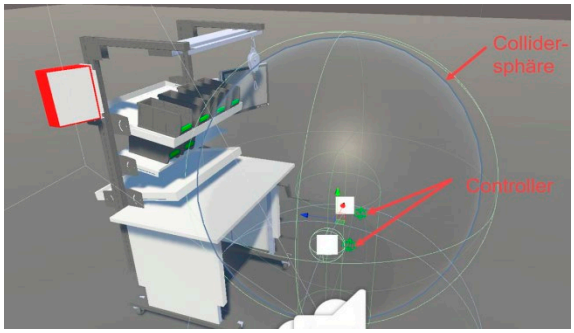

Fig. 2. Virtual test scenario with virtual measurement systems

The virtual measuring system measures the movements of the employees during the execution of a test task. These are, for example, the duration of a movement and directions of movements. Critical movements, such as permissible movement space, are output via a console and can be transferred to a design review report [6].

Summary

The paper at hand shows a systematic procedure for generating virtual test scenarios based on requirements. Besides the generation and modelling of the virtual environment, the appropriate selection of virtual measurement systems is a crucial step. This is facilitated by a systematic pre-selection and can be easily implemented. The procedure was demonstrated using the example of the design of an assembly workstation. In future studies, the process will be further automated to generate simple derivations of virtual test scenarios without manual effort.

References

[1] I. Gräßler, A new V-Model for interdisciplinary product engineering, *Engineering for a changing world 2017, (*2017).

[2] A. Lanzotti et al., Interactive tools for safety 4.0: virtual ergonomics and serious games in real working contexts, *Ergonomics*, Jg. 63, Nr. 3, S. 324-333, (2020).

[3] Buchholz, C.; Vorsatz, T.; Kind, S.; Stark, R.: "SHPbench – A Smart Hybrid Prototyping Based Environment for Early Testing, Verification and (user based) Validation of Advanced Driver Assistant Systems of Cars". In: *Procedia CIRP*, Jg. 60S. 139-144 (2017).

[4] S. Aromaa, K. Väänänen, Suitability of virtual prototypes to support human factors/ergonomics evaluation during the design, *Applied Ergonomics*, Jg. 56, S. 11-18, (2016).

[5] J. Wolfartsberger, Analyzing the potential of Virtual Reality for engineering design review, *Automation in Construction*, Jg. 104, 2019, S. 27-37.

[6] I. Gräßler, D. Roesmann, S. Hillebrand, J. Pottebaum, Information Model for Hybrid Prototyping in Design Reviews of Assembly Stations, *Procedia CIRP*, Jg. 112, 2022, S. 489-494.

DOI 10.5162/SMSI2023/P71

Pd Nanoparticles Decorated TiO_2 Nano-spheres for Hydrogen Gas Sensing at Room Temperature under Visible Light Conditions

Thilini Thathsara, Christopher J. Harrison, Rosalie K. Hocking, Mahnaz Shafiei
School of Science, Computing and Engineering Technologies, Swinburne University of Technology, Hawthorn, VIC 3122, Australia
mshafiei@swin.edu.au

Summary:
Visible light active hydrogen sensor can operate at ambient temperatures with enhanced performance making them a promising candidate for real-world applications. In this study, such sensor has been fabricated that employ heterojunctions containing Pd nanoparticles (NPs) decorated on TiO_2 nanospheres (Pd-decorated TiO_2 NS) using facile chemical methods. The sensor shows a response of 100.88% towards hydrogen with fast response and recovery (77 s and 470 s, respectively) at 30 ℃ under 565 nm visible light conditions and a voltage bias of 0.5 V.

Keywords: Nanoparticles, Nanospheres, Hydrogen sensing, Visible light, Room temperature.

Introduction

Hydrogen gas sensing has become important in recent times due to the increasing usage of hydrogen as an alternative energy source and feedstock. Hydrogen is highly flammable and explosive [1] and can pose a significant risk to human and environment safety in the event of leaks. Sensors that can detect hydrogen at low levels accurately and in real-time can prevent such incidents and ensure safe usage of hydrogen. Furthermore, development of hydrogen sensors contributes to advance the hydrogen economy and the adoption of hydrogen as a sustainable energy source [2].

Titanium dioxide (TiO_2) is widely used as a sensing material for hydrogen due to its high chemical stability and sensitivity to hydrogen gas. Additionally, TiO_2 is a low cost, abundant, and environmentally friendly material, making it an attractive choice for hydrogen sensing applications.

Sensors making use of visible light and operating at room temperature are generally more cost-effective compared to other types of hydrogen sensors, which can be expensive to produce and maintain. Therefore, in this endeavour, we aim to develop a hydrogen gas sensor with enhanced performance that can work at room temperature utilizing visible light.

Novelty

TiO_2 is an environmentally friendly sensing material, and the use of visible light instead of heat or other sources of energy makes these sensors more environmentally friendly compared to other types of hydrogen sensors that require low power [3]. In this work, we have successfully fabricated novel visible light active hydrogen sensing material that shows enhanced performance at 30 ℃ under voltage bias of 0.5 V.

Results and Conclusion

Figure 1 shows SEM image of the Pd-decorated TiO_2 NS. Monodispersed, agglomeration free, rigid TiO_2 nanospheres can be seen in the SEM image. The XRD analysis confirmed successful synthesis of Pd NPs decorated on the TiO_2 NS.

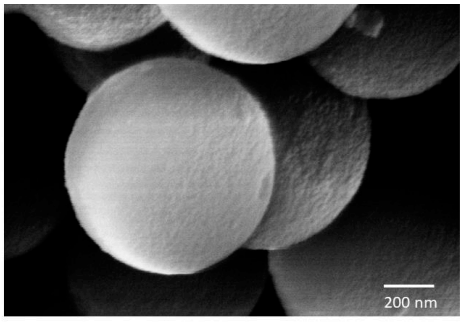

Fig. 1. SEM image of synthesized Pd-decorated TiO_2 NS.

To analyze hydrogen sensing properties, the operating temperature was optimized under dark and 565 nm visible light conditions. The sensor works at an optimum temperature of 50 ℃ under the dark condition with a response of

101.26% (using eq. (1)). However, the response (135 s) and recovery (1345 s) (Fig. 2) are significantly longer as compared to the condition under 565 nm visible light. When introducing 565 nm visible light to the sensor, a significant enhancement in response time (77 s) and recovery time (470 s) can be seen (Fig. 3). Furthermore, the working temperature was reduced from 50 ℃ to 30 ℃ under the light condition.

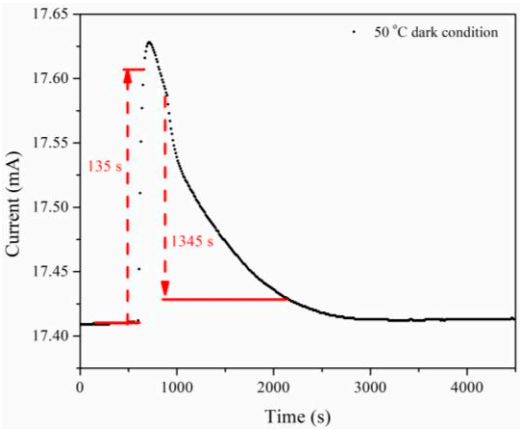

Fig. 2. Sensor response and recovery time towards 500 ppm hydrogen at 50 ℃ under dark conditions and 0.5 V.

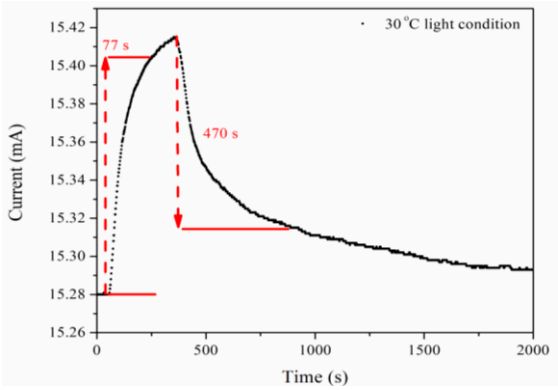

Fig. 3. Sensor response and recovery time towards 500 ppm hydrogen at 30 ℃ under 565 nm light conditions and 0.5 V.

Hydrogen sensing mechanism was studied to better understand the material behaviour at different conditions. Under the dark conditions, oxygen molecules presence in the air capture the electrons on the TiO_2 surface and form chemisorbed $O^-_{2(ads)}$. However, under 565 nm visible light the chemisorbed oxygen ion species react with photogenerated holes and electrons (due to the lowering the band gap energy) and generate photoinduced oxygen species that are loosely bound on the TiO_2 surface [4]. Therefore, loosely bound oxygen species easily reacts with hydrogen via $O^-_{2(h\nu)} + H_2 \rightarrow H_2O + e^-$ [5]. Under the dark conditions heat or another energy sources needs to be applied to desorb the chemically bound oxygen species on the TiO_2 surface. Therefore, under the dark condition 50 ℃ was required to activate the sensing layer. Furthermore, the Pd NPs act as a hydrogen collector as well as hydrogen dissociation agent to enhance the hydrogen sensing properties as follows; $Pd + \frac{x}{2}H_2 \rightarrow PdH_x$ and $2PdH_x + \frac{x}{2}O^-_{2(h\nu)} \rightarrow 2Pd + xH_2O + xe^-$.

According to the results, this study confirms development of novel nanomaterials for high performing gas sensors operating at a low temperature under visible light conditions that are promising for real-world applications.

Equations

$$R\% = \left(\frac{I_{air}}{I_{gas}}\right)\% \quad (1)$$

R: response magnitude.

I_{air}: Current of the sensor in the baseline condition.

I_{gas}: Current of the sensor in hydrogen environment.

Response time: The time taken to increase the baseline current to 90% of current change after exposure to hydrogen gas.

Recovery Time: The time taken to decrease the sensor current 90% back to the baseline current.

Acknowledgement

The authors acknowledge financial support from Australian Renewable Energy Agency (ARENA) and Future Energy Exports (FEnEx) CRC. S.K.T. Thathsara acknowledges the PhD scholarships under the Swinburne University Postgraduate Research Award (SUPRA).

References

[1] R. Ono, M. Nifuku, S. Fujiwara, S. Horiguchi, T. Oda, Minimum ignition energy of hydrogen–air mixture: Effects of humidity and spark duration, *Journal of Electrostatics,* 65, 87-93 (2007); doi: 10.1016.

[2] S. Chakraborty, S.K. Dash, R.M. Elavarasan, A. Kaur, D. Elangovan, S.T. Meraj, et al., Hydrogen energy as future of sustainable mobility, *Frontiers in Energy Research*, (2022); doi: 10.3389.

[3] T. Zhu, S.-P. Gao, The stability, electronic structure, and optical property of TiO_2 polymorphs, *The Journal of Physical Chemistry C*, 118, 11385-96 (2014); doi: 10.1021/jp412462m.

[4] S. Thathsara, C. Harrison, R. Hocking, M. Shafiei, Photoactive semiconducting metal oxides: Hydrogen gas sensing mechanisms, *International Journal of Hydrogen Energy*, (2022); doi:10.1016.

[5] S.W. Fan, A.K. Srivastava, V.P. Dravid, UV-activated room-temperature gas sensing mechanism of polycrystalline ZnO, *Applied Physics Letters*, 95, 142106 (2009): doi.10.1063/1.3243458.

DOI 10.5162/SMSI2023/P72

Angular Shift Compensation in Thermoformed Curved Thin-Film Interference Optical Filters

Hooman Banaei[1], Justin Boga[1], Bjoern Goetze[2], Johannes Kunsch[2]
[1] Everix Inc., 1468 N Goldenrod Rd, Suite 200, Orlando, FL 32807, USA
[2] Laser Components Germany GmbH, Werner-von-Siemens-Str. 15, 82140 Olching, Germany
hooman@everix.co

Summary:
Optical interference filters have an inherent blue shift at increasing angles of incidence (AOI). This angular shift leads to undesired constrains in optical sensor design. Curved filters can compensate such an angular shift considerably, enabling sensor designers to tighten the bandpass filter's bandwidth and improve SNR without compromising the field of view. This becomes possible since the optical filters are manufactured like optical fibers, i.e. fundamentally different from conventional material deposition. Work is under progress and results will be presented post-deadline.

Keywords: Optical Filters, Angular Shift Compensation, Thin-Film Filters, PMMA, Curved Dielectric Filters

Introduction

We did run into this subject since we developed a new technology for making optical bandpass filters for consumer type applications [1]. Later on, it turned out that this technology allows for dielectric optical filters that are within ballpark of conventionally manufactured filters but have the advantage of freeform. So, we took a closer look into industrial applications and traditional constrains.
Optical interference filters feature an inherent blue shift of bandgap and spectrum at increasing angles of incidence (AOI). This angular shift leads to undesired constrains in optical sensor design. For instance, a bandpass filter utilized to suppress ambient noise in a range finder or face/gesture recognition sensor should ideally be as narrow as the bandwidth of the laser source used. However, to accommodate for the significant angular shift in the optical filter transmission curve, sensor designers have to broaden the bandwidth of such a bandpass filter. This results in undesired ambient noise that reduces the sensor's Signal-to-Noise Ratio (SNR).
Sketches of the thermal drawing principle and associated equipment are given in Fig. 1 and Fig. 2. Acrylic/PMMA based materials are used and a typical optical bandpass does consist of 800-1300 layers. The thermal drift is appr. 0.1 nm/K.

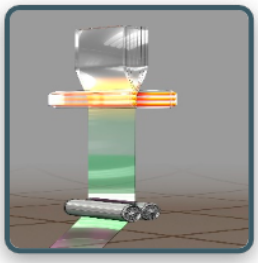

Fig.1 Dielectric optical interference filters are manufactured like optical fibers

Fig.2 Equipment for thermal drawing of optical filters

In this report, we demonstrate that 2- and 3-dimensionally curved filters can considerably compensate such an angular shift, enabling sensor designers to tighten the bandpass filter's bandwidth and improve SNR without compromising the field of view.

Description of the New Method or System

The thermal drawing technology provides the freedom of freeform filters. So, the basic idea is simple and illustrated in Fig.3: In order to avoid angular shift at angles of incidence under 45° the filter is shaped such, that the light enters this direction perpendicular.

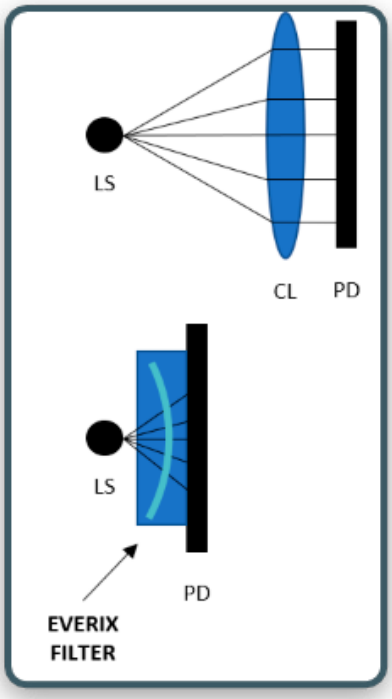

Fig.3 Basic sketch for angular correction by freeform filters in front of a photodetector.

Basically, this could also be achieved with conventional coating processes. However, in this case keeping film thickness independent of position becomes a challenge. Therefore, usually sub-complex designs are manufactured on curved substrates whereas the thermal drawing approach allows for more complex designs on curved substrates.

Results

Complex planar designs of thin film Single- and Multi-Notch Filters with typical FWHM of 5-8 % of the center wavelength and OD6 attenuation as well as bandpass filters with 5-100 nm FWHM have already been successfully implemented. Angular shift compensated filters are under work and results will be presented at the poster.

References

[1] H. E. Banaei, C.R. Nelson, Eyewear Article with Interference Filter, patent WO 2017/180828 A1, International Publication Date 19 October 2017

Collaborating Institutions and Organizations

- AHMT - German Working Group of Professors in Measurement Technology
- AISEM - Italian Association of Sensors and Microsystems (Italy)
- BAM - Federal Institute for Materials Research and Testing (Germany)
- BIPM - Bureau International de Poids and Mesures (France)
- CETIIAT - Centre Technique des Industries Aèrauliques et Thermiques (France)
- COOMET - Euro-Asian Cooperation of National Metrological Institutions
- EURAMET - The European Association of National Metrology Institutes
- METAS - Federal Institute of Metrology (Switzerland)
- GMA - Society for Measurement and Automatic Control (Germany)
- IMEKO - International Measurement Federation (Hungary)
- INTI - Instituto Nacional de Teconología Industrial (Argentina)
- Italian National Agency for New Technologies, Energy and Sustainable Economic Development (Italy)
- MSC - Measurement Science Conference (USA)
- NCSLI - National Conference of Standard Laboratories International (USA)
- NIST - National Instititute of Standards and Technology (USA)
- OVP - Österreichischer Verband für Elektrotechnik (Austria)
- PTB - Physikalisch-Technische Bundesanstalt (Germany)
- RISE - The Swedish Research Institute (Sweden)

Supporting Institutions and Publishing Partners:

AHMT

AMA Association for Sensors + Measurement

PTB Physikalisch-Technische Bundesanstalt Braunschweig und Berlin

BAM

DKD

eurolab

VDE

VDI

Journal of Sensors and Sensor Systems

OVE Österreichischer Verband für Elektrotechnik

AISEM